Design and Optimization of Turbomachinery for Thermodynamic Cycles Utilizing Low-Temperature Heat Sources

PhD Thesis

$$(EIv'')''=q-\rho A\ddot{v}$$

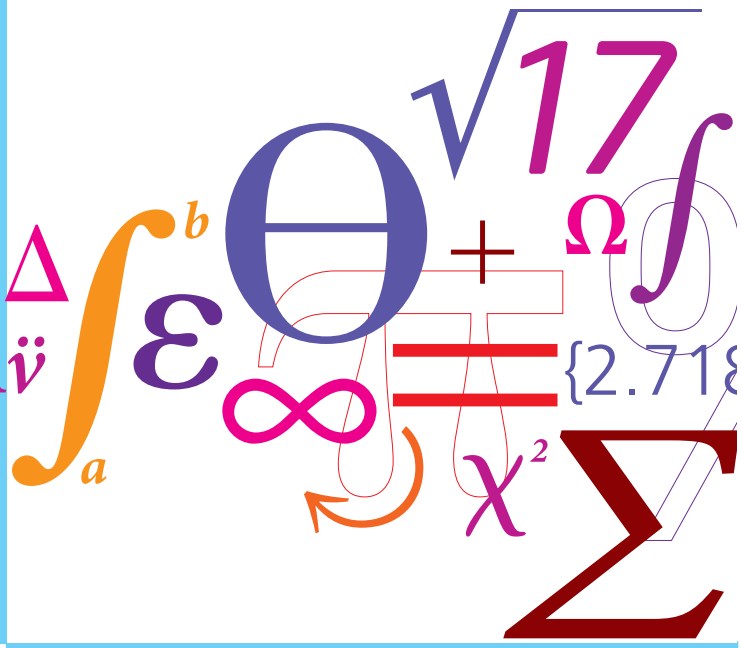

Andrea Meroni
DCAMM Special Report No. S251
May 2018

DTU Mechanical Engineering
Department of Mechanical Engineering

Design and Optimization of Turbomachinery for Thermodynamic Cycles Utilizing Low-Temperature Heat Sources

Ph.D. Thesis
submitted the 31st of May 2018
and defended the 23rd of November 2018
at the
TECHNICAL UNIVERSITY OF DENMARK

for the degree of Doctor of Philosophy

by
Andrea Meroni

under suggestion of:
Associate Professor Fredrik Haglind (DTU), main supervisor
Associate Professor Brian Elmegaard (DTU), co-supervisor
Associate Professor Giacomo Bruno Azzurro Persico (Politecnico di Milano), co-supervisor

and under the recommendation of:
Associate Professor Marvin Mikael Rokni (DTU)
Associate Professor Andrea Lazzaretto (University of Padova)
Professor Abdulnaser Ibrahim Sayma (City University London)

Design and Optimization of Turbomachinery for Thermodynamic Cycles Utilizing Low-Temperature Heat Sources

Copyright ©2018 by Andrea Meroni. All rights reserved.

Ph.D. Thesis
DCAMM Special Report no. S251
Printed by STEP
Font: Utopia typeset with LaTeX 2ε

DTU Mechanical Engineering
Section of Thermal Energy
Technical University of Denmark

Nils Koppels Allé, Bld. 403
DK-2800 Kongens Lyngby
Denmark
Phone: (+45) 4525 4319
Fax: (+45) 4525 1961
andmer@mek.dtu.dk
www.mek.dtu.dk
ISBN: 978-87-7475-541-8

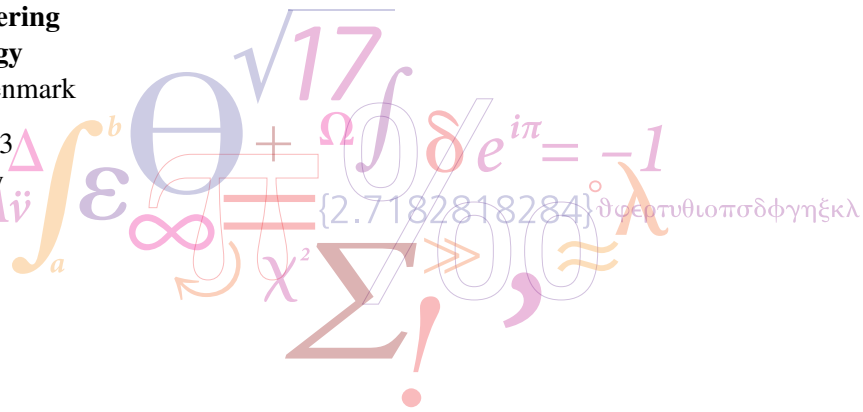

If you can't be a highway, just be a trail.
If you can't be the sun, be a star,
for it isn't by size that you win or you fail,
be the best of whatever you are.

— Martin Luther King

Preface

The present thesis was prepared at the Section of Thermal Energy, Department of Mechanical Engineering, Technical University of Denmark (DTU). It is submitted as partial fulfillment of the requirements for the degree of Doctor of Philosophy and is written as a monograph.

The work was conducted during more than three years, from December 2014 to May 2018, under the supervision of Associate Professor Fredrik Haglind (DTU) and co-supervision of Associate Professor Brian Elmegaard (DTU) and Giacomo Persico (Politecnico di Milano).

An external research stay was undertaken at the Department of Mechanical Engineering, Imperial College London (London, UK), under the supervision of Professor Ricardo Martinez-Botas, from June 2017 to October 2017.

The Ph.D. project was funded within the frame of the THERMCYC project ("Advanced thermodynamic cycles utilizing low-temperature heat sources"; project ID: 1305-00036B, see http://www.thermcyc.mek.dtu.dk/) by Innovations Fund Denmark, The Danish Council for Strategic Research in Sustainable Energy and Environment. Financial support was also received from the Otto Mønsted A/S Fond in the frame of ASME Turbo Expo 2016 conference.

Copenhagen, May 2018 Andrea Meroni.

Acknowledgments

In the first place, I would like to thank my supervisor, Prof. Fredrik Haglind, who gave me the opportunity to work on this project and provided guidance and support throughout this three-year experience. I would also like to thank all the people I worked with during these three years and in particular my colleagues at DTU, my co-supervisors Prof. Brian Elmegaard and Prof. Giacomo Persico, and the people at Imperial College London who all contributed to an inspiring, enriching and friendly atmosphere at work. My ultimate words of gratitude go to my family, who has always supported me in many ways from afar, and to my friends, the close and the distant ones.

Abstract

Organic Rankine cycle power systems and heat pump systems are considered as attractive technologies for the exploitation of excess heat into electricity and useful heat. However, the major barriers to the development of mass-produced low-temperature thermodynamic cycles are cost and efficiency. Expanders and compressors for organic Rankine cycle power systems and heat pumps are key components regarding cost and performance, and the use of reliable and accurate numerical models for these machines is currently regarded as one of the major challenges in the field.
This Ph.D. thesis investigates three turbomachinery technologies: axial and radial turbines for organic Rankine cycle power systems, and centrifugal compressors for heat pump systems. This work has two main objectives. The first one is to develop suitable mean-line models for the preliminary design and performance prediction of such machines. The second objective is to develop and apply design optimization methodologies which allow combining the machine and the cycle designs to identify suitable solutions from the performance and technical viewpoints.
First, a mean-line model for the preliminary design of axial-flow turbines is developed for single and multistage configurations operating with organic fluids. The model is validated against single-stage and multistage turbine test cases, two of which employ organic working fluids. A methodology for the combined design optimization of both the turbine and the organic Rankine cycle system is developed and applied to two case studies representative of key applications in the Danish sector. The results suggest that the methodology allows considering the trade-offs regarding cycle and turbine criteria, achieving more accurate results compared to the design of the system alone, and avoiding infeasible solutions in the preliminary design step.
Second, a mean-line model for the preliminary design and performance of single-stage radial-inflow turbines operating at high-pressure ratio conditions is developed. The model is calibrated with the data of six turbines operating at high-pressure ratio conditions from the literature and is validated with two additional turbines test cases, one of which employs an organic fluid. The calibration of the turbine, performed with an optimization process, allows a significant reduction in the deviation with the experimental data for both the isentropic efficiency and the mass flow rate.
Finally, a mean-line model for the preliminary design and performance estimation of centrifugal compressors is developed. The model is validated with five test cases from the open literature employing three different working fluids and is coupled to that of a heat pump system. The combined model is then optimized to design of a high-temperature heat pump system. The combined optimization methodology allows achieving more accurate results and identifying suitable solutions regarding preliminary design and performance.

Resumé

Organic Rankine cycle kraftprocesser og varmepumpesystemer betragtes som attraktive teknologier i forbindelse med udnyttelse af overskudsvarme til produktion af elektricitet og nyttig varme. De største barrierer for udvikling af masseproducerede lav-temperatur termodynamiske processer er høje omkostninger og lav effektivitet. Ekspansionsmaskiner og kompressorer til hhv. organic Rankine cycle kraftprocesser og varmepumper har en væsentlig indflydelse på systemernes omkostninger og ydeevne, og udviklingen af pålidelige og nøjagtige numeriske modeller for disse komponenter betragtes som en af de største udfordringer indenfor dette forskningsområde.
Denne ph.d.-afhandling undersøger tre turbomaskine-teknologier: aksiale og radiale turbiner til organic Rankine cycle krafprocesser, og centrifugalkompressorer til varmepumpesystemer. Dette arbejde har to centrale målsætninger. Det første er, at udvikle en egnet én-dimensionel model til indledende design og estimering af virkningsgrad for sådanne maskiner. Den anden målsætninger er, at udvikle og anvende designoptimeringsmetoder som gør det muligt at kombinere designprocessen for hhv. ekspansions- og kompressionsmaskiner med designprocessen for den termodynamiske proces, og dermed identificere egnede tekniske løsninger, som gør det muligt at opnå høj ydeevne.
Som det første, er en én-dimensionel model til fastlægning af det indledende design af aksialturbiner i ét- eller flertrinskonfigurationer til ekspansion af organiske arbejdsmedier blevet udviklet. Modellen er valideret mod eksperimentel testdata for ét- og flertrinsturbiner. To af testturbinerne var designet til og testet med organiske arbejdsmedier. En metode til kombineret optimering af turbine- og procesdesign for organic Rankine cycle kraftprocesser er udviklet og anvendt til applikationer som er relevante for dansk industri. Resultaterne antyder at designmetoden muliggør afvejninger vedrørende kraftproces- og turbinekriterier, hvorved der opnås mere præcise resultater i forhold til hvis designprocesserne er separerede. Derudover sikres det, at kraftprocessens design resulterer i randbetingelser som muliggør et fornuftigt turbinedesign.
Efter dette er en én-dimensionel model til fastlægning af indledende design og estimering af ydeevne for en ét-trinsturbine med radial indstrømning til drift ved høje trykforhold blevet udviklet. Modellen er kalibreret med data fra den videnskabelige litteratur fra seks turbiner som opererer ved høje trykforhold, og er yderligere valideret med to testturbiner, hvoraf den ene benytter en organisk væske. Ved at benytte en optimeringsalgoritme til at kalibrere inputparametrene til turbinemodellen, lykkedes det at reducere afvigelserne mellem de eksperimentelle data og de estimerede værdier fra modellen væsentligt.
Til slut er en én-dimensionel model til at fastlægge det indledende design og estimere ydeevnen for en centrifugalkompressorer udviklet. Modellen er valideret med eksperimentel data fra den videnskabelige litteratur fra fem testopstillinger for kompressorer i varmepumpesystemer som inkluderer brugen af tre forskellige arbejdsmedier. Kompressormodellen er efterfølgende sat sammen med en procesmodel for en varmepumpe, og den kombinerede model er benyttet til at optimere designet af en høj-temperatur varmepumpe. Den kombinerede optimeringsmetode gør det muligt at identificere egnede designløsninger for kompressor og varmepumper og at estimere ydeevnen for systemet med

høj præcision.

Papers and Presentations

Part of the work performed during the Ph.D. project resulted in peer-reviewed publications, which are listed hereafter. They are directly related to the main topics of this thesis.

Peer Reviewed Journal Publications

[P1] **Andrea Meroni**, Angelo La Seta, Jesper Graa Andreasen, Leonardo Pierobon, Giacomo Persico, and Fredrik Haglind. Combined Turbine and Cycle Optimization for Organic Rankine Cycle Power Systems — Part A: Turbine Model. Energies, Vol. 9, Issue 5, Number 313, p.1-15, 2016.

[P2] **Andrea Meroni**, Jesper Graa Andreasen, Giacomo Persico, and Fredrik Haglind. Optimization of organic Rankine cycle power systems considering multistage axial turbine design. Applied Energy, Vol. 209, p.339–354, 2018.

[P3] **Andrea Meroni**, Miles Robertson, Ricardo Martinez-Botas, and Fredrik Haglind. A methodology for the preliminary design and performance prediction of high-pressure ratio radial-inflow turbines. 2018. Energy, Vol. 164, p.1062–1078, 2018.

[P4] **Andrea Meroni**, Benjamin Zühlsdorf, Brian Elmegaard, and Fredrik Haglind. Design of centrifugal compressors for heat pump systems. Applied Energy, Vol. 232, p.139–156, 2018.

Peer Reviewed Conference Publications

[C1] **Andrea Meroni**, Jesper Graa Andreasen, Leonardo Pierobon, and Fredrik Haglind. Optimization of Cycle and Expander Design of an Organic Rankine Cycle Unit using Multi-component Working Fluids. ASME Turbo Expo 2016: Turbomachinery Technical Conference and Exposition, June 13-17 2016, Seoul, South Korea, p. 1–12.

Contents

Preface iv

Acknowledgements v

Abstract (English/Dansk) vii

Papers and Presentations xi

Contents xiv

Nomenclature xiv

1 Introduction 1
- 1.1 Background and motivation . . . 1
- 1.2 Literature review . . . 4
  - 1.2.1 Expanders for ORC systems . . . 4
  - 1.2.2 ORC axial-flow turbine modeling . . . 8
  - 1.2.3 ORC radial-inflow turbine modeling . . . 10
  - 1.2.4 Other aspects in ORC turbine modeling . . . 12
  - 1.2.5 Compressors for HP systems . . . 12
  - 1.2.6 Centrifugal compressors modeling for HP applications . . . 15
- 1.3 Objectives and methods . . . 16
- 1.4 Thesis structure . . . 18

2 Axial-flow turbines for ORC power systems 19
- 2.1 Introduction . . . 19
- 2.2 Methods . . . 20
  - 2.2.1 Design model for single-stage turbines . . . 21
  - 2.2.2 Design model for multistage turbines . . . 25
  - 2.2.3 Preliminary working fluid selection . . . 26
  - 2.2.4 Selection of the number of stages . . . 27
  - 2.2.5 Validation method . . . 28
  - 2.2.6 Sensitivity analysis . . . 30
  - 2.2.7 Optimization method . . . 31
  - 2.2.8 Case studies . . . 33
- 2.3 Results . . . 36
  - 2.3.1 Validation of single-stage turbine model . . . 36

2.3.2 Sensitivity analysis . . . 40
2.3.3 Validation of multistage turbine model . . . 42
2.3.4 Optimization of single-stage turbines . . . 45
2.3.5 Optimization of multistage turbines . . . 52
2.3.6 Cycle-turbine performance index . . . 54
2.4 Discussion . . . 57
2.5 Conclusion . . . 61

3 Radial-inflow turbines for ORC power systems 63
3.1 Introduction . . . 63
3.2 Methods . . . 64
3.2.1 Performance prediction methodology . . . 64
3.2.2 Empirical models for losses and flow deviation . . . 70
3.2.3 Sensitivity analysis . . . 72
3.2.4 Calibration method . . . 73
3.2.5 Validation method . . . 74
3.3 Results . . . 75
3.3.1 Sensitivity analysis . . . 75
3.3.2 Calibration . . . 75
3.3.3 Validation . . . 80
3.4 Discussion . . . 81
3.5 Conclusions . . . 82

4 Centrifugal compressors for heat pump systems 84
4.1 Introduction . . . 84
4.2 Methods . . . 85
4.2.1 Design model . . . 86
4.2.2 Off-design model . . . 90
4.2.3 Empirical models for losses and flow deviation . . . 91
4.2.4 Validation . . . 91
4.2.5 Case study and cycle modeling . . . 94
4.2.6 Design optimization methodology . . . 95
4.3 Results . . . 97
4.3.1 Validation . . . 97
4.3.2 Compressor design optimization . . . 100
4.4 Discussion . . . 102
4.5 Conclusion . . . 106

5 Conclusions 107
5.1 Summary of findings . . . 107
5.1.1 ORC axial-flow turbines . . . 107
5.1.2 ORC radial-inflow turbines . . . 109
5.1.3 Centrifugal compressors for HP systems . . . 109
5.2 Recommendations for future work . . . 110

Bibliography 111

A Axial turbine model **136**
A.1 Loss correlations . . . 136
A.1.1 Group 1 losses . . . 137
A.1.2 Group 2 losses . . . 140
A.2 Flow deviation correlations . . . 143
A.3 Blockage factor correlations . . . 144
A.4 Preliminary design formulas . . . 144
A.5 Validation data . . . 146

B Radial-inflow turbine model **148**
B.1 Loss correlations . . . 148
B.1.1 Nozzle . . . 148
B.1.2 Interspace . . . 149
B.1.3 Rotor . . . 149
B.2 Validation data . . . 151

C Centrifugal compressor model **153**
C.1 Loss correlations . . . 153
C.1.1 Impeller . . . 153
C.1.2 Diffuser . . . 155
C.2 Flow deviation correlations . . . 156
C.3 Preliminary design correlations . . . 156
C.4 Validation data . . . 157

D Articles **160**

List of Figures **243**

List of Tables **245**

Nomenclature

Abbreviation and acronyms

CC	Centrifugal Compressor
CFD	Computational Fluid Dynamics
GWP	Global Warming Potential
HP	Heat Pump
HPR	High-Pressure Ratio
HTHP	High-Temperature Heat Pump
ODP	Ozone Depletion Potential
ORC	Organic Rankine Cycle
RIT	Radial-Inflow Turbine
VD	Vaned Diffuser

Symbols

A	Cross-sectional area	[m^2]
AR	Vaned diffuser area ratio	[-]
AS	Vaned diffuser aspect ratio	[-]
b	Blade width, blade backbone length	[m]
BF	Blockage factor	[-]
c	Axial chord (axial turbine), chord (radial turbine)	[m]
C	Absolute velocity, cost	[m/s], [€]
C_f	Diffuser friction factor	[-]
C_0	Spouting velocity	[m/s]
COP	Coefficient of performance	[-]
CP	Diffuser pressure recovery coefficient	[-]
D	Diameter	[m]
D_f	Blade diffusion factor	[-]
D_H	Hydraulic diameter	[m]
e	Blade rear surface suction curvature	[m]
$\dot{m}$	Mass flow rate	[kg/s]
h	Specific enthalpy, blade height	[J/kg],[m]
h^*	Ratio of Rotor inlet to nozzle outlet blade height	[-]
Δh	Enthalpy drop	[J/kg]
I	Rothalpy	[J/kg]
k	Specific heat ratio	[-]
k_s	Blade surface roughness	[m]
K	Total pressure loss coefficient	[-]
K_a, K_r, K_{ar}	Coefficients in Eq. B.11	[-]
K_{p1}, K_{p2}, K_{p3}, K_{vs}, K_{inc}	Calibration coefficients	[-]
L_b	Blade length	[m]

L_z	Rotor axial length	[m]
L_H	Hydraulic length	[m]
LR	Ratio of splitter blades length over full blades length	[-]
M	Mach number	[-]
N	Rotational speed	[rpm]
N_{st}	Number of turbine stages	[-]
o	Blade throat/opening	[m]
p	Static pressure	[Pa]
P	Power	[W]
PI	Performance Index	[kW/€]
PR	Pressure ratio	[-]
$\dot{Q}$	Heat flow rate	[W]
r	Radius	[m]
R^*	Rotor to nozzle mean radius ratio	[-]
Re	Reynolds number	[-]
RRMSE	Relative Root Mean Square Error	[-]
s	Specific entropy	[J/(kgK)]
SP	Size Parameter	[m]
ss	Nozzle to rotor axial clearance	[m]
t	Trailing edge thickness	[m]
t_{cl}	Blade tip clearance	[m]
T	Temperature	[K]
U	Peripheral velocity	[m/s]
$\dot{V}_{comp,in}$	Compressor inlet volume flow rate	[m^3/s]
VFR	Volume flow rate ratio	[-]
W	Relative velocity	[m/s]
W_b	Blade work	[J/kg]
Z	Number of blades	[-]
Greek letters		
α	Absolute flow angle from the meridional direction	[°]
α_{FL}	Flaring angle	[°]
β	Relative flow angle from the meridional direction	[°]
γ	Nozzle wedge included angle	[°]
ε	Degree of admission, residual error	[-]
ε_w	Wake fraction at impeller exit	[-]
ζ	Kinetic energy loss coefficient	[-]
η	Efficiency	[-]
θ	Nozzle center angle	[°]
ρ	Density	[kg/m^3]

σ	Impeller slip factor	[-]
ϕ	Flow coefficient	[-]
χ	Stage degree of reaction, secondary flow mass fraction	[-]
ψ	Stage loading coefficient	[-]

Subscripts

0	Total, inducer inlet
1	Impeller or stage inlet
2	Nozzle exit (axial turbine), nozzle throat (radial turbine), impeller exit (centrifugal compressor)
21	Nozzle outlet (axial turbine)
3	Rotor exit (axial turbine), nozzle exit (radial turbine), vaneless diffuser exit (centrifugal compressor)
4	Rotor inlet (radial turbine), vaned diffuser throat (centrifugal compressor)
5	Rotor throat (radial turbine), vaned diffuser exit (centrifugal compressor)
6	Stage exit (radial turbine and centrifugal compressor)
a	Axial
b, bl	Blade
c, cl	Clearance
ch	Choking
el	Electric
ex	Exit
gear	Gearbox
gen	Generator
h	Hub
id	Ideal
imp	Impeller
inc	Incidence
ind	Inducer
is	Isentropic
m	Meridional, mean
min	Minimum
mix	Mixing
n,noz	Nozzle
p	Pump
pe	Post-expansion
pl	Passage
pp	Pinch point
o	Outlet
opt	Optimal
rel	Relative

r	Radial direction
rc	Recirculation
rel	Relative
rot	Rotor
s	Shroud
sc	Scavenge air
sf	Skin friction
st	Stage
t	Trailing edge, tangential, turbine
turb	Turbogenerator
th	Throat
tot	Total
ts	Total-to-static
tt	Total-to-total
vd	Vaned diffuser
vs	Interspace
wf	Working fluid

1 Introduction

This chapter delineates the background and motivation of this Ph.D. thesis. It provides an outlook on the significance of the topic and indicates possible ways for improving the design of turbomachinery for thermodynamic cycles utilizing low-temperature heat sources. A literature review draws the state of the art of expanders and compressors and indicates the main focus of this work. The end of this chapter outlines the objectives and methods of this thesis.

1.1 Background and motivation

The International Energy Agency [1] indicates that 81.4 % of world total primary energy supply depends on fossil fuels. The European Union redefined the roadmap for 2050 at the Paris climate conference in 2015 [2], with the aim to develop more climate-friendly and less energy-consuming economy. The new goals call for an 80 % reduction of greenhouse gas emissions by 2050 to below 1990 levels. Cost-efficient solutions need to be devised to make the low-carbon transition feasible and affordable. The Energy roadmap [1] envisaged an increasing share of renewable energy and more efficient use of energy.

Different measures can be adopted to increase the efficiency of current energy systems. The use of excess heat from industrial applications was regarded as an important way to decrease the energy demand, the CO_2 emissions as well as to achieve economic gains and improved energy efficiency [3]. Excess heat can be used for internal applications or can be recovered for power or heat generation. In this context, the literature indicates that there is a large unexploited waste heat potential. For example, in Denmark the total potential for heat recovery was estimated to be around 212 PJ per year, considering all end-users and utility companies [4]. This amount corresponds to 13 % of the net energy input for end users and producers. The two largest areas having the highest waste heat potential were identified in the transport and utility sectors. Two major energy sources that can be exploited were also identified. The first one is in the cooling/refrigeration, condensate and various industrial processes with heat source temperature below 60 °C, and the second is in the form of exhaust gas from various combustion and heating processes (with temperature in the range 120 °C to 400 °C). Heat recovery opportunities were also identified in UK industry [5]. The overall surplus heat was estimated as 52 PJ per year considering relevant UK industrial sites. The two major sources for heat recovery were at a temperature level below 100 °C for reuse on-site, and

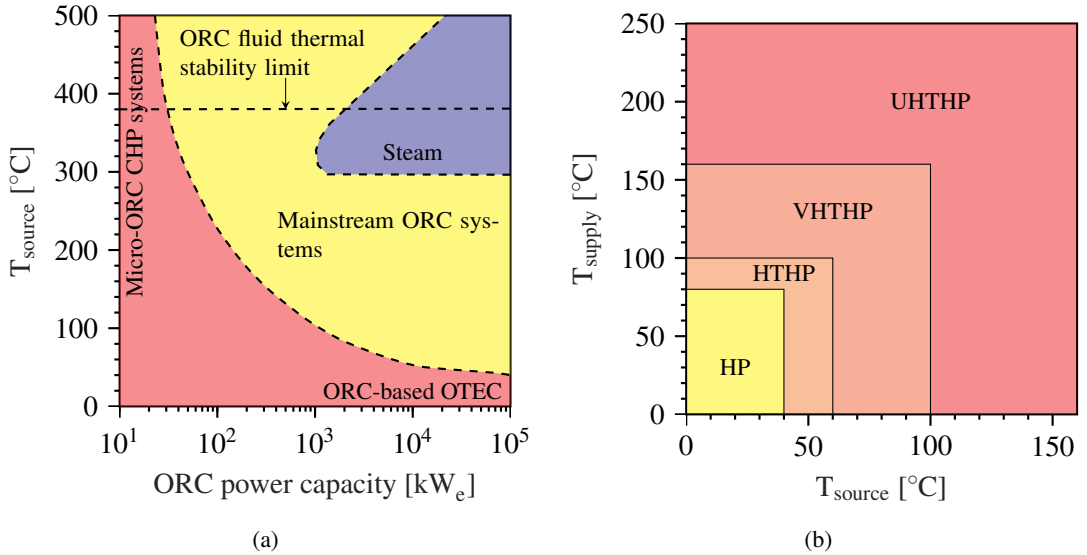

Figure 1.1: Current working domain of ORC and HP systems: (a) ORC domain based on system power capacity and heat source temperature (adapted from [6, 7]); (b) HP domain in terms of source and supply temperatures (adapted from [8, 9]).

the conversion of heat at a higher temperature level (in the range 200 °C to 1200 °C) into electricity.

Among the possible heat recovery technologies, thermodynamic cycles for power and heat generation utilizing low-temperature heat sources are regarded as the most viable and attractive solutions. Organic Rankine cycle (ORC) power systems are considered to be the "unrivalled technical solution for generating electricity from low-medium temperature heat sources of limited capacity" [10]. By applying the ORC technology to energy-intensive industrial processes in 27 EU countries, it was estimated to recover up to 72000 PJ of waste heat and to save 7.6 M ton of CO_2 [11]. Although the ORC power system has been a well-known technology for decades, the ORC market has experienced a rapid growth only since the early 2000s [12]. The success of ORC power systems is attributed to their inherent flexibility and their relatively high conversion efficiency for low temperatures and power outputs. The boundaries for the application of ORCs are changing over the years, and are expanding towards pioneering temperatures and power capacities [6, 10]. Figure 1.1(a) shows the current outlook for ORC applications. At high heat source temperatures and power capacities, ORCs are limited by the working fluid thermal stability limit and the competitiveness of steam Rankine cycles. On the other hand, at low temperatures and power capacities the ORC technology is limited by the inherently low values of efficiency and the high cost of the system and its components, hence resulting in an economically unattractive solution. The ORC field is still considered a niche market [13], and current research efforts are devoted to extending its application by developing ORC units suitable for high-volume production [6]. The expander is arguably the key component in an ORC, having unique features which require a dedicated design approach. In this respect, it is widely acknowledged that the design of a cost-competitive, technically sound and efficient expander plays a crucial role in the successful design of the system [14]. As a matter of facts, the expander cost usually represents between approximately 15 % and 70 % [12, 15–18] of the total cost of an ORC unit depending on the application, heat source temperature level, and

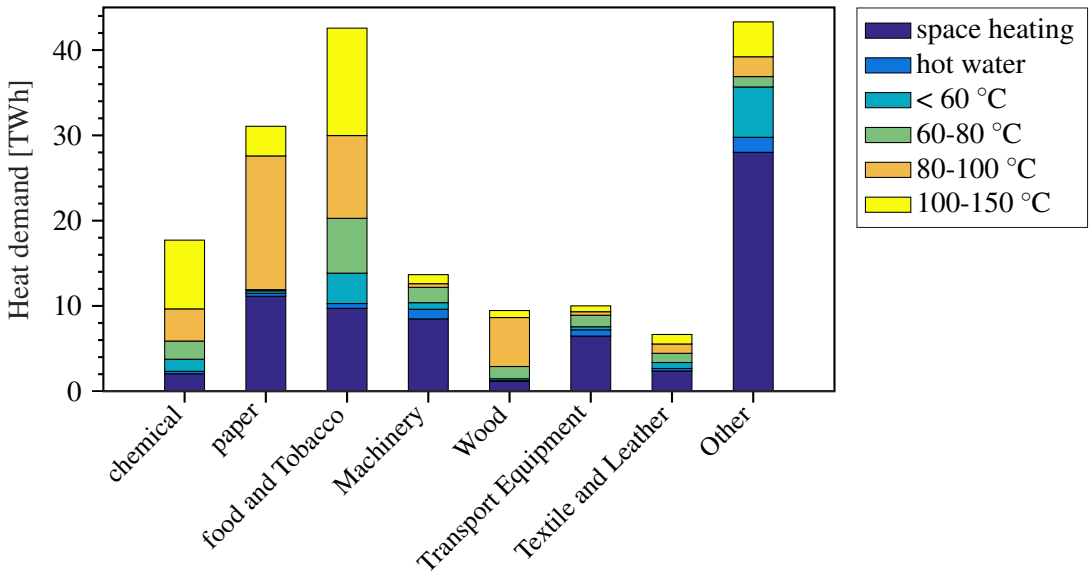

Figure 1.2: Heat demand by industrial sector in 33 European countries. Adapted from Ref. [21].

power capacity. Concurrently, it is important that the expander is efficient to increase the ORC net power output, reduce the payback time of the investment, and reduce the emissions of pollutants in systems running on fossil fuels. From a practical point of view, it is also important that the expander is technically simple, reliable and easily manufacturable.

At the same time, heat pump (HP) systems are now an established solution for the heat generation utilizing low-temperature heat sources. Heat pumps are used to upgrade waste heat at low temperature to high-temperature heat, which is more usable for domestic and industrial applications. A final energy conservation potential of 1717 PJ has been estimated for the application of the HP technology to the EU-28 industrial sector [19]. Numerous research efforts have been devoted to the development of HP units operating below 80 °C, and market solutions have been developed over the years [20]. However, there is an increasing demand for heat supplied at a higher temperature, depending on the specific industrial application. Figure 1.2 shows the heat demand in 33 European countries. Many industrial sectors require a large amount of heat supplied at values of temperature in the range 80 °C to 150 °C, which calls for the development of high-temperature heat pump (HTHP) systems or even very high-temperature heat pump (VHTHP) systems. Figure 1.1(b) shows the working domain of the current and future generation of heat pumps. High-temperature heat pumps are in the precommercial or market introduction phase while VHTHPs and ultra-high-temperature heat pump (UHTHP) systems are still in the research stage [9]. The lack of installed HP units delivering more than 90 °C is associated with a lack of cost-efficient solutions [22] and to technical challenges mainly related to the compressor technology [23]. From the thermodynamic viewpoint, the compressor is regarded as the component with the highest irreversible losses in the cycle [24]. From the technical perspective, the use of conventional compressor technologies for HTHPs is constrained by high discharge temperature and pressure, and cooling, lubrication and material compatibility issues [24–27] . For these reasons, the research is now focusing on the development of cost-competitive compressor solutions which can deliver high-temperature heat.

In light of the previous considerations, this Ph.D. thesis aims at investigating the possibilities for developing methodologies to improve the design of expanders and compressors for ORCs and HPs. The ultimate goal of the investigation is to promote the development of the next generation of ORCs and HPs in future energy systems.

1.2 Literature review

This section reviews state of the art for expanders and compressors in ORC and HP systems, respectively. The literature review serves to select some relevant technologies, which will be the main focus of the investigations in this thesis, and to indicate the major challenges and research directions concerning the selected technologies.

1.2.1 Expanders for ORC systems

Organic Rankine cycle power systems are used in a wide range of applications such as the exploitation of geothermal heat, solar energy, biomass, and heat recovery. Due to the wide operational range in which these systems need to operate, many different cycle configurations are adopted and, historically, many different expander types have been developed. Expanders can be divided into two categories: turboexpanders (also called turbines) and volumetric expanders (also called positive displacement devices). The reader is referred to Ref. [10] for a comprehensive overview of the different technologies.

A turbine stage usually consists of a static row of blades, namely the nozzle or stator, and of a rotating blade row, namely the rotor, see Figure 1.3. The scope of the nozzle vanes is to convert the fluid's enthalpy available at the turbine inlet into kinetic energy and to guide the flow to achieve optimal flow conditions for maximum work extraction in the rotor. Inside the rotor, the fluid expands and exchanges momentum with the blades. The rotor disks are connected to the turbine shaft which produces useful mechanical work. There are three main turbine configurations used in ORC units, and they are classified based on the relative motion of the fluid with respect to the axis of rotation of the shaft: a) axial-flow, b) radial-inflow (or centripetal), c) radial-outflow (or centrifugal) turbines.

Axial-flow turbines are usually employed for large mass flow rates and low pressure ratios. They are used in the single or multistage configuration for medium-to-large power capacities, typically in the range 100 kW to 15 MW [10]. The radial-inflow turbine (RIT) technology is applied to smaller mass flow rates and higher pressure ratios. Radial-inflow turbines are used in smaller-capacity systems, where the efficiency of axial turbines is penalized by the small blade heights and the use of partial admission. In this case, RITs allow achieving a higher efficiency than the axial counterpart with a single stage, even for large expansion ratios [6]. The power capacity of RITs ranges from tens of kW to a few MW. The radial-outflow turbine (ROT) technology has been successfully introduced in the market only recently. Radial-outflow turbines are usually employed in multistage arrangement and are particularly suited for high volumetric expansion ratios since their inherent increase of passage area during the expansion promotes the reduction of the stage exit flow velocity and the associated losses. Moreover, this turbine configuration is favored by the use of prismatic blades and multiple stages on the same rotor disk. The industrial commercialization

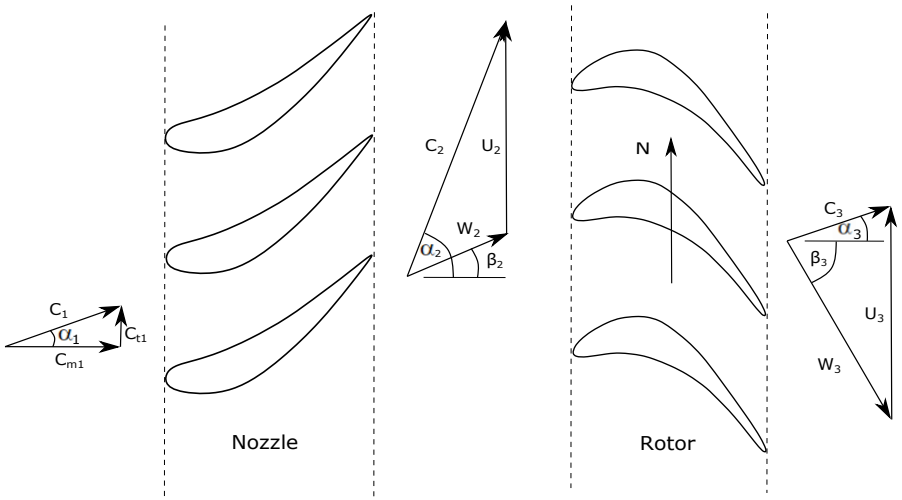

Figure 1.3: Exemplary turbine stage with nozzle, rotor and velocity triangles. See the Nomenclature for symbols.

and the research on ROTs are currently ongoing.

Volumetric expanders are employed for low-power outputs, usually below 150 kW [28]. In this range of power capacity, the turbine design is more challenging, and volumetric expanders may be a more cost-competitive solution than turbines. In a volumetric expander, the fluid is trapped in some chambers and is discharged after one working cycle. During the expansion, the pressure of the working fluid decreases due to an increase of the chamber's volume. These machines feature a stator and many rotors connected to the main shaft. Examples of positive displacement machines for ORC applications are scroll, screw, piston and rotary vane expanders. These solutions can be advantageous compared to turbines since they operate with a low rotational speed and can tolerate two-phase flows during the expansion, which would otherwise result in blade erosion issues in turbines. Compared to turbines, they can potentially be more cost-effective as they are retrofitted or derived from the refrigeration market, thus benefiting from scale economies. However, compared to turbines, the use of volumetric expanders is limited by technical challenges related to the maximum volumetric expansion ratio, the implementation of multistage configurations and the lower efficiency[6, 29].

Figure 1.4(a) provides a non-exhaustive list of the range of turbine power capacity for different ORC manufacturers and classified by expander type. ORMAT [44] is the world's leader ORC manufacturer with 62.9 % of the total installed power capacity, followed by Turboden [47] and Exergy [38], which hold around 13.4 % and 11.1 % of the total installed power capacity, respectively [12]. Figure 1.4 shows that the first three market leaders employ turbomachines: ORMAT and Turboden employ axial turbines while Exergy uses radial-outflow turbines. All three companies operate in the medium-large power output range between approximately 200-500 kW and 10-20 MW. Figure 1.5 highlights that, in the last two decades, axial turbines have dominated in the medium-large scale based on the number of installed units. All radial-outflow turbines units fall inside the medium-large scale; however, the number of installed units is much lower compared to the axial configuration. Some RIT units similar to that of ROT units have also been installed. In

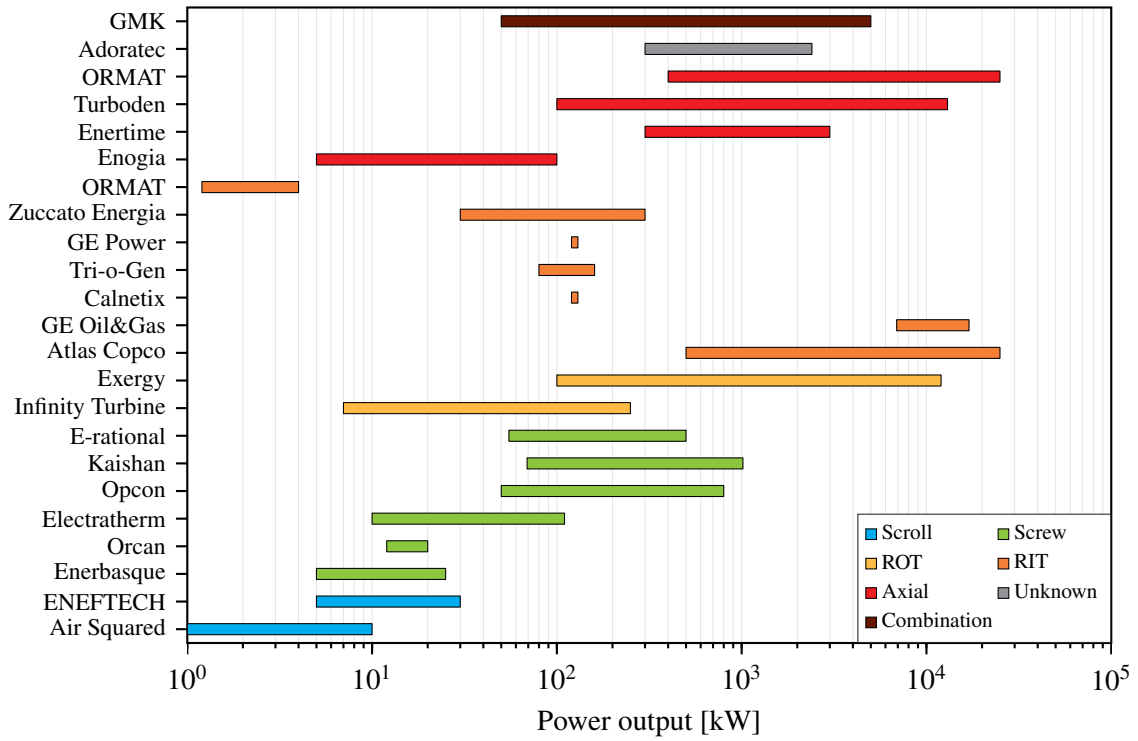

Figure 1.4: Installed ORC units by manufacturer, power output, and expander type. Data collected from the literature, see Refs. [6, 12, 13, 18] and from the company websites, see Refs. [30–49]. Companies which abandoned the development of their product line are not included. The term *unknown* indicates that the information on the expander type is not available. The term *combination* indicates that the manufacturer employs a combination of different expander technologies.

the small-power capacity, between 50 kW and 500 kW, there is an overlap of different expander technologies. Several axial turbines by Turboden have been installed in the range 100-500 kW. However, the majority of installed units are radial-inflow turbines. In this range, the companies GE Power [43], Calnetix [42], and Triogen [41] are the first three market players. Screw expanders are a competitive technology in the small-scale range of power capacity, although it was not possible to retrieve specific details on the number of installed units from the available sources in the literature. Figure 1.4(a) shows that many companies also cover applications in the mini- (50-10 kW) and micro-scale (< 10 kW). The latter is the typical power capacity range of volumetric machines such as scroll and screw expanders. It is worth noticing that a large number of installed units using turbomachines have also been installed in this range. Particularly relevant is the case of about 950 RITs manufactured by ORMAT since the early 1970s, many of which are still in operation [13, 50]. These units were powered by fossil fuels and were used for remote applications, where they delivered a power output in the range 0.2 kW to 4 kW. Presently, these numbers and considerations are only indicative since many companies did not share their specifications in the literature [12] and the information on their expander technology is unknown. There are also companies, such as GMK [49], which employ different expander types according to the application and the range of power capacity. Nevertheless, the literature highlights that the majority of commissioned expander units

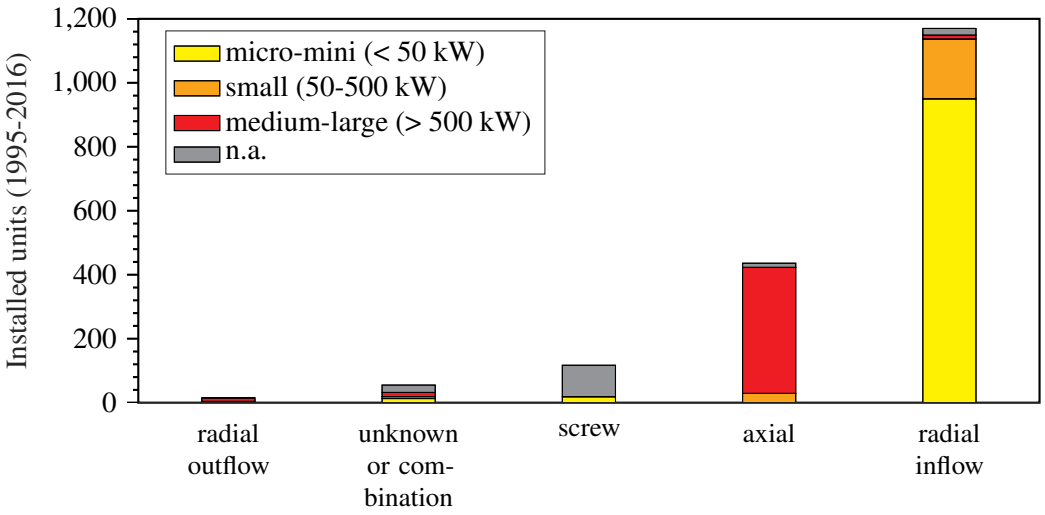

Figure 1.5: Number of installed units in the period 1995-2016. Data collected from the literature, see Refs. [6, 12, 13, 18] and from the company websites, see Refs [30–49]. The term "n.a." indicates that the data are not available.

are turboexpanders whereas volumetric machines are arguably in the precommercial or market introduction stage [6]. The axial and radial-inflow turbines were the two selected technologies for this work. The former is a well-established and mature technology for medium-large scale applications whereas the latter has been developed and applied with success in a large number of small-to-mini scale units. Hereafter, the dissertation will only refer to these two turbines.

The design and optimization of ORC systems are very challenging tasks as they require accurate and reliable models of the fluid thermodynamic properties, the cycle components and of their cost. They are regarded as the major barrier to achieving reliable results [51]. Regarding the components, the turbine design is especially challenging. The working fluid is an organic compound whose properties are very different from the steam or gases used in conventional power plants or turbochargers. The high molar mass of organic fluids makes it possible to design a turbine with a reduced number of stages compared to conventional gas and steam turbines, resulting in more compact and cost-effective solutions. On the other hand, the sound speed is reached at low values of expansion ratio, and the turbine often results in high-expansion ratios and supersonic flows which require the adoption of non-conventional design approaches [52]. The design challenge is further complicated by the non-ideal behavior of the working fluid, which demands the use of accurate real-gas equations of state.

The preliminary design is arguably the most crucial step in the whole design process of an ORC turbine [53]. Preliminary design models (also called *1D* or *mean-line models*) are employed in the first step of the design routine of an ORC turbine, before the use of more advanced techniques such as through-flow or aerodynamic analyses. The mean-line model formulation envisages the solution of balance equations of mass, energy, and momentum as well as the expressions for loss models to account for the entropy generation in the main stations of the stationary and rotating passages of the turbine. These models allow screening different turbine architectures and solutions in a relatively short time, saving computational efforts and costs in the subsequent detailed design

steps. A high-efficiency ORC turbine can be designed only if the mean-line design and analysis provide a realistic and highly-efficient solution [53]. Due to the inherent design challenges of ORC turbines, the development of a preliminary design model requires a dedicated approach which includes different aspects, see also Ref. [53]. First, a preliminary design tool for ORC turbines needs to be versatile: it should include the possibility to model any possible working fluid and to adopt a general formulation for the governing equations. Second, it needs to include proper modeling of choking and supersonic conditions in the blade rows as well as of the associated loss phenomena. Moreover, it should take into account the design of non-conventional geometries such as high-Mach number blade profiles and converging-diverging nozzles. Finally, due to the presence of real-gas phenomena, the thermo-physical properties of the working fluid are to be computed using accurate, real-gas equations of state. In order for these models to be reliable, they also need to be carefully validated and calibrated with detailed experimental data. At present, there are several aspects which hamper the development of accurate and reliable tools for the preliminary design, analysis, and optimization of ORC turbines. The most critical factor is probably the strong lack of detailed experimental and geometrical data for the validation of the numerical models. These data are not available in the open literature or are typically a confidential property of companies. The lack of data may result in unreliable numerical tools which, in turn, affect the correct evaluation of the ORC system design.

Once validated and reliable turbine models are available, the development of cost-competitive solutions can be performed by including accurate considerations on the expander design together with the ORC design process. In this way, it would be possible to 1) improve the accuracy of the cycle design, 2) avoid technically infeasible or challenging solutions, and 3) select more accurately a suitable working fluid. Compared to conventional steam or gas turbines, the possible use of different working fluids introduces an additional degree of freedom in the ORC system design. In principle, the most suitable working fluid should be selected to provide the best possible trade-off between the cycle and the components performance and technical feasibility. Many authors [54–57] highlighted that linking the thermodynamic cycle design, the expander design, and the working fluid selection is key for a successful ORC system design. At the same time, there are limited strategies in the literature to perform the ORC design accounting also for the expander design. This aspect has gained more attention only recently and is presented in more detail in the next sections.

1.2.2 ORC axial-flow turbine modeling

In the context of ORC axial-flow turbines, few mean-line models for single- and multistage turbines have been used by companies and research institutes. Some examples are AXTUR [58, 59] and zTurbo [60, 61]. These codes have been the object of intense development over the years, and their reliability has been successfully assessed by different companies [53]. However, comprehensive validation of such models has yet to be published in the literature (a partial validation of zTurbo was presented in Ref. [62]), especially including the data of an ORC turbine. As regards multistage ORC axial turbines, these are employed by different ORC companies [6]; however, the design and optimization methods for such turbines are still limited in the literature. Table 1.1 shows a collection of some ORC multistage turbines documented in the literature. In some experimental studies [63–67] the authors explained the design criteria for the ORC turbines of Table 1.1, but without presenting the details of their design and optimization methods. In other numerical studies [68–70] the authors employed Computational Fluid Dynamics (CFD) tools to analyze the flow and

Table 1.1: Documented multistage ORC axial turbines. From [72].

Author	Manufacturer	year	field	Power [kW]	N_{st}	Pressure ratio	N [rpm]	rm [mm]	fluid	Ref.
Verneau	Bertin & Cie	1977	solar	54	2	142	7700	145	*FC-75*	[66]
Osnaghi et al.	Gemmindustria	1979	solar	8	2	120	24000	90	C_6H_5Cl	[64]
Bado et al., Angelino et al., Barutti et al.	Gemmindustria	1979-1983	solar	35	4	116	6700	120	C_8F_{16}	[63, 73, 74]
Verneau	Bertin & Cie	1980	WHR	1350	2	100	14000	176	*Fluorinol 85*	[66]
Angelino et al.	Turboden	1984	WHR	100	2	24.9	3030	430	$C_6H_4Cl_2$	[65, 71]
Angelino et al.	Turboden	1984	WHR	100	2	13.64	3030	430	C_8H_{10}	[71]
Jokinen et al.	n/a	1998	WHR	25	2	>100	40000 - 48000	n/a	*toluene*	[67]
Obernberger and Hammerschmid	Turboden	2001	Biomass	400	2	n/a	n/a	n/a	*silicon oil*	[75]
Nasir et al.	Ormat Inc.	2003	WHR	4500	2	~ 30	3600	n.a.	*n-pentane*	[76]

performance of multistage ORC turbines. All the authors above [63, 64, 66–71], optimized the ORC turbine separately from the ORC system. In this respect, there is a need to publish detailed validation data and validated models for both single- and multistage ORC axial turbines in the open literature. The thorough development and validation of such models represents one of the objectives of this thesis, see Sec. 1.3.

Another key aspect of the preliminary design modeling of ORC axial turbines is the importance to account for accurate turbine design criteria in the system design process. The relation between the working fluid, the turbine, and the cycle designs was first shown in an international journal in the 1960s [54]. Nevertheless, the literature on ORC power systems is full of studies [77–83] where the details of the expander are neglected, and its performance is assumed by assigning a value in the expander isentropic efficiency. There are only limited studies, such as those by Astolfi et al. [15] and Martelli et al. [84], where the turbine performance was estimated more accurately by interpolation of a statistical correlation (developed for single-stage machines). Other studies by Da Lio et al. [85] and White and Sayma [86] performed the optimization of the cycle using performance maps previously generated with a mean-line model for single-stage axial and radial turbines, respectively. The coupling of turbine and cycle models was also proposed for single-stage radial turbines by Ventura and Rowlands [87], although using a database for the turbine performance data, and Uusitalo et al. [88], using a fixed value of turbine isentropic efficiency of 80 %. However, both works did not optimize the turbine design. Most recently, La Seta et al. [89] showed that a simple guess of turbine efficiency might provide a deviation up to 8 % in the ORC net power output if the turbine design is not properly considered. The results suggested the importance of simultaneously accounting for working fluid selection, ORC system design, and turbine design. To include all aspects, different methods have been developed in the literature, including the use of turbine efficiency correlations [90, 91] and non-dimensional design maps [58, 85, 92, 93]. Macchi and Astolfi [90] proposed recently a more advanced approach, which

includes the multistage turbine performance in the ORC system design and optimization. Using a mean-line model [94], they developed a correlation for the estimation of the isentropic turbine efficiency as a function of the size parameter and volume flow rate ratio for a different number of stages (up to three). The correlation can be used to optimize the thermodynamic cycle and evaluate the impact of the different number of stages. The approach proposed by Macchi and Astolfi [90] can be employed for ORC system optimization. At the same time, it does not yield a specific optimal solution for the selected application since the efficiency correlation assumes that the rotational speed is always optimized, the maximum number of stages is three, and the fluid is considered as an ideal gas. In addition to that, the approach above adopts the same design criteria for single and multistage turbines while other aspects such as the performance, cost, and technical criteria may introduce additional constraints in the design of the turbine, and different solutions might be preferred.

Based on the previous considerations, the second aspect of the novel contribution that is considered in this work is to design the ORC power system using a combined optimization of cycle and turbine designs. Such a methodology is applied to single- and multistage turbine layouts as well as to different case studies, and represents one of the objectives of this thesis, see Sec. 1.3.

1.2.3 ORC radial-inflow turbine modeling

Compared to axial turbines, RITs are used in applications demanding smaller mass flow rates and higher pressure ratios. Where cost and size are of primary concern, as in small-scale ORC power systems (< 500 kW), and depending on the specific application, the turbine may be designed at high-pressure ratio (HPR) conditions, usually above 3. The literature reports pressure ratios up to 100-150 [53, 66] for ORC systems exploiting moderate to high heat source temperatures. Under HPR conditions, the turbine features a high fluid-dynamic loading and the nozzle and the rotor may be close to choking or may even present supersonic flow conditions. When these phenomena occur inside the turbine, shock patterns and unsteady nozzle-rotor interaction effects may jeopardize the mechanical resistance of the blades as well as the turbine performance. The fluid operating under these conditions may not behave as a perfect gas. This situation holds especially true for organic fluids, whose expansion starts close to the saturated vapor line and often ends far from saturated conditions at the stage exit. This expansion involves a large change of the thermodynamic properties between the inlet and the outlet of the turbine, and the fluid exhibits real-gas effects. To cope with the aforementioned aspects, suitable tools need to be used already in the preliminary design and analysis of HPR radial-inflow turbines.

Choking conditions and real-gas effects were not considered in detail in the first mean line models presented in the literature since these tools were developed and calibrated based on the data of turbines operating at low-pressure ratios [129–132]. It was only in the last decade where the modeling of choking conditions and of real-gas equations [133–135] became relevant. However, only few publications included a detailed treatment and analysis of the phenomena occurring at HPR conditions, and these mostly relate to ORC applications. Some mean-line models have been developed to estimate the design efficiency of RITs for ORC applications such as those by Rahbar et al. [91], Da Lio et al. [136], and Mounier et al. [93]. These authors included the evaluation of the turbine design and efficiency at the design point only. Although choking conditions were included recently by Demierre et al. [126], the authors did not present the details of the modeling

Table 1.2: RITs designed and tested at pressure ratios above 3 from the open literature. From Ref. [95].

Author	Year	Application	Tested pressure ratio [-]	Fluid
Hiett and Johnston [96, 97]	1963	GT	1.3-5.0	Air
McLallin and Haas [98]	1980	GT	1.2-4.7	Air
Kidwell and Large [99]	1980	GT	2.0-5.0	Air
Rogo et al. [100]	1984	GT	2.0-7.0	Air
Ribaud and Mischel [101]	1986	GT	2.97-3.8	Air
Rogo [102]	1986	GT	2.0-7.0	Air
Rodgers [103]	1990	TC/GT	3.6,3.9,4.3	Air
Simonyi et al. [104]	1991	GT	3.0-5.8	Air
Pullen et al. [105]	1993	GT	1.1-4.7	Air
Huntsman et al. [106, 107]	1992, 1994	GT	$4.7^{(*)}$	Air
Jones [108]	1994	GT	1.0-9.0	Air
Spence and Artt [109]	1997	RES	1.3-4.0	Air
Atkinson [110]	1998	RES	1.3-3.7	Air
Doran et al. [111]	2001	TC	1.3-3.5	Air
Feng et al. [112]	2005	GT	1.1-3.1	Air
Spence et al. [113]	2007	TC	1.2-3.6	Air
Deng [114]	2007	RES	1.3-4.0	Air
Fu et al. [115, 116]	2012, 2015	GT	1.1-3.1	Air
Ino et al. [117]	1991	CR	7.0-12.0	Helium
Ghosh [118]	2008	CR	1.8-5.9	Air/Nitrogen
Larjola [119]	1988	ORC	$10.0^{(*)}$	R114
Van Buijtenen et al. [120]	2003	ORC	$120.5^{(*)}$	Toluene
Pei et al. [121]	2011	ORC	$7.1^{(*)}$	R123
Kang and Chung [122, 123]	2011, 2012	ORC	$4.1^{(*)}$	R245fa
Han et al. [124]	2014	ORC	$3.2^{(*)}$	R245fa
Demierre et al. [125, 126]	2014-2015	ORC	3.1-4.4	R134a
Kang [127]	2016	ORC	$4.1^{(*)}$	R245fa
Turunen-Saaresti et al. [128]	2017	ORC	$112.8^{(*)}$	MDM

GT = Gas Turbines. RES = Research. TC = Turbochargers. CR = Cryogenic systems. ORC = Organic Rankine cycles. $^{(*)}$ = documented design point only.

considering the different possible patterns which occur in the nozzle and the rotor when the turbine chokes. The most updated work in this respect is that by Baines and co-authors [97, 137–139]. Qiu and Baines [97] proposed a mean-line method to predict the performance at off-design conditions for choked and unchoked blade rows and validated the method with three test cases of HPR turbines. However, the details of the numerical strategy employed by the authors were not provided in their work as well as the detailed geometric data of the turbine test cases, which are not publicly available in the literature or are kept as confidential. To develop a reliable and accurate mean-line model, the development of a mean-line model requires validation and calibration using the experimental

data of different turbine test cases. In this respect, the literature shows a lack of comprehensive validation and calibration studies for HPR radial-inflow turbines. Glassman [140] calibrated its model using only the design point data of HPR turbines whereas Qiu and Baines used a set of loss coefficients calibrated with the data of some turbines operated at low-pressure ratio conditions [137–139], casting doubt on the actual reliability when using HPR turbines, especially under off-design conditions.

The literature review highlights the lack of suitable modeling tools for RITs in HPR applications as well as their validation. The development and validation of a RIT model for HPR conditions represent other objectives of this thesis, see Sec. 1.3.

1.2.4 Other aspects in ORC turbine modeling

There are also other important aspects regarding the improvement of the accuracy of the modeling tools for ORC turbines, and these are currently being investigated experimentally by different research institutes, in particular, Refs. [141–149]. First of all, the literature lacks empirical correlations developed for ORC turbines, casting doubt on the accuracy and suitability of mean-line numerical methods. In this respect, experimental studies need to be performed to validate the suitability of such numerical models. The second aspect that requires experimental activities is the validation of the available equations of state for the estimation of the thermo-physical properties of the working fluid. Both these aspects require dedicated experimental studies and, therefore, are outside the scope of this thesis. The parallel development of the aforementioned experimental studies and bespoke turbine design tools is key to the analysis and optimization of future ORC power systems.

1.2.5 Compressors for HP systems

As in ORC systems, the compressor technology of HPs can be categorized in turbomachines and volumetric machines. Historically, volumetric machines have been applied more extensively than turbomachines, and the preliminary selection of the most suitable compressor technology is based on two parameters: the required volume flow rate and the pressure ratio. Figure 1.6 shows the regions where each compressor technology exhibits better performance and has usually been applied. At volume flow rates lower than 200 m^3/s, positive displacement machines appear to be the preferred option. Reciprocating piston compressors in single or multistage arrangements are suited for the smallest volume flow rates and highest pressure ratios. Rotary compressors such as sliding vane, lobe and screw machines are employed for intermediate volume flow rates. At higher values, single and multistage centrifugal compressors can be used. For very high volume flow rates, multistage axial solutions can be considered. This chart provides only very approximate values, which should be used only for a rough preliminary selection. Once the technology has been selected, optimal values of rotational speed and size of the machine can be estimated with design charts such as that by Balje [151]. It is worth mentioning that both Figure 1.6 and the Balje chart [151] are based on statistical data of some compressors for conventional applications and may not be representative of the state-of-the-art technology. In this respect, a review of commercial units for HTHPs, displayed in Figure 1.7, shows that many technologies overlap in the same range of temperature and power capacities.

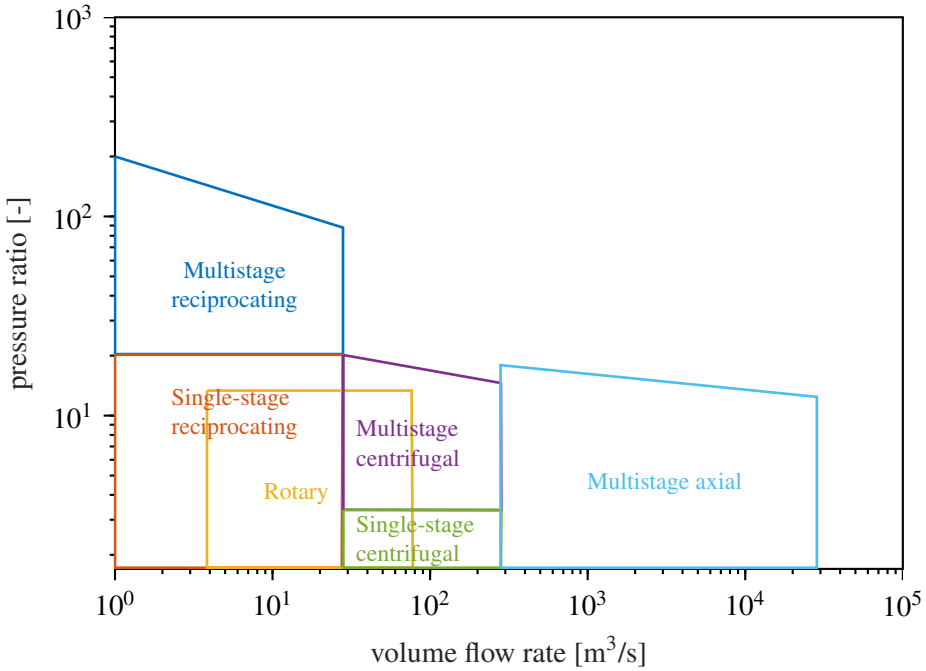

Figure 1.6: Charts for preliminary selection of compressor technology. Adapted from [150].

Among the possible compressor technologies, centrifugal compressor (CC) devices are receiving particular attention for the development of HTHPs. Compared to conventional volumetric machines, centrifugal compressors bear key advantages such as the potential to achieve higher efficiencies at high pressure ratios, a more compact design, and especially the possibility to use oil-free solutions, which avoids possible issues in the heat exchangers [162, 163]. The experimental activities on centrifugal compressors are numerous in the literature, and a non-exhaustive list of some well-documented cases is shown in Table 1.3. Some of the references in Table 1.3 are particularly relevant as they have been employed in the development and validation of numerical tools for CC design and analysis. Air compressors have been investigated since the early 1960s-1970s. Exemplary is the case of the Eckardt compressor [164–168], which was arguably the first CC prototype object of extensive research investigations, both experimentally and numerically. From the 1970s to the 2000s, fundamental research on CC for gas turbine applications was carried out by different research institutes [169–177], including NASA [178–180], to improve the design and performance of the machines and the prediction capability of the existing numerical tools. In the last decade, experimental investigations on CC were performed in new fields of application, using different working fluids and high values of rotational speed. Schiffmann and Favrat [126, 181, 182] published experimental and numerical results of a compressor consuming electric power of 1.8 kW at nominal conditions and with an outer diameter of 20 mm, which was designed for domestic HTHPs. The compressor featured a high rotational speed, in the range 150 krpm to 210 krpm, and was oil-free as the working fluid was employed to lubricate the gas foil bearings. The authors successfully tested the compressor which reached pressure ratios more than 3.3 and efficiencies above 78 %. Wright et al. [183] constructed a small-scale Brayton cycle loop (50 kW) to investigate

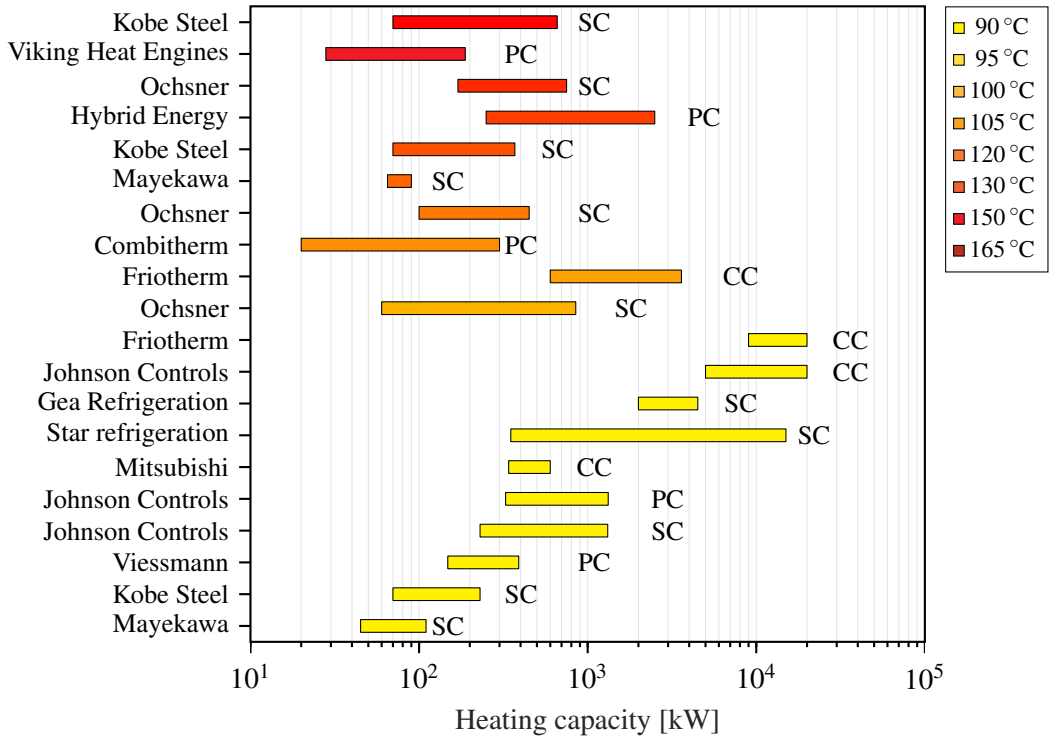

Figure 1.7: Manufacturers of high-temperature heat pumps based on maximum supply temperature and compressor type. SC = screw compressor; PC = piston compressor; CC = centrifugal compressor. Adapted from Refs. [8, 152–161].

the technical feasibility of CC operation close to the critical point of CO_2. The generated results could be used for the development of future Brayton cycles using supercritical fluids with solar, nuclear or fossil fuels heat sources. Casey et al. [184, 185] presented a study on the validation of a CC model for a vacuum blower and HPs with test cases using air as the working fluid. Madsbøll et al. [186] reported the design and testing of a CC unit using water vapor which could be used for HTHPs. Finally, Brasz [187] analyzed the use of new HFOs as the replacement for the existing HFCs in CC for the refrigeration industry. The studies above proved the technical feasibility of using CC for different applications and different working fluids in a wide operational range. Recently, new commercial units using HFOs have been developed [188, 189].

To design centrifugal compressors for the next generation of HPs, simple yet accurate numerical modeling tools need to be available. Most of the considerations made in Sec. 1.2.1 are also valid in this context. In particular, the implementation of cost-effective centrifugal compressor solutions requires reliable and accurate preliminary design models. These tools need to include the possibility to model any refrigerant in sufficient detail and need to be properly validated. Similarly to ORC turbines, there is a lack of data for validation of centrifugal compressors with different refrigerants, and this aspect can hamper the development of optimal and cost-competitive solutions. It is also arguable whether the empirical loss and deviation correlations employed in 1D models of centrifugal compressors can be directly applied to any compressor size, geometry and working fluid. For these reasons, more research is needed to investigate the suitability of the existing empirical models.

Table 1.3: Well-documented experimental activities on centrifugal compressors from the open literature.

Author	Year	Fluid	Application	P_{el} [kW] (at BEP)	N [krpm]	Max. PR [-]
Eckardt et al. [164–168]	1975	Air	Research	n.a.	10-16	3
Jones [190]	1977	Air	Gas Turbines	n.a.	25-40	7
Came [169]	1978	Air	Research	750	30-40	8.5
Dolan and Runstadler [170]	1979	Air	Research	750	37-75	4.3
Krain and Hah [171, 172]	1990	Air	Research	n.a.	n.a.	4.6
Hathaway et al. [178]	1992	Air	Gas Turbines	1115	1920	1.17
Colantuoni and Colella [173]	1993	Air	Gas Turbines	2000	30-43	10.5
Skoch et al. [179, 180]	1997	Air	Research	n.a.	13-22	4.5
Ziegler et al. [174–177]	2003	Air	Research	n.a.	21-35	3.7
Schiffman and Favrat [126, 181, 182]	2009-2010	R134a	HTHPs	1.8	150-210	3.3
Wright et al. [183]	2010	CO_2	S-CO_2 cycles	50	45-64	1.8
Casey et al. [184, 185]	2012-2013	Air	Blowers and HPs	n.a.	50-300	1.8
Madsbøll et al. [186]	2015	water	HTHPs	50	69-101	3.1
Brasz [187]	2013	R134a, R1234ze(E)	Refrigeration	33	n.a.	2.6

Table 1.4: Mean-line models developed for centrifugal compressors in the open literature.

Author	Ref.	Year	Model validation
Li et al.	[191]	2015	Off-Design, air compressor with vaneless and vaned diffusers
Kus and Nekså	[192]	2013	Design point, CO2 compressor
Casey	[193]	2012	0-D, Off-Design, tubocharger compressor
Vilim	[194]	2010	Design point, CO2 compressor
Schiffmann and Favrat	[182]	2009	Off-design maps, R134a compressor
Veres	[195]	2009	Off-design maps, three axial single and multi-stage compressors
Oh et al.	[196]	1997	Off-design maps, four air compressors
Aungier	[197]	1995	Off-design map, five air compressors with vaned and vaneless diffusers
Perdichizzi and Savini	[198]	1985	Off-design map, air compressor with vaned diffuser, off-design
Galvas	[199]	1973	Off-design map, air compressor with vaned diffuser, off-design
Rodgers	[200–203]	1964-1984	Off-design map, thirteen backswept air impellers with vaned diffuser
Coppage	[204]	1956	Aeroderivative air compressor, subsonic and supersonic conditions, off-design maps

1.2.6 Centrifugal compressors modeling for HP applications

Table 1.4 provides a non-exhaustive list of the mean-line models that were developed for CCs and their validation methods. The validation of the models described in Table 1.4 was performed using the experimental data for a single working fluid. The models which employed a working fluid that can be used in HP applications are those by Schiffmann and Favrat [182], Vilim [194] and Kus and Nekså [192]. In the design of heat pump systems, it is relevant to know whether a mean-line model validated with the data of a specific test case is suitable also for other geometries and working

fluids. This information serves to assess the accuracy and robustness of a mean-line model when used outside its validation boundaries.

Similarly to ORC turbines, the compressor mean-line model could be coupled to the system level modeling, thereby providing a combined design with the system. A common approach in the field, adopted by previous studies [205–210] is to neglect the details of the compressor design and performance in the preliminary design of the heat pump by setting a fixed value of compressor isentropic efficiency and volume flow rate. On the other hand, accounting for the compressor design and performance criteria in the preliminary design stage of the heat pump might be key to identify most suitable solutions from the technical viewpoint, avoiding the risk to design heat pump systems and compressors that are infeasible or too complex to be realized. In this context, the working fluid represents an additional degree of freedom in the design process, and can greatly affect both the system and the compressor designs. In this respect, a combined design of the energy system and the compressor is particularly important to ensure that the working fluid selection includes considerations on the performance and technical aspects of both the machine and the cycle. This approach, where the machine and the cycle designs are linked and optimized in the preliminary design step, was recently used in the context of ORC power systems, see Refs. [72, 89, 211] and Sec. 1.2.2. In the heat pump field, some authors linked the cycle design to that of the centrifugal compressor. Schiffmann and Favrat [182] optimized the design of a CC for different HP operating points to achieve the best seasonal performance of the compressor and the HP. They used a validated mean-line model of a CC. In a subsequent work, Schiffmann [212] proposed a method to design the centrifugal compressor by integrating the model of its mechanical subcomponents. Javed et al. [213] proposed a comprehensive method to perform the design of the compressor and the heat pump using different steps in the design process from preliminary design to 3D-CFD simulations of the impeller aerodynamics. The work of Javed et al. [213] is very detailed, and it was applied to a single working fluid. However, the computational efforts and the time required to run all simulations may not be suitable for a preliminary design process, which instead requires the use of a relatively short amount of time, especially if many different working fluids are investigated.

None of the authors mentioned above performed a cycle design where the most suitable working fluid is selected based on both cycle and compressor design criteria, and in all cases the fluid was selected a priori. Moreover, only Ref. [213] proposed to interface the cycle model to that of the compressor, ensuring the attainment of more accurate results. However, the use of 1D tools combined with CFD arguably requires considerable efforts regarding time and computational resources, and might not be compatible with the time and costs required in the very early step of the design process. According to the aspects above, the development and validation of a compressor mean-line tool for design and analysis, and the use of a methodology for the optimization with the HP system and the working fluid selection are additional objectives of this thesis.

1.3 Objectives and methods

This Ph.D. thesis has two main objectives. The first one is to develop suitable mean-line models for the preliminary design and performance prediction of ORC axial and radial-inflow turbines, and centrifugal compressors for HP systems. The second objective is to develop and apply design optimization methodologies which allow combining the machine and the cycle designs to identify suitable solutions from the performance and technical viewpoints. The main objectives are divided

into the following tasks, according to the turbomachinery technology:

Axial-flow turbines

i) To develop and validate mean-line modeling tools for single-stage and multistage axial-flow turbines operating with organic fluids.

ii) To develop a methodology that accounts for the turbine design criteria in the design of the ORC power system.

iii) To demonstrate the use of such a methodology in a case study relevant to ORC systems.

Radial-inflow turbines

iv) To develop and validate mean-line modeling tools for high-pressure ratio radial-inflow turbines operating with organic fluids.

Centrifugal compressors

v) To develop and validate mean-line modeling tools for centrifugal compressors operating with different working fluids.

vi) To develop a methodology for the combined optimization of a heat pump equipped with a centrifugal compressor.

vii) To apply the methodology to a case study relevant for HP systems.

The development of the modeling tools and methodologies above represents the first step towards the optimization of the next generation ORC power systems and HP systems.

The objectives (i)-(vii) are achieved for each particular technology using different methods, which are described in more detail in the next chapters. The mean-line models are based on the relevant modeling approaches from the literature and are written in the MATLAB [214] language. The numerical tools are developed in a way that results to be physically consistent, numerically stable, and has a general formulation which makes it adaptable to different applications. The developed models are formulated for a combined optimization with the energy system and are interfaced with state-of-art equations of state, hence accounting for the behavior of any working fluid of interest with suitable accuracy. In the case of axial turbines and centrifugal compressors, methodologies for the combined optimization of the machine and the cycle are developed for one or more case studies. In the case of radial-inflow turbines, a specific optimization methodology is used to calibrate the loss models to the considered experimental data of high-pressure ratio turbines from the literature. In all cases, the optimization is performed using evolutionary algorithms, which seek to optimize the system efficiency or power.

1.4 Thesis structure

This thesis is structured as follows:

Chapter 2 presents the development of numerical methods for the preliminary design, validation, and optimization of ORC axial-flow turbines. Moreover, this chapter presents the methodologies developed to include the turbine design criteria in the design and optimization of the ORC power system. Finally, it shows the application of the developed methods to the design of some reference case studies representative of low-temperature heat source applications used for power generation.

Chapter 3 presents the development of the numerical methods for the preliminary design, off-design and optimization of ORC radial-inflow turbines. Moreover, this chapter presents the methodology used to calibrate the model with the data of six well-documented HPR turbines from the open literature.

Chapter 4 presents the development of the numerical methods for the preliminary design, of-design and optimization of centrifugal compressors for HP systems. Also, the centrifugal compressor model is optimized for a case study of a HTHP to show the relevance of the application of the developed model.

Chapter 5 highlights the main outcomes of this work and draws the conclusions.

Appendix A describes the empirical correlations used in the axial turbine model and the data used for the validation.

Appendix B describes the empirical correlations used in the radial-inflow turbine model and the data used for the validation.

Appendix C describes the empirical correlations used in the centrifugal compressor model and the data used for the validation.

Appendix D includes a collection of the main published and unpublished papers related to this Ph.D. work.

2 Axial-flow turbines for ORC power systems

The work presented in this chapter is based on the results published in Refs. [72, 89, 211, 215] In particular, Refs. [89, 211, 215] refer to the development, the design and optimization of single-stage ORC axial turbines while Ref. [72] focuses on multistage ORC axial turbines.

2.1 Introduction

Axial-flow turbines were a selected technology in this work since they feature technological maturity, high performance, wide range of applicability, and the large availability of data in the literature. This chapter aims to fulfill the objectives defined in Sec. 1.3 for ORC axial-flow turbines.

The mean-line axial turbine model is developed to: (i) simulate axial-flow turbines operating with organic fluids and to (ii) perform a combined optimization with the ORC system design. The work is limited to consider steady-state analyses at design conditions and includes both single-stage and multistage turbine configurations. The development of the design models is based on the approaches presented in the literature; however, it is suitably modified to account for the use of organic working fluids. The mean-line models are validated using axial turbine test cases from the open literature, two of which are ORC turbines, and are selected based on the availability of sufficient and reliable data. Depending on the specific test case, the results of CFD simulations are also used as complementary tools to investigate the results of the mean-line models. A global sensitivity analysis is applied to the single-stage turbine model to reduce the number of decision variables and, consequently, the computational efforts required by the model optimization. A novel methodology for the combined optimization of the turbine and the cycle in both the single and multistage layout is developed. For the multistage turbine arrangement, two different turbine design approaches are proposed, and which designers can adopt according to their key decision criteria. The optimization methodology is then applied to two relevant case studies of waste heat recovery, in order to assess its suitability and to show how it can be used in a real application. Compared to the previous literature, see Section 1.2, the work proposed in this chapter introduces the following novel contributions: (i) it presents the detailed validation of a mean-line model of ORC axial turbines in the single- and multistage configurations, including the data of ORC turbines from the literature; (ii) it proposes a methodology for combined optimization of an ORC system and an ORC turbine, in which the turbine layout and performance become additional criteria for the working

fluid selection in a specific application; (iii) in the case of multistage turbines, it considers two alternative turbine design approaches, which designers may adopt according to their key decision criteria; (iv) it presents the combined optimal design of the ORC system and the turbine for two case studies, one of which includes the use of multi-component working fluids.

This chapter is structured as follows: Section 2.2.8 describes the mean-line modeling tool (named TURAX) for single- and multistage turbines, the model validation, the methodology for combined turbine and cycle optimization, and the selected case studies where the methodology was applied. Section 2.3 presents the results of the validation and the application of the methodology to the case studies. Section 2.4 discussed the results, and Section 2.5 draws the conclusions.

2.2 Methods

When axial turbines are considered, in their single or in the more general multistage layout, a specific methodology is developed to account for the design aspects of such machines into the preliminary design of the ORC power system [72].

The schematic workflow of the methodology adopted in this work is illustrated in Figure 2.1. The methodology considers two different approaches for turbine design: a *conservative design* and an *advanced design* approach. Section 2.2.4 explains the two approaches in more detail. The first step of the workflow is a working fluid preliminary selection (Sec. 2.2.3) based on the inputs from the selected case study (see Sec. 2.2.8). Then an assumed value of the isentropic turbine efficiency of 0.8 and a single stage are used to initiate the combined turbine and cycle optimization process. For each working fluid the turbine and the cycle are optimized with an iterative scheme (see Sec. 2.2.7). If the conservative approach is followed, a conservative turbine design is adopted, and the Mach number is constrained to a predefined value (see Sec. 2.2.4). The number of turbine stages is increased until the Mach number constraint is respected. Afterwards, the methodology computes a performance index (Sec. 2.3.5), which is used as an indicator of the combined effects of cycle and turbine designs. Eventually, the minimum number of stages in the *advanced design* approach and the suitability of the use of a gearbox are evaluated based on this parameter. Finally, the working fluids having the highest values of the performance index are selected, and the design solutions are compared based on technical and environmental criteria, and also on the specifications of the selected application.

The axial-flow turbine model presented in this work, named TURAX, originated from a MSc thesis work [216] and had been used in subsequent studies [72, 89, 211, 215]. The model is written in Matlab language [214] and provides the mean-line preliminary design and the efficiency prediction for an axial-flow turbine with one or more stages. In the present form, the model employs a steady-state analysis at design conditions.

The mean-line model formulation envisages the solution of balance equations of mass, energy, and momentum as well as the expressions for loss models to account for the entropy generation in the stationary and rotating passages of the turbine. A schematic of the axial turbine in the meridional plane and of the notation used in this chapter is shown in Figure 2.2.

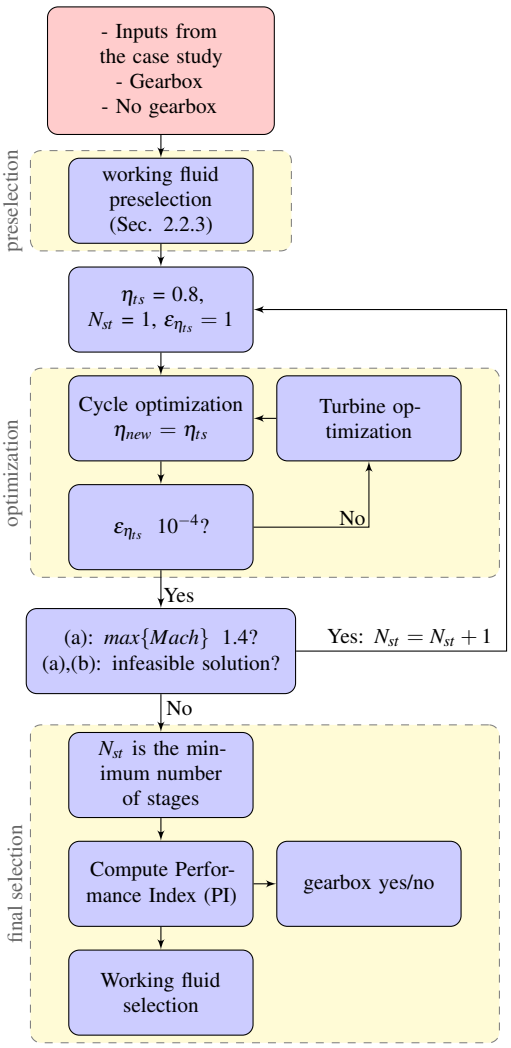

Figure 2.1: Methodology for combined optimization of the cycle and multistage turbine for (a) the conservative design approach and (b) the advanced design approach. From Ref. [72].

2.2.1 Design model for single-stage turbines

Figure 2.3 illustrates the workflow used to perform the design of a single-stage turbine. The parameters and inputs required by the model are the following:

a) Inlet total pressure p_{01}, inlet total temperature T_{01}, mass flow rate $\dot{m}$, outlet total pressure p_{03}. These parameters usually come from the ORC system model.

b) A set $\overline{X}$ of 12 turbine decision variables listed in the table of Figure 2.4. Note that this set is reduced to 10 variables after a sensitivity analysis study described in Sec. 2.2.6.

c) Additional geometrical specifications and constraints for the blade shape geometry, the nozzle-rotor clearance gap ss, the rotor tip clearance t_{cl}, the blade surface roughness k_s, the

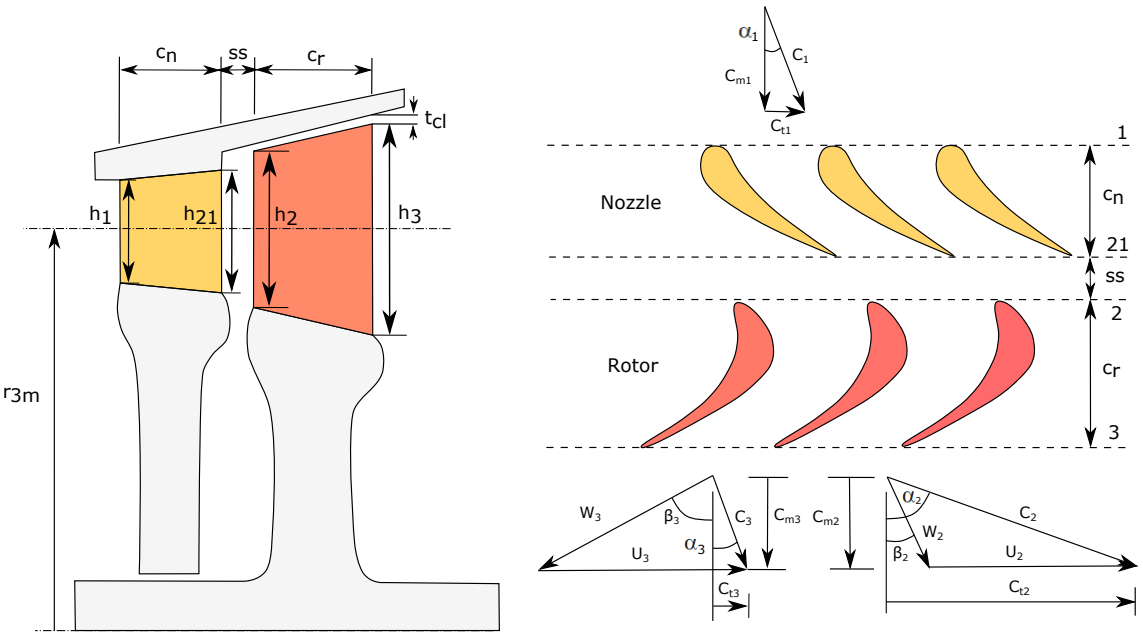

Figure 2.2: Schematic of the axial-flow turbine geometry and meridional cut layout.

nozzle to rotor mean radius ratio R^*.

d) A library for the computation of the thermo-physical properties of the working fluid. In the case of mixtures, the molar composition must also be specified. Two libraries available in TURAX for the estimation of the fluid's thermodynamic and transport properties are REFPROP [217] and CoolProp [218].

The turbine design model can be expressed in the general form

$$[\eta_{tt}, \eta_{ts}, geometry, flow] = f(T_{01}, p_{01}, p_{03}, \dot{m}, fluid, \overline{X}), \tag{2.1}$$

The outputs of the model are the turbine isentropic efficiency (expressed in terms of total-to-total and/or the total-to-static efficiencies, η_{tt} and η_{ts}), the turbine main geometrical parameters (here synthetically indicated with the term *geometry*), and the thermodynamic and fluid dynamic conditions ($flow$) at the nozzle and at the rotor inlet and outlet. Figure 2.3 illustrates that the design process is iterative and proceeds as follows:

(1) Guessed values of turbine stage and nozzle efficiencies are initially assumed.

(2) The outlet flow angles are estimated and, subsequently, the velocity triangles are computed. In order to compute the exit flow angles, the empirical correlation by Ainley and Mathieson [219] is used in case of subsonic flow conditions, and the empirical correlation by Vavra [220] is used for supersonic flow regimes.

(3) At each inlet and outlet station of a blade row, the thermodynamic and transport properties are calculated.

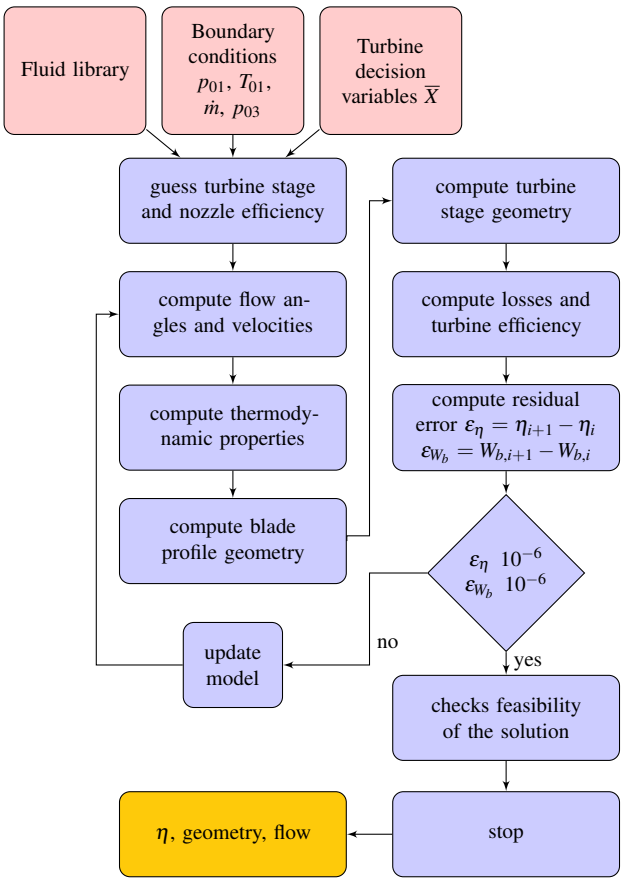

Figure 2.3: Flowchart of the single-stage axial turbine model. From Ref. [211].

(4) Nozzle and rotor blade profile geometry is computed. In case of a converging-diverging nozzle, the Deich's formula [221] is employed to calculate the blade opening. The profile loss correlations of Craig and Cox [222] are used for both converging and converging-diverging nozzle profiles. This approach was also adopted by Macchi [52].

(5) The meridional geometry of the turbine stage is computed.

(6) The velocity triangles at the hub and at the tip, required in the loss correlations, are computed using the free vortex assumption [223].

(7) Losses and efficiency are predicted. The method by Craig and Cox [222] is used to estimate the losses occurring in the turbine stage as it was considered as one of the most complete and reliable by some studies for ORC turbines [58, 65, 94, 224]. The correlation by Kacker and Ockapuu [225] is used to compute the shock losses in a blade row. The formula by Balje and Binsley [226] is employed for disk windage losses. The method by Suter and Traupel [227] is considered as one of the best available and comprehensive models [133, 228] and is used for the estimation of partial admission losses.

(8) If the nozzle exit Mach number is in the range 1.0 to 1.4, supersonic converging nozzle blades are used, allowing for a post-expansion downstream of the throat. For values of Mach number higher than 1.4, a supersonic adapted converging-diverging nozzle is used instead

Decision variable	Unit	Symbol
1) Stage inlet flow angle	°	α_1
2) Stage loading coefficient	-	$\psi = 2\Delta h_{is}/U_{3m}^2$
3) Nozzle minimum opening	m	o_{min}
4) Rotor opening	m	o_r
5) Nozzle axial chord	m	c_n
6) Rotor axial chord	m	c_r
7) Nozzle opening-to-pitch ratio	-	$(o/s)_n$
8) Rotor opening-to-pitch ratio	-	$(o/s)_r$
9) Rotational speed	rpm	N
10) Stage inlet axial velocity	m/s	C_{a1}
11) Rotor flow coefficient	-	$\phi_r = C_{a3}/U_{3m}$
12) Rotor inlet to nozzle outlet blade height	-	$h^* = h_2/h_{21}$

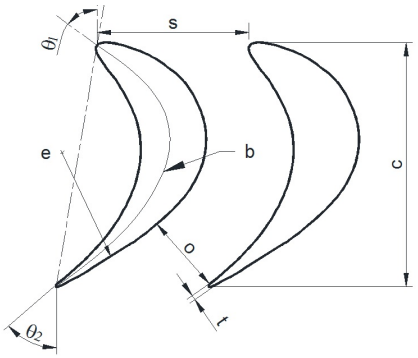

Figure 2.4: Decision variables and nomenclature in the blade-to-blade plane for the single-stage axial turbine model. From Ref. [211].

(see Sec. 2.2.4 for details). The rotor blades are converging with maximum Mach numbers at the rotor inlet and outlet of 0.8 and 1.4. This assumption serves to preserve the validity of the employed loss correlations and avoid excessive supersonic expansion losses [52]. For nozzle exit Mach numbers below 1.4, the throat is assigned the value of the minimum opening given as an input. Alternatively, the throat size is found by a mass balance between the throat and the nozzle exit sections assuming a constant blade height. In case of a supersonic adapted converging-diverging nozzle, the blade profile geometry is assumed to be optimized for supersonic flow conditions and, therefore, the profile loss increment due to Mach number effects is neglected as recommended by Dunham and Came [229].

(9) Blockage factors are applied to the mass balance equations to account for the effective passage area reduction due to boundary layer effects and the blade metal blockage. In this case, the method by Vavra [220] is used with an energy form factor of 0.9 [52].

(10) The residual error in efficiency and blade work between two consecutive iterations is calculated and the process iterates until it falls below a predefined threshold value (i.e. 10^{-6}).

(11) The final design is checked for being within a set of constraints related to manufacturability and technical feasibility. Table 2.2 shows the constraints used in this work.

The empirical correlations used in TURAX are reported in detail in Appendix A. The equations used to compute the thermodynamic and flow conditions in the different turbine sections are provided in standard turbomachinery textbooks and papers [52, 133, 220, 223, 230, 231], and are thereby not reported here.

If the objective of the design process is to generate an optimal turbine design, the set of decision variables $\overline{X}$ can be optimized using a dedicated optimization algorithm to yield the best value of a specified objective function (usually the turbine isentropic efficiency). The details of the optimization method are described in Sec. 2.2.7.

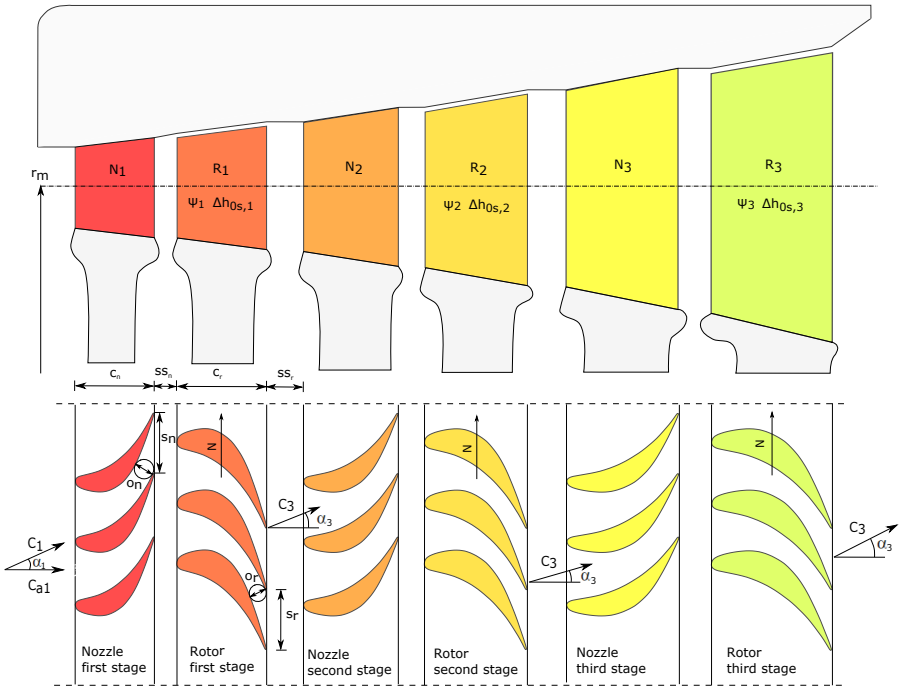

Figure 2.5: Schematic of the multistage axial-flow turbine geometry and meridional cut layout.

2.2.2 Design model for multistage turbines

The multistage turbine model is implemented by performing the design of many stages in series, as illustrated in Figure 2.5. Additional features are introduced to extend the single-stage model to the multistage layout:

(11) The set of decision variables for the multistage model is listed in Table 2.1. The design of the multistage machine is carried out by optimizing all the decision variables simultaneously according to the indications by Persico and Pini [90] for ORC turbines. Some variables need to be specified only once for the whole turbine stage, and these are the stage inlet axial velocity and the rotational speed by assuming that the stages share a common shaft.

(12) The distribution of the overall pressure ratio across the stages is optimized using the isentropic stage loading coefficient ψ_n. In the design of the turbine considering a constant mean radius, the mean peripheral speed U_m and the overall isentropic enthalpy drop $\Delta h_{0s,tot}$ are linked using ψ_n as follows:

$$\Delta h_{0s,tot} = \frac{U_m^2}{2} \cdot \sum_{n=1}^{N_{st}} \psi_n \tag{2.2}$$

Using Eq. 2.2 it is possible to compute the mean peripheral speed U_m and the isentropic enthalpy drop for each stage, and hence also the stage pressure ratio.

(13) It is assumed that the absolute flow angle and velocity at the exit of one stage is the same as that at the inlet of the next stage.

Table 2.1: Decision variables of the multistage turbine model. From Ref. [72].

Decision variable	Unit	Symbol	Stage
1) Isentropic stage loading coefficient	-	$\psi = \frac{2\Delta h_{is}}{U_{3m}^2}$	all
2) Nozzle minimum opening	m	o_{min}	all
3) Rotor opening	m	o_r	all
4) Nozzle axial chord	m	c_n	all
5) Rotor axial chord	m	c_r	all
6) Nozzle opening-to-pitch ratio	-	$(o/s)_n$	all
7) Rotor opening-to-pitch ratio	-	$(o/s)_r$	all
8) Rotational speed	rpm	N	first
9) Stage inlet axial velocity	m/s	C_{a1}	first
10) Rotor flow coefficient	-	$\phi_r = \frac{C_{a3}}{U_{3m}}$	all

2.2.3 Preliminary working fluid selection

When the design of the turbine and the ORC unit is performed, the most suitable working fluid needs to be selected. The selection process may be driven by the requirements of the specific application or can be part of the design process. In the latter case, it is convenient to perform a preliminary screening of some working fluids according to the indications found in the literature. This operation can save time and computational efforts in the subsequent steps when the turbine and the cycle are optimized following the methodologies of single- or multistage turbines illustrated in Figures 2.1 and 2.3.

The preliminary selection of the working fluids is based on indications from the literature [77, 232–235], and on the actual availability of the working fluids in commercial units [6, 233, 236]. Moreover, thermodynamic criteria require that the working fluid has a thermal stability limit higher than the hot fluid inlet temperature (boiler side) and a critical temperature higher than the minimum admissible temperature at the boiler inlet. Environmental criteria include a zero ozone depleting potential (ODP) [237] or a global warming potential (GWP) <150 [238]. In case of GWP >150, the fluids currently in use by manufacturers can be considered in the selection. In addition, technical aspects impose practical limitations on the maximum and minimum pressures in the ORC unit. Such constraints are provided by the recommendations from the literature, in particular by Rayegan et al. [239], Drescher and Brüggeman [240], and MAN Diesel & Turbo [241] for the case studies considered in this work. Excessive values of pressure inside the boiler and unstable operation are avoided by setting the maximum pressure limit to 0.8 times the reduced pressure. Finally, in case of multi-component working fluids, those mixtures whose equations of state do not contain accurately validated interaction parameters are discarded.

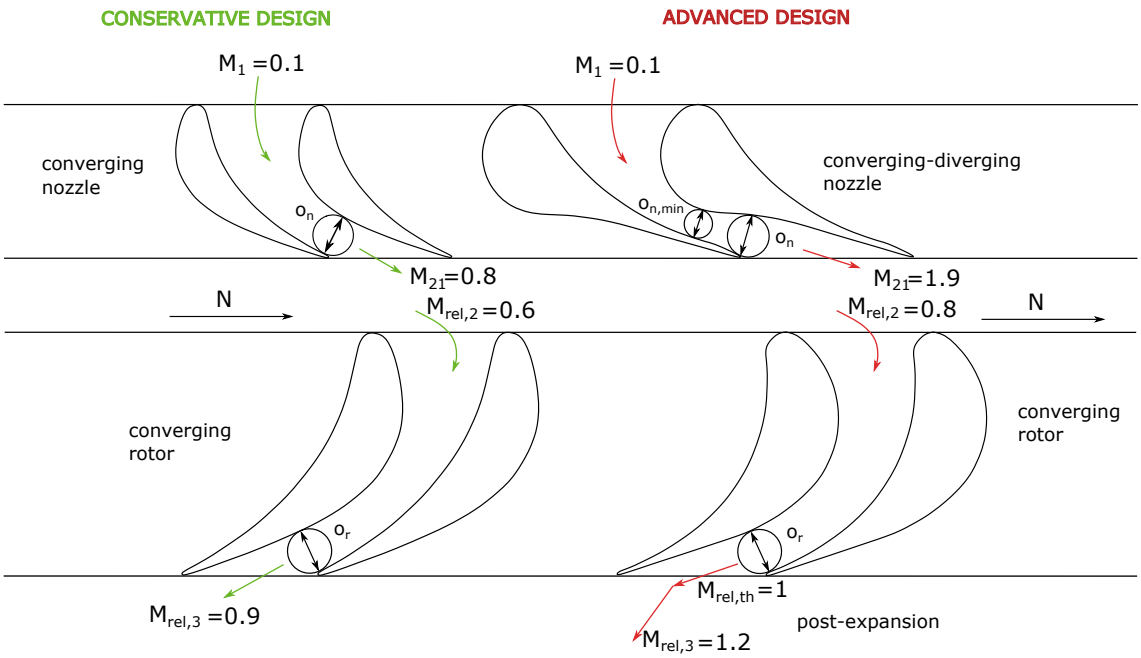

Figure 2.6: Exemplary blade profiles and representation of the conservative (left) and advanced (right) design approaches.

2.2.4 Selection of the number of stages

The optimal number of stages can be selected according to technical and economic criteria or aerodynamics and performance criteria. Some authors included the selection of the optimal number of stages in their work [15, 53, 84, 242]; however, a common method has not been established. This work proposes and analyses two different design approaches for the selection of the optimal number of stages: a *conservative design approach* and an *advanced design approach*.

Figure 2.6 depicts a representation of exemplary blade profiles and flow conditions for the conservative and advanced design approaches.

In the conservative design approach, the maximum Mach number at the nozzle outlet is set to the value 1.4. This method was adopted by different authors in the literature [60, 243, 244] and promotes a conservative ORC turbine design since the high losses related to supersonic flows are avoided, and a simple turbine geometry with converging nozzle blades is adopted. Moreover, this approach ensures the turbine reliability and good performance even at off-design conditions [63], and employs reliable loss estimation procedures from the literature [245].

On the other hand, the advanced design approach considers a more compact and loaded turbine stage featuring Mach numbers higher than 1.4 at the nozzle exit and converging-diverging nozzle blades. This approach was also adopted in the literature in the design of ORC turbines [66, 67].

2.2.5 Validation method

Single-stage turbine model

Two test cases were used for the validation of the single stage axial turbine model. The first one is the fourth stage of a multistage turbine which was in investigated at the University of Hannover in 1977 [246]. The experimental results of this test case were also used in subsequent studies [247, 248]. The experimental facility consisted in an open loop using air with turbine exhaust to the atmosphere. The stage was designed with free vortex design of the blades and a degree of reaction of 50 %. The experimental values of static pressure, total pressure, exit flow angles, and total temperature were measured in ten traverse points with a probe. The experimental error in the total pressure was 0.25 %. The geometry and operating conditions at the design point are reported in Table A.2. Together with the original experimental data, CFD results were also employed in this work to further assess the results of the turbine model. The CFD simulations were performed with ANSYS CFX® and using a 3D, unsteady model with the RANS $k-\omega$ SST model by Menter [249]. The study employed the standard CFD model for turbomachinery flow simulations in use at Politecnico di Milano [250]. The full 3D blade geometry was generated using the data by Kotzing and Evers [248], and the computational domain was discretized by means of a structured, flow-oriented, orthogonal mesh. A grid-sensitivity analysis was carried out using the polytropic efficiency as the indicator. The mesh was refined by a step of 400000 cells each time and, finally, a change in polytropic efficiency below 0.1 % was found for 3200000 cells. The final rotor grid is visualized in Figure 2.10(a). The stage inlet boundary conditions for the model simulations were imposed by using profiles of total pressure and temperature, a constant value of 10° in the flow angle and a turbulence intensity of 1 %. At the stage outlet, a mass flow rate of 6.786 kg/s was given as an additional boundary condition. On the lateral surfaces of the domain, periodic boundary conditions were imposed. The solver achieved the convergence of the momentum equations in the integral value of blade work for an accumulated time step of 100. The other parameters of the CFD simulations were set to the default values provided by ANSYS CFX®. The CFD tool predicted the flow physics and the stage efficiency within 1 % of the experimental data. In TURAX, the validation was performed by using a 50 % degree of reaction and imposing the actual blade height.

In the second test case, the single-stage turbine model was validated against the experimental data of a 3 kW ORC turbine [66] with impulse blading, using the fluid R113 and partial admission. The stage featured a converging-diverging nozzle with highly supersonic exit conditions (Mach number ~ 1.78), a transonic rotor and untwisted blades. A CFD analysis similar to that performed for the first test case was not possible since the original document did not provide the 3D geometry of the blades. At the same time, the validation of the mean-line model with this test case is still relevant considering the strong lack of reliable data on ORC turbines in the literature and the complex flow phenomena inside this turbine such as supersonic flows, partial admission, real gas effects and low Reynolds numbers. The effects of supersonic operating conditions in the nozzle and transonic conditions in the rotor were modeled as follows:

1. Profile losses for the converging-diverging shape of the nozzle were corrected using the suggestion by Craig and Cox [222].
2. Supersonic expansion losses at nozzle outlet were computed using the formula by Aungier [133].

In this specific case of validation, the introduction of the two correlations above had only a limited impact on the overall stage performance; however, it allowed achieving a more suitable distribution of losses and velocities in the nozzle and rotor. The original document of this test case did not provide the full details on the required data for the mean-line model and, consequently, some of the required parameters were estimated based on the available data. In particular, stage loading, opening-to-pitch ratios, flow coefficient, inlet axial velocity were obtained by the best match with nozzle inlet and rotor outlet blade heights, and with the number of nozzle and rotor blades. The main data for the geometry and operating conditions of the turbine are listed in Table A.1 in Appendix A.

Multistage turbine model

The validation of the multistage axial turbine model was performed using the experimental data of two turbines whose data are documented in the literature and contain sufficient information on the geometry, flow and performance conditions for the validation process. The two test cases are representative of the conservative and advanced design approaches, respectively. In the second test case some parameters related to the geometry were assumed and, therefore, a sensitivity analysis was carried out to evaluate the uncertainty of this assumption on the validation results.

The first test case used for validation is the Hannover turbine; however, in this case, the data of all the four stages are used. The turbine was operated at subsonic conditions using air and the experimental results were documented by Kötzing and Evers [248] and Hirsch and Denton [247]. At nominal conditions, the turbine generated 703 kW running at 7500 rpm with a total-to-static pressure ratio of approximately 2.6. The total-to-total efficiency was calculated from the experimental data as 91.3 % with an accuracy of 0.8 % [248, 251]. The blades were designed with the same criteria described in the validation of the single-stage turbine model. Kötzing and Evers [248] mentioned that the experimental results of the Hannover turbine could be affected by uncertainty. Therefore, to further assess the reliability of the validation, the results of the mean-line model were also compared to CFD simulations carried out by Gerolymos and Hanisch [252] and Croce et al. [253]. These simulation tools represent the state of the art of the modeling for the Hannover turbine test case [252–254] and were validated using the experimental data of other turbomachinery test cases [255, 256]. The data provided as inputs for the validation of the mean-line model are listed in Table A.2.

The geometric data of the turbine were directly provided in the original references or were extracted by interpolation. The absolute axial flow velocity at the inlet of the first stage was calculated by applying mass and energy balances. The turbine flow coefficients were computed by obtaining the match with the turbine geometry regarding mean radius and stage exit blade height. The blade profile after the opening in the rear suction side was considered to be straight, and the blade surface roughness was set to $2 \cdot 10^{-3}$ mm. Mass-weighted average flow and thermodynamic conditions at different turbine stations were calculated from the experimental and CFD data in order to allow for a direct comparison with the mean-line model. The pressure was computed as an area-weighted average. All the thermodynamic properties of air were estimated using the thermodynamic library REFPROP [217].

The second test case used for validation is a two-stage supersonic ORC turbine. The geometry and

experimental data for this turbine were reported by Verneau [66, 257] and Boy-Marcotte [258]. The turbine was originally employed for a small demonstration solar power plant. The overall design pressure ratio of the turbine is approximately 142; the first stage is of the impulse type with a converging-diverging nozzle and a transonic rotor while the second stage was designed for a 50 % reaction. The turbine operated with the working fluid FC-75, and generated 54 kW running at 7700 rpm with a total-to-static efficiency of 78 %. The data provided as inputs for the validation of the mean-line model with this test case are listed in Table A.2 in Appendix A. The blade angle at the outlet of the first rotor was not provided in the original references, and therefore the reported value of the exit flow angle 56.7° was imposed in the mean-line model to limit the uncertainty of the preliminary design validation. The stage loading coefficients for the two stages were found by obtaining the best match with the mean-line radius and the turbine peripheral speed. Some geometric parameters were not given in the original references and therefore were assumed as listed in Table A.2. In particular, nozzle and rotor throats were estimated using the cosine rule from the exit flow angle provided at the mean-line in Ref. [66], and the values of the trailing edge thickness and rotor tip clearance were estimated as in Macchi [52]. The blade profile after the opening in the rear suction side was consider to be straight and the blade surface roughness was set to $2 \cdot 10^{-3}$ mm. The absolute axial flow velocity at the inlet of the first stage was calculated by applying mass and energy balances. The working fluid FC-75 was not included in REFPROP, and consequently, its thermodynamic properties were estimated using the Peng-Robinson equation of state. The critical properties required by the equation of state were provided in Kluwick [259], and the method by Joback and Reid [260] was employed for the estimation of the ideal molar heat capacity coefficients, which could be estimated by the following expression:

$$c_p = A \cdot T + B \cdot T^2 + C \cdot T^3 + D \cdot T^4 \quad [J/(mol \cdot K)] \tag{2.3}$$

where c_p is expressed in $J \cdot mol^{-1} \cdot K^{-1}$ and the polynomial coefficients are A = -230.11, B = 2.6724, C = -0.0034, and D = 2.00 $\cdot 10^{-6}$.

2.2.6 Sensitivity analysis

The mean-line axial turbine model developed in this work was conceived for a coupled optimization together with the ORC system model. In this respect, it is important to ensure that the computational time and efforts in the turbine design are minimized. For this reason, a sensitivity analysis was first performed on the single-stage model to identify and, if possible, remove those parameters which have limited or negligible impact on the outputs, thereby reducing the number of required design variables for the optimization. To this end, the Morris screening method [261] was employed. The method allows combining the information obtained from a local sensitivity analysis to provide a global screening on the significance of the different design variables with limited computational resources. Moreover, Morris screening method is based on a statistical approach and accounts for the mutual interactions and the interdependence among the variables. The reader is referred to Ref. [261] for more details. In this work, all the twelve decision variables of the single-stage turbine model listed in Figure 2.4 were considered for the analysis. A sampling size of 50 and 6 screening levels were employed in Morris screening method, as they provided a reasonable compromise between the computational time and the achieved accuracy. The sensitivity analysis was applied to the single-stage test case of the Hannover turbine using the Matlab model originally developed by Sin et al. [262]. The decision variables were varied in the range ±25% of their nominal values

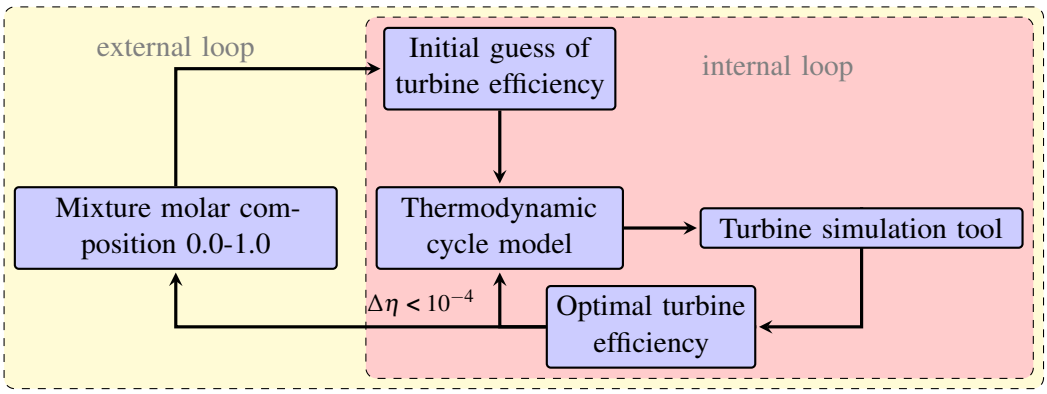

Figure 2.7: Methodology for combined optimization of the cycle and single-stage axial turbine using mixtures.

listed in Table A.1.

A sensitivity analysis was also applied in the validation process of the multistage turbine model. In this case, the objective was to assess the impact of the assumed geometric parameters on the validation results. To this end, a global sensitivity analysis based on the Monte Carlo method [263] was performed. Table A.2 shows the selected uncertain parameters and their assumed value, which was varied in the sensitivity analysis in the range $\pm$ 10 %. This range was selected to provide an expected flow deviation below 5° at the nozzle and rotor exit of the first and second stages, in agreement with the considered type of blading [264]. The Monte Carlo method was applied using a numerical model written in the Matlab environment and originally provided by Sin et al. [262]. The method used 500 samples for each parameter and a uniform distribution without correlation control.

2.2.7 Optimization method

In this work, turbine and cycle models were combined and optimized following the iterative procedure illustrated in Figure 2.1. Figure 2.7 illustrates the details of the cycle-turbine optimization methodology, including the specific case of multi-component working fluids.

The optimization process includes the following steps:

1. Given the specifications of the considered application, the cycle boundary conditions were provided (i.e. heat source temperature, condensation temperature, etc.)
2. The turbine isentropic efficiency was initially set to the constant value 0.8 (*internal loop* of Figure 2.7).
3. An optimization process based on evolutionary algorithms was applied to the cycle model and the boundaries for the turbine model in terms of inlet total temperature and pressure, mass flow rate and outlet total pressure were determined (*internal loop* of Figure 2.7).
4. The turbine model was optimized using an evolutionary algorithm and the new value of

turbine isentropic efficiency was used as an input to the following cycle model optimization (*internal loop* of Figure 2.7).

5. The combined turbine and cycle iteration process stopped when the difference in turbine isentropic efficiency between two consecutive iterations fell below a predefined threshold, i.e. 10^{-4} (*internal loop* of Figure 2.7).

6. When multi-component working fluids were considered, the iterative process was also performed for each value of molar composition with a composition step of 0.1 (*external loop* of Figure 2.7).

The optimization constraints used in the optimization of the turbine model are listed in Table 2.2. The optimization approach adopted in this work does not consider the use of a surrogate model, as it was done in Ref. [89], since that would require large computational efforts in generating numerous design points for each fluid and each stage. The combined turbine and cycle optimization was performed using the cycle net power output and the turbine efficiency as the objective functions, defined as follows [72]:

$$P_{net} = \dot{m}_{wf} \left(\Delta h_{0,t} - \Delta h_{0,p} \right) \tag{2.4}$$

$$\eta = \frac{\Delta h_{0,t}}{\Delta h_{ts} - \phi_{KE} \cdot \frac{{C_{a3}}^2}{2}} \tag{2.5}$$

where the parameter $\dot{m}_{wf}$ is the working fluid mass flow rate, and $\Delta h_{0,t}$ and $\Delta h_{0,p}$ are the total-to-total enthalpy drops across the turbine and the pump, respectively. The term Δh_{ts} indicates the total-to-static isentropic enthalpy difference across the turbine. The parameter ϕ_{KE} is the fraction of the kinetic energy recovered by a diffuser downstream the last stage and was set to 0.5.

The selected algorithm for cycle and turbine optimizations was a Particle Swarm algorithm [265] combined with a direct search method [266]. A population size of 2000 was chosen for the cycle and of 500 for the turbine optimization using Particle Swarm. These numbers ensured a good compromise between accuracy and time required for the simulations. In case of multi-component working fluids, a population size of 1000 and 20 iterations were used for the turbine model whereas a population size of 50 and 20 iterations were used in the cycle model. A smaller population size was selected for the cycle optimization as the use of thermodynamic libraries for mixtures heavily increased the computational time. The outcome of the Particle Swarm optimization was used as an input to the direct search method, which then rapidly converges to the local minimum of the problem. The use of a hybrid optimization method allowed a reduction in the computation time compared to the use of an evolutionary algorithm alone. For multistage turbines, two cases were considered during the optimization for fixed and optimized rotational speed. When the optimal value of rotational speed from the simulations was below that of the generator, i.e. 3600 rpm, the use of a gearbox was avoided. In this case, the rotational speed was instead set to 3600 rpm, 1800 rpm or 1200 rpm corresponding to the use of generators with 2, 4, or 6 poles. Moreover, to avoid possible stress issues on the blades, the rotor tip speed was constrained to the maximum value 500 m/s.

Table 2.2: Optimizing parameters and constraints of TURAX. Adapted from Ref. [215].

Decision variable	Symbol	Unit	Lower boundary	Upper boundary
Isentropic stage loading coefficient	ψ_{is}	[-]	2	6
Nozzle minum opening	$o_{n,min}$	[mm]	1	100
Rotor opening	o_r	[mm]	1	100
Nozzle axial chord	c_n	[m]	10	100
Rotor axial chord	c_r	[m]	10	100
Nozzle opening to pitch ratio	$(o/s)_n$	[-]	sin(13°)	sin(60°)
Rotor opening to pitch ratio	$(o/s)_r$	[-]	sin(13°)	sin(60°)
Stage inlet axial velocity	Ca_1	[m/s]	0	100
Rotor flow coefficient	ϕ_r	[-]	0	1
Rotor inlet relative Mach number	M_{w2}	[-]	0	0.8
Rotor outlet relative Mach number	M_{w3}	[-]	0	1.4
Flaring angle	α_{FL}	[°]	-25	25
Nozzle height to mean diameter ratio	$(h/D_m)_n$	[-]	0.001	0.25
Rotor height to mean diameter ratio	$(h/D_m)_r$	[-]	0.001	0.25
Nozzle chord to mean diameter ratio	$(c/D_m)_n$	[-]	0	0.25
Rotor chord to mean diameter ratio	$(c/D_m)_r$	[-]	0	0.25
Stage degree of reaction	χ	[-]	-0.1	0.9
Number of nozzle blades	z_n	[-]	10	130
Number of rotor blades	z_r	[-]	10	130
Rotor tip speed	U_{tip}	[m/s]	0	500
Nozzle and rotor Reynolds numbers	Re_n,Re_r	[-]	10^4	-
Nozzle and rotor trailing edge thickness to opening ratio	$(t/o)_n$,$(t/o)_r$	[-]	0.05	
Blade rear suction surface curvature	e_n,e_r	[m]	10^5	
Blade surface roughness	k_s	[m]	$2 \cdot 10^{-6}$	
Annulus blade height ratio	h^*	[-]	1.1	
Degree of admission	ε	[-]	1	
Minimum tip clearance	$min(t_{cl})$	[mm]	$2 \cdot 10^{-4}$	
Minimum trailing edge thickness	$min(t)$	[mm]	$2 \cdot 10^{-4}$	
Annulus to axial chord spacing	ss/c_n	[-]	0.5	
Rotational speed	N	[rpm]	3600	

2.2.8 Case studies

The case studies analyzed in this paper are all related to waste heat recovery from low-temperature heat, and are also representative of potentially relevant applications in Denmark. In the first case study, the combined turbine and cycle methodology was used to investigate the optimal designs using multi-component working fluids for single-stage turbines. In the second test case, pure fluids were considered, and the methodology was fully extended to multistage turbines following Figure 2.1.

Single-stage turbine model

Two case studies are considered in the application of the model to single-stage turbines. The first case study investigates the waste heat recovery from the jacket water from a marine diesel engine with a power output of approximately 60 MW. The jacket water is employed as a cooling agent

for the cylinder liners of the engine and is usually wasted into the fresh water cooling circuit. In this case, an ORC unit could harvest the available heat from the jacket water cooling system and produce electricity which may be used for on-board purposes. After cooling the cylinder liner, the jacket water has a temperature of 85 °C. The water is constrained to return to the engine at a temperature of 80 °C to provide the required cooling capacity. The second case study employs the same modeling conditions as the first case; however, no constraint on the hot fluid outlet temperature is imposed. This case can be representative for low-temperature heat recovery such as geothermal [267], solar [268] or waste heat recovery applications.

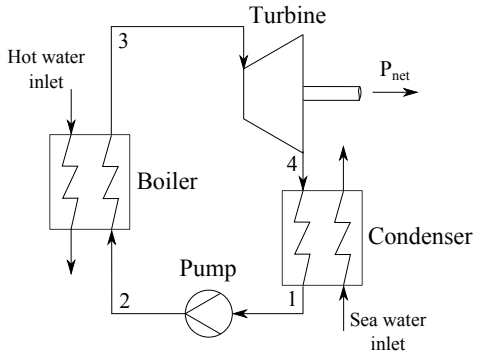

Parameter	Value	Unit
Hot water		
Inlet temperature	85	°C
Mass flow	120	kg/s
Pressure	1.5	bar
Condenser		
Coolant inlet temperature	27	°C
Coolant mass flow	100	kg/s
Outlet vapour quality	0	-
Cooling water pressure	1.5	bar
Pump		
Isentropic efficiency	0.8	-
Turbine		
Isentropic efficiency (first iteration)	0.85	-
Minimum outlet vapour quality	1	-

Figure 2.8: ORC unit and modeling conditions for the case of waste heat recovery from the jacket water of a 60 MW marine diesel engine. From Ref. [215].

A schematic of the investigated ORC unit is shown in Figure 2.8. The ORC system comprises a boiler, a single-stage turbine, a condenser and a pump. The jacket water coming from the engine provides the heat input to the ORC unit whereas the engine coolant is the heat sink at the condenser. The modeling of the heat exchangers followed an approach based on the UA values with the aim to better control the mean temperature difference in the heat transfer process. McLinden and Radermacher [269] and Högberg et al. [270] demonstrated that this modeling approach is especially valuable when the thermodynamic cycle performance is compared for different pure and multi-component working fluids. According to the UA-value approach, a total value of UA was set for the cycle and, during the cycle optimization, the UA-value distribution in the heat exchangers is optimized [271, 272].

In the first case study, the hot fluid outlet temperature was constrained to 80 °C and the cycle optimization variables were the boiler pressure and the fraction of the total UA value assigned to the boiler. To ensure a reasonable value of the pinch point in the range 3 K to 10 K, the total UA value was set to 500 kW/K. The second case study, without having a limitation on the outlet temperature of the hot fluid, employed the same optimization variables and, also, the superheating degree. In this case it would be possible to transfer more heat both in the boiler and in the condenser. Hence, the total UA value was set to 1500 kW/K, which ensured a pinch point in the range 3 K to 8 K. The heat exchangers were discretized and the UA values were calculated as follows:

$$UA = \sum_{j=1}^{n} (UA)_j = \sum_{j=1}^{n} \frac{\dot{Q}_j}{(\Delta T_{lm})_j} = \sum_{j=1}^{n} \left[\frac{\dot{m}_c (h_{c,o} - h_{c,i})}{(T_{h,o} - T_{c,i}) - (T_{h,i} - T_{c,o})} \cdot \ln \left(\frac{T_{h,o} - T_{c,i}}{T_{h,i} - T_{c,o}} \right) \right]_j \tag{2.6}$$

In Eq. 2.6, $\dot{Q}$ is heat transfer rate, ΔT_{lm} is the logarithmic mean temperature difference, T is the temperature. The subscript j refers to the cell j in the heat exchanger discretization, subscripts c and h refer to the cold and hot side of the heat exchanger and subscripts i and o refer to inlet and outlet [215]. The boiler was discretized in 30 cells and the condenser in 10 cells to provide a good trade-off regarding accuracy and computational time.

Multistage turbine model

The optimization methodology considering multistage turbines was applied to the waste heat recovery from a 37 MW diesel engine located on a container ship [241]. The possible waste heat sources include the exhaust gases, the jacket cooling water, and the scavenge air of the engine. The exhaust gases have a sulfur content of approximately 3 %. It was decided to design the ORC unit for 75 % engine load. Although the engine works at low load conditions for most of its time, this condition allowed the exploitation of the engine's waste energy without excessively oversizing the unit. The ORC unit and the corresponding modeling conditions are shown in Figure 2.9.

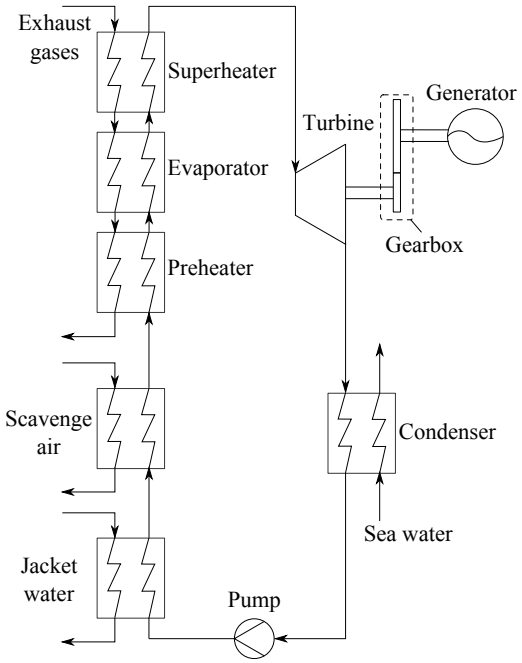

Parameter	Value	Unit
Exhaust gases		
Inlet temperature	235.85	°C
Mass flow	62.6	kg/s
Heat capacity	1.1	kJ/(kg · K)
Boiler		
Pinch point	20	°C
Minimum inlet temperature	135	°C
Condenser		
Fluid condensation temperature	30	°C
Pump		
Isentropic efficiency	0.7	-
Turbine		
Isentropic efficiency (initial iteration)	0.8	-
Minimum outlet vapour quality	1	-
Gearbox efficiency	0.97	-
Generator efficiency	0.95	-
Jacket water		
Available heat flow rate	9230	kW
Fluid outlet temperature	80	°C
Scavenge air		
Inlet temperature	166.3	°C
Available heat flow rate	9230	kW

Figure 2.9: ORC unit and modeling conditions for the case of waste heat recovery from from the exhaust gases, the scavenge air and the jacket water cooling system of a 37 MW marine diesel engine. From Ref. [215].

The working fluid requires a sufficient level of preheating at the pump outlet to avoid sulphuric acid condensation in the boiler [273]. This preheating is ensured by exploiting the waste heat from the exhaust gases but also from the jacket cooling water and the scavenge air. Moreover, sulphuric acid condensation was avoided by setting an additional constraint on the working fluid temperature at the boiler inlet of 135 °C. This number was selected according to the indications of Ref. [241].

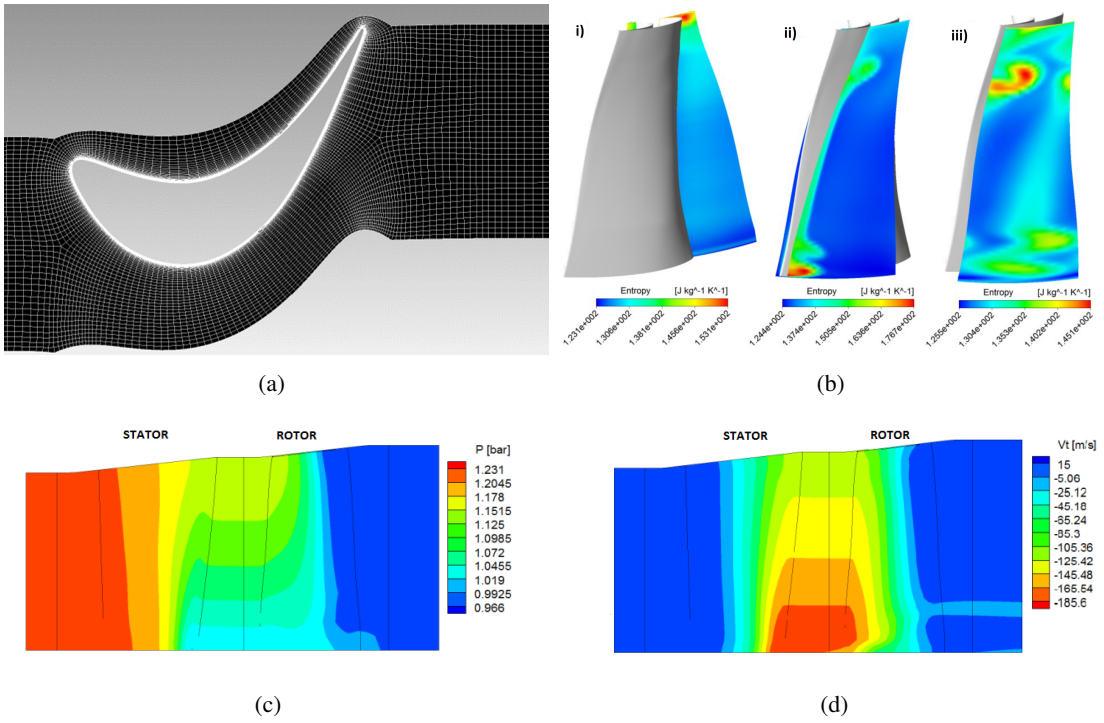

(a) (b)

(c) (d)

Figure 2.10: Computational results for the Hannover turbine test cases using the CFD tool ANSYS CFX®: (a) rotor mesh discretisation at the midspan; (b) contours of the specific entropy at i) the rotor inlet, ii) the rotor outlet, and iii) the measurement station; (c) static pressure field in the meridional plane; (d) contours of tangential velocity in the meridional plane. From [211].

The exhaust gases coming from the engine are used for the generation of 2 t/h service steam and, afterwards, enter the ORC boiler at 235.85 °C. In a preliminary analysis of the system, it was found that the recuperator is not necessary. The system design and performance are influenced by the insertion of a gearbox in the turbine unit, and this is discussed in Sec. 2.3. Finally, the modeling of the heat exchangers followed a pinch point approach.

2.3 Results

2.3.1 Validation of single-stage turbine model

The comparison of the results obtained with TURAX and CFD against the experimental data of the Hannover turbine is provided in Table 2.5. The values for CFD and for the experimental data are given as a mass-weighted average for the different quantities except for the pressure, calculated as an area-weighted average instead. The mass weighted average and the relative deviation with respect to the experimental data for the generic quantity (here indicated with φ) were calculated as

follows:

$$\overline{\varphi} = \frac{\int_A \rho C_a \varphi \, dA}{\int_A \rho C_a \, dA} \qquad Dev_\varphi = \frac{|\varphi - \overline{\varphi}_{exp}|}{\overline{\varphi}_{exp}} \tag{2.7}$$

The parameters ρ, C_a and A denote the density, the axial velocity and the cross-sectional area, respectively, while the subscript *exp* denotes the experimental datum. The deviation in the flow angles was calculated as the absolute difference between the predicted and the measured values.

The details of the CFD simulations are given in Figure 2.10 whereas the comparison with the experimental data for the static temperature and pressure profiles in spanwise direction at different turbine sections is shown in Figure 2.11. The experimental data are in good agreement with the average thermodynamic conditions and flow angles at nozzle outlet for both CFD and TURAX (see also Figures 2.11(a-b)). Along the blade span, CFD results and measured values have a good match, and the results of TURAX are close to those by CFD at the midspan. Both CFD and TURAX underpredict the uniform axial velocity profiles at the nozzle outlet. As a consequence, this results in a larger deviation for the absolute velocity at the nozzle outlet.

The comparison of the results indicates that the predicted deviation increases from the nozzle to the rotor outlet and suggests that the higher velocity in the experimental data at the nozzle outlet is also affected by the fluid-dynamic characteristics in the rotor. In particular, the deviation also increases from the midspan to the endwall regions for the axial and tangential velocities.

The complex fluid dynamics and loss mechanisms in the rotor blades are shows by the entropy field in Figure 2.10(b). Hirsch and Denton [247] highlighted that flow turning and secondary flow effects which are particularly strong at the root, and have an influence on the flow field along the blade span, are likely to stem from the low flow coefficient and aspect ratio (chord over blade span) of the turbine. These three-dimensional effects propagate towards the mid-line, affecting the overall flow field and are likely to generate the deviation between the experimental and the numerical values. As a result, values of deviation up to 10 % and 11.8 % are found at the nozzle exit for the flow angles and velocities.

Regarding the design geometry, TURAX predicted the stage mean radius within 1 %, the blade heights within 5 %, the flare angles within 8°, and underpredicted the number of nozzle blades by 1 unit. The performance of the turbine was compared in terms of total-to-total efficiency η_{tt}, and the nozzle and rotor kinetic energy loss coefficients, ζ_n and ζ_r, defined as:

$$\eta_{tt} = \frac{h_{01} - h_{03}}{h_{01} - h_{03s}} \qquad \zeta_n = \frac{h_2 - h_{2s}}{C_2^2/2} \qquad \zeta_r = \frac{h_3 - h_{3s}}{W_3^2/2} \tag{2.8}$$

The subscripts *1,2,3* denote the nozzle inlet, nozzle outlet, rotor outlet, respectively. The term h is the specific enthalpy, the subscript *0* denotes the total conditions, s indicates the isentropic conditions, and C and W denotes the absolute and relative velocities, respectively. The experimental total-to-total efficiency calculated as a mass-weighted average was approximately 91.6% The results indicate that CFD and TURAX overpredicted the measured value of isentropic efficiency by 1.7 %-points and 1.2 %-points, respectively. The lower values of experimental efficiency may be explained in light of the presence of fluid dynamic effects difficult to be captured by the numerical

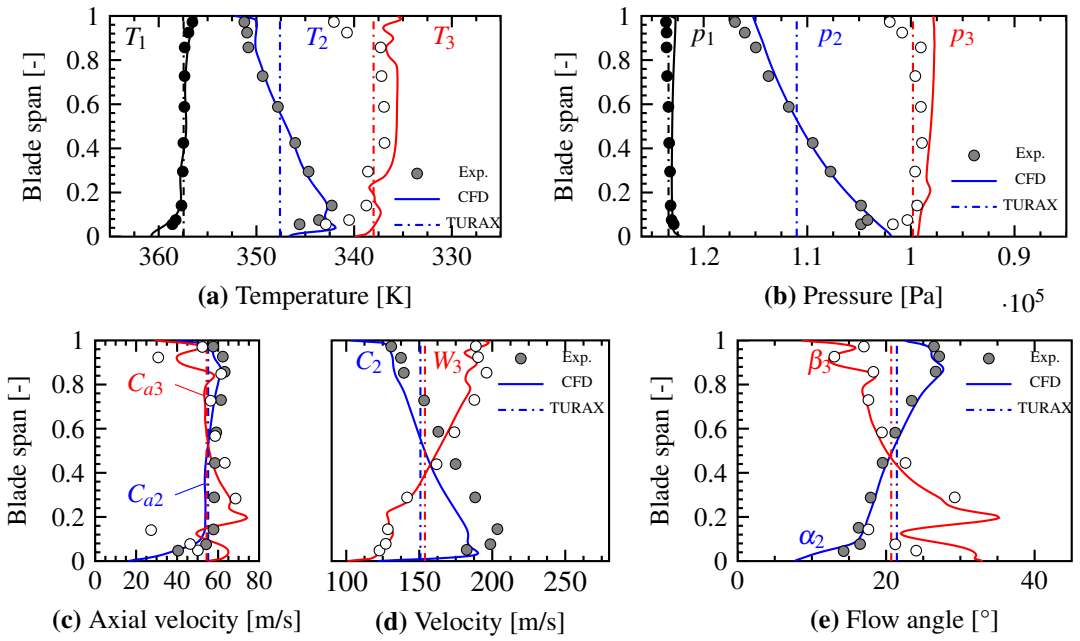

Figure 2.11: Experimental and numerical results for the fourth stage of the Hannover turbine in terms of (a) static temperature, (b) static pressure, (c) axial velocity, (d) absolute and relative velocity and (e) flow angles at the nozzle inlet, the nozzle outlet and the rotor outlet . From Ref. [211].

models such as flow turning, secondary flow effects and the presence of an unsteady stator-rotor interaction. The obtained value of stage efficiency can be related to the blade row parameters using approximate relations such as those proposed by Dixon and Hall [230]. In particular, at the nozzle outlet the higher value of absolute velocity in the experimental data for similar thermodynamic conditions suggests that the nozzle has a lower loss coefficient compared to the predicted results. At the same time, the higher value of the rotor loss coefficient computed from the measurements is responsible for the lower stage efficiency of the turbine.

The results of the validation of the single-stage axial turbine model with the fourth stage of the Hannover turbine suggest that TURAX is a reliable tool for performance prediction and preliminary design estimation since the maximum deviation obtained with the experimental data was $\pm 1.25\%$. This conclusion is further substantiated by the good agreement obtained in comparison with the average CFD data and the measurements.

Verneau turbine

The validation results for the ORC turbine investigated by Verneau [66] are shown in Figure 2.12. The nozzle and rotor outlet flow angles are predicted with excellent agreement while a good agreement is also achieved for the outlet velocities. The deviation in the predicted velocities influences the estimated value of the exit blade height, which, however, resulted only in a deviation of 0.3 mm. In this case of validation, the efficiency was compared in terms of total-to-static values

Table 2.3: Comparison between the predicted and measured quantities for the fourth stage of the Hannover turbine. From [211]. pp = percentage-points.

Parameter	Symbol	Units	Exp. data [246–248]	TURAX	CFD [274]	Error TURAX	Error CFD
Nozzle outlet absolute flow angle	α_2	°	69.84	68.55	68.45	1.29 °	1.39 °
Nozzle outlet relative flow angle	β_2	°	7.13	4.60	4.82	2.53 °	2.31 °
Nozzle outlet absolute velocity	C_2	-	170.8	150.8	153.84	11.8 %	9.95 %
Absolute Mach at nozzle outlet	M_2	-	0.457	0.406	0.412	11.2 %	9.9 %
Static pressure at nozzle outlet	p_2	bar	1.111	1.105	1.108	0.31 %	0.28 %
Static temperature at nozzle inlet	T_1	K	357.4	357.4	357.4	0.0 %	0.0 %
Static temperature at nozzle outlet	T_2	K	347.17	347.75	347.06	0.17 %	0.03 %
Rotor outlet relative flow angle	β_3	°	68.75	69.31	67.07	0.56 °	1.68 °
Rotor outlet absolute flow angle	α_3	°	2.45	5.91	7.58	3.46 °	5.13 °
Rotor outlet relative velocity	W_3	m/s	166.3	153.9	157.51	7.43 %	5.30 %
Static pressure at rotor outlet	p_3	bar	0.994	0.998	0.983	0.33 %	1.15 %
Static temperature at rotor outlet	T_3	K	337.86	337.96	336.60	0.03 %	0.37 %
Nozzle mean radius	r_{2m}	mm	181.5	180.1	181.5	0.77 %	0 %
Rotor mean radius	r_{3m}	mm	185	183.5	185	0.81 %	0 %
Nozzle inlet blade height	h_1	mm	89.2	89.2	89.2	0 %	0 %
Nozzle outlet (rotor inlet) blade height	h_2	mm	97	100.2	97	3.3 %	0 %
Rotor outlet blade height	h_3	mm	103	108.1	103	4.95 %	0 %
Nozzle flare angle	$\alpha_{FL,n}$	°	5.62	12.83	5.62	7.21 °	0 °
Rotor flare angle	$\alpha_{FL,r}$	°	7.89	12.04	7.89	4.15 °	0 °
Number of nozzle blades	z_n	-	29	28	29	1	0
Number of rotor blades	z_r	-	30	30	30	0	0
Nozzle kinetic energy loss coefficient	ζ_n	-	3.79 %	6.48 %	5.82 %	2.69 pp	2.03 pp
Rotor kinetic energy loss coefficient	ζ_r	-	9.08 %	6.76 %	6.66 %	2.32 pp	2.42 pp
Total-to-total stage efficiency	η_{tt}	-	91.62 %	92.84 %	93.32 %	1.22 pp	1.70 pp

defined as follows:

$$\eta_{ts} = \frac{h_{01} - h_{03}}{h_{01} - h_{3s}} \tag{2.9}$$

where h_{01} and h_{03} is the turbine inlet and outlet total enthalpies, and h_{3s} the turbine outlet static enthalpy following an isentropic expansion process. The value of η_{ts} predicted by TURAX was 64.3%, which deviates 1.3 %-points from the measured value. The rotor velocity coefficient is lower than the experimental one and indicates a higher relative contribution of the rotor losses. However, in absolute terms, the higher efficiency debit is calculated in the nozzle and is due to the higher value of kinetic energy at the outlet. The breakdown of the losses in the turbine is depicted in Figure 2.12. The nozzle blades feature a converging-diverging shape, and the profile losses are comparatively small. The first source of performance degradation in the stage are the nozzle secondary losses, which amount to 7.7 %-points of efficiency debit. These losses increase with the inlet to outlet velocity ratio and with the inverse of the aspect ratio (blade height over backbone length). In this case, the nozzle has a very small value of velocity ratio, approximately 0.04, and therefore the large secondary losses originate from the small nozzle aspect ratio, approximately 0.27, which produces strong secondary flows in the blade row. The highly supersonic flow conditions at the nozzle exit, characterized by an outlet Mach number of 1.76, suggest the presence of shock waves in the nozzle-rotor interspace which should involve additional losses, referred here as supersonic expansion losses. On the other hand, the rotor inlet features transonic flow conditions with a relative

Table 2.4: Comparison of results between TURAX and Verneau data [66]. pp = percentage-points. From Ref. [211].

Parameter	Symbol	Units	Verneau	TURAX	Err. (%)
Nozzle outlet flow angle	α_2	°	74.00	74.00	0 °
Absolute Mach at nozzle inlet	M_1	-	-	0.08	-
Axial Mach at nozzle outlet	M_{a2}	-	0.47	0.49	4.41 %
Absolute Mach at nozzle outlet	M_2	-	1.76	1.78	1.14 %
Nozzle velocity coefficient	C_2/C_{2s}	-	-	0.94	-
Rotor outlet relative flow angle	β_3	°	65.40	65.47	0.07 °
Relative Mach at rotor inlet	M_{W2}	-	1.13	1.12	0.76 %
Axial Mach at rotor outlet	M_{a3}	-	0.360	0.366	1.77 %
Relative Mach at rotor outlet	M_{W3}	-	0.880	0.883	0.34 %
Axial Mach numbers ratio	-	-	0.77	0.75	2.76 %
Rotor velocity coefficient	W_3/W_{3s}	-	-	0.73	-
Degree of reaction	χ	-	< 0	-0.3	-
Nozzle mean radius	r_{2m}	mm	48.0	47.6	1.01 %
Rotor mean radius	r_{3m}	mm	47.2	47.1	0.13 %
Nozzle inlet blade height	h_1	mm	3.37	3.37	0 %
Nozzle outlet blade height	h_{21}	mm	3.37	3.6	5.56 %
Rotor inlet blade height	h_2	mm	3.5	3.8	7.89 %
Rotor outlet blade height	h_3	mm	5.2	5.2	0 %
Nozzle flare angle	$\alpha_{FL,n}$	°	0	0.48	0.48 °
Upper rotor flare angle	$\alpha_{FL,ru}$	°	-0.18	1.17	1.35 °
Lower rotor flare angle	$\alpha_{FL,rl}$	°	8.06	5.33	2.73 °
Number of nozzle blades	z_n	-	22	23	1
Number of rotor blades	z_r	-	72	72	0
Total-to-static stage efficiency	η_{ts}	%	63	64.3	1.29 pp
Power output	$\dot{W}$	kW	3	3.22	7.1 %

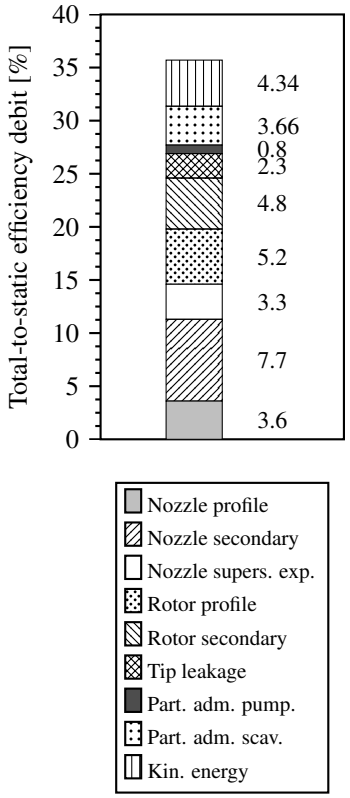

Figure 2.12: Comparison of results between TURAX and Verneau data [66]. pp = percentage-points. The breakdown of losses is shown in the chart.

Mach number of approximately 1.13. The profile losses in the rotor increase as the high value of the Mach number produces other shock waves in correspondence of the blades leading edge. The very high velocity ratio (above 1) and the very low aspect ratio in the rotor significantly affect the rotor secondary losses. Additional losses are also produced by the high value of rotor exit kinetic energy, which amounts to approximately 4.3 %-points of efficiency debit. The tip leakage losses in the rotor represent a small contribution in this case since the pressure drop across the rotor is small due to the low stage degree of reaction. The partial admission losses represent a significant contribution to the overall losses, and they have a similar magnitude as the kinetic energy losses. These losses are mainly due to the waste of energy due to the filling of inactive passages in the blade rows, denoted with the term scavenging losses. Finally, the deviation in terms of turbine power output between TURAX and the experimental results is 7.1 %, which corresponds to 0.22 kW.

2.3.2 Sensitivity analysis

The results of the application of the sensitivity analysis using Morris screening method are presented in Figure 2.13. The two black lines are drawn in the chart and connect standard error and deviation

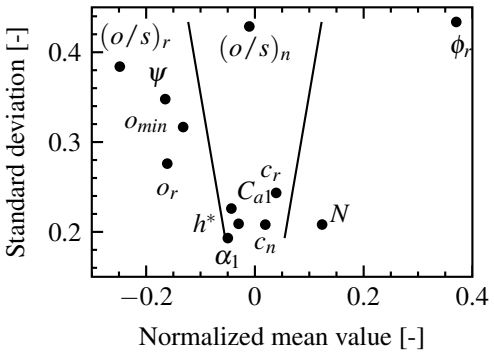

Parameter	Unit	Symbol	Signif.
1) Stage inlet flow angle	°	α_1	no
2) Stage loading coefficient	-	ψ	yes
3) Nozzle minimum opening	m	o_{min}	yes
4) Rotor opening	m	o_r	yes
5) Nozzle axial chord	m	c_n	no
6) Rotor axial chord	m	c_r	no
7) Nozzle opening-to-pitch ratio	-	$(o/s)_n$	no
8) Rotor opening-to-pitch ratio	-	$(o/s)_r$	yes
9) Rotational speed	rpm	N	yes
10) Stage inlet axial velocity	m/s	C_{a1}	no
11) Rotor flow coefficient	-	ϕ_R	yes
12) Rotor inlet to nozzle outlet blade height	-	h^*	no

Figure 2.13: Sensitivity analysis and significance of decision variables of the axial turbine model. Morris screening method [261] applied to the Hannover turbine test case. From Ref. [211].

for each decision variable. The chart is to be interpreted in the following way [261]: 1) a significant contribution to the change of turbine efficiency for a decision variable is represented by a large deviation in the mean value; 2) non-linear effects and/or interactions among different variables are indicated by a high value of standard deviation; 3) a variable whose contribution to the efficiency is less significant compared the other variables appears inside the wedge formed by the two black lines. In this case, the variable can be removed from the list of model input parameters. The results of the sensitivity analysis are also indicated in the table of Figure 2.13. The Morris plot suggests that all the parameters are interdependent as they show non-zero values of standard deviation. To make a definitive conclusion on the significance of a single decision variable and decide whether to keep it or discard it, the relevance from both the results of the Morris plot and the design viewpoint is considered. The following list summarizes the findings of the sensitivity analysis considering the aspects above:

- ψ, o_{min}, o_r, $(o/s)_r$, N, ϕ_r are outside the wedge in the Morris plot, and they are strictly connected to the turbine design characteristics. Consequently, they are considered as important parameters in the study.
- The nozzle opening-to-pitch $(o/s)_n$ is a less significant decision variable according to the Morris chart. At the same time, it shows a strong interdependency with the other decision variables due to the high value of standard deviation. From the design viewpoint, this variable is paramount to compute the exit flow angle in the nozzle blade row and allows estimating the pitch and number of blades. For these reasons, this parameter is not discarded.
- The stage inlet axial velocity C_{a1} is within the wedge of the Morris plot and, therefore, provides a less significant contribution ion the turbine efficiency compared to the other variables. However, the value of C_{a1} is important from the design point of view as it determines the actual nozzle blade height at the inlet. This aspect is especially relevant from the technical viewpoint and becomes a key factor in the design and manufacturing of small-scale turbines [224]. Therefore, this parameter was not excluded from the list of necessary design input parameters.
- The decision variable c_n and c_r represent the nozzle and rotor axial chord and are considered

as less significant parameters from the Morris screening method. However, they are related to the values of the flaring angles in the stage, which represent an important constraint during the optimization of the design of the stage and allow enlarging the space for the possible design solutions. Moreover, they can be relevant in application where the turbine size is an important criterion as they directly relate to the turbine length in the axial direction. For these reasons, these two parameters are not discarded.

- The stage inlet flow angle α_1 is a less significant parameter in the Morris plot. This decision variable can also be fixed from the design viewpoint by assuming that the flow at the design point enters completely in the axial direction.
- Finally, the decision variable h^*, which represents the ratio between rotor inlet and nozzle outlet blade heights, is also a less significant variable according to the Morris chart. The parameter h^* is associated with the tip clearance and annulus losses in the performance prediction method by Craig and Cox [222] and used in TURAX. However, this decision variable shows a limited impact on the turbine design and the efficiency since it is bound to the small range 1.0 to 1.1 by typical design constraints [222]. Consequently, it was removed from the initial list of input parameters.

2.3.3 Validation of multistage turbine model

Four-stage subsonic turbine

The validation results of the multistage turbine model with the four-stage Hannover turbine are shown in Table 2.5. The deviation between the numerical and experimental values is expressed by Eq. 2.7. The CFD data by Gerolymos et al. [252] and Croce et al. [253] are used in Eq. 2.7 in place of the experimental data in case the latter are unavailable or uncertain. The comparison in terms of angle is expressed as the absolute difference between two values.

Good agreement is found in terms of total temperature and pressure at the outlet of the stages and with both experimental and CFD data, with a deviation up to 0.5 %. The static pressure at the outlet of the stages has a deviation up to 1.7 %. The comparison of the velocities is performed with respect to CFD results, given the lack of similar reliable data in the measurements. A maximum deviation of 3.5 % in the absolute velocity C_3 with the CFD data [253] is probably related to the discrepancy in the static pressure. The measured data for the rotor outlet relative flow angle β_3 were not available in the original references; however, a deviation within 3° is suggested by comparison with the available CFD data by Gerolymos et al. [252]. A higher deviation with the measured data, up to 8°, is found for the absolute flow angle at the nozzle outlet α_3, and it is associated with the discrepancy in the values of C_3. A comparison of the profiles of total temperature, total pressure, absolute flow angle and velocity at the exit of each stage is shown in Figure 2.14. The experimental results show a higher discrepancy with the numerical profiles; however, TURAX and CFD achieve a reasonable match in most cases. The design geometry predicted by TURAX in the meridional plane is represented in Figure 2.15. The small deviation for the velocities and the thermodynamic quantities results in a close match for the blade heights, with a deviation within 3 %. The total-to-total efficiency was predicted to be within 0.2 %-points with respect to CFD data and within 1.72 %-points with respect to the experimental values. Finally, the validation results are satisfactory and suggest that TURAX is suitable for the preliminary estimation of the performance

Table 2.5: Comparison between numerical and experimental results [247, 248] for the four-stage Hannover turbine. From Ref. [72].

Symbol	Units	Exp. data	TURAX	CFD	Dev.	Exp. data	TURAX	CFD	Dev.
		Stage 1				Stage 2			
T_{03}	K	384.81	384.60	382.72$^{(*)}$	0.05%	363.12	363.43	362.13$^{(*)}$	-0.09%
p_{03}	Pa	$2.12{\cdot}10^5$	$2.11{\cdot}10^5$	$2.09{\cdot}10^5$ $^{(*)}$	0.32%	$1.70{\cdot}10^5$	$1.70{\cdot}10^5$	$1.69{\cdot}10^5$ $^{(*)}$	-0.02%
p_3	Pa	$2.07{\cdot}10^5$	$2.08{\cdot}10^5$		-0.62%	$1.66{\cdot}10^5$	$1.67{\cdot}10^5$		-0.91%
C_3	m/s	73.33	57.96	59.78$^{(**)}$	3.05%	73.0	60.02	60.19$^{(**)}$	0.28%
β_3			65.93	65.85$^{(**)}$	0.08		66.62	66.97$^{(**)}$	-0.35
α_3		0.62	-3.47	4.65$^{(*)}$	4.10	-4.76	2.30	6.67$^{(*)}$	-7.06
$h1$	m	0.0595	0.0594		0.17%	0.0675	0.0682		-1.04%
h_{21}	m	0.0635	0.0635		0.00%	0.0725	0.0736		-1.52%
h_3	m	0.0675	0.0682		-1.04%	0.0775	0.0766		1.16%
DR	-		0.347	n.a.			0.4269		
η_{st}	-	89.91%	91.49%	91.45%$^{(*)}$	0.0%	92.52%	92.22%	92.10%$^{(*)}$	0.1%
		Stage 3				Stage 4			
T_{03}	K	340.377	341.95	341.40$^{(*)}$	-0.46%	321.034	320.23	319.57$^{(*)}$	0.25%
p_{03}	Pa	$1.35{\cdot}10^5$	$1.35{\cdot}10^5$	$1.36{\cdot}10^5$ $^{(**)}$	-0.18%	$1.05{\cdot}10^5$	$1.05{\cdot}10^5$	$1.05{\cdot}10^5$ $^{(*)}$	-0.17%
p_3	Pa	$1.31{\cdot}10^5$	$1.32{\cdot}10^5$		-1.06%	$1.01{\cdot}10^5$	$1.03{\cdot}10^5$		-1.70%
C_3	m/s	73.193	60.79	60.33$^{(**)}$	-0.77%	81.401	62.04	64.30$^{(**)}$	3.52%
β_3			67.40	67.04$^{(**)}$	0.36		68.28	65.22$^{(**)}$	3.06
α_3		-2.159	4.39	4.70$^{(*)}$	6.55	-0.608	7.35	-0.57 $^{(*)}$	-7.96
$h1$	m	0.0775	0.0767		1.03%	0.0892	0.0885		0.78%
h_{21}	m	0.0833	0.0846		-1.50%	0.0961	0.0988		-2.81%
h_3	m	0.0892	0.0885		0.78%	0.1030	0.1026		0.39%
DR	-		0.47				0.54		
η_{st}	-	n/a	92.55%	92.80%$^{(*)}$	0.2%	n/a	92.94%	92.73%$^{(**)}$	0.2%
η_{tt}	-	91.3 %	93.02 %	92.96 %	1.72 pp				

$^{(*)}$ = Gerolymos et al. [252]. $^{(**)}$ = Croce et al. [253]. pp = percentage-points. n/a = not available.

and geometry at the design point considering multistage turbines with subsonic conditions and blades with a high aspect ratio.

Two-stage supersonic ORC turbine

The validation results for the two-stage supersonic ORC turbine described by Verneau [66, 257] are provided in Table 2.6.

A good agreement is found by comparing the thermodynamic quantities in both stages. A maximum deviation of 3 % is computed for the first stage whereas a maximum deviation of 8.5 % for the second stage. A deviation up to 6.3 % is found in terms of static pressure and absolute Mach number for the exit of the first and the second stage. This number is likely to be associated with the deviation in the values of velocity. The turbine meridional geometry predicted by TURAX is shown in Figure 2.15 in red whereas the original geometry [66] is depicted in black. The values of blade height at inlet and outlet of each stage and the number of blades are within 3 % deviation; however, the discrepancy increases at the outlet of the second stage where the deviation is up to 5.6 %. The overall turbine total-total-efficiency was overpredicted by 1.76 %-points with TURAX

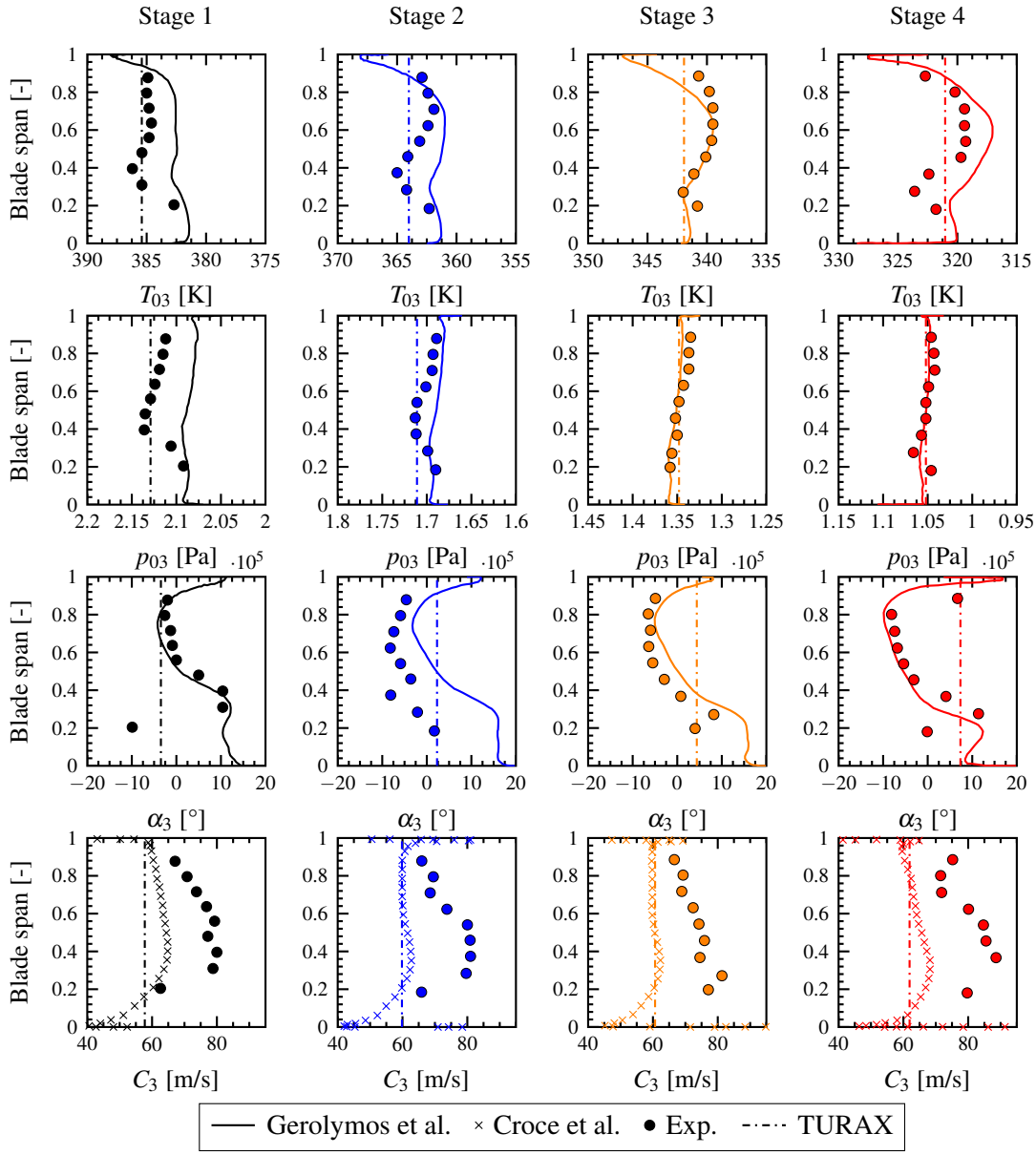

Figure 2.14: Profiles of total temperature, total pressure, absolute flow angle, absolute velocity at the stage outlet. Data from experimental results [248], Gerolymos et al. [252], Croce at al. [253] and TURAX for the Hannover turbine test case [72].

compared to the measured values of Verneau.

The results of the uncertainty analysis using the Monte Carlo method are shown in Figure 2.16. The most influential parameters in terms of the output turbine efficiency are the opening-to-pitch ratios in the second stage and that in the nozzle of the first stage. These parameters are responsible for the estimation of the exit flow angle in the blade rows. The other parameters such as the tip clearance, trailing edge thickness-to-opening ratios are less significant to the output efficiency and provided only a marginal change in efficiency. Considering the complexity of modeling the two-stage

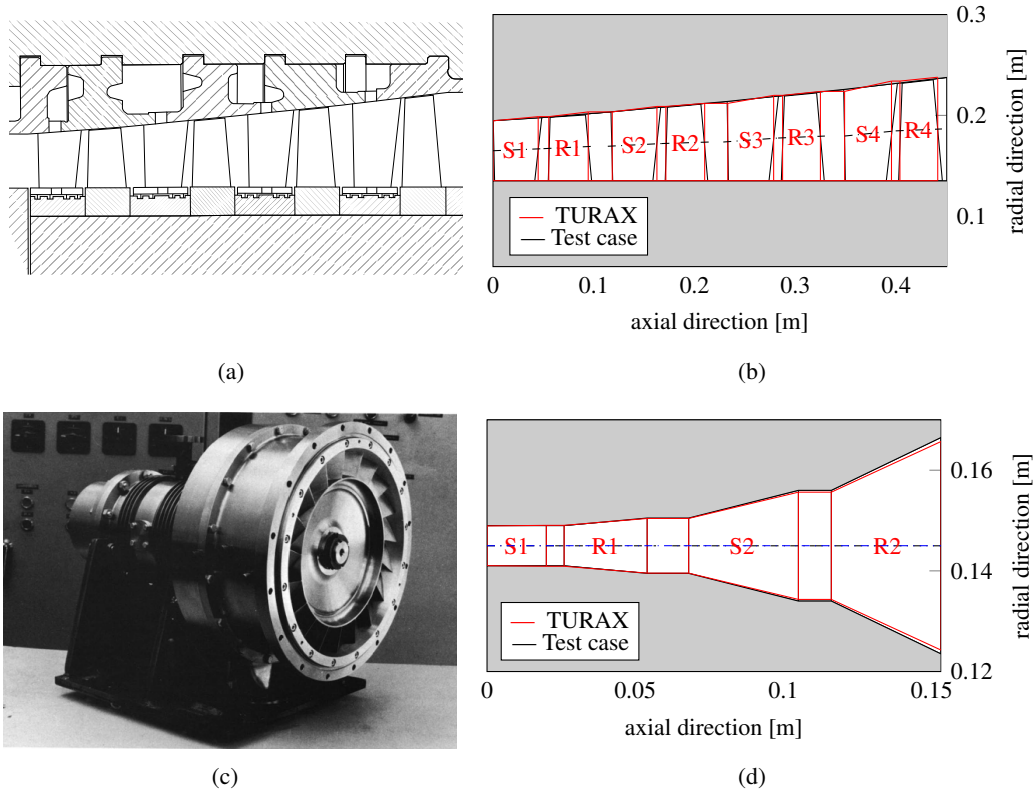

Figure 2.15: (a) Four-stage subsonic Hannover turbine test case (adapted from [248]); (b) meridional cut layout of the four-stage Hannover turbine; (c) two-stage supersonic ORC turbine test case [258]; (d) meridional cut layout of the two-stage supersonic ORC turbine. From Ref. [72].

supersonic turbine accurately with an organic fluid, the achieved deviation within 2 %-points is considered as a satisfactory result and suggests that TURAX can also be considered validated in the multistage layout.

2.3.4 Optimization of single-stage turbines

Thermodynamic Cycle Design

Figure 2.17 illustrates the change of the two-phase envelope in the entropy-temperature diagram with the molar composition for the two considered mixtures.

Constrained Hot Fluid Outlet Temperature Figures 2.18(a) and 2.18(b) illustrate the results of the optimization for the single-stage turbine considering a limit on the hot fluid outlet temperature. The maximum net power output is achieved using pure fluids and is primarily governed by the trend in the cycle rather than that of the turbine. The maximum turbine efficiency is obtained

Table 2.6: Comparison of results between TURAX and Verneau [66, 257] data on a two-stage ORC turbine. From Ref. [72].

		Stage 1				Stage 2			
Parameter	Units	Verneau	TURAX	St.dev.	Dev.	Verneau	TURAX	St.dev.	Dev.
α_2	°	74	73.99	0.95	0.00	60	58.87	2.44	1.12
β_2	°	59.20	59.55	1.56	0.36	-33	-29.24	8.54	3.75
Ca_2	m/s	65	65.46	4.11	0.7%	49	53.16	7.72	8.5%
C_2	m/s	235	237.41	1.39	1.0%	98	102.56	9.42	4.7%
W_2	m/s	126	129.15	2.2	2.5%	58.5	61.38	4.9	5.0%
M_2	-	2.45	2.48	0.014	2.5%	1.02	1.06	0.1	4.9%
M_{w2}	-	1.32	1.35	0.02	2.4%	0.61	0.64	0.05	5.0%
p_2	Pa	$3.08{\cdot}10^4$ (*)	$3.00{\cdot}10^4$	996	-2.9%	15292	$1.43{\cdot}10^4$	1650	-6.3%
T_2	K	459.40 (*)	458.79	0.25	-0.1%	457.15	457.14	0.74	-0.1%
W_3	m/s	130	127.76	0	-1.7%	118	116.57	6.76	-1.2%
Ca_3	m/s	71	70.14	0	-1.2%	49	49.1	0	0.2%
C_3	m/s	72	70.87	0	-1.6%	49	50.89	1.64	3.9%
M_{w3}	-	1.35	1.33	0	-1.3%	1.24	1.22	0.07	-1.7%
M_3	-	0.75	0.74	0	-1.5%	0.51	0.53	0.02	3.8%
β_3	°	56.7	56.7	0	0.00	65	65	1.55	-0.01
α_3	°	-6.8	-8.21	0	-1.41	-10	-12.62	8.22	-2.62
T_{03}	K	461.23 (*)	460.78	0.06	-0.1%	454.11	454.38	0.1	0.1%
T_3	K	459.77 (*)	458.86	0.06	-0.2%	453.2	453.4	0.09	0.0%
p_3	Pa	$2.24 \cdot 10^4$	$2.1 \cdot 10^4$	0.74	-6.3%	7900	$7.78{\cdot}10^3$	72.1	-1.5%
p_{03}	Pa	$2.76{\cdot}10^4$ (*)	$2.77{\cdot}10^4$	0	0.1%	9021.9	$8.98{\cdot}10^4$	0	-0.5%
h_1	m	0.008	0.0079	0	1.3%	0.011	0.0109	0	1.2%
h_2	m	0.008	0.0082	0	-2.1%	0.022	0.0214	0.001	2.8%
h_3	m	0.011	0.0109	0	1.3%	0.043	0.0415	0	3.4%
z_n	-	25	27	1	2.00	30	30	2	0.46
z_r	-	121	122	0	1	19	20	1	1
DR (theor.)	-	0.086	0.093	0.009	0.01	0.50	0.47	0.09	-0.03
Power	kW	40	40.78	0.089	-2.0%	14	14.28	0.14	-2.0%
η_{st}	-	75 %	73.21 %	0.29 pp	1.8 pp	82 %	80.96 %	1.25 pp	1 pp
η_t	-	78 %	79.72 %	0.40 pp	1.76 pp				

(*) = computed from the design point velocity triangles. St.dev. = standard deviation from the uncertainty analysis. pp = percentage-points.

for pure R245fa and isobutane for the two mixtures R245fa/pentane and propane/isobutane. The optimal turbine efficiency is aligned with the trend of the cycle except for the binary mixture R245fa/pentane in the molar composition range (0/1) to (0.5/0.5). Although propane/isobutane has a larger change in turbine efficiency across the entire molar composition range, the cycle net power output remains approximately constant. The optimal results are given by pure R245fa and pentane with similar values of net power output and turbine efficiency of approximately 200 kW and an efficiency of 0.88. The optimal results also yield a ratio of total UA-value ratio between boiler and condenser of about 0.5 for all cases.

Unconstrained Hot Fluid Outlet Temperature. Figures 2.18(c) and 2.18(d) show the results of the optimization for the case where the hot fluid outlet temperature is not constrained. In this case the mixture R245fa/pentane with molar composition (0.5/0.5) and the propane/isobutane mixture with composition (0.2/0.8) yield the maximum net power output. Concurrently, the maximum turbine efficiency for both binary mixtures is provided by the pure fluids. Figure 2.18(d) indicates that the

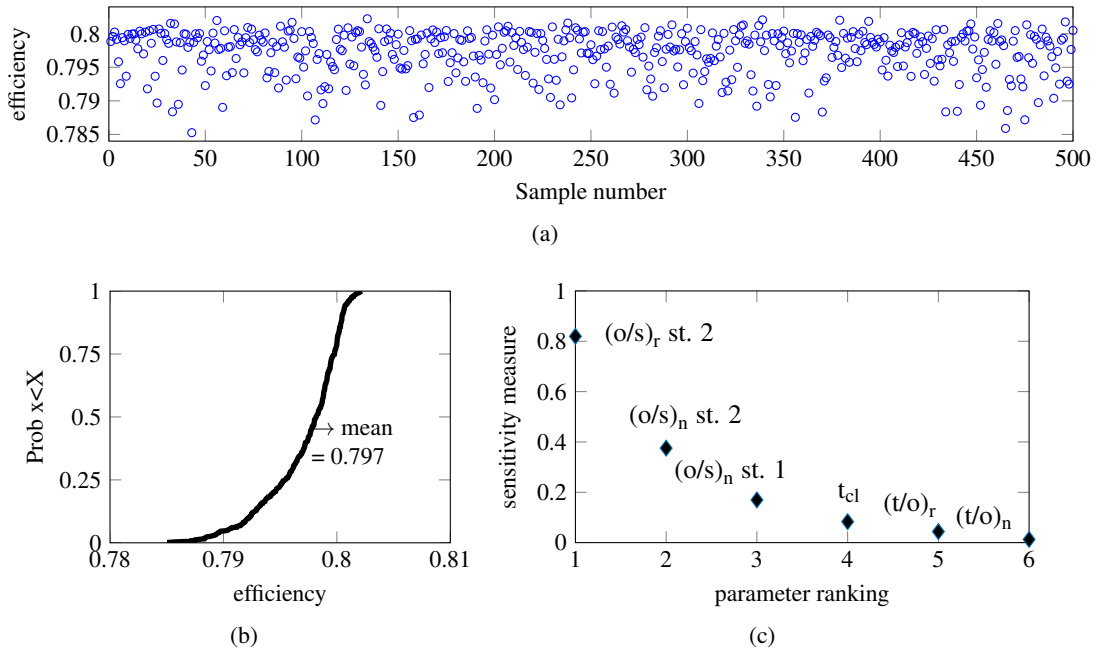

Figure 2.16: Results of the uncertainty analysis on the assumed parameters of the two-stage supersonic turbine: (a) scatterplot of uncertainty in turbine efficiency; (b) corresponding cumulative distribution function; (c) ranking of the uncertain parameters based on significance level. From Ref. [72].

use of a constant turbine efficiency not only changes the maximum net power output, but it also shifts the location of the optimal mixture composition from about (0.2/0.8) to (0.4/0.6). Conversely, in the case of the mixture R245fa/pentane the assumption of a constant turbine efficiency provides different values of net power output but does not change the location of the optimal composition since the optimal efficiency is nearly constant over the entire molar composition range. The optimal UA-ratio resulted in being 0.5 when the output temperature of the hot fluid is not constrained. The results for both cases suggest that the use of binary mixtures is more favorable when the heat source temperature is not constrained by a lower limit, and the heat source realizes a larger temperature difference. Figures 2.19(a) and 2.19(b) show the temperature-thermal power diagram for the mixture R245fa/pentane. When the hot fluid temperature difference is small, from 85 °C to 80 °C in Figure 2.19(a), pure fluids are the best solution as they can provide the best match between the heat source profile (in red) and that of the working fluid (in black). On the other hand, Figure 2.19(b) shows that when a lower limit does not constrain the outlet temperature of the hot fluid, which varies in the range 85 °C to 72 °C, the profiles are better matched by exploiting the temperature glide of a mixture of two fluids.

As a result, the optimal net power output profile is affected by that of the temperature glide. Figure 2.20 shows the optimal trends of the hot fluid temperature difference ΔT_{hf}, the working fluid temperature glide in the boiler, and the superheating degree. The maximum net power output obtained in Figure 2.18(c) occurs when ΔT_{hf} matches the temperature glide of the working fluid. Consequently, peaks of net power output are observed at molar composition (0.1/0.9), (0.4/0.6) and (0.5/0.5). When the hot fluid outlet temperature is constrained, and the ΔT_{hf} is lower, the

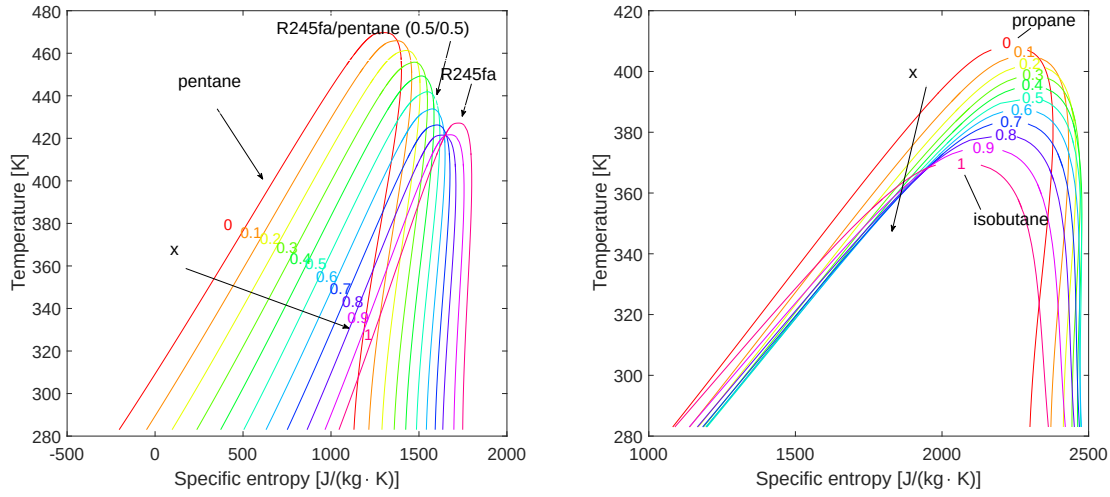

(a) (b)

Figure 2.17: Specific entropy-temperature diagram for the following binary mixtures in the molar composition range 0.0 to 1.0: (a) R45fa/pentane and (b) propane/isobutane.

temperature glide is better matched at high or low values of the molar composition, indicating that it has a detrimental effect on the net power output and hence the pure fluids result to be the preferred choice. The fluids R245fa and the binary mixture (0.5/0.5) R245fa/pentane yield the maximum values of net power output. In a real application, also other factors need to be considered when selecting the most suitable working fluids such as technical aspects, environmental and safety issues, turbine design and manufacturability aspects, and economic criteria [54, 234]. The best designs obtained from the combined optimization are detailed in Table 2.7. Regarding the heat exchangers, pure isobutane shows a higher condensing pressure and a lower volume flow rate, suggesting the use of a more compact condenser than pure R245fa. When the hot fluid outlet temperature is unconstrained, the mixture propane/isobutane (0.2/0.8) shows higher condensing and evaporating pressure and almost half of the volumetric flow rate of the mixture R245fa/pentane (0.5/0.5), thereby suggesting the use of smaller condenser than R245fa/pentane (0.5/0.5).

Preliminary Turbine Design

In terms of turbine performance, pure fluids always resulted in the highest isentropic efficiency. In particular, the fluid R245fa/pentane resulted in a nearly flat trend of the efficiency across the entire composition range whereas the fluid propane/isobutane showed a variation of approximately 8 %-points in the molar composition range. The change can be explained in light of the breakdown of losses in the turbine for each value of molar composition shown in Figure 2.21(a) for the case with hot fluid outlet temperature limit. The mixture R45fa/pentane has lower losses than propane/isobutane, and they do not exhibit a significant change in the molar composition range. Figure 2.21(a) indicates that the loss contributions providing a change in the efficiency of propane/isobutane are mostly due to secondary flows and tip leakage effects. These effects are governed by design values of the nozzle and rotor blade heights. Figure 2.21(b) depicts the variation of the turbine

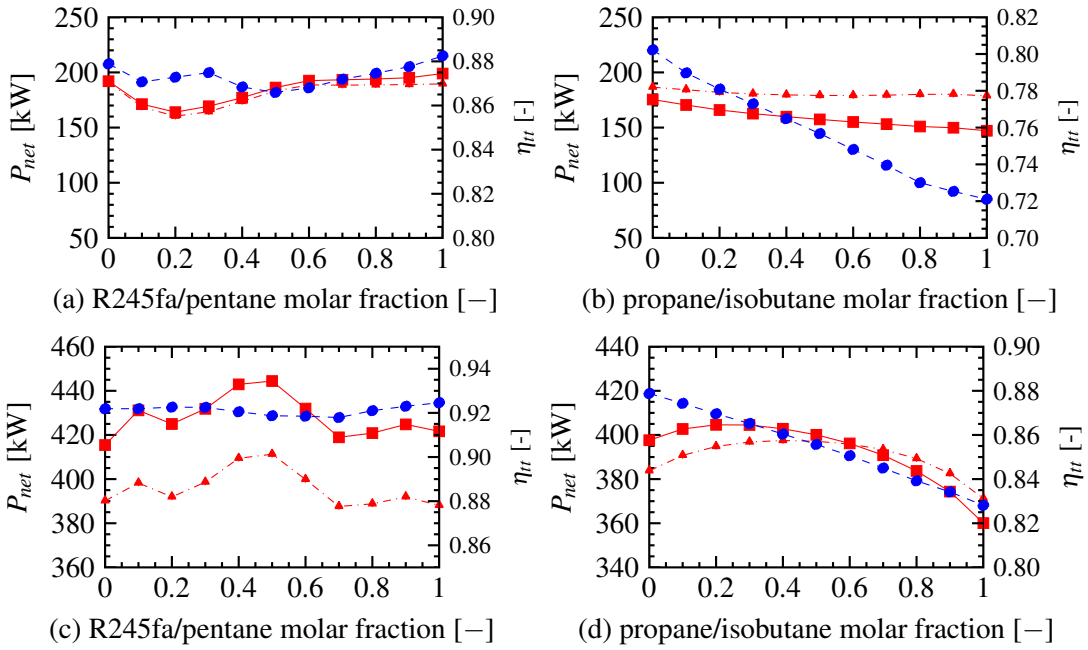

Figure 2.18: Optimal power output for the optimal cycle and constant η_{tt} (▲), for the optimal cycle and optimal η_{tt} (■), and the optimal total-to-total turbine efficiency (●) vs. molar composition of the selected mixtures. Heat source with (a,b) and without (c,d) limitation on the heat source outlet temperature. Adapted From Ref. [215].

blades aspect ratio (height over backbone length) and shows that much lower values are achieved for propane/isobutane. Low values of aspect ratio increase the generation of secondary flows in the blade channels, leading to high values of secondary losses. At the same time, a small blade height results in a higher tip clearance to throat area ratio, which in turn yields high values of tip clearance losses. Although the trend of the aspect ratio for R245fa/pentane of Figure 2.21(b) is non-monotonic, its change across the entire molar composition range is only marginal to the increase of secondary and tip clearance losses, hence showing an almost flat efficiency profile for the mixture R245fa/pentane. Another way to explain the different values of efficiency for the two mixtures is by resorting to the volume flow rate ratio (VFR) and size parameter (SP) which were proposed by Macchi and Perdichizzi [58] as key parameters to describe the performance of axial flow turbines. The VFR inherently expresses the compressibility effects of the working fluid while SP is a measure of the turbine dimensions. If the turbine has a high VFR, low efficiency is obtained due to the high flow deflection in blade passages and the high Mach numbers. On the other hand, a small SP results in a low turbine performance since the small size increases tip clearance losses and secondary flow effects. Similar values of VFR in the range 2 to 3 are observed for both mixtures in Figure 2.21(c); however, significantly different values of SP are obtained (2-4 cm for propane/isobutane vs. 7-10 cm for R245fa/pentane). This explains the lower values of efficiency for the propane/isobutane mixture compared to R245fa/pentane, whose values of VFR and SP in the molar composition range do not significantly affect the losses.

Regarding the technical feasibility of turbine preliminary design, the following aspects are consid-

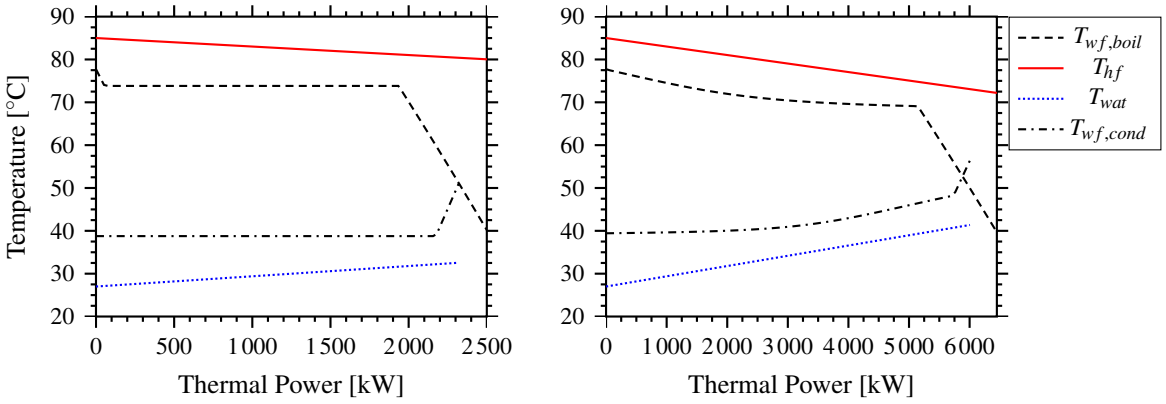

(a) R245fa/pentane (1/0). Temperature constraint (b) R245fa/pentane (0.5/0.5). No temperature constraint

Figure 2.19: Temperature-thermal power diagram for the optimal R245fa/pentane mixture with and without outlet temperature limit. From Ref. [215].

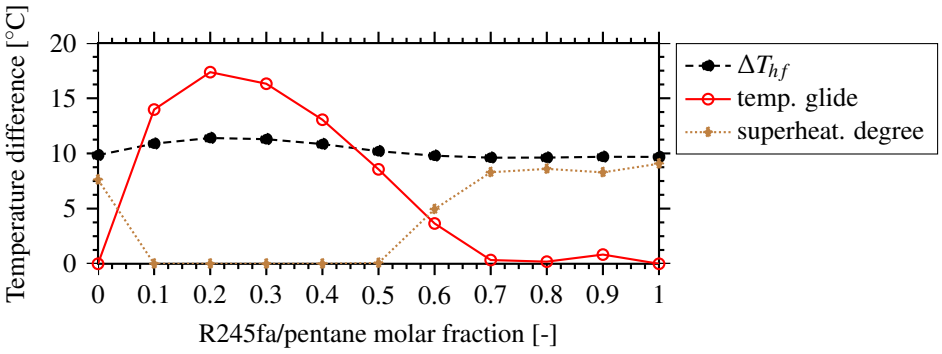

Figure 2.20: Hot fluid, working fluid temperature glide and superheating in the evaporator. No temperature constraint. From Ref. [215].

ered:

1) All fluid candidates feature a single-stage solution, whose technical feasibility is substantiated by the values of VFR and SP which suggest high values of turbine efficiency [58].

2) It is possible to manufacture the blade heights of the nozzle and the rotor in all cases. The shortest blade is found for pure propane in the case of constrained hot fluid outlet temperature and is 5.6 mm. This value is well within the range of typical blade heights for small-scale axial flow turbines (1.5 mm to 6.5 mm) documented in the literature [66, 242, 275].

3) Nozzle and rotor blades can be manufactured using untwisted profiles since the hub-to-tip radius ratios are higher than 0.9, and radial effects will not have significant effects in the turbine fluid dynamics [223].

4) The final turbine designs feature mean diameters in the range 479 mm to 657 mm and a relatively short length in the axial direction, in the range 25 mm to 35 mm, due to the short

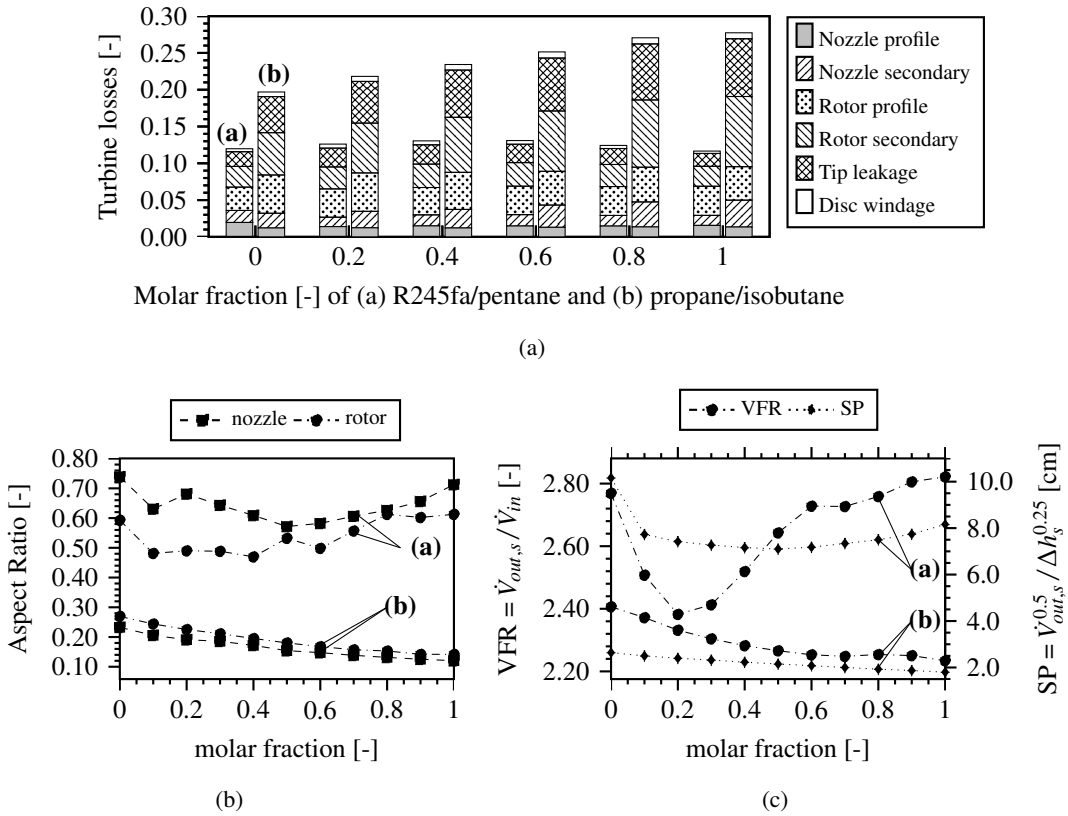

Figure 2.21: Breakdown of losses in terms of (a) turbine efficiency debit; (b) aspect ratio; (c) volume flow rate (VFR) and size parameter (SP). In the figure, the two mixtures are (a) R245fa/pentane and (b) propane/isobutane at their optimal molar compositions and for the cases with and without outlet temperature limit, respectively. Adapted from Ref. [215].

axial chords.

5) The optimal number of nozzle and rotor blades resulted in being in the range 120 to 130 and is within the expected range of values found in the ORC turbine investigated in the literature [66, 276].

6) Due to the low values of exit Mach number, nozzle and rotor blades feature converging blade profiles. With this type of blades, a post-expansion downstream the throat until Mach number of 1.4 can be used at off-design conditions to provide a further expansion.

7) The turbine design features a high degree of reaction, between 0.55 and 0.76. A low-reaction design would provide high stage loading, rotor blades with good mechanical resistance, less thrust on the rotor and lower tip leakage flow [277]. Low reaction designs would yield highly cambered rotor blades, featuring a strong boundary layer separation and a corresponding penalty in efficiency. High reaction designs would result in high tip leakage flows in the rotor, produce a high axial thrust on the rotor, may increase the mechanical losses and require special care in the design of bearings. As an advantage, the high reaction blade profiles feature low Mach numbers, good performance at off-design conditions and avoid to employ

an expensive diaphragm in the nozzle due to its low pressure drop [278]. Moreover, if 50 % reaction blades are adopted, cost reductions and ease of manufacturing are expected as similar blade profiles can be used for both the nozzle and the rotor.

8) Table 2.7 shows that there is an appreciable difference between total-to-total and total-to-static values of isentropic turbine efficiency, indicating that high kinetic energy losses are present at the turbine discharge. For this reason, in this study, it is assumed that such kinetic energy can be recovered using a diffuser downstream the turbine stage and before entering the condenser.

9) The final designs feature high values of turbine efficiency, and therefore the insertion of a gearbox can be conveniently avoided. However, it may be considered only if a further reduction in turbine mean diameter and size are required.

Regarding the turbine design, pure R45fa resulted to be the best fluid for the case with constrained hot fluid outlet temperature since it yields the smallest turbine size and volume, a lower number of blades and higher blade heights compared pure pentane. In the case of unconstrained temperature at the outlet of the hot fluid, the mixture R245fa/pentane (0.5/0.5) resulted in the best values of turbine efficiency and the lowest values of pressure in the heat exchangers. In this respect, the turbine size is 60 % bigger than the optimal propane/isobutane mixture; however, the larger net power output of the cycle might justify the higher turbine cost.

2.3.5 Optimization of multistage turbines

The list of preselected working fluids for the test case of the waste heat recovery from a 37 MW marine diesel engine is shown in Table 2.8. This case study considers multistage turbine configurations, has a heat source temperature of 235 °C and only pure working fluids are considered.

The optimum net power output for the different fluids is shown in Figures 2.22(c-d) while the turbine efficiency and the number of stages are shown in Figures 2.24, respectively. Both the conservative and the advanced design approaches are compared in the figures.

The application of the methodology presented in this chapter resulted in unfeasible single- and two-stage turbine designs for the fluid MM. Three stages are required to achieve a feasible solution with this fluid following the advanced design approach while five stages are required in the conservative design approach. In terms of net power output, the working fluid n-butane has the highest ranking and is followed by R245fa, isopentane, and n-pentane. When the rotational speed is not optimized and is set to a fixed value, a reduction in the power output is observed since the rotational speed is not at the optimal value to minimize the turbine losses. The fluid R245fa has a lower optimal rotational speed than n-butane (approximately 7200 rpm), and consequently yield the highest performance. Using a conservative design approach, all the solutions require two or three stages and feature values of isentropic efficiency in the range 85 % to 93 %. In the case of the fluid MM, a solution with two or three stages using the conservative design approach could not be found due to the excessive values of the flaring angles and the Mach numbers found in the blade rows. There is not a significant change in the required number of stages for optimized or constant rotational speed, although a lower number of stages is required of n-pentane and n-butane as they are running

Table 2.7: Optimal turbine and cycle design parameters. From Ref. [215].

		R245fa/pentane		propane/isobut.	
Parameter	Unit	Temp. limit	No limit	Temp. limit	No limit
Cycle					
Optimal molar composition	-	(1/0)	(0.5/0.5)	(0/1)	(0.2/0.8)
Mass flow rate, $\dot{m}$	kg/s	11.98	24.75	6.92	16.99
Turbine outlet pressure, P_{cond}	bar	2.40	2.80	5.13	6.73
Turbine inlet pressure, P_{boil}	bar	6.74	6.41	11.83	13.40
Turbine inlet temperature, T_{in}	K	350.46	351.13	350.80	353.79
Cycle net power output, P_{net}	kW	198.97	444.43	175.43	404.59
Boiler UA-value, $(UA)_{boil}$	W/K	250	750	250	750
Max. condenser volume flow	m^3/s	0.93	2.17	0.56	1.09
Max. boiler volume flow	m^3/s	0.009	0.027	0.013	0.032
Turbine					
Isentropic efficiency (t-t), η_{tt}	%	88.00	91.87	80.22	87.43
Isentropic efficiency (t-s), η_{ts}	%	73.56	82.98	60.52	67.87
Stage loading coefficient, ψ	-	4.15	3.27	4.85	4.74
Rotor flow coefficient, ϕ_r	-	0.50	0.44	0.54	0.49
Degree of reaction, χ	-	0.66	0.57	0.76	0.72
Specific diameter, D_m/SP	-	5.86	5.21	9.56	6.56
Specific speed, $D_m \Delta h_s^{1/4} / \dot{V}_{out,s}^{1/2}$	-	0.039	0.053	0.020	0.031
Nozzle outlet Mach number, M_2	-	0.88	0.86	0.71	0.69
Rotor inlet Mach number, M_{W2}	-	0.27	0.25	0.21	0.22
Rotor outlet Mach number, M_{W3}	-	1.24	1.01	1.22	1.09
Mean diameter, D_m	mm	479	600	560	554
Nozzle blade height, h_2	mm	13.3	27.5	5.6	14.0
Rotor outlet blade height, h_3	mm	16.6	28.5	7.3	14.9
Nozzle axial chord, c_n	mm	10.8	12	10.1	10.3
Rotor axial chord, c_r	mm	13.9	15.6	12.1	10.4
Nozzle opening, o_n	mm	3.3	3.7	3.1	3.6
Rotor opening, o_r	mm	3.8	4.5	3.1	3
Nozzle blade pitch, s_r	mm	14.8	16.1	13.8	16.0
Rotor blade pitch, s_n	mm	14.4	15.3	13.7	13.3
Number of nozzle blades, z_n	-	102	118	128	110
Number of rotor blades, z_r	-	106	124	130	130
Turbine volume	dm^3	5.77	10.40	6.87	6.56

Table 2.8: Selected working fluid candidates for the case study of waste heat recovery from a 37 MW marine diesel engine with heat source temperature of 235 °C**. From Ref. [72].**

Fluid	T_c [K]	GWP [-]	ODP [-]	tox./flamm.(*) [-]	Thermal stability limit [K]	Condensation pressure(**) [bar]	Manufacturer [-]	Ref. [-]
n-pentane	469.7	4 ± 2	0	4/1	573.15-588.15	0.82	Ormat Atlas Copco	[279–281]
isopentane	460.3	4 ± 3	0	4/1	500.15-588.15	1.09	Ormat Atlas Copco	[279–281]
MM	518.7	∼0	0	3/0	573.15	0.07	Turboden	[282–284]
n-hexane	507.8	4-6	0	3/1	n.a.	0.25	-	
cyclopentane	511.7	<25	0	3/1	513.15-548.15	0.51	Ormat Turboden GE Oil& Gas Atlas Copco Aqylon	[280, 281, 284–289]
benzene	562.0	3.4	0	3/2	>723.15	0.16	-	[279]
cyclohexane	553.6	4-6	0	3/1	n.a.	0.16	-	
toluene	591.7	3.3	0	3/2	>588.15;	0.0489	Tri-o-gen Aqylon	[10, 41, 279, 289–291]
n-butane	425.1	4	0	4/1	563.15-693.15	2.83	Atlas Copco Ormat Turboden	[280, 281]
R245fa	427.2	1030	0	0/2	523.15-573.15	1.78	GE-Energy Calnetix Cryostar Atlas Copco	[281, 284, 292–294]
ethanol	514.71	0	0	3/2	550	0.10	E-rational -	

(*) = According to standard NPFA 704. (**) at 30 °C. n.a. = datum not available.

on higher values of rotational speed, respectively 9000 rpm and 14000 rpm. At the same time, the advantages given by the insertion of a gearbox might be compensated by the higher cost of the investment and by its efficiency penalty. Since the results highlight that the use of different fluid entails very different levels of cost and complexity, an additional analysis should be performed in terms of technical and economic criteria to provide a suitable comparison among the working fluid candidates.

2.3.6 Cycle-turbine performance index

The most suitable working fluids can be found by comparing the different solutions in Figure 2.22(a) on the same basis for the considered application. A specific figure of merit was employed to simultaneously account for (a) the different levels of system complexity given by the number of turbine stages; (b) the cost of the turbine related to its dimensions; (c) the cost introduced by the possible use of a gearbox. To this end, a performance index was expressed as the ratio of the

electrical net power output and the cost of the turbogenerator as follows:

$$PI = \frac{P_{el}}{C_{turb}} \qquad [kW_{el}/k€_t] \tag{2.10}$$

In Eq. 2.10, $P_{el} = P_{net} \cdot \eta_{gear} \cdot \eta_{gen}$ is the net electrical power output of the cycle including the generator efficiency η_{gen} and, if present, the gearbox efficiency η_{gear}. The cost of turbogenerator unit is C_{turb} and is expressed in k€. The turbine represents between 15 % and 70 % of the total cost in the ORC system [12, 15, 16, 295–297] depending on power output, heat source temperature and system architecture. For this reason, the cost of the turbogenerator unit is considered in the denominator of Eq. 2.10. The correlation by Astolfi et al. [15] was employed in this study to predict the cost of the turbogenerator since it was developed from the authors experience with ORC companies. The correlation applies for power outputs above 1000 kW, and therefore it can be used with confidence for the designs presented in this work. The turbogenerator cost is expressed by Eq. 2.11, where C_t is the turbine cost, C_{gen} is the generator cost and C_{gear} is the cost of the gearbox. The turbine cost, expressed in Eq. 2.12, also accounts for the number of stages n, the size parameter of the last stage SP, a reference value for the size parameter SP_0, the reference cost of the turbine C_0, and the reference value for the turbine electric power $P_{el,0}$.

$$C_{turb} = C_t + C_{gen} + C_{gear} \tag{2.11}$$

$$C_t = C_0 \left(\frac{n}{n_0}\right)^{0.5} \left(\frac{SP}{SP_0}\right)^{1.1} \tag{2.12}$$

$$C_0 = 1230\ k€,\ n_0 = 2,\ SP_0 = 0.18\ m \tag{2.13}$$

$$C_{gen} = C_0 \left(\frac{P_{el}}{P_{el,0}}\right)^{0.67} \tag{2.14}$$

$$C_0 = 200\ k€,\ P_{el,0} = 5000\ kW \tag{2.15}$$

$$C_{gear} = 0.4 \cdot C_{gen} \tag{2.16}$$

For each fluid, the value of PI is illustrated in Figure 2.22, and Table 2.9 provides the details of the optimal solutions.

The fluid n-butane ranks as the best working fluid candidate for both the conservative and the advanced design approaches. In the former case, the turbine would employ a two-stage configuration whereas, in the latter, it would use a single-stage design. In Both cases, the turbine employs a gearbox.

Regarding size and cost, the fluid n-butane results in the smallest turbine diameter and the lowest cost and R245fa ranks as the second option. Fluid such as MM, toluene, and ethanol present a lower value of PI since they exhibit large turbine dimensions and a higher number of stages. The resulting solutions in the meridional plane are depicted in Figure 2.23. Single-stage turbines have a large blade deflection, and a smaller size in axial direction whereas the two-stage designs present a lower value of rotational speed and, therefore, reduce the mechanical stress on sealing and bearings.

In the advanced design approach, the solutions with high values of PI feature a small number of

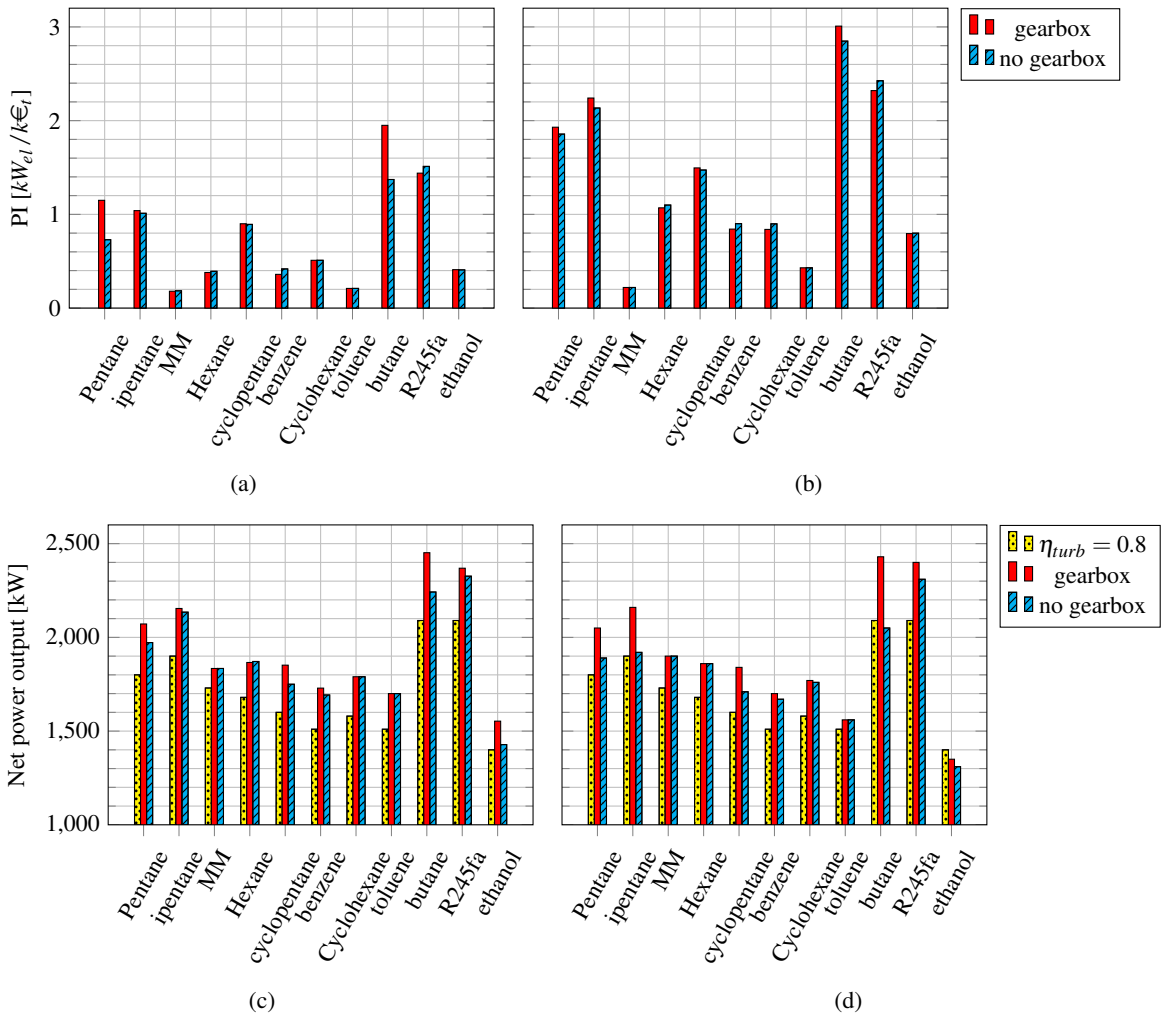

Figure 2.22: Performance Index (PI) and optimal net power output of the working fluid candidates according to (a,c) the conservative and (b,d) the advanced design approaches. From Ref. [72].

stages as shown in Table 2.9. In the conservative design approach, the solutions with the highest value of PI feature two or three stages. The fluid MM has a low value of PI as it requires five stages to accommodate the large expansion ratio. According to [90], it is unusual to design axial turbines having more than three stages.

For those fluids whose efficiency increment was lower than 4 %-points, such as R245fa, n-pentane, and n-hexane, the use of the gearbox resulted in a higher cost which was not offset by the increase in net electrical power output, obtaining a lower PI value. Beneficial effects by the insertion of a gearbox were, instead, obtained by the fluid n-butane. In this case, the use of a gearbox increased the turbine efficiency by 6-7 %-points and, at the same time, resulted in a lower number of stages.

Table 2.9: Ranking of the optimal working fluid candidates. From Ref. [72].

Fluid	PI	N_{st}	Gearbox	N	r_m	U_{tip}	P_{el}	C_{turb}	p_{max}	p_{min}	$\frac{\dot{Q}_{sc}}{\dot{Q}_{sc,max}}$
	$\left[\frac{kW}{k€_t}\right]$	-	-	[rpm]	[m]	$\left[\frac{m}{s}\right]$	$[kW_{el}]$	$[k€_t]$	[bar]	[bar]	[-]
Conservative Design											
butane	1.95	2	yes	14371	0.16	281.4	2203	1128	30.37	2.83	0.54
R245fa	1.51	2	no	3600	0.37	229.8	2210	1462	29.21	1.78	0.51
Pentane	1.15	2	yes	9128	0.24	264.1	1909	1655	14.46	0.82	0.35
ipentane	1.04	3	yes	7673	0.23	214.9	1985	1903	22.11	1.09	0.35
cyclopentane	0.90	2	yes	7885	0.28	266.0	1706	1894	8.84	0.51	0.24
ethanol	0.41	3	yes	5939	0.43	307.4	1431	3499	6.60	0.10	0.13
Hexane	0.39	3	no	3600	0.51	193.7	1778	4530	5.59	0.25	0.32
Cyclohexane	0.38	2	no	3600	0.52	242.8	1656	4377	4.05	0.16	0.23
benzene	0.36	3	no	3600	0.46	204.4	1644	4511	4.24	0.16	0.19
toluene	0.21	3	no	1800	0.96	177.8	1563	7345	1.93	0.05	0.19
MM	0.18	5	yes	1200	1.09	194.5	1742	9454	2.53	0.07	0.41
Advanced Design											
butane	3.01	1	yes	20647	0.16	312.62	2238	744	30.00	2.83	0.54
R245fa	2.43	1	no	3600	0.48	185.52	2191	903	29.21	1.78	0.51
ipentane	2.24	1	yes	14362	0.20	337.16	1986	886	22.11	1.09	0.35
Pentane	1.93	1	yes	11149	0.28	356.3	1890	980	14.63	0.82	0.35
cyclopentane	1.50	1	yes	11313	0.26	323.55	1705	1135	8.82	0.51	0.24
Hexane	1.10	1	no	3600	0.68	284.86	1769	1608	5.56	0.25	0.29
benzene	0.90	1	no	3600	0.77	307.11	1590	1766	4.24	0.16	0.19
Cyclohexane	0.90	1	no	3600	0.74	293.12	1669	1857	4.06	0.16	0.24
ethanol	0.80	1	no	3600	1.21	458.84	1240	1551	6.60	0.10	0.13
toluene	0.43	1	no	1800	1.92	325.16	1465	3368	1.93	0.05	0.19
MM	0.22	1	no	1200	1.23	323.55	1805	8242	2.54	0.07	0.41

2.4 Discussion

The highest PI values was achieved by the single-stage n-butane turbine using the advanced design approach and was approximately 1.5 times higher than that using a two-stage configuration. Consequently, such an advanced design approach would be the best solution as long as the challenging aerodynamic design features are accepted.

The literature indicates that the selection of the most suitable number of stages relies on different factors and is also specific to the considered application. A conservative ORC design approach which gave priority to high values of turbine efficiency at part load and avoided the use of loss models for supersonic flows, considered to be less reliable at that time, was employed 1970s and 1980s in Italy [63, 65, 71], see Table 1.1. This approach was also employed since a higher number of stages could reduce the rotational speed of the turbine unit, and possibly avoid the use of a gearbox. Each stage featured a pressure ratio in the range 3.2 to 5.0 and employed reaction blades. Angelino and Invernizzi [245] recommended the use of two-stage turbines rather than a single-stage design to improve the turbine efficiency and also to reduce the loading imposed on the

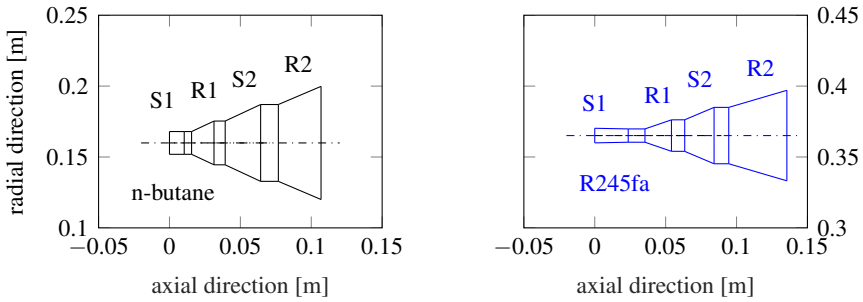

(a)

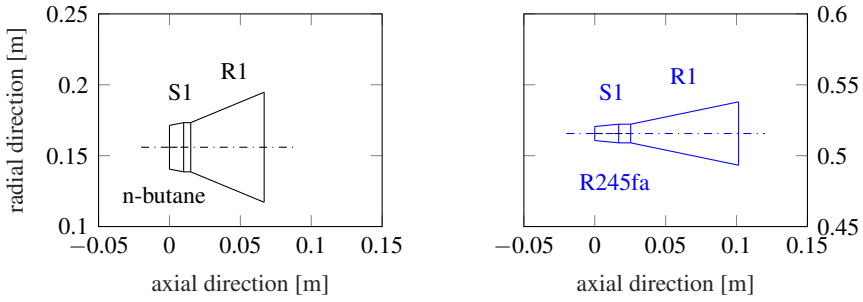

(b)

		Conservative design					Advanced design				
Stage	Param	n-but.	R245fa	n-pent.	isop.	cyclop.	n-but.	R245fa	n-pent.	isop.	cyclop.
1	χ	0.45	0.27	0.45	0.44	0.44	0.20	0.22	0.21	0.26	0.23
	M_2	1.18	1.40	1.27	1.18	1.26	1.86	1.96	2.23	2.07	2.01
	M_{w3}	1.05	1.00	1.15	1.00	1.15	1.18	1.30	1.40	1.40	1.34
2	χ	0.53	0.38	0.50	0.44	0.52	-	-	-	-	-
	M_2	1.03	1.20	1.16	1.08	1.10	-	-	-	-	-
	M_{w3}	1.09	1.07	1.15	0.97	1.16	-	-	-	-	-
3	χ	-	-	-	0.55	-	-	-	-	-	-
	M_2	-	-	-	0.93	-	-	-	-	-	-
	M_{w3}	-	-	-	1.01	-	-	-	-	-	-

Figure 2.23: Meridional profile geometry of the two best working fluid candidates, and Mach numbers and stage reactions of the five best working fluid candidates: (a) conservative and (b) advanced design approaches. From Ref. [72].

heat exchangers.

At the same time, the use of advanced design approaches was documented by other authors in the open literature. Pressure ratios in the range 6 to 150 were employed in the design of single and

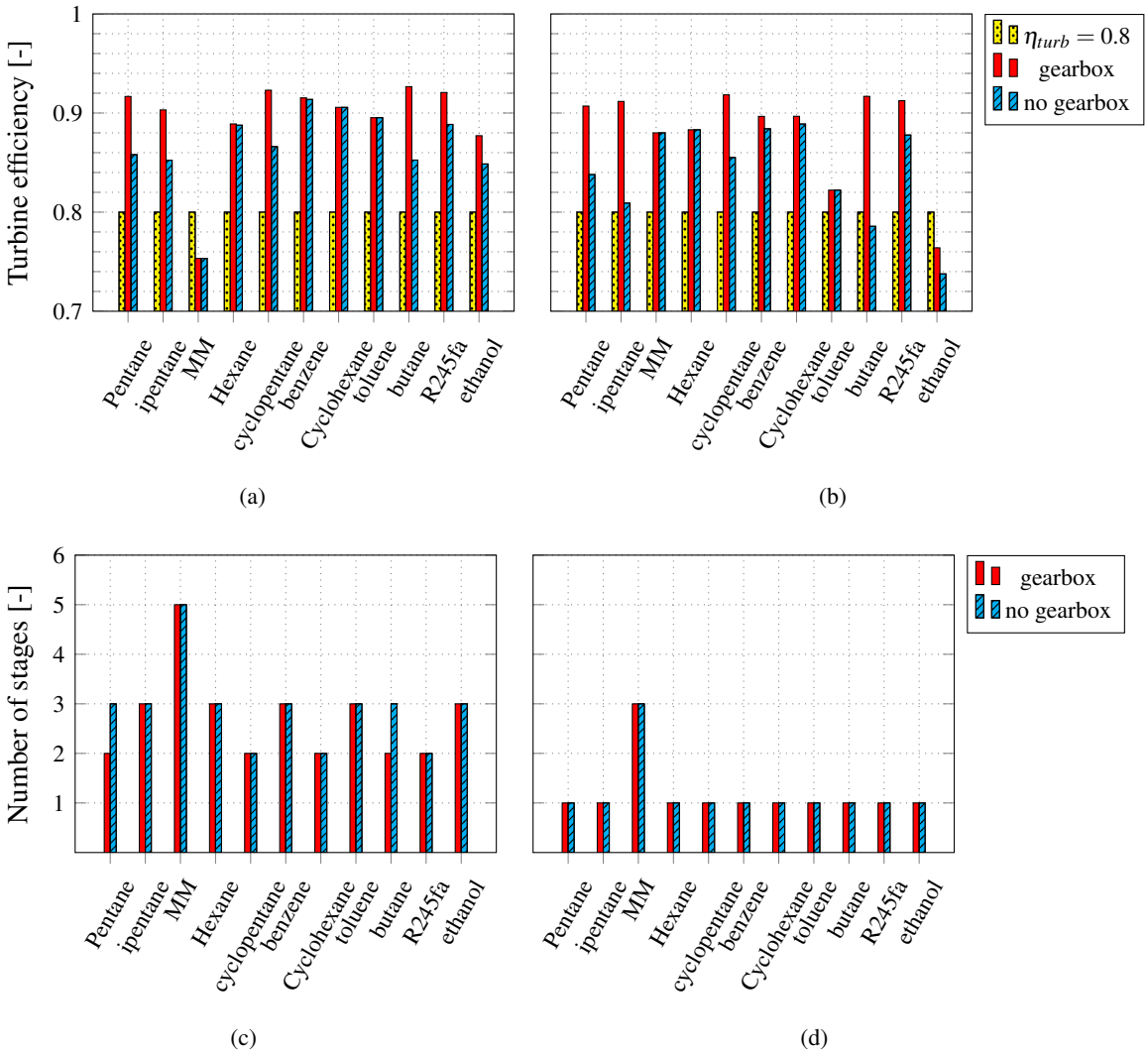

Figure 2.24: Turbine design efficiency and minimum number of stages of the working fluid candidates according to (a,c) the conservative and (b,d) the advanced design approaches. From Ref. [72].

two-stage ORC turbines described and tested by Verneau [66]. The turbines featured converging-diverging nozzles with exit Mach number up to 2.74 and a transonic rotor with inlet relative Mach number of 1.1 or higher. The measured value of total-to-static turbine efficiency was about 0.78 at the design point for the two-stage turbines, and a rapid degradation in the performance was observed at off-design conditions. Another case where the advanced design approach was adopted is reported by Bronicki [50], who described his experience in the design and testing of ORC turbines since 1960. The advanced design approach was used in single-stage turbines as the nozzle exit Mach numbers were in the range 2.5 to 3.5.

In the late 1990s, a two-stage ORC axial turbine was designed and tested by Jokinen et al. [67]. The

turbine operated with toluene and adopted a two-stage design following the indications by Verneau [66]. The high value of overall pressure ratio, approximately 100, required the use of two stages since the same authors considered that a highly-loaded single-stage design required high blade deflections and provided very low values of turbine efficiency at part loads. The two-stage turbine featured relative Mach numbers above 1 at the exit of the blade rows with subsonic inlet conditions. A higher pressure ratio, approximately 120, was considered by Osnaghi et al. [64] in the design of an ORC turbine for medium temperature solar power plant. In this case, a two-stage solution was adopted. The advanced design approach was selected here to use a minimum number of stages, and resulted in supersonic converging-diverging nozzles with exit Mach number of 1.9 and transonic rotor profiles. The value of thermodynamic efficiency computed from the experimental measures was 0.77, and rapid decay in the efficiency was observed at off-design operation by reducing the rotational speed.

The aforementioned studies suggest that the optimal solution with n-butane found in this work, featuring a pressure ratio of 10.3, would use a single-stage configuration for the advanced design approach and would require a minimum number of two stages for a conservative design. These considerations agree with the results found by the application of the optimization methodology presented in this work, and further substantiate the validity of this approach. As a matter of facts, the value of turbine efficiency found in this work adopting the advanced design approach are higher than those in the literature (i.e. >90 %). This discrepancy may come from the lack of completely reliable loss correlations for supersonic flow conditions. At the same time, the design of supersonic turbines involves inherent challenges, as recently highlighted by Pini et al. [298] and Rodriguez-Fernandez and Persico [299]. The authors showed that the use of novel CFD-based shape-optimization techniques could improve the performance of the turbine compared to traditional aerodynamic design techniques. Moreover, the turbine optimization using multi-point methods allow achieving further improvement considering also off-design operation [90].

Other possible challenges of supersonic ORC turbines are mechanical issues related to the high stresses on the blades and the bearings, and additional losses and stresses arising from the centrifugal forces due to the large chords and flaring angles.

If mechanical and stress issues make the design of the n-butane turbine too complex or challenging, the turbine employing R245fa can be the second best candidate since it features lower values of Mach number in the blade rows and it operates at a lower speed. Such conditions facilitate the design of sealing and of the bearing system.

Regarding environmental aspects, n-butane is highly flammable but has minor hazard issues. In this regard, flammable working fluids have been used so far in the design and operation of ORC units by many companies. Although the refrigerant R245fa is now employed by many ORC companies, as highlighted in Table 2.8, a phase-out is expected in the mid-term due to its high value of GWP [300]. New environmentally-friendly refrigerants, such as R1233ZE(Z) and R1233zd(E) would represent an ideal solution; however, they were discarded in the preliminary design process due to their comparatively low value of thermal stability.

2.5 Conclusion

This chapter presented a methodology for the optimal design of ORC power systems based on cycle and turbine design criteria. The methodology focused on the use of single- and multistage axial turbine criteria for the design of the ORC system. To this end, a conservative and an advanced turbine design approaches were introduced and represent key decision criteria in the methodology.

To perform the design of the axial turbine, a turbine model named TURAX was presented and validated in its single and multistage formulation with the existing, well-documented data of different turbines from the open literature. The validation of TURAX with two single-stage turbine test cases, one of which is an ORC turbine, suggests a performance prediction within 1.3 %-points at the design point. This value is consistent with the prediction range of $\pm$ 1.25 %-points declared by the performance prediction method by Craig and Cox used in the mean-line model. Regarding thermodynamic and flow conditions, the design model has a deviation up to 10 %, and similar values are found in the estimation of the blade heights. The uncertainty in the estimation of the exit flow angles, the losses and the experimental uncertainty greatly affect the values of deviation obtained in the results. For example, Hirsch and Denton [247] showed that the use of different correlations for the performance estimation using through-flow methods, the uncertainty is in the range $\pm$2% for the efficiency and $\pm$20% for the losses. A sensitivity analysis using the Morris screening method allowed identifying the most important decision variables in the model from the performance and design viewpoint. Finally, 10 variables were selected as the most significant for the design and optimization of the turbine. In its multistage version, TURAX was validated with two test cases: a four-stage subsonic turbine using air and a two-stage supersonic ORC turbine. These test cases were representative for the conservative and advanced design approaches, respectively. The validation of the turbine model in its more general multistage layout substantiates the results already found in the single-stage model since the deviation in efficiency is up to 2 %-points, and the deviation for the flow conditions and the design geometry is up to 8.5 %.

The developed methodology and the models were then applied to two case studies. The first case study focused on the design of a single-stage axial turbine using multi-component working fluids for the WHR from the jacket water cooling system of a 60 MW marine diesel engine. The second case study investigated the optimal ORC system and turbine designs for the WHR from the exhaust gases, the scavenge air and the jacket water cooling system of a 37 MW marine diesel engine. In this case, pure fluids and multistage turbine design criteria were considered. The application of the combined turbine and cycle optimization methodology to the first case study resulted to be advantageous especially in the presence of a heat source temperature variation higher than 5 °C and for the mixture propane/isobutane. For a hot fluid temperature change up to 5 °C, resulting from a constraint on the outlet temperature of the heat source, pure fluids performed better than mixtures and a very small change in net power output was observed compared to the use of a constant value of isentropic efficiency. However, for higher values of hot fluid temperature change, better performance was found for mixtures and a change in net power output up to 8 % was observed compared to a guessed value in turbine efficiency, which makes it relevant to consider the combined optimization methodology. The fluid R245fa/pentane (0.5/0.5) provided the best cycle and turbine performance and is the recommended option. Where environmental and technical aspects lead to the use of another fluid, the fluid propane/isobutane (0.2/0.8) would be the second best choice. The combined optimization methodology was then used to design an ORC system in the second case study, which included considerations on multistage turbine criteria. In this case, cycle and

turbine designs showed trade-off in terms of performance and led to the identification of the best fluids featuring small size, reduced number of turbine stages, low cost and high turbine and cycle performance. The fluid n-butane ranked as the first option, and featured a single-stage configuration with highly supersonic flows in the advanced design approach, whereas it featured a two-stage reaction turbine in the conservative design approach. A literature review on the experimental studies conducted on ORC multistage turbines validated the suitability of the results obtained by the methodology. If the design of the turbine with n-butane faces technical and aerodynamic challenges, the fluid R245fa can be used as the second option due to its lower flammability and the lower rotational speed, which would simplify the design of sealing and bearings. The adoption of a gearbox solution was discussed. It was found that it was advantageous to use a gearbox when the fluid investigated exhibits an increase in turbine efficiency up to 6-7 %-points.

The methodology presented in this chapter was limited to considerations on the cycle and the expander. In this respect, it is relevant to expand the methodology by including additional aspects such as off-design considerations and the performance of the other cycle components such as the pump and the heat exchangers. Finally, the optimal designs were obtained using a preliminary design method. The use of more advanced design techniques is recommended to study the resulting designs regarding aerodynamics, structural analysis, and noise and off-design considerations.

3 Radial-inflow turbines for ORC power systems

The work presented in this chapter was carried out during the external research stay at Imperial College London and during the following months. The work is unpublished and has been recently submitted for publication, see Ref. [95].

3.1 Introduction

The background and motivations for this work were presented in Chapter 1.4. This chapter presents the development of steady-state, mean-line models for HPR radial-inflow turbines, in both the design and the off-design modes. The models include different numerical modeling strategies to treat unchoked and choked flow conditions, and the subsonic and supersonic flow regimes. The models are developed using a generic formulation of the governing equations including real-gas effects to investigate any fluid of interest. Given the lack of validated models for high-pressure ratio turbines in the literature, the off-design model is calibrated with the data of some well-documented experimental test cases from the open literature. A global sensitivity analysis using the Monte Carlo method is employed to identify the importance of the calibration coefficients in regard to the choking mass flow rate and the turbine isentropic efficiency. The calibration method uses a novel approach, based on an optimization algorithm, which aims to minimize the predicted deviation between the experimental and the numerical data considering all the measured operating points of the turbines. Finally, the results of the calibration are assessed by validating the off-design model with other two additional test cases, which present different features than the original test cases, and one of which is an ORC turbine.

In this case, the off-design tool is developed to: (i) calibrate the model over a wide range of operating conditions, (ii) comply with those ORC applications featuring important variations of the system operating conditions.

The primary novel contributions of this work are the following: (1) a detailed mean-line modeling strategy addressing choking conditions in the blade rows at design and off-design operation; (2) a calibration method based on a multi-objective optimization algorithm, which aims to minimize the predicted deviation between the measured operating point and the numerical model for each of the test cases; (3) a set of loss models calibrated for HPR radial-inflow turbines.

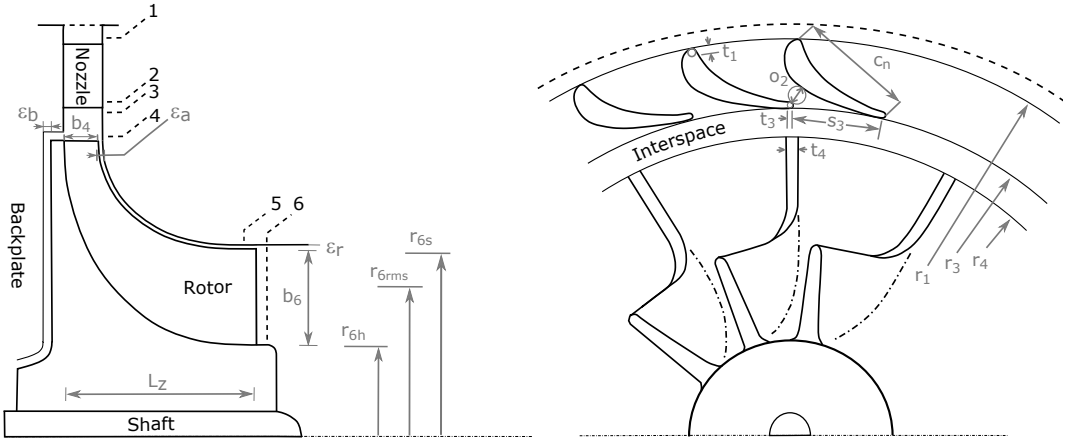

Figure 3.1: Representation of the geometry of the radial-inflow turbine. From Ref. [95].

This chapter has the following structure: Section 2 introduces the employed methodology and the methods. Section 3 presents the calibration results. Section 4 discusses the results, and Section 5 draws the conclusion.

3.2 Methods

3.2.1 Performance prediction methodology

The MATLAB [214] language was employed to develop a steady-state, mean-line model with the aim (i) to perform the design and performance prediction using a comprehensive numerical strategy which includes the treatment of unchoked and choked flow conditions in the blade rows; (ii) to apply it to HPR radial-inflow turbines operating with any working fluid and application; (iii) to be robust, stable and with short simulation time.

In the mean-line approach of the model, the thermodynamic and flow conditions at every main turbine station are representative of mass-weighted averaged conditions over the whole section. In the turbine model, three subcomponents were modeled: the nozzle, the nozzle-rotor interspace, and the rotor. A schematic of the turbine in the meridional plane is shown in Figure 3.1, which highlights the main stations, the terminology and the symbols used in this paper. In each station and between two stations, mass and energy balances, and loss equations are solved to determine all the average thermodynamic and flow conditions. The thermodynamic library CoolProp [218], which employs state-of-the-art equations of state, was used to compute the fluid properties. The core of the methodology focuses on identifying the choking conditions in each blade row, independently of the actual thermodynamic and flow conditions. Choking conditions in a blade row are defined as the situation where the flow is at sonic conditions at the point of minimum flow area. If the process is isentropic, it can be shown that this situation corresponds to the maximum possible mass flow rate per unit area [301]. Four distinct choking flow patterns may occur in a nozzled turbine, and

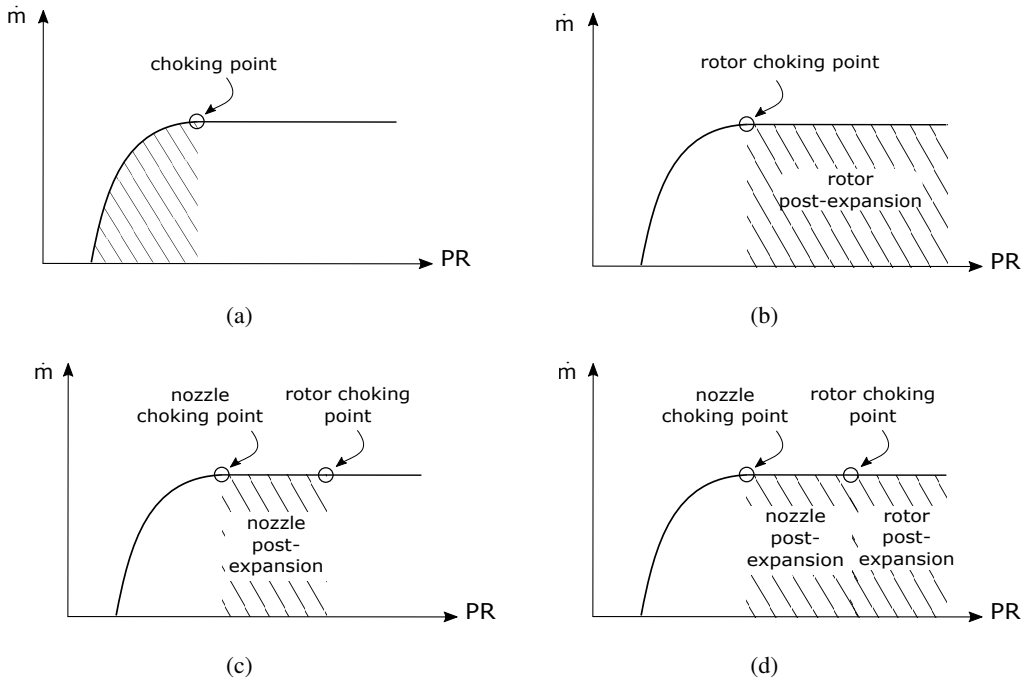

Figure 3.2: Illustration of the possible turbine flow patterns occurring at off-design conditions: (a) Nozzle and rotor unchoked; (b) rotor choked and nozzle unchoked; (c) nozzle choked and rotor unchoked; (d) nozzle and rotor choked. From Ref. [95].

these are shown in Figure 3.2: (a) both the nozzle and the rotor are unchoked, (b) the nozzle is unchoked and the rotor is choked, (c) the nozzle is choked and the rotor is unchoked, and (d) both the nozzle and the rotor are choked.

There are different approaches to the design and off-design mean-line modeling [302], and the strategy adopted in this work is shown in Figure 3.3.

Design modeling strategy

The preliminary design modeling strategy is illustrated in Figure 3.3(a). The set of inputs to the mean-line model are the inlet total temperature T_{01} and pressure p_{01}, the rotational speed N, the mass flow rate $\dot{m}$, and the stage total-to-static pressure ratio PR_{ts}. These values usually come from the specifications of the thermodynamic cycle, except for N, which is often set by design constraints or is optimized. In addition to the aforementioned inputs, a set of decision variables describing the turbine geometry and loading conditions are provided as indicated in Table 3.1. The modeling strategy illustrated in Figure 3.3(a) relates to a specified set of decision variables, and it can be coupled to an optimization algorithm to determine the optimal combination of geometrical and fluid dynamic variables. The first step in the modeling strategy (*Step 0*) is to identify which is the first component to choke since the maximum mass flow rate that the turbine can accommodate is limited by the choking. To this end, the nozzle choking conditions are first calculated using a numerical method. The governing equations expressed as mass balance, energy balance, and loss

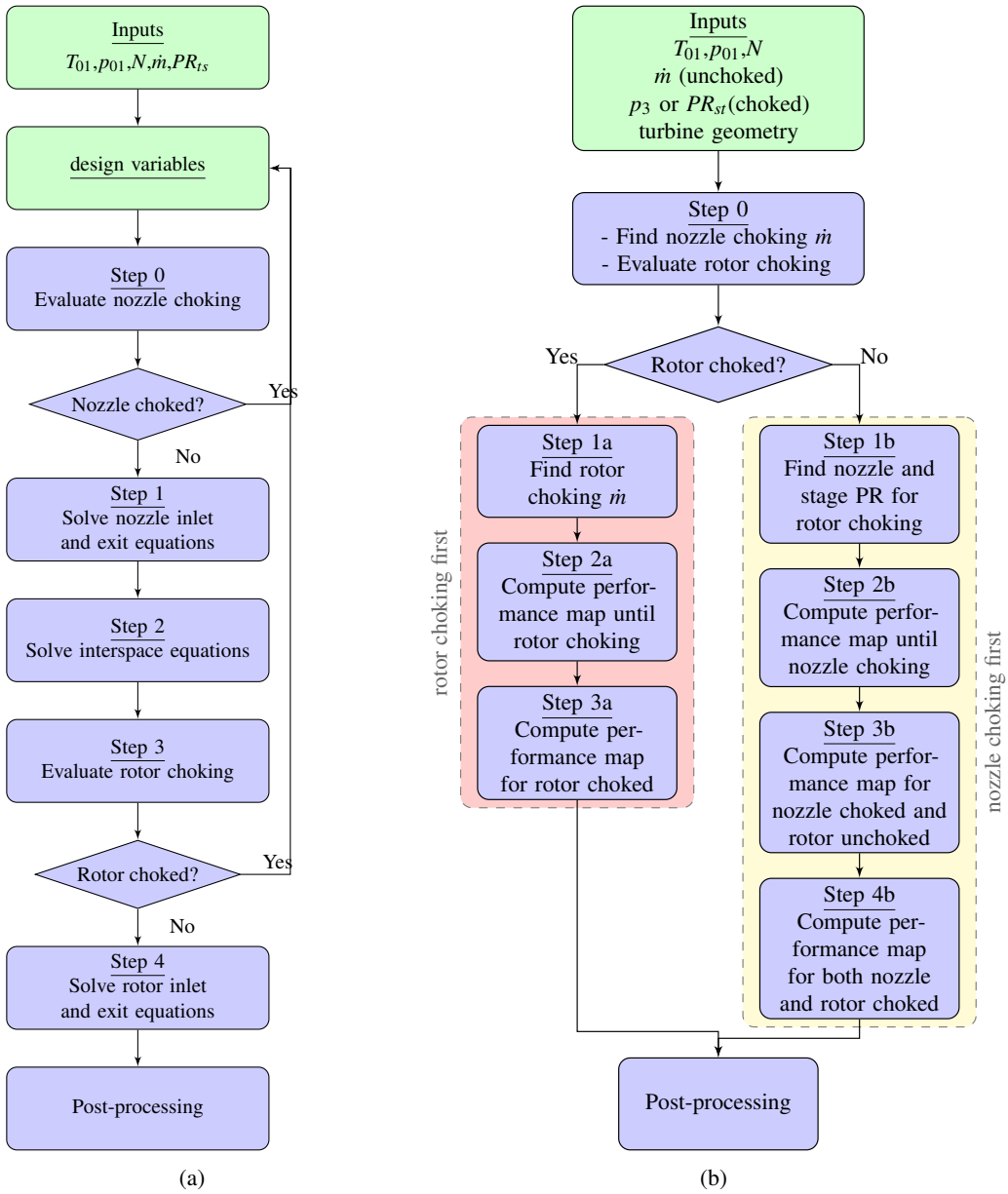

Figure 3.3: modeling strategy for high-pressure ratio RITs: (a) preliminary design model; (b) off-design model. From Ref. [95].

equations accounting for the entropy generation in the nozzle are, respectively:

$$C_2 = \frac{\dot{m}}{\rho_2 \cdot cos(\alpha_2) \cdot A_2 (1 - BF_2)} \tag{3.1}$$

$$h(\rho_2, T_2) = h_{01} - \frac{1}{2} C_2^2 \tag{3.2}$$

$$\sum_{n=1}^{n_{losses}} \Delta h_{loss,n} - h(\rho_2, T_2) + h(p_2, s_{01}) = 0 \tag{3.3}$$

Table 3.1: Decision variables of the design model for RITs.

Decision variable	Unit	Symbol
1) Velocity ratio	-	$\frac{U_4}{C_0} = \frac{U_4}{\sqrt{2\Delta h_{0,is}}}$
2) Nozzle inlet-outlet radius ratio	-	(r_1/r_3)
3) Nozzle opening-to-pitch ratio	-	$(o/s)_n$
4) Interspace radius ratio	-	(r_3/r_4)
5) Rotor inlet width over exit blade height	-	(b_4/b_6)
6) Rotor outlet-inlet radius ratio	-	(r_{6s}/r_4)
7) Rotor exit hub-to-shroud radius ratio	-	$\nu = (r_{6h}/r_{6s})$
8) Rotor opening-to-pitch ratio	-	$(o/s)_r$
9) Rotational speed	rpm	N

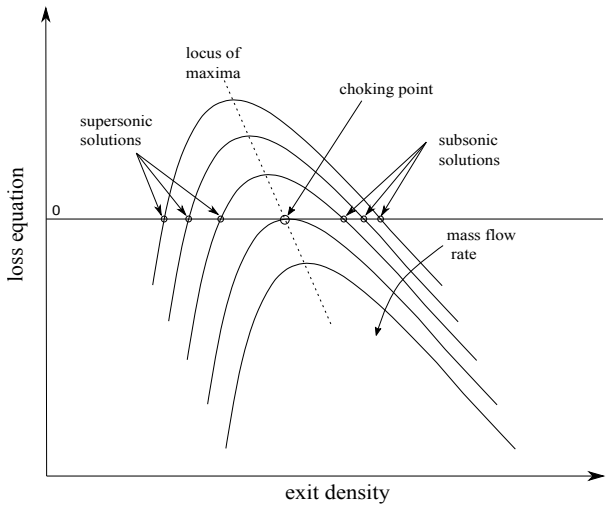

Figure 3.4: Identification of the choking point for a blade row. From Ref. [95].

where ρ_2 is the density, α_2 the absolute flow angle, A_2 the cross-sectional area, C_2 the absolute velocity, and p_2 the static pressure at the nozzle outlet. The mass flow rate in Eq. 3.1 may be reduced by a blockage factor BF_2, which take into account the effects of the metal blockage and boundary layer. The term h indicates the specific enthalpy, and h_{01} and s_{01} the total specific enthalpy and entropy at the nozzle inlet, respectively. The term $\Delta h_{loss,n}$ represents the specific loss contribution in the blade row, calculated using an empirical model, see Sec. 3.2.2. The nozzle exit flow angle under subsonic conditions was computed using an empirical correlation, see Sec. 3.2.2. Figure 3.4 illustrates the left-hand side of Eq. 3.3 expressed as a function of ρ_2 and $\dot{m}$. This representation serves to determine the choking point uniquely . For a specified value of the mass flow rate, the function at the left hand side of Eq. 3.3 has a non-monotonic trend, a concave shape and a single point of maximum. The value of mass flow rate corresponding to the situation where the curve crosses the x-axis was identified as the *choking mass flow rate*, and the associated point

of maximum as the *choking point*. For values of mass flow rate smaller than the choking mass flow rate, the maximum of the curve lies above the x-axis, which is crossed in two points by the function. These two points correspond to subsonic (higher density) and supersonic (lower density) solutions. Therefore, the choking point is also identified as the situation where the subsonic and supersonic numerical solutions coincide. On the other hand, for values of mass flow rate higher than the choking value, the function does not cross the x-axis, being the point of maximum below the x-axis, and there is no solution to the set of Eqs. 3.1-3.3 (*Step 1*). From the physical viewpoint, this is consistent with the fluid dynamic situation occurring in the turbine: the machine cannot physically accommodate a mass flow rate higher than the choking value, unless a different geometry or inlet conditions are prescribed. In the design modeling strategy, the numerical routine stops and warns the user to change the inlet conditions or the decision variables of the model. If choking conditions are not reached, Eqs. 3.1-3.3 (*Step 1*) are solved together with the mass continuity, the energy balance, the momentum balance and the loss equation in the nozzle-rotor interspace (*Step 2*), which are expressed as follows:

$$C_4 = \frac{\dot{m}}{\rho_4 \cdot cos(\alpha_4) \cdot A_4(1 - BF_4)} \tag{3.4}$$

$$h(\rho_4, T_4) = h_{01} - \frac{1}{2}C_4^2 \tag{3.5}$$

$$\frac{C_3 sin\alpha_3}{C_4 sin\alpha_4} = \frac{r_4}{r_3} + \frac{2\pi C_f \rho_4 C_4 sin\alpha_4 (r_3^2 - r_3 r_4)}{\dot{m}} \tag{3.6}$$

$$\Delta h_{vs,loss} - h(\rho_4, T_4) + h(p_4, s_3) = 0 \tag{3.7}$$

where the term $\Delta h_{vs,loss}$ and C_f denote the vaneless space loss and the friction factor, respectively. The two terms are computed using empirical correlations. Equation 3.6 was based on the formulation by Stanitz [303], according to Whitfield and Baines [304]. To solve Eqs. 3.4-3.7, a trust region solver in MATLAB [214] was employed using initial guess values for α_4 and ρ_4. Once the nozzle choking conditions are determined, the next step (*Step 3*) is to identify the rotor choking conditions. The following set of equations for the rotor are solved:

$$W_5 = \frac{\dot{m}}{\rho_5 \cdot cos(\beta_5) \cdot A_5(1 - BF_5)} \tag{3.8}$$

$$h(\rho_5, T_5) = I_4 - \frac{1}{2}W_5^2 + \frac{1}{2}U_5^2 \tag{3.9}$$

$$\sum_{n=1}^{n_{loss}} \Delta h_{loss,n} - h(\rho_5, T_5) + h(p_5, s_4) = 0 \tag{3.10}$$

where $I_4 = h_4 + 0.5W_4^2 - 0.5U_4^2$ corresponds to the rothalpy term. In the design mode, the rotor exit flow angle β_5 was not provided by the empirical correlation and, instead, was computed by assigning the exit static pressure p_5 given the total-to-static pressure ratio specified as an input. In the off-design mode, since the exit pressure is unknown, β_5 is provided by an empirical correlation (Sec. 3.2.2) to close the set of equations. Similarly to the analysis in the nozzle, the left-hand side of Eq. 3.10 was expressed as a function of the rotor exit density ρ_5, and the resulting trend is like that of Figure 3.4. However, a major difference with the nozzle modeling is that the function also depends on the rotational speed of the rotor. The design routine ended if the specified mass flow

rate resulted in being higher than the choking value in the rotor. Otherwise, the governing equations were solved, and the design routine proceeded to the post-processing operations.

Off-design modeling strategy

The off-design modeling strategy is illustrated in Figure 3.3(b). In the off-design mode, the full turbine geometry and turbine inlet conditions are specified and performance maps are generated as the output. The mass flow rate $\dot{m}$ was given as an input and performance maps were generated until choking conditions. When the turbine reached choking conditions, the solution strategy changed: the mass flow rate was set to the choking value; however, the outlet pressure could assume an infinitude of values. In this case, there is not a single solution to the numerical problem and, to cope with this issue, the static pressure at the turbine outlet was also specified. The modeling strategy could also employ the stage pressure ratio as an input from the beginning; however, it was found that giving the mass flow rate as the input until choking resulted in faster computational time. Since the workflow of Figure 3.3(b) refers to a specified rotational speed value, an iterative scheme was applied to produce performance maps in a range of rotational speeds.

Identification of the choking point (Steps 0, 1a and 1b) The identification of the first blade row to choke is the first step of the off-design modeling strategy (*Step 0*) as in the design mode. The solution of the nozzle equations employed the set of Eqs. 3.1-3.3. The point at which the locus of maxima of Eq. 3.3 is zero in the nozzle corresponds to the choking condition (see also Figure 3.4), and is determined using a numerical solver. Using the nozzle choking mass flow rate, it was evaluated whether the rotor was already choked by solving Eqs. 3.4-3.10. Depending on the result, different flow patterns were identified and the modeling strategy changed accordingly. If the rotor choked first, the choking flow patterns a) and b) of Figure 3.2 were considered (Steps 1a-3a in Figure 3.3(b)). The choking condition at which the peak of the function in Eq. 3.10 is zero was computed using a numerical solver, enabling the identification of the values of choking density and mass flow rate (*Step 1a*). If the nozzle choked first, the flow patterns a), c) and d) of Figure 3.2 were considered (Steps 1b-4b in Figure 3.3(b)). In this case, the solution strategy determined the rotor choking condition found at higher expansion ratios (*Step 1b*). The rotor inlet static pressure was changed until Eqs. 3.8-3.10 go to zero. The critical values of nozzle and stage pressure ratio were determined and used in subsequent steps of the methodology.

Nozzle and rotor unchoked (Steps 2a and 2b) The mass flow rate was varied from a lower limit up to the choking point and the turbine performance maps were computed. This operation was repeated for each value of mass flow rate and Eqs. 3.1-3.10 were sequentially solved to calculate the values of stage pressure ratio and the efficiency.

Nozzle unchoked and rotor choked (Step 3a) In this case, the mass flow rate was set to the choking value, and the nozzle flow could not further expand since only the rotor exit pressure could change, and this could not affect the flow upstream the throat [301]. Therefore, also the total-to-static stage pressure ratio was provided as an input. The expansion downstream of the rotor throat was allowed using a post-expansion. The thermodynamic and flow conditions at the

throat were computed using mass energy balances, Eqs. 3.8 and 3.9. In this case, the choking density determined in *Step 1a* was provided as input. For values of pressure ratio higher than the rotor choking condition, the set of post-expansion equations in terms of mass and energy balances, and losses was solved. The governing equations were applied between the throat end the exit to determine the turbine exit density ρ_6 as follows:

$$W_6 = \sqrt{2 \cdot (I_4 - h(\rho_6, p_6)) + U_6^2} \tag{3.11}$$

$$\beta_6 = -cos^{-1}\left[\dot{m}_{ch,rot} / (\rho_6 W_6 A_5 (1 - BF_5))\right] \tag{3.12}$$

$$\Delta h_{pe,rot} - h(\rho_6, p_6) + h(p_6, s_5) = 0 \tag{3.13}$$

where $\Delta h_{pe,rot}$ is the post-expansion loss, s_5 denotes the specific entropy at the throat, and $\dot{m}_{ch,rot}$ is choking mass flow rate of the rotor.

Nozzle choked and rotor unchoked (Step 3b) Mass and energy balances between the nozzle inlet and the throat were used to determine the thermodynamic and flow parameters at the choked throat. For a value of pressure ratio higher than the choking value, a post-expansion process was considered after the nozzle throat. In this case, the following set of equations was solved for the nozzle exit density ρ_3:

$$C_3 = \sqrt{2 \cdot (h_{01} - h(\rho_3, p_3))} \tag{3.14}$$

$$\alpha_3 = cos^{-1}\left[\dot{m}_{ch,noz} / (\rho_3 C_3 A_2 (1 - BF_2))\right] \tag{3.15}$$

$$\Delta h_{pe,noz} - h(\rho_3, p_3) + h(p_3, s_2) = 0 \tag{3.16}$$

where $\Delta h_{pe,noz}$ is the post-expansion losses, s_2 is the specific entropy at the throat, and $\dot{m}_{ch,rot}$ denotes the rotor choking mass flow rate.

Both nozzle and rotor choked (Step 4b) In case both the nozzle and the rotor were choked, further expansion was possible using a post-expansion after the rotor throat solving Eqs. 3.14-3.16.

3.2.2 Empirical models for losses and flow deviation

The equations employed to determine the thermodynamic and flow conditions in the different turbine stations require the use of empirical correlations for the flow angle and the losses. These are described in detail in Appendix B. The blockage factors used in the mass balance equations are usually dependent on the specific test case that is considered. The best agreement with the data of the six test cases employed in this work was found for $BF = 0$ and, therefore, possible blockage effects were neglected. The numerical correlations of the losses occurring in the blade rows were originally based on the models by Baines [137], although with some modifications. In the field

of radial turbines, the literature [302] indicates that there is a strong lack of techniques used to predict nozzle losses based on geometry and flow conditions. For this reason, nozzle losses have often been neglected as they were considered of a much lower magnitude than those in the rotor [137]. Although this may hold true for low-pressure ratio turbines, the experimental investigations [98, 305] on high-pressure ratio turbines and numerical analyses [306, 307] on very high-pressure ratio RITs (i.e. PR > 100) suggest that the nozzle losses should be included. At the same time, a suitable nozzle model is required to obtain meaningful results regarding flow conditions at the rotor inlet and the stage performance prediction.

The nozzle losses used in this work were the following three: the passage loss, the trailing edge loss, and the post-expansion loss. The most reliable nozzle passage losses in the literature [308] are arguably those by Rodgers [132] and Rohlik [309]. In this work, the loss model by Rodgers [132] was adopted since it is directly computed based on the nozzle geometry and flow conditions without using the boundary layer parameters, which are less straightforward to predict. The original loss model by Rodgers [132] neglects the losses due to trailing edge and shock waves effects by assuming that the trailing edge to chord ratio is less than 2 % and that Mach numbers are lower than 1.2.

To fully extend the loss prediction to HPR conditions, the losses due to the trailing edge blockage and to Mach numbers higher than 1.2 at the blade exit were also included in the mean-line model. The loss correlation by Glassman [140] was employed to model the trailing edge loss. In this respect, Refs. [134, 140, 310] argued that it could be a more meaningful formulation than that used by Baines [137] since it considers the actual blade blockage. Aungier's [133] correlation was employed to estimate the post-expansion loss.

The loss model by Khastner and Bhinder [129], frequently employed in the literature [134, 302, 304], was also used here to compute the losses in the nozzle-rotor interspace. The friction factor in the interspace was computed using Japikse's formulation [311]:

$$C_f = k \left(\frac{1.8 \cdot 10^5}{Re_4} \right)^{0.2} \tag{3.17}$$

where Re_4 is the Reynolds number at the rotor inlet and k is an empirical coefficient. Equation 3.17 was used to model the interspace loss in RITs following Whitfield and Baines [304]. The coefficient k can vary in the range 0.005 to 0.02 in practical applications, and Japikse [311] recommended to use the value 0.01.

The rotor passage, clearance, and incidence losses were modelled with the correlations by Baines [137] and the trailing edge and post-expansion losses were modelled by the correlations by Glassman [140], consistently with the nozzle losses. Additional losses included the effects of friction by the rotor disc, modelled as a sudden enthalpy rise at constant static pressure [304], and predicted following Daily and Nece [312].

The final set of loss models is shown in Table 3.2 . Initially, all the coefficients K_{p1}, K_{p2}, K_{p3}, K_{vs} and K_{inc} were considered for calibration in this work; however, the final set was selected after a dedicated sensitivity analysis, described in Sec. 3.2.3.

As opposed to the axial turbine field, there is a strong lack of correlations for the flow deviation

Table 3.2: Loss correlations.

Loss mechanism	Loss model	Reference
Nozzle passage	$\Delta h_{pl,noz} = K_{p1}\frac{0.05}{Re_3^{0.2}}\left[\frac{3\tan\alpha_3}{s_3/c_n}+\frac{s_3\cos\alpha_3}{b_3}\right]\frac{1}{2}C_3^2$	Rodgers [132]
Nozzle trailing edge	$\Delta h_{t,noz} = \left(\frac{Z_n t_3}{2\pi r_3 cos\alpha_3}\right)^2 \frac{1}{2}C_3^2 \cdot Y_3^{(*)}$	Glassman [140]
Nozzle post-expansion	$\Delta h_{pe,noz} = \left(\frac{M_3 - M_2}{M_3}\right)^2 \frac{1}{2}C_3^2 \cdot \frac{1}{Y_3^{(*)}}$	Aungier [133]
Interspace	$\Delta h_{vs} = K_{vs} C_f \left(\frac{L}{D}\right)\frac{1}{2}\left(\frac{C_3+C_4}{2}\right)^2$	Kastner and Bhinder [129]
Rotor incidence	$\Delta h_{inc,rot} = K_{inc}(sin\lvert\beta_4 - \beta_{4,opt}\rvert)^2 \frac{1}{2}W_4^2$	Baines [137]
Rotor passage	$\Delta h_{pl,rot} = K_p\{K_{p2}\left(\frac{L_H}{D_H}\right) + 0.68K_{p3}\left[1-\left(\frac{r_{6rms}}{r_4}\right)^2\right]\left(\frac{cos\beta_6}{b_6/c_r}\right)\}\frac{1}{2}\left(W_4^2+W_6^2\right)$	Baines [137]
Rotor clearance	$\Delta h_c = \frac{U_4^3 Z_r}{8\pi}\left(K_a\varepsilon_a C_a + K_r\varepsilon_r C_r + K_{ar}\sqrt{\varepsilon_a\varepsilon_r C_a C_r}\right)$	Baines [137]
Rotor trailing edge	$\Delta h_{t,rot} = \left(\frac{Z_r t_6}{\pi(r_{6s}+r_{6h})cos\beta_6}\right)^2 \frac{1}{2}W_6^2 \cdot Y_6^{(*)}$	Glassman [140]
Rotor post-expansion	$\Delta h_{pe,rot} = \left(\frac{M_{6,rel} - M_5}{M_{6,rel}}\right)^2 \frac{1}{2}W_6^2 \cdot \frac{1}{Y_6^{(*)}}$	Aungier [133]
Rotor disc friction	$\Delta h_{df} = 0.25K_f\frac{\overline{\rho}U_4^3 r_4^2}{\dot{m}}$ where $\overline{\rho} = \frac{\rho_4+\rho_6}{2}$ $Re_4 = \frac{\rho_4 U_4 r_4}{\mu_4}$ if $Re_4 < 3\cdot10^5$ $K_f = 3.7(\varepsilon_b/b_4)^{0.1}Re_4^{-0.5}$ if $Re_4 > 3\cdot10^5$ $K_f = 0.102(\varepsilon_b/b_4)^{0.1}Re_4^{-0.2}$	Daily and Nece [312]

$^{(*)}\ Y_3 = \left[1+\frac{k_3-1}{2}M_3^2\right]^{\frac{k_3}{1-k_3}}$; $Y_6 = \left[1+\frac{k_6-1}{2}M_{6,rel}^2\right]^{\frac{k_6}{1-k_6}}$

angles in RITs. In this work, the exit flow angle at unchoked conditions for the nozzle and the rotor was estimated with the cosine rule, as follows:

$$\alpha_2 = cos^{-1}(o_2/s_2) \quad \beta_5 = cos^{-1}(o_5/s_5) \tag{3.18}$$

where o is the throat opening, and s is the vane spacing.

3.2.3 Sensitivity analysis

The objectives of the sensitivity analysis, which was applied to the off-design model, were the following: i) identify the calibration coefficients which have a larger impact on the output mass flow rate and isentropic efficiency; ii) remove the calibration coefficients having a small impact on the changes in mass flow rate and efficiency, with the aim to minimize the computational efforts of

the calibration process; iii) identify a range of values in which the calibration coefficients satisfy the choking conditions required by the different test cases.

The global sensitivity analysis used the Monte Carlo method [263], which, in comparison to methods based on a local sensitivity study, also considers the possible interactions between the different variables. The model described in 2.2.6 was employed for the analysis. The input calibration coefficients were assigned a uniform probability distribution without imposing a correlation matrix on the input parameters, and for each coefficient 500 samples were generated. In the application of the sensitivity analysis, all turbine test cases described in Sec. 3.2.4 were considered.

3.2.4 Calibration method

Six test cases were selected from the open literature for the application of the methodology presented in Sec. 3.2.1. The following criteria were employed in the selection of the six test cases from Table 1.2 : 1) the original references present reliable data and include sufficient details on geometry, flow conditions, and performance maps at HPR conditions; 2) they all have the same geometric configurations with a nozzle and without a volute or a diffuser. The geometry and input data employed in the test cases are shown in Table B.1 in Appendix B.

The calibration methodology sought to identify the values of the calibration loss coefficients (and hence the loss models) yielding the minimum deviation between the model and experimental data in terms of the mass flow rate and efficiency maps. In mathematical terms, the set of calibration coefficients can be expressed by the array

$$\overline{X} = \{K_{p1}, K_{p2}, K_{p3}, K_{inc}\} \tag{3.19}$$

where K_{p1},K_{p2},K_{p3}, and K_{inc} are the calibration coefficients in the loss models of Table 3.2. Therefore, the calibration aimed to minimize the overall relative root mean square error (RRMSE) in terms of mass flow rate and efficiency. The optimization function, f, was expressed as:

$$f = min\{\frac{1}{n_t}\sum_{i=1}^{n_t} RRMSE(\eta_{is,i}(\overline{X})), \frac{1}{n_t}\sum_{i=1}^{n_t} RRMSE(\dot{m}_i(\overline{X}))\} \tag{3.20}$$

$$RRMSE(\eta_{is}) = \sqrt{\frac{1}{n_p}\sum_{j=1}^{n_p}\left(\frac{\eta_{is,exp,j} - \eta_{is,mod,j}(\overline{X})}{\eta_{is,exp,j}}\right)^2} \tag{3.21}$$

$$RRMSE(\dot{m}) = \sqrt{\frac{1}{n_p}\sum_{j=1}^{n_p}\left(\frac{\dot{m}_{exp,j} - \dot{m}_{mod,j}(\overline{X})}{\dot{m}_{exp,j}}\right)^2} \tag{3.22}$$

where η_{is} denotes isentropic efficiency, $\dot{m}$ the mass flow rate, $i = 1,..,n_t$ the test cases and $j = 1,...,n_p$ the points in the map. The subscript *exp* refers to the experimental data whereas *mod* refers to the numerical data.

The multi-objective optimization, based on a genetic algorithm, was performed using 150 generations. During the optimization process, the set $\overline{X}$ of the calibration coefficients was changed to find the combination yielding the minimum RRMSE values. This approach is mathematically consistent; however, it does not ensure always that the solution is physically consistent. Therefore, two different scenarios were considered and analyzed. In the first one, the optimization was per-

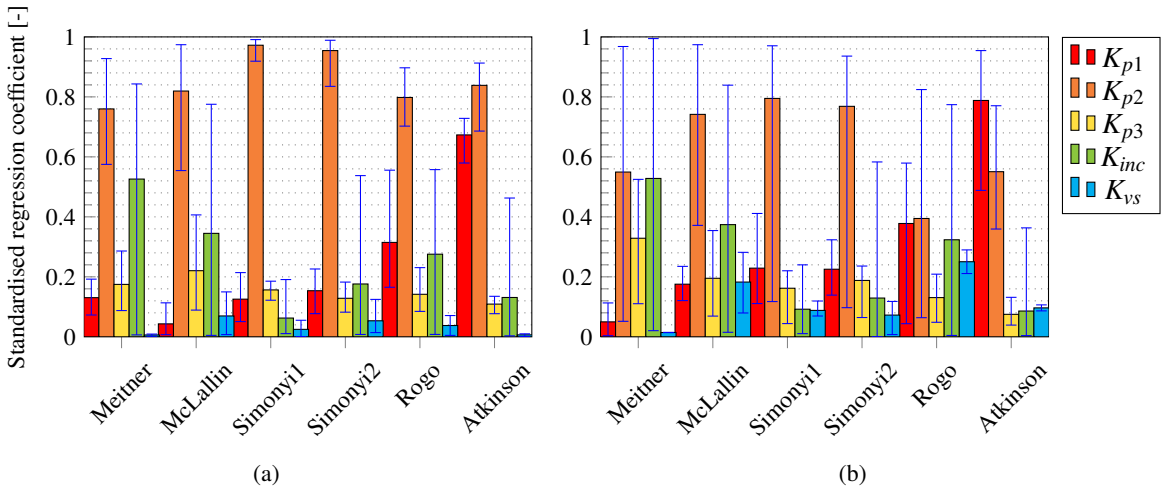

Figure 3.5: Significance level of the calibration coefficients: (a) on the turbine total-to-static isentropic efficiency; (b) on the mass flow rate. The bars indicate the standard deviation from the mean value. The analysis employed the test cases listed in Table B.1. From Ref. [95].

formed without any constraints in the possible values of the calibration coefficients. Therefore, the optimizer was free to find the solution that minimized the RRMSE values from the purely mathematical viewpoint. In a second case, the optimization was run using predefined constraints on the calibration coefficients, which were found by the sensitivity analysis as those values ensuring the correct prediction of the choking point in all the speed lines of the test case data.

3.2.5 Validation method

After the calibration process, the design and off-design models were validated with the objective to further assess the suitability of the loss models in the prediction of turbine performance. The validation of the design model was performed using the six test cases used for calibration of the off-design model. The suitability of the off-design model was assessed by validating it with the data of two additional test cases, with different geometric features than those used for calibration. The first test case was documented by Demierre et al. [125, 126] and is a 2 kW ORC turbine. This test case was chosen as it presents the full geometric details of the ORC turbine as well the operating points at off-design conditions. The turbine was tested with the organic fluid R134a in the range of pressure ratios 3.1 to 4.4 and rotational speeds 147 krpm to 206 krpm. The difference of this test case with respect to those used for calibration is that it employs a diffuser. This component was modelled using the approach described by Moustapha et al. [302] and using a total pressure recovery coefficient of 0.55. The second test case is the Ricardo C80 turbine, which differed from the test cases used for calibration for the presence of a volute. In this test case, described in Refs. [96, 97], the turbine was tested up to a pressure ratio of 5.0. The validation with this test case was performed by assuming that the losses in the volute were small and could be embedded in the nozzle losses. The throat size, which was not included in the original data, was computed using the

formulation by Li et al. [313]:

$$o_2 = 2r_3 sin\left(\frac{\theta}{2}\right) cos\left(\frac{\theta}{2} - \alpha_{3b} - \frac{\gamma}{2}\right) \tag{3.23}$$

In Eq. 3.23, the vane trailing edge is assumed to have a wedge shape with included angle $\gamma = 11°$ and with the center angle in the radial plane calculated as $\theta = 2\pi/Z_s$.

3.3 Results

3.3.1 Sensitivity analysis

The results of the global sensitivity analysis in terms of efficiency and the mass flow rate are shown in Figure 3.5. The results of the sensitivity analysis for the isentropic efficiency suggest that the calibration coefficient K_{p2}, related to the friction losses in the rotor passage, is the most significant one since the values of standardized regression coefficients are in the range 0.76 to 0.98. After K_{p2}, the coefficients K_{p1} and K_{inc}, related to nozzle passage losses and rotor incidence loses, rank as the second most important ones in some of the cases. The coefficient K_{p3} results to provide the smallest change in turbine efficiency, and therefore the analysis suggests that it is the least significant one. In terms of mass flow rate, the results are similar to those presented for the efficiency and indicate that K_{p2} is the most significant parameter, although it has a lower mean value and a larger scatter. The coefficient K_{p1} appears to have a strong influence in the determination of the mass flow rate in the last test case, and this suggests it has a stronger impact on the nozzle losses. The analysis suggests that the significance level of the calibration coefficient varies and it depends on the specific test case. At the same time, the coefficient K_{vs} shows the smallest values of mean and variance, and for this reason, it was not included as a coefficient for calibration. This choice enabled a reduction of the computational time of the calibration without an appreciable change in the accuracy of the results. Finally, the sensitivity analysis was employed to identify the ranges of the calibration coefficients fulfilling the identification of the choking point in the different cases. These ranges were subsequently employed for the constrained optimization process in the calibration.

3.3.2 Calibration

The results of the multi-objective optimization are shown in Figure 3.6. They are expressed in terms of the RRMSE in isentropic efficiency, $RRMSE_\eta$ and mass flow rate, $RRMSE_m$, and for the unconstrained and constrained optimization cases. After approximately 120 generations, the optimal Pareto front in Figure 3.6 was found. The optimal $RRMSE_\eta$ and $RRMSE_m$ are in the range 2.05 % to 2.17 and 1.45 % to 1.56 %, respectively, for the unconstrained optimization. In the constrained optimization, the identification of the choking point using constraints reduced the solution space, and therefore the optimal solutions are in the range 2.13 % to 2.8 % for $RRMSE_\eta$. As for $RRMSE_m$, values similar to those of the unconstrained optimization were found. The Pareto front consists of multiple optimal points, each of them identified by a set of calibration coefficients. The most suitable point in the front can be selected depending on key-decision criteria of the designer. In this work, the optimal point in the front was selected by assigning an equal weight to the two objective functions, resulting in the optimal calibration coefficients indicated in Table

Table 3.3: Optimal set of calibration coefficients for an equal weight of $RRMSE_\eta$ and $RRMSE_m$ in the pareto front. From Ref. [95].

	unconstrained	constrained
K_{p1}	1.3881	1.4152
K_{p2}	0.637	0.5903
K_{p3}	0.1042	0.4036
K_{inc}	0.8952	0.8754

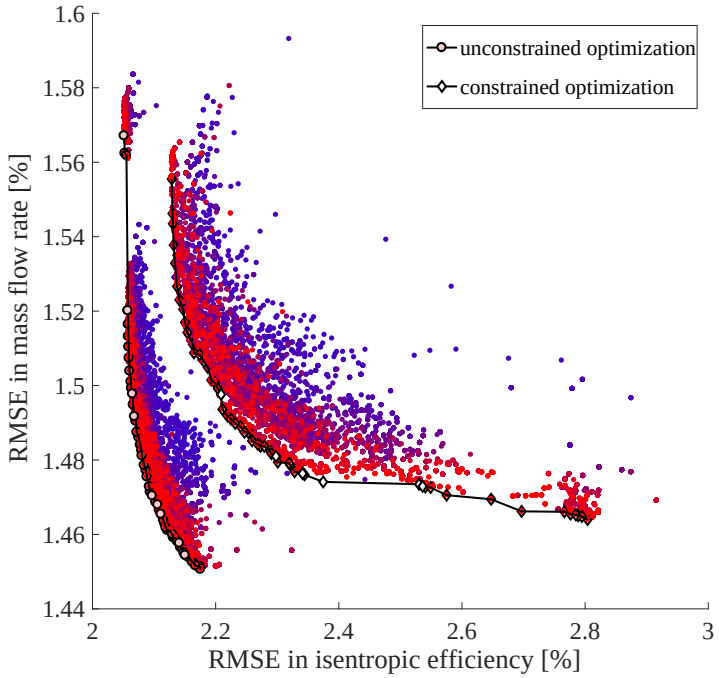

Figure 3.6: Optimal pareto fronts from the unconstrained and constrained multi-objective optimizations. The colours indicate the evolution of the pareto front from the initial (●) to the final (●) generations. From Ref. [95].

3.3. The results indicate that, compared to Baines' [137] values, a higher nozzle loss coefficient is required to obtain the best match with the test cases. Also, lower values of primary, secondary and incidence losses are required in the rotor.

The comparison of the results regarding $RRMSE_\eta$ and $RRMSE_m$ is illustrated in Figure 3.7 for the different cases. The calibration allowed reducing the overall $RRMSE_\eta$ from 5.88 % to 2.11 % and 2.04 % for the cases of constrained and unconstrained optimization, respectively. The overall deviation in mass flow rate reduced from 2.38 % to to 1.54 % and 1.33 %, respectively. A reduction in the deviation for the single test cases is also observed. It was observed that the difference in the optimal values between the constrained and unconstrained optimization cases was small, as also indicated in Table 3.3. The Figures 3.8 and 3.9 compared the performance maps before and after

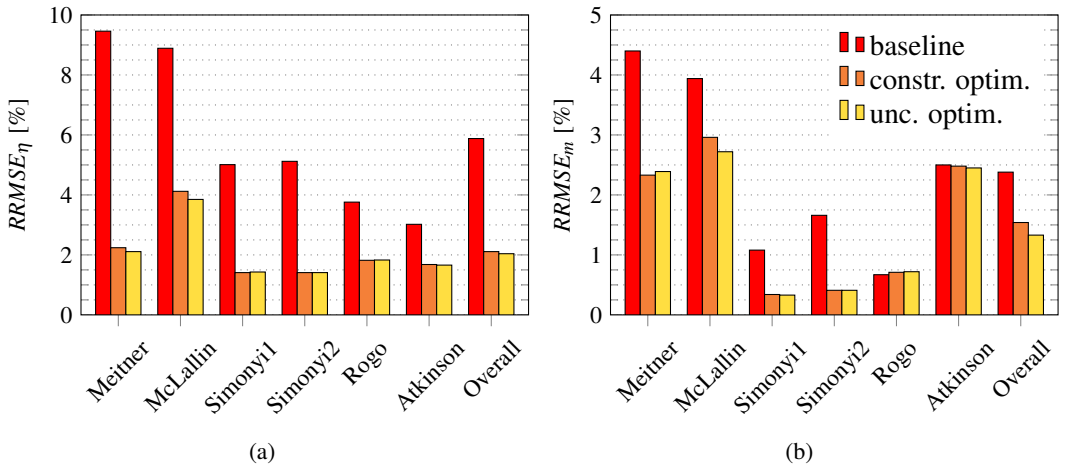

Figure 3.7: Comparison of RRMSE values for the different test cases before and after the optimization process: (a) RRMSE in isentropic efficiency; (b) RRMSE in mass flow rate. From Ref. [95].

the calibration process for three exemplary test cases.

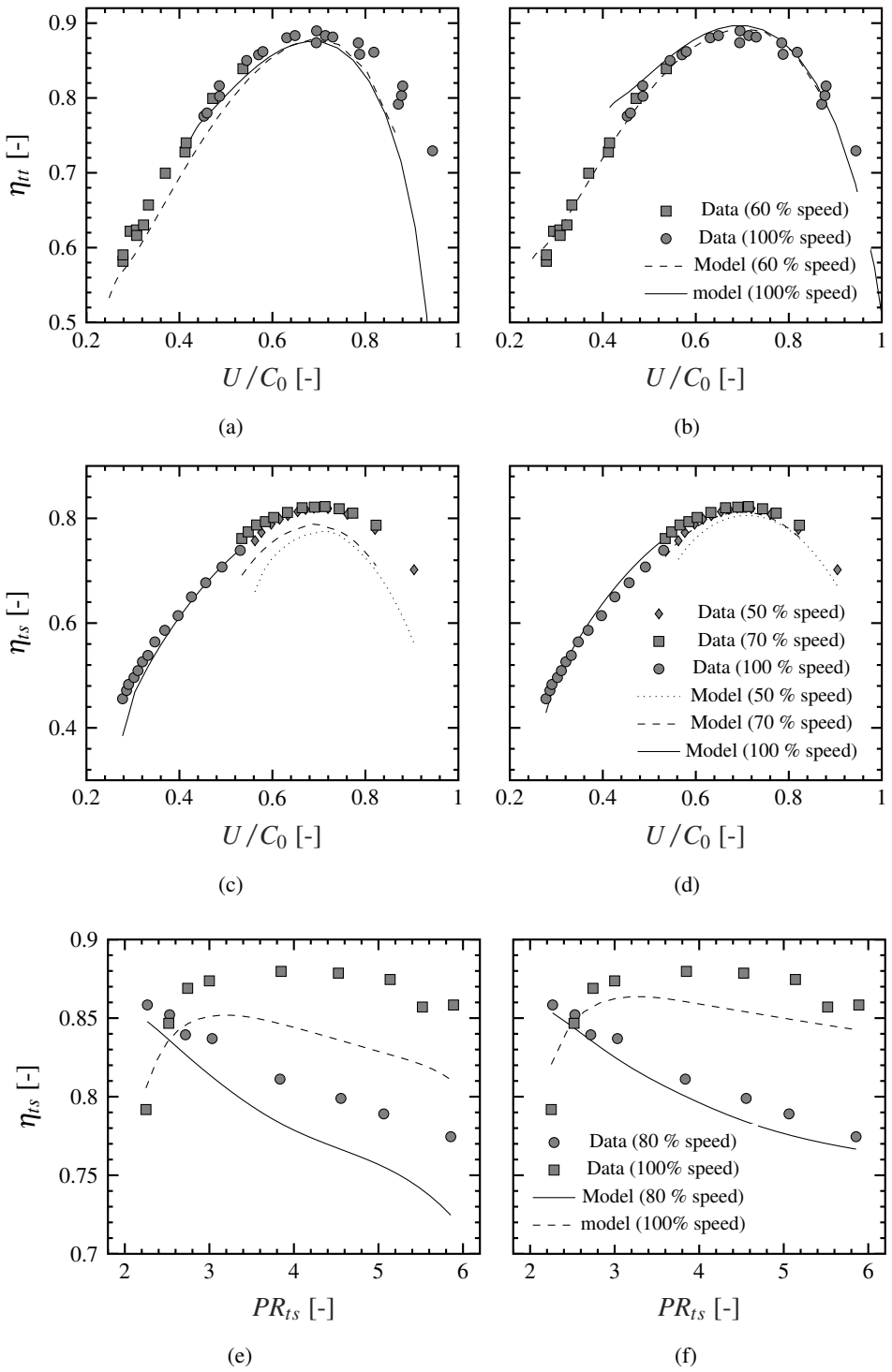

Figure 3.8: Exemplary isentropic efficiency maps before (a,c,e) and after (b,d,f) the multi-objective optimization: (a,b) Metiner and Glassmann [314] test case; (c,d) McLallin [98] test case; (e,f) Rogo [102] test case. From Ref. [95].

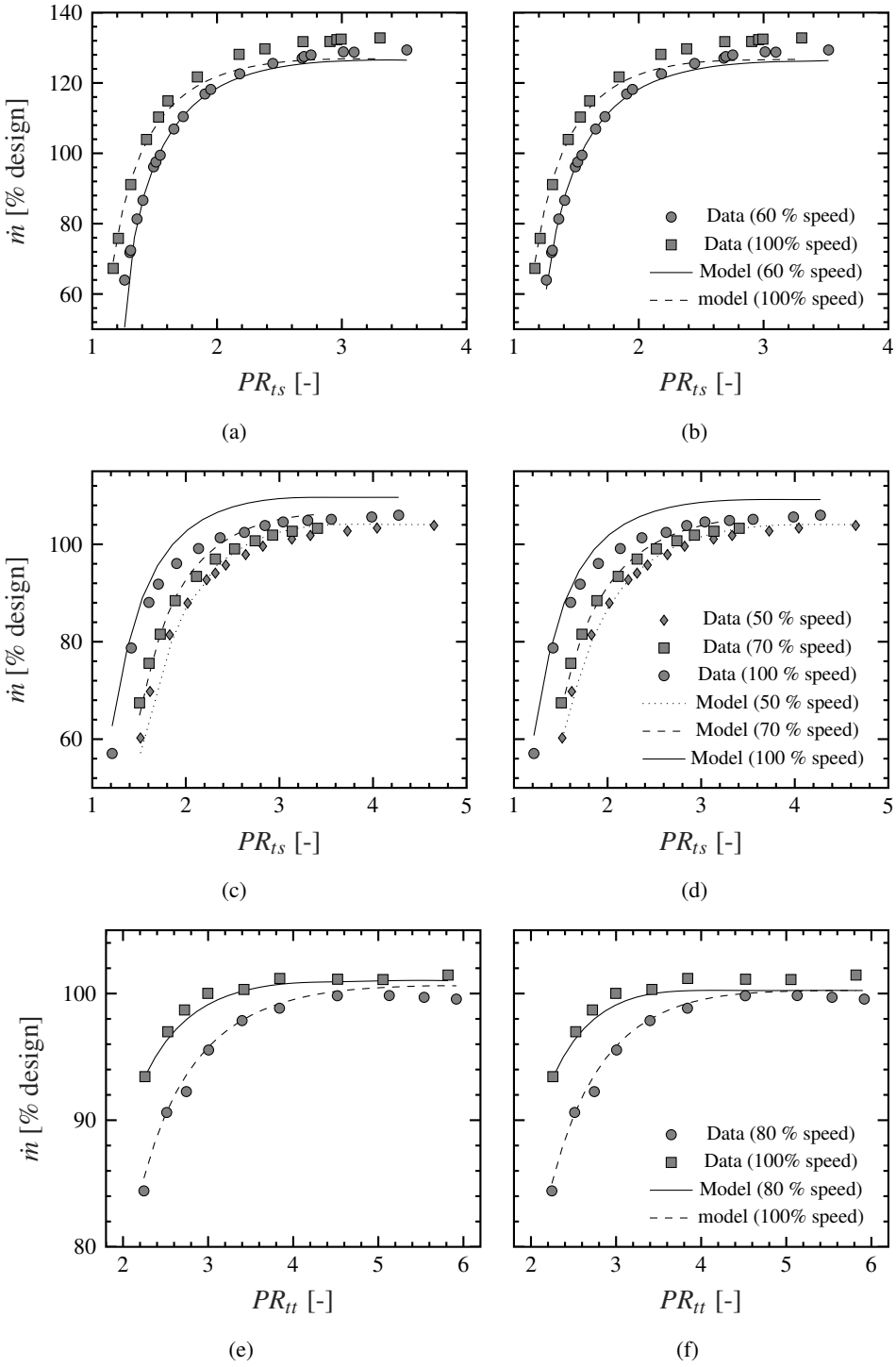

Figure 3.9: Exemplary mass flow rate maps before and after the multi-objective optimization: (a,b) Meitner and Glassmann [314] test case; (c,d) McLallin [98] test case; (e,f) Rogo [102] test case. From Ref. [95].

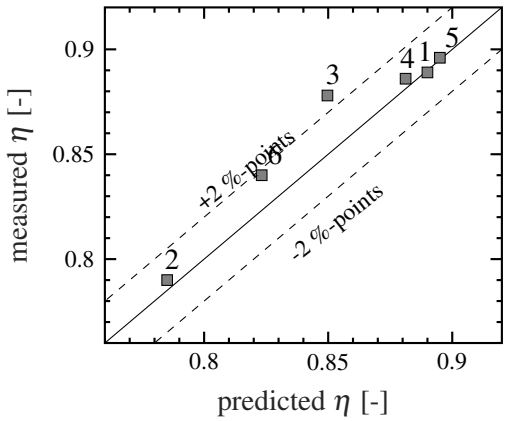

Test case	No.	PR_{ts} [-]	$\dot{m}$ [kg/s]	N [rpm]	U/C_0 [-]	η [-]	η_{exp} [-]	deviation [%]
Meitner and Glassman	1	1.54	0.260	29550	0.700	0.890 (t-t)	0.889 (t-t)	0.10%
Mc Lallin	2	3.23	0.187	31456	0.609	0.785 (t-s)	0.790 (t-s)	-0.49%
Rogo	3	4.54	1.044	164000	0.655	0.850 (t-t)	0.878 (t-t)	-2.83%
Simonyi rotor 1	4	4.99	2.361	19919	0.674	0.881 (t-t)	0.886 (t-t)	-0.48%
Simonyi rotor 2	5	4.99	2.350	18923	0.641	0.895 (t-t)	0.896 (t-t)	-0.10%
Atkinson	6	3.50	0.850	39000	0.700	0.823 (t-s)	0.840 (t-s)	-1.68%

(t-t) = total-to-total efficiency; (t-s) = total-to-static efficiency

Figure 3.10: Validation of the turbine design model. From Ref. [95].

3.3.3 Validation

In the validation of the design models, Figure 3.10 shows that the efficiency deviated in the range 0.1 %-points to 2.83 %-points depending on the test case, with the highest deviation found in the turbine investigated by Rogo [102]. Since the best fit is computed using all the measured operating points, the optimizer found the best fit at the expense of a higher deviation for the 100 % speed line.

The validation results for the test case of the turbine investigated by Demierre et al. [125, 126] are provided in Figures 3.11(a) and 3.11(b). The mean-line model shows a deviation within 1 % in the mass flow rate for all operating conditions, and seems to overestimate the value of total-to-static efficiency across all points. The values predicted with the numerical model have a deviation up to 5 % which is inside the range of uncertainty of the experimental data.

The validation results for the Ricardo turbine C80 are provided in 3.11(c) and 3.11(d). In the Ricardo turbine C80, the nozzle chokes first. Using Eq. 3.23 to estimate the nozzle throat opening, the $RRMSE_m$ is 1.75 %, as shown in Figure 3.11(d). It was noted that, in this specific case, the cosine rule used to compute the nozzle opening underpredicted the mass flow rate by 20 %. This result suggests that it essential to know the geometry accurately at the throat as this can have a large impact on the mass flow rate and, consequently, on the efficiency.

As for the efficiency, the best match is obtained at lower values of rotational speed and velocity

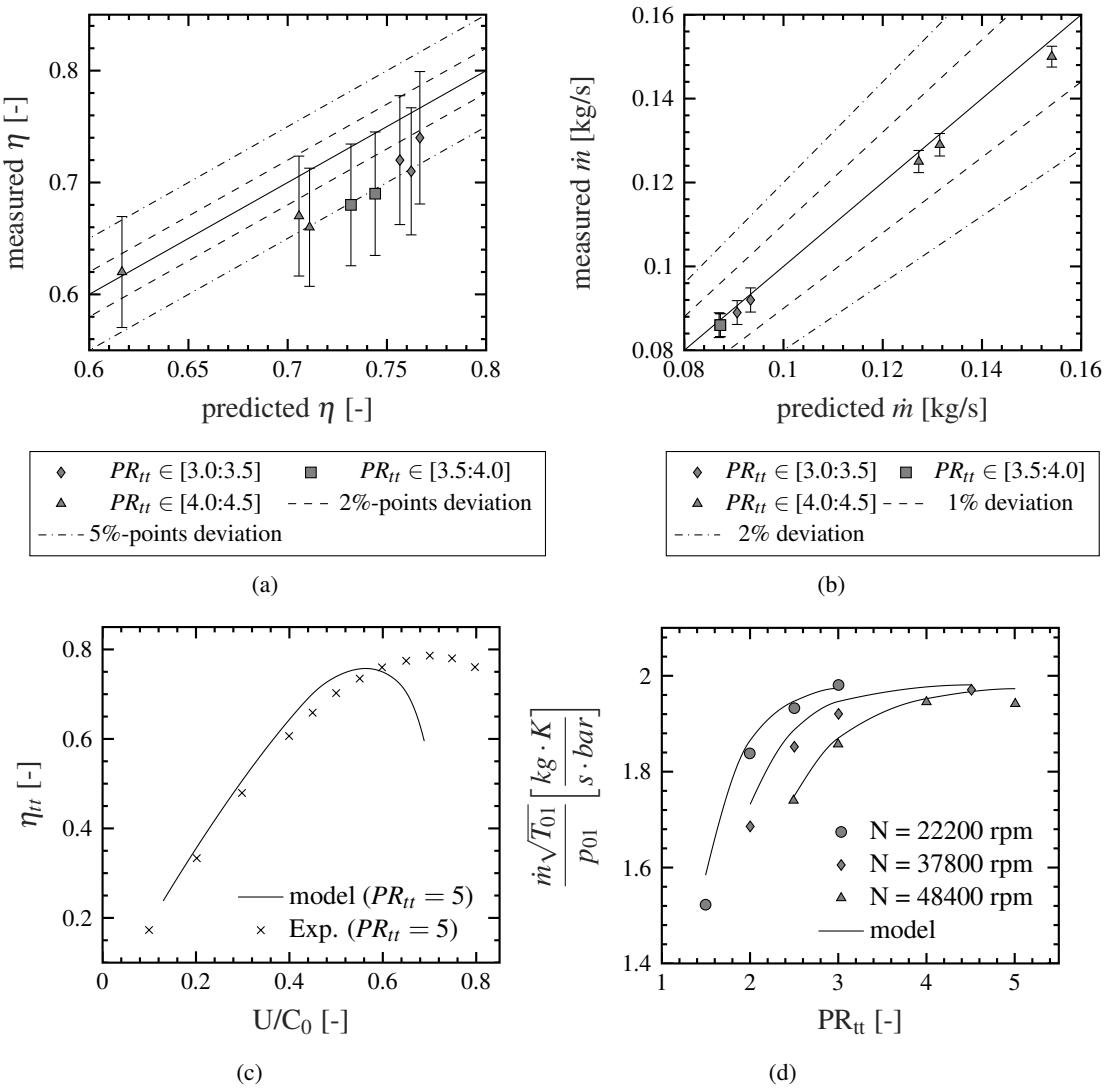

Figure 3.11: Validation of the off-design turbine model: (a,b) turbine by Demierre et al. [125, 126]; Ricardo C80 turbine [96, 97]. The error bars represent the uncertainty in the experimental measurements. From Ref. [95].

ratio U/C_0 whereas the losses are higher at higher speeds and the peak of the efficiency curve is located at lower values of U/C_0, approximately 0.55.

3.4 Discussion

This work identified the optimal coefficients for the loss models by achieving the best possible match with the experimental data regarding the flow rate and turbine efficiency. The resulting model can be used to perform the preliminary design and to predict the turbine efficiency for HPR turbines. At the same time, it was not assessed how suitable the the loss models could be to estimate

the flow conditions inside and between the blade rows since this was outside the scope of this work. For this reason, definitive conclusions are to be drawn only after careful evaluation with the internal flow conditions from experimental data and the results of high-fidelity CFD simulations.

An important aspect that requires a proper discussion is the model accuracy obtained in the results. After the calibration, it was possible to achieve values of accuracy in the range $\pm$ 2.1 %. In order to evaluate whether this accuracy is acceptable, a comparison with the accuracy of other performance prediction methods from the literature is performed here. A deviation within 1 %-point in performance prediction was achieved by Glassman [140], who calibrated the loss models to the data of three RITs operating at low-pressure ratio conditions. Values of $\pm$ 2 % in efficiency were obtained by Rodgers [132] in the validation of a RIT model. The model by Baines [137, 139, 302] showed an accuracy of 3.20 %-points in efficiency, corresponding to an RRMSE value of 5.80 % at the best efficiency points, in the validation with the data of 30 turbines. The RRMSE value obtained by Baines [137, 139, 302] is in the same order of magnitude of that obtained in this work before the optimization, see Figure 3.7. The performance prediction models presented by the aforementioned authors highlight values of accuracy in the range 1 %-point to 3.8 %-points. This suggests that the accuracy of 2.1 %-points obtained with the present model is acceptable.

The test cases used to calibrate the model presented in this work all featured conventional design characteristics such as rotor inlet radial blades, no volute and diffuser, air as the working fluid, and rotor tip diameters in the range 116 to 370 mm. The same accuracy is not expected for turbines having different characteristics. As a matter of facts, the validation of the same model with the test case by Demierre et al. [125, 126], whose turbine tip diameter was 18 mm, the working fluid is R134a, and features a diffuser, showed a deviation in the values of isentropic turbine efficiency up to 5 %-points. The validation with another test case, the Ricardo C80 turbine, featuring an 80 degree nozzle and a volute, suggested that knowing the size of the throat accurately is paramount to predict the mass flow rate accurately, and suggests the use of suitable correlations for the estimation of the throat opening, such as Eq. 3.23.

Finally, it is remarked that the results and methodologies presented here are suitable to HPR turbines operating with any working fluid and in the gas phase. The accuracy of the performance prediction model is expected to be in the range of the calibrated model for turbines having geometric and fluid-dynamic characteristics similar to those of the calibration test cases. In other situations, it is suggested that the mass flow rate is computed in a reasonable range if the turbine geometry is well-defined whereas a lower accuracy in efficiency must be expected when using turbines with different geometric and fluid-dynamic features.

3.5 Conclusions

This chapter presented a methodology for the preliminary design and performance prediction of high-pressure ratio turbines. This was the first time that a comprehensive methodology including performance prediction models, calibration, validation and analysis of the results was presented based on the experimental data of turbines operating at high pressure ratio. To this end, a single-stage, mean-line model of a radial-inflow turbine was developed, including the details of the employed numerical strategy for the treatment of the possible choking flow conditions. A global sensitivity analysis allowed determining the most important calibration coefficients to be applied

to the loss models. The loss coefficients were calibrated by minimizing the predicted deviation in efficiency and mass flow rate across all the measured data at off-design conditions. The calibration method used for the first time a multi-objective optimization based on a genetic algorithm, which provided a significant reduction in the predicted deviation with the experimental data in comparison to the baseline case (no optimization). In this respect, the deviation, expressed in relative RMSE values, decreased from 5.9 % to 2.1 % in terms of efficiency and from 2.4 % to 1.5 % in terms of mass flow rate.

The calibrated loss coefficients provided a deviation of 2.83 % for the design model efficiency. Afterwards, the calibrated model was used in the validation with an ORC turbine and another air turbine, whose design and fluid-dynamic features where different from those used in the calibration. The validation with the ORC turbine yielded a deviation within 1 % in the mass flow rate and about 5 % in efficiency. The validation with the second test case of an air turbine provided acceptable results in mass flow rate and efficiency, and highlighted that a correct estimation of the actual throat size is paramount. Future work should be devoted to use the developed tool and methodologies for the design, analysis and optimization of ORC power systems.

4 Centrifugal compressors for heat pump systems

The work presented in this chapter is unpublished work, see Ref. [315].

4.1 Introduction

The background and motivations for this work were presented in Chapter 1.4. This chapter presents a methodology for the combined design of heat pumps and centrifugal compressors.

For centrifugal compressors, steady-state mean-line models for the design, and off-design are developed following an approach similar to that of RITs. The models offer the possibility to include different working fluids thanks to the general formulation of the governing equations and the use of accurate equations of state for the estimation of the fluid's thermodynamic and transport properties. To account for the possibility of choking conditions in the blade rows, the onset of choking is predicted using a specific numerical method. The compressor model is then validated at the design and off-design conditions with the data of five test cases, including three different working fluids: air, the refrigerant R134a, and CO_2. Afterwards, it is combined with the model of a high-temperature heat pump and the combined model is optimized for different working fluids to determine the solution that optimizes the performance from both the heat pump and the compressor viewpoints. The main novel contributions of this chapter, concerning the review of the literature in Sec. 1.2.5, are the following: (1) a thorough CC model validation for different test cases including three different working fluids (air, R134a and CO_2); (2) a methodology for the combined optimization of a heat pump equipped with CCs, enabling the selection of the most suitable working fluid.

The structure of this chapter is the following: Section 2 presents the compressor models, the validation and the optimization methods. Section 3 presents the results of the compressor model validation and the optimization methodology. Section 4 discusses the results, and Section 5 draws the conclusions.

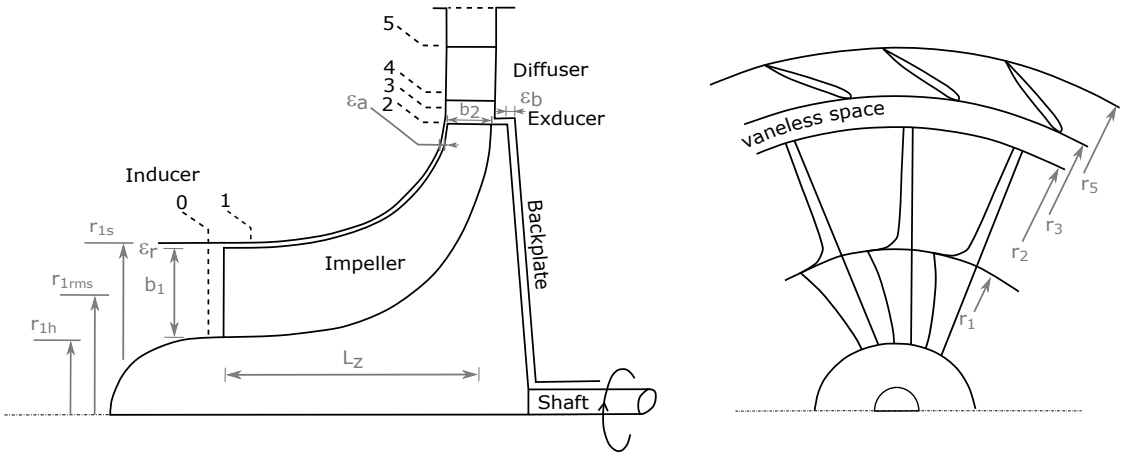

Figure 4.1: Schematic of the centrifugal compressor geometry. From Ref. [315].

4.2 Methods

This work employed a steady-state, mean-line model for the performance prediction of CCs at design and off-design conditions. The model, implemented in the MATLAB language [214], followed a mean-line approach in which the thermodynamic and flow conditions were computed at the mean streamline in the compressor meridional plane, and were representative of mass-weighted averaged conditions over the whole section. The subcomponents which were considered in the compressor modeling were the impeller, the vaneless diffuser and the vaned diffuser. A schematic of the compressor model is illustrated in Figure 4.1, where the main stations and the terminology used in this chapter are also highlighted. Mass and energy balances and loss equations accounting for the entropy generation were solved to determine the thermodynamic and flow conditions in the main stations. Real-gas equations of state were used to compute the thermodynamic and fluid transport properties of the fluids using the thermodynamic libraries CoolProp [218] and REFPROP [217].

A paramount aspect of the development of the compressor model was to account for choking conditions, which determine the maximum allowable mass flow rate through the compressor. When the speed of sound is reached within the compressor passages, the flow is said to be choked [301]. Usually, the choking point is experienced in the impeller blades or in the vaned diffuser, in correspondence of the points of minimum flow area [316]. In the impeller, choking also depends on the rotational speed as this will affect the values of local relative velocity inside the impeller blades. It is important to detect choking in the machines since when this occurs the mass flow rate cannot be increased, determining a constraint on the compressor operational range and a sudden drop in the performance. The modeling strategy adopted in the compressor models identifies the choking point by screening the possibility of choking conditions in the impeller inlet, the impeller outlet, or in the vaned diffuser.

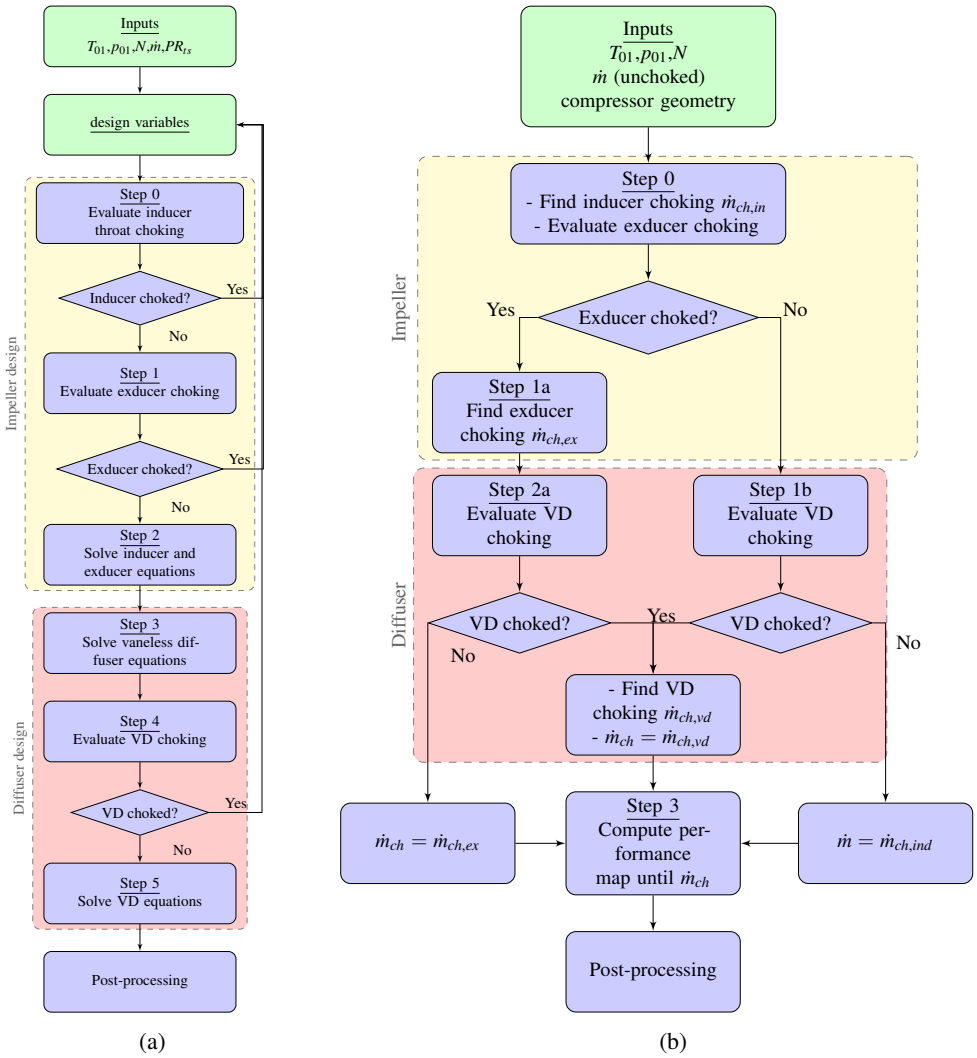

Figure 4.2: modeling strategy for centrifugal compressors: (a) preliminary design model; (b) analysis model. From Ref. [315].

4.2.1 Design model

The workflow of the preliminary design model is shown in Figure 4.2(a). The model inputs are the following: the inlet total temperature T_{01}, the inlet total pressure p_{01}, the rotational speed N, the mass flow rate $\dot{m}$, and the stage total-to-static pressure ratio PR_{ts}. The inputs also include a set of decision variables related to geometry and loading conditions which are to be provided. The design variables and the optimization constraints used in this work are shown in Table 4.1. The boundaries come from the literature [182, 198] and are expressed using upper and lower bounds in order to ensure that the design solutions are manufacturable, physically meaningful and technically feasible. Mechanical stress issues on the blades are avoided by setting an upper limit to the tip speed based on recommendations from the literature. Since the modeling strategy described in Figure 4.2(a) relates to a given set of decision variables, an optimization strategy was applied to

Table 4.1: Design variables and optimization constraints of the compressor design model. From Ref. [315].

Decision variable	Description	Units	Lower boundary	Upper boundary
$\psi_{is} = \Delta h_{0,is}/U_2^2$	Isentropic stage loading coefficient	[-]	0.3	1.1
N	Rotational speed	[krpm]	1	210
r_{1s}/r_2	Inlet shroud to tip radius ratio	[-]	0.4	0.7
r_{1h}/r_{1s}	Inlet hub to shroud radius ratio	[-]	0.25	0.7
b_2/r_2	Exit blade width over radius	[-]	0.02	0.8
β_{2b}	Impeller exit blade angle	[°]	-45	0
β_{1b}	Impeller inlet average blade angle	[°]	-70	-20
Optional decision variable				
Z_r	Number of total impeller blades	[-]	6	60
Additional constraints				
$M_{1s,rel}$	Relative Mach number at impeller inlet shroud	[-]	0	1.4
$M_{1,rel}$	Relative Mach number at impeller inlet	[-]	0	0.9
W_2/W_{1s}	Ratio of exit to inlet shroud relative velocities	[-]	0.25	-
α_2	Impeller exit absolute flow angle	[°]	-	85
o_1	Impeller inlet throat	[mm]	1.49	50
χ	Stage degree of reaction	[-]	-0.1	0.9
U_2	Impeller exit peripheral speed	[m/s]	0	400
r_3/r_2	Vaneless diffuser radius ratio	[-]	1.05	2
Fixed values (if not specified)				
t_b	Blade thickness	[mm]	0.2	
ε	Impeller clearance	[mm]	0.15	
ε_b	Impeller backface clearance	[mm]	1	
k_s	Impeller surface roughness	[mm]	0.002	
b_3/b_2	Diffuser width ratio	[-]	1	
CP	Diffuser pressure coefficient	[-]	0.44	

determine the set of variables leading to the optimal compressor design, see Sec. 4.2.5. According to the specifications of the selected application, some decision variables can also be fixed and not optimized. For example, the number of impeller blades can be set as an input or can be optimized. In case of the design model, they were computed from an empirical correlation, as follows [317]:

$$Z_r = 12.03 + 2.544 PR_{tt} \qquad \text{(without splitters)} \tag{4.1}$$

$$Z_r = -4.527 e^{1.865/PR_{tt}} + 32.22 \qquad \text{(with splitters)} \tag{4.2}$$

Where Z_r is the number of impeller blades and PR_{tt} the stage total-to-total pressure ratio. The design model was implemented following the guidelines by Japikse and Baines [168] and Whitfield and Baines [304].

The modeling strategy illustrated in Figure 4.2(a) starts by evaluating if the compressor is choked for the set of specified design and input variables (*Step 0*). If the stage results to be choked, the compressor is not able to accommodate the mass flow rate specified as an input, and the decision variables are to be changed. The choking condition is determined using a numerical method. The equations in the inducer throat regarding mass continuity, energy balance, and the isentropic process

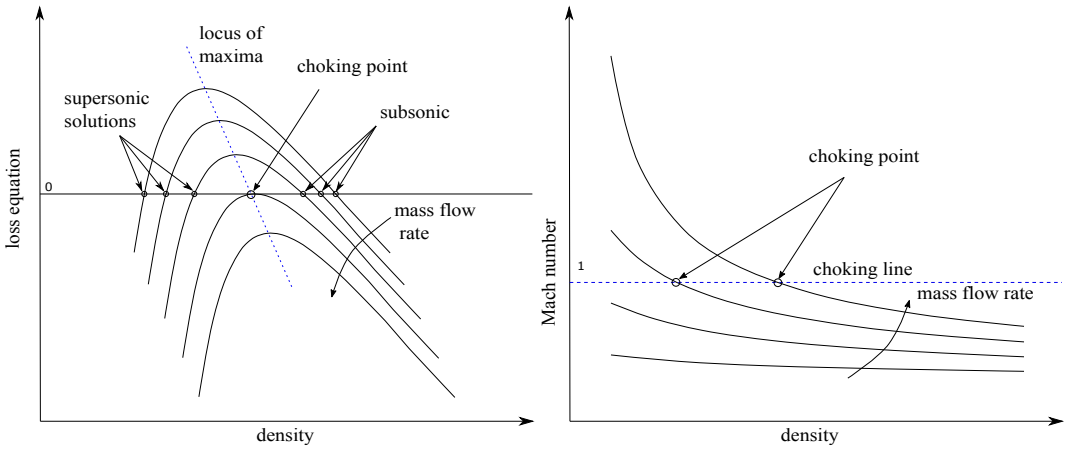

Figure 4.3: Identification of the choking point for a blade row: (a) residual of the loss equation, and (b) Mach number. From Ref. [315].

equation equation are the following:

$$W_1 = \dot{m}/(\rho_1 A_{th,1}) \tag{4.3}$$

$$h_1 = h_{01} - \frac{1}{2}W_1^2 + \frac{1}{2}U_{1,rms}^2 \tag{4.4}$$

$$s_{01} - s_1 = 0 \tag{4.5}$$

In Eqs. 4.3 to 4.5 the parameters ρ_1, $A_{th,1}$, W_1, $U_{1,rms}$, and h_1 denote the density, flow area, relative velocity, root-mean-square average peripheral speed, static specific enthalpy at the inducer throat section, respectively. The term h_{01} is the total specific enthalpy, and s_{01} and s_1 denote the total and static specific entropies, respectively. It is assumed that the process from the inducer inlet to the throat is isentropic in Eq. 4.5. Figure 4.3(a) shows that the left-hand side of Eq. 4.5 can be expressed as a function of ρ_1 and $\dot{m}$ for the specified inlet and geometric conditions.

As explained in Chapter 3.5, the residual function in Figure 4.3(a) shows a non-monotonic behavior with a maximum. The condition at which the peak of this function crosses the abscissa was identified as the *choking condition*. Eqs. 4.5 has two solutions at small values of $\dot{m}$, one representing the solution for subsonic conditions and the other for supersonic conditions. At higher values of mass flow rate, the maximum of the function shifts downwards and eventually crosses the density axis. This condition corresponds to choking, where numerically the subsonic and supersonic solution coincide, and physically the sonic conditions are reached at the point of minimum relative flow area in the blade passage. If a higher mass flow rate is employed, there is no solution to the system of equations, as shown in Figure 4.3(a). To produce a compressor design which complies with the specified mass flow rate, a different set of decision variables needs to be employed. If there is no choking at the inducer section, the modeling strategy proceeds and it checks whether choking conditions occur at the exducer section (*step 1*). The equations for mass and momentum balances

and the losses at the exducer section 2 are expressed as follows:

$$C_{2m} = \dot{m}/(\rho_2 A_2) \tag{4.6}$$

$$h_{02} = h_{01} + C_{2t}U_2 - C_{1t}U_{1,rms} \tag{4.7}$$

$$\sum_{n=1}^{n_{loss}} \Delta h_{loss,imp} - h_{02} + h(p_{02}, s_{01}) = 0 \tag{4.8}$$

where $\Delta h_{loss,imp}$ denotes the n^{th} impeller loss, which is computed using the empirical correlations described in Sec. 4.2.3. Equation 4.7 requires an expression for the tangential component of the rotor exit absolute velocity, C_{2t}. This is provided using the component in the meridional direction, C_{2m}, and the slip factor σ, which is an indication of the flow deviation at the impeller exit. Once the slip factor is known from empirical correlations, a slip velocity can be computed and C_{2t} and C_2 are provided as follows:

$$C_{2t} = \sigma U_2 - C_{2m}\tan(|\beta_{2b}|) \tag{4.9}$$

$$C_2 = \sqrt{C_{2m}^2 + C_{2t}^2} \tag{4.10}$$

$$h_2 = h_{02} - \frac{1}{2}C_2^2 \tag{4.11}$$

The evaluation of the possible choking at the exducer section is carried out in the same way as the inducer. The left-hand side of Eq. 4.8 is a function of the mass flow rate and the impeller exit density, and has a trend similar to that of Figure 4.3(a). If choking conditions occur, or if the specified mass flow rate is higher than the choking value, the modeling strategy exits the design routine. Alternatively, the set of Eqs. 4.6-4.8 are solved, and the thermodynamic and flow conditions at the impeller exit section are found (*Step 2*). If there is not a diffuser, the design routine terminates, and the model performs the post-processing operations necessary to compute the performance and the final design of the machine.

In the presence of a vaneless diffuser, the total pressure loss coefficient K and the ideal pressure coefficients were computed based on the specified stage exit total pressure p_{03} and pressure coefficient CP as follows:

$$K = \frac{p_{02} - p_{06}}{p_{02} - p_2} \tag{4.12}$$

$$p_3 = p_2 + CP(p_{02} - p_2) \tag{4.13}$$

$$CP_{id} = CP + K \tag{4.14}$$

The vaneless diffuser exit state was then determined by solving the following set of equations for the exit density ρ_3 [168]:

$$h_3 = h(\rho_3, p_3) \tag{4.15}$$

$$C_3 = \sqrt{2(h_{02} - h_3)} \tag{4.16}$$

$$\dot{m} - C_3\rho_3 A_2 cos(\alpha_2)(1 - CP_{id})^{-0.5} = 0 \tag{4.17}$$

According to Japikse [316], the vaneless diffuser cannot be choked since it has no throat section. However, in the presence of a vaned diffuser (VD), which has a throat section at the inlet, the modeling strategy requires further evaluation of the choking conditions occurring in this component (*Step 4*). To this end, the equations in the vaned diffuser throat are formulated as:

$$C_4 = \dot{m}/(\rho_4 A_{th,4}) \tag{4.18}$$

$$h_4 = h_{03} - \frac{1}{2}C_4^2 \tag{4.19}$$

$$S_{03} - S_4 = 0 \tag{4.20}$$

Using the numerical solution strategy employed for the impeller, it is checked that the vaned diffuser is not choked at its throat section. If it is choked, the design routine ends. Otherwise, the equations at the diffuser exit are solved as follows (*Step 5*):

$$C_5 = \dot{m}/(\rho_5 \cos\alpha_5 A_5) \tag{4.21}$$

$$h_5 = h_{03} - \frac{1}{2}C_5^2 \tag{4.22}$$

$$\sum_{n=1}^{n_{loss}} \Delta h_{loss,vd} - h_{03} + h(p_5, S_3) = 0 \tag{4.23}$$

The design mode has the stage total-to-static pressure ratio specified, and therefore also the exit static pressure p_5. Accordingly, the exit flow angle α_5 is computed from the solution of Eqs. 4.21 to 4.23 to match p_5. However, in the off-design mode, p_5 is not known beforehand. To close the set of vaned diffuser equations, the exit flow angle was approximated with the vane exit angle assuming that the exit flow deviation is negligible.

4.2.2 Off-design model

The off-design modeling strategy is shown in Figure 4.2(b). In the off-design strategy, the compressor geometry is provided as an input, and the model generates compressor performance maps as the output. To generate the maps, the mass flow rate $\dot{m}$ is required as input whereas the stage pressure ratio and efficiency are model outputs. The stage performance is computed for each value of mass flow rate and a single speed line whereas full performance maps are generated using an iterative scheme for the different values of rotational speed. The starting point of the off-design strategy is to evaluate if the inducer or the exducer is choked first for the assigned inputs and conditions and compressor geometry (*Step 0*). The inducer throat was modeled using Eqs. 4.3-4.5. The choking mass flow rate at the inducer throat is determined by solving for the zero of the locus of maxima of the left-hand side of Eq. 4.5. The resulting value of choking mass flow rate is then used to evaluate whether the exducer is already choked by screening the location of the peak of the function at the left-hand side of Eq. 4.8. Two different paths in the modeling strategy are followed accordingly.

In case the exducer choked, the value of choking mass flow rate was determined by solving for the zero of the locus of maxima of Eq. 4.8. The performance maps for the unchoked flow regime were computed by varying the mass flow rate until the choking value (*step 3*). The following set of one-dimension equations [303] was solved in each point of the vaneless space after the impeller, to

provide the thermodynamic and flow conditions:

$$C_m \frac{dC_m}{dr} - \frac{C_t^2}{r} + C_f \frac{C^2 \cos(\alpha)}{b} + \frac{1}{\rho}\frac{dp}{dr} = 0 \tag{4.24}$$

$$C_m \frac{dC_t}{dr} + \frac{C_m C_t}{r} + C_f \frac{C^2 \sin(\alpha)}{b} = 0 \tag{4.25}$$

$$\frac{1}{\rho}\frac{d\rho}{dr} + \frac{1}{C_m}\frac{dC_m}{dr} + \frac{1}{b}\frac{db}{dr} + \frac{1}{r} = 0 \tag{4.26}$$

$$h_{02} - h - \frac{1}{2}C^2 = 0 \tag{4.27}$$

The vaneless space width b is provided at every point along the vaneless space by interpolation between the inlet and outlet values. The term C_f in Eqs. 4.24 and 4.25 denotes the vaneless space friction factor, and was estimated using a correlation by Japikse [311] as $C_f = k(1.8 \cdot 10^5 / Re)^{0.2}$. Japikse [311] recommended using values between 0.005 and 0.02 for k. In this work the best match with the data used for validation was found for the value 0.005. To solve the system of equations 4.24-4.27, a MATLAB ODE15i solver [214] was employed using initial values of C_m, C_t, ρ and p at the impeller outlet.

Steps 2a and *1b* were added to the modeling strategy to evaluate whether the diffuser choked before the impeller. The vaned diffuser choking mass flow rate was determined by solving for the zero fo the locus of maxima in the set of Eqs. 4.21-4.23.

4.2.3 Empirical models for losses and flow deviation

The set of loss models used in this work, shown in Table 4.2, was selected as the different loss models were employed by many authors, they are well-described in the original references, and provided a good match with the experimental data of the validation.

The slip factor in Eqs. 4.6-4.8 was estimated according to the correlation by Wiesner [318], and further improved by Aungier [197] to account for splitter blades a limiting value for high inlet-to-outlet impeller radius ratios. Additional information on the employed correlations for losses and flow deviation is included in Appendix C.

4.2.4 Validation

Five well-documented test cases from the open literature were used for the validation of the mean-line model. The test cases featured three different working fluids: air, R134a, and CO_2. The input data used for validation are listed in Table C.1 in Appendix C. In the analysis mode, the actual compressor geometry was fully assigned, and the performance of the model was compared to that of the experimental test cases. In the design mode, the specifications of the design point were assigned as well as the full geometry of the impeller. However, the diffuser ratio was an output and it was computed to match the stage exit pressure prescribed by the input pressure ratio.

Table 4.2: Loss correlations. From Ref. [315].

Loss mechanism	Loss model	Reference
Impeller incidence	$\Delta h_{inc} = \frac{1}{2} W_1^2 sin^2 \lvert \beta_{1,opt} - \beta_1 \rvert$	Galvas [199]
	$\beta_{1,opt} = tan^{-1}[(A_1/A_{th,1}) tan\beta_{1b}]$	
Impeller friction	$\Delta h_{sf} = 4 C_{fi} \frac{L_b}{d_{hb}} \overline{W}^2$	Galvas [199]
	$\overline{W} = max\{\sqrt{(W_1^2 + W_2^2)/2}), \sqrt{(W_{th,1}^2 + W_2^2)/2}\}$	Aungier [197]
	$L_b \approx \frac{\pi}{8}(2r_2 - (r_{1s} + r_{1h}) - b_2 + 2L_z)\left(\frac{2}{(cos\beta_{1s} + cos\beta_{1h})/2 + cos\beta_{2b}}\right)$	Jansen [319]
	$d_{hb} = \frac{2r_2}{\frac{Z_r}{\pi cos\beta_{2b}} + \frac{2r_2}{b_2}} + \frac{2r_{1s}}{\frac{2}{1 - r_{1h}/r_{1s}} + \frac{2Z_r}{\pi(1 + r_{1h}/r_{1s})}\sqrt{1 + tan^2\beta_{1bs}\left(1 + \frac{(r_{1h}/r_{1s})^2}{2}\right)}}$	Galvas [199]
Impeller blade loading	$\Delta h_{bl} = 0.05 D_f^2 U_2^2$	Coppage [204]
	$D_f = 1 - \frac{W_2}{W_1} + c_{df}\frac{\Delta h_0}{U_2^2}\frac{W_2}{W_{1s}}\left(\frac{Z_r}{\pi}\left(1 - \frac{r_{1s}}{r_2}\right) + 2\frac{r_{1s}}{r_2}\right)^{-1}$	
Impeller clearance	$\Delta h_{cl} = 0.6\frac{\overline{\varepsilon}}{b_2}\lvert C_{2t}\rvert\sqrt{\frac{4\pi}{b_2 Z_r}\frac{r_{1s}^2 - r_{1h}^2}{(r_2 - r_{1s})(1 + \rho_2/\rho_1)}\lvert C_{2t}\rvert C_{1m}}$	Jansen [319]
	$\overline{\varepsilon} = (\varepsilon_a + \varepsilon_r)/2$	
Impeller mixing	$\Delta h_{mix} = \frac{1}{1 + tan^2(\alpha_2)}\left(\frac{1 - \varepsilon_w - b^*}{1 - \varepsilon_w}\right)^2 \frac{1}{2} C_2^2$	Johnston and Dean [320]
	$\chi = 0.93\varepsilon_w^2 + 0.07\varepsilon_w$ where $b^* = 1, \quad \chi = 0.15$	Japikse [316]
Impeller disc friction	$\Delta h_{df} = 0.25\frac{\rho_i U_2^3 r_2^2 K_f}{\dot{m}}$ where $\rho_i = (\rho_1 + \rho_2)/2$	Daily and Nece [312]
	if $Re_2 = \frac{\rho_2 U_2 r_2}{\mu_2} < 3 \cdot 10^5 \qquad K_f = 3.7\frac{(\varepsilon_b/b_2)^{0.1}}{Re_2^{0.5}}$	
	if $Re_2 = \frac{\rho_2 U_2 r_2}{\mu_2} > 3 \cdot 10^5 \qquad K_f = 0.102\frac{(\varepsilon_b/b_2)^{0.1}}{Re_2^{0.2}}$	
Impeller recirculation(*)	$\Delta h_{rc} = 8 \cdot 10^{-5} sinh(3.5 \cdot \alpha_2^3) D_f^2 U_2^2$	Oh et al. [196]
Vaned diffuser incidence	$\Delta h_{vd,inc} = 0.6 sin^2 \lvert \alpha_3 - \alpha_{3b} \rvert \frac{1}{2} C_3^2$	Conrad [321]
Vaned diffuser friction	$\Delta h_{vd,sf} = 2 C_{f,vd} C_{m,vd}^2 \frac{L_{b,vd}}{d_{hb,vd}}$	Conrad [321]
	$L_{b,vd} = \frac{r_5 - r_3}{cos\left(\frac{\alpha_{3b} + \alpha_{5b}}{2}\right)} \qquad d_{hb,vd} = \frac{o_4 b_4}{o_4 + b_4} + \frac{o_5 b_5}{o_5 + b_5}$	

(*) the flow angle is expressed in radians

Air compressors

Three experimental test cases employed air as the working fluid. These test cases are a family of compressors which were extensively documented and investigated in the literature. Japikse claimed that this set of compressors was the most comprehensive set of experimental data for CCs in the literature [167]. The three compressors were named *Eckardt compressors*, in honor of Dr. Dietrich Eckardt who tested them in the 1970s. The experimental results for the three test cases were published in a number of scientific papers [164, 166, 322]. The tests were conducted using laser two-focus velocimetries, high-frequency pressure transducers, and conventional pneumatic probes. The experimental data have an accuracy of $\pm$ 1 % in terms of mass flow rate, $\pm$ 3 rpm in the rotational speed, $\pm$ 0.07 °C in the temperature for the baseline or $\pm$ 0.2 °C with recovery factor

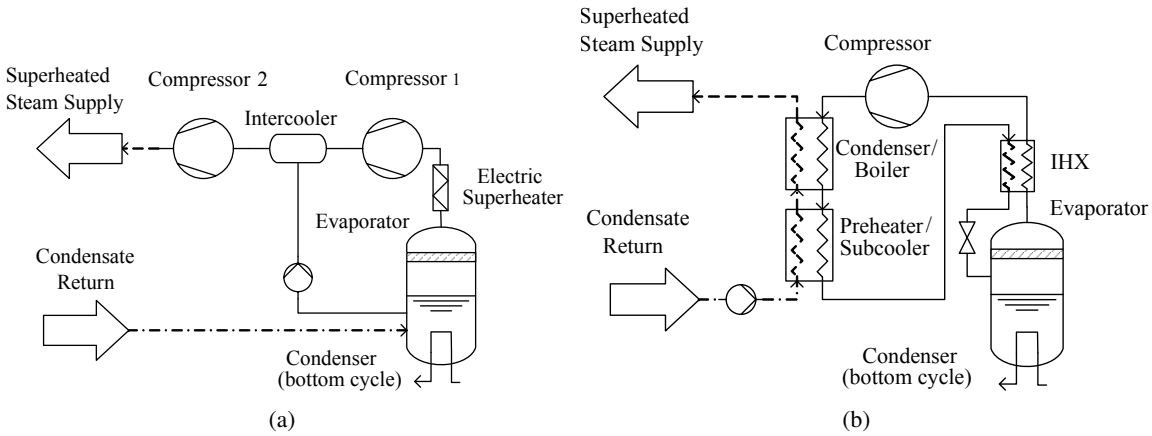

Figure 4.4: Layout of the HP cycle for steam generation using: (a) an open-loop with steam and (b) a closed-loop with other working fluids. From Ref. [315].

error, ± 2 % on impeller exit or diffuser inlet area, ± 0.25 % in nominal pressure pr ± 0.5 % for r/r_2 1.1 and angles to ± 0.25 ° nominal or ± 0.5 ° for r/r_2 1.1. Japikse [167] considered these values of accuracy to meet or exceed common research standards in the late 1980s.

R134a compressor

The test case employing R134a is a compressor with a vaneless diffuser which was designed and tested for domestic heat pump applications by Schiffmann and Favrat [182]. This test case is particularly significant to assess the suitability of the mean-line model to predict the performance of a compressor using a refrigerant, as commonly used in heat pump applications. The geometric and experimental details are reported in Refs. [126, 182, 323, 324]. The geometric and modeling details of the compressor are listed in Table C.1. The compressor was tested at values of rotational speed up to 210 krpm, and gas lubricated bearings were employed to allow for oil-free operation. The accuracy of the measurement probes was ± 0.2 K in the temperature, ± 0.002 MPa in the pressure, ± 0.5 % in the mass flow rate, and ± 0.1 % in the electric power [182]. The test results demonstrated the technical feasibility of the compressor for small-scale heat pump applications. The machine achieved values of pressure ratio up to 3.3, power up to 1.8 kW and internal isentropic efficiency up to 79 %. The details of the internal flow measurements were not provided.

CO_2 compressor

The last test case is a compressor using supercritical CO_2 which was tested at Sandia National Laboratories (SNL) [183]. The compressor was designed for the development of advanced Brayton cycles using supercritical working fluids. Like the previous test case, the presence of experimental data of a CC operating with a working fluid used in the refrigeration field makes this test case particularly relevant to test the suitability of the developed mean-line model. At the same time, the numerical model faces the challenges of computing the thermodynamic conditions close to the critical point, where large deviations from the ideal gas laws and also large variations in the

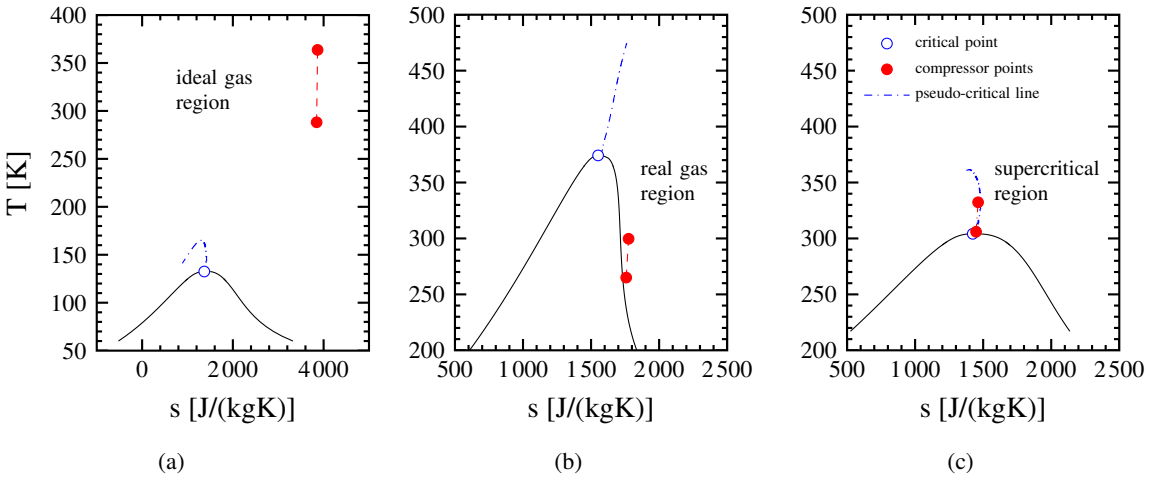

Figure 4.5: Entropy-temperature diagram for the test cases used for validation: (a) air compressors; (b) R134a compressor; (c) CO_2 compressor.

fluid properties are experienced. The compressor has an impeller and a vaned diffuser. The impeller has 6 main blades and 6 six splitter blades, and the vaned diffuser has 17 wedge-shaped vanes. The compressor geometry and the inputs to the mean-line model are provided in Table C.1. The compressor was supported by gas bearings and employed a high-speed permanent magnet motor/alternator and labyrinth gas seals to reduce the rotor cavity pressure. The machine was tested up to 65 krpm, achieving a pressure ratio of 1.65 and a mass flow rate of 1.8 kg/s. The experimental report indicated an accuracy in the measurement of the temperature of $\sim$0.2 K for resistance thermometry devices, and $\sim$0.1 K for thermocouples. The obtained results demonstrated that it was possible to operate the compressor in a stable and controlled way close to the critical point.

For this test case, CFD results were also available in the literature. As an additional source of validation, CFD results were compared to the mean-line model results. The CFD simulations were performed by Pecnik et al. [325] for the impeller only configuration and by Rinaldi et al. [326] including a vaned diffuser. The CFD simulation tool described in Refs. [325, 326] is representative for the current state of the art in the numerical modeling of centrifugal compressors with CO_2 .

Figure 4.5 shows the entropy-temperature diagram and the compressor operating points at design conditions for the different test cases. Figure 4.5 further highlights the differences and challenges in the thermodynamic and modeling conditions in each case.

4.2.5 Case study and cycle modeling

The combined compressor and cycle optimization was applied to design a HTHP system considering different working fluids. The heat pump cycle was part of a cascade heat pump system used for high-temperature steam generation. The steam is supplied at 150 °C using a heat source at 100 °C. The heat source is provided by a bottom cycle, which is not included in the present analysis. The bottom cycle, which is assumed to have constant operating conditions, exploits low-temperature

Table 4.3: Modeling conditions of the heat pump cycle. From Ref. [315].

Parameter	Value	Unit
Evaporator		
T_{eva}	100	°C
p_{eva}	$p_{sat}(T_{eva})$	Pa
Condenser		
T_{supply}	150	°C
ΔT_{pp}	3	°C
p_{cond}	$p_{sat}(T_{supply} + \Delta T_{pp})$	Pa
Subcooling (closed-loop only)		
ΔT_{sc}	5	°C

heat as excess heat or that from district heating.

The heat pump system is illustrated in Figure 4.4. Two different layout were analyzed and compared, as shown in Figure 4.4: an open-loop cycle using steam, and closed-loop cycle using other working fluids. The open-loop cycle using steam is used as a reference since this is currently the benchmark for HTHPs used for steam generation. The layout shown in Figure 4.4(a) was employed for steam, which required a two-stage compressor. In fact, a preliminary screening suggested that the compressor featured a high pressure ratio (above 5) and a high rotational speed. These two aspects can make the design of a single-stage compressor challenging due to high Mach numbers in the blade rows, and the associated loss phenomena, and the high tip speeds, which may compromise the structural integrity of the impeller. Other authors [186, 327, 328] made similar considerations on the design of steam compressors, and recommended to limit the maximum design pressure ratio to 3.5 to achieve values of tip speed up to 550 m/s. The intercooler between the two stages was introduced to improve the overall compression efficiency [328]. Moreover, an electric superheater was conceived as a safety measure to avoid two-phase conditions at the compressor inlet and outlet, which may result in droplet formation reducing the compressor's reliability and lifetime. The distribution of the pressure ratio across the two compressor stages was computed by the geometric mean of the overall compression ratio. In the open-loop, direct contact heat exchangers are employed since the working fluid is the same as the supplied steam.

The modeling conditions of the heat pump cycle are listed in Table 4.3. The HP cycle evaporates at 100 °C and supplies heat at 150 °C. The working fluids investigated in the closed-loop cycle were selected according to the following criteria: (i) operation below the critical point; (ii) zero ozone depletion potential; (iii) global warming potential <150; (iv) possibility to compute the fluid properties with CoolProp [218] and/or REFPROP [217]. The following fluids were selected: pentane, isopentane, cyclopentane, R1233zd(E), and MM. To avoid two-phase conditions at the compressor outlet, a minimum value of superheat was imposed.

4.2.6 Design optimization methodology

To perform a simultaneous optimization of both the centrifugal compressor and the heat pump designs, the two numerical models were coupled and optimized. Figure 4.6 shows the adopted optimization strategy.

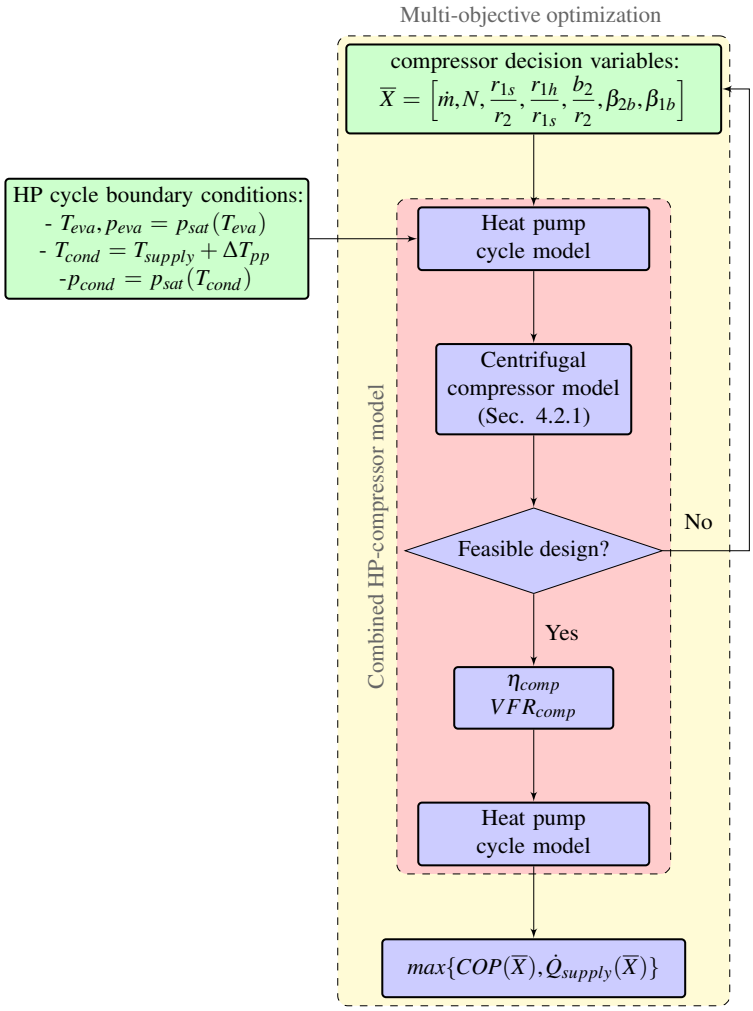

Figure 4.6: Methodology for the combined multi-objectived optimization of the heat pump cycle and the centrifugal compressor.

The inputs of the combined model are the boundary conditions of the HP model and a set of decision variables $\overline{X}$ for the compressor. In the combined model, the heat pump model provided the inlet temperature and pressure, and the outlet pressure for the compressor model. Afterwards, the resulting compressor design is checked for being within the optimization and technical constraints, and for avoiding choking conditions in the blade rows. If the compressor design is feasible, the corresponding values of compressor isentropic efficiency and volume flow rate are used by the heat pump model to compute the values of COP and supply heat flow rate $\dot{Q}$. The compressor was optimized using the mass flow rate as an additional decision variable with the aim to maximize the cycle COP and the supply heat flow rate. The objective functions were expressed as:

$$[max(COP), max(\dot{V}_{comp,in})] = f(\overline{X}) \tag{4.28}$$

$$\overline{X} = \left[\dot{m}, N, \frac{r_{1s}}{r_2}, \frac{r_{1h}}{r_{1s}}, \frac{b_2}{r_2}, \beta_{2b}, \beta_{1b}\right] \tag{4.29}$$

The cycle specifications set the thermodynamic state at the compressor inlet, and hence maximizing the $\dot{Q}_{supply}$ is equivalent to maximizing the compressor inlet volume flow rate $\dot{V}_{comp,in}$. The optimization was performed using the list of constraints for the decision variables provided in Table 4.1. The impeller outlet diameter was fixed, and the cycle requirements set the pressure ratio. Therefore, also the compressor isentropic stage loading coefficient $\psi = \Delta h_{0,is}/U_2^2$ was fixed, and it was not optimized together with the other variables. Equation 4.1 was employed to find the optimal number of blades. In the application of the optimization to the considered case study, it was decided to compared different solutions and draw possible comparisons with the existing state-of-the-art machines, and hence the compressor outlet diameter was set to the value 110 mm. This number corresponds to the tip diameter of the steam compressor for HTHPs described by Madsbøll et al. [186] for a similar heat pump application. Similarly, a different set of decision variables may be used depending on the objective of the study. For example, the compressor impeller diameter might also be considered in the optimization, or the rotational speed may be set to a predefined value due to design constraints. One of the fluids investigated in the study was steam. In this case, a two-stage compressor was required (see Sec. 4.2.5), and the two stages were assumed to be mounted on the same shaft. Between the two stages, an intercooler was employed and the mass flow rate to the second stage was computed from a mass and energy balance at the intercooler. The total number of decision variables for the two-stage compressor was 12. The multi-objective optimization process employed a genetic algorithm solver available in MATLAB [214] with 500 individuals and 200 generations. In the optimization of the two-stage compressor with the genetic algorithm, 1000 individuals were used instead due to the higher number of decision variables.

4.3 Results

4.3.1 Validation

The validation results for the three Eckardt impellers [164, 166, 322] is shown in Figure 4.7. Impeller O shows a deviation in pressure ratio up to 1.4 % of the experimental data, impeller A by up to 6 %, and impeller B of up to 7 %. in the case of impeller B, the highest deviation is achieved at 16 krpm and for both low and high mass flow rates. The efficiency prediction is close to the trend of the measured data for impeller O, which has a deviation up to 2 %-points. The prediction for impeller A seems to follow the experimental trends, although the trend is not perfectly matched for all the speed line and the efficiency is underpredicted by up to 2 %-points at the best efficiency point. The maximum discrepancy is 6.7 %-points at higher mass flow rates. The efficiency prediction for impeller B is similar to that of impeller A, although the best efficiency point is estimated to be at 10-19 % lower values than the experimental value. The overall deviation in pressure ratio and efficiency is satisfactory, and the trends of the speed lines suggest that the compressor behavior can be predicted with consistency for the three Eckardt compressors.

The validation with the case of the R134a compressor is shown in Figure 4.8(a) in terms of pressure ratio. The trend of the mean-line model is in good agreement with that of the experimental data, notwithstanding the inherent challenges for this test case to accurately model mini and micro-scale turbomachinery (the maximum shaft power of the compressor is 1.5 kW). The highest deviation in the pressure ratio, found at high and low values of rotational speed and in proximity of the choking point, is 7 %. In terms of isentropic efficiency, a higher deviation is experienced as shown

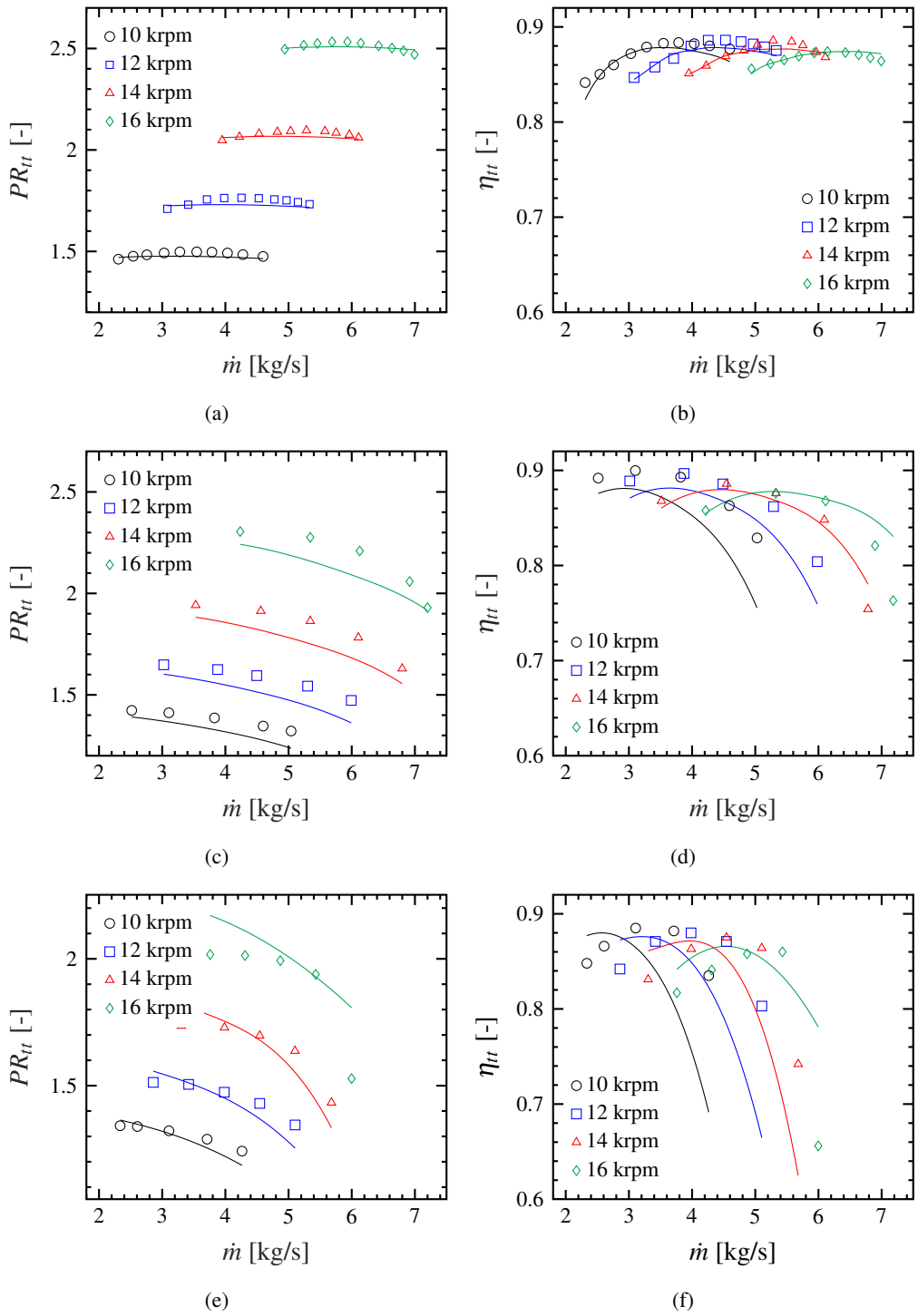

Figure 4.7: Comparison between the measured (○) and predicted (–) pressure ratio and isentropic efficiency for different Eckardt impellers: (a,b) impeller O; (c,d) impeller A; (e,f) impeller B. From Ref. [315].

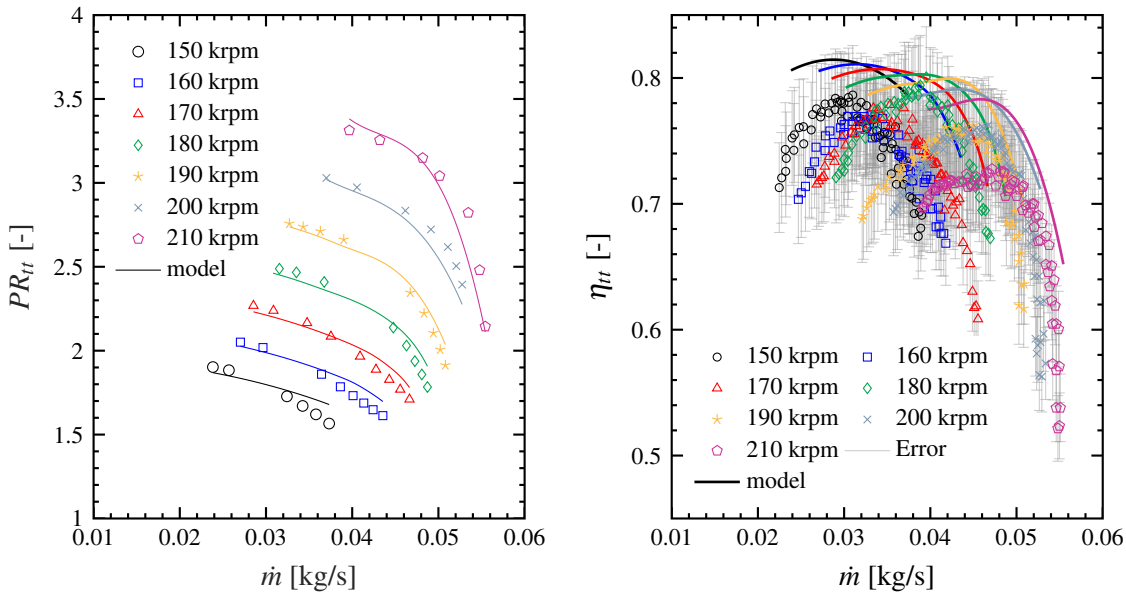

(a) (b)

Figure 4.8: Comparison between the measured and predicted results for the compressor operated with R134a and studied by Schiffmann and Favrat [182, 329]: (a) pressure ratio and (b) the isentropic efficiency. From Ref. [315].

in Figure 4.8(b), especially close to the surge and choking points. The error bars in Figure 4.8(b) were extrapolated from Refs. [182, 329]. They were computed using the propagation method approximated by the first order Taylor series. The experimental uncertainty in the compressor isentropic efficiency was only available for this validation test case. It is suggested that the deviation near surge is due to the presence of inlet recirculation flows. The maximum deviation is up to 8 %-points for some speed lines.

The validation with the Sandia compressor is shown in Figure 4.9. The experimental trends are followed with good agreement except for the 55 krpm speed line, where deviation up to 17 % in the enthalpy rise and the peak efficiency is shifted to a 25 % lower flow coefficient. The trend of CFD data with the experiments highlights that CFD has also a shift of about 25 % in the peak efficiency, especially relevant at low rotational speed. Rinaldi et al. [326] concluded that the results are in a reasonable agreement with the measured data, considering the challenges of accurately predicting the flow conditions close to the critical point of CO_2.

The validation of the design model is provided in Table 4.4. The prediction in isentropic efficiency is up to 3.7 % deviation for the three Eckardt impellers, approximately 7 % for the R134a compressor, and approximately 6.5 % for the Sandia compressor. The comparison with the designed diffusers highlights that the diffuser radius ratio is generally overestimated by the model, the largest increase being from 1.65 to 2.23, suggesting that higher losses are predicted by the model. The results found in the design model validation agree with those of the off-design model at the design point and suggest that the preliminary design model is suitable for different working fluids.

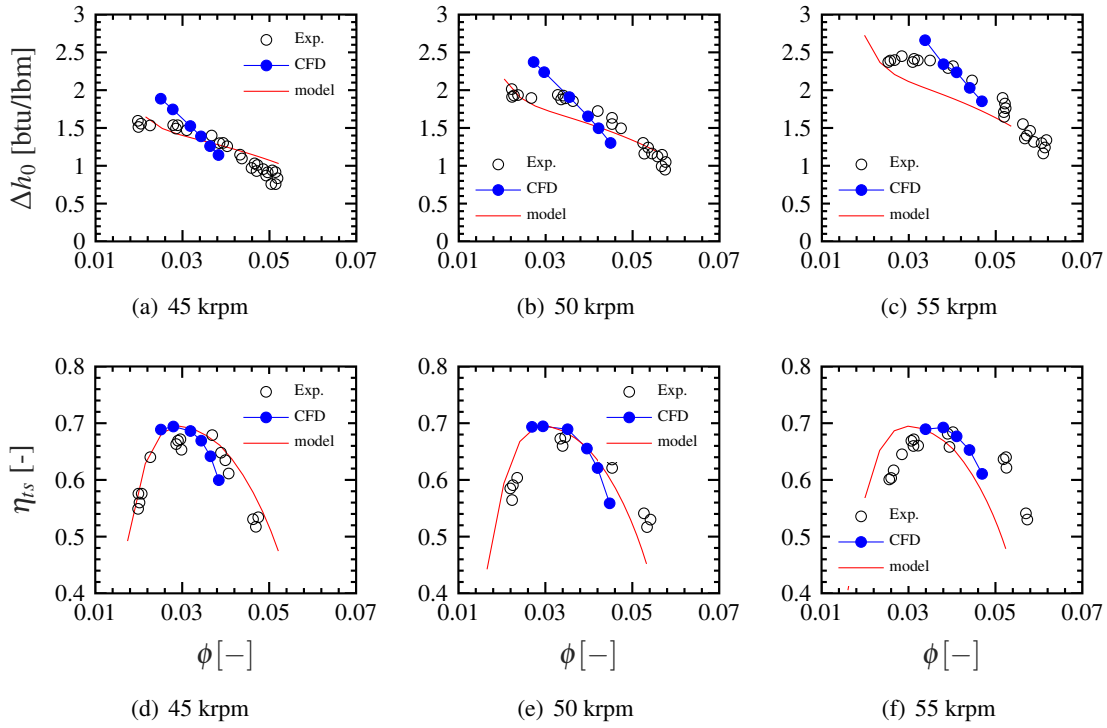

Figure 4.9: Comparison between the measured and predicted enthalpy rise and isentropic total-to-static efficiency as a function of the flow coefficient $\phi = \dot{m}/(\rho_{01} U_2 d_2^2)$ for the Sandia compressor impeller with vaned diffuser. Experimental data from Ref. [183] and state-of-the-art CFD data from Ref. [326]. From Ref. [315].

4.3.2 Compressor design optimization

The Pareto fronts of the optimal solutions of the multi-objective optimization are plotted in Figure 4.10 for the COP and the supply heat flow rate $\dot{Q}_{supply}$. In the plots, the best solution is arbitrarily indicated with a red dot, corresponding to the point with the equal weight of the two objective functions. For some working fluids, the shape of the Pareto front is not smooth and rather pronounced. This peculiarity is primarily determined by the values of optimal mass flow rate. In fact, it is found that each point in the Pareto front has an optimal value of mass flow rate given by the trade-off in terms of cycle performances and the minimum value to avoid the onset of choking conditions in the compressor stage.

The open-loop configuration with steam achieves the highest values of COP and $\dot{Q}_{supply}$, which are respectively 5.46 and 1733.6 kW at the best point. The second best performance is obtained by cyclopentane with a COP of 4.74 and $\dot{Q}_{supply}$ of 1224.7 kW, which is 30 % lower than steam. The third best performance in terms of COP is attributed to MM, having a COP of 4.54 although only 242.4 kW as for $\dot{Q}_{supply}$. Lower values of COP are seen for n-pentane and isopentane, which also deliver supply heat flow rates that are 19 % and 6 % lower than steam, respectively. The worst performance in terms of COP is attributed to R1233zd(E), having a 57 % lower COP than steam and a supply heat flow rate of 742.6 kW. The Pareto front for the compressor performance is shown in Figure 4.11. The highest volume flow rate at the compressor inlet is found for steam in this

Table 4.4: Validation of the design model. From Ref. [315].

	Eckardt O	Eckardt A	Eckardt B	Schiffmann	Sandia
No	1	2	3	4	5
PR_{tt}[-]	2	1.81	1.67	2.35	1.26
$\dot{m}$[kg/s]	5.32	4.54	4.54	0.039	2.15
N [krpm]	14	14	14	180	50
ψ_{is}	0.7824	0.62	0.53	0.5	0.41
Diffuser radius ratio (model)	1.6859	1.8017	1.8769	2.2289	1.3709
Diffuser radius ratio (actual)	1.687	1.687	1.687	1.65	1.3697
η_{model}	0.885	0.869	0.843	0.744	0.717
η_{exp}	0.886	0.876	0.875	0.800	0.673
deviation	-0.03%	-0.84%	-3.70%	-7.03 %	6.52 %

case and amounts to approximately 1.07 m^3/s. At the same time, the two-stage steam compressor features the lowest values of total-to-static efficiency of 0.69 and 0.68 in the first and second stage, respectively. The other fluids experience a different trend: they exhibit a lower volume flow rate than steam but show a higher efficiency.

The details of the optimization results are listed in Table 4.5, and the meridional cut layout of the obtained compressors is visualized in Figure 4.12. The different working fluids feature optimal mass flow rates in the range 0.64 kg/s (steam) to 7.85 kg/s (R1233zd(E)), and values of optimal rotational speed in the range 28.8 krpm (R1233zd(E)) to 85 krpm (steam). The optimal values of rotational speed result in values of tip speed within 500 m/s. Values close to this limit are found for steam, due to the higher rotational speed.

Regarding the optimal design characteristics, the different compressor stages feature a significant backsweep, above 40° for all fluids, except for steam which has nearly radial blades. The optimal solutions feature values of r_{1s}/r_2 close to the upper limit for the hydrocarbons and for the first stage of the steam compressor. All compressor stages have a relatively high fluid dynamic loading as shown by the high values of the relative Mach number at the inlet, $M_{1s,rel}$, which are above 1 at the shroud. Exception is made for the fluid R1233zd(E) and the second stage with steam.

The optimal throat size is in the range 4.1 mm to 7.4 mm. These values suggest that the blades can be manufactured with a conventional five-axis milling machine. Moreover, a similar number of blades are found for the different designs, between 18 and 22, suggesting that they will have similar manufacturing costs.

Regarding the efficiency, the fluid R1233zd(E) yielded the most efficient compressor with values of total-to-total and total-to-static efficiency of approximately 0.91 and 0.79, respectively, which are about 10 %-points higher than those of the steam vapor compressors. At the same time, the higher efficiency of the R1233zd(E) compressor is still not enough to overcome the thermodynamic advantages offered by the open-loop cycle with steam.

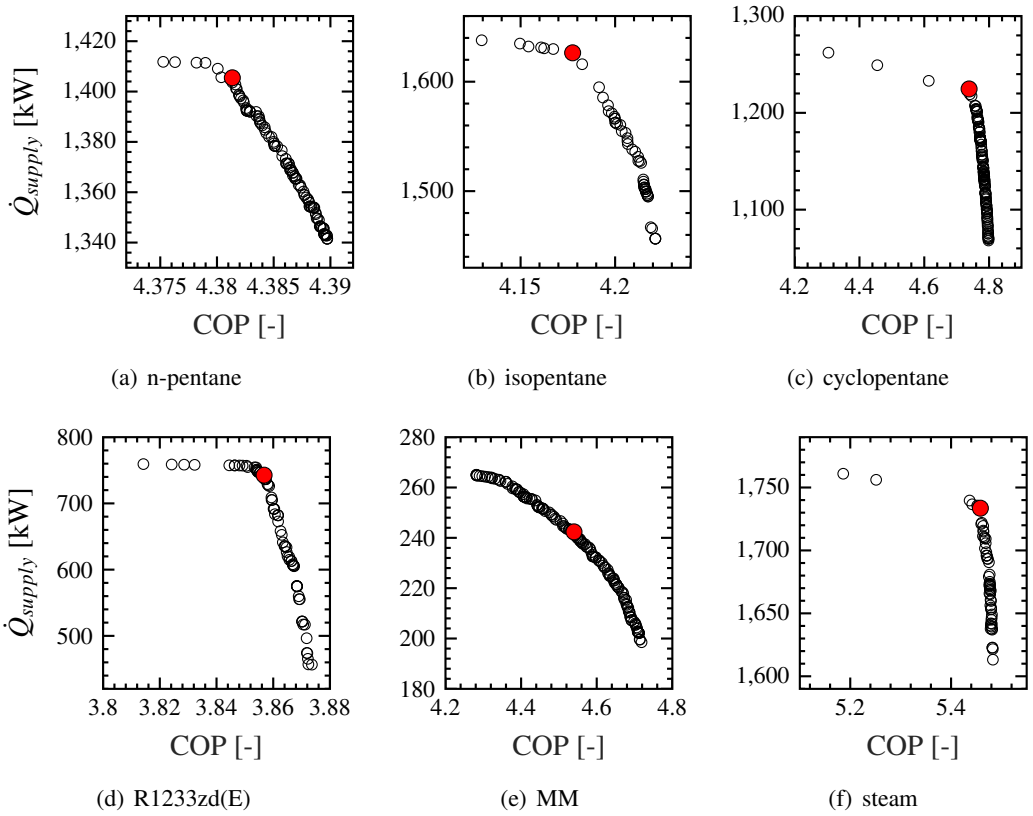

(a) n-pentane (b) isopentane (c) cyclopentane

(d) R1233zd(E) (e) MM (f) steam

Figure 4.10: Pareto fronts of the optimal solutions in terms of COP and supply heat flow rate for the selected working fluids. The solution having an equal weight of the two objective functions is indicated with the symbol ●. From Ref. [315].

4.4 Discussion

The model validation suggested the suitability of the model to predict the performance at the design and off-design points for different working fluids and geometries. The open-loop cycle using steam yields the highest performance in terms of COP and $\dot{V}_{comp,in}$, and it would be the best choice among all working fluid candidates. The results of the combined optimization also suggest that cyclopentane might be employed in case of possible design issues with the steam compressor. In this case, the lower rotational speed of the compressor, approximately 48 krpm, would be beneficial for the mechanical design of the machine and a lower COP and supply heat flow rate are expected.

Previous studies [205–210] used a fixed value of compressor isentropic efficiency when selecting the fluid for heat pump applications.

The results showed that volume flow rates in the range 0.1 m^3/s to 1.0 m^3/s are achieved for compressors with a similar size, fixed by the impeller inlet diameter. The large variation of the volume flow rate suggests that it does not only depend on the compressor size, but also on the stage pressure ratio, the maximum mass flow rate, the rotational speed and the employed working fluid. The considerations above also suggest that the volumetric heating capacity (supplied heat flow rate

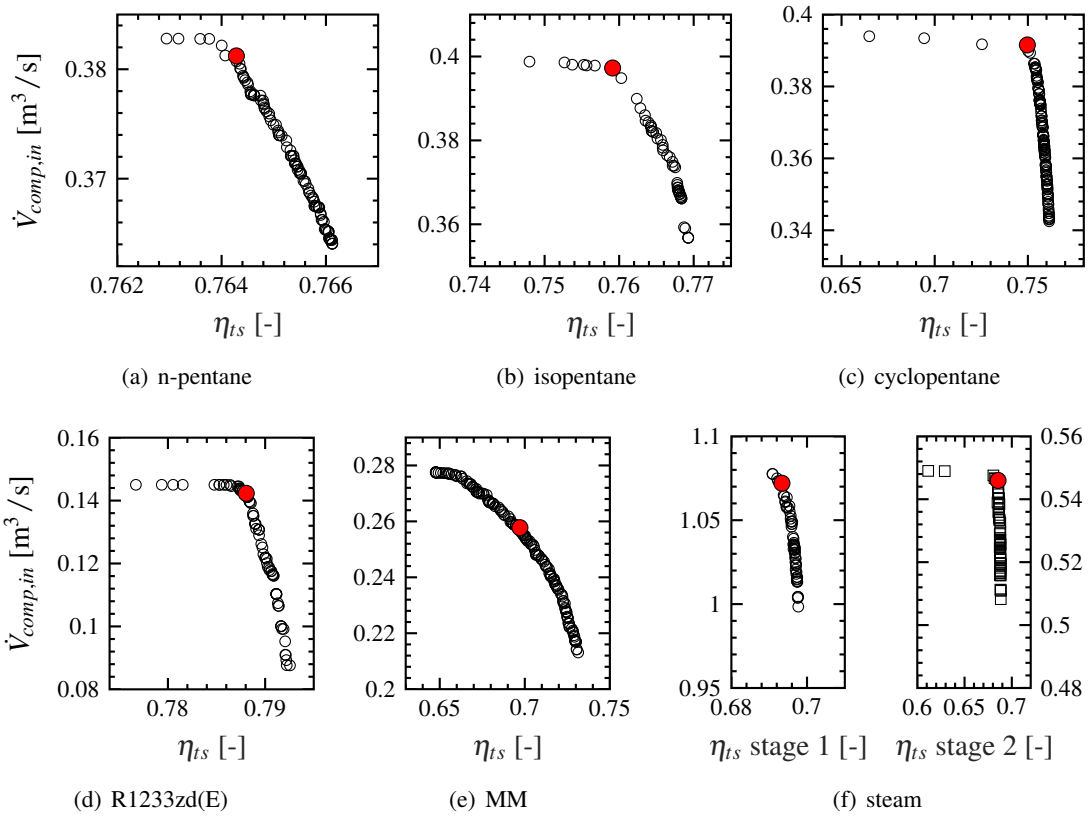

(a) n-pentane (b) isopentane (c) cyclopentane

(d) R1233zd(E) (e) MM (f) steam

Figure 4.11: Pareto fronts of the optimal solutions in terms of compressor isentropic efficiency and inlet volume flow rate for the selected working fluids. The solution having an equal weight of the two objective functions is indicated with the symbol ●. From Ref. [315].

over compressor inlet volume flow rate) might not the most suitable indicator to estimate the size and cost of the centrifugal compressor. In this respect, a coupled analysis of the compressor and the heat pump cycle for design purposes would be recommended. Also, the combined compressor and cycle designs suggest that different values of compressor efficiency and volume flow rate are obtained for the different fluids, and indicates the importance of providing a combined design of the HP and the compressor.

Regarding the best solution, the open-loop cycle with steam yielded the highest values of COP and supply heat flow rate, and therefore is considered to be the preferred solution. Concurrently, the design of the compressor with steam is more challenging, and it requires a more expensive compressor due to the presence of two stages. The steam compressor results in high values of rotational speed, very lower values of mass flow rate and efficiency. The design of a suitable steam compressor appears to be a fluid dynamic and technical challenge. Moreover, the presence of two stages implies the use of a more expensive machine, although this may be partly offset by the absence of surface heat exchangers and the higher system COP provided by the open-loop cycle.

Regarding the compressor geometry, the steam compressor should run at 85 krpm, having a peripheral speed of about 490 m/s, with transonic conditions at the impeller inlet, and an isentropic

Table 4.5: Optimal compressor design for different working fluids. From Ref. [315].

Parameter	Units	Pentane	Isopentane	Cyclopentane	R1233zd(E)	MM	Steam (stage 1)	Steam (stage 2)
T_{01}	[K]	391.2	390.4	387.1	376.2	406.9	373.2	397.7
p_{01}	[bar]	59.27	7.22	4.16	10.42	1.00	1.01	2.29
PR_{tt}	[-]	2.828	2.721	2.965	2.765	3.745	2.255	2.255
$\dot{m}$	[kg/s]	5.73	7.45	3.88	7.85	1.30	0.64	0.69
N	[rpm]	46000	43985	48000	28802	34000	85001	85001
r_{1s}/r_2	[-]	0.70	0.70	0.70	0.53	0.70	0.70	0.68
r_{1h}/r_{1s}	[-]	0.33	0.27	0.34	0.32	0.29	0.26	0.64
b_2/r_2	[-]	0.14	0.18	0.17	0.11	0.19	0.27	0.12
β_{2b}	[°]	-43.6	-44.8	-44.7	-43.1	-44.91	-13.05	-5.16
β_{1b}	[°]	-45.1	-47.7	-49.7	-34.5	-50.6	-34.3	-44.6
T_{03}	[K]	428.9	429.1	430.4	429.6	429.9	476.1	504.6
U_2	[m/s]	264.9	253.3	276.5	165.9	195.8	489.6	489.6
C_3	[m/s]	105.9	88.4	118.7	67.6	81.0	199.3	212.6
β_2	[°]	-53.2	-55.3	-55.0	-55.1	-57.3	-33.5	-25.0
α_2	[°]	65.7	70.1	70.6	72.2	76.7	69.2	67.2
$M_{1s,rel}$	[-]	1.09	1.08	1.08	0.84	1.03	1.02	0.85
$M_{1,rel}$	[-]	0.89	0.88	0.88	0.71	0.81	0.88	0.76
$M_{2,rel}$	[-]	0.69	0.61	0.56	0.55	0.46	0.35	0.37
M_2	[-]		1.02	0.97	1.02	1.08	0.83	0.86
r_{1s}	[m]	0.0385	0.0384	0.0384	0.0291	0.0371	0.0384	0.0371
r_{1h}	[m]	0.0127	0.0105	0.0131	0.0094	0.0106	0.0098	0.0236
r_2	[m]	0.055	0.055	0.055	0.055	0.055	0.055	0.055
L_z	[m]	0.036	0.0391	0.0353	0.0276	0.0371	0.0401	0.0189
b_1	[m]	0.0257	0.0279	0.0252	0.0197	0.0265	0.0286	0.0135
b_2	[m]	0.0079	0.0099	0.0093	0.0058	0.0085	0.0147	0.0065
b_3	[m]	0.0079	0.0099	0.0093	0.0058	0.0085	0.0147	0.0065
Z_r	[-]	19	19	20	19	22	18	18
$Z_{r,splitter}$	[-]	0	0	0	0	0	0	0
r_3	[m]	0.0735	0.0836	0.0738	0.0738	0.0735	0.1016	0.0996
o_1	[m]	0.0058	0.0052	0.005	0.0051	0.0041	0.0068	0.0074
χ	[-]	0.755	0.738	0.764	0.748	0.743	0.704	0.636
η_{ts}	[-]	0.764	0.759	0.750	0.788	0.697	0.693	0.686
η_{tt}	[-]	0.892	0.851	0.886	0.907	0.838	0.796	0.797
COP	[-]	4.38	4.18	4.74	3.86	4.54	5.46	
$\dot{V}_{in}$	[m^3/s]	0.38	0.40	0.39	0.14	0.26	1.07	
Q_{supply}	[kW]	1405.5	1626.4	1224.68	742.6	242.4	1733.6	

efficiency of about 0.69. The results are confirmed by the findings of other authors in the literature. Šarevski and Šarevski [327] presented the characteristics of centrifugal compressors with steam for refrigeration and heat pump systems. They concluded that a single stage solution is limited by a maximum pressure ratio of 3.5. They recommended a two-stage solution for a temperature lift of 20 °C to 45 °C. These considerations are confirmed by the results in this work, and especially by the fact that a single-stage solution resulted in excessive values of tip speed, supersonic Mach numbers in the blade rows with the presence of choking conditions.

The optimal blade angles of the steam compressors considered by Šarevski and Šarevski [327] were in the range -15° to 0° with a Mach number at the impeller inlet in the range 0.85 to 0.95, which corresponds to those obtained by the combined cycle and compressor optimization methodology. The construction and initial tests of a steam compressor for a HTHP were recently presented by

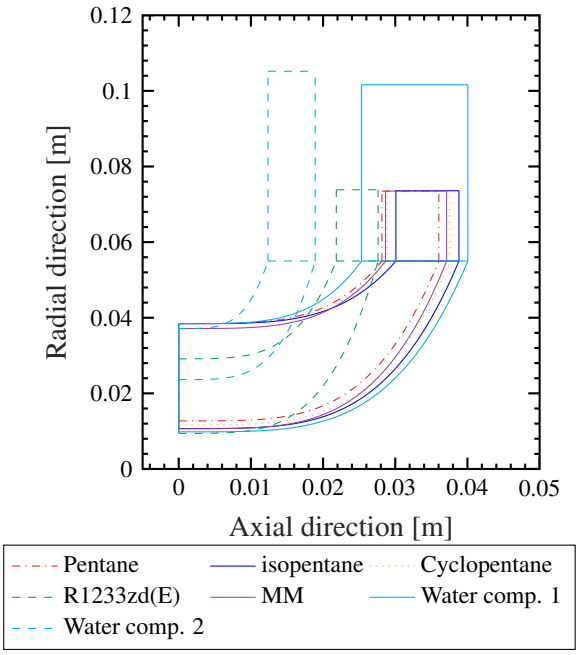

(a)

Figure 4.12: Meridional cut layout of the optimal compressor designs. From Ref. [315].

Madsbøll et al. [186]. The compressor was designed for 95 krpm and had blade angles of $-10°$. The maximum isentropic efficiency was 0.719 at 84.4 krpm, which is 2.9 %-points higher than that obtained by the mean-line model in this work. Another centrifugal compressor using steam was studied by Süß [330] in the context of refrigeration applications. The maximum cycle COP using the developed CC was 14, which was a surprising result considering that it is 3 and 4 times higher than state-of-the-art equipment in the field. The compressor at 90 krpm showed a value of efficiency of 70 % which is 1 %-point higher than that predicted in this work. Another work by Bantle [331] used a turbocharger retrofitted for mechanical vapor recompression in steam driers. The compressor at full capacity (90 krpm) reached a pressure ratio of 2.4 with an efficiency of 72 %, a mass flow rate of 0.125 kg/s and a temperature of 225 °C. The results are similar to those obtained in the first stage steam compressor. However, the efficiency is 3 %-points lower, and the mass flow rate is 5.1 times smaller than the value found in this work since the compressor was designed for a 5 to 6 times lower heating capacity. Moreover, Bantle [332] recently presented a continuation of the work in Ref. [331], and a two-stage compressor is presented for a HTHP application. The compressor featured values of Mach numbers (0.96-1.27 at the tip) and outlet diameters (115 mm and 146 mm) similar to those employed in this study, although the pressure ratio distribution across the two stages is different (2 in the first stage and 3.2 in the second one). The considerations above, demonstrating that similar fluid-dynamic values and parameters values also also found in other works, indicate the suitability of the methodology presented in this study.

4.5 Conclusion

This chapter presented a mean-line compressor model for design and analysis purposes, a model validation and a methodology for the combined optimization with a heat pump system. The validation of the compressor model was performed with five test cases including three different working fluids: air, R134a, and CO_2. The mean-line model in the analysis mode showed to capture well the trend of the experimental data and showed agreement with the experimental results and a deviation up to 7 % in the mass flow rate and 8 %-points in the efficiency. The validation with the design model had a deviation up to 7 % in the compressor isentropic efficiency. The results from the validation suggested that the model can be used in design and analysis modes with acceptable accuracy for different geometries and working fluids.

A methodology for the combined optimization of the centrifugal compressor and the heat pump system was presented and, subsequently, was applied to the design of a high-temperature heat pump supplying steam at 150 °C. The cycle and compressor models were combined and the resulting model was optimized in terms of two objective functions: the system COP and the supply heat flow rate. Five working fluid candidates were selected and analyzed in a closed-loop configuration while steam was analyzed in an open-loop configuration.

The application of the methodology was key to achieve accurate results and compare them for different working fluids regarding cycle and compressor performance and technical viability.

The results of the methodology showed that the open-loop cycle with steam had the highest values of COP and supply heat flow rate, which were respectively 5.48 and 1734 kW. However, the use of steam requires a more challenging compressor design, characterized by a two-stage configuration, higher values of rotational speed, high flow velocities in the channels, and a lower isentropic efficiency. These findings were substantiated by the studies of other authors and confirmed the suitability of the adopted optimization methodology. As an alternative to steam, cyclopentane ranked as the second-best option in terms of COP and could be considered if the steam cycle would be too expensive or technically challenging. In this case, in fact, the compressor would run at the lower rotational speed of 48 krpm, would have a single stage and a higher efficiency.

5 Conclusions

5.1 Summary of findings

ORC power systems and HP systems are considered to be attractive propositions for the generation of electricity and heat using low-temperature heat sources. However, the major barrier to the mass production of this new generation of low-temperature thermodynamic cycles is the development of cost-competitive solutions. In this respect, expanders and compressors are key components regarding cost and performance for ORC and HP systems, and the development of reliable and accurate numerical models for the preliminary design and performance prediction is currently considered to be a major challenge in the field.

The present work had two main objectives, which were divided into sub-objectives according to the different technologies. The first objective was to develop suitable mean-line models for the preliminary design and the analysis of axial and radial-inflow turbines for ORC systems, and centrifugal compressors for heat pumps. The second objective was to develop and apply optimization methodologies which allowed combining the machine and cycle designs to identify suitable solutions from the performance and technical viewpoints.

5.1.1 ORC axial-flow turbines

In the context of ORC axial turbines, a mean-line model for the preliminary design of single-stage and multistage ORC axial turbines (named TURAX) was presented as well as a methodology for the combined design optimization of axial turbines and the ORC system. The mean-line design model was validated with the experimental data of single and multistage turbines from the open literature, including two ORC axial turbines. The validation in the single-stage configuration suggests that the turbine efficiency is predicted within 1.3 %-points. This range is in agreement with the $\pm 1.25\%$ range of accuracy declared by the employed performance prediction method. The turbine thermodynamic and flow conditions are predicted within 10 %. A sensitivity analysis identified 10 decision variables as the most important ones for the design and optimization of the turbine. The validation of the multistage turbine model shows a deviation up to 2 %-points in the efficiency and up to 8.5 % in the design geometry. The validation results suggest that the model can be used for preliminary design purposes with expected values of uncertainty within those found in the validation.

A combined methodology for the design of the system and the turbine was presented. The turbine and the ORC system models were combined, and the optimization of the combined system was performed for two case studies. The first case study investigated the waste heat recovery from the jacket water cooling system of a 60 MW marine diesel engine where the jacket cooling water temperature was available at 85 °C. A single-stage turbine design was investigated as well as the use of binary mixtures since they are considered thermodynamically advantageous for low-temperature heat sources. Two binary mixtures were selected and analyzed: pentane/R245fa and propane/isobutane. The second case study investigated the waste heat recovery from a 37 MW marine diesel engine using the exhaust gases, scavenge air, and jacket water cooling system as the heat sources. The waste heat of the exhaust gases was the major energy source and was available at the temperature of 235 °C. In this case, the optimization methodology was further extended to include multistage axial turbines operating with pure fluids, and to include preliminary technical and economic considerations. A conservative and advanced design approaches were analyzed based on turbine loading and Mach numbers inside the blade rows. Moreover, a performance index was presented, enabling the designer to simultaneously account for multiple turbine design aspects in the ORC system design.

The results of the first case study indicate that it is relevant to use the combined turbine and cycle optimization methodology. The estimated net power output deviates in the range 3% to 21% compared to a simple guess in turbine isentropic efficiency, depending on the values of molar composition and on the selected mixture. Moreover, the methodology allows improving the accuracy in the identification of the optimal molar composition since a shift from 0.2 to 0.4 for the mixture propane/isobutane is observed. Finally, the use of the methodology suggests that pure fluids are the most suitable working fluids when the hot fluid temperature difference is below 5 °C whereas multi-component working fluids yield a better cycle performance for a higher temperature difference since they can better match the heat source temperature profile in the boiler. The two best mixtures are R245fa/pentane (0.5/0.5) and propane/isobutane (0.2/0.8). The application of the optimization methodology to the first test case results also in turbine designs which are technically feasible as they feature acceptable blade heights (> 5 mm), untwisted blades, large diameters (479 mm to 657 mm), a number of blades in the range 102 to 130, converging blade profiles, and reaction blades. Moreover, the insertion of a gearbox can be avoided.

The results of the second case study, for a heat source with higher temperature level, further highlight the presence of trade-offs regarding cycle and turbine performance and designs. The trade-off is primarily guided by the large pressure ratio across the turbine, which ultimately depends on the selected working fluid. In this case, the optimal solution is sought as a compromise of multiple criteria such as the turbine and cycle performance, the turbine size and cost, and the number of stages. Moreover, the optimization methodology allows the designer to select the most suitable solution according to his key decision criteria. When an advanced design approach is followed, the optimal solution is n-pentane with a single-stage turbine configuration and highly supersonic flows. Conversely, the use of a conservative design approach simplifies the mechanical and aerodynamic design of the turbine, and the optimal solution is a two-stage reaction turbine with n-pentane. The use of a gearbox is found to be advantageous for those solutions whose turbine isentropic efficiency increases by 6-7 %-points.

5.1.2 ORC radial-inflow turbines

In the context of ORC radial-inflow turbines, this thesis presented a methodology for the preliminary design and performance prediction of high-pressure ratio turbines. The work is the first of its kind to present a comprehensive methodology for high-pressure ratio turbines including performance prediction models, calibration, validation and analysis of the results.

A mean-line model for the preliminary design and performance of radial-inflow turbines was presented, including the details of the numerical modeling strategy for the treatment of choking conditions in the blade rows. The turbine model was then calibrated using the literature data of six radial-inflow turbines operating at high pressure ratios. The calibration methodology was based on a genetic algorithm, and it allowed minimizing the predicted deviation across all the experimental data points. The use of this calibration approach is key to improve the model accuracy with respect to the experimental test cases since the predicted deviation, expressed as the relative average RMSE, decreases from 5.9 % to 2.1 % in the efficiency and from 2.4 % to 1.5 % in the mass flow rate. The validation of the design model for the same test cases shows a maximum deviation of 2.83 %.

Finally, the analysis model was validated with the data from other two test cases, one of which is an ORC turbine. The validation with the ORC turbine suggests a deviation up to 1 % in the mass flow rate and up to 5 % in the isentropic efficiency. The validation with the other test case, an air turbine operated up to a pressure ratio of 5, provides acceptable results regarding mass flow rate and efficiency. The validation of this case also highlights that a correct estimation of the throat size is paramount to obtain accurate results.

5.1.3 Centrifugal compressors for HP systems

In the field of centrifugal compressors for heat pumps, a mean-line model for the preliminary design and performance of centrifugal compressors was presented as well as a methodology for a combined optimization with a heat pump system. The mean-line model was validated with five test cases including three different working fluids: air, R134a, and CO_2.

The mean-line model, validated in the analysis mode, shows a deviation with the experimental data up to 7 % in the mass flow rate and 8 %-points in the efficiency. The validation of the design model shows deviations up to 7 % in the isentropic efficiency. The values of deviation are acceptable and, in the test case using R134a, fall within the range of experimental uncertainty. Moreover, the trend of the results predicted with the model appears to follow the experimental trends. For these reasons, and in the absence of more accurate and reliable experimental data, the results of the mean-line model are considered to be acceptable.

The mean-line model in the design mode was then combined to that of a heat pump system for a coupled optimization. The heat pump was designed to supply steam at 150 °C and was optimized for the maximum COP and supply heat flow rate considering different working fluids. An open-loop configuration was considered for steam, being the current benchmark for this type of application, while a closed-loop system was considered for five other selected working fluids. The combined optimization methodology allows achieving more accurate results regarding the heat pump performance, and allows comparing the different solutions in terms of both cycle and

compressor designs compared to a simple guess of turbine efficiency. The results also highlight that the widely employed assumption that the compressor size is directly related to the volume inlet flow rate might not be suitable for heat pumps using centrifugal compressors. In fact, although the compressors feature the same impeller outer diameter, and therefore have a similar size, they show volume flow rates in the range 0.1 m^3/s to 1.0 m^3/s. This result suggests that other factors determine the compressor inlet volume flow rate such as the stage pressure ratio, the maximum allowable mass flow rate, the compressor rotational speed and the working fluid properties. Moreover, the results suggest the importance of coupling the compressor and cycle models for analysis and design optimization purposes. The best working fluid is found to be steam with a heat pump COP of 5.48 and a supply heat flow rate of 1734 kW. At the same time, the use of the combined compressor and cycle optimization allows identifying that water requires a two-stage compressor with challenging characteristics such as a rotational speed of 85 krpm, transonic flow conditions in the impeller, and a lower isentropic efficiency of about 0.69 for the two compressor stages. These findings are further confirmed by the work of other researchers who investigated water vapor compressors for similar applications.

5.2 Recommendations for future work

The mean-line models developed in this work were validated with different test cases from the open literature. In this respect, it would be relevant to validate the models with the measured data of the internal flows in the blade rows. Such an operation would allow for more accurate validation of the models' prediction capabilities and assessment of the suitability of the existing loss correlations for the prediction of the internal flow characteristics. This type of validation is especially relevant for the radial-inflow turbine and centrifugal compressor models since a validation with the internal flow measurements was partially carried out in the context of the axial turbine model.

Another important aspect is the developmental of loss correlations tailored to ORC turbines and HP centrifugal compressors. To this end, experimental investigations on real machines are required.

More accurate experimental results are also needed for centrifugal compressors in heat pump applications due the large uncertainty ($\sim$8%) found in the experimental data of the test cases used for validation.

The third topic for possible future work is the development of detailed mean-line models for the preliminary design and performance prediction of supersonic ORC turbines featuring converging-diverging nozzle profiles. Although the models used in this work for converging-diverging nozzles were based on the existing information from the literature, the correlations for losses and performance prediction at supersonic conditions are extremely limited and were developed for ideal gases, casting doubt on their reliability using real-gas flows.

The fourth topic for future work is to investigate the optimal turbine and compressor designs, obtained with the mean-line models, using advanced design techniques to assess the suitability of the solutions from the aerodynamic and technical viewpoints.

The last aspect which is considered for future work is to extend the combined optimization methodology to radial-inflow turbines and including off-design considerations.

Bibliography

[1] IEA Headline Energy Data. URL http://www.iea.org/statistics.

[2] European Commission. 2050 low-carbon economy - Climate Action. URL https://ec.europa.eu/clima/policies/strategies.

[3] Sarah Broberg Viklund and Magnus Karlsson. Industrial excess heat use: Systems analysis and CO2 emissions reduction. *Applied Energy*, 152:189–197, 2015.

[4] B. Huang, F. Bühler, and F.M. Holm. Industrial Energy Mapping: THERMCYC WP6. Technical report, 2015.

[5] G. P. Hammond and J. B. Norman. Heat recovery opportunities in UK industry. *Applied Energy*, 116:387–397, 2014.

[6] Piero Colonna, Emiliano Casati, Carsten Trapp, Tiemo Mathijssen, Jaakko Larjola, Teemu Turunen-Saaresti, and Antti Uusitalo. Organic Rankine Cycle Power Systems: From the Concept to Current Technology, Applications, and an Outlook to the Future. *Journal of Engineering for Gas Turbines and Power*, 137(10):100801, 2015.

[7] Mario Gaia. 30 Years of Organic Rankine Cycle Development. In *First International Seminar on ORC Power Systems, September 22-23*, pages 11–23, Delft, The Netherlands, 2011.

[8] Cordin Arpagaus, Frédéric Bless, Jürg Schiffmann, and Stefan S. Bertsch. Review on High Temperature Heat Pumps. Market Overview and Research Status. In *European Heat Pump Summit, October 24-25*, pages 1–23, Nuremberg, Germany, 2017.

[9] Danish Technological Institute. Development of ultra-high temperature hybrid heat pump for process application. URL https://www.dti.dk/projects/project-development-of-ultra-high-temperature-hybrid-heat-pump-for-process-application/37430.

[10] Ennio Macchi and Marco Astolfi. *Organic rankine cycle (ORC) power systems : technologies and applications*. Woodhead Publishing Limited, Duxford, United Kingdom, 2016.

[11] F. Campana, M. Bianchi, L. Branchini, A. De Pascale, A. Peretto, M. Baresi, A. Fermi, N. Rossetti, and R. Vescovo. ORC waste heat recovery in European energy intensive industries: Energy and GHG savings. *Energy Conversion and Management*, 76:244–252, 2013.

[12] T. Tartière, B. Obert, and L. Sanchez. Thermo-economic optimization of subcritical and transcritical ORC systems. In *Second International Seminar on ORC Power Systems, October 7-8*, pages 1–12, Rotterdam, The Netherlands, 2013.

[13] L. Y. Bronicki. History of Organic Rankine Cycle systems. In Ennio Macchi and Marco Astolfi, editors, *Organic Rankine Cycle (ORC) Power Systems : Technologies and Applications*, chapter 2, pages 25–66. Woodhead Publishing Limited, Duxford, United Kingdom, 2016.

[14] Ennio Macchi. The choice of working fluid: the most important step for a successful organic Rankine cycle (and an efficient turbine). In *Second International Seminar on ORC Power Systems, Keynote Lecture, October 7-8*, Rotterdam, The Netherlands, 2013.

[15] Marco Astolfi, Matteo C. Romano, Paola Bombarda, and Ennio Macchi. Binary ORC (Organic Rankine Cycles) power plants for the exploitation of medium-low temperature geothermal sources - Part B: Techno-economic optimization. *Energy*, 66:435–446, 2014.

[16] S. Lecompte, H. Huisseune, and Martijn van den Broek. Part load based thermo-economic optimization of the Organic Rankine Cycle (ORC) applied to a combined heat and power (CHP) system. *Applied Energy*, 111:871–881, 2013.

[17] Steven Lecompte, Sanne Lemmens, Henk Huisseune, Martijn van den Broek, and Michel De Paepe. Multi-Objective Thermo-Economic Optimization Strategy for ORCs Applied to Subcritical and Transcritical Cycles for Waste Heat Recovery. *Energies*, 8(4):2714–2741, 2015.

[18] Sylvain Quoilin, Sébastien Declaye, Bertrand F. Tchanche, and Vincent Lemort. Thermo-economic optimization of waste heat recovery Organic Rankine Cycles. *Applied Thermal Engineering*, 31(14):2885–2893, 2011.

[19] S. Wolf and M. Blsels. Model-based quantification of the contribution of industrial heat pumps to the European climate change mitigation strategy. In *Proceedings of the ECEEE Industrial Efficiency Conference 2016, September 12-14*, pages 477–487, Kalkscheune, Berlin, Germany, 2016.

[20] Cordin Arpagaus, Frédéric Bless, Jürg Schiffmann, and Stefan S. Bertsch. Multi-temperature heat pumps: A literature review. *International Journal of Refrigeration*, 69:437–465, 2016.

[21] P. Nellissen and S. Wolf. Heat pumps in non-domestic applications in Europe: potential for an energy revolution. Technical report, Emerson Climate Technologies GmbH., 2014.

[22] Jonas Kjær Jensen. *Industrial heat pumps for high temperature process applications: A numerical study of the ammonia-water hybrid absorption-compression heat pump*. PhD thesis, Technical University of Denmark (DTU), Lyngby, Denmark, 2016.

[23] Opeyemi Bamigbetan, Trygve M. Eikevik, Petter Nekså, and Michael Bantle. Review of vapour compression heat pumps for high temperature heating using natural working fluids. *International Journal of Refrigeration*, 80:197–211, 2017.

[24] M Zehnder. *Efficient air-water heat pumps for high temperature lift residential heating, including oil migration aspects*. PhD thesis, École polytechnique fédérale de Lausanne, 2004.

[25] M. Youbi-Idrissi, J. Bonjour, C. Marvillet, and F. Meunier. Impact of refrigerant-oil solubility on an evaporator performances working with R-407C. *International Journal of Refrigeration*, 26(3):284–292, 2003.

[26] M. Youbi-Idrissi, J. Bonjour, M. F. Terrier, C. Marvillet, and F. Meunier. Oil presence in an evapoator: Experimental validation of a refrigerant/oil mixture enthalpy calculation model. *International Journal of Refrigeration*, 27(3):215–224, 2004.

[27] M. Youbi-Idrissi and J. Bonjour. The effect of oil in refrigeration: Current research issues and critical review of thermodynamic aspects. *International Journal of Refrigeration*, 31(2): 165–179, 2008.

[28] Vincent Lemort and Arnaud Legros. Positive displacement expanders for Organic Rankine Cycle systems. In Ennio Macchi and Marco Astolfi, editors, *Organic Rankine Cycle (ORC) Power Systems : Technologies and Applications*, chapter 12, pages 361–396. Woodhead Publishing Limited, Duxford, United Kingdom, 2016.

[29] Marco Astolfi. Technical options for Organic Rankine Cycle systems. In Ennio Macchi and Marco Astolfi, editors, *Organic Rankine Cycle (ORC) Power Systems : Technologies and Applications*, chapter 3, pages 67–89. Woodhead Publishing Limited, Duxford, United Kingdom, 2016.

[30] Air Squared. Air Squared. URL https://airsquared.com/content/.

[31] Enerbasque. Enerbasque. URL http://enerbasque.com/en/.

[32] Orcan Energy AG. Orcan - The Efficiency Company. URL http://www.orcan-energy.com/en/home.

[33] ElectraTherm. ElectraTherm. URL https://electratherm.com/.

[34] Opcon energy Systems. OES – Opcon Energy System. URL http://opconenergysystem.com/en/home/.

[35] Kaishan Technologies. Organic Rankine Cycle (ORC) Expander Power Plant—Renewable Energy Technology. URL http://kaishantechnologies.com/products/organic-rankine-cycle-orc-expander-power-plant-renewable-energy-technology/.

[36] E-RATIONAL. E-Rational - Value for Heat. URL http://www.e-rational.net/.

[37] Infinity Turbine. Infinity Turbine - Waste Heat to Power - ORC. URL http://www.infinityturbine.com/.

[38] Exergy S.p.A. Exergy - Green power through innovation. URL http://exergy-orc.com/.

[39] Atlas Copco. ORC Solutions References — Atlas Copco Gas and Process. URL http://www.atlascopco-gap.com/orc-solutions-references/.

[40] Zuccato Energia. Zuccato Energia. URL http://www.zuccatoenergia.it/index.php/en/.

[41] Triogen. Triogen - Power From Heat. URL http://www.triogen.nl/.

[42] Calnetix Technologies. Calnetix Technologies - Organic Rankine Cycle Systems. URL https://www.calnetix.com/organic-rankine-cycle-systems.

[43] GE Power & Water. Clean Cycle II R-Series. URL https://www.gepower.com/.

[44] Ormat Technologies Inc. Ormat Technologies Inc. - Renewable Energy Expertise. URL http://www.ormat.com/en/home/a/main/.

[45] Enogia. Enogia. URL http://www.enogia.com/.

[46] Enertime. ORC modules - Enertime Solutions. URL http://www.enertime.com/en/technology/solutions/orc-modules.

[47] Turboden S.p.A. TURBODEN - clean energy ahead. URL https://www.turboden.com/turboden-orc-technology/1062/the-orc-technology.

[48] Adoratec. adoratec-products. URL http://www.adoratec.com/productnav.html.

[49] INTEC GMK. GMK - Gesellschaft für Motoren und Kraftanlagen mbH. URL http://www.gmk.info/.

[50] L. Y. Bronicki. Experience with high speed organic Rankine cycle turbomachinery. In *Conference on High Speed Technology, August*, pages 47–61, Lappeenranta, Finland, 1988.

[51] Marco Astolfi, E Martelli, and Leonardo Pierobon. Thermodynamic and technoeconomic optimization of Organic Rankine Cycle systems. In Ennio Macchi and Marco Astolfi, editors, *Organic Rankine Cycle (ORC) Power Systems : Technologies and Applications*, chapter 7, pages 173–250. Woodhead Publishing Limited, Duxford, United Kingdom, 2016.

[52] Ennio Macchi. Design criteria for turbines operating with fluids having a low speed of sound. Technical report, Von Karman Institue for Fluid Dyanmics, 1977.

[53] G. Persico and M. Pini. Fluid dynamic design of Organic Rankine Cycle turbines. In Ennio Macchi and Marco Astolfi, editors, *Organic Rankine Cycle (ORC) Power Systems: Technologies and Applications*, pages 253–297. Woodhead Publishing Limited, Duxford, United Kingdom, 2016.

[54] H. Tabor and L. Bronicki. Establishing criteria for fluids for small vapor turbines. *SAE Technical Paper*, 640823:561–575, 1964.

[55] Daniele Fiaschi, Giampaolo Manfrida, and Francesco Maraschiello. Thermo-fluid dynamics preliminary design of turbo-expanders for ORC cycles. *Applied Energy*, 97:601–608, sep 2012.

[56] Stefano Clemente, Diego Micheli, Mauro Reini, and Rodolfo Taccani. Bottoming organic Rankine cycle for a small scale gas turbine: A comparison of different solutions. *Applied Energy*, 106:355–364, 2013.

[57] E. Maria Mondejar, Marcus Thern, and Magnus Genrup. Aerodynamic Considerations in the Thermodynamic Analysis of Organic Rankine Cycles. In *ASME 2014 Power Conference, July 28-31*, pages 1–8, Baltimore, Maryland, USA, 2014.

[58] E. Macchi and A. Perdichizzi. Efficiency Prediction for Axial-Flow Turbines Operating with Nonconventional Fluids. *Journal of Engineering for Power*, 103(4):718, 1981.

[59] G. Lozza, E. Macchi, and A. Perdichizzi. On the Influence of the Number of Stages on the Efficiency of Axial-Flow Turbines. In *Proceedings of the ASME Turbo Expo, March 18-22*, pages 1–10, London, UK, 1982.

[60] Matteo Pini, Giacomo Persico, Emiliano Casati, and Vincenzo Dossena. Preliminary Design of a Centrifugal Turbine for Organic Rankine Cycle Applications. *Journal of Engineering for Gas Turbines and Power*, 135(4):042312, 2013.

[61] E. Casati, S. Vitale, M. Pini, G. Persico, and P. Colonna. Centrifugal Turbines for Mini-ORC Power Systems. *Journal of Engineering for Gas Turbines and Power*, 136(12):122607, 2014.

[62] E. Casati, S. Vitale, M. Pini, G. Persico, and P. Colonna. Preliminary Design Method For Small Scale Centrifugal ORC Turbines. In *Proceedings of the 2nd International Seminar on ORC Power Systems, 7-8 October*, pages 1–32, Rotterdam, The Netherlands, 2013.

[63] G. Bado, G. Tomei, T. Angelino, M. Gaia, and E. Macchi. The Ansaldo 35 kW solar power system. In *Sun II - ISES Silver Jubilee Congress, May 38- June 1*, volume 1, pages 1090–1094, Atlanta, Georgia, USA, 1979.

[64] C. Osnaghi, G. Angelino, F. Bassi, and E. Bollina. Progetto e realizzazione di un motore a fluido organico con espansione a turbina da accoppiarsi con un impianto solare a media concentrazione. Technical report, 1979.

[65] G. Angelino, M. Gaia, and E. Macchi. Medium temperature 100 kW ORC engine for total energy systems. In H. Ehringer, G. Hoyaux, and P.A. Pilavachi, editors, *Energy Conservation in Industry—Combustion, Heat Recovery and Rankine Cycle Machines*, pages 177–189. Springer Netherlands, Brussels and Luxembourg, Belgium and Luxembourg, 1983.

[66] A. Verneau. Supersonic turbines for organic fluid Rankine cycles from 3 to 1300 kW. *Small High Pressure Ratio Turbines, (VKI Lecture Series 1987-2007) Von Karman Institute For Fluid Dynamics, Rhode-Saint-Genése, Belgium*, 1987.

[67] T. Jokinen, J. Larjola, and I. Mikhaltsev. Power unit for research submersible. In *International Conference on Electric Ship (ElecShip 98), September 2-4*, volume 1, pages 114–118, Istanbul, Turkey, 1998.

[68] Luca Sciacovelli and Paola Cinnella. Numerical study of multistage transcritical organic Rankine cycle axial turbines. *Journal of Engineering for Gas Turbines and Power*, 136(8): 82604, 2014.

[69] Piotr Klonowicz, Jan Surwiło, Lukasz Witanowski, Tomasz K Suchocki, Zbigniew Kozanecki, and Piotr Lampart. Design and numerical study of turbines operating with MDM as working fluid. *Open Engineering*, 5(1):485–499, 2015.

[70] Jan Surwilo, Piotr Lampart, and Mariusz Szymaniak. CFD analysis of fluid flow in an axial multi-stage partial-admission ORC turbine. *Open Engineering*, 5(1):360–364, 2015.

[71] G. Angelino, M. Gaia, and E. Macchi. Medium Temperature 100 kW ORC Engine for Total Energy Systems - Experimental Results. Technical Report 1, 1984.

[72] Andrea Meroni, Jesper Graa Andreasen, Giacomo Persico, and Fredrik Haglind. Optimization of organic Rankine cycle power systems considering multistage axial turbine design. *Applied Energy*, 209:339–354, 2018.

[73] G. Angelino, M. Gaia, E. Macchi, A. Barutti, C. Maccio, and G. Tomei. Test results of a medium temperature solar engine. *International Journal of Ambient Energy*, 3(3):115–126, 1982.

[74] A. Barutti, W. Pedrick, G. Angelino, M. Gaia, and E. Macchi. Ansaldo Solar Thermal and Photovoltaic Plants Located at Ballajura, Western Australia. In *8th Solar World Congress, Biennial Congress of the International Solar Energy Society, August 14-19*, volume 3, pages 1572–1576, Perth, Australia, 1983.

[75] I. Obernberger and A. Hammerschmid. Biomass fired CHP plant based on an ORC cycle–Project ORC-STIA-Admont. *Final Report, Bios-energy systems*, pages 1–12, 2001.

[76] Pervaiz Nasir, Steve Jones, Daniel Schochet, and N. Sparks. Utilization of Turbine Waste Heat to Generate Electric Power at Neptune Plant. URL http://www.ormat.com/en/home/a/main/.

[77] Jian Song, Yin Song, and Chun-wei Gu. Thermodynamic analysis and performance optimization of an Organic Rankine Cycle (ORC) waste heat recovery system for marine diesel engines. *Energy*, 82:976–985, 2015.

[78] E. Yun, H Park, S.Y. Yoon, and K.C. Kim. Dual parallel organic Rankine cycle (ORC) system for high efficiency waste heat recovery in marine application. *Journal of Mechanical Science and Technology*, 29(6):2509–2515, 2015.

[79] Min-Hsiung Yang and Rong-Hua Yeh. Analyzing the optimization of an organic Rankine cycle system for recovering waste heat from a large marine engine containing a cooling water system. *Energy Conversion and Management*, 88:999–1010, 2014.

[80] Min-Hsiung Yang and Rong-Hua Yeh. Thermodynamic and economic performances optimization of an organic Rankine cycle system utilizing exhaust gas of a large marine diesel engine. *Applied Energy*, 149:1–12, 2015.

[81] Andrea Toffolo, Andrea Lazzaretto, Giovanni Manente, and Marco Paci. A multi-criteria approach for the optimal selection of working fluid and design parameters in Organic Rankine Cycle systems. *Applied Energy*, 121:219–232, 2014.

[82] Daniel Maraver, Javier Royo, Vincent Lemort, and Sylvain Quoilin. Systematic optimization of subcritical and transcritical organic Rankine cycles (ORCs) constrained by technical parameters in multiple applications. *Applied Energy*, 117:11–29, 2014.

[83] Jacopo Vivian, Giovanni Manente, and Andrea Lazzaretto. A general framework to select working fluid and configuration of ORCs for low-to-medium temperature heat sources. *Applied Energy*, 156:727–746, 2015.

[84] Emanuele Martelli, Federico Capra, and Stefano Consonni. Numerical optimization of Combined Heat and Power Organic Rankine Cycles - Part A: Design optimization. *Energy*, 90:310–328, 2015.

[85] Luca Da Lio, Giovanni Manente, and Andrea Lazzaretto. Predicting the optimum design of single stage axial expanders in ORC systems: Is there a single efficiency map for different working fluids? *Applied Energy*, 167:44–58, 2016.

[86] Martin White and Abdulnaser I. Sayma. Improving the economy-of-scale of small organic rankine cycle systems through appropriate working fluid selection. *Applied Energy*, 183: 1227–1239, 2016.

[87] Carlos André de Miranda Ventura and Andrew Stewart Rowlands. Design and performance estimation of radial inflow turbines coupled with a thermodynamic cycle analysis procedure. In *ASME ORC 2013: 2nd International Seminar on ORC Power Systems, October 7-8*, pages 1–5, Rotterdam, The Netherlands, 2013.

[88] Antti Uusitalo, Teemu Turunen-Saaresti, Aki Gronman, Juha Honkatukia, and Jari Backman. Combined Thermodynamic and Turbine Design Analysis of Small Capacity Waste Heat Recovery ORC. In *ASME ORC 2015: 3nd International Seminar on ORC Power Systems, 12-14 October*, pages 1–10, Brussels, Belgium, 2015.

[89] Angelo La Seta, Andrea Meroni, Jesper Graa Andreasen, Leonardo Pierobon, Giacomo Persico, and Fredrik Haglind. Combined Turbine and Cycle Optimization for Organic Rankine Cycle Power Systems – Part B: Application on a Case Study. *Energies*, 9(6):393, 1–17, 2016.

[90] Ennio Macchi and Marco Astolfi. Axial flow turbines for Organic Rankine Cycle applications. In Ennio Macchi and Marco Astolfi, editors, *Organic Rankine Cycle (ORC) Power Systems: Technologies and Applications*, chapter 9, pages 299–319. Woodhead Publishing Limited, Duxford, United Kingdom, 2016.

[91] Kiyarash Rahbar, Saad Mahmoud, and Raya K. Al-Dadah. Optimized efficiency maps and new correlation for performance prediction of ORC based on radial turbine for small-scale applications. In *3rd International Seminar on ORC Power Systems, October 12-14, 2015, Brussels, Belgium*, pages 1–10, 2015.

[92] Luca Da Lio, Giovanni Manente, and Andrea Lazzaretto. New efficiency charts for the optimum design of axial flow turbines for organic Rankine cycles. *Energy*, 77:447–459, 2014.

[93] V. Mounier, L.E. Olmedo, and Jurg Schiffmann. Small scale radial inflow turbine performance and pre-design maps for Organic Rankine Cycles. *Energy*, 143:1072–1084, 2018.

[94] Giovanni Lozza. A comparison between the Craig-Cox and the Kacker-Okapuu methods of turbine performance prediction. *Meccanica*, 17(4):211–221, 1982.

[95] Andrea Meroni, Miles Robertson, Ricardo Martinez-Botas, and Fredrik Haglind. A methodology for the preliminary design and performance prediction of high-pressure ratio radial-inflow turbines. *Energy [submitted for publication]*, 2018.

[96] G. F. Hiett and I. H. Johnston. Experiments Concerning the Aerodynamic Performance of Inward Flow Radial Turbines. *Proceedings of the Institution of Mechanical Engineers, Conference Proceedings*, 178(9):28–42, 1963.

[97] Xuwen Qiu and Nick Baines. Performance Prediction for High Pressure-Ratio Radial Inflow Turbines. In *ASME Turbo Expo 2007: Power for Land, Sea, and Air, 14-17 May 2007, Montreal, Canada*, pages 945–956. American Society of Mechanical Engineers, 2007.

[98] Kerry L. McLallin and Jeffrey E. Haas. Experimental Performance and Analysis of 15.04-Centimeter-Tip-Diameter, Radial-Inflow Turbine with Work Factor of 1.126 and Thick Blading. Technical report, NASA, Washington D.C., USA, 1980.

[99] J.R. Kidwell and G.D. Large. Advanced technology components for model GTP305-2 aircraft auxiliary power system. Final report for period 6 May 1975-15 Jul 1979. Technical report, AiResearch Mfg. Co., Phoenix, AZ, USA, 1980.

[100] C. Rogo, T. Hajek, and A.G. Chen. Variable stator radial turbine. Technical report, NASA, 1984.

[101] Y. Ribaud and C. Mischel. Study and experiments of a small radial turbine for auxiliary power units. In *ASME 1986 International Gas Turbine Conference and Exhibit, 8-12 June 1986, Dusseldorf, West Germany*, pages V002T04A003–V002T04A003. American Society of Mechanical Engineers, 1986.

[102] Casimir Rogo. Variable area radial turbine fabrication and test program. Technical report, NASA, Washington D.C., USA, 1986.

[103] C. Rodgers. Review of mixed flow and radial turbine options. In *26th Joint Propulsion Conference, 16-18 July 1990, Orlando, Florida, USA*, page 2414, 1990.

[104] P. Susan Simonyi, Richard J. Roelke, Roy G. Stabe, Brentley C. Nowlin, and Danielle Dicicco. Aerodynamic evaluation of two compact radial-inflow turbine rotors. Technical report, NASA, Washington D.C., USA, 1995.

[105] K.R. Pullen, N.C. Baines, and S.H. Hill. The Design and Evaluation of a High Pressure Ratio Radial Turbine. In *ASME 1992 International Gas Turbine and Aeroengine Congress and Exposition, June 1–4*, pages V001T01A050–V001T01A050, Cologne, Germany, 1992. American Society of Mechanical Engineers.

[106] I. Huntsman, H.P. Hodson, and S.H. Hill. The Design and Testing of a Radial Flow Turbine for Aerodynamic Research. *Journal of Turbomachinery*, 114(2):411–418, 1992.

[107] I. Huntsman and H. Hodson. An experimental assessment of the aerodynamic performance of a low-speed radial inflow turbine. In *30th Joint Propulsion Conference and Exhibit, June 27-29*, pages 1–8, Indianapolis, IN, USA, 1994.

[108] Anthony C. Jones. Design and Test of a Small, High Pressure Ratio Radial Turbine. *Journal of Turbomachinery*, 118(2):362–370, 1996. ISSN 15288900, 0889504x.

[109] S.W.T. Spence and D.W. Artt. Experimental performance evaluation of a 99.0 mm radial inflow nozzled turbine with different stator throat areas. *Proceedings of the Institution of Mechanical Engineers, Part A: Journal of Power and Energy*, 211(6):477–488, 1997.

[110] M. J. Atkinson. *The design of efficient radial turbines for low power applications*. PhD thesis, University of Sussex, Brighton, United Kingdom, 1998.

[111] W.J. Doran, S.W.T Spence, and D.W. Artt. Experimental performance evaluation of a 99.0 mm radial inflow nozzled turbine with varying shroud profiles. *Proceedings of the Institution of Mechanical Engineers, Part A: Journal of Power and Energy*, 215(2):267–280, 2001.

[112] Zhengping Feng, Qinghua Deng, and Jun Li. Aerothermodynamic Design and Numerical Simulation of Radial Inflow Turbine Impeller for a 100 kW Microturbine. In *ASME Turbo Expo 2005: Power for Land, Sea, and Air, June 6-9 June*, pages 873–880, Reno, Nevada, USA, 2005. American Society of Mechanical Engineers.

[113] S.W. Spence, R.S. Rosborough, David Artt, and Geoffrey McCullough. A Direct Performance Comparison of Vaned and Vaneless Stators for Radial Turbines. *Journal of turbomachinery*, 129(1):53–61, 2006.

[114] Qinghua Deng, Jiufang Niu, Jingru Mao, and Zhenping Feng. Experimental and Numerical Investigation on Overall Performance of a Radial Inflow Turbine for 100kW Microturbine. In *ASME Turbo Expo 2007: Power for Land, Sea, and Air, 14-17 May 2007, Montreal, Canada*, pages 919–926. American Society of Mechanical Engineers, 2007.

[115] Lei Fu, Yan Shi, Qinghua Deng, Huaizhi Li, and Zhenping Feng. Integrated Optimization Design for a Radial Turbine Wheel of a 100 kW-Class Microturbine. *Journal of Engineering for Gas Turbines and Power*, 134(1):12301, 2011.

[116] Lei Fu, Zhen-ping Feng, Guo-jun Li, Qing-hua Deng, Yan Shi, and Tie-yu Gao. Experimental validation of an integrated optimization design of a radial turbine for micro gas turbines. *Journal of Zhejiang University SCIENCE A*, 16(3):241–249, 2015.

[117] N. Ino, A. Machida, K. Ttsugawa, Y. Arai, M. Matsuki, H. Hashimoto, and A. Yasuda. Development of High Expansion Ratio Helium Turbo Expander. *Advances in Cryogenic Engineering*, 37(pt B):835–844, 1991.

[118] Subrata Kumar Ghosh. *Experimental and computational studies on cryogenic turboexpander*. PhD thesis, National Institute of Technology Rourkela, Rourkela, India, 2008.

[119] J. Larjola. ORC power plant based on high speed technology. In *Conference on High Speed Technology, 21-24 August 1988, Lappeenranta, Finland*, pages 63–77, 1988.

[120] J.P. Van Buijtenen, J. Larjola, T. Turunen-Saaresti, J. Honkatukia, H. Esa, J. Backman, and A. Reunanen. Design and validation of a new high expansion ratio radial turbine for ORC application. In *Proceedings of the Fifth European Conference on Turbomachinery*, pages 1–14, 2003.

[121] Gang Pei, Jing Li, Yunzhu Li, Dongyue Wang, and Jie Ji. Construction and dynamic test of a small-scale organic rankine cycle. *Energy*, 36(5):3215–3223, 2011.

[122] Seok Hun Kang and Dae Hun Chung. Design and Experimental Study of Organic Rankine Cycle (ORC) and Radial Turbine. In *ASME 2011 Turbo Expo: Turbine Technical Conference and Exposition, June 6–10 June*, pages 1037–1043, Vancouver, British Columbia, Canada, 2011.

[123] Seok Hun Kang. Design and experimental study of ORC (organic Rankine cycle) and radial turbine using R245fa working fluid. *Energy*, 41(1):514–524, 2012.

[124] Sangjo Han, JongBeom Seo, and Bum-Seog Choi. Development of a 200 kW ORC radial turbine for waste heat recovery. *Journal of Mechanical Science and Technology*, 28(12): 5231–5241, 2014.

[125] Jonathan Demierre, Daniel Favrat, Jürg Schiffmann, and Johannes Wegele. Experimental investigation of a Thermally Driven Heat Pump based on a double Organic Rankine Cycle and an oil-free Compressor-Turbine Unit. *International Journal of Refrigeration*, 44:91–100, 2014.

[126] Jonathan Demierre, Antonio Rubino, and Jürg Schiffmann. Modeling and Experimental Investigation of an Oil-Free Microcompressor-Turbine Unit for an Organic Rankine Cycle Driven Heat Pump. *Journal of Engineering for Gas Turbines and Power*, 137(3):1–10, 2015.

[127] Seok Hun Kang. Design and preliminary tests of ORC (organic Rankine cycle) with two-stage radial turbine. *Energy*, 96:142–154, 2016.

[128] Teemu Turunen-Saaresti, Antti Uusitalo, and Juha Honkatukia. Design and testing of high temperature micro-ORC test stand using Siloxane as working fluid. *Journal of Physics: Conference Series*, 821(1):12024, 2017.

[129] L. J. Kastner and F. S. Bhinder. A Method for Predicting the Performance of a Centripetal Gas Turbine Fitted With a Nozzle-Less Volute Casing. In *ASME 1975 International Gas Turbine Conference and Products Show, March 2-6*, pages 1–11, Houston, Texas, USA, 1975.

[130] A. J. Glassman. NASA contributions to radial turbine aerodynamic analyses. In *Automotive Technol. Develop. Contractor Coord. Meeting, November 11-13*, pages 1–20, Dearborn, MI, USA, 1980.

[131] A. Perdichizzi and G. Lozza. Design Criteria and Efficiency Prediction for Radial Inflow Turbines. In *Gas Turbine Conference and Exhibition, May 31-June 4*, pages 1–9, Anaheim, California, USA, 1987.

[132] Colin Rodgers. Mainline performance prediction for radial inflow turbines. Technical report, Von Karman Inst. for Fluid Dynamics, Lecture Series on Small High Pressure Ratio Turbines, 1987.

[133] Ronald H. Aungier. *Turbine Aerodynamics: Axial-Flow and Radial-Flow Turbine Design and Analysis*. ASME Press, New York, USA, 2006.

[134] Subrata K. Ghosh, R. K. Sahoo, and Sunil K. Sarangi. Mathematical Analysis for Off-Design Performance of Cryogenic Turboexpander. *Journal of Fluids Engineering*, 133(3):031001, 2011.

[135] Carlos A.M. Ventura, Peter A. Jacobs, Andrew S. Rowlands, Paul Petrie-Repar, and Emilie Sauret. Preliminary design and performance estimation of radial inflow turbines: An automated approach. *Journal of Fluids Engineering*, 134(3):31102, 2012.

[136] Luca Da Lio, Giovanni Manente, and Andrea Lazzaretto. A mean-line model to predict the design efficiency of radial inflow turbines in organic Rankine cycle (ORC) systems. *Applied Energy*, 205:187–209, 2017.

[137] N. C. Baines. A meanline prediction method for radial turbine efficiency. In *Sixth International Conference on Turbocharging and air management systems, November 3-5*, pages 45–56, London, UK, 1998.

[138] N. C. Baines. Radial and mixed flow turbine options for high-boost turbochargers. In *Seventh International Conference on Turbochargers and Turbocharging, 14-15 May*, pages 35–44, London, UK, 2002.

[139] N.C. Baines. Radial turbines: an integrated design approach. In *6th Conference on Turbomachinery: Fluid Dynamics and Thermodynamics, November 7-11*, pages 1–10, Lille, France, 2005.

[140] Arthur J. Glassman. Enhanced analysis and users manual for radial-inflow turbine conceptual design code RTD. Technical report, NASA, Washington D.C., USA, 1995.

[141] A. Spinelli, V. Dossena, P. Gaetani, C. Osnaghi, and D. Colombo. Design of a Test Rig for Organic Vapours. In *Asme Turbo Expo 2010, June 14-18*, pages 109–120, Glasgow, UK, 2010.

[142] M. Pini, A. Spinelli, Vincenzo Dossena, Paolo Gaetani, and Francesco Casella. Dynamic simulation of a test rig for organic vapours. In *5th Conference on Energy Sustainability, ASME EsFuelCell 2011, August 7-10*, pages 7–10, Washington DC, USA, 2011.

[143] Andrea Spinelli, Matteo Pini, Vincenzo Dossena, Paolo Gaetani, and Francesco Casella. Design, Simulation, and Construction of a Test Rig for Organic Vapors. *Journal of Engineering for Gas Turbines and Power*, 135(4):10, 2013.

[144] A. Spinelli, G. Cammi, M. Zocca, S. Gallarini, F. Cozzi, P. Gaetani, V. Dossena, and A. Guardone. Experimental observation of non-ideal expanding flows of Siloxane MDM vapor for ORC applications. *Energy Procedia*, 129:1125–1132, 2017.

[145] Adam Joseph Head, Carlo De Servi, Emiliano Casati, Matteo Pini, and Piero Colonna. Preliminary Design of the ORCHID: A Facility for Studying Non-Ideal Compressible Fluid Dynamics and Testing ORC Expanders. In *ASME Turbo Expo 2016: Turbomachinery Technical Conference and Exposition, June 13-17*, page V003T25A001, Seoul, South Korea, 2016.

[146] Miles C. Robertson, Aaron W. Costall, Peter J. Newton, and Ricardo F. Martinez-Botas. Radial Turboexpander Optimization Over Discretized Heavy-Duty Test Cycles for Mobile Organic Rankine Cycle Applications. In *ASME Turbo Expo 2016: Turbomachinery Technical Conference and Exposition, June 13-17*, pages 1–14, Seoul, South Korea, 2016.

[147] Maximilian Passmann, Felix Reinker, Karsten Hasselmann, Stefan aus der Wiesche, and Franz Joos. Development and Design of a Two-Stage Contraction Zone and Test Section of an Organic Rankine Cycle Wind Tunnel. In *ASME Turbo Expo 2016: Turbomachinery Technical Conference and Exposition, June 13-17*, volume 3, page V003T25A006, Seoul, South Korea, 2016. ASME.

[148] Braden Twomey, Andras Nagy, Hugh Russell, Andrew Rowlands, Jason Czapla, Rajinesh Singh, and Ingo de M Ventura, Carlos A Jahn. The University of Queensland Refrigerant and Supercritical CO2 Test Loop. In *ASME Turbo Expo 2016: Turbomachinery Technical Conference and Exposition, June 13-17*, page V003T25A013, Seoul, South Korea, 2016.

[149] H. Russel, A. Rowlands, C. Ventura, and I. Jahn. Design and Testing Process for a 7kW Radial Inflow Refrigerant Turbine at the University of Queensland. In *ASME Turbo Expo 2016: Turbomachinery Technical Conference and Exposition, June 13-17*, page V008T23A036, Seoul, South Korea, 2016.

[150] David H. Robison and Peter J. Beaty. Compressor Types, Classifications, And Applications. In *21st Turbomachinery Symposium, September 28- October 1*, pages 1–6, Dallas, Texas, USA, 1992.

[151] O.E. Balje. *Turbomachines-A guide to design, selection, and theory*. John Wiley and Sons, New York, NY, USA, 1981.

[152] Hybrid Energy. Hybrid Energy - High temperature heat pumps. URL http://www.hybridenergy.no/.

[153] Kobelco. Kobelco. URL http://www.kobelco.co.jp/products/.

[154] Mayekawa Global. Heat Pumps - MAYEKAWA Global (MYCOM). URL http://www.mayekawa.com/products.

[155] Ochsner Energy Technology. Ochsner Energy Technology. URL http://ochsner-energietechnik.com/.

[156] Combitherm. Heatpumps - Combitherm Apparate. URL http://www.combitherm.de/heatpumps.html.

[157] Friotherm. Friotherm Unitop. URL http://www.friotherm.com/en/products/unitop/.

[158] Star Refrigeration. Star Refrigeration Products. URL http://www.star-ref.co.uk/our-products/neatpump/neatpump-brochure.aspx.

[159] Gea Group. Chillers heat pumps and refrigeration systems. URL https://www.gea.com/en/productgroups/.

[160] Johnson Controls Denmark ApS. HeatPAC HPX, . URL http://www.sabroe.com/en/products/chillers-and-heat-pumps/heatpac-hpx/.

[161] ltd. Mitsubishi Heavy Industries Thermal Systems. Water to Water Heat Pump (industrial use) - MITSUBISHI HEAVY INDUSTRIES THERMAL SYSTEMS, LTD. URL https://www.mhi-mth.co.jp/en.

[162] J. Schiffmann and D. Favrat. Design, experimental investigation and multi-objective optimization of a small-scale radial compressor for heat pump applications. *Energy*, 35(1): 436–450, 2009.

[163] J Schiffmann. Integrated Design and Multi-objective Optimization of a Single Stage Heat-Pump Turbocompressor. *Journal of Turbomachinery*, 137(7):071002, 2015.

[164] D. Eckardt. Instantaneous Measurements in the Jet-Wake Discharge Flow of a Centrifugal Compressor Impeller. *Journal of Engineering for Power*, 97(3):337, 1975.

[165] D. Eckardt. Detailed Flow Investigations Within a High-Speed Centrifugal Compressor Impeller. *Journal of Fluids Engineering*, 98(3):390, 1976.

[166] D. Eckardt, K.J. Trültzsch, and W. Weimann. *Vergleichende Strömungsuntersuchungen an drei Radialverdichter-Laufrädern mit konventionellen Meßverfahren*. PhD thesis, 1977.

[167] D. Japikse. A Critical Evaluation of Three Centrifugal Compressors With Pedigree Data Sets: Part 5—Studies in Component Performance. *Journal of Turbomachinery*, 109(1):1, 1987.

[168] D. Japikse and N. Baines. *Introduction to turbomachinery*. Concepts ETI, Norwich, VT, USA, 1994.

[169] P. M. Came. The Development, Application and Experimental Evaluation of a Design Procedure for Centrifugal Compressors. *Proceedings of the Institution of Mechanical Engineers*, 192(1):49–67, 1978.

[170] Francis X. Dolan and Jr. Runstadler, Peter W. Design, development, and test of a laser velocimeter for a small 8:1 pressure ratio centrifugal compressor. Technical report, 1979.

[171] H. Krain. Swirling Impeller Flow. *Journal of Turbomachinery*, 110(1):122, 1988.

[172] C. Hah and H. Krain. Secondary Flows and Vortex Motion in a High-Efficiency Backswept Impeller at Design and Off-Design Conditions. *Journal of Turbomachinery*, 112(1):7, 1990.

[173] S. Colantuoni and A. Colella. Aerodesign and Performance Analysis of a Radial Transonic Impeller for a 9:1 Pressure Ratio Compressor. *Journal of Turbomachinery*, 115(3):573, 1993.

[174] Kai U. Ziegler, Heinz E. Gallus, and Reinhard Niehuis. A Study on Impeller-Diffuser Interaction—Part II: Detailed Flow Analysis. *Journal of Turbomachinery*, 125(1):183, 2003.

[175] Kai U. Ziegler, Heinz E. Gallus, and Reinhard Niehuis. A Study on Impeller-Diffuser Interaction—Part I: Influence on the Performance. *Journal of Turbomachinery*, 125(1):173, 2003.

[176] Stefan Ubben and Reinhard Niehuis. Experimental Investigation of the Diffuser Vane Clearance Effect in a Centrifugal Compressor Stage With Adjustable Diffuser Geometry—Part I: Compressor Performance Analysis. *Journal of Turbomachinery*, 137(3):031003, 2014.

[177] Stefan Ubben and Reinhard Niehuis. Experimental Investigation of the Diffuser Vane Clearance Effect in a Centrifugal Compressor Stage With Adjustable Diffuser Geometry: Part II — Detailed Flow Analysis. *Journal of Turbomachinery*, 137(3):V02DT42A043, 2014.

[178] M. D. Hathaway, J. R. Wood, and C. A. Wasserbauer. NASA Low-Speed Centrifugal Compressor for Three-Dimensional Viscous Code Assessment and Fundamental Flow Physics Research. *Journal of Turbomachinery*, 114(2):295, 1992.

[179] Gary J. Skoch, P.S. Prahst, M.P. Wernet, J.R. Wood, and A.J. Strazisar. Laser anemometer measurements of the flow field in a 4:1 pressure ratio centrifugal impeller. In *ASME 1997 International Gas Turbine and Aeroengine Congress and Exhibition, June 2-5 1997*, page V001T03A049, Orlando, Florida, USA, 1997.

[180] T.F. McKain and G.J. Holbrook. Coordinates for a high performance 4:1 pressure ratio centrifugal compressor. Technical report, 1997.

[181] J. Schiffmann and D. Favrat. Experimental investigation of a direct driven radial compressor for domestic heat pumps. *International Journal of Refrigeration*, 32(8):1918–1928, 2009.

[182] J. Schiffmann and D. Favrat. Design, experimental investigation and multi-objective optimization of a small-scale radial compressor for heat pump applications. *Energy*, 35(1): 436–450, 2009.

[183] Steven A. Wright, Ross F. Radel, Milton E. Vernon, Gary E. Rochau, and Paul S. Pickard. Operation and Analysis of a Supercritical CO2 Brayton Cycle. Technical report, 2010.

[184] Mick V Casey, D Krähenbuhl, and C Zwyssig. The Design of Ultra-High-Speed Miniature Centrifugal Compressors. In *10th European Conference on Turbomachinery, Fluid Dynamics and Thermodynamics, April 15-19*, page 14, Lappeenranta, Finland, 2013.

[185] Dongdong Zhao, Krahenbuhl Daniel, Benjamin Blunier, Christof Zwyssig, Manfeng Dou, and Abdellatif Miraoui. Design and control of an ultra high speed turbo compressor for the air management of fuel cell systems. In *2012 IEEE Transportation Electrification Conference and Expo, ITEC 2012, June 18-20*, pages 1–6, Dearborn, MI, USA, 2012.

[186] H. Madsbøll, M. Weel, and A. Kolstrup. Development of a water vapor compressor for high temperature heat pump applications. In *24th IIR International Congress of Refrigeration, August 16-22*, pages 1–8, Yokohama, Japan, 2015.

[187] J J Brasz. Oil-free centrifugal refrigeration compressors: from HFC134a to HFO1234ze(E). In *8th International Conference on Compressors and their Systems, September 9-10*, pages 467–475, London, UK, 2013.

[188] Johnson Controls Denmark ApS. York chiller heralds adoption of R1233zd, . URL https://www.coolingpost.com/world-news/.

[189] Danfoss. Turbocor. URL https://www.danfoss.com/en/products/compressors/.

[190] M.G. Jones. The Performance of a 6.5 Pressure Ratio Centrifugal Compressor having a Radially-Vaned Impeller. Technical report, Aeronautic Research Council London, 1977.

[191] Pei Yuan Li, Chu Wei Gu, and Yin Song. A new optimization method for centrifugal compressors based on 1D calculations and analyses. *Energies*, 8(5):4317–4334, 2015.

[192] Bartosz Kus and Petter Nekså. Development of one-dimensional model for initial design and evaluation of oil-free CO2 turbo-compressor. *International Journal of Refrigeration*, 36 (8):2079–2090, 2013.

[193] Michael Casey and Chris Robinson. A Method to Estimate the Performance Map of a Centrifugal Compressor Stage. *Journal of Turbomachinery*, 135(2):021034, 2012.

[194] Richard B. Vilim. A one-dimensional compressor model for super-critical carbon dioxide applications. In *2010 International Conference on Advances in Nuclear Power Plants (ICAPP'10), June 13-17*, pages 1–12, San Diego, CA, USA, 2010.

[195] Joseph Veres. Axial and Centrifugal Compressor Mean Line Flow Analysis Method. In *47th AIAA Aerospace Sciences Meeting including The New Horizons Forum and Aerospace Exposition, January 5-8*, pages 1–38, Orlando, Florida, USA, 2009. American Institute of Aeronautics and Astronautics.

[196] H. W. Oh, E. S. Yoon, and M. K. Chung. An optimum set of loss models for performance prediction of centrifugal compressors. *Proceedings of the Institution of Mechanical Engineers, Part A: Journal of Power and Energy*, 211(4):331–338, 1997.

[197] R. H. Aungier. Mean Streamline Aerodynamic Performance Analysis of Centrifugal Compressors. *Journal of Turbomachinery*, 117(3):360, 1995.

[198] A. Perdichizzi and M. Savini. Aerodynamic and geometric optimization for the design of centrifugal compressors. *International Journal of Heat and Fluid Flow*, 6(1):49–56, 1985. ISSN 0142727X.

[199] M.R. Galvas. Fortran program for predicting off-design performance of centrifugal compressors. Technical report, 1973.

[200] Colin Rodgers. Typical Performance Characteristics of Gas Turbine Radial Compressors. *Journal of Engineering for Power*, 86(2):161, 1964.

[201] C. Rodgers. A Diffusion Factor Correlation for Centrifugal Impeller Stalling. *Journal of Engineering for Power*, 100(4):592, 1978.

[202] Collin Rodgers. Efficiency of centrifugal compressor impellers. In *AGARD 282 conference proceedings, May 7-9*, pages 1–14, Brussels, Belgium, 1980.

[203] Collin Rodgers. Static pressure recovery characteristics of some radial vaneless diffusers. *Canadian Aeronautics and Space Journal*, 30:42–54, 1984.

[204] J.E. Coppage and F. Dallenbach. Study of supersonic radial compressors for refrigeration and pressurization systems. Technical report, Garret Corp., 1956.

[205] Marwan Chamoun, Romuald Rulliere, Philippe Haberschill, and J.F. Berail. Water vapour as refrigerant for a new high temperature heat pump. In *23rd IIR International Congress of Refrigeration, August 21-26*, pages 1–8, Prague, Czech Republic, 2011.

[206] P. De Larminat and Damien Arnon. Natural or synthetic refrigerants - what options for high temperature heat pumps? In *10th IIR Gustav Lorentzen Conference on Natural Refrigerants, June 25-27*, pages 1–8, Delft, The Netherlands, 2012.

[207] Piotr A. Domanski, J. Steven Brown, Jaehyeok Heo, Janusz Wojtusiak, and Mark O. McLinden. A thermodynamic analysis of refrigerants: Performance limits of the vapor compression cycle. *International Journal of Refrigeration*, 38(1):71–79, 2014.

[208] Mark O. McLinden, Andrei F. Kazakov, J. Steven Brown, and Piotr A. Domanski. A thermodynamic analysis of refrigerants: Possibilities and tradeoffs for Low-GWP refrigerants. *International Journal of Refrigeration*, 38(1):80–92, 2014.

[209] Chieko Kondou and Shigeru Koyama. Thermodynamic assessment of high-temperature heat pumps using low-GWP HFO refrigerants for heat recovery. *International Journal of Refrigeration*, 53:126–141, 2015.

[210] Opeyemi Bamigbetan, Trygve Magne Eikevik, Petter Nekså, and Michael Bantle. Evaluation of Natural working fluids for the Development of high temperature heat pumps. In *12th IIR Gustav Lorentzen Conference on Natural Refrigerants GL2016, August 21-24*, pages 1–8, Edimburgh, UK, 2016.

[211] Andrea Meroni, Angelo La Seta, Jesper Graa Andreasen, Leonardo Pierobon, Giacomo Persico, and Fredrik Haglind. Combined Turbine and Cycle Optimization for Organic Rankine Cycle Power Systems – Part A: Turbine Model. *Energies*, 9(5):313, 1–15, 2016.

[212] J. Schiffmann. Integrated Design and Multi-objective Optimization of a Single Stage Heat-Pump Turbocompressor. *Journal of Turbomachinery*, 137(7):071002, 2015.

[213] Adeel Javed, Cordin Arpagaus, Stefan Bertsch, and Jürg Schiffmann. Small-scale turbocompressors for wide-range operation with large tip-clearances for a two-stage heat pump concept. *International Journal of Refrigeration*, 69:285–302, 2016.

[214] The Mathworks Inc. MATLAB - MathWorks, 2016. URL http://www.mathworks.com/products/matlab/.

[215] Andrea Meroni, Jesper Graa Andreasen, Leonardo Pierobon, and Fredrik Haglind. Optimization of Cycle and Expander Design of an Organic Rankine Cycle Unit using Multi-component Working Fluids. In *ASME Turbo Expo 2016: Turbomachinery Technical Conference and Exposition, June 13-17*, pages 1–12, Seoul, South Korea, 2016.

[216] Paolo Gabrielli. Design and optimization of turbo-expanders for organic Rankine cycles. Master's thesis, Technical University of Denmark, 2014.

[217] Eric W. Lemmon, Marcia L. Huber, and Mark O. McLinden. NIST reference fluid thermodynamic and transport properties–REFPROP, 2002.

[218] Ian H. Bell, Jorrit Wronski, Sylvain Quoilin, and Vincent Lemort. Pure and pseudo-pure fluid thermophysical property evaluation and the open-source thermophysical property library coolprop. *Industrial and Engineering Chemistry Research*, 53(6):2498–2508, 2014.

[219] D. G. Ainley and G. C. R. Mathieson. A Method of Performance Estimation for Axial-Flow Turbines. Technical report, Aeronautical Research Council Great Britain, 1951.

[220] M. Vavra. Axial flow turbines. Technical report, 1969.

[221] M.E. Deich, G. A. Filippov, and L.Ya. Lazarev. *Atlas of Axial Turbine Blade Cascades*. C.E. Trans. 4563-4564. CEGB Information Services, 1965.

[222] H. R. M. Craig and H. J. A. Cox. Performance estimation of axial flow turbines. *Proceedings of the Institution of Mechanical Engineers*, 185(1):407–424, 1970.

[223] H. I. H. Saravanamuttoo, G. F. C. Rogers, and Henry Cohen. *Gas Turbine Theory (5th Ed.)*. 2001.

[224] Piotr Klonowicz, Florian Heberle, Markus Preißinger, and Dieter Brüggemann. Significance of loss correlations in performance prediction of small scale, highly loaded turbine stages working in Organic Rankine Cycles. *Energy*, 72:322–330, 2014.

[225] S. C. Kacker and U. Okapuu. A Mean Line Prediction Method for Axial Flow Turbine Efficiency. *Journal of Engineering for Gas Turbines and Power*, 104(1):111–119, 1982.

[226] O. E. Balje and R. L. Binsley. Axial Turbine Performance Evaluation. Part A Loss-Geometry Relationships. *Journal of Engineering for Gas Turbines and Power*, 90(4):341–348, 1968.

[227] W. Traupel. *Thermische Turbomaschinen. Vol. 1 : Thermodynamisch-strömungstechnische Berechnung*. Springer, 1966.

[228] Ennio Macchi and Giovanni Lozza. Comparison of Partial vs Full Admission for Small Turbines at Low Specific Speeds. In *ASME 1985 International Gas Turbine Conference and Exhibit, March 18-21*, pages 1–8, Houston, Texas, USA, 1985.

[229] J. Dunham and P. M. Came. Improvements to the Ainley-Mathieson method of turbine performance prediction. *Journal of Engineering for Gas Turbines and Power*, 92(3):252–256, 1970.

[230] S.L. Dixon and C.A. Hall. *Fluid Mechanics and Thermodynamics of Turbomachinery*. Oxford, UK, sixth edition, 2010.

[231] Michael H. Vavra. *Aero-thermodynamics and Flows in Turbomachines*. J. Wiley, 1960.

[232] Ulrik Larsen, Leonardo Pierobon, Fredrik Haglind, and Cecilia Gabrielii. Design and optimisation of organic Rankine cycles for waste heat recovery in marine applications using the principles of natural selection. *Energy*, 55(45):803–812, 2013.

[233] Sylvain Quoilin, Martijn Van Den Broek, Sébastien Declaye, Pierre Dewallef, and Vincent Lemort. Techno-economic survey of Organic Rankine Cycle (ORC) systems. *Renewable and Sustainable Energy Reviews*, 22:168–186, 2013.

[234] Junjiang Bao and Li Zhao. A review of working fluid and expander selections for organic Rankine cycle. *Renewable and Sustainable Energy Reviews*, 24(1):325–342, 2013.

[235] Dongxiang Wang, Xiang Ling, Hao Peng, Lin Liu, and LanLan Tao. Efficiency and optimal performance evaluation of organic Rankine cycle for low grade waste heat power generation. *Energy*, 50(1):343–352, 2013.

[236] Henrik Öhman and Per Lundqvist. Screw expanders in ORC applications, review and a new perspective. In *3rd International Seminar on ORC Power Systems, October 12-14, Brussels, Belgium*, pages 1–10, 2015.

[237] Ozone Secretariat UNEP, Montreal Protocol on Substances that Deplete the Ozone Layer, US Government Printing Office, 1987. Technical report.

[238] Official Journal of the European Union, Regulation (EU) no 517/2014 of the European parliament and of the council on fluorinated greenhouse gases and repealing regulation (EC) no 842/2006. Technical report.

[239] R. Rayegan and Y. X. Tao. A procedure to select working fluids for Solar Organic Rankine Cycles (ORCs). *Renewable Energy*, 36(2):659–670, 2011.

[240] Ulli Drescher and Dieter Brüggemann. Fluid selection for the Organic Rankine Cycle (ORC) in biomass power and heat plants. *Applied thermal engineering*, 27(1):223–228, 2007.

[241] MAN Diesel & Turbo. Waste Heat Recovery System (WHRS) - Marine Engines & Systems. Technical report, aug 2015. URL http://marine.man.eu/.

[242] Costante Invernizzi, Paolo Iora, and Paolo Silva. Bottoming micro-Rankine cycles for micro-gas turbines. *Applied thermal engineering*, 27(1):100–110, 2007.

[243] G. Angelino, C. Invernizzi, and G. Molteni. The potential role of organic bottoming Rankine cycles in steam power stations. *Proceedings of the Institution of Mechanical Engineers, Part A: Journal of Power and Energy*, 213(2):75–81, 1999.

[244] C. Maccio, G. Tomei, G. Angelino, M. Gaia, and E. Macchi. Operational experience of a 3.0 kW solar powered water pump. In *Silver Jubilee Congress, May 28- June 1*, volume 1, pages 1501–1505, Atlanta, GA, USA, 1979.

[245] G. Angelino and C. Invernizzi. Cyclic methylsiloxanes as working fluids for space power cycles. *Journal of solar energy engineering*, 115(3):130–137, 1993.

[246] Dipl.-Ing. Gerhard Groschup. *Strömungstechnische Untersuchung einer Axialturbinenstufe im Vergleich zum Verhalten der erben Gitter ihrer Beschaufelung*. PhD thesis, Technische Universität Hannover, 1977.

[247] Ch. Hirsch and J. D. Denton. Through Flow Calculations in Axial Turbomachines. AGARD Advisory Report N.175. Technical report, AGARD. Propulsion and Energetics Panel. Working Group 12, 1981.

[248] P. Kötzing and B. Evers. Test case e/tu, 4-stage low speed turbine. AGARD Advisory Report N.275. Technical report, AGARD, 1990.

[249] Florian R. Menter. Zonal Two Equation k-omega, Turbulence Models for Aerodynamic Flows. *AIAA paper*, (2906):21, 1993.

[250] G. Persico, A. Mora, P. Gaetani, and M. Savini. Unsteady aerodynamics of a low aspect ratio turbine stage: Modeling issues and flow physics. *Journal of Turbomachinery*, 134(6): 61030, 2012.

[251] N. Herzog, M. Binner, J. R. Seume, and K. Rothe. Verification of low-flow conditions in a multistage turbine. In *ASME Turbo Expo 2007: Power for Land, Sea, and Air*, pages 563–574. American Society of Mechanical Engineers, 2007.

[252] G. A. Gerolymos and C. Hanisch. Multistage three-dimensional Navier-Stokes computation of off-design operation of a four-stage turbine. *Proceedings of the Institution of Mechanical Engineers, Part A: Journal of Power and Energy*, 213(4):243–261, 1999.

[253] Giulio Croce, Luca Ratto, and Antonio Satta. A Navier Stokes Solver for Axisymmetric Turbomachinery Analysis. In *5th European conference on Computational Fluid Dynamics, June 14-17 June*, pages 1–12, Lisbon, Portugal, 2010.

[254] Carlo Cravero, Paolo Macelloni, and Giuseppe Briasco. Three-Dimensional Design Optimization of Multistage Axial Flow Turbines Using a RSM Based Approach. In *ASME Turbo Expo 2012: Turbine Technical Conference and Exposition, June 11-15, Copenhagen, Denmark*, pages 1873–1884. American Society of Mechanical Engineers, 2012.

[255] G. A. Gerolymos and I. Vallet. Tip-clearance and secondary flows in a transonic compressor rotor. In *ASME 1998 International Gas Turbine and Aeroengine Congress and Exhibition*, page V001T01A093, 1998.

[256] G. A. Gerolymos. Implicit multiple-grid solution of the compressible Navier-Stokes equations using k-epsilon turbulence closure. *AIAA journal*, 28(10):1707–1717, 1990.

[257] A. Verneau. Waste Heat Recovery by Organic Fluid Rankine Cycle. In *Proceedings from the First Industrial Energy Technology Conference, April 22-25*, pages 940–952, Houston, Texas, USA, 1979.

[258] J. L. Boy-Marcotte. 100-1000 kW (el) medium-power distributed-collector solar system. *Electric Power Systems Research*, 3(1):41–51, 1980.

[259] Alfred Kluwick. *Nonlinear waves in real fluids*. Springer, 1991.

[260] Kevin G. Joback and Robert C. Reid. Estimation of pure-component properties from group-contributions. *Chemical Engineering Communications*, 57(1-6):233–243, 1987.

[261] M. D. Morris. Factorial Sampling Plans for Preliminary Computational Experiments. *Technometrics*, 133(2):295–302, 1991.

[262] Gurkan Sin, Krist V. Gernaey, and Anna Eliasson Lantz. Good Modeling Practice for PAT Applications: Propagation of Input Uncertainty and Sensitivity Analysis. *Biotechnology Progress*, 25(4):1043–1053, 2009.

[263] N. Metropolis and S. Ulam. The Monte Carlo Method. *Journal of the American Statistical Association*, 44(247):335–341, 1949.

[264] C. Osnaghi. *Teoria delle turbomacchine*. 2013.

[265] J. Kennedy. Particle swarm optimization. In *Encyclopedia of Machine Learning*, pages 760–766. Springer, 2010.

[266] Charles Audet and J. E. Dennis. Analysis of generalized pattern searches. *Siam Journal on Optimization*, 13(3):889–903, 2003.

[267] Florian Heberle, Markus Preißinger, and Dieter Brüggemann. Zeotropic mixtures as working fluids in Organic Rankine Cycles for low-enthalpy geothermal resources. *Renewable Energy*, 37(1):364–370, 2012.

[268] Bertrand Fankam Tchanche, George Papadakis, Gregory Lambrinos, and Antonios Frangoudakis. Fluid selection for a low-temperature solar organic Rankine cycle. *Applied Thermal Engineering*, 29(11):2468–2476, 2009.

[269] M.O. O. McLinden and R. Radermacher. Methods for comparing the performance of pure and mixed refrigerants in the vapour compression cycle. *International Journal of Refrigeration*, 10(6):318–325, 1987.

[270] M. Högberg, L. Vamling, and T. Berntsson. Calculation methods for comparing the performance of pure and mixed working fluids in heat pump applications. *International Journal of Refrigeration*, 16(6):403–413, 1993.

[271] Young Jin Baik, Minsung Kim, Ki Chang Chang, Young Soo Lee, and Hyung Kee Yoon. A comparative study of power optimization in low-temperature geothermal heat source driven R125 transcritical cycle and HFC organic Rankine cycles. *Renewable Energy*, 54:78–84, 2013.

[272] J. G. Andreasen, U. Larsen, and F. Haglind. Design of organic Rankine cycles using a non- conventional optimization approach. In *28th international conference on Efficiency, Cost, Optimization, Simulation and Environmental Impact of Energy Systems (ECOS), June 29-July 3*, pages 1–13, Pau, France, 2015.

[273] Jesper Graa Andreasen, Andrea Meroni, and Fredrik Haglind. A Comparison of Organic and Steam Rankine Cycle Power Systems for Waste Heat Recovery on Large Ships. *Energies*, 10(4):547, 1–23, 2017.

[274] Stefano Calvi. Analisi e validazione di solutori CFD ad alta e bassa fedelta' per turbomacchine. MSc thesis, 2015.

[275] Antti Uusitalo. Working Fluid Selection and Design of Small-scale Waste Heat Recovery Systems Based on Organic Rankine Cycles, 2014.

[276] G. Angelino, E. Macchi, and M. Gaia. *Design, Construction and Testing of a Hermetically Sealed 100 kW Organic Rankine Cycle Engine for Medium Temperature (200-400 C) Heat Recovery: Final Report*. Commission of the European Communities; Directorate-general Science, Research and Development, 1985.

[277] P. J. Walker and J. A. Hesketh. Design of low-reaction steam turbine blades. *Proceedings of the Institution of Mechanical Engineers, Part C: Journal of Mechanical Engineering Science*, 213(2):157–171, 1998.

[278] S. Havakechian and R. Greim. Aerodynamic design of 50 per cent reaction steam turbines. *Proceedings of the Institution of Mechanical Engineers, Part C: Journal of Mechanical Engineering Science*, 213(1):1–25, 1999.

[279] Wendy C. Andersen and Thomas J. Bruno. Rapid screening of fluids for chemical stability in organic Rankine cycle applications. *Industrial & Engineering Chemistry Research*, 44 (15):5560–5566, 2005.

[280] Ormat Technologies. Green Energy You Can Rely On, 2016. URL http://www.ormat.com.

[281] Atlas Copco. EG, EGi, EEGi-Series — Atlas Copco Gas and Process, 2016. URL http://www.atlascopco-gap.com/products/expanders/eg-egi-eegi-series/.

[282] Markus Preißinger and Dieter Brüggemann. Thermal stability of hexamethyldisiloxane (MM) for high-temperature organic Rankine cycle (ORC). *Energies*, 9(3):183, 2016.

[283] Dwight E. Williams. Volatile Methyl Siloxanes: Environmentally Sound Solvent Systems. ACS Publications, 2000.

[284] Turboden. Turboden: Clean Energy Ahead, 2016. URL http://www.turboden.eu.

[285] Ennio Macchi. Theoretical basis of the Organic Rankine cycle. In Ennio Macchi and Marco Astolfi, editors, *Organic Rankine Cycle (ORC) Power Systems : Technologies and Applications*, chapter 1, pages 3–24. Elsevier Science, 2016.

[286] Marco Pasetti, Costante M Invernizzi, and Paolo Iora. Thermal stability of working fluids for organic Rankine cycles: An improved survey method and experimental results for cyclopentane, isopentane and n-butane. *Applied Thermal Engineering*, 73(1):764–774, 2014.

[287] Daniel M. Ginosar, Lucia M. Petkovic, and Donna Post Guillen. Thermal stability of cyclopentane as an organic Rankine cycle working fluid. *Energy & Fuels*, 25(9):4138–4144, 2011.

[288] GE Oil & Gas - ORegen. URL http://www.geoilandgas.com.

[289] Aqylon - Smarter Power. URL http://www.aqylon.com/products-range/.

[290] W. J. Collins, R. G. Derwent, C. E. Johnson, and D. S. Stevenson. The oxidation of organic compounds in the troposphere and their global warming potentials. *Climatic Change*, 52(4): 453–479, 2002.

[291] Gerald C. Straty, M. J. Ball, and T. J. Bruno. PVT of toluene at temperatures to 673 K. *Journal of Chemical and Engineering Data*, 33(2):115–117, 1988.

[292] Gianfranco Angelino and Costante Invernizzi. Experimental investigation on the thermal stability of some new zero ODP refrigerants. *International Journal of Refrigeration*, 26(1): 51–58, 2003.

[293] Calnetix. Organic Rankine Cycle Systems, 2016. URL http://www.calnetix.com/organic-rankine-cycle-systems.

[294] Cryostar- Clean Energy. URL http://www.cryostar.com/web/power-electricity.

[295] Sanne Lemmens. A perspective on costs and cost estimation techniques for organic Rankine cycle systems. In *Proceedings of the 3rd International Seminar on ORC Power Systems (ASME ORC 2015), Brussels, Belgium*, pages 12–14, 2015.

[296] Sylvain Quoilin, Sébastien Declaye, Bertrand F Tchanche, and Vincent Lemort. Thermo-economic optimization of waste heat recovery Organic Rankine Cycles. *Applied thermal engineering*, 31(14):2885–2893, 2011.

[297] Steven Lecompte, Sanne Lemmens, Henk Huisseune, Martijn van den Broek, and Michel De Paepe. Multi-Objective Thermo-Economic Optimization Strategy for ORCs Applied to Subcritical and Transcritical Cycles for Waste Heat Recovery. *Energies*, 8(4):2714–2741, 2015.

[298] Matteo Pini, Giacomo Persico, David Pasquale, and Stefano Rebay. Adjoint method for shape optimization in real-gas flow applications. *Journal of Engineering for Gas Turbines and Power*, 137(3):32604, 2015.

[299] P. Rodriguez-Fernandez and G. Persico. Automatic design of ORC turbine profiles using evolutionary algorithms. In *Proceedings of the Third International Seminar on ORC Power Systems, October 12-14, Brussels, Belgium*, pages 1–10, 2015.

[300] Jeff Tollefson. Nations agree to ban refrigerants that worsen climate change. \url{http://www.nature.com}.

[301] S. L. Dixon and C. A. Hall. *Fluid Mechanics and Thermodynamics of Turbomachinery*. Butterworth-Heinemann, Oxford, UK, seventh edition, 2014.

[302] Hany Moustapha, Mark F. Zelesky, Nicholas C. Baines, and David Japikse. *Axial and Radial Turbines*. Concepts NREC, White River Junction, VT, USA, 2003.

[303] John D. Stanitz. One-dimensional compressible flow in vaneless diffusers of radial-and mixed-flow centrifugal compressors, including effects of friction, heat transfer and area change. Technical report, NASA, 1952.

[304] A. Whitfield and N. C. Baines. *Design of radial turbomachines*. John Wiley and Sons Inc., New York, NY, USA, 1990.

[305] Filippo Rubechini, Michele Marconcini, Andrea Arnone, Alberto Scotti Del Greco, and Roberto Biagi. Special Challenges in the Computational Fluid Dynamics Modeling of Transonic Turbo-Expanders. *Journal of Engineering for Gas Turbines and Power*, 135(10): 102701, 2013.

[306] John Harinck, David Pasquale, Rene Pecnik, Jos van Buijtenen, and Piero Colonna. Performance improvement of a radial organic Rankine cycle turbine by means of automated computational fluid dynamic design. *Proceedings of the Institution of Mechanical Engineers, Part A: Journal of Power and Energy*, 227(6):637–645, 2013.

[307] Enrico Rinaldi, Rene Pecnik, and Piero Colonna. Unsteady Operation of a Highly Supersonic Organic Rankine Cycle Turbine. *Journal of Turbomachinery*, 138(12):121010, 2016.

[308] D. W. Artt and S. W. T. Spence. A loss analysis based on experimental data for a 99.0 mm radial inflow nozzled turbine with different stator throat areas. *Proceedings of the Institution of Mechanical Engineers, Part A: Journal of Power and Energy*, 212(1):27–42, 1998.

[309] Harold E. Rohlik and Milton G. Kofskey. Recent radial turbine research at the NASA Lewis Research Center. In *ASME 1972 International Gas Turbine and Fluids Engineering Conference and Products Show, 26-30 March 1972, San Francisco, California, USA*, page V001T01A041. American Society of Mechanical Engineers, 1972.

[310] Hyung-Chul Jung and Susan Krumdieck. Meanline design of a 250 kW radial inflow turbine stage using R245fa working fluid and waste heat from a refinery process. *Proceedings of the Institution of Mechanical Engineers, Part A: Journal of Power and Energy*, 230(4):402–414, 2016.

[311] David Japikse. Advanced diffusion levels in turbocharger compressors and component matching. In *1st International Conference on Turbocharging and Turbochargers, April 26-28*, pages 143–155, London, UK, 1982.

[312] J. W. Daily and R. E. Nece. Chamber Dimension Effects on Induced Flow and Frictional Resistance of Enclosed Rotating Disks. *Journal of Basic Engineering*, 82(1):217–230, 1960.

[313] Shuo Li, Eric M. Krivitzky, and Xuwen. Qiu. Meanline Modeling of a Radial-Inflow Turbine Nozzle With Supersonic Expansion. In *ASME Turbo Expo 2016: Turbomachinery Technical Conference and Exposition, June 13-17*, page V02DT42A036, Seoul, South Korea, 2016.

[314] P. L. Meitner and A. J. Glassman. Computer Program for Off-Design Performance Analysis of Radial Inflow Turbines with Rotor Blade Sweep. Technical report, NASA, Washington D.C., USA, 1983.

[315] Andrea Meroni, Benjamin Zühlsdorf, Brian Elmegaard, and Fredrik Haglind. Design of centrifugal compressors for heat pump systems. *[To be submitted]*, 2018.

[316] David Japikse. *Centrifugal compressor design and performance*. Concepts ETI Inc., Wilder, VT, USA, 1996.

[317] Cheng Xu and Ryoichi S. Amano. Empirical design considerations for industrial centrifugal compressors. *International Journal of Rotating Machinery*, 2012:1–15, 2012.

[318] F. J. Wiesner. A Review of Slip Factors for Centrifugal Impellers. *Journal of Engineering for Gas Turbines and Power*, 89(4):558–566, 1967.

[319] W. Jansen. A method for calculating the flow in a centrifugal impeller when entropy gradients are present. In *Royal Society conference on internal aerodynamics (turbomachinery), 19-21 July*, pages 133–146, Cambridge, UK, 1967.

[320] J. P. Johnston and R. C. Dean. Losses in Vaneless Diffusers of Centrifugal Compressors and Pumps: Analysis, Experiment, and Design. *Journal of Engineering for Power*, 88(1):49, 1966. ISSN 00220825.

[321] O. Conrad, K. Raif, and M. Wessels Of. The calculation of performance maps for centrifugal compressors with vane-island diffusers. In *Proceedings of the Twenty-fifth Annual International Gas Turbine Conference and Exhibit and Twenty-second Annual Fluids Engineering Conference, March 9-13*, pages 135–147, New Orleans, Louisiana, USA, 1980. American Society of Mechanical Engineers.

[322] D. Eckardt. Flow field analysis of radial and backswept centrifugal compressor impellers. I-Flow measurements using a laser velocimeter. In *Proceedings of the Twenty-fifth Annual International Gas Turbine Conference and Exhibit and Twenty-second Annual Fluids Engineering Conference, March 9-13*, pages 77–86, New Orleans, Louisiana, USA, 1980.

[323] J. Schiffmann and D. Favrat. Theoretical design of a high-speed low power radial turbo-compressor. In *6th European Turbomachinery Conference, 7-11 March*, pages 1–11, Lille, France, 2005.

[324] Jürg Schiffmann and Daniel Favrat. High-Speed Low Power Radial Turbocompressor For Oil-Free Heatpumps. In *International Compressor Engineering Conference at Purdue, July 17-20*, pages 1–8, 2006.

[325] Rene Pecnik, Enrico Rinaldi, and Piero Colonna. Computational Fluid Dynamics of a Radial Compressor Operating With Supercritical CO2. *Journal of Engineering for Gas Turbines and Power*, 134(12):122301, 2012.

[326] E. Rinaldi, R. Pecnik, and P. Colonna. Computational Fluid Dynamic Simulation of a Supercritical CO2 Compressor Performance Map. *Journal of Engineering for Gas Turbines and Power*, 137(7), 2015.

[327] M. N. Šarevski and V. N. Šarevski. Characteristics of water vapor turbocompressors applied in refrigeration and heat pump systems. *International Journal of Refrigeration*, 35(5): 1484–1496, 2012.

[328] V. N. Šarevski and M. N. Šarevski. Energy efficiency of the thermocompression refrigerating and heat pump systems. In *International Journal of Refrigeration*, volume 35, pages 1067–1079, 2012.

[329] Jürg Schiffmann. Small-scale and oil-free turbocompressor for refrigeration applications. In *22nd International Compressor Engineering Conference at Purdue, 14-17 July*, pages 1–11, West Lafayette, Indiana, USA, 2014.

[330] Juergen Süß. A centrifugal compressor cooling system using water as working fluid. In *12th IIR Gustav Lorentzen Conference on Natural Refrigerants (GL2016), August 21-24*, pages 1–7, Edimburgh, UK, 2016.

[331] Michael Bantle. Turbo-compressors: Prototype tests of mechanical vapour re-compression for steam driers. In *12th IEA Heat Pump Conference, June*, Rotterdam, The Netherlands, 2017.

[332] Michael Bantle. Steam compression and the development of a cost effective turbo compressor. In Brian Elmegaard, Benjam Zühlsdorf, Lars Reinholdt, and Michael Bantle, editors, *Book of presentations of the International Workshop on High Temperature Heat Pumps.*, pages 137–141. Kgs. Lyngby: Technical University of Denmark (DTU), 2017.

[333] J. H. Horlock. Losses and efficiencies in axial-flow turbines. *International Journal of Mechanical Sciences*, 2(1-2):48–75, 1960.

[334] Charles A. Wasserbauer and Arthur J. Glassman. Fortran program for predicting off-design performance of radial-inflow turbines. 1975.

[335] Ronald H. Aungier. *Centrifugal compressors: a strategy for aerodynamic design and analysis*. ASME Press, New York, NY, USA, 2000.

[336] Barend W. Botha and Adriaan Moolman. Determining the impact of the different losses on centrifugal compressor design. *R&D journal*, 21(3):1–9, 2005.

[337] Klaus Schlichting, Hermann Gersten, Egon Krause, Herbert Oertel, and Katherine Mayes. *Boundary-layer theory*. Springer, 1955.

[338] J.D. Stanitz. Some Theoretical Aerodynamic Investigations of Impellers in Radial and Mixed-Flow Centrifugal Compressors. *Transactions of the ASME*, 74:473–476, 1952.

[339] Xuwen Qiu, David Japikse, Jinhui Zhao, and Mark R. Anderson. Analysis and Validation of a Unified Slip Factor Model for Impellers at Design and Off-Design Conditions. *Journal of Turbomachinery*, 133(4):041018, 2011.

[340] B. Monge. *Design of supercritical carbon dioxide centrifugal compressors*. PhD thesis, University of Seville, Seville, Spain, 2014.

A Axial turbine model

A.1 Loss correlations

This appendix reports the main information on the loss correlations and the performance prediction method adopted in the axial turbine model TURAX. There are different performance prediction methods implemented in TURAX: Craig and Cox [222], Traupel [227], Aungier [133] and Soderberg [301]. As mentioned in Chapter 2.5, the method by Craig and Cox [222] was selected in this work since it is comprehensive and it was used by some researchers in the field of ORC turbines. The full details regarding the Craig and Cox performance prediction method are fully described in Ref. [222] and, therefore, are not reported here. However, for the sake of completeness, the different loss correlations are reported here. Note that the blade and flow angles reported in the charts of this appendix are referred to the tangential direction, as opposed to the angle convention used in the other chapters.

According to Craig and Cox [222], the losses in a turbine stage are conventionally divided into two categories: group 1 and group 2 losses. Group 1 losses include all the losses contributing to the reduction of the blade work produced by a change in tangential momentum of the fluid passing through the rotor blades. These losses are subdivided in profile, secondary and annulus losses. The profile losses are due to the friction in the blade profiles and in the blade wakes. The secondary losses stem from the friction on the walls at root and tip of the blades and secondary flow effects. The annulus losses are related to sudden enlargements in the fluid path or the presence of wall cavities. Group 2 losses are associated to work lost as part of the fluid does not participate to the generation of useful work on the rotor blades but leaks over the rotor tip or through diaphragm glands. Moreover, the output work is further reduced by the windage and bearing losses, and partial admission losses. Other loss contributions such as those due to the presence of liquid droplets in the blade rows when expanding in the two-phase region are not included in TURAX since the expansion of organic fluids ends in the superheated vapor region. Note that the classification of the losses as described above assumes that all the losses are non-interacting. This assumption is a simplification which does not occur in reality; however, treating separately each loss contribution allows formulating the losses in a mathematical way that is convenient to make considerations on the performance prediction and on the turbine design.

The stage efficiency is calculated as follows:

$$\eta_{tt} = \frac{\Delta h_{eul}}{\Delta h_{eul} + \text{Group 1 losses}} - \text{Group 2 losses} \tag{A.1}$$

$$\text{Group 1 losses} = (X_p + X_s + X_a)_{nozzle} \frac{C_2^2}{2} + \left(X_p + X_s + X_a \frac{C_3^2}{W_3^2} \right)_{rotor} \frac{W_3^2}{2} \tag{A.2}$$

$$\text{Group 2 losses} = \Delta\eta_k + \Delta\eta_{dw} + \Delta\eta_{pa} \tag{A.3}$$

where $\Delta h_{eul} = U_2 C_{2t} - U_3 C_{3t}$ is the Euler work done on the rotor blades by a change of tangential momentum of the fluid, X_p the kinetic energy loss coefficient for the profile losses, X_s for the secondary losses, and X_a for the losses in the annulus or due to wall cavities. For convenience, Group 2 losses are computed as efficiency debits as this is the simplest way they are derived from experimental data. In Equation A.3, $\Delta\eta_k$ is the efficiency debit due to leakage at the rotor tip, $\Delta\eta_{dw}$ that due to disc windage, $\Delta\eta_{pa}$ that due to the presence of partial admission. Craig and Cox [222] provided the calculation of the different loss terms from empirical charts, which are reported below for convenience.

A.1.1 Group 1 losses

For each blade row, the kinetic energy coefficient of the profile loss is calculated with the following expression:

$$X_p = x_{pb} N_{pr} N_{pi} N_{pt} c_M + (\Delta x_p)_t + (\Delta x_p)_{s/e} + (\Delta x_p)_m \tag{A.4}$$

The first term in Equation A.4 is the profile loss contribution due to a so-called basic profile loss (x_{pb}) corrected for Reynolds number effects (N_{pr}), incidence effects at off-design conditions (N_{pi}), and the effects of trailing edge thickness losses (N_{pt}). The second term in Equation A.4 is a profile loss increment due to trailing edge thickness losses ($(\Delta x_p)_t$). The third term is a profile loss increment due to blade back radius losses ($(\Delta x_p)_{s/e}$), and the last term is a profile loss due to supersonic Mach number effects for convergent blade profiles $(\Delta x_p)_m$.

The basic profile loss is the friction loss in the blades under subsonic flow conditions, and for the optimal blade incidence when the incidence loss is minimum. A basic profile loss parameter, $x_p(s/b)sin(\beta)$, is calculated in Figure A.1 as a function of a modified lift coefficient $F_L(s/b)$ and a blade contraction ratio, defined as the ratio of the internal passage width from the inlet to the throat. In this nomenclature, s is the blade pitch, b is the blade backbone length, and β is the flow angle in the relative coordinate system. The lift coefficient is provided in Figure A.1(b) as a function of the inlet and exit flow angles in the blade row. In particular, the inlet flow angle is that corresponding to a minimum incidence loss condition (design point) while the outlet flow angle is that corresponding to subsonic flow conditions. A correlation for the contraction ratio of average blade profiles is illustrated in Figure A.2(a). The basic loss profile X_b is then corrected for the effect of the Reynolds number using the factor N_{pr} in Figure A.2(b), and to zero trailing edge conditions using the factor N_t in Figure A.3. The profile loss correction for incidence effects, the factor N_{pi}, is computed using other figures in Craig and Cox [222]. However, these are not reported here since the axial turbine model presented in this work considered design conditions only, for which the incidence loss is minimum and $N_{pi} = 1$. The profile loss increment due to trailing edge effects, $(\Delta x_p)_t$, is provided

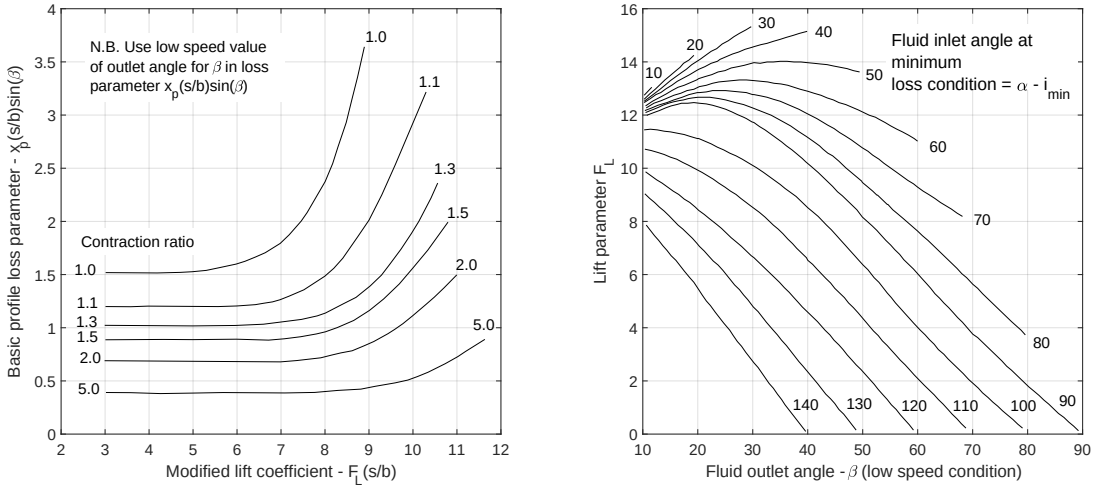

(a) (b)

Figure A.1: Estimation of (a) basic profile loss x_p and (b) lift parameter F_L. Adapted from Craig and Cox [222].

in Figure A.3 as a function of the trailing-edge-thickness to pitch ratio (te/s).

The profile loss increment due to blade back radius losses applies to those profiles designed with a pronounced convex suction surface downstream of the throat. This increment is estimated in Figure A.4(a), where it is shown that it increases with the pitch to back blade radius ratio and with the outlet Mach number.

The profile loss increment due to Mach number effects applies when the relative isentropic Mach number at the blade exit is above one and is shown in Figure A.4(b). The correlation applies only to convergent blade profiles.

In Equation A.4, the term c_M is a multiplier coefficient for the presence of shock losses in the blade rows. The factor is computed according to Kacker and Ockapuu [225] as follows:

$$c_M = 1 + 0.25 \left[\left(\frac{M - 0.4}{0.4} \right)^{1.75} - 1 \right] \qquad \text{for M} > 0.8 \tag{A.5}$$

$$c_M = 1 \qquad \text{for M} \leq 0.8 \tag{A.6}$$

where M denotes the Mach number at the inlet of the blade row in the relative coordinate system. Equation A.5 assumes that shock waves form already before reaching sonic conditions at the inlet of the blade passages.

For each blade row, the kinetic energy coefficient of the secondary loss is calculated with the expression:

$$X_s = (x_s)_b (N_s)_r (N_s)_{h/b} \tag{A.7}$$

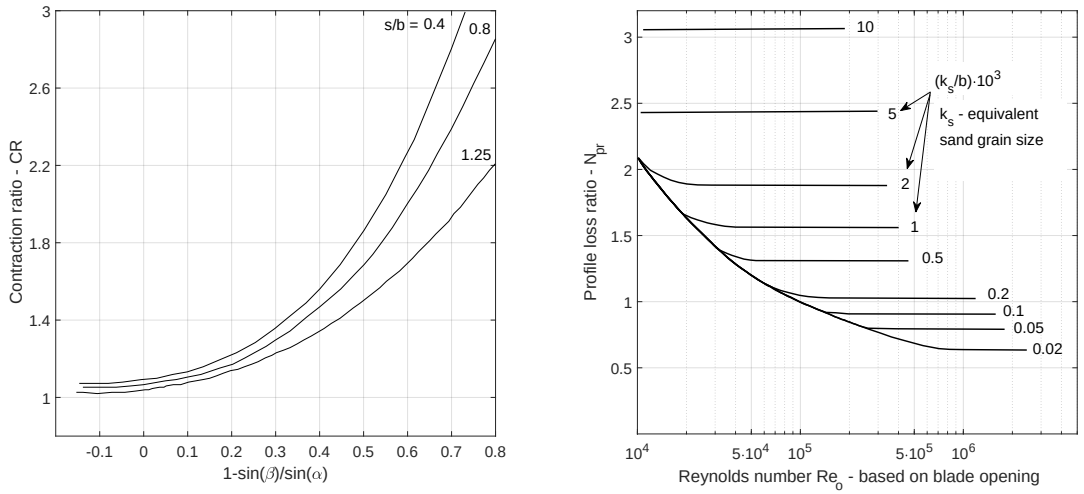

(a) (b)

Figure A.2: (a) Contraction ratio for average profiles and (b) profile loss ratio against Reynolds number effect. Adapted from Craig and Cox [222].

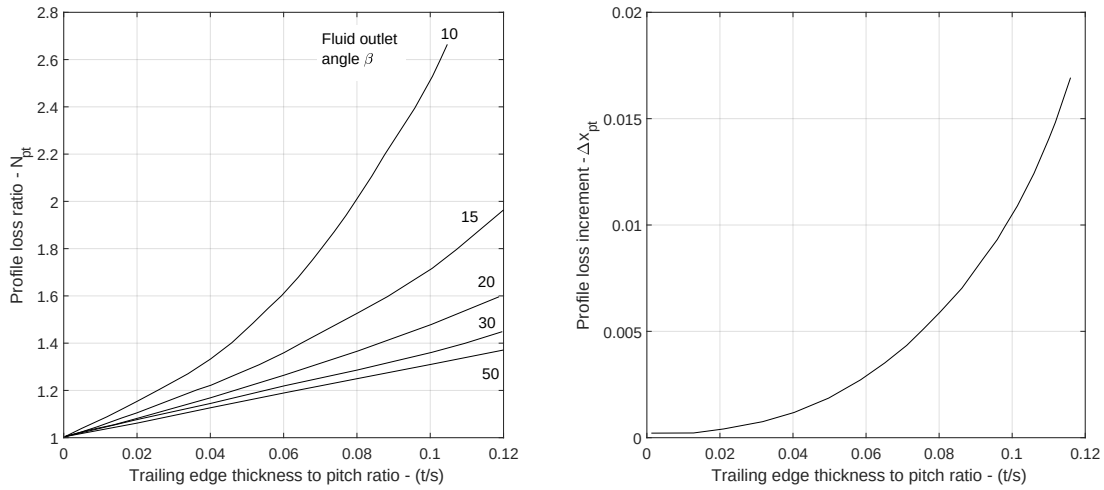

(a) (b)

Figure A.3: Trailing edge thickness losses. Adapted from Craig and Cox [222].

where $(x_s)_b$ is a basic secondary loss coefficient, and $(N_s)_r$ and $(N_s)_{h/b}$ are two correction factors accounting for Reynolds number and blade aspect ratio effects, respectively. The parameter $(x_s)_b$ is calculated from Figure A.5(a) as a function of the relative inlet-to-outlet velocity ratio across the blades and of the lift coefficient. The multiplier $(N_s)_r$ is computed from Figure A.2(b) as in the case of the profile losses whereas the factor $(N_s)_{h/b}$ incorporating the effects of the blade aspect ratio is given in Figure A.5(b).

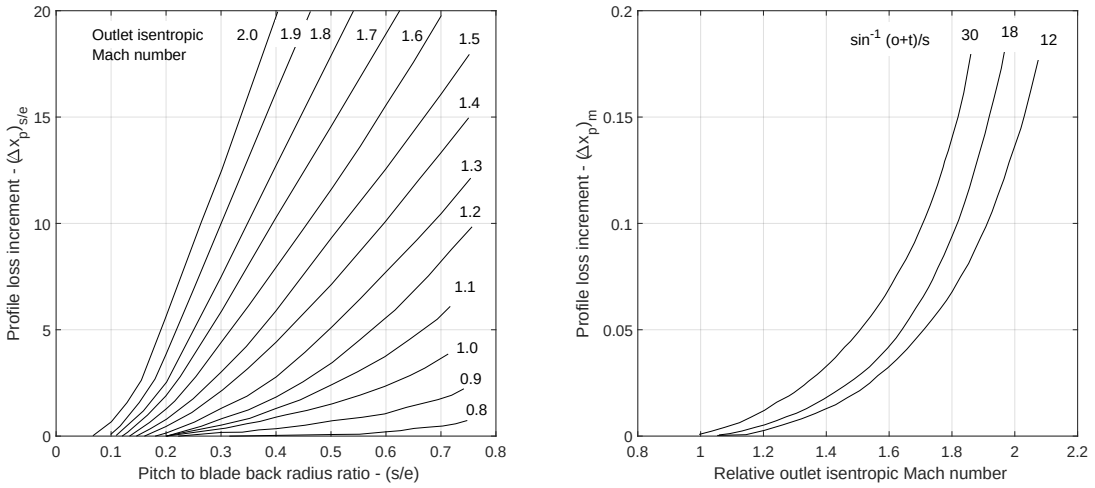

(a) (b)

Figure A.4: Profile loss increment for (a) blade back radius losses and (b) Mach number loss for convergent blading. Adapted from Craig and Cox [222].

Annulus wall losses are computed from Figure A.6. In this work, only a controlled expansion was considered.

A.1.2 Group 2 losses

The losses due to rotor tip clearance effects are provided as efficiency debit by the following expressions:

$$\Delta\eta_k = F_k \frac{A_k}{A_t}\eta_0 \qquad \text{for shrouded blades} \tag{A.8}$$

$$\Delta\eta_k = 1.5F_k \frac{A_k}{A_t}\eta_0 \qquad \text{for unshrouded blades} \tag{A.9}$$

where η_0 is the blading efficiency, A_k is the leakage area , A_t is the total area (hub to shroud) at the throat, and F_k is a leakage factor which is provided in Figure A.7 for shrouded blades. In case of unshrouded blades, Craig and Cox [222] suggested multiplying the factor F_k from Figure A.7 by 1.5.

The losses due to the windage and friction effects on the rotor disc are computed using the following

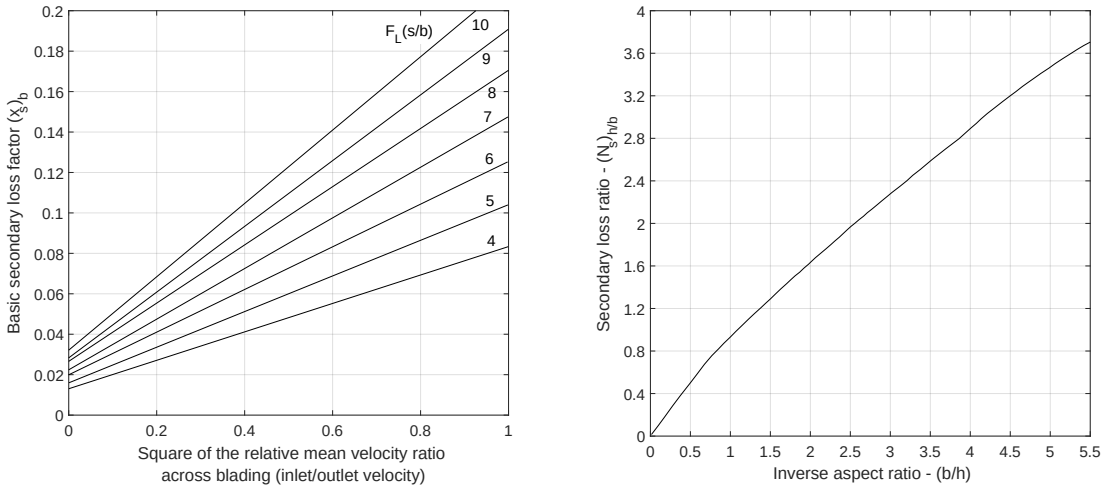

(a) (b)

Figure A.5: (a) Secondary loss-basic loss factor and (b) Secondary loss- aspect ratio factor. Adapted from Craig and Cox [222].

expressions [226]:

$$\Delta\eta_{dw} = \frac{P_d}{\dot{m}\Delta h_{0,is}} \tag{A.10}$$

$$P_d = C_{df} U_r^3 \overline{\rho} \frac{\overline{r}_{hub}^2}{2} \tag{A.11}$$

$$U_r = 2\pi N \overline{r}_{hub} \quad \overline{\rho} = \frac{\rho_2 + \rho_3}{2} \quad \overline{r}_{hub} = \frac{r_{hub,2} + r_{hub,3}}{2} \tag{A.12}$$

$$C_{df} = max\{c_1; c_2; c_3; c_4\} \tag{A.13}$$

$$c_1 = \frac{2\pi B^{-1}}{Re_d} \quad c_2 = \frac{3.7(B^{0.1})}{Re_d^{0.2}} \quad c_3 = \frac{0.08B^{-\frac{1}{6}}}{Re_d^{0.25}} \quad c_4 = \frac{0.102(B^{0.1})}{Re_d^{0.2}} \tag{A.14}$$

$$Re_d = Re_r \frac{\overline{r}_{hub} U_r}{o_r W_3} \tag{A.15}$$

$$B = \frac{0.75ss}{\overline{r}_{hub}} \tag{A.16}$$

where P_d is the mechanical power lost due to disc friction and windage effects, $\Delta h_{0,is}$ is the stage isentropic total enthalpy drop, $\dot{m}$ is the working fluid mass flow rate. The terms o_r, W_3 and ss denote the rotor throat, the rotor exit relative velocity, and the axial distance between the nozzle exit and the rotor inlet.

Partial admission losses are modeled using the correlation by Suter and Traupel [227], which is considered to be the best available by Craig and Cox [222]. Partial admission refers to a specific turbine operation where a fraction ε_{adm} of the total admission arc through the nozzle blades is blocked. The correlations estimate the partial admission losses as two efficiency debit contributions: the pumping (also called *ventilation* or *windage*) losses and the sector-end scavenging (also called

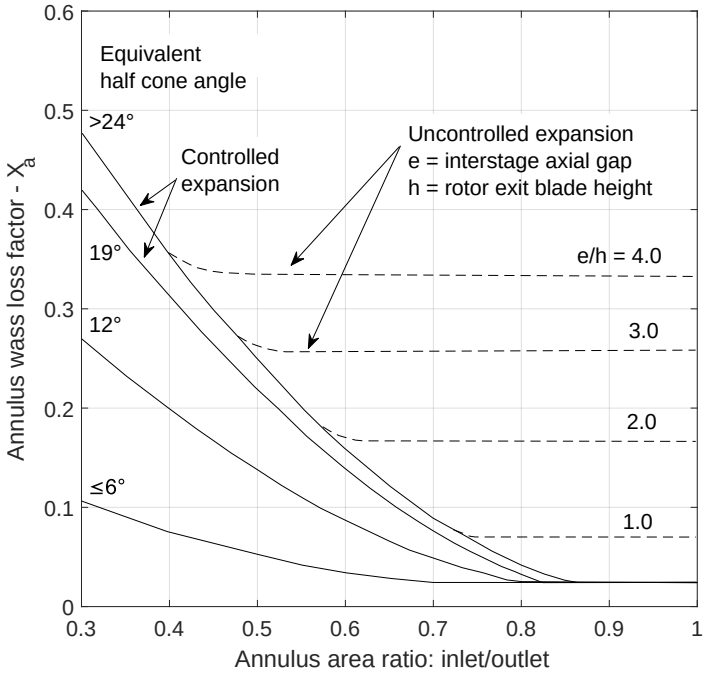

Figure A.6: Annulus wall loss. Adapted from Craig and Cox [222].

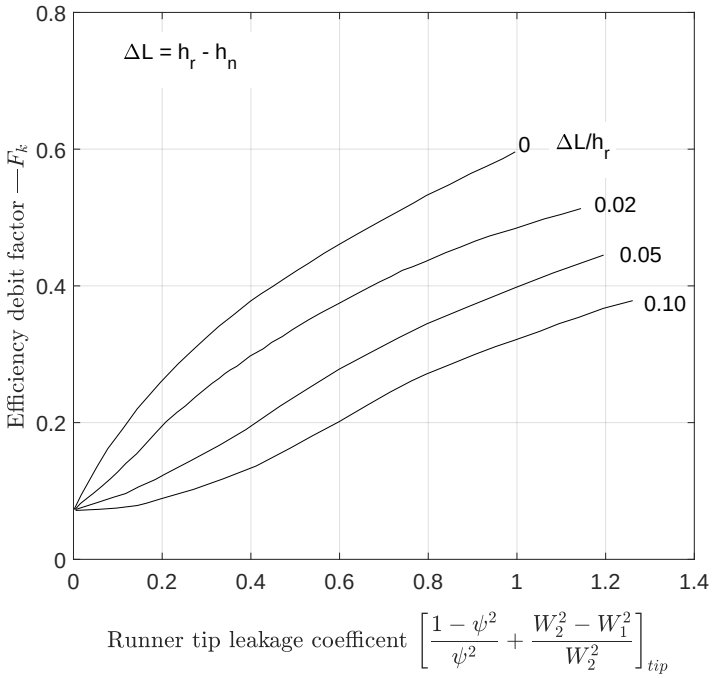

Figure A.7: Shrouded efficiency loss. Adapted from Craig and Cox [222].

filling-emptying) losses [133]. The first type of losses occurs when some of the flow in the active blade passages in the rotor re-enters inactive passages to produce windage losses. The second type of losses is due to the presence of rotor blades which are only partially filled and, therefore, operate at reduced mass flow rate resulting in wasted energy. The equations used to compute the partial admission losses are the following:

$$C_{bl} = 0.019 + 1.1\left(0.125 - \frac{h_r}{2\bar{r}_r}\right)^2 \tag{A.17}$$

$$\psi_{is} = 2\frac{\Delta h_{0,is}}{\bar{U}_r^2} \tag{A.18}$$

$$\Delta\eta_{pa,pl} = C_{bl}\frac{1-\varepsilon_{adm}}{\varepsilon_{adm}\phi_n\psi_{is}} \tag{A.19}$$

$$\Delta\eta_{pa,sc} = \frac{0.3c_r}{2\bar{r}_r\varepsilon_{adm}\sqrt{\psi_{is}}} \tag{A.20}$$

where h_r is the average rotor blade height, $\bar{r}_r$ the average rotor radius, $\psi_{is} = 2\Delta h_{0,is}/U_{3m}^2$ the isentropic stage loading coefficient, c_r the rotor axial chord, and ϕ_n is the nozzle flow coefficient.

A.2 Flow deviation correlations

The flow angle at the exit of a blade row is computed using empirical correlations based on the opening-to-pitch ratio and the exit flow conditions. The following formula by Ainley and Mathieson [219] is employed for subsonic flow conditions at the exit:

$$\theta = cos^{-1}(o/s) \quad [radians] \tag{A.21}$$

$$\alpha^* = (1.1485\theta - 0.1897) \quad [radians] \tag{A.22}$$

$$\alpha = \alpha_{sub} = \alpha^*(deg) + 4\left(\frac{s}{e}\right) \quad \text{for M} \leq 0.5 \quad [degrees] \tag{A.23}$$

$$\alpha = \alpha_{sub}(rad) + 2(M-0.5)(\theta - \alpha_{sub}(deg)) \quad \text{for M} > 0.5 \quad [radians] \tag{A.24}$$

where s is the blade pitch, o the throat, and e the blade rear suction side curvature radius. Note that a consistent application of the above equations requires the conversion of α^* in degrees in Equation A.23, and the use of the angles in radians in Equation A.24, where the angle α can subsequently be converted in degrees. In case of a converging nozzle with supersonic flow conditions at the exit, the formula by Vavra [220] is used. Such a formula is derived by applying energy, momentum and continuity equations from the blade exit opening to the downstream conditions assumed to be

uniform. The final formula is the following:

$$K = \gamma/(\gamma-1) \tag{A.25}$$

$$A_1 = -K\left(\frac{p_{ex}}{p_{th}}\right)tan(\theta) \tag{A.26}$$

$$A_2 = \sqrt{\left(1-\frac{p_{ex}}{p_{th}}\right)\left[2KM_{th}^2 - 1 - \left(\frac{\gamma+1}{\gamma-1}\right)\frac{p_{ex}}{p_{th}}\right] + \left[K\frac{p_{ex}}{p_{th}}tan(\theta)\right]^2} \tag{A.27}$$

$$A_3 = 1 + \gamma M_{th}^2 - \left(\frac{p_{ex}}{p_{th}}\right) \tag{A.28}$$

$$\Delta\alpha = tan^{-1}\left(\frac{A_1 + A_2}{A_3}\right) \tag{A.29}$$

$$\alpha = \theta - \Delta\alpha \tag{A.30}$$

The terms p_{ex} and p_{th} indicate the static pressure at the exit and the throat, respectively. The term M_{th} is the Mach number at the throat, and γ is the specific heat ratio evaluated at the exit conditions. In case an adapted converging-diverging nozzle is used, the flow angle is computed using the cosine rule, Equation A.21.

A.3 Blockage factor correlations

In TURAX the restriction of the effective passage area due to the boundary layer growth is considered using restriction factors applied to the mass continuity equation. The following restriction factor ζ from Vavra [220] is used for each blade row:

$$\zeta = \frac{1}{1+\left(\frac{H}{K}\right)\cdot X_p^*} \qquad X_p^* = \frac{X_{p,noM}}{1+X_p+X_a+X_s} \tag{A.31}$$

where (H/K) is an energy factor form assumed to be equal to 0.9 following the approach by Macchi [52]. Note that the term $X_{p,noM}$ is the profile loss kinetic energy coefficient after removing the loss contributions and terms related to Mach number effects.

A.4 Preliminary design formulas

Some additional expressions are needed to determine part of the geometric parameters required in the empirical correlations. These formulas are provided hereafter.

The blade backbone length (here denoted b) and the profile chord (here denoted ch) are required for the estimation of the nozzle and rotor profile losses. An approximate method is used to determine this values based on the knowledge of the axial chord (here indicated with c) and the inlet and outlet geometric angles ($\alpha_{1,bl}$ and $\alpha_{2,bl}$). The blade geometry is assumed to be a circular arc followed by

a straight part after the throat.

$$\Lambda_1 = \left(\frac{(180° - \alpha_{1,bl}) + \alpha_{2,bl}}{2} \right) \tag{A.32}$$

$$\Lambda_2 = \left(\frac{c - o \cdot cos(\alpha_{2,bl})}{sin(\Lambda_1)} \right) \tag{A.33}$$

$$ch = \sqrt{[s \cdot cos^2(\alpha_{2,bl}) + \Lambda_2 \cdot cos(\Lambda_1)]^2 + c^2} \tag{A.34}$$

$$\Lambda_3 = 180° - \alpha_{1,bl} - \alpha_{2,bl} \tag{A.35}$$

$$b = s \cdot cos(\alpha_{2,bl}) + \frac{\Lambda_2}{2sin(\Lambda_3/2)} \Lambda_3 \tag{A.36}$$

If a converging-diverging nozzle is present, the opening-to-throat ratio can be computed using Deich's formula [221]:

$$q = \frac{M(\gamma+1)}{2} \left[1 + \frac{M^2(\gamma-1)}{2} \right]^{\frac{\gamma+1}{2(\gamma-1)}} \tag{A.37}$$

$$\frac{o_{ex}}{o_{th}} = 1 + (0.5M - 0.4) \left(\frac{1}{q} - 1 \right) \tag{A.38}$$

where M is the Mach number at the exit of the blade row in the relative coordinate system, and γ is the specific heat ratio computed using the blade exit flow conditions. In the design routine of TURAX, the minimum opening o_{min} is assigned as a decision variable. This term corresponds to o_{th} in Equation A.38, and hence the exit opening is straightforwardly calculated. Alternatively, if the nozzle is adapted to supersonic flow conditions, the opening-to-throat ratio is calculated as a mass balance between the throat (indicated with "*th*") at sonic conditions and the prescribed blade exit conditions (indicated with "*ex*"):

$$\frac{o_{ex}}{o_{th}} = \frac{\rho_{th} a_{th}}{\rho_{ex} C_{ex}} \tag{A.39}$$

In both Equations A.38 and A.39 the diverging part of the nozzle is assumed to have a constant blade height.

Other expressions used to compute the main geometric characteristics of the turbine are used in TURAX, i.e., the calculation of the blade height from the mass continuity equation, the estimation of the flaring angles, the mean radius, the number of blades, the nozzle-rotor axial gap and so forth. These calculations can be found in many turbomachinery textbooks [133, 223, 301, 302] and, for brevity, are not included in this appendix.

A.5 Validation data

Table A.1: Decision variables (1-12) and input variables of TURAX for the Hannover [246, 247] and Verneau [66] single-stage turbine test cases. From Ref. [211].

			Hannover turbine		Verneau turbine	
Parameter	Symbol	Units	Nozzle	Rotor	Nozzle	Rotor
(1) Inlet flow angle	α_1	°	10		$0^{(**)}$	
(2) Stage loading coefficient	ψ	-	$2.1^{(*)}$		$4.4^{(*)}$	
Nozzle **(3)** and rotor **(4)** throat opening	$o_{n,min}$, o_r	mm	15	14	1.76	1.75
Nozzle **(5)** and rotor **(6)** axial chord	c_n, c_r	mm	48.2	37.1	$12.5^{(**)}$	12.5
Nozzle **(7)** and rotor **(8)** opening to pitch ratio	$(o/s)_n$, $(o/s)_r$	-	$0.378^{(*)}$	$0.358^{(*)}$	$0.277^{(*)}$	$0.425^{(*)}$
(9) Rotational speed	N	rpm	7200		18000	
(10) Inlet axial velocity	C_{a1}	m/s	$55.9^{(*)}$		$10.1^{(*)}$	
(11) Rotor flow coefficient	ϕ_r	-	$0.39^{(*)}$		$0.52^{(*)}$	
(12) Rotor inlet to nozzle outlet blade height	h^*	-	1		1.039	
Degree of admission	ε	-	1		0.4	
Mass flow rate	$\dot{m}$	kg/s	6.786		0.18	
Total inlet temperature	T_{01}	K	$358.69^{(*)}$		403	
Total inlet pressure	p_{01}	Pa	$1.2486 \cdot 10^5$ $^{(*)}$		$6.8 \cdot 10^5$	
Total outlet pressure	p_{03}	Pa	$0.998 \cdot 10^5$ $^{(*)}$		$1.21 \cdot 10^5$ $^{(*)}$	
Rotor to nozzle mean radius ratio	R^*	-	1.019		0.99	
nozzle-rotor axial clearance	ss	mm	34.36		$6.3^{(**)}$	
Radius of blade rear suction side curvature	e_n, e_r	mm	109.00	166.57	10^{8} $^{(**)}$	10^{8} $^{(**)}$
Trailing edge thickness to blade opening ratio	$(t/o)_n$, $(t/o)_r$	-	0.0253	0.0357	0.07	0.172
Blade surface roughness	k_s	mm	$2 \cdot 10^{-3}$ $^{(**)}$		$2 \cdot 10^{-3}$ $^{(**)}$	
Rotor tip clearance	t_{cl}	mm	0.24		-	
Inlet width arc	-	mm	29.60	34.95	-	
Backbone length	b_n, b_r	mm	62.10	57.63	-	
Trailing edge thickness	t_n, t_r	mm	0.38	0.50	0.3	$0.3^{(**)}$

$^{(*)}$ = estimated value $^{(**)}$ = assumed value

Table A.2: Decision and input variables of TURAX for the Hannover [247, 248] and Verneau [66, 257] multistage turbine test cases. From Ref.[72].

		Hannover turbine								Verneau turbine			
		Stage 1		Stage 2		Stage 3		Stage 4		Stage 1		Stage 2	
Symbol	Units	Nozzle	Rotor	Nozzle	Rotor	Nozzle	Rotor	Nozzle	Rotor	Nozzle	Rotor	Nozzle	Rotor
ψ	-	2.61		2.61		2.61		2.61		4.62		1.48	
$o_{n,min}$, o_r	mm	12.24	13.52	13.01	13.65	13.84	13.79	14.78	13.94	1.00	3.50	1.52	2.03
c_n, c_r	mm	44.80	39.10	44.30	38.50	45.50	37.50	46.50	37.50	20.00	28.00	37.00	37.00
$(o/s)_n$, $(o/s)_r$	-	0.332	0.393	0.342	0.383	0.353	0.372	0.365	0.360	$0.276^{(**)}$	0.467	$0.500^{(**)}$	$0.423^{(**)}$
N	rpm	7500								7700			
C_{a1}	m/s	57.8								1.23			
ϕ_r	-	0.435		0.440		0.430		0.42		0.61		0.42	
$\dot{m}$	kg/s	7.8								1.6			
α_1	°	-5.57								0			
T_{01}	K	404.63								489			
p_{01}	Pa	$2.58 \cdot 10^5$								$11.2 \cdot 10^5$			
p_{03}	Pa	$1.05 \cdot 10^5$								$0.09 \cdot 10^5$			
ss	mm	235		200		195		180		300		300	
ss_{st}	mm	610		595		640		643		500		500	
$(t/o)_n$, $(t/o)_r$	-	0.0361	0.0302	0.0361	0.0284	0.0360	0.0267	0.0360	0.0249		$0.05^{(**)}$		
t_{cl}	mm	0.4									$0.2^{(**)}$		

$^{(*)}$ = estimated value. $^{(**)}$ = assumed value with uncertainty.

B Radial-inflow turbine model

B.1 Loss correlations

This section describes the set of loss models listed in Table 3.2. The losses are categorized based on the component (nozzle, interspace, and rotor losses) and based on the type (internal and external losses).

B.1.1 Nozzle

The nozzle losses are the passage loss, the trailing edge loss, and the post-expansion loss. The following formulation by Rodgers [132] was used to estimate the nozzle passage losses:

$$\Delta h_n = \frac{0.05}{Re_3^{0.2}} \left[\frac{3\tan\alpha_3}{s_3/c_n} + \frac{s_3\cos\alpha_3}{b_3} \right] \frac{1}{2} C_3^2 \tag{B.1}$$

where s_3 is the nozzle exit pitch, c_n the chord, b_3 the exit width, α_3 the absolute flow angle at the nozzle exit, and C_3 the absolute velocity at the nozzle exit. The parameter $Re_3 = C_3 b_3 \rho_3 / \nu_3$ is the Reynolds number at the nozzle exit, being ν_3 the dynamic viscosity of the working fluid at the nozzle exit. Rodger's formulation [132] assumes that trailing edge and shock losses are negligible provided that the trailing edge to chord ratio is less than 2 % and that Mach numbers are lower than 1.2. To extend the loss modeling to higher Mach numbers and remove the limitations on the trailing edge to chord ratio, other two losses are introduced. The trailing edge loss can be computed assuming a sudden expansion between the throat and a section immediately downstream of the trailing edge. While the formula by Baines [137] expresses it as a reduction of meridional velocity component, a more physical formulation is that based on the actual blade blockage [134, 140, 310]. Nozzle trailing edge losses are computed following Glassman [140] with the expression:

$$\Delta h_{t,noz} = \left(\frac{Z_n t_3}{2\pi r_3 cos\alpha_3} \right)^2 \frac{1}{2} C_3^2 \left[1 + \frac{k_3 - 1}{2} M_3^2 \right]^{\frac{k_3}{1-k_3}} \tag{B.2}$$

In Equation B.2, Z_n is the number of nozzle blades, M_3 the absolute Mach number at the exit, and $k_3 = c_p/c_v$ is the specific heat ratio at the nozzle exit. Equation B.2 was converted from a total pressure loss coefficient into enthalpy loss coefficient using the formula proposed by Horlock

[333]. The nozzle post-expansion losses occur when the flow at the nozzle exit is over-expanded to supersonic discharge Mach numbers. In this case, shock waves form in correspondence of the trailing edge and produce additional losses in the turbine. The nozzle post-expansion loss correlations follow the approach by Aungier [133]. However, in this case, the formula was adapted to consider an expansion right after choking using the average value of the Mach number at the throat, M_2. The equation reads:

$$\Delta h_{pe,noz} = \left(\frac{M_3 - M_2}{M_3}\right)^2 \frac{1}{2} C_3^2 \left[1 + \frac{k_3 - 1}{2} M_3^2\right]^{\frac{k_3}{1-k_3}} \tag{B.3}$$

Aungier [133] claimed that is unreasonable to expect that post-expansion losses depend on the profile losses, and therefore Equation B.3 is only a function of the throat and exit flow conditions. Note also that the losses in Equation B.3 increase with the second power of $(M_3 - M_2)$.

B.1.2 Interspace

The loss in the interspace between rotor and nozzle was not considered in the original work by Baines [137]. In the present work, The following correlation by Khastner and Bhinder [129] is used:

$$\Delta h_{vs} = C_f \left(\frac{L}{D}\right) \frac{1}{2} \left(\frac{C_3 + C_4}{2}\right)^2 \tag{B.4}$$

where C_f is the friction factor in the interspace, and L and D are the hydraulic length and diameter, respectively. Equation B.4 was frequently employed in the literature [134, 302, 304]. The friction factor in the interspace is computed using Japikse's formulation [311]:

$$C_f = k \left(\frac{1.8 \cdot 10^5}{Re_4}\right)^{0.2} \tag{B.5}$$

Equation B.5 is used to model the interspace loss in RITs following Whitfield and Baines [304]. The coefficient k can vary in the range 0.005 to 0.02 in practical applications, and Japikse [311] recommended to use the value 0.01.

B.1.3 Rotor

The rotor losses are classified in internal and external losses. The internal losses are those occurring within the blade rows and internal to the blade passages. Internal losses comprise the passage, clearance, incidence, trailing edge and post-expansion losses. The external losses are associated with the loss of performance due to phenomena occurring outside the blade rows.

The losses inside the rotor blade passage can be expressed by a single formulation. This practice is particularly meaningful for radial turbines where the three-dimensional characteristics of the flow make it hard to separate the effects of friction and secondary losses like in the axial turbine practice.

The rotor passage loss is formulated following Baines [137] in a single formulation as:

$$\Delta h_{pl,rot} = K_p \{K_{p2} \left(\frac{L_H}{D_H}\right) + 0.68 K_{p3} \left[1 - \left(\frac{r_{6rms}}{r_4}\right)^2\right] \left(\frac{cos\beta_6}{b_6/c_r}\right)\} \frac{1}{2} \left(W_4^2 + W_6^2\right) \tag{B.6}$$

with $K_p = 0.11$. The same coefficient is multiplied by a factor of 2 if $(r_4 - r_{6s})/b_6 < 0.2$ in order to account for the higher secondary losses due to high blade passage curvature. The mean passage hydraulic length and diameter, are defined as

$$L_H = \frac{\pi}{4} \left[\left(l_z - \frac{b_4}{2}\right) + \left(r_4 - r_6 + \frac{b_6}{2}\right)\right] \tag{B.7}$$

$$D_H = \frac{1}{2} \left[\left(\frac{4\pi r_4 b_4}{2\pi r_4 + Z_r b_4}\right) + \left(\frac{2\pi (r_{6s}^2 - r_{6h}^2)}{\pi (r_{6s} + r_{6h}) + Z_r b_6}\right)\right] \tag{B.8}$$

The passage loss formulation is derived from modifications to the original passage loss by NASA [334]. The coefficients K_{p2} and K_{p3} are calibrated based on the experimental test data as described in Chapter 3.5. The flow at the nozzle exit approaches the rotor inlet with a certain angle of incidence which affects the rotor fluid dynamics and the losses. However, only at one single operating point the incidence loss is minimum. The experimental results [304] suggested that then minimum incidence loss does not coincide with the point of zero incidence, and therefore an optimum incidence angle exists. The following correlation by Baines [137] is used to predict the rotor incidence losses:

$$\Delta h_{inc,rot} = K_{inc} (sin|\beta_4 - \beta_{4,opt}|)^2 \frac{1}{2} W_4^2 \tag{B.9}$$

In Equation B.9, the optimal incidence angle $\beta_{4,opt}$ is calculated as [304]:

$$\beta_{4,opt} = tan^{-1} \left[-1.98 \frac{tan(\alpha_4)}{(Z_r + Z_{r,split})(1 - 1.98/(Z_r + Z_{r,split}))}\right] \tag{B.10}$$

where Equation B.10 accounts for the number of full rotor blades Z_r and splitter blades $Z_{r,split}$.

A clearance gap is present between the rotor blade tip and the shroud to avoid friction and mechanical issues during the impeller rotation. At the same time, this gap results in a performance degradation since part of the fluid leaks through the gap driven the pressure differential between the pressure and suction sides. The experimental investigations [302] carried out on radial-inflow turbines have shown that the axial and radial clearance, respectively at the rotor inlet and exit, contribute differently to the total loss. These studies [302] highlighted that the radial clearance is a more relevant parameter than the axial clearance. The penalty in efficiency given by the radial clearance is rather strong, and therefore it is recommended to keep it to the minimum value allowed by manufacturing constraints and technology. The rotor clearance loss is expressed according to the correlation by Baines [137], which incorporates the separate effects of the axial and radial clearance

gaps:

$$\Delta h_c = \frac{U_4^3 Z_r}{8\pi}\left(K_a \varepsilon_a C_a + K_r \varepsilon_r C_r + K_{ar}\sqrt{\varepsilon_a \varepsilon_r C_a C_r}\right) \tag{B.11}$$

$$C_a = \frac{1-(r_{6s}/r_4)}{C_{m4} b_4} \tag{B.12}$$

$$C_r = \left(\frac{r_{6s}}{r_4}\right)\frac{L_z - b_4}{C_{m6} r_6 b_6} \tag{B.13}$$

The three terms in Equation B.11 are representative of the effects of axial, radial clearance and the interaction effects between them. The calibration of the loss model with some turbine experimental data yielded $K_a = 0.4$, $K_r = 0.75$, and $K_{ar} = -0.3$.

The trailing edge loss in the rotor is computed similarly to the nozzle, using the following expression:

$$\Delta h_{t,rot} = \left(\frac{Z_r t_6}{\pi(r_{6s}+r_{6h})cos\beta_6}\right)^2 \frac{1}{2} W_6^2 \left[1 + \frac{k_6 - 1}{2} M_{6,rel}^2\right]^{\frac{k_6}{1-k_6}} \tag{B.14}$$

Equation B.14 was converted from a total pressure loss coefficient into enthalpy loss coefficient using the formula proposed by Horlock [333].

The rotor post-expansion loss for supersonic conditions is modeled similarly to the nozzle, according to the following expression modified from Aungier [133]

$$\Delta h_{pe,rot} = \left(\frac{M_{6,rel} - M_5}{M_{6,rel}}\right)^2 \frac{1}{2} W_6^2 \left[1 + \frac{k_6 - 1}{2} M_{6,rel}^2\right]^{\frac{k_6}{1-k_6}} \tag{B.15}$$

External losses occur outside the blade rows producing additional heat that increases the fluid enthalpy while expanding in the rotor. In this set of loss models, the external losses comprise disk windage losses and were introduced in the turbine model by a sudden enthalpy rise at constant pressure at the turbine exit (mixing process). The disk windage loss is due to leakage flows between the turbine disk backface and the backplate. The empirical correlation by Daily and Nece [312] is the often quoted in the literature [304], and is employed as follows:

$$\Delta h_{df} = 0.25 K_f \frac{\overline{\rho} U_4^3 r_4^2}{\dot{m}} \quad where \quad \overline{\rho} = \frac{\rho_4 + \rho_6}{2} \;\; Re_4 = \frac{\rho_4 U_4 r_4}{\mu_4} \tag{B.16}$$

$$if \quad Re_4 \;\; 3 \cdot 10^5 \quad K_f = 3.7(\varepsilon_b/b_4)^{0.1} Re_4^{-0.5} \tag{B.17}$$

$$if \quad Re_4 \;\; 3 \cdot 10^5 \quad K_f = 0.102(\varepsilon_b/b_4)^{0.1} Re_4^{-0.2} \tag{B.18}$$

$$\tag{B.19}$$

B.2 Validation data

Appendix B. Radial-inflow turbine model

Table B.1: Data of the HPR turbines selected for calibration. From Ref. [95].

	Test case	Meitner and Glassman	McLallin et al.	Simonyi rotor 1	Simonyi rotor 2	Rogo	Atkinson
	Ref.	[314]	[98]	[104]	[104]	[102]	[110]
				Input conditions			
T_{01}	[K]	377.778	322.2	477.78	477.78	394	418
p_{01}	[Pa]	38610.6	137900	333706.3	333706.3	164000	354550
N	[rpm]	29550;17730	9437-34602	17927-21911	15138-22708	12751-15939	26277-40795
				Stator			
b_1	[m]	0.0147	0.0109	0.021	0.021	0.015	0.008
b_3	[m]	0.015	0.008	0.012	0.012	0.015	0.008
r_1	[m]	0.073	0.097	0.224	0.224	0.251	0.111
r_3	[m]	0.060	0.084	0.194	0.194	0.194	0.092
Z_n	[-]	14	29	36	36	15	17
t_3	[m]	0.001	0.001	0.0003	0.0003	0.003	0.0012
α_{3b}	[deg]	72.47	76	70	70	77	76
o_2	[m]	0.0073	0.0036	0.0091	0.0092	0.0174	0.0095
				Rotor			
b_4	[m]	0.015	0.008	0.012	0.012	0.016	0.0077
r_4	[m]	0.058	0.075	0.185	0.185	0.177	0.0867
r_{6s}	[m]	0.041	0.047	0.118	0.118	0.114	0.0609
r_{6h}	[m]	0.014	0.023	0.076	0.076	0.051	0.0261
β_{4b}	[deg]	0	0	0	0	0	0
β_{6b}	[deg]	-56.86	-58	-55.3	-53.86	-60	-60
Z_r	[-]	22	12	14	14	13	14
t_6	[m]	0.0002	0.004	0.001	0.001	0.00076	0.0024
o_5	[m]	0.0048	0.0065	0.02	0.02	0.01706	0.0223
l_z	[m]	0.040	0.04572	0.046	0.043	0.107	0.0399
ε_a	[m]	0.0003	0.0003	0.0005	0.0002	0.0004	0.00075
ε_r	[m]	0.0004	0.0003	0.0002	0.0004	0.0004	0.0004
ε_b	[m]	0.0003	0.0003	0.0003	0.0003	0.0009	0.00075

C Centrifugal compressor model

C.1 Loss correlations

There are numerous empirical correlations for the losses and the exit flow deviation for centrifugal compressors, and they are documented in many different scientific publications, i.e. see Refs [196, 304, 316, 335, 336]. As mentioned in Chapter 4.5, the set of empirical correlations used in this work for centrifugal compressors was chosen based on the literature and since they yielded the best match with the experimental data. The losses are categorized in impeller internal losses, impeller external losses, and diffuser losses. For the nomenclature used in this Appendix, see the corresponding Chapter 4.5

C.1.1 Impeller

The losses internal to the impeller passage are those related to incidence, skin friction, blade loading, and clearance. The flow to the inlet of the impeller will pass smoothly into the impeller passage at only one operating point [304]. At other operating points, the inlet flow will produce higher losses in the impeller passage. The difference between the inlet blade and flow angles is termed *incidence*, and there exists a value of incidence which is optimal. This value does not usually coincide with the zero incidence condition, and the incidence loss models have the objective to determine the optimal incidence angle and the magnitude of the incidence loss. The loss model by Galvas [199] is selected as it presents a simple and clear way to compute the optimal incidence angle using the blockage from the blade leading edge thickness and the root-mean-square value of the inlet radius. The optimal incidence angle $\beta_{1,opt}$ and the incidence losses Δh_{inc} are calculated as follows:

$$\beta_{1,opt} = tan^{-1}[(A_1/A_{th,1})tan\beta_{1b}] \tag{C.1}$$

$$\Delta h_{inc} = \frac{1}{2}W_1^2 sin^2|\beta_{1,opt} - \beta_1| \tag{C.2}$$

where A_1 and $A_{th,1}$ are the impeller inlet and throat areas, respectively. The term β_{1b} is the impeller inlet blade angle, W_1 is the relative inlet velocity, and β_1 the relative inlet flow angle.

The impeller skin friction loss is associated with the entropy gradients generated by the shear forces exerted on the fluid in the boundary layer. In centrifugal compressors, such losses have traditionally

been modeled as friction losses through a pipe of equivalent hydraulic length and diameter. The model developed by Galvas [199] was found to provide the better match with the test cases used to validate the model. The skin friction loss is calculated using the following expressions:

$$\Delta h_{sf} = 4C_{fi}\frac{L_b}{d_{hb}}\overline{W}^2 \tag{C.3}$$

$$L_b \approx \frac{\pi}{8}(2r_2 - (r_{1s}+r_{1h}) - b_2 + 2L_z)\left(\frac{2}{(cos\beta_{1s}+cos\beta_{1h})/2 + cos\beta_{2b}}\right) \tag{C.4}$$

$$d_{hb} = \frac{2r_2}{\frac{Z_r}{\pi cos\beta_{2b}} + \frac{2r_2}{b_2}} + \frac{2r_{1s}}{\frac{2}{1-\lambda} + \frac{2Z_r}{\pi(1+\lambda)}\sqrt{1+tan^2\beta_{1bs}\left(1+\frac{\lambda^2}{2}\right)}} \tag{C.5}$$

$$\overline{W} = max\left(\sqrt{(W_1^2+W_2^2)/2)}, \sqrt{(W_{th,1}^2+W_2^2)/2}\right) \tag{C.6}$$

In Equation C.3, L_b is the blade length, C_{fi} is a skin friction coefficient computed using the correlations by Schlichting [337] (adapted from Aungier [335]). The blade length in Equation C.4 is approximated using a formulation by Jansen [319], and it was found to provide the best estimation of the actual impeller length compared to other methods found in the literature, i.e., see Refs. [199, 204]. The average velocity in the impeller passage, $\overline{W}$ in Equation C.6, is computed using the method by Aungier [197], which produces a rapid increase of the friction losses close to the choking point and is consistent with the physical trend of the speed lines.

Diffusion and blade loading losses are also present in the impeller passage due to boundary layer growth and separation and to secondary flows. They are computed using the correlation by Coppage [204] based on the definition of a diffusion factor D_f

$$D_f = 1 - \frac{W_2}{W_1} + c_{df}\frac{\Delta h_0}{U_2^2}\frac{W_2}{W_{1s}}\left[\frac{Z_r}{\pi}\left(1-\frac{r_{1s}}{r_2}\right) + 2\frac{r_{1s}}{r_2}\right]^{-1} \tag{C.7}$$

$$c_{df} = 0.75 \quad \textit{without splitter blades} \qquad c_{df} = 0.6 \quad \textit{with splitter blades} \tag{C.8}$$

$$\Delta h_{bl} = 0.05 D_f^2 U_2^2 \tag{C.9}$$

Equation C.8 shows that the empirical coefficient c_{df} reduces in the presence of splitter blades, and hence also the diffusion factor and the blade loading losses [304].

Clearance losses result from fluid's leakage from the pressure to the suction side of the blades for unshrouded impellers. These are provided by Jansen's correlation [319]:

$$\Delta h_{cl} = 0.6\frac{\overline{\varepsilon}}{b_2}|C_{2t}|\sqrt{\frac{4\pi}{b_2 Z_r}\frac{r_{1s}^2 - r_{1h}^2}{(r_2 - r_{1s})(1+\rho_2/\rho_1)}|C_{2t}|C_{1m}} \tag{C.10}$$

where $\overline{\varepsilon} = (\varepsilon_a + \varepsilon_r)/2$ is the average clearance in the impeller passage.

The losses external to the impeller passage are added as a sudden enthalpy rise at constant pressure at the impeller exit section, representative of a mixing process at the immediately downstream of the impeller. The external losses are the impeller mixing losses, the disk friction and recirculation losses. The mixing loss results from the non-uniform discharge of the flow from the impeller and

this contribution is calculated based on the jet/wake theory [304], following the jet/wake model presented by Johnston and Dean [320] and reproposed in other works [192, 196]. The expression for the mixing loss Δh_{mix} is the following:

$$\Delta h_{mix} = \frac{1}{1+tan^2(\alpha_2)} \left(\frac{1-\varepsilon_w-b^*}{1-\varepsilon_w} \right)^2 \frac{1}{2} C_2^2 \tag{C.11}$$

$$\chi = 0.93\varepsilon_w^2 + 0.07\varepsilon_w \tag{C.12}$$

where ε_w is the fraction of the blade-to-blade spacing occupied by the wake, χ is the secondary flow mass fraction and b^* the ratio of diffuser inlet width to impeller tip width. Equation C.12 stems from a curve fit of the data from three different Eckardt impellers studied by Japikse [316]. Japikse [316] recommended the parameter χ to vary between 0.15 and 0.35, and in this work the value 0.015 is used. The term b^* is instead assumed to be unity in the developed model.

The fluid flowing in the impeller backface gap produces shear forces in its interaction with the rear face of the impeller and the nearby stationary surfaces. This enthalpy rise is termed disc friction loss. According to Whitfield and Baines [304], the most quoted approach is that by Daily and Nece [312], who computed the disc friction losses according to the following expressions:

$$\Delta h_{df} = 0.25 \frac{\rho_i U_2^3 r_2^2 K_f}{\dot{m}} \quad \text{where} \quad \rho_i = (\rho_1 + \rho_2)/2 \tag{C.13}$$

$$K_f = 3.7 \frac{(\varepsilon_b/b_2)^{0.1}}{Re_2^{0.5}} \quad \text{for} \quad Re_2 = \frac{\rho_2 U_2 r_2}{\mu_2} < 3 \cdot 10^5 \tag{C.14}$$

$$K_f = 0.102 \frac{(\varepsilon_b/b_2)^{0.1}}{Re_2^{0.2}} \quad \text{for} \quad Re_2 = \frac{\rho_2 U_2 r_2}{\mu_2} > 3 \cdot 10^5 \tag{C.15}$$

where ε_b is the rotor backface clearance gap.

Finally, an additional enthalpy rise may result from the recirculation of low momentum fluid from the vaneless space back to the impeller passage. This loss is computed using the model by Oh et al. [196] which produces a rapid increase of this loss at low mass flow rates compared to the models by Jansen [319], Coppage et al. [204] and Aungier [335]. This model was found to yield a good agreement with the experimental data trend of the compressors used for validation in Chapter 4.5 for lower mass flow rates on the same speed line.

$$\Delta h_{rc} = 8 \cdot 10^{-5} sinh(3.5 \cdot \alpha_2^3) D_f^2 U_2^2 \tag{C.16}$$

C.1.2 Diffuser

The losses in the vaneless diffuser are estimated using the procedures already described in Chapter 4.5 and are not reported here. The prediction of the losses in the vaned diffuser is a rather complex topic, and for this reason, the reader is referred to specific books for more details [316, 335]. A simple model is implemented in this work, which considers two type of losses: the vaned diffuser incidence losses and the friction losses. Incidence losses are given by an expression from Conrad

[321]:

$$\Delta h_{vd,inc} = 0.6 sin^2|\alpha_3 - \alpha_{3b}|\frac{1}{2}C_3^2 \tag{C.17}$$

Vaned diffuser friction losses are computed using the classical pipe flow correlation from the work of Conrad [321]:

$$\Delta h_{vd,sf} = 2C_{f,vd}C_{m,vd}^2\frac{L_{b,vd}}{d_{hb,vd}} \tag{C.18}$$

$$C_{m,vd} = (C_5 + max\{C_3, C_4\})/2 \tag{C.19}$$

$$L_{b,vd} = \frac{r_5 - r_3}{cos\left(\frac{\alpha_{3b}+\alpha_{5b}}{2}\right)} \qquad d_{hb,vd} = \frac{o_4 b_4}{o_4 + b_4} + \frac{o_5 b_5}{o_5 + b_5} \tag{C.20}$$

C.2 Flow deviation correlations

Different slip factors correlations have been proposed in the literature, and those by Wiesner [318], Stanitz [338] and the recent model by Qiu et al. [339] are arguably the most often employed. The following formulas are employed in this work:

$$\sigma = 1 - \frac{\sqrt{cos\beta_{2b}}}{Z_r^{0.7}} \tag{C.21}$$

Equation C.21 holds up to the limiting radius ratio given by

$$(r_1/r_2)_{lim} = \frac{\sigma - \sigma^*}{1 - \sigma^*} \tag{C.22}$$

$$\sigma^* = sin(19^\circ + 0.2(90 - |\beta_{2b}|)) \tag{C.23}$$

If r_1/r_2 is higher than the limiting value $(r_1/r_2)_{lim}$, a corrected value of the slip factor is computed as follows:

$$\sigma_{cor} = \sigma\left[1 - \left(\frac{(r_1/r_2) - (r_1/r_2)_{lim}}{1 - \sigma_{lim}}^{\sqrt{(90-\beta_{2b})/10}}\right)\right] \tag{C.24}$$

C.3 Preliminary design correlations

In the design model, the number of blades is calculated as a function of the total-to-total stage pressure ratio using an empirical correlation derived from a pool of compressor data [317] as depicted in Figure C.1.

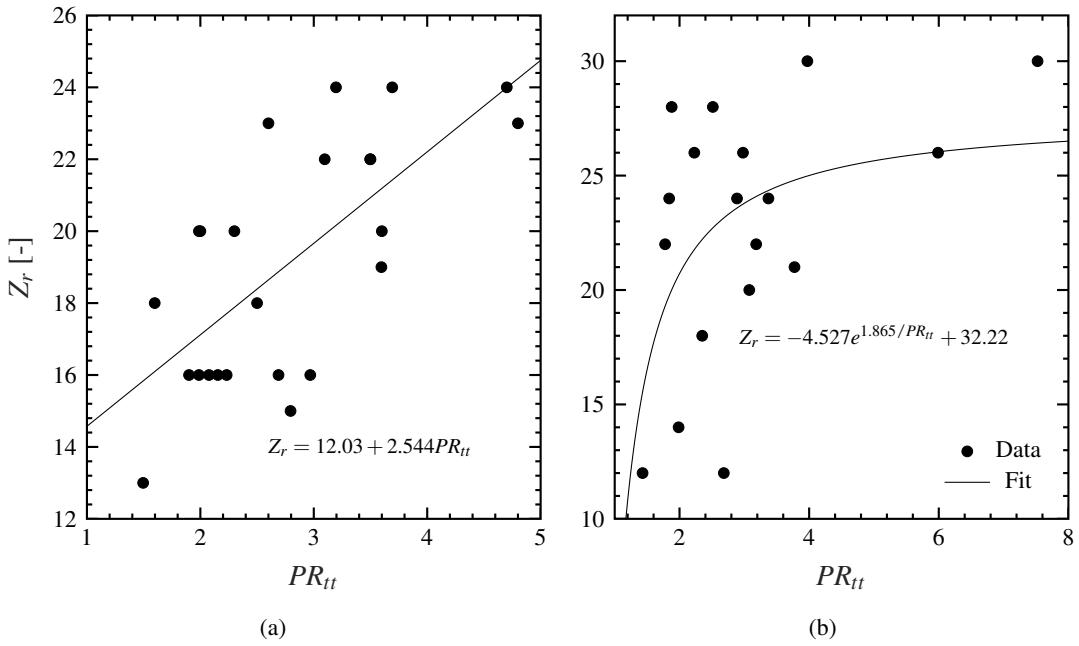

Figure C.1: Number of total impeller blades for centrifugal compressors: (a) without splitter blades; (b) with splitter blades. Adapted from [317].

C.4 Validation data

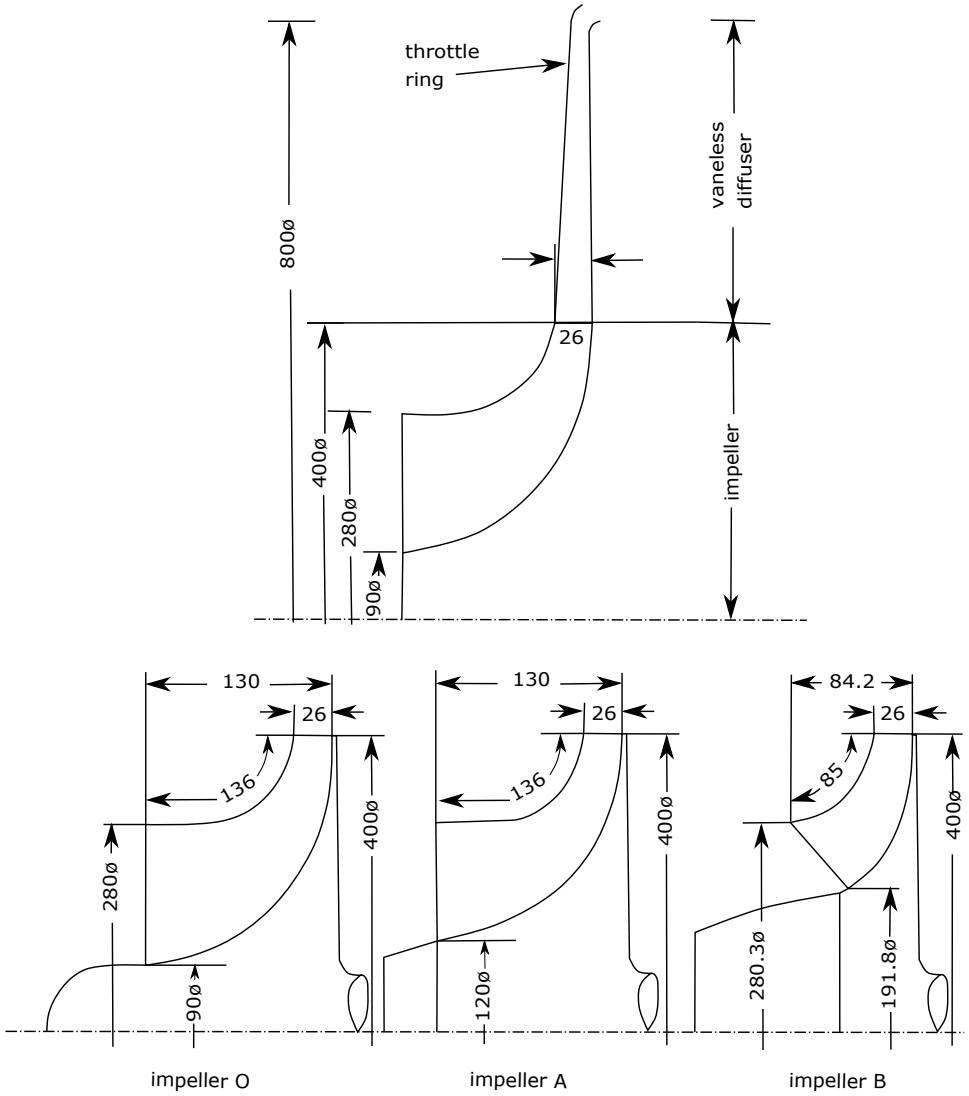

Figure C.2: Meridional layout of Eckardt's centrifugal compressor stages (dimensions in mm). Adapted from Ref. [167].

Table C.1: Data of the experimental centrifugal compressors.

Ref.	Units	Eckardt Impeller O [164–167]	Eckardt Impeller A [164–167]	Eckardt Impeller B [164–167]	Schiffmann and Favrat [126, 181, 182, 323, 329]	Sandia [183, 194, 325, 326, 340]
			Input conditions			
Fluid	-	Air	Air	Air	R134a	CO_2
T_{01}	K	288.15	288.15	288.15	265	305.97
p_{01}	$10^5 \cdot$ Pa	1.01325	1.01325	1.01325	1.65	76.9
N	krpm	14-16	14-16	14-16	150-210	45-55
			Impeller			
r_{1s}	m	0.14	0.14	0.14	0.0056	0.0094
r_{1h}	m	0.045	0.06	0.0959	0.002	0.00254
r_2	m	0.2	0.2	0.2	0.01	0.01868
b_2	m	0.026	0.026	0.026	0.0012	0.00171
L_z	m	0.13	0.13	0.13	0.007693	0.1137
$Z_{r,full}$	-	20	20	20	9	6
$Z_{r,splitter}$	-	0	0	0	9	6
$LR_{splitter}$	-	0	0	0	0.5	0.7
β_{1bs}	°	-63	-63	-60	-56	-50
β_{1bh}	°	-32	-40	-45	-30.23	-40
β_{2b}	°	0	-30	-40	-45	-50
ε_a	mm	0.372	0.235	0.372	0.15	0.254
ε_r	mm	0.372	0.19	0.372	0.15	0.254
ε_b	mm	0.372	0.235	0.372	1	0.254
k_s	mm	0.002	0.002	0.002	0.01	0.01
t_{b1}	mm	2.11	2.11	2.11	0.1	0.762
t_{b2}	mm	1.08	1.08	1.08	0.1	0.762
			Vaneless Diffuser			
r_3/r_2	-	1.69	2.69	3.69	1.65	1.02
b_3/b_2	-	0.51	0.51	0.51	0.75	1
			Vaned Diffuser			
AR	-	-	-	-	-	2.81
AS	-	-	-	-	-	0.55
LWR	-	-	-	-	-	3.41
Z_{vd}	-	-	-	-	-	17
α_{3b}	°	-	-	-	-	71.5
α_{5b}	°	-	-	-	-	71.5
t_{b3}	m	-	-	-	-	0
t_{b5}	m	-	-	-	-	0.00335
X_{b52}	-	-	-	-	-	1
X_{r52}	-	-	-	-	-	1.37
			Inducer			
r_0	m	-	-	-	0.01	-
L_{ind}	m	-	-	-	0.02	-
$k_{s,ind}$	mm	-	-	-	0.1	-
			Volute			
r_4	m	-	-	-	0.0045	-

D Articles

energies

MDPI

Article

Combined Turbine and Cycle Optimization for Organic Rankine Cycle Power Systems—Part A: Turbine Model

Andrea Meroni [1,*], Angelo La Seta [1], Jesper Graa Andreasen [1], Leonardo Pierobon [1], Giacomo Persico [2] and Fredrik Haglind [1]

[1] Department of Mechanical Engineering, Technical University of Denmark, Nils Koppels Allé, Building 403, Kongens Lyngby 2800, Denmark; anlse@mek.dtu.dk (A.L.S.); jgan@mek.dtu.dk (J.G.A.); lpier@mek.dtu.dk (L.P.); frh@mek.dtu.dk (F.H.)

[2] Laboratorio di Fluidodinamica delle Macchine, Dipartimento di Energia, Politecnico di Milano, Via Lambruschini 4, Milan I-20156, Italy; giacomo.persico@polimi.it

* Correspondence: andmer@mek.dtu.dk; Tel.: +45-4525-4319

Academic Editor: Sylvain Quoilin

Received: 21 March 2016; Accepted: 18 April 2016; Published: 25 April 2016

Abstract: Axial-flow turbines represent a well-established technology for a wide variety of power generation systems. Compactness, flexibility, reliability and high efficiency have been key factors for the extensive use of axial turbines in conventional power plants and, in the last decades, in organic Rankine cycle power systems. In this two-part paper, an overall cycle model and a model of an axial turbine were combined in order to provide a comprehensive preliminary design of the organic Rankine cycle unit, taking into account both cycle and turbine optimal designs. Part A presents the preliminary turbine design model, the details of the validation and a sensitivity analysis on the main parameters, in order to minimize the number of decision variables in the subsequent turbine design optimization. Part B analyzes the application of the combined turbine and cycle designs on a selected case study, which was performed in order to show the advantages of the adopted methodology. Part A presents a one-dimensional turbine model and the results of the validation using two experimental test cases from literature. The first case is a subsonic turbine operated with air and investigated at the University of Hannover. The second case is a small, supersonic turbine operated with an organic fluid and investigated by Verneau. In the first case, the results of the turbine model are also compared to those obtained using computational fluid dynamics simulations. The results of the validation suggest that the model can predict values of efficiency within $\pm$ 1.3%-points, which is in agreement with the reliability of classic turbine loss models such as the Craig and Cox correlations used in the present study. Values similar to computational fluid dynamics simulations at the midspan were obtained in the first case of validation. Discrepancy below 12% was obtained in the estimation of the flow velocities and turbine geometry. The values are considered to be within a reasonable range for a preliminary design tool. The sensitivity analysis on the turbine model suggests that two of twelve decision variables of the model can be disregarded, thus further reducing the computational requirements of the optimization.

Keywords: organic Rankine cycle (ORC); axial turbine design; combined optimization; turbine experimental validation; turbine sensitivity analysis

1. Introduction

The effective exploitation of medium-to-low temperature heat sources demands power generation technologies which are efficient, flexible and cost-competitive. In this context, Organic Rankine Cycle (ORC) power systems represent an advantageous proposition due to their technical

feasibility, inherent simplicity, and the possibility to be used in combination with renewable energy sources and decentralized power plants.

In their simplest configuration, ORC power systems consist of a pump, a boiler, an expander and a condenser. The expander is arguably a crucial component owing to design complexities often associated with the presence of real-gas phenomena and supersonic flow conditions, and since it can greatly affect both the overall energetic efficency and the total cost of the system. As an example, Stine *et al*. [1] estimated an expander cost of almost 30% on the whole plant investment. Lecompte *et al*. [2] performed a techno-economic optimization of an ORC, indicating a relative incidence between 22% and 34% on the overall plant costs according to the selected working fluid. Cayer *et al*. [3] showed that the investment cost of a turboexpander can be as high as 50% of the total cost of the ORC system.

One of the preliminary design steps of an ORC unit is the selection of a suitable expander type. Volumetric machines such as scroll, screw, piston, and rotary vane expanders are competitive solutions in the lower power output range (<50 kW), are easier to manufacture and can be cheaper compared to turboexpanders. Furthermore, they operate at lower rotational speeds and can tolerate two-phase flows during expansion, which can lead to blade erosion issues in turbomachines. However, the applicability of volumetric expanders is limited by a maximum volume ratio and by low values of efficiency. Bao and Zhao [4] have reported maximum volume ratios of approximately eight and maximum efficiency of approximately 70%. Axial and radial turboexpanders are employed for high flow rates and large pressure ratios, typically in the power range above 50 kW [5]. In the ORC field, Fiaschi *et al*. [6] have suggested the use of radial inflow turbines as advantageous solutions in the small power range due to their compact structure, higher enthalpy drop per stage and insensitivity to load variation at off-design. In the context of radial turboexpanders, novel architectures have been studied by Persico *et al*. [7], Pini *et al*. [8] and Casati *et al*. [9], who have highlighted the specific flow features and advantages of centrifugal turbine configurations for high-temperature and small-power output applications. Axial turbines are generally adopted for high mass flow rates and in multistage configurations [10,11]. Many ORC manufacturers [12,13] employ axial turbines for small to large scale applications. Uusitalo [14] has recommended the use of axial stages for high values of turbine specific speed. Klonowicz *et al*. [15] have highlighted that axial-flow turbine configurations usually have better structural properties than their radial counterparts because, in the latter, the centrifugal force acts perpendicularly to the blades. Several methods are available for axial-flow turbine analysis, according to the design phase and objective of the study. At the early stage, a one-dimensional tool can be used to estimate turbine performance and the design of the annulus line.

The objective of this two-part paper is to provide a methodology for the combined optimal design of a turbine and an ORC power system. The axial-flow turbine configuration was selected due its technological maturity, the high performance achievable already with a single stage, the wide range of applicability, the possibility of adopting multiple stages or partial admission for very low or high mass flow rates, and the large availability of data and scientific publications in the literature. The model presented herein, named TURAX, has been particularly conceived to (i) simulate axial-flow turbines operating with organic fluids and to (ii) perform a coupled optimization with the design of the ORC system. In this respect, the use of a reliable, accurate and computationally efficient model is of paramount importance. Part A outlines a description and an extensive validation of the mean-line model, in order to ensure reliability and accuracy of results. In addition, a global sensitivity analysis on the main parameters is presented, in order to identify the most significant decision variables for turbine design and optimization, and reduce the computational efforts when the model is coupled to the thermodynamic cycle. The validation was carried out considering the experimental data of two well-documented test cases from literature, one of which features an ORC turbine. In the first case, the model was also validated using computational fluid dynamics (CFD) simulations, in order to provide a comparison with state-of-the-art modeling techniques. The simultaneous optimization of the expander and cycle design is applied on a case study and is presented in part B.

One-dimensional numerical tools for preliminary turbine design similar to those presented in this paper have been developed in the past [8,16,17]. However, in comparison with previous works, a much more thorough validation of the code is presented in this paper, based on the best available and documented data from literature. In this respect, the model is also validated using the data of an ORC axial turbine, for which no other well-documented references are found in the literature. Another novel approach is that a global sensitivity analysis is carried out in order to reduce the number of decision variables and, consequently, the computational efforts required by the model optimization. Moreover, in comparison to previous works, TURAX enables the user to select a suitable optimization method among genetic algorithm, population-based methods, direct search methods, gradient-based methods, or a combination of the previous ones, in order to tailor the solution strategy to the specific requirements of the considered application. The coupling of expander and cycle tools to estimate the design of an ORC system has been presented by Ventura and Rowlands [18] and Uusitalo *et al*. [19]. One difference compared with the present work is that a radial inflow turbine configuration was considered in both studies, whereas an axial turbine design is considered herein. Moreover, both of the cited works did not optimize the design of the turbine: Ventura and Rowlands [18] obtained the turbine performance from a database, whereas Uusitalo *et al*. [19] set the expander efficiency to 80%. Conversely, in the present work, a simultaneous optimization of both cycle and expander designs is carried out. In conclusion, to the authors' best knowledge, this is the first time that a thorough validation of a mean-line axial turbine model is presented and that the design tool is coupled with an ORC cycle model for the simultaneous optimization of both expander and cycle designs using advanced optimization algorithms.

Part A is structured as follows: Section 2 explains the methods for validation and sensitivity analysis. Section 3 presents the results. Conclusions are given in Section 4.

2. Axial Turbine Model

2.1. Modeling Approach

The axial turbine model, TURAX, originated from an MSc thesis work [20] and has been used in a subsequent study [21]. The model is written in Matlab language [22] and provides the mean-line preliminary design and the efficiency prediction for an axial-flow turbine.

The model requires the following inputs:

a) A set of boundary conditions: inlet total pressure p_{01}, inlet total temperature T_{01}, mass flow rate $\dot{m}$, outlet total pressure p_{03}. These are typically inputs from cycle calculations.
b) An array $\overline{X}$ of 12 turbine decision variables listed in the table of Figure 1.
c) Specifications on blade shape geometry, clearance between nozzle and rotor *ss*, blade tip clearance t_{cl}, surface roughness k_s, nozzle to rotor mean radius ratio R^*.
d) A fluid library: the fluid can be a pure component or a mixture at a specified molar composition. For instance, the user can select the fluid thermophysiscal property libraries REFPROP® [23] or CoolProp [24].

The model can be expressed in the analytical form:

$$[\eta_{tt}, geometry, flow] = f(T_{01}, p_{01}, p_{03}, \dot{m}, fluid, \overline{X}), \quad (1)$$

where the outputs are the isentropic efficiency (*i.e.*, the total-to-total efficiency η_{tt}), the turbine main geometrical parameters (*geometry*), and the thermo-fluid-dynamic features ($flow$) at nozzle and rotor inlet and outlet. The working principle for a single-stage turbine is illustrated in Figure 1. The calculation process is iterative and proceeds as follows:

1. In the first iteration, assumption of the guessed values of turbine stage and nozzle efficiencies.

2. Estimation of outlet flow angles and velocities. The former are estimated with the correlation of Ainley and Mathieson [25] for subsonic flow regimes. The Vavra correlation [26] is used for supersonic flow conditions.
3. Calculation of thermodynamic properties.
4. Calculation of nozzle and rotor blade profile geometry and outlet flow angles. The Deich's formula [27] is used to calculated the blade opening for converging-diverging nozzle. The profile loss correlations of Craig and Cox used for nozzle converging profiles are also adopted for a supersonic configuration. This approach, supported by Macchi [28], is based on the large number of efficient converging-diverging nozzles which were designed and tested according to Deich's method.
5. Calculation of turbine stage geometry.
6. Estimation of losses and efficiency. The method by Craig and Cox [29] is used since it is considered by a number of references as one of the most complete and reliable [15,30,31]. Shock losses in a blade row are computed according to Kacker and Ockapuu [32]. Disk windage losses are estimated according to Balje and Binsley [33]. Partial admission losses are calculated using the method by Suter and Traupel [34], which is considered as one of the best available and comprehensive models [11,35].
7. In order to account for the area restriction due to the influence of the boundary layer, restriction factors are applied to the mass balance equation using the method of Vavra [26] with an energy form factor of 0.9 [28].
8. Calculation of the error on efficiency and blade work. The process iterates until the residual error between two consecutive iterations is below a predefined threshold value (*i.e.*, 10^{-6}).

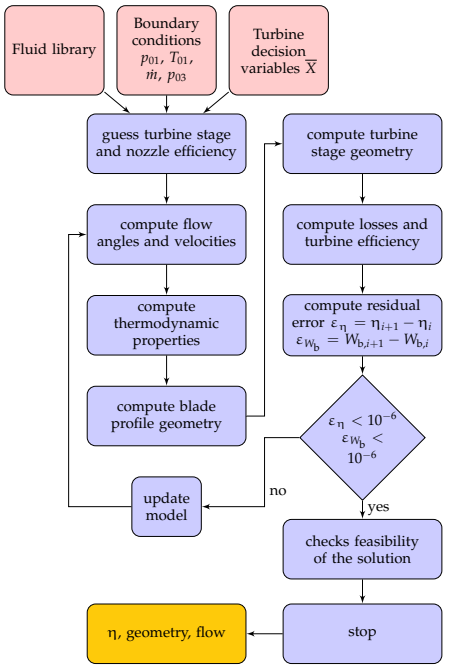

Decision variable	Unit	Symbol
1) Stage inlet flow angle	°	α_1
2) Stage loading coefficient	-	$\psi = 2\Delta h_{is}/U_{3m}^2$
3) Nozzle minimum opening	m	o_{min}
4) Rotor opening	m	o_r
5) Nozzle axial chord	m	c_n
6) Rotor axial chord	m	c_r
7) Nozzle opening-to-pitch ratio	-	$(o/s)_n$
8) Rotor opening-to-pitch ratio	-	$(o/s)_r$
9) Rotational speed	rpm	N
10) Stage inlet axial velocity	m/s	C_{a1}
11) Rotor flow coefficient	-	$\phi_r = C_{a3}/U_{3m}$
12) Rotor inlet to nozzle outlet blade height	-	$h^* = h_2/h_{21}$

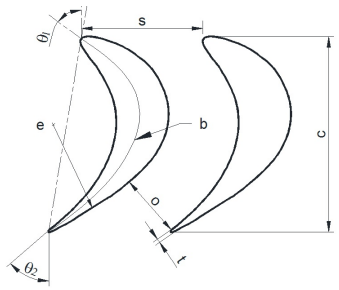

Figure 1. Axial turbine model flowchart, decision variables and nomenclature in the blade-to-blade plane.

9. In order to produce a feasible solution, the algorithm checks that the resulting turbine design satisfies a set of predefined constrains in the end of the iterative loop. The user can specify the

values of the desired constraints in the model. An example of such constraints is provided in part B.

The detailed equations for turbine design can be found in textbooks and papers on the topic [11,26,28,36–38] and are therefore not reported here.

2.2. Validation

The model was validated considering two reference cases. The first case is the last stage of a four-stage turbine investigated at the Technical University of Hannover by Groschup [39] in 1977, and subsequently used as reference for further studies [40,41]. The working fluid is air and the turbine facility is an open loop configuration with exhaust to the atmosphere. The blading is of the free-vortex type with 50% degree of reaction. Total and static pressure, flow angles and total temperature were measured for ten traverse points with a probe. A total pressure measurement error in the order of 0.25% was reported . Table 1 lists the turbine operating conditions and geometry at the design point.

In the present work, CFD simulations on the flow in the same turbine were performed using ANSYS CFX®. The results are included as reference for the validation of TURAX. The CFD simulations were performed using a 3D, unsteady model with the RANS $k-\omega$ SST model by Menter [42], applying the standard CFD model for turbomachinery flow simulations in use at Politecnico di Milano [43]. The reliability of this model was assessed against experiments performed at Politecnico di Milano. The CFD model predicted accurately the fully three-dimensional and unsteady flow physics, and estimated the stage efficiency within 1% of experimental data. For the Hannover turbine test case, the three-dimensional blade profiles were generated using the data available in Kotzing and Evers [41]. The computational domain was discretized using a structured, orthogonal and flow-oriented mesh. A grid-sensitivity analysis was performed using the turbine polytropic efficiency [37] as an indicator. Different tests were run by refining the mesh with a step of 400,000 cells each time. A change in polytropic efficiency below 0.1% was achieved using 110 layers in spanwise direction and about 3,200,000 cells in the computational domain. Figure 2a shows an example of the final rotor grid. The model was set up using profiles of total pressure, total temperature, a constant inlet flow angle of 10°, and turbulence intensity of 1% as boundary conditions at the nozzle inlet. The total pressure and temperature profiles at the inlet were interpolated from the experimental data of the turbine. A constant mass flow rate of 6.786 kg/s was imposed as boundary condition at the stage outlet. In addition, periodic boundary conditions were imposed on the lateral surfaces of the blade channel. Convergence in the residual values of the momentum equations in the integral value of blade work was reached for a value of 100 in the accumulated time step of the solver. ANSYS CFX® default settings were used for the other parameters in the simulation setup. The validation of TURAX was performed imposing a stage degree of reaction of 0.5 and the actual stage inlet blade height.

The second case of validation is a low-power output turbine operated with an organic fluid and documented by Verneau [44]. The turbine was developed for waste heat recovery applications of automotive engines. The turbine is of the impulse type and it operates with the fluid R113 and partial admission. The measured total-to-static efficiency is 63% and the delivered power output is 3 kW. The stage is highly-loaded featuring a converging-diverging nozzle with supersonic exit conditions and transonic conditions in the rotor. Due to the small blade heights, untwisted profiles were adopted. The report of Verneau does not include the specific data of the blade profiles, therefore it was not possible to carry out a CFD analysis as in the other case study. Nonetheless, considering the complexity of the phenomena within the turbine (*i.e.*, supersonic flows, partial admission, real fluid behavior, low Reynolds number), this case of validation is useful to highlight advantages and limitations of a mean-line model for the estimation of the preliminary design of an ORC turbine. Moreover, the interest in the analysis of this specific case comes also from the strong lack of reliable and accurate data on ORC turbines in the open literature. For this case of validation, two correlations were employed in addition to those presented in Section 2.1:

1. A correction in the profile losses suggested by Craig and Cox [29] in order to account for the converging-diverging shape of the nozzle.
2. A formula due to Aungier [11] in order to include supersonic expansion losses at nozzle outlet.

Table 1. Decision variables **(1–12)** and input variables of TURAX for the Hannover [39,40] and Verneau [44] turbine test cases.

			Hannover Turbine		Verneau Turbine	
Parameter	**Symbol**	**Units**	**Nozzle**	**Rotor**	**Nozzle**	**Rotor**
(1) Inlet flow angle	α_1	°	10		0 (**)	
(2) Stage loading coefficient	ψ	-	2.1 (*)		4.4 (*)	
Nozzle **(3)** and rotor **(4)** throat opening	$o_{n,min}$, o_r	mm	15	14	1.76	1.75
Nozzle **(5)** and rotor **(6)** axial chord	c_n, c_r	mm	48.2	37.1	12.5 (**)	12.5
Nozzle **(7)** and rotor **(8)** opening to pitch ratio	$(o/s)_n$, $(o/s)_r$	-	0.378 (*)	0.358 (*)	0.277 (*)	0.425 (*)
(9) Rotational speed	N	rpm	7200		18,000	
(10) Inlet axial velocity	C_{a1}	m/s	55.9 (*)		10.1 (*)	
(11) Rotor flow coefficient	ϕ_r	-	0.39 (*)		0.52 (*)	
(12) Rotor inlet to nozzle outlet blade height	h^*	-	1		1.039	
Degree of admission	ε	-	1		0.4	
Mass flow rate	$\dot{m}$	kg/s	6.786		0.18	
Total inlet temperature	T_{01}	K	358.69 (*)		403	
Total inlet pressure	p_{01}	Pa	1.2486×10^5 (*)		6.8×10^5	
Total outlet pressure	p_{03}	Pa	0.998×10^5 (*)		1.21×10^5 (*)	
Rotor to nozzle mean radius ratio	R^*	-	1.019		0.99	
nozzle-rotor axial clearance	ss	mm	34.36		6.3 (**)	
Radius of blade rear suction side curvature	e_n, e_r	mm	109.00	166.57	10^8 (**)	10^8 (**)
Trailing edge thickness to blade opening ratio	$(t/o)_n$, $(t/o)_r$	-	0.0253	0.0357	0.07	0.172
Blade surface roughness	k_s	mm	2×10^{-3} (**)		2×10^{-3} (**)	
Rotor tip clearance	t_{cl}	mm	0.24		-	
Inlet width arc	-	mm	29.60	34.95	-	
Backbone length	b_n, b_r	mm	62.10	57.63	-	
Trailing edge thickness	t_n, t_r	mm	0.38	0.50	0.3	0.3 (**)

(*) = estimated value (**) = assumed value.

It was observed that the introduction of these two correlations has a limited impact on the estimate of the overall stage performance. However, it allowed having a better redistribution of losses between the nozzle and the rotor, and consequently a better match in the velocities. Another approach is found in Macchi [28], where the nozzle losses for supersonic flows have been taken into account including the profile losses for converging nozzle and the correction from Vavra [26]. Since not all data required for the validation were provided in the reference, stage loading, opening-to-pitch ratios, flow coefficient, inlet axial velocity were estimated by obtaining the best possible match with nozzle inlet and rotor outlet blade heights, and with the number of nozzle and rotor blades. Furthermore, uniform entry conditions to tip seals were considered. The main data on geometry and operating parameters of the turbine are listed in Table 1.

2.3. Sensitivity Analysis

Since the axial turbine model is to be coupled to the thermodynamic cycle model, it is important to ensure that it is as computationally efficient as possible. However, the number of decision variables for a turbine model optimization can be very large and can exponentially increase the computational requirements. Therefore, a sensitivity analysis was performed on the turbine model with the aim to indicate which decision variables have the biggest influence on turbine efficiency, and, possibly, to reduce the number of required decision variables by removing those that have limited or negligible impact on the solution. The sensitivity analysis was performed according to the Morris screening method [45]. The information obtained from a local sensitivity analysis is combined in order to provide a global preliminary screening of the most important decision variables in the model by using limited computational efforts. In addition, the method allows highlighting the mutual interactions and the interdependence among the variables. The Morris screening method is based on statistical

analysis. The reader is referred to the original paper by Morris [45] for additional details. In this context, the original decision variables subjected to the analysis were twelve. The method requires using a value of sampling size and of number of screening levels in each decision variable domain. These two parameters are an arbitrary choice of the analyst, and different values can be selected [45,46]. In the present work, six screening levels and a value sampling size of 50 were used, in order to obtain a satisfactory compromise between accuracy and calculation time. The sensitivity analysis was performed using the model developed by Sin *et al.* [47] and was based on the Hannover turbine test case. The decision variables were varied in the range ±25% of their nominal values of Table 1.

3. Results

3.1. Hannover Turbine

Table 2 shows the comparison of TURAX and CFD results with the experimental data of the Hannover turbine test case. CFD and experimental values are reported as mass-weighted averages except for pressure, which is provided as area-weighted average. The mass-weighted average and the relative error for the generic quantity φ were computed as:

$$\overline{\varphi} = \frac{\int_A \rho C_a \varphi \, dA}{\int_A \rho C_a \, dA} \qquad Err_\varphi = \frac{|\varphi - \overline{\varphi}_{exp}|}{\overline{\varphi}_{exp}}, \tag{2}$$

where ρ, C_a and A are the density, axial velocity and cross-sectional area. The subscript exp refers to measured experimental data. The error in flow angles and geometric angles is provided in degrees. Figure 2 shows the some details of CFD simulations. Figure 3 shows static temperature and pressure profiles in spanwise direction at different turbine sections. The experimental points are reported in the chart. The average thermodynamic conditions and flow angles at nozzle outlet (see also Figure 3a–b) of CFD and TURAX are in good agreement with experiments. Experimental and CFD results show a good match along the blade span, and CFD values are close to those of TURAX at midspan. The axial velocity profiles of Figure 3c are uniform at the nozzle outlet, although they appear to be underestimated by both tools. As a result, higher discrepancy in the estimation of average absolute velocity is found. The higher velocity at the nozzle outlet from experimental data can also be related to the fluid-dynamic characteristics in the rotor. The results show that the prediction error increases from nozzle to rotor. These differences are more evident in the axial and relative velocity profiles where the mismatch increases in the endwall regions. Figure 2b shows the entropy field in the rotor, which highlights the complex loss mechanisms in the rotor row. Hirsch and Denton [40] remark that the low flow coefficient and aspect ratio (chord over blade span) of the turbine are likely to be the cause of flow turning and secondary flow effects which become particularly strong at the root, and have influence on the flow field along the blade span. These 3D effects propagate toward the midspan. As a consequence of the error propagation along the stage and the difficulty in predicting the large change of flow angles and velocities in the spanwise direction, TURAX and the CFD model show a discrepancy in the average flow angles and velocities at nozzle outlet as high as 10% and 11.8%, respectively, by comparison with the experimental data.

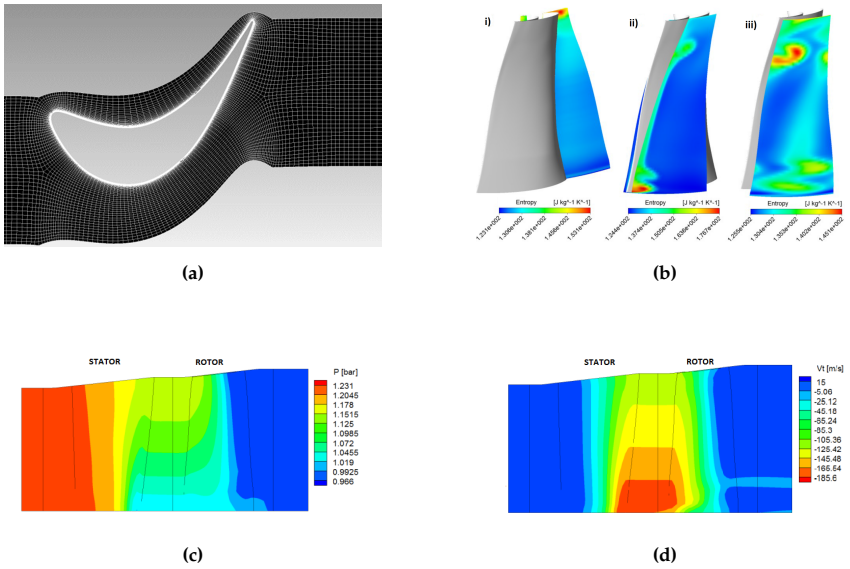

Figure 2. Computational fluid dynamics (CFD) results of the Hannover turbine using ANSYS CFX®: (**a**) details of the rotor grid at the midspan; (**b**) entropy field in streamwise direction at (i) the rotor inlet, (ii) the rotor outlet, and (iii) the measurement station; (**c**) contours of static pressure in the meridional plane; (**d**) contours of tangential velocity in the meridional plane. Adapted from Calvi [48].

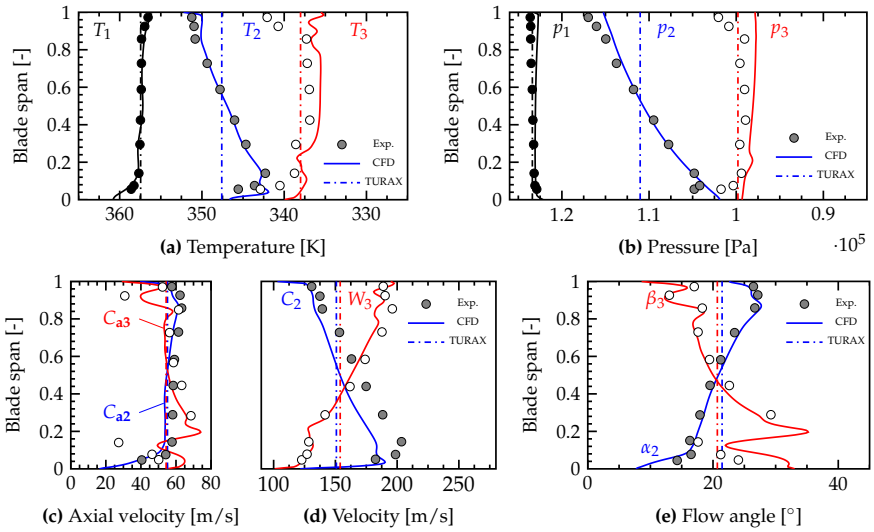

Figure 3. Profiles of (**a**) static temperature, (**b**) pressure, (**c**) axial velocity, (**d**) absolute and relative velocity and (**e**) flow angles at nozzle inlet, nozzle outlet and rotor outlet. Experimental, CFD and TURAX data of the Hannover turbine test case are shown in the charts.

Table 2. Comparison of results obtained with TURAX, CFD, and experimental investigations on the Hannover turbine. pp = percentage-points.

Parameter	Symbol	Units	Exp. Data [39–41]	TURAX	CFD [48]	Error TURAX	Error CFD
Nozzle outlet absolute flow angle	α_2	°	69.84	68.55	68.45	1.29 °	1.39 °
Nozzle outlet relative flow angle	β_2	°	7.13	4.60	4.82	2.53 °	2.31 °
Nozzle outlet absolute velocity	C_2	-	170.8	150.8	153.84	11.8%	9.95%
Absolute Mach at nozzle outlet	M_2	-	0.457	0.406	0.412	11.2%	9.9%
Static pressure at nozzle outlet	p_2	bar	1.111	1.105	1.108	0.31%	0.28%
Static temperature at nozzle inlet	T_1	K	357.4	357.4	357.4	0.0%	0.0%
Static temperature at nozzle outlet	T_2	K	347.17	347.75	347.06	0.17%	0.03%
Rotor outlet relative flow angle	β_3	°	68.75	69.31	67.07	0.56 °	1.68 °
Rotor outlet absolute flow angle	α_3	°	2.45	5.91	7.58	3.46 °	5.13 °
Rotor outlet relative velocity	W_3	m/s	166.3	153.9	157.51	7.43%	5.30%
Static pressure at rotor outlet	p_3	bar	0.994	0.998	0.983	0.33%	1.15%
Static temperature at rotor outlet	T_3	K	337.86	337.96	336.60	0.03%	0.37%
Nozzle mean radius	r_{2m}	mm	181.5	180.1	181.5	0.77%	0%
Rotor mean radius	r_{3m}	mm	185	183.5	185	0.81%	0%
Nozzle inlet blade height	h_1	mm	89.2	89.2	89.2	0%	0%
Nozzle outlet (rotor inlet) blade height	h_2	mm	97	100.2	97	3.3%	0%
Rotor outlet blade height	h_3	mm	103	108.1	103	4.95%	0%
Nozzle flare angle	$\alpha_{FL,n}$	°	5.62	12.83	5.62	7.21 °	0 °
Rotor flare angle	$\alpha_{FL,r}$	°	7.89	12.04	7.89	4.15 °	0 °
Number of nozzle blades	z_n	-	29	28	29	1	0
Number of rotor blades	z_r	-	30	30	30	0	0
Nozzle kinetic energy loss coefficient	ζ_n	-	3.79%	6.48%	5.82%	2.69 pp	2.03 pp
Rotor kinetic energy loss coefficient	ζ_r	-	9.08%	6.76%	6.66%	2.32 pp	2.42 pp
Total-to-total stage efficiency	η_{tt}	-	91.62%	92.84%	93.32%	1.22 pp	1.70 pp

The mean-line model provided accuracy within 1% in the estimation of the mean radius, within 5% in the blade heights, within 8° in the flare angles, and underestimated the number of blades by one unit. The performance of the turbine stage was evaluated through the total-to-total efficiency η_{tt} and the nozzle and rotor kinetic energy loss coefficients, ζ_n and ζ_r, defined as

$$\eta_{tt} = \frac{h_{01} - h_{03}}{h_{01} - h_{03s}} \qquad \zeta_n = \frac{h_2 - h_{2s}}{C_2^2/2} \qquad \zeta_r = \frac{h_3 - h_{3s}}{W_3^2/2}, \tag{3}$$

where *1,2,3* refer to nozzle inlet, nozzle outlet, and rotor outlet, h is the specific enthalpy, *0* refers to total conditions, *s* refers to isentropic conditions, and C and W are the absolute and relative velocities, respectively. The mass-weighted average value of efficiency from experimental results was calculated as approximately 91.6%. Both CFD simulations and TURAX overestimated the efficiency of the stage by 1.7 and 1.2%-points, respectively. The presence of effects difficult to predict accurately such as 3D turning, secondary flow effects as well as of the unsteady stator-rotor interaction might explain the lower value of turbine efficiency obtained in the experiments. The blade row parameters can be related to the efficiency of the stage by resorting to approximate relations such as those proposed by Dixon and Hall [37]. For similar thermodynamic conditions at the nozzle outlet, the higher value of absolute velocity in the experimental measurements results in a lower nozzle loss coefficient whilst a higher experimental rotor loss coefficient contributes to the lower turbine efficiency.

In this case of validation, TURAX proved to be a reliable tool by comparison with both experimental and CFD results since the discrepancy in the estimated efficiency was in the order of 1%. In addition, it provided very good agreement with average CFD values and acceptable agreement with experiments, thus making it suitable for preliminary design estimation.

3.2. Verneau Turbine

Figure 4 shows the results of the validation of TURAX with the ORC turbine investigated by Verneau [44]. Excellent agreement is obtained in the estimation of nozzle and rotor outlet flow angles and good agreement is obtained in the prediction of velocities. The error on the flow velocities affects the values of blade heights, which nevertheless differ by only 0.3 mm. The performance prediction was performed using the total-to-static efficiency:

$$\eta_{ts} = \frac{h_{01} - h_{03}}{h_{01} - h_{3s}}. \quad (4)$$

TURAX predicted a value of 64.3%, which is within 1.3%-points of the measured value. The relative contribution of losses is higher in the rotor, as highlighted by the lower value of rotor velocity coefficient. However, a higher efficiency debit is computed for the nozzle, due to the higher kinetic energy at the outlet. The chart in Figure 4 shows the breakdown of turbine losses. The blade profile is adapted to a converging-diverging shape and the profile losses in the nozzle result in being comparatively small. Nozzle secondary losses represent the first source of performance degradation, with approximately 7.7%-points of efficiency debit. Secondary losses in a blade row increase for high inlet to outlet velocity ratios and low aspect ratios (blade height over backbone length). The nozzle exhibits a very small velocity ratio (about 0.04), thus the biggest contribution to secondary losses stems from the small value of aspect ratio (*ca.* 0.27), which generates strong secondary flows within the blade row. The high Mach number at the nozzle trailing edge suggests the presence of shock waves in the stator-rotor gap leading to additional losses, here referred to as supersonic expansion losses. Transonic flow conditions are encountered at the rotor inlet. Consequently, profile losses increase due to the presence of shock waves generated at the leading edge of the rotor blades. The high velocity ratio (*i.e.*, >1) and the low aspect ratio significantly increase the secondary losses in the rotor. At the same time, the high velocity at the outlet results in significant discharge kinetic energy losses (around 4.3%-points). Tip leakage losses depend on the aerodynamic loading of the rotor. In this case, it provides only a marginal efficiency debit since the turbine has a very low degree of reaction, therefore the pressure drop typically associated with this type of loss is small. Finally, partial admission losses provide a contribution on the same order of magnitude as the kinetic energy losses. In this case, most of the wasted energy comes from the filling of inactive passages within the blade row, referred to as scavenging losses. The difference in power output obtained by TURAX and that reported by Verneau is 7.1%, corresponding to 0.22 kW.

Parameter	Symbol	Units	Verneau	TURAX	Err. (%)
Nozzle outlet absolute flow angle	α_2	°	74.00	74.00	0 °
Absolute Mach at nozzle inlet	M_1	-	-	0.08	-
Axial Mach at nozzle outlet	M_{a2}	-	0.47	0.49	4.41%
Absolute Mach at nozzle outlet	M_2	-	1.76	1.78	1.14%
Nozzle velocity coefficient	C_2/C_{2s}	-	-	0.94	-
Rotor outlet relative flow angle	β_3	°	65.40	65.47	0.07 °
Relative Mach at rotor inlet	M_{W2}	-	1.13	1.12	0.76%
Axial Mach at rotor outlet	M_{a3}	-	0.360	0.366	1.77%
Relative Mach at rotor outlet	M_{W3}	-	0.880	0.883	0.34%
Axial Mach numbers ratio	-	-	0.77	0.75	2.76%
Rotor velocity coefficient	W_3/W_{3s}	-	-	0.73	-
Degree of reaction	χ	-	< 0	-0.3	-
Nozzle mean radius	r_{2m}	mm	48.0	47.6	1.01%
Rotor mean radius	r_{3m}	mm	47.2	47.1	0.13%
Nozzle inlet blade height	h_1	mm	3.37	3.37	0%
Nozzle outlet blade height	h_{21}	mm	3.37	3.6	5.56%
Rotor inlet blade height	h_2	mm	3.5	3.8	7.89%
Rotor outlet blade height	h_3	mm	5.2	5.2	0%
Nozzle flare angle	$\alpha_{FL,n}$	°	0	0.48	0.48 °
Upper rotor flare angle	$\alpha_{FL,ru}$	°	-0.18	1.17	1.35 °
Lower rotor flare angle	$\alpha_{FL,rl}$	°	8.06	5.33	2.73 °
Number of nozzle blades	z_n	-	22	23	1
Number of rotor blades	z_r	-	72	72	0
Total-to-static stage efficiency	η_{ts}	%	63	64.3	1.29 pp
Power output	$\dot{W}$	kW	3	3.22	7.1%

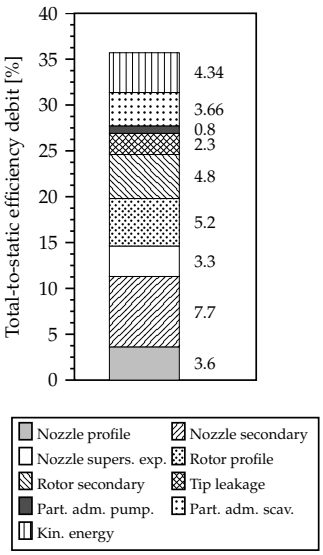

Figure 4. Comparison of results between TURAX and Verneau data [44]. pp = percentage-points. The breakdown of losses is shown in the chart.

3.3. Sensitivity Analysis

Figure 5 presents the results in the standard deviation-mean value diagram. Two black lines are drawn in the chart, which connect standard error and mean value of each decision variable. According to Morris [45]: (1) a large deviation of the mean value implies that a variable can be considered important in terms of affecting the model output, *i.e.*, it provides a significant contribution to the change of turbine efficiency; (2) a high value of standard deviation implies that a variable produces non-linear effects and/or has strong interactions with other variables; (3) if a variable is inside the wedge formed by the two lines, it can be considered as less important than the others, thus it can possibly be screened out from the set of the input parameters. The table in Figure 5 shows the results of the analysis. All parameters show mutual interdependency since they have non-zero standard deviations in the Morris plot. The selection criterion of the decision variables is based both on significance from the sensitivity analysis results and on importance from a design viewpoint.

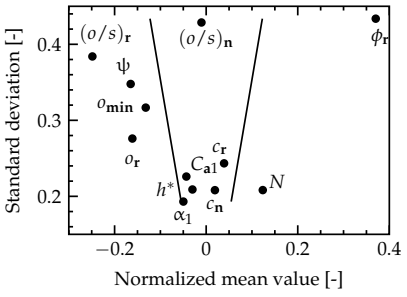

Parameter	Unit	Symbol	Signif.
1) Stage inlet flow angle	°	α_1	no
2) Stage loading coefficient	-	ψ	yes
3) Nozzle minimum opening	m	o_{min}	yes
4) Rotor opening	m	o_r	yes
5) Nozzle axial chord	m	c_n	no
6) Rotor axial chord	m	c_r	no
7) Nozzle opening-to-pitch ratio	-	$(o/s)_n$	no
8) Rotor opening-to-pitch ratio	-	$(o/s)_r$	yes
9) Rotational speed	rpm	N	yes
10) Stage inlet axial velocity	m/s	C_{a1}	no
11) Rotor flow coefficient	-	ϕ_R	yes
12) Rotor inlet to nozzle outlet blade height	-	h^*	no

Figure 5. Sensitivity analysis and significance of decision variables of the axial turbine model. Morris screening method [45] applied to the Hannover turbine test case.

- ψ, o_{min}, o_r, $(o/s)_r$, N, ϕ_r are indicated as significant parameters. Moreover, they tightly relate to the design features of the stage.
- The nozzle opening-to-pitch $(o/s)_n$ is not important according to the results. However, it is affected by a high standard deviation compared to the others, which implies strong interactions with the other parameters in the model. In addition, it cannot be disregarded from the design viewpoint since it relates to the estimation of nozzle pitch and outlet flow angle, and allows determining the number of nozzle blades.
- The stage inlet velocity C_{a1} is screened as an insignificant parameter for the performance of the turbine. However, the value of C_{a1} is strictly related to nozzle inlet blade height, which is a relevant aspect in the design and manufacturing of an axial turbine. This aspect becomes particularly critical for small-scale expanders, as highlighted, for example, by Klonowicz *et al.* [15]. Consequently, this variable was not excluded from the decision variables.
- Nozzle and rotor axial chords, c_n and c_r, do not significantly affect the efficiency according to Morris's method. However, they tightly relate to the estimation of flaring angles. The optimization of the parameters c_n and c_r in the model would enable one to broaden the space of feasible design solutions. Furthermore, they relate to the actual length of the turbine and can be relevant for applications where compactness is a relevant decision criterion.
- The stage inlet flow angle α_1 does not provide a significant contribution to the efficiency. From the design point of view, it is a common practice to set it to the value of zero. Thus, it can be conveniently screened out from the decision variables of the model.
- The rotor inlet to nozzle outlet blade height ratio h^* can be screened out in the model. Although related to tip clearance and annulus losses in the Craig and Cox correlations, it shows a limited impact on both preliminary design and efficiency of the turbine due to the short range of variation given by typical design constraints (*i.e.*, 1.0–1.1) [29].

4. Conclusions

In this paper, the axial-flow turbine computational model TURAX was presented, including a thorough validation and a global sensitivity analysis. The validation of the axial turbine model, TURAX, considering two very different test cases confirms that the design performance can be predicted within 1.3%-points, which is in agreement with the commonly accepted prediction accuracy of the empirical loss model used in the code, namely the Craig and Cox correlation. The thermodynamic conditions at the different turbine sections can be accurately predicted by TURAX. The model provided values of velocity and flow angles in good agreement with CFD at the midspan for the case of validation of a subsonic, reaction turbine using air. Maximum discrepancy in the order of 10% was found for both TURAX and CFD models when comparing the flow results with experimental measurements, and blade heights and geometry were predicted in the same order of accuracy as velocities. In a second test case, TURAX showed a good match in the comparison with the experimental data from an ORC turbine, notwithstanding the complexity of the case addressing real fluid behavior, supersonic flows, shock waves in the blade channels, partial admission, low aspect ratio, converging-diverging nozzle, and rotor impulse blades. The fluid-dynamic features were predicted within 5% accuracy and the blade heights within 8% accuracy. In both cases, the discrepancy in the results can largely depend on the uncertainty in the outlet flow angle and loss correlations, and on the uncertainty in the experimental measurements. Hirsch and Denton [40] have shown that, using different correlations applied to through-flow methods, the accuracy in the estimation of turbine efficiency and losses can be $\pm$2%-points and $\pm$20%, respectively. The global sensitivity analysis using the Morris screening method combined with design considerations resulted in the selection of a minimum of 10 decision variables, which will be used for model optimization purposes as shown in the second part of this paper.

Acknowledgments: The research work was conducted within the frame of the THERMCYC project ("Advanced thermodynamic cycles utilizing low-temperature heat sources"; see http://www.thermcyc.mek.dtu.dk/) funded by InnovationsFonden, The Danish Council for Strategic Research in Sustainable Energy and Environment.

Author Contributions: Andrea Meroni wrote the first draft and contributed to the turbine model improvement, validation and sensitivity analysis. Angelo La Seta contributed to the model development and to a first validation. Jesper Graa Andreasen and Leonardo Pierobon contributed to the model development and improvement. Giacomo Persico provided the CFD results and contributed to the analysis and discussion of the model validation. Fredrik Haglind contributed to the discussion and provided guidance throughout the work. All authors contributed to the first and second revisions, read and approved the final manuscript.

Conflicts of Interest: The authors declare no conflict of interest.

Nomenclature

A Cross-sectional area (m^2)
C Absolute velocity ($m \cdot s^{-1}$)
D_m Mean diameter of the stage (m)
Err Error (-)
M Mach number (-)
N Rotational speed (rpm)
R^* Rotor to nozzle mean radius ratio (-)
Re Reynolds number (-)
T Temperature (K)
U Peripheral velocity ($m \cdot s^{-1}$)
U_{tip} Tip Speed ($m \cdot s^{-1}$)
W Relative velocity ($m \cdot s^{-1}$)
W_b Blade work ($J \cdot kg^{-1}$)
$\dot{m}$ Mass flow rate ($kg \cdot s^{-1}$)
b Blade backbone length (m)
c Axial chord (m)

e Blade rear surface suction curvature (m)
h Blade height [m]; specific enthalpy ($J \cdot kg^{-1}$)
h^* Ratio of Rotor inlet to nozzle outlet blade height (-)
k_s Blade surface roughness (m)
o Blade opening (m)
p Pressure (Pa)
r radius (m)
ss Nozzle to rotor axial clearance (m)
t Trailing edge thickness (m)
t_{cl} Blade tip clearance (m)
z Number of blades (-)

Abbreviations and acronyms
CFD Computational Fluid Dynamics
ORC Organic Rankine Cycle

Greek letters
α Absolute flow angle (°)
α_{FL} Flaring angle (°)
β Relative flow angle (°)
χ Stage degree of reaction (-)
ϵ Degree of admission (-); residual error (-)
η Turbine isentropic efficiency (-)
ϕ Flow coefficient (-)
ψ Stage loading coefficient (-)
ρ Density ($kg \cdot m^{-3}$)
φ Generic quantity (-)
ζ Kinetic energy loss coefficient (-)

Subscripts
0 Total conditions
1 Nozzle inlet
2 Rotor inlet
21 Nozzle outlet
3 Rotor outlet
a Axial component
m Referred to the mean diameter
min Referred to the minimum opening
n Nozzle
o Outlet
r Rotor
s Isentropic conditions
ts Total-to-static
tt Total-to-total
W Referred to the relative coordinate system

References

1. Stine, W.B.; Harrigan, R.W. *Solar Energy Fundamentals and Design*; John Wiley and Sons, Inc.: New York, NY, USA, 1985.
2. Lecompte, S.; Huisseune, H.; van den Broek, M.; De Schampheleire, S.; De Paepe, M. Part load based thermo-economic optimization of the Organic Rankine Cycle (ORC) applied to a combined heat and power (CHP) system. *Appl. Energy* **2013**, *111*, 871–881.
3. Cayer, E.; Galanis, N.; Nesreddine, H. Parametric study and optimization of a transcritical power cycle using a low temperature source. *Appl. Energy* **2010**, *87*, 1349–1357.

Appendix D. Articles

4. Bao, J.; Zhao, L. A review of working fluid and expander selections for organic Rankine cycle. *Renew. Sustain. Energy Rev.* **2013**, *24*, 325–342.
5. Quoilin, S.; Broek, M.V.D.; Declaye, S.; Dewallef, P.; Lemort, V. Techno-economic survey of Organic Rankine Cycle (ORC) systems. *Renew. Sustain. Energy Rev.* **2013**, *22*, 168–186.
6. Fiaschi, D.; Manfrida, G.; Maraschiello, F. Design and performance prediction of radial ORC turboexpanders. *Appl. Energy* **2015**, *138*, 517–532.
7. Persico, G.; Pini, M.; Dossena, V.; Gaetani, P. Aerodynamics of Centrifugal Turbine Cascades. *J. Eng. Gas Turbines Power* **2015**, *137*, doi:10.1115/1.4030261.
8. Pini, M.; Persico, G.; Casati, E.; Dossena, V. Preliminary Design of a Centrifugal Turbine for Organic Rankine Cycle Applications. *J. Eng. Gas Turbines Power* **2013**, *135*, doi: 10.1115/1.4023122.
9. Casati, E.; Vitale, S.; Pini, M.; Persico, G.; Colonna, P. Centrifugal Turbines for Mini-ORC Power Systems. *J. Eng. Gas Turbines Power* **2014**, *136*, 1–11.
10. Colonna, P.; Casati, E.; Trapp, C.; Mathijssen, T.; Larjola, J.; Turunen-Saaresti, T.; Uusitalo, A. Organic Rankine Cycle Power Systems: From the Concept to Current Technology, Applications, and an Outlook to the Future. *J. Eng. Gas Turbines Power* **2015**, *137*, 1–19.
11. *TurbinAungier, R.H. e Aerodynamics*; American Society of Mechanical Engineers Press: New York, NY, USA, 2006.
12. Turboden. Turboden: Clean Energy Ahead. 2016. Available online: http://www.turboden.eu (accessed on 1 January 2016).
13. Ormat Technologies. Green Energy You Can Rely On. 2016. Available online: http://www.ormat.com (accessed on 1 January 2016).
14. Uusitalo, A. Working Fluid Selection and Design of Small-scale Waste Heat Recovery Systems Based on Organic Rankine Cycles. Ph.D. Thesis, Lappeenranta University of Technology, Lappeenranta, Finland, 2014.
15. Klonowicz, P.; Heberle, F.; Preißinger, M.; Brüggemann, D. Significance of loss correlations in performance prediction of small scale, highly loaded turbine stages working in Organic Rankine Cycles. *Energy* **2014**, *72*, 322–330.
16. Lozza, G.; Macchi, E.; Perdichizzi, A. On the influence of the number of stages on the efficiency of axial-flow turbines. In Proceedings of the 27th American Society of Mechanical Engineers, International Gas Turbine Conference and Exhibit, American Society of Mechanical Engineers, London, UK, 18–22 April 1982.
17. Da Lio, L.; Manente, G.; Lazzaretto, A. New efficiency charts for the optimum design of axial flow turbines for organic Rankine cycles. *Energy* **2014**, *77*, 447–459.
18. Ventura, C.A.D.M.; Rowlands, A.S. Design and performance estimation of radial inflow turbines coupled with a thermodynamic cycle analysis procedure. In Proceedings of the ASME ORC 2013: 2nd International Seminar on ORC Power Systems, Rotterdam, The Netherlands, 7–8 October 2013; pp. 1–5.
19. Uusitalo, A.; Turunen-Saaresti, T.; Gronman, A.; Honkatukia, J.; Backman, J. Combined Thermodynamic and Turbine Design Analysis of Small Capacity Waste Heat Recovery ORC. In Proceedings of the ASME ORC 2015: 3nd International Seminar on ORC Power Systems, Brussels, Belgium, 12–14 October 2015; pp. 1–10.
20. Gabrielli, P. Design and Optimization of Turbo-Expanders for Organic Rankine Cycles. Master's Thesis, Technical University of Denmark, Copenhagen, Denmark, 2014.
21. La Seta, A.; Andreasen, J.G.; Pierobon, L.; Persico, G.; Haglind, F. Design of Organic Rankine Cycle Power Systems Accounting for Expander Performance. In Proceedings of the 3rd International Seminar on ORC Power Systems, Brussels, Belgium, 12–14 October 2015; pp. 1–12.
22. Mathworks. MATLAB 2015b Documentation. Available online: http://www.mathworks.com (accessed on 1 January 2016).
23. Lemmon, E.W.; Huber, M.L.; McLinden, M.O. *NIST reference fluid thermodynamic and transport properties–REFPROP*; U.S. Department of Commerce: Gaithersburg, MD, USA, 2002.
24. Bell, I.H.; Wronski, J.; Quoilin, S.; Lemort, V. Pure and pseudo-pure fluid thermophysical property evaluation and the open-source thermophysical property library CoolProp. *Ind. Eng. Chem. Res.* **2014**, *53*, 2498–2508.
25. Ainley, D.G.; Mathieson, G.C.R. *A Method of Performance Estimation for Axial-Flow Turbines*; Technical Report; Aeronautical Research Council Great Britain: London, UK, 1951.

26. Vavra, M. *Axial Flow Turbines. Flow in Turbines. (VKI Lecture Series 15)*; Von Karman Institute For Fluid Dynamics: Rhode-Saint-Genése, Belgium, 1969; pp. 1–117.
27. Deich, M. *Atlas of Axial Turbine Blade Cascades*; Deich, M.E., Filippov, G.A., Lazarev, L.Ya., Eds.; Maschinostroenie Publishing House: Moscow, Russia, 1965; pp. 4563–4564.
28. Macchi, E. *Design Criteria for Turbines Operating with Fluids having a Low Speed of Sound. Closed Cycle Gas Turbines. (VKI Lecture Series 100)*; Von Karman Institute For Fluid Dynamics: Rhode-Saint-Genése, Belgium, 1977; Volume 2, pp. 1–34.
29. Craig, H.; Cox, H. Performance estimation of axial flow turbines. *Proc. Inst. Mech. Eng.* **1970**, *185*, 407–424.
30. Macchi, E.; Perdichizzi, A. Efficiency Prediction for Axial-Flow Turbines Operating with Nonconventional Fluids. *J. Eng. Power* **1981**, *103*, 718–724.
31. Lozza, G. A comparison between the Craig-Cox and the Kacker-Okapuu methods of turbine performance prediction. *Meccanica* **1982**, *17*, 211–221.
32. Kacker, S.C.; Okapuu, U. A Mean Line Prediction Method for Axial Flow Turbine Efficiency. *J. Eng. Power* **1982**, *104*, 111–119.
33. Balje, O.E.; Binsley, R.L. Axial Turbine Performance Evaluation. Part A Loss-Geometry Relationships. *J. Eng. Gas Turbines Power* **1968**, *90*, 341–348.
34. Traupel, W. *Thermische Turbomaschinen: Thermodynamisch-Strömungstechnische Berechnung*; Springer: Berlin, Germany, 1966; Volume 1.
35. Macchi, E.; Lozza, G. Comparison of Partial *vs.* Full Admission for Small Turbines at Low Specific Speeds. In Proceedings of the ASME 1985 International Gas Turbine Conference and Exhibit, Houston, Texas, 18–21 March 1985.
36. Saravanamuttoo, H.I.H.; Rogers, G.F.C.; Cohen, H. *Gas Turbine Theory*; Pearson Education Limited: Essex, UK, 2001.
37. Dixon, S.L.; Hall, C.A. *Fluid Mechanics and Thermodynamics of Turbomachinery*; Butterworth-Heinemann: Waltham, MA, USA, 2010; pp. 105–107.
38. Vavra, M.H. *Aero-thermodynamics and Flows in Turbomachines*; John Wiley & Sons: New York, NY, USA, 1960.
39. Groschup, D.I.G. Strömungstechnische Untersuchung einer Axialturbinenstufe im Vergleich zum Verhalten der erben Gitter ihrer Beschaufelung. Ph.D. Thesis, Technische Universität Hannover, Hannover, Germany, 1977.
40. Hirsch, C.; Denton, J. *Through Flow Calculations in Axial Turbomachines. AGARD Advisory Report N.175*; Technical Report; AGARD, Propulsion and Energetics Panel, Working Group 12: Neuilly Sur Seine, France, 1981.
41. Kötzing, P.; Evers, B. *Test Case e/tu-4, 4-stage Low Speed Turbine. AGARD Report No.275 AR-275*; Technical Report; AGARD: Neuilly Sur Seine, France, 1990.
42. Menter, F.R. *Zonal Two Equation $k-\omega$ Turbulence Models for Aerodynamic Flows*, In Proceedings of the 23rd Fluid Dynamics, Plasmadynamics, and Lasers Conference, Orlando, FL, USA, 6–9 July 1993.
43. Persico, G.; Mora, A.; Gaetani, P.; Savini, M. Unsteady aerodynamics of a low aspect ratio turbine stage: Modeling issues and flow physics. *J. Turbomach.* **2012**, *134*, doi:10.1115/1.4004021.
44. Verneau, A. *Supersonic turbines for organic fluid Rankine cycles from 3 to 1300 kW*; Small High Pressure Ratio Turbines, (VKI Lecture Series 1987-2007); Von Karman Institute For Fluid Dynamics: Rhode-Saint-Genése, Belgium, 1987.
45. Morris, M.D. Factorial Sampling Plans for Preliminary Computational Experiments. *Technometrics* **1991**, *133*, 295–302.
46. Saltelli, A.; Tarantola, S.; Campolongo, F.; Ratto, M. *Sensitivity Analysis in Practice: A Guide to Assessing Scientific Models*; John Wiley & Sons: Chichester, West Sussex, UK, 2004.
47. Sin, G.; Gernaey, K.V.; Lantz, A.E. Good Modeling Practice for PAT Applications: Propagation of Input Uncertainty and Sensitivity Analysis. *Biotechnol. Prog.* **2009**, *25*, 1043–1053.
48. Calvi, S. Analisi e validazione di solutori CFD ad alta e bassa fedeltá per turbomacchine. Master's Thesis, Politecnico di Milano, Milan, Italy, 2015.

© 2016 by the authors; licensee MDPI, Basel, Switzerland. This article is an open access article distributed under the terms and conditions of the Creative Commons Attribution (CC-BY) license (http://creativecommons.org/licenses/by/4.0/).

Proceedings of ASME Turbo Expo 2016: Turbomachinery Technical Conference and Exposition
GT2016
June 13-17, 2016, Seoul, South Korea

GT2016-58065

OPTIMIZATION OF CYCLE AND EXPANDER DESIGN OF AN ORGANIC RANKINE CYCLE UNIT USING MULTI-COMPONENT WORKING FLUIDS

Andrea Meroni *
Department of Mechanical Engineering
Technical University of Denmark
DK-2800 Kgs. Lyngby, Denmark
Email: andmer@mek.dtu.dk

Jesper Graa Andreasen
Department of Mechanical Engineering
Technical University of Denmark
DK-2800 Kgs. Lyngby, Denmark
Email: jgan@mek.dtu.dk

Leonardo Pierobon
Department of Mechanical Engineering
Technical University of Denmark
DK-2800 Kgs. Lyngby, Denmark
Email: lpier@mek.dtu.dk

Fredrik Haglind
Department of Mechanical Engineering
Technical University of Denmark
DK-2800 Kgs. Lyngby, Denmark
Email: frh@mek.dtu.dk

ABSTRACT

Organic Rankine cycle (ORC) power systems represent attractive solutions for power conversion from low temperature heat sources, and the use of these power systems is gaining increasing attention in the marine industry. This paper proposes the combined optimal design of cycle and expander for an organic Rankine cycle unit utilizing waste heat from low temperature heat sources. The study addresses a case where the minimum temperature of the heat source is constrained and a case where no constraint is imposed. The former case is the waste heat recovery from jacket cooling water of a marine diesel engine onboard a large ship, and the latter is representative of a low-temperature geothermal, solar or waste heat recovery application. Multi-component working fluids are investigated, as they allow improving the match between the temperature profiles in the heat exchangers and, consequently, reducing the irreversibility in the ORC system. This work considers mixtures of R245fa/pentane and propane/isobutane. The use of multi-component working fluids typically results in increased heat transfer areas and different expander designs compared to pure fluids. In order to properly account for turbine performance and design constraints in the cycle calculation, the thermodynamic cycle and the turbine are optimized simultaneously in the molar composition range of each mixture. Such novel optimization approach enables one to identify to which extent the cycle or the turbine behaviour influences the selection of the optimal solution. It also enables one to find the composition for which an optimal compromise between cycle and turbine performance is achieved. The optimal ORC unit employs pure R245fa and provides approximately 200 kW when the minimum hot fluid temperature is constrained. Conversely, the mixture R245fa/pentane (0.5/0.5) is selected and provides approximately 444 kW when the hot fluid temperature is not constrained to a lower value. In both cases, a compact and efficient turbine can be manufactured.

*Address all correspondence to this author.

Copyright © 2016 by ASME

1 INTRODUCTION

In the last two decades, the increasing demand of fossil fuels paved the way to the research and development of more efficient, environmentally-friendly technologies. Organic Rankine cycle systems represent a well-established solution for the exploitation of medium-to-low temperature heat sources, due to its inherent flexibility and simplicity compared to conventional power plants [1]. Current research efforts are devoted to improve the performance of the cycle and extend its applicability range toward pioneering temperature and power capacities. In this respect, the selection of the optimal working fluid and of the optimal expander design plays a key role in determining the efficiency of the system.

The working fluid can be a pure substance or the combination of two or more components. Mixtures of pure fluids can increase the efficiency of the cycle due to the the presence of a temperature glide during the heat addition and rejection processes. This feature can be conveniently used to reduce the temperature mismatch with the heat source. As a consequence, lower irreversibility and a higher system performance are achieved [2]. Many authors investigated the thermodynamic advantages of mixtures over pure working fluids in the past. Heberle et al. [3] showed that the use of R227ea/R245fa as a working fluid can provide efficiency improvements up to 15 % in an ORC exploiting low-enthalpy geothermal resources below 120 °C. Chys et al. [4] estimated a potential rise up to 16 % and 6 % utilizing zeotropic mixtures of refrigerants and hydrocarbons for heat source temperatures of 150 °C and 250 °C. From a technical and economic point of view, important trade-offs between cycle and components' behaviour can arise. Andreasen et al. [5] showed that the use of hydrocarbon mixtures with optimal composition utilizing a 90 °C heat source provides the best performance and increases the size of the heat exchangers. Further complexity might be expected due to composition shift [6] and reduced heat transfer [7] related to the non-ideal behaviour and mass transfer phenomena of mixtures.

The expander is arguably the key-component in an ORC unit. However, the analysis of the effect of mixtures on the design of the expander was considered only in few works. Braimakis et al. [8] and Chaitanya Prasad et al. [9] resorted to using a size parameter $\dot{V}_{out,s}^{0.5}/\Delta h_s^{0.25}$ and volume flow rate ratio $\dot{V}_{out}/\dot{V}_{in}$ to describe the preliminary design of the expander, neglecting a more detailed analysis of geometric and flow features of the machine. In addition, most of the cycle models rely on the assumption of constant isentropic efficiency of the turbine, neglecting the interdependency between the component and the system performance. La Seta et al. [10] recently presented a methodology where cycle and expander design are simultaneously optimized. Results highlighted the importance of accounting for the expander design, as a change up to 10 % in the turbine isentropic efficiency was found when it was optimized.

Organic Rankine cycle units for solar, geothermal, biomass and industrial waste heat recovery applications have been extensively investigated. A novel field of investigation is the waste heat recovery from the diesel engines onboard large ships. There is an enormous unexploited potential from different sources such as the exhaust gases, scavenge air, jacket water and lubricant systems of the engine. As an example, Larsen et al. [11] investigated the case of waste heat recovery utilizing the exhaust gases of the main engine in a temperature range between 180 °C and 360 °C. In order to further increase the power available onboard the ship and reduce the fuel consumption, ORC units exploiting low-temperature heat have also been recently considered. For example, Yang et al. [12] performed a thermo-economic optimization of an ORC utilizing the waste heat from the jacket water cooling system. Among the six working fluids analysed, R1234yf and R1234ze were found to be the best from the thermo-economic performance viewpoint, while R245fa showed the lowest operating pressures. To the best authors' knowledge, the design and optimization of an ORC unit using multi-component working fluids to recover waste heat from the jacket water cooling system has never been investigated before.

This work presents a methodology where cycle and expander designs are combined and optimized through an iterative method. Two binary mixtures are considered: R245fa/pentane and propane/isobutane. A steady-state cycle model is coupled with a single-stage axial expander model to provide the optimum point in the range of molar composition of the fluids. This approach enables one to identify the molar composition for which the optimal compromise between cycle and expander design is achieved. Results are compared to those obtained assuming a constant isentropic efficiency of the turbine. Maraver et al. [13] showed that a constraint on the minimum outlet temperature of the heat source can pose limitations on the cycle design, and the selection of the optimal working fluid can be greatly affected in a practical application. Thus, two case studies were investigated in this work. The first case is the waste heat recovery from the jacket water from a marine engine with hot fluid outlet temperature constrained to a lower limit. The second case is representative of a more general heat recovery application with the same heat source inlet temperature but with no limitation on the outlet temperature. Such case can be typical of low-temperature geothermal, solar or waste heat recovery applications. For example, Heberle et al. [3] analyzed zeotropic mixtures of different working fluids for inlet temperature of geothermal water between 80 and 180 °C. Tchanche et al. [14] compared the theoretical performance of different working fluids with hot water temperature below 90 °C for solar applications.

This paper is structured as follows: Section 2 presents the methods. Results are given and discussed in Sec. 3. Conclusions are drawn in Sec. 4.

Copyright © 2016 by ASME

2 METHODS

The two case studies analysed in this paper are both related to waste heat recovery from low temperature heat. The first represents waste heat recovery from the jacket water from a marine engine with a power output of approximately 60 MW. The jacket water is used for cooling the cylinder liners and the heat is traditionally rejected to the fresh water cooling circuit. In the present study, an ORC unit recovers waste heat from the jacket water and converts it into useful electricity. The temperature of the jacket water at the inlet to the ORC unit is 85 °C. In order to ensure appropriate cooling for the engine, the cooling medium must be returned at a temperature of 80 °C. This imposes a constraint on the jacket water outlet temperature from the ORC boiler.

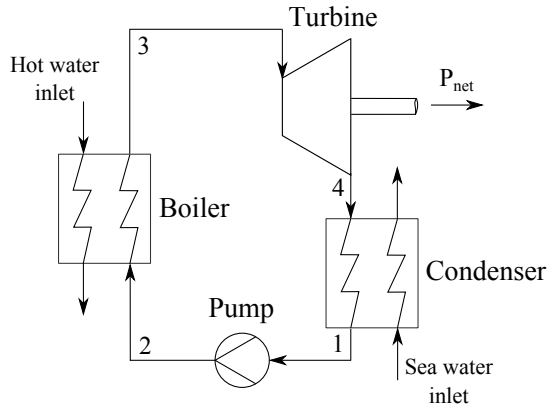

FIGURE 1: ORGANIC RANKINE CYCLE UNIT

TABLE 1: ORC UNIT MODELLING CONDITIONS

Parameter	Value	Unit
Hot water		
Inlet temperature	85	°C
Mass flow	120	kg/s
Pressure	1.5	bar
Condenser		
Coolant inlet temperature	27	°C
Coolant mass flow	100	kg/s
Outlet vapour quality	0	-
Cooling water pressure	1.5	bar
Pump		
Isentropic efficiency	0.8	-
Turbine		
Isentropic efficiency (first iteration)	0.85	-
Minimum outlet vapour quality	1	-

Figure 1 shows a sketch of the ORC unit, which consists of a boiler, a turbine, a condenser and a pump. The heat input to the ORC unit is provided through the boiler from the hot water stream and heat is rejected to the coolant in the condenser. Table 1 lists the modelling conditions for the ORC unit, the hot water and the coolant.

The heat exchangers were modelled using *UA* values rather than minimum pinch point temperature differences, in order to control the mean temperature difference of the heat transfer process. This is especially important when comparing the performance of pure and mixed working fluids, as demonstrated by McLinden and Radermacher [15] and Högberg et al. [16] for vapour compression cycles.

The modelling of the cycle followed the procedure outlined by Baik et al. [17] and Andreasen et al. [18], where a total cycle *UA*-value was assigned to the cycle and the distribution of the total *UA*-value to the heat exchangers was optimized. The cycle was optimized with the objective of maximising the net power output, which was calculated as

$$P_{net} = \dot{m}_{wf}\left(h_{03} - h_{04} - (h_{02} - h_{01})\right) \tag{1}$$

where $\dot{m}_{wf}$ is the working fluid mass flow, h is the mass specific enthalpy, the indexes *1* to *4* refer to the thermodynamic state points of Fig. 1 and *0* indicates total quantities.

For the case study concerning heat recovery from the jacket water cooling system, the temperature of the hot water at the outlet of the boiler was fixed at 80 °C. In this case the decision variables for the optimization were the boiler pressure and the fraction of the total *UA*-value which was assigned to the boiler. The total *UA*-value was set to $UA_{tot} = 500$ kW/K, since this ensured to obtain a pinch point value between 3 and 10 K in the entire molar composition range.

For the generic case, without a limitation on the hot water outlet temperature, the decision variables were the boiler pressure, the superheating degree and the fraction of the total *UA*-value which was assigned to the boiler. When the temperature of the hot water was not constrained, it was possible to transfer more heat to the ORC unit. The size of the heat exchangers was therefore allowed increasing compared to the previous case by increasing the total *UA*-value to $UA_{tot} = 1500$ kW/K, since this ensured to obtain reasonable pinch point values within 3-8 K.

The *UA*-values were calculated in the following way by discretization of the heat exchangers

$$UA = \sum_{j=1}^{n} (UA)_j = \sum_{j=1}^{n} \frac{\dot{Q}_j}{(\Delta T_{lm})_j} = \sum_{j=1}^{n} \left[\frac{\dot{m}_c (h_{c,o} - h_{c,i})}{(T_{h,o} - T_{c,i}) - (T_{h,i} - T_{c,o})} \cdot \ln\left(\frac{T_{h,o} - T_{c,i}}{T_{h,i} - T_{c,o}} \right) \right]_j \tag{2}$$

Copyright © 2016 by ASME

TABLE 2: OPTIMIZING PARAMETERS AND CONSTRAINTS OF TURAX

Decision variables	Unit	Lower boundary	Upper boundary	Constraints	Unit	Lower boundary	Upper boundary	Fixed parameters	Unit	Value
ψ	-	2	6	M_{W2}	-	0	0.8	$(t/o)_n$,$(t/o)_r$	-	0.05
$o_{n,min}$	m	0.001	0.100	M_{W3}	-	0	1.4	e_n,e_r	m	10^5
o_r	m	0.001	0.100	α_{FL}	$^\circ$	-25	25	k_s	m	$2\cdot10^{-6}$
c_n	m	0.010	0.100	$(h/D_m)_n$, $(h/D_m)_r$	-	0.001	0.25	hhh	-	1.1
c_r	m	0.010	0.100	$(c/D_m)_n$, $(c/D_m)_r$	-	0	0.25	ε	-	1
$(o/s)_n$	-	sin(13°)	sin(60°)	χ	-	-0.1	0.9	$min(t_{cl})$	m	$2\cdot10^{-4}$
$(o/s)_r$	-	sin(13°)	sin(60°)	z_n, z_r	-	10	130	$min(t_n)$,$min(t_r)$	-	$2\cdot10^{-4}$
Ca_1	$m\cdot s^{-1}$	0	100	U_{tip}	$m\cdot s^{-1}$	0	500	ss/c_n	-	0.5
ϕ_r	-	0	1	Re_n, Re_r	-	10^4	-	N	rpm	3600

$\psi = \Delta h_s/U_{3m}^2$ stage loading coefficient
$\phi_r = Ca_3/U_{3m}$ rotor flow coefficient
(h/D_m) = blade height to mean diameter
(t/o) = trailing edge thickness to opening
ε = degree of admission
M_{W2} = rotor inlet relative Mach number
$o_{n,min}$ = nozzle minimum opening
(c/D_m) = axial chord to mean diameter
e = blade rear suction surface curvature
hhh = annulus blade height ratio
M_{W3} = rotor outlet relative Mach number
(o/s) = opening-to-pitch ratio
ss/c_n = annulus to axial chord spacing
k_s = blade surface roughness
t = blade trailing edge thickness
c = axial chord
α_{FL} = flaring angle
U_{tip} = blade tip speed
t_{cl} = blade tip clearance
z = number of blades

where $\dot{Q}$ is heat transfer rate, ΔT_{lm} is the logarithmic mean temperature difference, T is temperature, subscript j refers to cell j, subscripts c and h refer to the cold and hot side of the heat exchanger and subscripts i and o refer to inlet and outlet. For the boiler 30 cells were used for the discretisation and for the condenser 10 cells were used. These numbers ensured a reasonable trade-off between computational time and accuracy.

2.1 The Axial Turbine Simulation Tool - TURAX

The low expansion ratios (i.e. 2-4) which are found in the case studies make it possible to design an efficient single-stage expander, thus avoiding the need for more advanced and expensive architectures. The preliminary design and the isentropic total-to-total efficiency of the axial turbine were estimated using a mean-line code written in the Matlab® language [19], named TURAX. A brief description of the model, which was introduced in a previous work [10], is provided in this section. The turbine model is based on the efficiency prediction method of Craig and Cox [20]. The correlations developed in the method were based on cascade test data from a large number of steam and gas turbines. The authors claimed efficiency prediction accuracy of $\pm1.25\%$. At present, there is scarce information about the accuracy of the method with organic fluids and mixtures, and several test rigs are under development [21, 22] to investigate the real gas behaviour of these fluids. Nonetheless, there are a number of previous publications [23–25] which employed the Craig and Cox method in ORC field. In their experience, this method is considered as the most reliable one. Other empirical correlations are also used in TURAX.

1. The outlet flow angles of a blade row were estimated with the correlation by Ainley and Mathieson [26]. Vavra's correlation [27] is used for supersonic flow conditions
2. In case of converging-diverging nozzle, the opening was calculated using Deich's formula [28]
3. Shock losses in a blade row were computed according to Kacker and Ockapuu [29]
4. Disk windage losses were estimated according to Balje and Binsley [30]

The total-to-total isentropic efficiency of the turbine can be expressed as

$$\eta_{tt} = f(T_{01}, p_{01}, p_{03}, \dot{m}, fluid, \overline{X}) \tag{3}$$

where T_{01}, p_{01}, p_{03} are the total temperature and pressures at inlet and outlet of the stage, $\dot{m}$ is the mass flow rate, $fluid$ is the selected working fluid, $\overline{X}$ is a set of 9 decision variables related to geometrical and flow features of the stage. The efficiency was maximised by means of a constrained optimization of $\overline{X}$. Additional constraints on the model variables are required, in order to avoid infeasible designs in the solution space [31]. Finally, some model parameters are set to fixed values, in order to reduce the number of optimization variables. Table 2 lists the decision variables of $\overline{X}$, the fixed parameters and constraints.

2.2 Working Fluids

In the present paper, the mixtures R245fa/pentane and propane/isobutane were selected due to the following reasons:

a) The thermodynamic properties can be accurately estimated by experimental validation of their interaction parameters.

Copyright © 2016 by ASME

Equations of state are available for mixtures of hydrocarbons and refrigerants [32–34].

b) All fluids are commercially available and can be employed in ORC power plants. R245fa, pentane, isobutane are used by different manufacturers [35–39]. Propane and isobutane were also used as working fluids in a geothermal binary power plant documented by DiPippo [40].
c) R245fa achieved high performance for the same application in a recent work by Andreasen et al. [18].
d) Another work [5] showed that the mixture propane/isobutane (0.77/0.33) delivers the best power output among low-GWP mixtures in subcritical configuration for a waste heat recovery unit with a 90° C heat source.
e) A subcritical cycle configuration can be used since the critical temperature and pressure of the selected fluids are always higher than those required in the case study.

The thermodynamic properties of each mixture were computed using REFPROP® version 9.0 [41].

2.3 Optimization

The present work combines a constrained optimization of the cycle and the expander, performed through an iterative approach. The objective function of the optimization is the net power output of the ORC unit. The optimisation procedure was executed by combining a particle swarm alghorith with a pattern search method using the Matlab® Optimization Toolbox [42]. The former is population-based method whilst the latter is a direct search method. The reader is referred to Kennedy [43] and Audet et al. [44] for more details. Particle swarm was run with a population size of 1000 and 20 iterations for the turbine model whereas a population size of 50 and 20 iterations were used in the cycle model. A larger population size was selected for the turbine optimization, due to the large number of decision variables. Subsequently, results were used as initial values for the direct search method, which converges more rapidly. This hybrid optimization approach allowed reducing the computational time of using solely a population-based algorithm but with a higher number of iterations.

For every mixture, the following steps were executed:

1. The boundary conditions of the cycle were provided (i.e. heat source temperature, condensation temperature, etc.)
2. A constant isentropic efficiency of the expander, set to the value 0.85, was used in the first iteration
3. The cycle was optimized in the whole molar composition range with a binary mixture composition step of 0.1
4. The inlet temperature, pressure, mass flow rate and the outlet pressure of the expander were used as boundary conditions for the preliminary design of the same device
5. The turbine was optimized in the whole composition range
6. The values of isentropic efficiency of the turbine at each molar composition were used to perform the new cycle simulation

3 RESULTS AND DISCUSSION

3.1 Thermodynamic Cycle Design

Constrained Hot Fluid Outlet Temperature The optimization results of the case with a limit on the minimum heat source temperature are shown in Figs. 2A and 2B. Results with constant turbine efficiency (red triangle markers) and with optimized turbine efficiency (red square markers) are indicated in the charts. Pure fluids yield the maximum net power output for all mixture compositions. In all cases, the optimal power output profile is dominated by the optimal cycle trend, and the optimization of the expander has only a marginal influence. For R245fa/pentane, the maximum isentropic turbine efficiency is obtained with pure R245fa. For propane/isobutane, the maximum isentropic turbine efficiency is using pure isobutane, although the optimal value is practically constant over the entire composition range. From the turbine viewpoint, the plots suggest that the profile of the optima is aligned with that of the cycle for propane/isobutane, and for R245fa/pentane in the molar composition range (0.5/0.5)-(1/0). For propane/isobutane, a more pronounced change in turbine efficiency is observed, leading to an almost flat net power output curve. Nevertheless, this case exhibits the lowest performance in terms of both the cycle and the turbine. Therefore, pure R245fa or pentane can be conveniently chosen, yielding a maximum power output of approximately 200 kW with a turbine efficiency of approximately 0.88. The optimal distribution of the UA-value ratio between boiler and condenser is around 0.5 for all cases.

Unconstrained Hot Fluid Outlet Temperature. The optimization results of this case are shown in Fig. 2C and 2D. The maximum net power output is obtained using a mixture. A molar composition (0.5/0.5) yields the maximum net power using R245fa/pentane and a (0.2/0.8) composition provides the maximum using a propane/isobutane mixture. Considering only turbine performance, the optimal efficiency is found using a pure fluid. In addition, it can be seen that the use of a constant turbine efficiency provides significantly different net power output profiles only when propane/isobutane is used. For R245fa/pentane the optimal turbine efficiency is nearly constant over the entire composition range. This results in a shift in the power profile, without changing its shape and the location of the optimal composition. Conversely, the use of optimized turbine efficiency with propane/isobutane had a stronger impact, so that the maximum shifts from molar composition (0.4/0.6) to (0.2/0.8). Finally, the

Copyright © 2016 by ASME

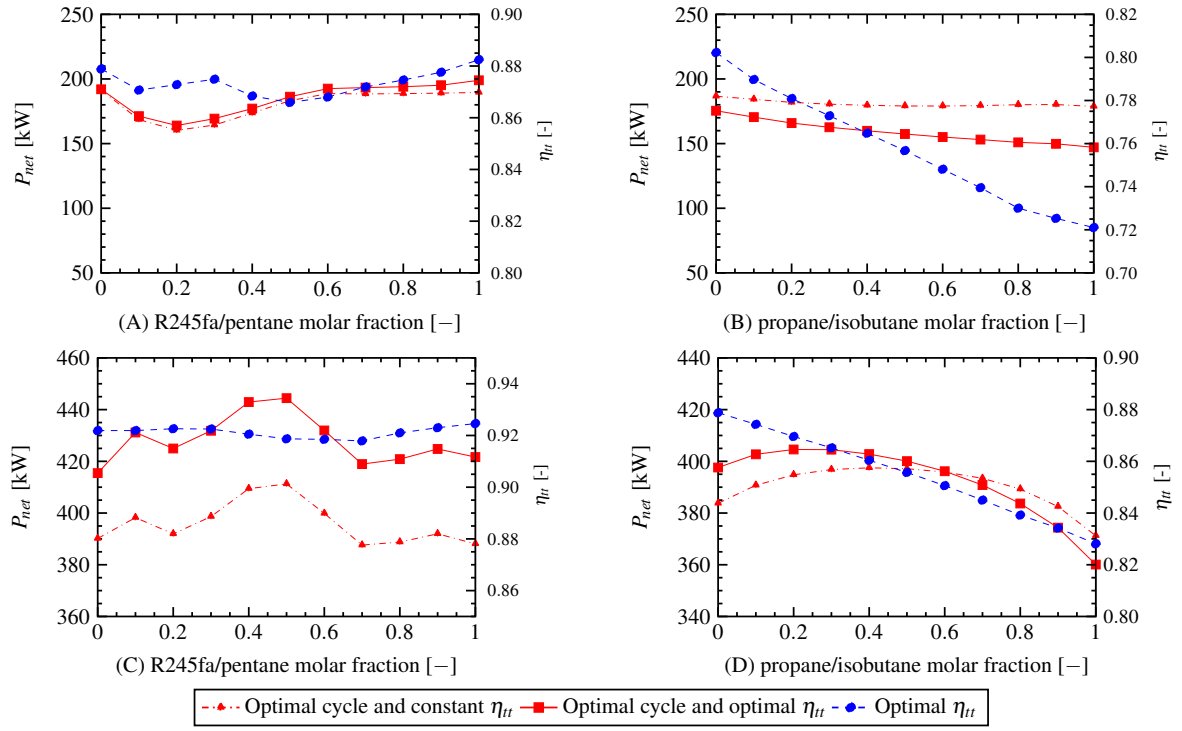

FIGURE 2: OPTIMAL POWER OUTPUT AND TOTAL-TO-TOTAL TURBINE EFFICIENCY VS. MOLAR COMPOSITION OF THE SELECTED MIXTURES. HEAT SOURCE WITH (A),(B) AND WITHOUT (C),(D) LIMITATION ON THE HEAT SOURCE OUTLET TEMPERATURE

optimal UA-ratio is around 0.5 also in this case. The previous results indicate that mixed working fluids are more attractive solutions when the heat source temperature is not bound to a lower limit. The thermodynamic reason can be explained by resorting to the heat power-temperature diagram of Fig. 3, referred to mixture R245fa/pentane. Figures 3A and 3B illustrate the thermal power-temperature diagram for the cases with and without outlet temperature constraint, respectively. In the latter, the hot water (red line) is cooled from 85 to 80 °C. Due to the small temperature change, the use of a mixture does not exhibit particular advantages, and pure R245fa (black line) is found to be the best solution. However, when the heat source temperature is not bound to a lower limit, and is cooled to approximately 72 °C, a mixture of R245fa and pentane (black line in the right figure) provides advantages over a pure fluid. In fact, the trend of the net power output is strongly influenced by the temperature glide. Figure 4 depicts the variation of the temperature glide of evaporation, the degree of superheating and the temperature difference of the hot fluid from the inlet to the location of the bubble point ΔT_{hf} for R245fa/pentane. The temperature profiles of the boiler are matched when ΔT_{hf} matches the temperature glide and the degree of superheat is zero. This occurs at mole compositions of (0.1/0.9) and (0.5/0.5), which explains the peaks in net power output depicted in Fig. 2C. A good match is also achieved at (0.4/0.6) which consequently results in a high net power output. Note also that the trend of the temperature glide in Fig. 4 is opposite of the power profile in Fig. 2A. This indicates that the temperature glide has a negative effect on the net power output when the hot fluid outlet temperature is constrained.

Although pure R245fa and the mixture (0.5/0.5) R245fa/pentane give the maximum net power output for the two cases, the selection of a suitable working fluid should also account for other aspects such as cycle technical viability, safety issues, turbine design and manufacturability, environmental and economic considerations [45, 46]. Table 3 shows the details of the selected cycle and turbine optimal designs. Despite the higher net power output of pure R245fa, it is arguable that the higher pressures and smaller volume flow rate of pure isobutane

Copyright © 2016 by ASME

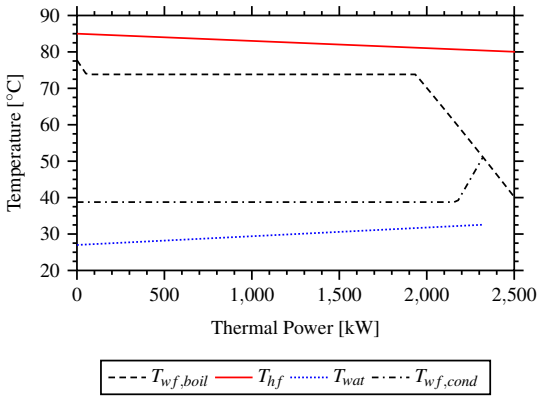

(A) R245fa/pentane (1/0). Temperature constraint

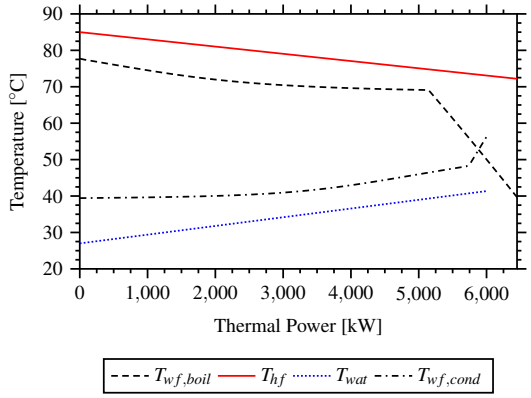

(B) R245fa/pentane (0.5/0.5). No temperature constraint

FIGURE 3: TEMPERATURE-THERMAL POWER DIAGRAM FOR THE OPTIMAL R245FA/PENTANE MIXTURE WITH AND WITHOUT OUTLET TEMPERATURE LIMIT

would result in a more compact condenser. When the minimum temperature is not limited, the mixture R245fa/pentane (0.5/0.5) shows lower condensing and evaporating pressures, and almost as twice the maximum volumetric flow rate of propane/isobutane (0.2/0.8), thus suggesting the use of a bigger condenser.

3.2 Preliminary Turbine Design

The maximum efficiency among the optimal expanders is found using a pure fluid independently of the temperature constraint. It is noted that the efficiency profile has a flat behaviour and small change with the composition using R245fa/pentane, but propane/isobutane exhibits ca. 8 %-points of efficiency decay in the composition range. As an example, Fig. 5A shows

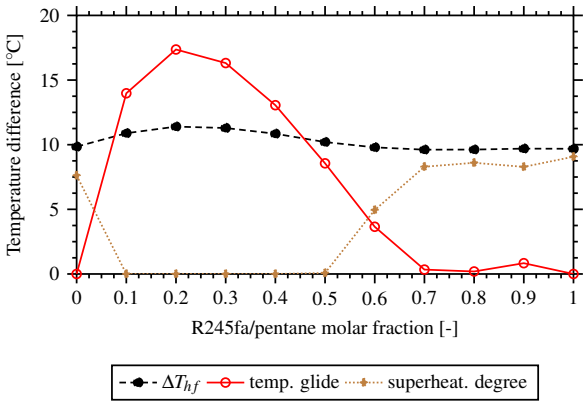

FIGURE 4: HOT FLUID, WORKING FLUID TEMPERATURE GLIDE AND SUPERHEATING IN THE EVAPORATOR. NO TEMPERATURE CONSTRAINT

the breakdown of losses in the whole range of molar composition for the case with boiler outlet temperature constraint. R245fa/pentane has lower losses than propane/isobutane and that the losses do not change significantly with the molar composition. Propane/isobutane has similar values of profile losses but the addition of isobutane increases secondary and tip leakage losses. This effect can be related to a reduction of the blade height. Higher secondary losses are due to a progressive reduction of blade aspect ratio (height over backbone length) of the turbine, which in turn enhances the generation of secondary flows in the blade channels. Figure 5B shows that both mixtures lead to low aspect ratio (< 1) turbine designs, but propane/isobutane has less than half the values of R245fa/pentane. As a result, the former mixture exhibits higher secondary losses. The higher tip leakage is also linked to a smaller blade height, which can be related to the increases of clearance area in relation to the blade throat area. It can be noticed that the trend of aspect ratio for R245fa/pentane is not monotone, but the higher aspect ratio highlights that the change of secondary losses is only marginal and the efficiency profile remains almost flat. The efficiency trends can also be explained resorting to volume flow rate ratio (VFR) and size parameter (SP), in accordance with the analysis of Macchi and Perdichizzi [31]. The former is representative of the compressibility effects of the fluid whereas the latter is representative of the actual dimensions of the turbine. On the one hand, high values of VFR entail low values of efficiency due to increased losses associated to higher deflection in the blade rows and the higher Mach numbers. On the other hand, a small turbine, thus a small SP, penalizes the achievable efficiency due to increased radial clearance effects and shorter blades. Figure 5C shows that both mixtures have VFR values in the same or-

Copyright © 2016 by ASME

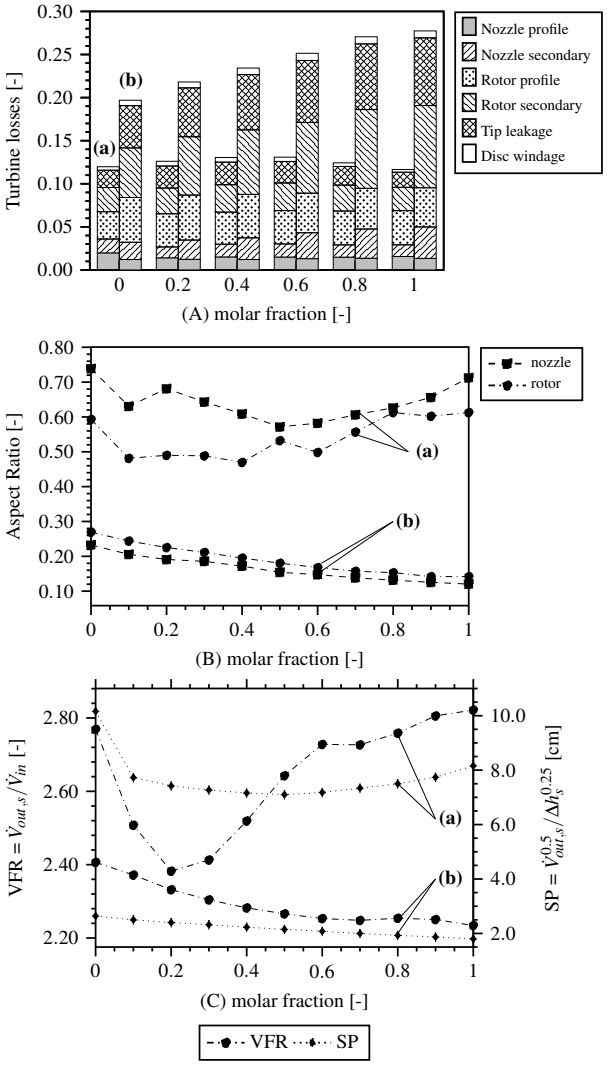

FIGURE 5: BREAKDOWN OF LOSSES FOR THE OPTIMAL R245FA/PENTANE (a) AND PROPANE/ISOBUTANE (b) MOLAR COMPOSITION RANGE WITH OUTLET TEMPERATURE LIMIT

der of magnitude (i.e. 2-3) but different SP values (i.e. 2-4 cm vs. 7-10 cm). As a result, the turbine with the smaller size and employing propane/isobutane shows a lower efficiency. Moreover, for this mixture the reduction in SP more than offsets that of VFR, leading to a lower efficiency. The higher VFR and SP for R245fa/pentane are such that the relative change of these two in the molar composition range does not affect significantly the losses.

Some considerations regarding the feasibility of the obtained preliminary axial turbine designs can be made:

1) A single-stage solution confirms to be feasible for all the fluid candidates. In fact, the low values of volume flow rate ratios (i.e. in the range 2-2.5) and size parameter (i.e. 0.03-0.07 m) are within the range for which high efficiency values of the turbine can be expected [31].

2) Nozzle and rotor blades heights are long enough to be manufacturable in all cases. The smallest value, found in the stator using pure propane with minimum hot fluid temperature constraint, is 5.6 mm. As an example, Verneau [47] documented nozzle blade heights as low as 3.5 mm using a small axial turbine with an organic fluid and partial admission; Invernizzi et al. [48] used rotor blade heights as low as 6.5 mm; Uusitalo [49] set a lower manufacturability constraint on stator blade heights to 1.5 mm in the development of an ORC radial turbine prototype.

3) The hub-to-tip radius ratios are higher than 0.9, thus radial effects are not expected to play an important role in the fluid-dynamic of the turbine and untwisted blades can be manufactured [50].

4) The turbine designs result to have mean diameter between 479 and 657 mm and short axial length between 25 and 35 mm, due to small nozzle and rotor axial chords.

5) A number of blades between 102 and 130 was found in the optimal designs. These values can be found in other ORC applications using axial turbines such as documented by Verneau [47], and even higher values were used by Angelino [51].

6) Converging blades can be used for both nozzle and rotor. A post-expansion process between throat and the blade row downstream can be considered for stator outlet Mach numbers as high as 1.4 according to Deich's method [28], thus avoiding the need for converging-diverging blades. The method can be applied also to rotor blades according to Macchi [52].

7) The optimal designs entail a high reaction turbine, with degree of reaction between 0.55 and 0.76. Advantages and limitations of low and high reaction designs were discussed by Walker and Hesket [53] and Havakechiam and Greim [54], respectively. Low reaction blades enable high stage loading with low interstage swirl, robust rotor blades, less thrust on the rotor and lower tip leakage flows. This would result in highly cambered rotor blades and in the risk of high boundary layer separation and lower efficiency. On the other hand, the larger pressure ratio in the rotor of high reaction turbines could result in higher leakage losses and axial thrust, which

Copyright © 2016 by ASME

may set demands for the design of thrust bearings and may increase the mechanical losses. High reaction designs ensure to have low Mach number, good performance at off-design and avoid a costly diaphragm due to the lower nozzle pressure drop. The option of near 50 % reaction blades would also enable the designer to use similar profiles for both stator and rotor, with consequent cost reduction and easier manufacture.

8) The big difference between total-to-static and total-to-total efficiency values in Tab. 3 shows that high kinetic energy losses are associated with the selected designs. Nonetheless, it is assumed to completely recover such losses using a diffuser before entering the condenser.

9) The gearbox can be conveniently avoided, considering the high efficiency values of the estimated designs. However, it might be taken into account if, for example, a reduction in the mean diameter would be preferred in order to further reduce the volume of the turboexpander.

Pure R245fa is found to be the optimal working fluid also for the turbine when the hot fluid temperature is constrained. In fact, it provided the highest value of efficiency, the smallest turbine volume, requires less number of blades, and higher blade heights with respect to pure pentane. When the temperature was not limited in the boiler, R245fa/pentane (0.5/0.5) provided the best turbine performance and lowest heat exchangers pressures. Although the expander volume increased by +60 % with respect to the optimal propane/isobutane mixture, the larger net power output of the cycle might arguably justify the additional turbine cost.

TABLE 3: OPTIMAL TURBINE AND CYCLE DESIGN PARAMETERS

Parameter	Unit	R245fa/pentane		propane/isobut.	
		Temp. limit	No limit	Temp. limit	No limit
Cycle					
Optimal molar composition	-	(1/0)	(0.5/0.5)	(0/1)	(0.2/0.8)
Mass flow rate, $\dot{m}$	kg/s	11.98	24.75	6.92	16.99
Turbine outlet pressure, P_{cond}	bar	2.40	2.80	5.13	6.73
Turbine inlet pressure, P_{boil}	bar	6.74	6.41	11.83	13.40
Turbine inlet temperature, T_{in}	K	350.46	351.13	350.80	353.79
Cycle net power output, P_{net}	kW	198.97	444.43	175.43	404.59
Boiler UA-value, $(UA)_{boil}$	W/K	250	750	250	750
Max. condenser volume flow	m^3/s	0.93	2.17	0.56	1.09
Max. boiler volume flow	m^3/s	0.009	0.027	0.013	0.032
Turbine					
Isentropic efficiency (t-t), η_{tt}	%	88.00	91.87	80.22	87.43
Isentropic efficiency (t-s), η_{ts}	%	73.56	82.98	60.52	67.87
Stage loading coefficient, ψ	-	4.15	3.27	4.85	4.74
Rotor flow coefficient, ϕ_r	-	0.50	0.44	0.54	0.49
Degree of reaction, χ	-	0.66	0.57	0.76	0.72
Specific diameter, D_m/SP	-	5.86	5.21	9.56	6.56
Specific speed, $D_m\Delta h_s^{1/4}/\dot{V}_{out,s}^{1/2}$	-	0.039	0.053	0.020	0.031
Nozzle outlet Mach number, M_2	-	0.88	0.86	0.71	0.69
Rotor inlet Mach number, M_{W2}	-	0.27	0.25	0.21	0.22
Rotor outlet Mach number, M_{W3}	-	1.24	1.01	1.22	1.09
Mean diameter, D_m	mm	479	600	560	554
Nozzle blade height, h_2	mm	13.3	27.5	5.6	14.0
Rotor outlet blade height, h_3	mm	16.6	28.5	7.3	14.9
Nozzle axial chord, c_n	mm	10.8	12	10.1	10.3
Rotor axial chord, c_r	mm	13.9	15.6	12.1	10.4
Nozzle opening, o_n	mm	3.3	3.7	3.1	3.6
Rotor opening, o_r	mm	3.8	4.5	3.1	3
Nozzle blade pitch, s_r	mm	14.8	16.1	13.8	16.0
Rotor blade pitch, s_n	mm	14.4	15.3	13.7	13.3
Number of nozzle blades, z_n	-	102	118	128	110
Number of rotor blades, z_r	-	106	124	130	130
Turbine volume	dm^3	5.77	10.40	6.87	6.56

4 CONCLUSION

This paper presented a methodology where both cycle and expander designs were simultaneously optimized. The method was applied to two case studies utilizing a low-temperature heat source. A limitation on the minimum hot fluid temperature was analysed in the first case, while no constraint was set in the second case. The working fluid mixtures R245fa/pentane and propane/isobutane were investigated. Results suggest that the combined optimization methodology is advantageous, especially in the presence of a heat source temperature variation higher than 5 °C and for the mixture propane/isobutane. When the outlet temperature is constrained, only a small change in the maximum net power output is observed compared to assuming a constant isentropic efficiency. However, a change of 8 % in the optimal objective function and a shift in the maximum optimal composition are seen for propane/isobutane in the second case study. In the first case study, pure fluids provide the maximum net power output. R245fa results to be the optimal working fluid for both cycle and turbine, yielding approximately 200 kW of net power output, the lowest cycle operating pressures, the smallest turbine with a maximum efficiency of 88 % and the lowest number of blades. Multi-component working fluids yield the best performance when the heat source outlet temperature is not bound. A trade-off is seen between expander size and maximum net power output in this case. R245fa/pentane (0.5/0.5) provides the best cycle and expander performance, and also results in the biggest expander. Due to the 60 % smaller turbine size and the more compact condenser, the choice of Propane/isobutane (0.2/0.8) can be eventually considered whereby the application is limited by space constraints.

Copyright © 2016 by ASME

ACKNOWLEDGMENT

The research work was conducted within the frame of the THERMCYC project ("Advanced thermodynamic cycles utilizing low-temperature heat sources"; see http://www.thermcyc.mek.dtu.dk/) funded by Innovations-Fonden, The Danish Council for Strategic Research in Sustainable Energy and Environment. The financial support is gratefully acknowledged.

REFERENCES

[1] Colonna, P., Casati, E., Trapp, C., Mathijssen, T., Larjola, J., Turunen-Saaresti, T., and Uusitalo, A., 2015. "Organic Rankine Cycle Power Systems: From the Concept to Current Technology, Applications, and an Outlook to the Future". *Journal of Engineering for Gas Turbines and Power,* ***137***(10), pp. 1–19.

[2] Angelino, G., and Colonna Di Paliano, P., 1998. "Multicomponent working fluids for organic Rankine cycles (ORCs)". *Energy,* ***23***(6), pp. 449–463.

[3] Heberle, F., Preißinger, M., and Brüggemann, D., 2012. "Zeotropic mixtures as working fluids in Organic Rankine Cycles for low-enthalpy geothermal resources". *Renewable Energy,* ***37***(1), pp. 364–370.

[4] Chys, M., van den Broek, M., Vanslambrouck, B., and De Paepe, M., 2012. "Potential of zeotropic mixtures as working fluids in organic Rankine cycles". *Energy,* ***44***(1), pp. 623–632.

[5] Andreasen, J., Larsen, U., Knudsen, T., Pierobon, L., and Haglind, F., 2014. "Selection and optimization of pure and mixed working fluids for low grade heat utilization using organic Rankine cycles". *Energy,* ***73***, pp. 204–213.

[6] Zhao, L., and Bao, J., 2014. "The influence of composition shift on organic Rankine cycle (ORC) with zeotropic mixtures". *Energy Conversion and Management,* ***83***, pp. 203–211.

[7] Jung, D., McLinden, M., Radermacher, R., and Didion, D., 1989. "Horizontal flow boiling heat transfer experiments with a mixture of R22/R114". *International journal of heat and mass transfer,* ***32***(1), pp. 131–145.

[8] Braimakis, K., Karellas, S., Preiinger, M., Brggemann, D., and Panopoulos, K., 2015. "Low grade waste heat recovery with subcritical and supercritical Organic Rankine Cycle based on natural refrigerants and their binary mixtures". *Energy,* ***88***, pp. 80–92.

[9] Chaitanya Prasad, G., Suresh Kumar, C., Srinivasa Murthy, S., and Venkatarathnam, G., 2015. "Performance of an organic Rankine cycle with multicomponent mixtures". *Energy,* ***88***, pp. 1–7.

[10] La Seta, A., Andreasen, J. G., Pierobon, L., Persico, G., and Haglind, F., 2015. "Design of organic Rankine cycle power systems accounting for expander performance". In 3rd International Seminar on ORC Power Systems, Brussels, 12-14 Oct.

[11] Larsen, U., Pierobon, L., Haglind, F., and Gabrielii, C., 2013. "Design and optimisation of organic Rankine cycles for waste heat recovery in marine applications using the principles of natural selection". *Energy,* ***55***(45), pp. 803–812.

[12] Yang, M.-H., and Yeh, R.-H., 2015. "Thermo-economic optimization of an organic Rankine cycle system for large marine diesel engine waste heat recovery". *Energy,* ***82***, pp. 256–268.

[13] Maraver, D., Royo, J., Lemort, V., and Quoilin, S., 2014. "Systematic optimization of subcritical and transcritical organic rankine cycles (orcs) constrained by technical parameters in multiple applications". *Applied Energy,* ***117***, pp. 11–29.

[14] Tchanche, B. F., Papadakis, G., Lambrinos, G., and Frangoudakis, A., 2009. "Fluid selection for a low-temperature solar organic Rankine cycle". *Applied Thermal Engineering,* ***29***(11), pp. 2468–2476.

[15] McLinden, M. O., and Radermacher, R., 1987. "Methods for comparing the performance of pure and mixed refrigerants in the vapour compression cycle". *International Journal of Refrigeration,* ***10***(6), pp. 318–325.

[16] Högberg, M., Vamling, L., and Berntsson, T., 1993. "Calculation methods for comparing the performance of pure and mixed working fluids in heat pump applications". *International Journal of Refrigeration,* ***16***(6), pp. 403–413.

[17] Baik, Y. J., Kim, M., Chang, K. C., Lee, Y. S., and Yoon, H. K., 2013. "A comparative study of power optimization in low-temperature geothermal heat source driven R125 transcritical cycle and HFC organic Rankine cycles". *Renewable Energy,* ***54***, pp. 78–84.

[18] Andreasen, J., Larsen, U., and Haglind, F., 2015. "Design of organic rankine cycles using a non-conventional optimization approach". In 28th International Conference on Efficiency, Cost, Optimization, Simulation and Environmental Impact of Energy Systems, 29 Jun. - 03 Jul. , Pau, France, pp. 1–12.

[19] Mathworks. MATLAB 2015b Documentation. www.mathworks.com.

[20] Craig, H., and Cox, H., 1970. "Performance estimation of axial flow turbines". *Proceedings of the Institution of Mechanical Engineers,* ***185***(1), pp. 407–424.

[21] Spinelli, A., Pini, M., Dossena, V., Gaetani, P., and Casella, F., 2013. "Design, simulation, and construction of a test rig for organic vapors". *Journal of Engineering for Gas Turbines and Power,* ***135***(4), pp. 1–10.

[22] Mathijssen, T., Gallo, M., Casati, E., Nannan, N., Zamfirescu, C., Guardone, A., and Colonna, P., 2015. "The flexible asymmetric shock tube (fast): a ludwieg tube facility for wave propagation measurements in high-temperature vapours of organic fluids". *Experiments in Fluids,* ***56***(10), pp. 1–12.

[23] Macchi, E., and Perdichizzi, A., 1981. "Efficiency prediction for axial-flow turbines operating with nonconventional fluids". *Journal of Engineering for Gas Turbines and Power,* ***103***(4), pp. 718–724.

[24] Lozza, G., 1982. "A comparison between the Craig-Cox and the Kacker-Okapuu methods of turbine performance prediction". *Meccanica,* ***17***(4), pp. 211–221.

[25] Klonowicz, P., Heberle, F., Preißinger, M., and Brüggemann, D., 2014. "Significance of loss correlations in performance prediction of small scale, highly loaded turbine stages working in Organic Rankine Cycles". *Energy,* ***72***, pp. 322–330.

[26] Ainley, D. G., and Mathieson, G. C. R., 1951. A method of performance estimation for axial-flow turbines. Tech. rep., Aeronautical Research Council Great Britain.

[27] Vavra, M., 1969. Axial flow turbines. Tech. rep., Von Karman

Copyright © 2016 by ASME

Institute For Fluid Dynamics, Rhode-Saint-Genése, Belgium.
[28] Deich, M., 1965. *Atlas of Axial Turbine Blade Cascades: By M.E. Deich, G.A. Filippov and L.Ya. Lazarev*. C.E. Trans. 4563-4564. CEGB Information Services.
[29] Kacker, S. C., and Okapuu, U., 1982. "A Mean Line Prediction Method for Axial Flow Turbine Efficiency". *Journal of Engineering for Power,* ***104***, p. 111.
[30] Balje, O. E., and Binsley, R. L., 1968. "Axial turbine performance evaluation .a. loss-geometry relationships". *Journal of Engineering for Power,* ***90***(4), p. 341.
[31] Macchi, E., and Perdichizzi, A., 1981. "Efficiency Prediction for Axial-Flow Turbines Operating with Nonconventional Fluids". *Journal of Engineering for Power,* ***103***(4), pp. 718–724.
[32] Lemmon, E. W., 2004. "Equations of State for Mixtures of R-32, R-125, R-134a, R-143a, and R-152a". *Journal of Physical and Chemical Reference Data,* ***33***(2), p. 593.
[33] Kunz, O., Klimeck, R., Wagner, W., and Jaeschke, M., 2007. "The GERG-2004 Wide-Range Equation of State for Natural Gases and Other Mixtures". pp. 1–555.
[34] Outcalt, S. L., and Lemmon, E. W., 2013. "Bubble-Point Measurements of Eight Binary Mixtures for Organic Rankine Cycle Applications". *Journal of Chemical & Engineering Data,* ***58***(6), pp. 1853–1860.
[35] Turboden, 2016. Turboden: Clean Energy Ahead. www.turboden.eu. Accessed Jan. 1, 2016.
[36] Ormat Technologies, 2016. Green Energy You Can Rely On. www.ormat.com. Accessed Jan. 1, 2016.
[37] Atlas Copco, 2016. EG, EGi, EEGi-Series Atlas Copco Gas and Process. http://www.atlascopco-gap.com/products/expanders/eg-egi-eegi-series. Accessed Jan. 1, 2016.
[38] Calnetix, 2016. Organic Rankine Cycle Systems. http://www.calnetix.com/organic-rankine-cycle-systems. Accessed Jan. 1, 2016.
[39] Quoilin, S., Broek, M. V. D., Declaye, S., Dewallef, P., and Lemort, V., 2013. "Techno-economic survey of Organic Rankine Cycle (ORC) systems". *Renewable and Sustainable Energy Reviews,* ***22***, pp. 168–186.
[40] DiPippo, R., 2012. *Geothermal power plants: principles, applications, case studies and environmental impact*. Butterworth-Heinemann. Chapter 8.
[41] Lemmon, E. W., Huber, M. L., and McLinden, M. O., 2002. NIST reference fluid thermodynamic and transport properties–REFPROP.
[42] Coleman, T., Branch, M. A., and Grace, A., 1999. *Optimization Toolbox for Use with MATLAB: User's Guide, Version 2*. Math Works, Incorporated.
[43] Kennedy, J., 2010. "Particle swarm optimization". In *Encyclopedia of Machine Learning*. Springer, pp. 760–766.
[44] Audet, C., and Dennis, J. E., 2003. "Analysis of generalized pattern searches". *Siam Journal on Optimization,* ***13***(3), pp. 889–903.
[45] Tabor, H., and Bronicki, L., 1964. Establishing criteria for fluids for small vapor turbines. Tech. rep., SAE Technical Paper.
[46] Bao, J., and Zhao, L., 2013. "A review of working fluid and expander selections for organic rankine cycle". *Renewable and Sustainable Energy Reviews,* ***24***, pp. 325–342.
[47] Verneau, A. "Supersonic Turbines for Organic Fluid Rankine Cycles From 3 to 1300 kW". *Small High Pressure Ratio Turbines*. (VKI Lecture Series 1987-2007) Von Karman Institute For Fluid Dynamics, Rhode-Saint-Genése, Belgium.
[48] Invernizzi, C., Iora, P., and Silva, P., 2007. "Bottoming micro-Rankine cycles for micro-gas turbines". *Applied thermal engineering,* ***27***(1), pp. 100–110.
[49] Uusitalo, A., 2014. "Working Fluid Selection and Design of Small-scale Waste Heat Recovery Systems Based on Organic Rankine Cycles". Doctoral thesis Lappeenranta University of Technology.
[50] Saravanamuttoo, H. I. H., Rogers, G. F. C., and Cohen, H., 2001. *Gas turbine theory*. Pearson Education.
[51] Angelino, G., Macchi, E., and Gaia, M., 1985. *Design, Construction and Testing of a Hermetically Sealed 100 kW Organic Rankine Cycle Engine for Medium Temperature (200-400 °C) Heat Recovery: Final Report*. Commission of the European Communities; Directorate-general Science, Research and Development.
[52] Macchi, E. "Design criteria for turbines operating with fluids having a low speed of sound". *Closed Cycle Gas Turbines*. (VKI Lecture Series 100) Von Karman Institute For Fluid Dynamics, Rhode-Saint-Genése, Belgium.
[53] Walker, P., and Hesketh, J., 1998. "Design of low-reaction steam turbine blades". *Proceedings of the Institution of Mechanical Engineers, Part C: Journal of Mechanical Engineering Science,* ***213***(2), pp. 157–171.
[54] Havakechian, S., and Greim, R., 1999. "Aerodynamic design of 50 per cent reaction steam turbines". *Proceedings of the Institution of Mechanical Engineers, Part C: Journal of Mechanical Engineering Science,* ***213***(1), pp. 1–25.

Nomenclature

(o/s)	Opening-to-pitch ratio [-]
(t/o)	Trailing edge thickness to opening ratio [-]
C	Absolute velocity [$m \cdot s^{-1}$]
Ca	Axial velocity [$m \cdot s^{-1}$]
D_m	Mean diameter of the stage [m]
M_W	Relative Mach number [-]
N	Rotational speed [rpm]
P_{net}	Cycle net power output [kW]
Re	Reynolds number [-]
T	Temperature [K]
U	Peripheral velocity [$m \cdot s^{-1}$]
U_{tip}	Tip Speed [$m \cdot s^{-1}$]
W	Relative velocity [$m \cdot s^{-1}$]
ΔT_{ml}	Logarithmic mean temperature difference [K]
$\dot{Q}$	Thermal power [W]
$\dot{m}$	Mass flow rate [$kg \cdot s^{-1}$]
c	Axial chord [m]
c/D_m	Chord to mean diameter ratio [-]
h	Blade height [m]; specific enthalpy [$J \cdot kg^{-1}$]
h/D_m	Blade height to mean diameter ratio [-]
hhh	Rotor inlet to nozzle outlet blade height ratio [-]

Copyright © 2016 by ASME

k_s	Blade surface roughness [m]
o	Blade opening [m]
p	Pressure [Pa]
ss	Annulus axial spacing [m]
t_{cl}	Tip clearance [m]
z	Number of blades [-]
UA	Overall heat transfer coefficient times area [$W \cdot K^{-1}$]
e	Blade rear suction surface curvature [m]
t	Trailing edge thickness [m]

Abbreviations and acronyms

AR	Aspect ratio of the blade
ORC	Organic Rankine cycle
SP	Size parameter of the turbine [m]
VFR	Volume flow rate ratio of the turbine [-]

Greek letters

α_{FL}	Flaring angle [°]
χ	Stage degree of reaction [-]
ε	Degree of admission [-]
η_{tt}	Turbine total-to-total isentropic efficiency [-]
ϕ	Flow coefficient [-]
ψ	Stage loading coefficient [-]

Subscripts

1	Referred to the nozzle inlet
2	Referred to the rotor inlet
3	Referred to the rotor outlet
boil	Referred to the boiler
c	Referred to the cold side fluid
cond	Referred to the condenser
h	Referred to the hot side fluid
hf	Referred to the hot fluid
i	Referred to the inlet
in	Referred to the inlet
in	Referred to the turbine inlet
m	Referred to the mean diameter
min	Referred to the minimum opening
n	Referred to the nozzle; number of discretizations in the heat exchangers
o	Referred to the outlet
r	Referred to the rotor
s	Referred to isentropic conditions
ts	Referred to total-to-static conditions
tt	Referred to total-to-total conditions
w	Referred to the relative coordinate system
wat	Referred to water
wf	Referred to the working fluid

Copyright © 2016 by ASME

Appendix D. Articles

Applied Energy 209 (2018) 339–354

Contents lists available at ScienceDirect

Applied Energy

journal homepage: www.elsevier.com/locate/apenergy

Optimization of organic Rankine cycle power systems considering multistage axial turbine design

Andrea Meroni[a,*], Jesper Graa Andreasen[a], Giacomo Persico[b], Fredrik Haglind[a]

[a] Department of Mechanical Engineering, Technical University of Denmark, Nils Koppels Allé, Building 403, 2800 Kongens Lyngby, Denmark
[b] Dipartimento di Energia, Politecnico di Milano, Via Lambruschini 4, 20156 Milano, Italy

HIGHLIGHTS

- A design methodology for ORC considering multistage axial turbine design is presented.
- A multistage axial turbine model is presented and validated.
- The methodology is applied to a waste heat recovery case on a container ship.
- n-butane and R245fa show the best trade-off between cycle and turbine design.
- The best solutions feature a single-stage with highly supersonic flow conditions.

ARTICLE INFO

2010 MSC:
00-01
99-00

Keywords:
Organic Rankine cycle
Axial turbine
Multistage turbine
Waste heat recovery
Marine diesel engine
Optimization

ABSTRACT

Organic Rankine cycle power systems represent a viable and efficient solution for the exploitation of medium-to-low temperature heat sources. Despite the large number of commissioned units, there is limited literature on the design and optimization of organic Rankine cycle power systems considering multistage turbine design. This work presents a preliminary design methodology and working fluid selection for organic Rankine cycle units featuring multistage axial turbines. The method is then applied to the case of waste heat recovery from a large marine diesel engine. A multistage axial turbine model is presented and validated with the best available data from literature. The methodology allows the identification of the most suitable working fluid considering the trade-off between cycle and multistage turbine designs. The results of the optimization of cycle and turbine suggest that the fluid n-butane yields the best compromise in terms of cycle net power output, turbine cost and efficiency for the considered case study. When a conservative design approach is adopted, the turbine features a two-stage configuration with supersonic converging nozzles and post-expansion. Conversely, a single-stage turbine featuring a supersonic converging-diverging nozzle and Mach number up to 2 is the resulting ideal choice when a more advanced design approach is implemented.

1. Introduction

Organic Rankine cycle power systems are employed in a range of different fields such as biomass applications, geothermal heat recovery, industrial waste heat recovery and solar applications. Compared to gas and steam turbines, the relatively small enthalpy drop in the expansion is advantageous for the ORC turbine design since it allows for the use of only one or a few turbine stages. For a given external heat source, the preliminary design of the ORC systems is performed by optimization of the thermodynamic cycle, which is typically hampered by technical and practical constraints. The system components such as the expander, heat exchangers and pump can be included in the cycle optimization or can be optimized in a subsequent stage of the design process.

Even though different aspects can be included in the preliminary design of ORC systems, a number of authors [1–4] have highlighted that the expander and working fluid are the two key elements.

Song et al. [5], Yun et al. [6], Yang and Yeh [7,8] and Andreasen et al. [9] performed design and optimization of ORC systems for marine applications but neglected the details of the expander design. Toffolo et al. [10], Maraver et al. [11] and Vivian et al. [12] proposed different methodologies for selecting the optimal working fluid and cycle configuration in ORC systems; however, in all cases the isentropic turbine efficiency was set to a fixed value. Astolfi et al. [13] and Martelli et al. [14] performed detailed thermodynamic and techno-economic analyses

* Corresponding author.
E-mail addresses: andmer@mek.dtu.dk (A. Meroni), jgan@mek.dtu.dk (J.G. Andreasen), giacomo.persico@polimi.it (G. Persico), frh@mek.dtu.dk (F. Haglind).

http://dx.doi.org/10.1016/j.apenergy.2017.09.068
Received 7 April 2017; Received in revised form 17 August 2017; Accepted 10 September 2017
Available online 22 September 2017
0306-2619/ © 2017 Elsevier Ltd. All rights reserved.

Nomenclature

C	absolute velocity [m·s^{-1}]; cost [k€]
Dev.	deviation [–]
M	Mach number [–]
N	rotational speed [rpm]
P	cycle power output [kW]
PI	performance index [kW·k€$^{-1}$]
PR	pressure ratio [–]
Re	Reynolds number [–]
T	temperature [K]
U	peripheral velocity [m·s^{-1}]
W	relative velocity [m·s^{-1}]
$\dot{Q}_{sc}$	scavenge air heat flow rate [W]
$\dot{m}$	mass flow rate [kg·s^{-1}]
c	axial chord [m]
c_p	molar heat capacity [J·kg^{-1}·K^{-1}]
e	blade rear surface suction curvature [m]
h	blade height [m]; specific enthalpy [J·kg^{-1}]
k_s	blade surface roughness [m]
n	number of stages [–]
o	blade opening [m]
p	pressure [Pa]
r	radius [m]
ss	nozzle to rotor axial clearance [m]
ss_{st}	interstage axial clearance [m]
t	trailing edge thickness [m]
t_{cl}	blade tip clearance [m]
z	number of blades [–]
DR	stage degree of reaction [–]
SP	turbine size parameter [m]
UA	overall heat transfer coefficient times area [kW·K^{-1}]

Abbreviations and acronyms

CFD	computational fluid dynamics
GWP	global warming potential
ODP	ozone depleting potential
ORC	organic Rankine cycle
TURAX	axial turbine simulation tool

Greek letters

α	absolute flow angle [°]
β	relative flow angle [°]
ϵ	residual error [–]
η	turbine isentropic efficiency [–]
ϕ	flow coefficient [–]
ψ	isentropic stage loading coefficient [–]

Subscripts

0	total conditions
1	nozzle inlet
2	rotor inlet
3	rotor outlet
a	axial component
c	critical
el	electrical
gear	gearbox
gen	generator
m	referred to the mean diameter
max	maximum
min	referred to the minimum opening
n	nozzle
net	net power
o	outlet
r	rotor
s	isentropic conditions
st	referred to one stage
t	turbine
tip	referred to the blade tip
tot	referred to the total turbine expansion
ts	total-to-static
tt	total-to-total
turb	turbogenerator
w	referred to the relative coordinate system

on ORC systems including multistage turbine optimization for geothermal and biomass applications, respectively. The aforementioned authors designed the ORC system by means of an assumption of the turbine efficiency, or estimated the turbine performance by interpolation of a statistical correlation developed for single-stage machines. Da Lio et al. [15] tackled the issue by constructing performance maps for single-stage axial turbines including the critical temperature of the working fluid as an additional parameter. Recently, White and Sayma [16] proposed a coupled analysis and optimization process of a small-scale ORC and a single-stage radial turbine with the aim to improve the economy-of-scale of the system. The authors developed performance maps based on a modified similitude theory to predict the performance of the turbine and of the ORC system.

In previous publications the present authors [17,18] developed a methodology for a coupled optimization of an organic Rankine cycle unit and an axial turbine, and demonstrated that it is essential to include the design of the turbine in order to make accurate estimations of the cycle performance. In Refs. [17,18], a single-stage axial turbine model was validated and employed. However, multistage turbine solutions are more suitable for applications requiring large power output and high expansion ratio, since they ensure better efficiency and limit the turbine loading under these conditions [19]. Multistage axial turbine arrangements are used by many ORC manufacturers, as documented in Colonna et al. [20], and a number of exemplary turbines have been documented, see Table 1. However, the literature on their design and optimization procedures is very limited. Some authors [21–25] presented the main criteria used in the development of the turbines in Table 1, however without providing the full details of their design and optimization methods. Other authors [26–28] have focused only on the analysis of the flow and performance of multistage ORC turbines using CFD techniques for a given turbine geometry. In all previous references, i.e. Refs. [21–28], the multistage turbine design was decoupled from the optimization of the ORC system. To the best of our knowledge, the most advanced approach where the multistage turbine performance is included in the ORC system optimization, is that proposed recently by Macchi and Astolfi [19]. They constructed a priori correlations to predict the turbine isentropic efficiency as a function of the size parameter and volume flow rate ratio for a fixed number of stages (up to three). The formula was developed using a mean-line model [34] employing ideal gas assumptions and optimizing the rotational speed. By using the proposed correlations, the thermodynamic cycle can be optimized to assess the impact of the different number of stages on the system performance. The approach by Macchi and Astolfi [19] is very general; however, it does not provide a specific optimal design for the considered application, i.e. the rotational speed is always set to the optimal value, the fluid is considered as an ideal gas, and the number of stages is limited to three. Moreover, the approach follows the same design philosophy for single and multi-stage turbine

Appendix D. Articles

Table 1
Documented multistage ORC axial turbines.

Author	Manufacturer	Year	Field	Power [kW]	N_{st}	Pressure ratio	N [rpm]	rm [mm]	Fluid	Ref.
Verneau	Bertin & Cie	1977	Solar	54	2	142	7700	145	*FC-75*	[24]
Osnaghi et al.	Gemmindustria	1979	Solar	8	2	120	24,000	90	C_6H_5Cl	[22]
Bado et al., Angelino et al., Barutti et al.	Gemmindustria	1979–1983	Solar	35	4	116	6700	120	C_8F_{16}	[21,29,30]
Verneau	Bertin & Cie	1980	WHR	1350	2	100	14,000	176	*Fluorinol 85*	[24]
Angelino et al.	Turboden	1984	WHR	100	2	24.9	3030	430	$C_6H_4Cl_2$	[23,31]
Angelino et al.	Turboden	1984	WHR	100	2	13.64	3030	430	C_8H_{10}	[31]
Jokinen et al.	n/a	1998	WHR	25	2	> 100	40,000–48,000	n/a	*Toluene*	[25]
Obernberger and Hammerschmid	Turboden	2001	Biomass	400	2	n/a	n/a	n/a	*Silicon oil*	[32]
Nasir et al.	Ormat Inc.	2003	WHR	4500	2	~30	3600	n.a.	*n-pentane*	[33]

configurations; whereas in real applications key decision criteria such as performance, cost, working fluid limitations and technical aspects may set additional constraints on the turbine design, leading to different solutions.

There are a few mean-line models for multistage ORC turbine design in use by companies and research institutes, including AXTUR [35], used in the aforementioned approach by Macchi and Astolfi [19], and zTurbo [36,37]. These codes underwent intense development, and their reliability was successfully assessed by several companies [38]; however, their detailed validation has yet to be published in the scientific literature (even though, in the case of zTurbo, a partial validation was presented in Ref. [39]). For this reason, there is the need to publish validation details of multistage ORC turbine models in the open literature.

The objective of this paper is to extend the design methodology of ORC power systems by including the optimal preliminary design of the axial turbine in the most general multistage layout. To this end, the paper presents a comprehensive strategy for turbine model validation, cycle and turbine combined optimization, and analysis of the results. This work is limited to consider steady-state analyses at design conditions. A multistage turbine model is developed and validated with two well-documented test cases from the literature, one of which is an ORC turbine. The design methodology for cycle and turbine is presented, and two different turbine design approaches are proposed. Then, the methodology is applied to the case of waste heat recovery from a large marine diesel engine, in order to show how it can be used in a real application.

This paper introduces several novel elements: (i) it presents the detailed validation of a mean-line model of ORC multistage axial turbines; (ii) it considers two alternative turbine design approaches, which designers may adopt according to their key decision criteria; (iii) it proposes a methodology for combined optimization of an ORC system and an ORC multistage turbine, in which the turbine layout and performance become additional criteria for the working fluid selection in a specific application.

Compared to the method used by Macchi and Astolfi [19], the methodology presented here allows optimizing the cycle and turbine for a specific application and including real-gas models. Overall the results and the method provide a solid contribution to state-of-the-art, of relevance for researchers as well as engineers and decision-makers.

The paper is structured as follows: Section 2 presents the case study, the methods for the cycle and turbine designs, the criteria for the working fluid selection, and the validation of the multistage turbine model. Section 3 presents the results of the turbine model validation and of the optimization with the ORC system. Section 4 discusses the results. Conclusions are drawn in Section 5.

2. Methods

Fig. 1 illustrates a schematic of the workflow methodology adopted in this study. Two different turbine design approaches were adopted, namely *conservative design* and *advanced design*, which are explained in more detail in Section 2.4. Based on the inputs from the case study (Section 2.1), a working fluid preselection process was performed (Section 2.2). As a starting point, an isentropic turbine efficiency of 0.8 and a single-stage design were assumed. Then, cycle and turbine were optimized for each working fluid candidate following an iterative process described in Section 2.6. In the conservative design approach, the maximum Mach number in the optimized turbine solutions was checked for being within a predefined value to ensure a conservative turbine design (see Section 2.4). If the constraint was not satisfied, a new combined optimization step was performed using an additional turbine stage. Finally, a performance index was computed (Section 3.3), incorporating the effects of both turbine and cycle designs. This parameter was also used to select the minimum number of stages in the *advanced design* approach and to decide on the possible insertion of a gearbox. A number of fluid candidates having the highest performance index was selected. The selection of the most suitable working fluid is

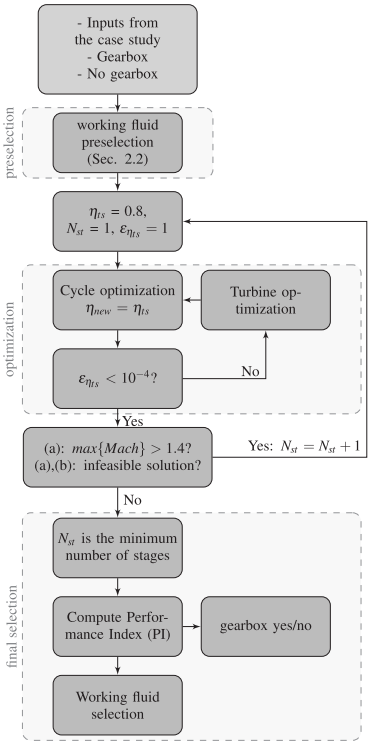

Fig. 1. Flow chart of the adopted methodology for the cases with (a) conservative design and (b) advanced design.

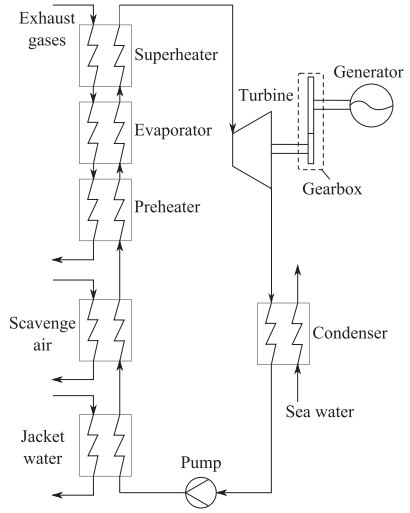

Fig. 2. Organic Rankine cycle unit.

discussed (Section 4) based on technical and environmental aspects, and the requirements of the specific application. The aforementioned steps and the validation of the multistage turbine model are described hereafter.

2.1. Case study and cycle modelling

The selected case study is the waste heat recovery from the exhaust gases, jacket cooling water and scavenge air of a 37 MW diesel engine aboard a container ship [40]. The engine employs a heavy fuel oil with sulphur content, of about 3% and operates most of the time at low loads. In order to exploit fully the engine's waste heat, without oversizing the unit, we chose to design the ORC system at 75% engine load. Fig. 2 shows a sketch of the ORC unit, and Table 2 lists the ORC modelling conditions. In addition to the exhaust gases, the jacket water and scavenge air were included as heat sources in order to obtain a higher system net power output from the ORC unit, and to preheat the working fluid at the pump outlet to the required level to avoid sulphuric acid condensation [41]. We found that a recuperator is not required. When the exhaust gases exit the engine, they are first used for generating service steam (2 t/h) for onboard heating purposes. After the service steam-boiler, the exhaust gases enter the ORC at 235.85 °C. The temperature of the working fluid at the boiler inlet was limited to 135 °C to avoid sulphuric acid condensation [40]. The turbine can potentially be equipped with a gearbox, affecting both the system performance and turbine design. The suitability of the gearbox solution is discussed in Section 3. The heat exchangers in the cycle were modelled with a pinch point approach.

Table 2
Modelling conditions of the ORC unit.

Parameter	Value	Unit
Exhaust gases		
Inlet temperature	235.85	°C
Mass flow	62.6	kg/s
Heat capacity	1.1	kJ/(kg·K)
Boiler		
Pinch point	20	°C
Minimum inlet temperature	135	°C
Condenser		
Fluid condensation temperature	30	°C
Pump		
Isentropic efficiency	0.7	–
Turbine		
Isentropic efficiency (initial iteration)	0.8	–
Minimum outlet vapour quality	1	–
Gearbox efficiency	0.97	–
Generator efficiency	0.95	–
Jacket water		
Available heat flow rate	9230	kW
Fluid outlet temperature	80	°C
Scavenge air		
Inlet temperature	166.3	°C
Available heat flow rate	9230	kW

2.2. Preliminary working fluid selection

In order to screen the suitability of the different working fluid candidates, some preselection criteria were used. Fluid candidates were selected according to indications in the literature [5,42–45] for a waste heat recovery source of 235 °C, and according to their availability in commercial units [20,43,46]. The working fluids were discarded in the case they presented the following attributes: a thermal stability limit lower than the hot fluid inlet temperature, a critical temperature lower than the minimum admissible temperature at the boiler inlet, a non-zero ozone depleting potential (ODP) [47] or a global warming potential (GWP) > 150 [48]. In the latter case, exception was made for those fluids currently used by manufacturers. Practical limitations on maximum and minimum pressures allowed in the ORC unit were also considered based on the indications by Rayegan et al. [49], Drescher and Brüggeman [50], and MAN Diesel & Turbo [40]. Finally, the work was limited to subcritical cycle operation, with a maximum limit of 0.8 in reduced pressure, in order to avoid excessive pressure in the boiler and problems during operating conditions close to the critical point. Table 3 shows the list of preselected working fluids.

2.3. Multistage axial turbine model

TURAX is a mean-line model for the design and performance prediction of single and multistage axial turbines. In its present status the model is limited to steady-state analyses at design conditions. The model has been particularly conceived (i) to simulate axial-flow turbines operating with organic fluids and (ii) to perform a coupled optimization with the design of the ORC system. The details of the single-stage axial turbine model were presented in previous publications [17,18]. The main features of the multistage axial turbine model are described hereafter:

(1) TURAX performs the design of a multistage turbine by simultaneous optimization of each stage variable, in agreement with the indications by Persico and Pini [38] for ORC turbines. The decision variables of the multistage model are given in Table 4. The stage inlet axial velocity is specified only for the first stage, and the rotational speed is the same for all stages, since they are assumed to be mounted on the same shaft. In total 8 variables per stage are specified as input, in addition to rotational speed and stage inlet axial velocity.
(2) The pressure ratio of each stage is optimized based on the isentropic stage loading coefficient ψ_n. For a constant radius turbine design, the following relation holds:

$$\Delta h_{0s,tot} = \frac{U_m^2}{2} \cdot \sum_{n=1}^{N_{st}} \psi_n \quad (1)$$

By means of Eq. (1) it is possible to compute the mean peripheral speed U_m and isentropic enthalpy drop $\Delta h_{0s,tot}$, thus also the total

Table 3
Preliminary screening of working fluid candidates.

Fluid	T_c [K]	GWP [–]	ODP [–]	Tox./flamm.(*) [–]	Thermal stability limit [K]	Condensation pressure(**) [bar]	Manufacturer [–]	Ref. [–]
n-pentane	469.7	4 ± 2	0	4/1	573.15–588.15	0.82	Ormat Atlas Copco	[51–53]
isopentane	460.3	4 ± 3	0	4/1	500.15–588.15	1.09	Ormat Atlas Copco	[51–53]
MM	518.7	~0	0	3/0	573.15	0.07	Turboden	[54–56]
n-hexane	507.8	4–6	0	3/1	n.a.	0.25	–	
cyclopentane	511.7	< 25	0	3/1	513.15–548.15	0.51	Ormat Turboden GE Oil & Gas Atlas Copco Aqylon	[57–59,52,53,56,60,61]
benzene	562.0	3.4	0	3/2	> 723.15	0.16	–	[51]
cyclohexane	553.6	4–6	0	3/1	n.a.	0.16	–	
toluene	591.7	3.3	0	3/2	> 588.15;	0.0489	Tri-o-gen Aqylon	[57,62,51,63,64,61]
n-butane	425.1	4	0	4/1	563.15–693.15	2.83	Atlas Copco Ormat	[53,52]
R245fa	427.2	1030	0	0/2	523.15–573.15	1.78	Turboden GE-Energy Calnetix Cryostar Atlas Copco E-rational	[65,56,53,66–68]
ethanol	514.71	0	0	3/2	550	0.10	–	

(*) = According to standard NPFA 704.
(**) At 30°C. n.a. = datum not available.

pressure ratio distribution across the stages.
(3) The flow angle and absolute velocity at the outlet of a stage were assumed to be the same as those at the inlet of the subsequent stage.
(4) The method by Craig and Cox [69] was employed, since it is the most comprehensive for the preliminary design of an ORC turbine. [23,34,35,70]. The loss correlations used in the model were described in a previous work [17]. Supersonic converging nozzle blades are used for exit Mach numbers between 1 and 1.4, allowing a post-expansion downstream the blade opening. For higher Mach numbers, a supersonic adapted converging-diverging nozzle is used instead. In order to preserve the validity of the employed loss correlations and avoid high losses due to supersonic conditions, the rotor shape is converging with maximum relative Mach numbers at the rotor inlet and outlet of 0.8 and 1.4, respectively [71]. If the nozzle exit flow has a Mach number below 1.4, the throat is calculated as the minimum opening provided as input. Alternatively, it is calculated by a mass balance between the throat and the outlet of the nozzle, assuming a constant blade height in the divergent part. When an adapted converging-diverging nozzle was used, the blade profile design was assumed to be optimized, and the profile loss increment due to high Mach numbers is neglected as recommended in Dunham and Came [72].

Table 4
Decision variables of the multistage turbine model.

Decision variable	Unit	Symbol	Stage
(1) Isentropic stage loading coefficient	–	$\psi = \frac{2\Delta h_{is}}{U_{3m}^2}$	all
(2) Nozzle minimum opening	m	o_{min}	all
(3) Rotor opening	m	o_r	all
(4) Nozzle axial chord	m	c_n	all
(5) Rotor axial chord	m	c_r	all
(6) Nozzle opening-to-pitch ratio	–	$(o/s)_n$	all
(7) Rotor opening-to-pitch ratio	–	$(o/s)_r$	all
(8) Rotational speed	rpm	N	first
(9) Stage inlet axial velocity	m/s	C_{a1}	first
(10) Rotor flow coefficient	–	$\phi_r = \frac{C_{a3}}{U_{3m}}$	all

2.4. Selection of the number of stages

The selection of the optimal number of stages may be based on a techno-economic analysis or on turbine aerodynamics and performance considerations. A number of different approaches to this topic can be found in Refs. [13,14,38,73]. Nonetheless, an unequivocal method for the selection of the number of stages of ORC turbines has not been identified in the literature. This paper presents and compares two different approaches.

The first approach (denoted as *conservative approach*) follows a conservative turbine aerodynamic design, where the maximum Mach number in each stage is set to 1.4. This method allows avoiding excessive losses related to highly-supersonic flow conditions in the blade rows and the use of a simpler blade design (i.e. converging nozzle blades with post-expansion), and it can ensure higher reliability and performance at off-design conditions [21]. Moreover, it avoids using the conventional loss estimation procedures for highly supersonic flow conditions, for which not fully reliable correlations are available [74]. This method was adopted by previous authors [36,75,76] in the design of ORC turbines.

A more compact solution would possibly employ converging-diverging nozzle blades with highly supersonic flows. For this reason, a second approach (denoted as *advanced approach*) is presented. In this case, the turbines have a higher stage loading and are designed with adapted converging-diverging nozzles. This approach was adopted by some other authors, see i.e. [24,25], in the design of ORC turbines.

2.5. Turbine model validation

This multistage axial turbine model was validated using the design data of two reference turbines, having the most comprehensive and detailed information on experimental characterization and turbine geometry. The two test cases can be considered representative of the conservative and the advanced design approach, respectively. In addition, in the second test case, an uncertainty analysis was carried out in order to quantify the effects of the uncertainty in the assumed input parameters, on the results. The uncertainty analysis was applied only to

Table 5
Decision and input variables of TURAX for the Hannover [77,78] and Verneau [24,85] turbines test cases.

		Hannover turbine								Verneau turbine			
		Stage 1		Stage 2		Stage 3		Stage 4		Stage 1		Stage 2	
Symbol	Units	Nozzle	Rotor	Nozzle	Rotor	Nozzle	Rotor	Nozzle	Rotor	Nozzle	Rotor	Nozzle	Rotor
ψ	–	2.61		2.61		2.61		2.61		4.62		1.48	
$o_{n,min}$,o_r	mm	12.24	13.52	13.01	13.65	13.84	13.79	14.78	13.94	1.00	3.50	1.52	2.03
c_n,c_r	mm	44.80	39.10	44.30	38.50	45.50	37.50	46.50	37.50	20.00	28.00	37.00	37.00
$(o/s)_n$,$(o/s)_r$	–	0.332	0.393	0.342	0.383	0.353	0.372	0.365	0.360	0.276(**)	0.467	0.500(**)	0.423(**)
N	rpm	7500										7700	
C_{a1}	m/s	57.8										1.23	
ϕ_r	–	0.435		0.440		0.430		0.42		0.61		0.42	
$\dot{m}$	kg/s	7.8										1.6	
α_1	°	−5.57										0	
T_{01}	K	404.63										489	
p_{01}	Pa	$2.58{\cdot}10^5$										$11.2{\cdot}10^5$	
p_{03}	Pa	$1.05{\cdot}10^5$										$0.09{\cdot}10^5$	
ss	mm	235		200		195		180		300		300	
ss_{st}	mm	610		595		640		643		500		500	
$(t/o)_n$,$(t/o)_r$	–	0.0361	0.0302	0.0361	0.0284	0.0360	0.0267	0.0360	0.0249			0.05(**)	
t_{cl}	mm	0.4										0.2(**)	

(*) = estimated value.
(**) = assumed value with uncertainty.

the second test case, since the geometry of the first test case is well defined.

Four-stage subsonic turbine. The first case study is a subsonic four-stage turbine operated with air whose design performance and flow characteristics are described in Kötzing and Evers [77] and in Hirsch and Denton [78]. The turbine generates 703 kW at 7500 rpm, has a total-to-static pressure ratio of approximately 2.6 and a calculated total-to-total efficiency of 91.3% with an estimated accuracy of 0.8% [77,79]. The blades are of the free-vortex type, designed for a 50% degree of reaction in the middle section. Kötzing and Evers [77] suggested the presence of uncertainty in the experimental data. In order to improve the reliability of the validation, the results of TURAX were also compared to the Computational Fluid-Dynamic (CFD) data documented in Gerolymos and Hanisch [80] and Croce et al. [81]. These two are representative of state-of-the-art modelling techniques for multistage turbines [80–82] and have been validated using other experimental turbomachinery data [83,84].

Table 5 lists the input data used for model validation. Blade opening, pitch, stator-rotor axial clearance and interstage axial gap at the mean-line section were extracted by interpolation from the design data in the references. The axial velocity at the turbine inlet was computed by mass and energy balances. Flow coefficients were found by obtaining the actual turbine mean-line diameter and the best possible match with the actual blade height at the stage outlet. A straight blade profile in the rear suction side after the opening and a surface roughness of $2{\cdot}10^{-3}$ mm were used in the calculations. Thermodynamic and flow conditions at the different turbine sections used for the comparison were estimated by applying mass-weighted averages to the experimental and CFD profiles, except for the pressure that was estimated as an area-weighted average. The thermodynamic properties of air were computed using REFPROP [86].

Two-stage ORC turbine. The second reference case for the validation of the multistage turbine model is a supersonic two-stage turbine used for a small demonstration solar power plant, whose design data and test results are presented by Verneau [24,85] and Boy-Marcotte [87]. The turbine features a first, highly-loaded impulse stage with converging-diverging nozzle blades, and a second stage with 50% reaction blading. The fluorochemical FC-75 is employed as the working fluid and the turbine produces approximately 54 kW at 7700 rpm with a measured total-to-static efficiency of 78%.

Table 5 shows the input data used in the validation of TURAX. Since the blade angle at the first rotor outlet was not provided, the actual value of the flow angle 56.7° was imposed in order to limit the uncertainty of preliminary calculations. The stage loading coefficients in the two stages were selected in order to match the actual mean radius and peripheral speed. The geometric data that were not provided by Verneau were assumed as indicated in Table 5. Opening-to-pitch ratios in the first stage nozzle and in the second stage were estimated using the cosine rule of the mean-line exit flow angles given in Ref. [24]. The throat at the nozzle and rotor exit in the second stage were computed based on the assumed values of opening-to-pitch and the known pitch. Trailing edge to opening ratios and tip clearance were assumed as in Macchi [71]. The axial velocity at the turbine inlet was computed by mass and energy balances. A straight blade profile in the rear suction side after the throat and a surface roughness of $2{\cdot}10^{-3}$ mm were used. The thermodynamic properties of FC-75 were computed using the Peng-Robinson equation of state. The critical properties of FC-75 were used as in Kluwick [88] and the ideal molar heat capacity coefficients were estimated with the method by Joback and Reid [89]. The ideal molar heat capacity c_p, expressed in $J{\cdot}mol^{-1}{\cdot}K^{-1}$, was computed as a fourth-degree polynomial function of temperature with coefficients $A = -230.11$, $B = 2.6724$, $C = -0.0034$, and $D = 2.00 \cdot 10^{-6}$.

The uncertainty analysis using the Monte Carlo method [90] was carried out on the assumed parameters in order to evaluate the effect of their uncertainty on the results. The 6 uncertain parameters and their assumed values are indicated in Table 5. They were varied in the range ± 10%, which was selected to yield less than 5° of flow deviation at the rotor outlet in the second stage and at the nozzle outlet in the first stage, as expected for the type of blading employed in the test case [91]. A number of 500 samples was used for each variable, and a uniform distribution without correlation control was applied. A model in the Matlab environment originally developed by Sin et al. [92] and modified for the scope of this work was used.

2.6. Design optimization

In this work, turbine and cycle models were combined and optimized following the iterative procedure illustrated in Fig. 1 and described in Section 2. The optimization boundaries are described in La Seta et al. [18]. However, the approach in [18] was based on the use of

a surrogate model for the turbine, whereas a new approach was adopted in this study since it does not require the computational efforts of generating numerous design points for each fluid and number of stages. The objective function of the cycle and turbine optimizations are the net power output and the turbine efficiency, respectively, defined as

$$P_{net} = \dot{m}_{wf}(\Delta h_{0,t} - \Delta h_{0,p}), \quad \eta = \frac{\Delta h_{0,t}}{\Delta h_{ts} - 0.5 \cdot \frac{C_{a3}^2}{2}} \tag{2}$$

The parameter $\dot{m}_{wf}$ is the working fluid mass flow rate, and $\Delta h_{0,t}$ and $\Delta h_{0,p}$ are the total-to-total enthalpy drops across the turbine and the pump, respectively. The term Δh_{ts} denotes the total-to-static isentropic enthalpy drop across the turbine, and the coefficient 0.5 indicates that 50% of the kinetic energy is assumed to be recovered by a diffuser downstream the last stage. Cycle and turbine designs were optimized by means of a hybrid optimization approach combining Particle Swarm optimization with a direct search method. A population size of 2000 and 500 for cycle and turbine were selected, since they provided a good compromise between accuracy and computational time. The turbine was designed considering the cases of optimized and fixed rotational speed. If the optimal rotational speed was lower or equal to that required by the generator (3600 rpm aboard the ship), the gearbox was not used and the rotational speed was fixed to the value 3600, 1800 or 1200 rpm. A maximum value of 500 m/s for the rotor blade tip speed was imposed as the optimization constraint, in order to limit mechanical stress issues.

3. Results

3.1. Validation

Four-stage subsonic turbine. Table 6 shows the results of the validation. The deviation between experimental and TURAX values is expressed as $Dev = (TURAX - datum)/datum$, where *datum* refers to the corresponding experimental value. When experimental data are not available for comparison or are considered uncertain, the deviation is calculated with respect to the CFD data by Gerolymos et al. [80] and Croce et al. [81]. The deviation in the flow angles is expressed in absolute difference.

The total pressure and temperature at the outlet of the different stages, p_{03} and T_{03}, show good agreement with experimental and CFD data, with deviations smaller than 0.5%. The deviation in static pressure p_3 is higher and up to 1.7%. Notwithstanding the lack of reliable velocity data in the experimental results, the comparison between TURAX and CFD calculations of Croce et al. [81] shows a maximum discrepancy of 3.5% in absolute velocity C_3, possibly due to the discrepancy in static pressure. Although experimental data of the rotor outlet relative flow angle β_3 were not provided, the comparison with the CFD data of Gerolymos et al. [80] suggests agreement within 3°. The absolute flow angle at the rotor outlet α_3 has a deviation up to 8° with experimental data. This high value might stem from the discrepancy in C_3. Fig. 3 shows the profiles of the main quantities at the exit of each stage. Despite the difference between the experimental and predicted velocity profiles, the average values of TURAX provide a reasonable match with the CFD profiles. Fig. 4 shows the meridional turbine layout obtained with TURAX. The blade heights are computed with good accuracy, with less than 3% deviation, as a result of the relatively small discrepancies in the flow and thermodynamic quantities. The predicted total-to-total efficiency of the stages resulted to be within 0.2%-points of the CFD values, and within 1.72%-points of the experimental values. The results of this validation are considered to be satisfactory and confirm that TURAX is suitable for the preliminary design and performance prediction of multistage turbine architectures featuring subsonic flow conditions and high-aspect ratio blade profiles.

Two-stage supersonic ORC turbine. Table 7 reports the results of the validation with the two-stage ORC turbine described by Verneau [24,85]. The values of standard deviation obtained with the uncertainty analysis are shown in absolute terms. The thermodynamic and flow

Table 6
Comparison of results obtained with TURAX, CFD, and experimental investigations [77,78] on the four-stage Hannover turbine.

Symbol	Units	Exp. data	TURAX	CFD	Dev.	Exp. data	TURAX	CFD	Dev.
		Stage 1				Stage 2			
T_{03}	K	384.81	384.60	382.72*	0.05%	363.12	363.43	362.13*	−0.09%
p_{03}	Pa	$2.12 \cdot 10^5$	$2.11 \cdot 10^5$	$2.09 \cdot 10^5$ *	0.32%	$1.70 \cdot 10^5$	$1.70 \cdot 10^5$	$1.69 \cdot 10^5$ *	−0.02%
p_3	Pa	$2.07 \cdot 10^5$	$2.08 \cdot 10^5$		−0.62%	$1.66 \cdot 10^5$	$1.67 \cdot 10^5$		−0.91%
C_3	m/s	73.33	57.96	59.78**	3.05%	73.0	60.02	60.19**	0.28%
β_3			65.93	65.85**	0.08		66.62	66.97**	−0.35
α_3		0.62	−3.47	4.65*	4.10	−4.76	2.30	6.67*	−7.06
$h1$	m	0.0595	0.0594		0.17%	0.0675	0.0682		−1.04%
h_{21}	m	0.0635	0.0635		0.00%	0.0725	0.0736		−1.52%
h_3	m	0.0675	0.0682		−1.04%	0.0775	0.0766		1.16%
DR	-		0.347	n.a.			0.4269		
η_{st}	-	89.91%	91.49%	91.45%*	0.0%	92.52%	92.22%	92.10%*	0.1%
		Stage 3				Stage 4			
T_{03}	K	340.377	341.95	341.40*	−0.46%	321.034	320.23	319.57*	0.25%
p_{03}	Pa	$1.35 \cdot 10^5$	$1.35 \cdot 10^5$	$1.36 \cdot 10^5$ **	−0.18%	$1.05 \cdot 10^5$	$1.05 \cdot 10^5$	$1.05 \cdot 10^5$ *	−0.17%
p_3	Pa	$1.31 \cdot 10^5$	$1.32 \cdot 10^5$		−1.06%	$1.01 \cdot 10^5$	$1.03 \cdot 10^5$		−1.70%
C_3	m/s	73.193	60.79	60.33**	−0.77%	81.401	62.04	64.30**	3.52%
β_3			67.40	67.04**	0.36		68.28	65.22**	3.06
α_3		−2.159	4.39	4.70*	6.55	−0.608	7.35	−0.57 *	−7.96
$h1$	m	0.0775	0.0767		1.03%	0.0892	0.0885		0.78%
h_{21}	m	0.0833	0.0846		−1.50%	0.0961	0.0988		−2.81%
h_3	m	0.0892	0.0885		0.78%	0.1030	0.1026		0.39%
DR	–		0.47				0.54		
η_{st}	–	n/a	92.55%	92.80%*	0.2%	n/a	92.94%	92.73%**	0.2%
η_{tt}	–	91.3%	93.02%	92.96%	1.72 pp				

pp = percentage-points. n/a = not available.
* = Gerolymos et al. [80].
** = Croce et al. [81].

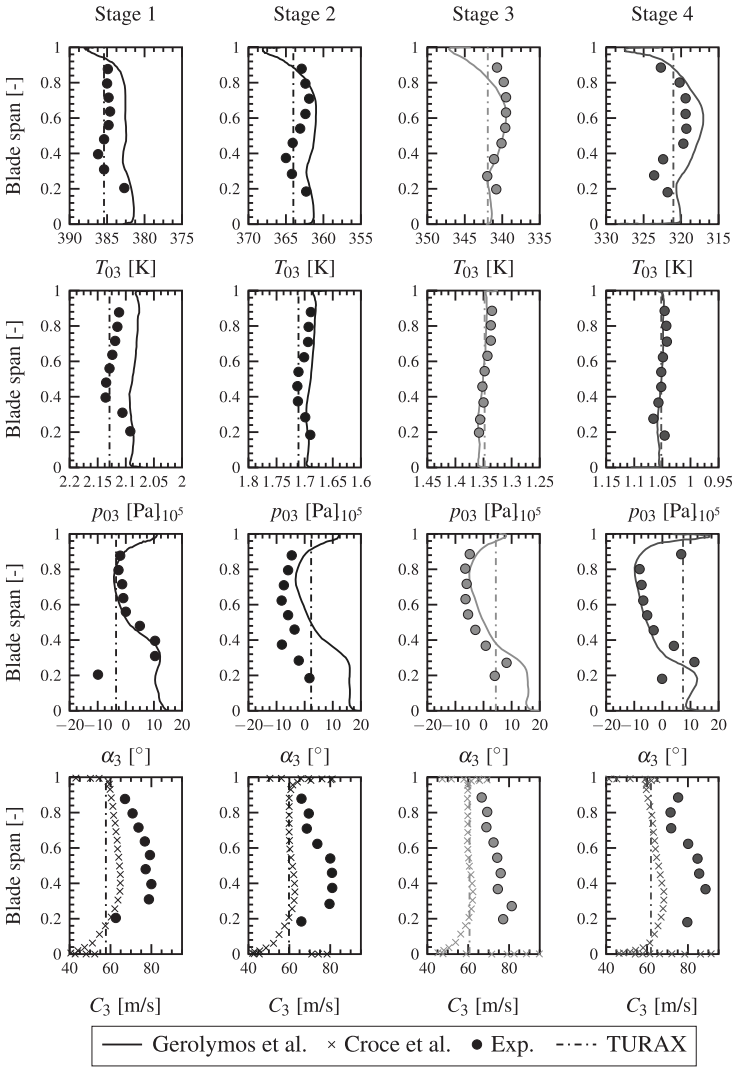

Fig. 3. Profiles of total temperature, total pressure, absolute flow angle, absolute velocity at the stage outlet. Data from experimental results [77], Gerolymos et al. [80], Croce et al. [81] and TURAX for the Hannover turbine test case.

quantities in the two stages show a good agreement with the data of Verneau, with deviations up to 3% in the first stage and 8.5% in the second stage. Static pressure and absolute Mach number at the first and the second stage outlet, respectively, show a mismatch up to 6.3% which is possibly related to the discrepancy in the velocity values. Fig. 4 shows the meridional profile of the turbine computed by TURAX (red) and the original profile (black) from Verneau [24]. Blade heights and number of blades are calculated with less than 3% deviation except at the turbine outlet, where the deviation is up to 5.6%. TURAX computed total-to-static efficiency values of 73.22% and 81.53% for the first and the second stage, respectively. The predicted efficiency was 79.76% and differed by 1.76%-points from the experimental value of Verneau. Fig. 5 shows the scatter plot of turbine efficiency after uncertainty propagation and the ranking of the uncertain parameters. The parameters with a greater impact on the results were the opening-to-pitch ratio, responsible for the calculation of the exit flow angle, and the blade surface roughness, responsible for frictional effects on the blades. The stage inlet flow angle, tip clearance, trailing edge thickness-to-opening ratio and backbone surface curvature provided only a marginal change in efficiency. Moreover, the data of Verneau are in many cases comprised in the standard deviation range of TURAX. In light of the complexity of phenomena related to the design of a two-stage supersonic turbine with an organic fluid, the obtained discrepancy of less than 2%-points is considered satisfactory for a preliminary design tool.

3.2. Design optimization

Fig. 8 shows the cycle net power output, Fig. 9 the turbine efficiency and Fig. 10 the minimum required number of stages obtained by the optimization for both the conservative and the advanced approaches.

Fig. 8 highlights that different values of net power output can be obtained depending on turbine modelling criteria and configurations.

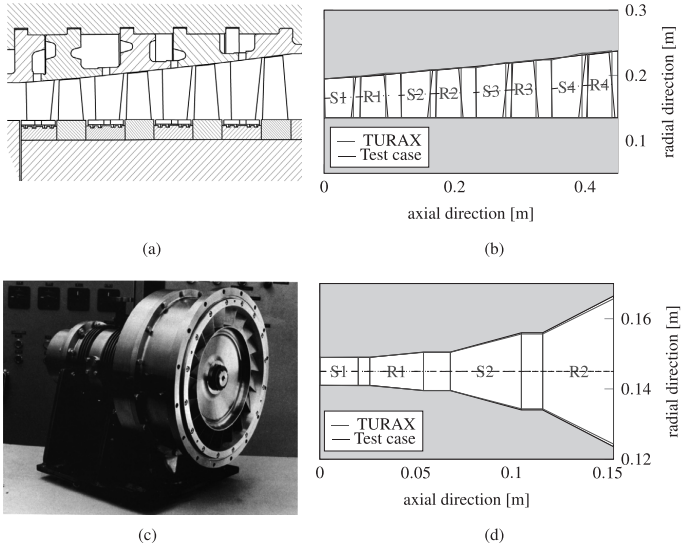

Fig. 4. (a) Subsonic turbine test case (adapted from [77]); (b) meridional cut layout of the subsonic turbine; (c) supersonic ORC turbine test case [87]; (d) meridional cut layout of the supersonic ORC turbine.

For the fluid MM, the adoption of the methodology presented in this work results in unfeasible design solutions for one and two stages. Feasible solutions are found using three stages with the advanced design and five stages in the case a conservative approach is preferred. Different values of net power output are obtained when the turbine is optimized together with the cycle. From the thermodynamic perspective, n-butane ranks as the most promising candidate, followed by R245fa, isopentane and n-pentane. When the turbine design is

Table 7
Comparison of results between TURAX and Verneau [24,85] data on a two-stage ORC turbine.

		Stage 1				Stage 2			
Parameter	Units	Verneau	TURAX	St.dev.	Dev.	Verneau	TURAX	St.dev.	Dev.
α_2	°	74	73.99	0.95	0.00	60	58.87	2.44	1.12
β_2	°	59.20	59.55	1.56	0.36	−33	−29.24	8.54	3.75
Ca_2	m/s	65	65.46	4.11	0.7%	49	53.16	7.72	8.5%
C_2	m/s	235	237.41	1.39	1.0%	98	102.56	9.42	4.7%
W_2	m/s	126	129.15	2.2	2.5%	58.5	61.38	4.9	5.0%
M_2	–	2.45	2.48	0.014	2.5%	1.02	1.06	0.1	4.9%
M_{w2}	–	1.32	1.35	0.02	2.4%	0.61	0.64	0.05	5.0%
p_2	Pa	$3.08 \cdot 10^4$ *	$3.00 \cdot 10^4$	996	−2.9%	15,292	$1.43 \cdot 10^4$	1650	−6.3%
T_2	K	459.40 *	458.79	0.25	−0.1%	457.15	457.14	0.74	−0.1%
W_3	m/s	130	127.76	0	−1.7%	118	116.57	6.76	−1.2%
Ca_3	m/s	71	70.14	0	−1.2%	49	49.1	0	0.2%
C_3	m/s	72	70.87	0	−1.6%	49	50.89	1.64	3.9%
M_{w3}	–	1.35	1.33	0	−1.3%	1.24	1.22	0.07	−1.7%
M_3	–	0.75	0.74	0	−1.5%	0.51	0.53	0.02	3.8%
β_3	°	56.7	56.7	0	0.00	65	65	1.55	−0.01
α_3	°	−6.8	−8.21	0	−1.41	−10	−12.62	8.22	−2.62
T_{03}	K	461.23 *	460.78	0.06	−0.1%	454.11	454.38	0.1	0.1%
T_3	K	459.77 *	458.86	0.06	−0.2%	453.2	453.4	0.09	0.0%
p_3	Pa	$2.24 \cdot 10^4$	$2.1 \cdot 10^4$	0.74	−6.3%	7900	$7.78 \cdot 10^3$	72.1	−1.5%
p_{03}	Pa	$2.76 \cdot 10^4$ *	$2.77 \cdot 10^4$	0	0.1%	9021.9	$8.98 \cdot 10^4$	0	−0.5%
h_1	m	0.008	0.0079	0	1.3%	0.011	0.0109	0	1.2%
h_2	m	0.008	0.0082	0	−2.1%	0.022	0.0214	0.001	2.8%
h_3	m	0.011	0.0109	0	1.3%	0.043	0.0415	0	3.4%
z_n	–	25	27	1	2.00	30	30	2	0.46
z_r	–	121	122	0	1	19	20	1	1
DR (theor.)	–	0.086	0.093	0.009	0.01	0.50	0.47	0.09	−0.03
Power	kW	40	40.78	0.089	−2.0%	14	14.28	0.14	−2.0%
η_{st}	–	75%	73.21%	0.29 pp	1.8 pp	82%	80.96%	1.25 pp	1 pp
η_t	–	78%	79.72%	0.40 pp	1.76 pp				

St.dev. = standard deviation from the uncertainty analysis. pp = percentage-points.
* = computed from the design point velocity triangles.

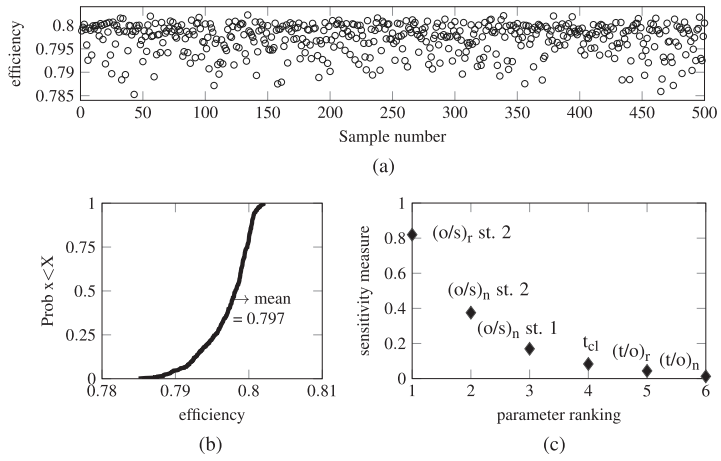

Fig. 5. Results of the uncertainty analysis on the assumed parameters of the two-stage supersonic turbine: (a) scatterplot of uncertainty in turbine efficiency; (b) corresponding cumulative distribution function; (c) ranking of the uncertain parameters based on significance level.

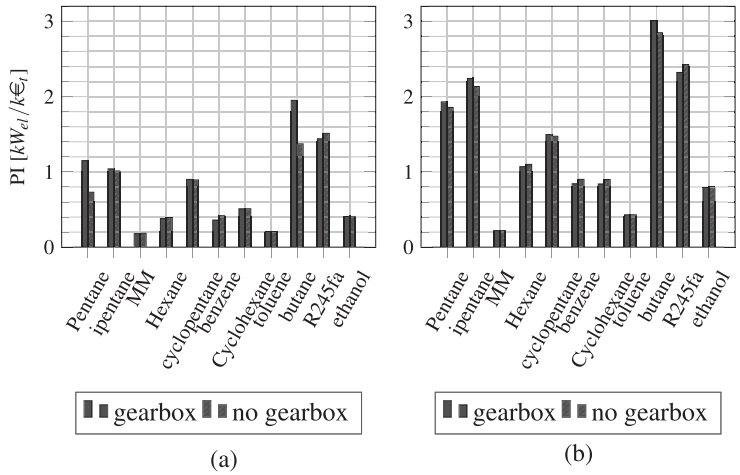

Fig. 6. Performance Index (PI) of the working fluid candidates according to (a) the conservative and (b) the advanced design approaches.

optimized for constant rotational speed, the net power output declines in most of the cases, since the machine is not operating at the optimal specific speed. In this case, R245fa outperforms n-butane thanks to the lower optimal rotational speed (approximately 7200 rpm). When a conservative design approach is adopted, almost all solutions except MM require two or three stages, with turbine efficiencies between 85% and 93% in most cases. Not much difference is observed in the required number of stages with optimized or constant rotational speed, except for n-pentane and n-butane due to the higher values of rotational speed between 9000 and 14,000 rpm. The adoption of an advanced design approach always leads to optimal turbines featuring a single stage. In the case of MM, it is not possible to find suitable design solutions for one stage, primarily due to the excessive flaring angles and relative Mach numbers at the stage exit. The advantages of increasing the rotational speed with a gearbox might be offset by the additional efficiency penalty and the cost due to the insertion of such a component. The results suggest that the different power output values correspond to different turbine designs and that might lead to different levels of cost and complexity. Therefore, a dedicated analysis must be performed in order to identify whether one design solution outperforms another, considering both technical and economic criteria.

3.3. Cycle-turbine performance index

It is useful to compare the solutions of Fig. 8 on a common basis in order to find the most suitable working fluid for the considered application. In this respect a figure of merit was used, which enables one to consider at the same time (a) the higher system complexity resulting from the increased number of stages; (b) the cost of the expander based on its size; and (c) the possible cost of the gearbox. A Performance Index (PI) is defined here as the ratio of the electrical net power output to the cost of the turbogenerator unit:

$$PI = \frac{P_{el}}{C_{turb}}] \quad [\mathrm{kW_{el}/k€_t}] \tag{3}$$

where $P_{el} = P_{net} \cdot \eta_{gear} \cdot \eta_{gen}$ is the net electrical power output of the cycle, considering the generator efficiency η_{gen} and, possibly, the gearbox efficiency η_{gear}. The variable C_{turb} denotes the cost of the turbogenerator in k€. The use of the turboexpander cost in the denominator is justified by the fact that the turbine represents between 15% and 70% of the total cost in the ORC system [13,93–97] depending on power output, heat source temperature and system architecture. In this work, the cost of the turbogenerator was estimated using the correlation by Astolfi et al.

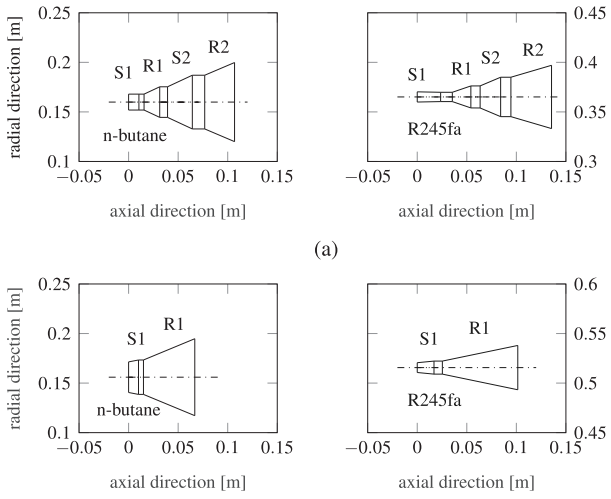

Fig. 7. Meridional profile geometry of the two best working fluid candidates, and Mach numbers and stage reactions of the five best working fluid candidates: (a) conservative and (b) advanced design approaches.

		Conservative design					Advanced design				
Stage	param	n-but.	R245fa	n-pent.	isop.	cyclop.	n-but.	R245fa	n-pent.	isop.	cyclop.
1	DR	0.45	0.27	0.45	0.44	0.44	0.20	0.22	0.21	0.26	0.23
	M_2	1.18	1.40	1.27	1.18	1.26	1.86	1.96	2.23	2.07	2.01
	M_{w3}	1.05	1.00	1.15	1.00	1.15	1.18	1.30	1.40	1.40	1.34
2	DR	0.53	0.38	0.50	0.44	0.52	-	-	-	-	-
	M_2	1.03	1.20	1.16	1.08	1.10	-	-	-	-	-
	M_{w3}	1.09	1.07	1.15	0.97	1.16	-	-	-	-	-
3	DR	-	-	-	0.55	-	-	-	-	-	-
	M_2	-	-	-	0.93	-	-	-	-	-	-
	M_{w3}	-	-	-	1.01	-	-	-	-	-	-

[13], which was developed based on the experience gained by the authors with ORC manufacturers. The formula is valid for a power output higher than 1000 kW, which applies to the designs in this paper. Eq. (4) shows the total cost of the turbogenerator unit, expressed as the sum of the turbine cost (C_t), generator cost (C_{gen}) and possible gearbox cost (C_{gear}). The parameter n is the number of stages, SP is the size parameter of the last stage, SP_0 the reference turbine size parameter, C_0 the basic reference cost, and $P_{el,0}$ the reference turbine electric power.

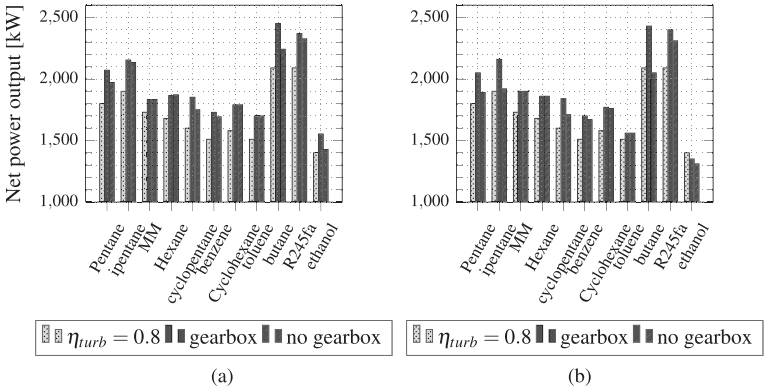

Fig. 8. Optimal net power output of the working fluid candidates according to (a) the conservative and (b) the advanced design approaches.

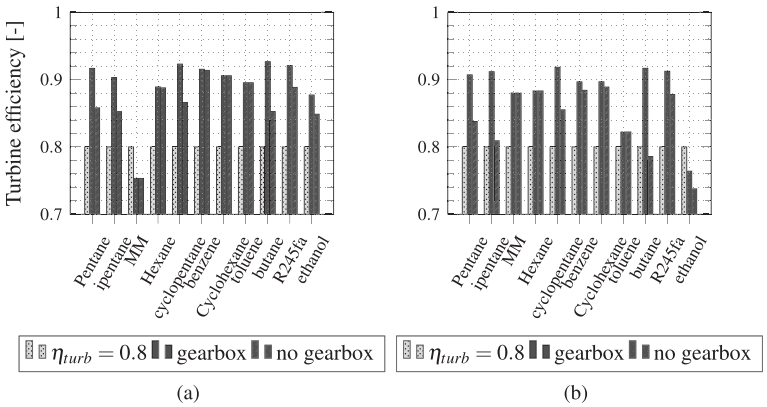

Fig. 9. Turbine design efficiency of the working fluid candidates according to (a) the conservative and (b) the advanced design approaches.

$$C_{turb} = C_t + C_{gen} + C_{gear} \quad (4)$$

$$C_t = C_0\left(\frac{n}{n_0}\right)^{0.5}\left(\frac{SP}{SP_0}\right)^{1.1}$$

C_0 = 1230 k€, n_0 = 2, SP_0 = 0.18 m

$$C_{gen} = C_0\left(\frac{P_{el}}{P_{el,0}}\right)^{0.67}$$

C_0 = 200 k€, $P_{el,0}$ = 5000 kW

$C_{gear} = 0.4 \cdot C_{gen}$

Fig. 6 shows the values of PI of the optimal solutions for each fluid, and Table 8 shows the characteristics of the obtained solutions.

In both the conservative and the advanced approaches, the ORC systems with the highest PI would employ n-butane, but would feature a two-stage and a single-stage turbine with gearbox, respectively.

The fluid n-butane has the smallest turbine diameter, and results in the lowest cost, followed by R245fa. The working fluids yielding large turbine sizes and more stages such as MM, toluene and ethanol, are further penalized in the fluid rank. Fig. 7 shows that single-stage turbines feature rotor blades with higher deflection and more compact size in the axial direction. On the other hand, the two-stage configurations allow a conservative design of sealing and bearings due to the lower rotational speed. Table 8 shows that the smaller number of stages of the advanced designs results in a higher PI, while the best solutions in the conservative approach have two and three stages. In particular, the five-stage turbine with MM is greatly penalized by the additional complexity. Moreover, turbine designs with more than three stages are unusual [38].

Notwithstanding the higher net electrical power output, the additional cost and efficiency penalty of the gearbox result in a lower PI for many fluids such as R245fa, n-pentane, and n-hexane due to an efficiency increase lower than 4%-points. On the other hand, a gearbox solution for n-butane is beneficial since it provides a comparatively higher turbine efficiency by 6–7%-points and a reduced number of stages.

4. Discussion

The single-stage, highly supersonic n-butane turbine yielded the best PI value, which is approximately 1.5 times higher than that of the two-stage solution. Thus, the advanced approach would be the preferred option, provided that an aerodynamic design featuring supersonic concepts is accepted.

The review of the existing literature on single and multistage turbines suggests that the criteria for selecting the optimal number of stages depend on a multitude of factors and on the requirements of the specific application. For example, Angelino et al. [23,31] and Bado

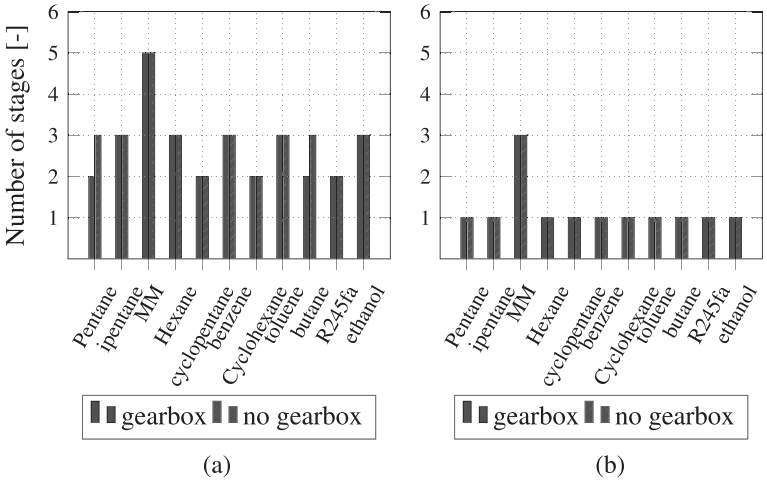

Fig. 10. Minimum number of stages of the working fluid candidates according to (a) the conservative and (b) the advanced design approaches.

Table 8
Ranking of the optimal working fluid candidates.

Fluid	PI	N_{st}	Gearbox	N	r_m	U_{tip}	P_{el}	C_{turb}	p_{max}	p_{min}	$\frac{\dot{Q}_{sc}}{\dot{Q}_{sc,max}}$
	$\left[\frac{kW}{k€_f}\right]$	–	–	[rpm]	[m]	$\left[\frac{m}{s}\right]$	[kW_{el}]	[$k€_f$]	[bar]	[bar]	[–]
Conservative design											
butane	1.95	2	yes	14,371	0.16	281.4	2203	1128	30.37	2.83	0.54
R245fa	1.51	2	no	3600	0.37	229.8	2210	1462	29.21	1.78	0.51
Pentane	1.15	2	yes	9128	0.24	264.1	1909	1655	14.46	0.82	0.35
ipentane	1.04	3	yes	7673	0.23	214.9	1985	1903	22.11	1.09	0.35
cyclopentane	0.90	2	yes	7885	0.28	266.0	1706	1894	8.84	0.51	0.24
ethanol	0.41	3	yes	5939	0.43	307.4	1431	3499	6.60	0.10	0.13
Hexane	0.39	3	no	3600	0.51	193.7	1778	4530	5.59	0.25	0.32
Cyclohexane	0.38	2	no	3600	0.52	242.8	1656	4377	4.05	0.16	0.23
benzene	0.36	3	no	3600	0.46	204.4	1644	4511	4.24	0.16	0.19
toluene	0.21	3	no	1800	0.96	177.8	1563	7345	1.93	0.05	0.19
MM	0.18	5	yes	1200	1.09	194.5	1742	9454	2.53	0.07	0.41
Advanced design											
butane	3.01	1	yes	20,647	0.16	312.62	2238	744	30.00	2.83	0.54
R245fa	2.43	1	no	3600	0.48	185.52	2191	903	29.21	1.78	0.51
ipentane	2.24	1	yes	14,362	0.20	337.16	1986	886	22.11	1.09	0.35
Pentane	1.93	1	yes	11,149	0.28	356.3	1890	980	14.63	0.82	0.35
cyclopentane	1.50	1	yes	11,313	0.26	323.55	1705	1135	8.82	0.51	0.24
Hexane	1.10	1	no	3600	0.68	284.86	1769	1608	5.56	0.25	0.29
benzene	0.90	1	no	3600	0.77	307.11	1590	1766	4.24	0.16	0.19
Cyclohexane	0.90	1	no	3600	0.74	293.12	1669	1857	4.06	0.16	0.24
ethanol	0.80	1	no	3600	1.21	458.84	1240	1551	6.60	0.10	0.13
toluene	0.43	1	no	1800	1.92	325.16	1465	3368	1.93	0.05	0.19
MM	0.22	1	no	1200	1.23	323.55	1805	8242	2.54	0.07	0.41

et al. [21] suggest that a conservative design approach was mainly followed between the 1970s and 1980s in Italy, see Table 1. The main rationale behind these designs was to prioritise high efficiency values at part load as well as to avoid the use of highly supersonic blade rows since loss models had, at that time, comparatively low reliability. Moreover, the higher number of stages could reduce the optimal rotational speed, thereby avoiding the use of a gearbox. Reaction blade profiles were employed in each stage, with a pressure ratio per stage estimated between 3.2 and 5.0. In terms of turbine efficiency, Angelino and Invernizzi [74] suggested the use of two-stage turbines instead of the single-stage one in order to obtain high performance and avoid excessive loading in the heat exchangers.

Notwithstanding the inherent challenges of more advanced designs, other authors documented the use of such high pressure ratio ORC turbines. Verneau [24] described the testing of different single and two-stage ORC turbines featuring pressure ratios between 6 and 150. An advanced design approach was considered here as the first stage stator was highly loaded and featured a converging-diverging nozzle with an exit Mach number up to 2.74. The relative inlet Mach number to the rotor was 1.1 or higher. The first stage pressure ratio was between 6 and 150 while the second was 2 or 3. For the two-stage turbines, Verneau [24] documented isentropic total-to-static turbine efficiencies of about 0.78 at the design point and a rapid performance decay at off-design operation.

Bronicki [98] reported his experience on designing and testing ORC turbines since 1960 and using high speed turbogenerator technology. Stator Mach numbers for single-stage units were between 2.5 and 3.5, indicating that an advanced design approach was followed. The overall stage efficiency for a 600 W unit was measured as 0.77.

Jokinen et al. [25] presented the results of a two-stage ORC axial turbine using toluene which was designed and tested in the late 1990s. The selection criteria of the number of stages were based on considerations from the work of Verneau [24]. The stage pressure ratio was above 100, and the authors noted that a single-stage unit would have caused design problems and resulted in low efficiency at part-load due to the high blade deflection. The final design featured subsonic relative velocity to each blade passage inlet and supersonic flow conditions to the exit.

Osnaghi et al. [22] presented the design of an 8 kW two-stage ORC turbine with a pressure ratio of about 120 and conceived for a medium temperature solar power plant. To minimize the number of stages, an advanced design approach was adopted resulting in a two-stage turbine featuring converging-diverging nozzles with exit Mach numbers of about 1.9 and transonic rotors. The design value of thermodynamic efficiency calculated from measurements was approximately 0.7, and the efficiency dropped rapidly when reducing the rotational speed.

The survey of the available literature suggests that the optimal n-butane turbine, having a pressure ratio of about 10.3, is in a range where two stages are required following the conservative design approach and one stage would be sufficient for the advanced design approach. This is in good agreement with the results obtained using the methodology presented here, further confirming the validity of the methodology. In fact, the values of isentropic efficiency estimated by the present model in the advanced design approach appear to be comparatively higher than those documented in the literature (i.e. $> 90\%$). This deviation might be due to the lack of fully reliable loss and deviation correlations for supersonic conditions. However, it needs to be stressed that there are inherent difficulties associated with the aerodynamic design of supersonic turbines. As a matter of fact, recent studies on ORC supersonic turbines by Pini et al. and Persico and Rodriguez-Fernandez and Persico [99,100] have shown that novel CFD-based shape-optimization techniques allow for achieving consistent performance gains with respect to traditional aerodynamic design methods. These methods can also include multi-point turbine operation, thus minimizing the efficiency penalty at off-design conditions [38].

Besides aerodynamic difficulties, for supersonic turbines Horn [101] highlighted some possible challenges related to mechanical stresses on blades and on the bearing system, additional losses and centrifugal stresses on the blade due to the large rotor chords and flaring angles.

In the case where the design and operation of an advanced n-butane turbine are considered too problematic, R245fa can be the second best working fluid candidate, thanks to the relatively lower flow velocity (and hence Mach number) and rotational speed, allowing for a more conservative design of bearings and seals.

Regarding environmental aspects, the best fluid, n-butane, is highly flammable and has minor hazard issues. Until now, the use of flammable fluids is allowed in ORC plants, and they have been constructed and operated by many manufacturers. The fluid R245fa is currently used by a number of ORC manufacturers (see Table 3); however, it should be phased out on a mid-term horizon due to the relatively high GWP [102]. The use of new working fluids such as R1233ZE(Z) and R1233zd(E) would represent ideal solutions from an environmental perspective, although they were discarded in the early selection step due to their low thermal stability limit for the considered application.

5. Conclusions

This paper presented, for the first time in the literature, a methodology for the design of ORC power systems based on cycle and multistage turbine design criteria. In addition, it presented, for the first time, a mean-line model of an ORC multistage axial turbine that is validated and discussed, and two different design approaches for such turbines. The turbine model was developed and validated against a four-stage subsonic turbine and a two-stage supersonic ORC turbine, representative of a conservative and an advanced design approach, respectively. After a working fluid preselection process, a coupled optimization of cycle and turbine designs was performed for single and multistage turbine arrangements, which was then applied to the case study of waste heat recovery aboard large ships. The validation indicates overall satisfactory results in the comparison with the available data from the open literature, with 2%-points prediction accuracy in efficiency, and up to 8.5% in flow conditions and design geometry.

The results suggest that taking into account the turbine design yields different solutions and choices. The turbine efficiency varies approximately between 74% and 93% when different fluids and design criteria are employed.

The fluid n-butane demonstrates the best trade-off between cycle and expander design. The results indicate that the optimal solution with n-butane features a single-stage configuration with highly supersonic flows, whereas it features a two-stage reaction turbine when a more conservative design approach is followed. These results are in agreement with the experimental findings of ORC multistage turbines documented in the literature and further confirm the validity of the presented methodology. The fluid R245fa resulted to be the second best fluid. Provided that its high GWP value is accepted, it can be used in place of n-butane since it is non-flammable and it has a lower optimal rotational speed than the expander designed with n-butane, which simplifies the design of bearings and sealings. Due to the additional cost for the systems, the adoption of a gearbox results in a better performance index only for those fluids, such as n-butane and n-pentane, where an increase of turbine efficiency up to 6–7%-points is observed.

Finally it is noted that the methodology presented herein was limited to the design of the cycle and expander. For future work it would be relevant to address also off-design conditions and include the performance of the heat exchangers and the pump. Moreover, it is recommended to employ advanced design techniques to investigate potential aerodynamic, structural, noise and off-design issues of highly supersonic turbines.

Acknowledgments

The research work was conducted within the frame of the THERMCYC project (“Advanced thermodynamic cycles utilizing low-temperature heat sources”; see http://www.thermcyc.mek.dtu.dk/) funded by InnovationsFonden, The Danish Council for Strategic Research in Sustainable Energy and Environment.

References

[1] Tabor H, Bronicki L. Establishing criteria for fluids for small vapor turbines. In: SAE national transportation, powerplant, and fuels and lubricants meeting; 1964. p. 561–75.
[2] Fiaschi D, Manfrida G, Maraschiello F. Thermo-fluid dynamics preliminary design of turbo-expanders for ORC cycles. Appl Energy 2012;97:601–8. http://dx.doi.org/10.1016/j.apenergy.2012.02.033.
[3] Clemente S, Micheli D, Reini M, Taccani R. Bottoming organic Rankine cycle for a small scale gas turbine: a comparison of different solutions. Appl Energy 2013;106:355–64. http://dx.doi.org/10.1016/j.apenergy.2013.02.004.
[4] Mondejar EM, Thern M, Genrup M. Aerodynamic considerations in the thermodynamic analysis of organic Rankine cycles. In: Proceedings of the ASME 2014 power conference, July 28–31; 2014. p. 1–8.
[5] Song J, Song Y, Gu C-w. Thermodynamic analysis and performance optimization of an Organic Rankine Cycle (ORC) waste heat recovery system for marine diesel engines. Energy 2015;82:976–85. http://dx.doi.org/10.1016/j.energy.2015.01.108.
[6] Yun E, Park H, Yoon SY, Kim KC. Dual parallel organic Rankine cycle (ORC) system for high efficiency waste heat recovery in marine application. J Mech Sci Technol 2015;29(6):2509–15.
[7] Yang M-H, Yeh R-H. Analyzing the optimization of an organic Rankine cycle system for recovering waste heat from a large marine engine containing a cooling water system. Energy Convers Manage 2014;88:999–1010.
[8] Yang M-H, Yeh R-H. Thermodynamic and economic performances optimization of an organic Rankine cycle system utilizing exhaust gas of a large marine diesel engine. Appl Energy 2015;149:1–12. http://dx.doi.org/10.1016/j.apenergy.2015.03.083.
[9] Andreasen JG, Larsen U, Haglind F. Design of organic Rankine cycles using a non-conventional optimization approach. In: Proceedings of the 28th international conference on efficiency, cost, optimization, simulation and environmental impact of energy systems, June 30–July 3, Pau, France; 2015. p. 1–12.
[10] Toffolo A, Lazzaretto A, Manente G, Paci M. A multi-criteria approach for the optimal selection of working fluid and design parameters in Organic Rankine Cycle systems. Appl Energy 2014;121:219–32. http://dx.doi.org/10.1016/j.apenergy.2014.01.089.
[11] Maraver D, Royo J, Lemort V, Quoilin S. Systematic optimization of subcritical and transcritical organic Rankine cycles (ORCs) constrained by technical parameters in multiple applications. Appl Energy 2014;117:11–29. http://dx.doi.org/10.1016/j.apenergy.2013.11.076.
[12] Vivian J, Manente G, Lazzaretto A. A general framework to select working fluid and configuration of ORCs for low-to-medium temperature heat sources. Appl Energy 2015;156:727–46. http://dx.doi.org/10.1016/j.apenergy.2015.07.005.
[13] Astolfi M, Romano MC, Bombarda P, Macchi E. Binary ORC (Organic Rankine Cycles) power plants for the exploitation of medium–low temperature geothermal sources–Part B: Techno-economic optimization. Energy 2014;66:435–46.
[14] Martelli E, Capra F, Consonni S. Numerical optimization of combined heat and power organic Rankine cycles–Part A: design optimization. Energy 2015;90:310–28.
[15] Da Lio L, Manente G, Lazzaretto A. Predicting the optimum design of single stage axial expanders in ORC systems: Is there a single efficiency map for different working fluids? Appl Energy 2016;167:44–58. http://dx.doi.org/10.1016/j.apenergy.2016.01.020.
[16] White M, Sayma AI. Improving the economy-of-scale of small organic Rankine cycle systems through appropriate working fluid selection. Appl Energy 2016;183:1227–39. http://dx.doi.org/10.1016/j.apenergy.2016.09.055.
[17] Meroni A, La Seta A, Andreasen JG, Pierobon L, Persico G, Haglind F. Combined turbine and cycle optimization for organic Rankine cycle power systems—Part A: turbine model. Energies 2016;9(5):313. http://dx.doi.org/10.3390/en9050313.
[18] La Seta A, Meroni A, Andreasen JG, Pierobon L, Persico G, Haglind F. Combined turbine and cycle optimization for organic Rankine cycle power systems—Part B: application on a case study. Energies 2016;9(6):393. http://dx.doi.org/10.3390/en9060393.
[19] Macchi E, Astolfi M. Axial flow turbines for Organic Rankine Cycle applications. In: Macchi E, Astolfi M, editors. Organic Rankine Cycle (ORC) power systems: technologies and applications. Elsevier Science; 2016. p. 299–319 [chapter 9].
[20] Colonna P, Casati E, Trapp C, Mathijssen T, Larjola J, Turunen-Saaresti T, et al. Organic Rankine Cycle power systems: from the concept to current technology, applications, and an outlook to the future. J Eng Gas Turb Power 2015;137(10):1–19.
[21] Bado G, Tomei G, Angelino T, Gaia M, Macchi E. The Ansaldo 35 kW solar power system. In: Sun II – ISES silver jubilee congress, May, Atlanta, Georgia, vol. 1; 1979. p. 1090–4.
[22] Osnaghi C, Angelino G, Bassi F, Bollina E, Ferrari P, Gaia M, et al. Progetto e realizzazione di un motore a fluido organico con espansione a turbina da accoppiarsi con un impianto solare a media concentrazione. In: II Seminario Informativo dell'attivitá del sottoprogetto 'Energia Solare', vol. 3; 1979.
[23] Angelino G, Gaia M, Macchi E. Medium temperature 100 kW ORC engine for total energy systems. Energy conservation in industry-combustion, heat recovery and Rankine cycle machines. Springer; 1983. p. 177–89.
[24] Verneau A. Supersonic turbines for organic fluid Rankine cycles from 3 to 1300 kW. In: Small high pressure ratio turbines, (VKI lecture series 1987–2007) Von Karman Institute For Fluid Dynamics, Rhode-Saint-Genése, Belgium; 1987. p. 1–55.
[25] Jokinen T, Larjola J, Mikhaltsev I. Power unit for research submersible. In: International conference on electric ship (ElecShip 98), Istanbul, Sept, vol. 1; 1998. p. 114–8.
[26] Sciacovelli L, Cinnella P. Numerical study of multistage transcritical organic Rankine cycle axial turbines. J Eng Gas Turb Power 2014;136(8):082604.

Appendix D. Articles

[27] Klonowicz P, Surwio J, Witanowski L, Suchocki TK, Kozanecki Z, Lampart P. Design and numerical study of turbines operating with MDM as working fluid. Open Eng 2015;5(1):485–99. http://dx.doi.org/10.1515/eng-2015-0050.

[28] Surwilo J, Lampart P, Szymaniak M. CFD analysis of fluid flow in an axial multi-stage partial-admission ORC turbine. Open Eng 2015;5(1):360–4. http://dx.doi.org/10.1515/eng-2015-0042.

[29] Angelino G, Gaia M, Macchi E, Barutti A, Maccio C, Tomei G. Test results of a medium temperature solar engine. Int J Ambient Energy 1982;3(3):115–26.

[30] Barutti A, Pedrick W, Angelino G, Gaia M, Macchi E. Ansaldo solar thermal and photovoltaic plants located at Ballajura, Western Australia. In: 8th solar world congress, biennial congress of the international solar energy society,14–19 August, Perth, Australia, vol. 3; 1983. p. 1572–6.

[31] Angelino G, Gaia M, Macchi E. Medium temperature 100 kW ORC engine for total energy systems - experimental results. Commission of the European Communities, Report EUR 9236 (1); 1984. p. 421.

[32] Obernberger I, Hammerschmid A. Biomass fired CHP plant based on an ORC cycle–Project ORC-STIA-Admont. Final report, bios-energy systems; 2001. p. 1–12.

[33] Nasir P, Jones S, Schochet D, Sparks N. Utilization of turbine waste heat to generate electric power at neptune plant. < http://www.ormat.com/research/papers/utilization-turbine-waste-heat-generate-electric-power-neptune-plant > [accessed Oct. 1, 2016].

[34] Lozza G, Macchi E, Perdichizzi A. On the influence of the number of stages on the efficiency of axial-flow turbines. In: ASME 1982 international gas turbine conference and exhibit. American Society of Mechanical Engineers; 1982. p. 1–10.

[35] Macchi E, Perdichizzi A. Efficiency prediction for axial-flow turbines operating with nonconventional fluids. J Eng Power 1981;103(4):718–24.

[36] Pini M, Persico G, Casati E, Dossena V. Preliminary design of a centrifugal turbine for organic Rankine cycle applications. J Eng Gas Turb Power 2013;135(4):042312. http://dx.doi.org/10.1115/1.4023122.

[37] Casati E, Vitale S, Pini M, Persico G, Colonna P. Centrifugal turbines for mini-ORC power systems. J Eng Gas Turb Power 2014;136(December 2014):1–11. http://dx.doi.org/10.1115/1.4027904.

[38] Persico G, Pini M. Fluid dynamic design of Organic Rankine Cycle turbines. In: Macchi E, Astolfi M, editors. Organic Rankine Cycle (ORC) power systems: technologies and applications. Elsevier Science; 2016. p. 253–97 [chapter 8].

[39] Casati E, Vitale S, Pini M, Persico G, Colonna P. Preliminary design method for small scale centrifugal ORC turbines; 2013. < http://www.asme-orc2013.nl/uploads/File/PPT%20155.pdf > [accessed Aug. 15, 2017].

[40] MAN Diesel & Turbo. Waste heat recovery system (WHRS) – marine engines & systems; Aug. 2015. < http://marine.man.eu/ > .

[41] Andreasen JG, Meroni A, Haglind F. A comparison of organic and steam Rankine cycle power systems for waste heat recovery on large ships. Energies 2017;10(4):547. http://dx.doi.org/10.3390/en10040547. (23 pp.), 547 (23 pp.).

[42] Larsen U, Pierobon L, Haglind F, Gabrielii C. Design and optimisation of organic Rankine cycles for waste heat recovery in marine applications using the principles of natural selection. Energy 2013;55(45):803–12. http://dx.doi.org/10.1016/j.energy.2013.03.021.

[43] Quoilin S, Broek MVD, Declaye S, Dewallef P, Lemort V. Techno-economic survey of Organic Rankine Cycle (ORC) systems. Renew Sustain Energy Rev 2013;22:168–86. http://dx.doi.org/10.1016/j.rser.2013.01.028.

[44] Bao J, Zhao L. A review of working fluid and expander selections for organic Rankine cycle. Renew Sustain Energy Rev 2013;24:325–42. http://dx.doi.org/10.1016/j.rser.2013.03.040.

[45] Wang D, Ling X, Peng H, Liu L, Tao L. Efficiency and optimal performance evaluation of organic Rankine cycle for low grade waste heat power generation. Energy 2013;50(1):343–52. http://dx.doi.org/10.1016/j.energy.2012.11.010.

[46] Öhman H, Lundqvist P. Screw expanders in orc applications, review and a new perspective. In: 3rd International seminar on ORC power systems, October 12–14, Brussels, Belgium; 2015. p. 1–10.

[47] Ozone Secretariat UNEP. Montreal protocol on substances that deplete the ozone layer. Tech. rep. US Government Printing Office; 1987.

[48] Official Journal of the European Union. Regulation (EU) no 517/2014 of the European parliament and of the council on fluorinated greenhouse gases and repealing regulation (EC) no 842/2006. Tech. rep.

[49] Rayegan R, Tao Y. A procedure to select working fluids for Solar Organic Rankine Cycles (ORCs). Renew Energy 2011;36(2):659–70.

[50] Drescher U, Brüggemann D. Fluid selection for the Organic Rankine Cycle (ORC) in biomass power and heat plants. Appl Therm Eng 2007;27(1):223–8.

[51] Andersen WC, Bruno TJ. Rapid screening of fluids for chemical stability in organic Rankine cycle applications. Ind Eng Chem Res 2005;44(15):5560–6.

[52] Green Energy You Can Rely On. < www.ormat.com > [accessed Oct. 1, 2016].

[53] EG, EGi, EEGi-Series - Atlas Copco Gas and Process. < http://www.atlascopco-gap.com/products/expanders/eg-egi-eegi-series > [accessed Oct. 1, 2016].

[54] Preißinger M, Brüggemann D. Thermal stability of hexamethyldisiloxane (MM) for high-temperature organic Rankine cycle (ORC). Energies 2016;9(3):183.

[55] Williams DE. Volatile methyl siloxanes: environmentally sound solvent systems. ACS Publications; 2000.

[56] Turboden: Clean Energy Ahead. < www.turboden.eu > [accessed Oct. 1, 2016].

[57] Macchi E. Theoretical basis of the Organic Rankine cycle. In: Macchi E, Astolfi M, editors. Organic Rankine Cycle (ORC) power systems: technologies and applications. Elsevier Science; 2016. p. 3–24 [chapter 1].

[58] Pasetti M, Invernizzi CM, Iora P. Thermal stability of working fluids for organic Rankine cycles: an improved survey method and experimental results for cyclopentane, isopentane and n-butane. Appl Therm Eng 2014;73(1):764–74.

[59] Ginosar DM, Petkovic LM, Guillen DP. Thermal stability of cyclopentane as an organic Rankine cycle working fluid. Energy Fuels 2011;25(9):4138–44.

[60] Ge oil & gas – ORegen. < http://www.geoilandgas.com > [accessed Oct. 1, 2016].

[61] Aqylon - Smarter Power. < http://www.aqylon.com/products-range/ > [accessed Oct. 1, 2016].

[62] Collins W, Derwent R, Johnson C, Stevenson D. The oxidation of organic compounds in the troposphere and their global warming potentials. Clim Change 2002;52(4):453–79.

[63] Straty GC, Ball M, Bruno T. PVT of toluene at temperatures to 673 K. J Chem Eng Data 1988;33(2):115–7.

[64] Triogen – Power From Heat. < http://www.triogen.nl/ > [accessed Oct. 1, 2016].

[65] Angelino G, Invernizzi C. Experimental investigation on the thermal stability of some new zero ODP refrigerants. Int J Refrig 2003;26(1):51–8.

[66] Calnetix – Organic Rankine Cycle Systems. < http://www.calnetix.com/organic-rankine-cycle-systems > [accessed Oct. 1, 2016].

[67] Cryostar – Clean Energy. < http://www.cryostar.com/web/power-electricity > [accessed Oct. 1, 2016].

[68] E-Rational – Value for Heat. < http://www.e-rational.net/ > [accessed Oct. 1, 2016].

[69] Craig H, Cox H. Performance estimation of axial flow turbines. Proc Inst Mech Eng 1970;185(1):407–24.

[70] Klonowicz P, Heberle F, Preißinger M, Brüggemann D. Significance of loss correlations in performance prediction of small scale, highly loaded turbine stages working in Organic Rankine Cycles. Energy 2014;72:322–30. http://dx.doi.org/10.1016/j.energy.2014.05.040.

[71] Macchi E. Design criteria for turbines operating with fluids having a low speed of sound. Closed Cycle Gas Turbines. (VKI Lecture Series 100) Von Karman Institute For Fluid Dynamics, Rhode-Saint-Genése, Belgium 2; 1977. p. 1–34.

[72] Dunham J, Came P. Improvements to the Ainley-Mathieson method of turbine performance prediction. J Eng Power 1970;92(3):252–6.

[73] Invernizzi C, Iora P, Silva P. Bottoming micro-Rankine cycles for micro-gas turbines. Appl Therm Eng 2007;27(1):100–10.

[74] Angelino G, Invernizzi C. Cyclic methylsiloxanes as working fluids for space power cycles. J Sol Energy Eng 1993;115(3):130–7.

[75] Angelino G, Invernizzi C, Molteni G. The potential role of organic bottoming Rankine cycles in steam power stations. Proc Inst Mech Eng, Part A: J Power Energy 1999;213(2):75–81.

[76] Maccio C, Tomei G, Angelino G, Gaia M, Macchi E. Operational experience of a 3.0 kW solar powered water pump. In: Sun II, vol. 1; 1979. p. 1501–5.

[77] Kötzing P, Evers B. Test case e/tu, 4-stage low speed turbine. AGARD Advisory Report N.275. Tech. rep. AGARD.

[78] Hirsch C, Denton J. Through flow calculations in axial turbomachines. AGARD Advisory Report N.175. Tech. rep. AGARD. Propulsion and Energetics Panel. Working Group 12; 1981.

[79] Herzog N, Binner M, Seume J, Rothe K. Verification of low-flow conditions in a multistage turbine. ASME Turbo Expo 2007: power for land, sea, and air. American Society of Mechanical Engineers; 2007. p. 563–74.

[80] Gerolymos G, Hanisch C. Multistage three-dimensional Navier-Stokes computation of off-design operation of a four-stage turbine. Proc Inst Mech Eng, Part A: J Power Energy 1999;213(4):243–61.

[81] Croce G, Ratto L, Satta A, A Navier Stokes solver for axisymmetric turbomachinery analysis. In: 5th European conference on computational fluid dynamics, 14–17 June, Lisbon, Portugal; 2010. p. 1–12.

[82] Cravero C, Macelloni P, Briasco G. Three-dimensional design optimization of multistage axial flow turbines using a RSM based approach. In: ASME Turbo Expo 2012: turbine technical conference and exposition, June 11–15. Copenhagen, Denmark: American Society of Mechanical Engineers; 2012. p. 1873–84.

[83] Gerolymos G, Vallet I. Tip-clearance and secondary flows in a transonic compressor rotor. In: ASME 1998 international gas turbine and aeroengine congress and exhibition. American Society of Mechanical Engineers; 1998. p. V001T01A093–V001T01A093.

[84] Gerolymos G. Implicit multiple-grid solution of the compressible Navier-Stokes equations using k-epsilon turbulence closure. AIAA J 1990;28(10):1707–17.

[85] Verneau A. Waste heat recovery by organic fluid Rankine cycle. In: Proceedings from the first industrial energy technology conference, April 22–25, Houston, TX; 1979. p. 940–52.

[86] Lemmon EW, Huber ML, McLinden MO. NIST reference fluid thermodynamic and transport properties–REFPROP; 2013.

[87] Boy-Marcotte J. 100–1000 kW (el) medium-power distributed-collector solar system. Electr Power Syst Res 1980;3(1):41–51.

[88] Kluwick A. Nonlinear waves in real fluids. Springer; 1991.

[89] Joback KG, Reid RC. Estimation of pure-component properties from group-contributions. Chem Eng Commun 1987;57(1–6):233–43.

[90] Metropolis N, Ulam S. The Monte Carlo method. J Am Stat Assoc 1949;44(247):335–41. http://dx.doi.org/10.1080/01621459.1949.10483310.

[91] Osnaghi C. Teoria delle turbomacchine. Società Editrice Esculapio; 2013.

[92] Sin G, Gernaey KV, Lantz AE. Good modeling practice for PAT applications: propagation of input uncertainty and sensitivity analysis. Biotechnol Prog 2009;25(4):1043–53.

[93] Lecompte S, Huisseune H, van den Broek M, De Schampheleire S, De Paepe M. Part load based thermo-economic optimization of the Organic Rankine Cycle (ORC) applied to a combined heat and power (CHP) system. Appl Energy 2013;111:871–81.

[94] Lemmens S. A perspective on costs and cost estimation techniques for organic Rankine cycle systems. In: Proceedings of the 3rd international seminar on ORC power systems (ASME ORC 2015), Brussels, Belgium; 2015. p. 12–4.

[95] Quoilin S, Declaye S, Tchanche BF, Lemort V. Thermo-economic optimization of waste heat recovery Organic Rankine Cycles. Appl Therm Eng

2011;31(14):2885–93.
[96] Lecompte S, Lemmens S, Huisseune H, van den Broek M, De Paepe M. Multi-objective thermo-economic optimization strategy for ORCs applied to subcritical and transcritical cycles for waste heat recovery. Energies 2015;8(4):2714–41.
[97] Tartière T, Obert B, Sanchez L. Thermo-economic optimization of subcritical and transcritical ORC systems. In: ASME ORC 2013–international seminar on ORC power systems; 2013. p. 1–12.
[98] Bronicki L. Experience with high speed organic Rankine cycle turbomachinery. In: Conference on high speed technology, Lappeenranta University of Technology, August, Lappeenrata, Finland; 1988. p. 21–4.
[99] Pini M, Persico G, Pasquale D, Rebay S. Adjoint method for shape optimization in real-gas flow applications. J Eng Gas Turb Power 2015;137(3):032604.
[100] Rodriguez-Fernandez P, Persico G. Automatic design of ORC turbine profiles using evolutionary algorithms. In: Proceedings of the third international seminar on ORC power systems, October 12–14, Brussels, Belgium; 2015. p. 1–10.
[101] Horn G, Norris T, Whybrow J. Turbine flow problems of binary cycles employing high density fluids. Proc Inst Mech Eng 1968;183(1):165–78.
[102] Tollefson J. Nations agree to ban refrigerants that worsen climate change. < http://www.nature.com > [accessed Feb. 1, 2017].

Energy 164 (2018) 1062–1078

Contents lists available at ScienceDirect

Energy

journal homepage: www.elsevier.com/locate/energy

A methodology for the preliminary design and performance prediction of high-pressure ratio radial-inflow turbines

Andrea Meroni [a, *], Miles Robertson [b], Ricardo Martinez-Botas [b], Fredrik Haglind [a]

[a] Department of Mechanical Engineering, Technical University of Denmark, Nils Koppels Allé, Building 403, 2800 Kongens, Lyngby, Denmark
[b] Department of Mechanical Engineering, Imperial College London, City and Guilds Building, South Kensington Campus, London, SW7 2AZ, UK

ARTICLE INFO

Article history:
Received 2 May 2018
Received in revised form
24 July 2018
Accepted 6 September 2018
Available online 12 September 2018

2010 MSC:
00–01
99-00

Keywords:
Radial inflow turbine
Validation
Mean-line model
High-pressure ratio
Organic Rankine cycle

ABSTRACT

Modern power generation technologies, such as organic Rankine cycle power systems, require turboexpanders operating with high-efficiency and high power density. These features often lead to high-pressure ratios machines, characterised by the presence of choking and supersonic flow conditions. This paper proposes a comprehensive methodology for the preliminary design and performance prediction of radial-inflow turbines operating at high-pressure ratios. A steady-state, mean-line model of a radial-inflow turbine is developed including real-gas effects and a detailed modelling strategy for the treatment of choking flow conditions. In addition, a set of loss models tailored to high-pressure ratio radial-inflow turbines is developed. After a global sensitivity analysis, the model is calibrated by means of a multi-objective optimisation with a Genetic Algorithm and using the data of six high-pressure ratio turbines with total-to-total pressure ratios up to 5.8. The calibration method allows a significant reduction in the overall predicted deviation of the turbine isentropic efficiency and mass flow rate. The design model yields predicted deviations in isentropic efficiency within ± 3 %-points and the off-design model within 5%. The methodology and the results are intended to be used as a benchmark for the future development of radial-inflow turbines in high-pressure ratio applications.

© 2018 Elsevier Ltd. All rights reserved.

1. Introduction

Radial-inflow turbines (RITs) are used extensively within many areas of the power generation field. Conventional applications range from large-scale hydroelectric power plants to small-scale units used in automotive turbochargers, aircraft auxiliary power units, cryogenic systems, and space power generation [34]. In all these applications, the radial-inflow configuration features key advantages over its axial counterpart such as the lower cost and ease of manufacturing, higher efficiency, and reduced size and number of stages [34,35]. The specific requirements of the selected applications may result in a turbine operating at high-pressure ratio (HPR) conditions, usually above 3. This may be particularly significant in cases where cost and size are limiting factors.

The pressure ratio across the turbine depends on the specifications of the thermodynamic cycle, i.e. heat source and heat sink temperatures, and on the selected working fluid. In the context of organic Rankine cycle (ORC) power systems, pressure ratios up to 100–150 [36,37] can be achieved in combination with moderate to high heat source temperatures. Such pressure ratios are characterised by the presence of nozzle and/or rotor choking conditions and supersonic flows. The latter entail the formation of shock patterns and result in an unsteady nozzle-rotor fluid dynamic interaction which may compromise the mechanical integrity and the performance of the blade rows. Moreover, depending on the application, the working fluid operating at high pressure ratios might not behave like a perfect gas. For organic fluids, the expansion starts close to the critical point and typically ends far from the saturation line at the turbine outlet. In such conditions, the fluid exhibits a large change in the thermodynamic properties, making it important to consider real-gas effects. The aforementioned aspects make the design and performance prediction of HPR turbines significantly different from those of lower pressure ratio turbines, and therefore require numerical tools and strategies tailored for high-pressure ratio applications.

Different authors, including Refs. [6,14,38–40], pointed out the lack of publicly available and well-documented data regarding the

* Corresponding author.
E-mail addresses: andmer@mek.dtu.dk (A. Meroni), miles.robertson09@imperial.ac.uk (M. Robertson), r.botas@imperial.ac.uk (R. Martinez-Botas), frh@mek.dtu.dk (F. Haglind).

https://doi.org/10.1016/j.energy.2018.09.045
0360-5442/© 2018 Elsevier Ltd. All rights reserved.

RIT geometry and internal flow conditions, which hampers the development of reliable and accurate performance prediction tools. This lack of published stage performance data is even greater for HPR turbines. A compilation of RITs designed and tested at pressure ratios above 3 from the open literature is reported in Table 1. In order to fill this gap, Sauret [41] and Li et al. [42] resorted to aerodynamic investigations with CFD models on specific HPR turbines tested in the literature.

At the same time, the use of one-dimensional (or mean-line) models is often regarded as the most important step for the preliminary design and performance prediction of a turbine, and allows for significant cost and time savings in the whole turbine design process [36] compared to more advanced design methods. However, preliminary mean-line modelling strategies and validation studies for RITs operating at HPRs are very limited and the existing methods mostly rely on the data for low-pressure ratio conditions.

The first mean-line modelling strategies documented in the open literature were based on data of low-pressure ratio turbines [43–46]. These models did not consider real-gas equations of state as well as detailed choking considerations in their formulation. Since the 2000s, real-gas equations of state could be embedded in the numerical models and other models were developed [39,47,48]. In recent years, other authors presented a number of mean-line models for the design and off-design analysis of RITs, especially for ORC power systems. However, only few authors included choking considerations which occur in the nozzle and/or in the rotor at high pressure ratios. Rahbar et al. [49], Da Lio et al. [50], and Mounier et al. [51] developed mean-line models to predict the design efficiency of RITs for ORC applications. The proposed models included the treatment of choking conditions at the design point only. Demierre et al. [31] developed a mean-line model of an ORC turbine considering also choking conditions, however, the authors did not present a detailed modelling strategy for the prediction of the different possible choking patterns in the turbine.

Table 1
RITs designed and tested at pressure ratios above 3 from the open literature.

Author	Year	Field	Pressure ratio [–]	Fluid
Hiett and Johnston [1,2]	1963	GT	1.3–5.0	Air
McLallin and Haas [3]	1980	GT	1.2–4.7	Air
Kidwell and Large [4]	1980	GT	2.0–5.0	Air
Rogo et al. [5]	1984	GT	2.0–7.0	Air
Ribaud and Mischel [6]	1986	GT	2.97–3.8	Air
Rogo [7]	1986	GT	2.0–7.0	Air
Rodgers [8]	1990	TC/GT	3.6,3.9,4.3	Air
Simonyi et al. [9]	1991	GT	3.0–5.8	Air
Pullen et al. [10]	1993	GT	1.1–4.7	Air
Huntsman et al. [11,12]	1992	GT	4.7(*)	Air
Jones [13]	1994	GT	1.0–9.0	Air
Spence and Artt [14]	1997	RES	1.3–4.0	Air
Atkinson [15]	1998	RES	1.3–3.7	Air
Doran et al. [16]	2001	TC	1.3–3.5	Air
Feng et al. [17]	2005	GT	1.1–3.1	Air
Spence et al. [18]	2007	TC	1.2–3.6	Air
Deng [19]	2007	RES	1.3–4.0	Air
Fu et al. [20,21]	2012	GT	1.1–3.1	Air
Ino et al. [22]	1991	CR	7.0–12.0	Helium
Ghosh [23]	2008	CR	1.8–5.9	Air/N_2
Larjola [24]	1988	ORC	10.0(*)	R114
Van Buijtenen et al. [25]	2003	ORC	120.5(*)	Toluene
Pei et al. [26]	2011	ORC	7.1(*)	R123
Kang and Chung [27,28]	2011	ORC	4.1(*)	R245fa
Han et al. [29]	2014	ORC	3.2(*)	R245fa
Demierre et al. [30,31]	2014	ORC	3.1–4.4	R134a
Kang [32]	2016	ORC	4.1(*)	R245fa
Turunen-Saaresti et al. [33]	2017	ORC	112.8(*)	MDM

GT = Gas Turbines. RES = Research. TC = Turbochargers. CR = Cryogenic systems. ORC = Organic Rankine cycles. (*) = documented design point only.

The mean-line method by Baines [52] is probably the most updated in the field as it has been object of refinements and improvements, see Refs. [53,54]. Based on the previous work by Baines [52–54], Qiu and Baines [2] were the first to propose a mean-line method to compute the turbine flow capacity for unchoked and choked conditions, and for the subsonic, transonic and supersonic flow regimes. The authors validated their model using three test cases. Although Qiu and Baines [2] presented a method which considered choking conditions for HPR turbines, they did not present the details of their numerical modelling strategy and the geometry and flow data of the test cases are not fully available in the open literature or come from private communications, respectively.

Another fundamental aspect in the development of a mean-line model is the validation and/or calibration process with experimental data. Glassmann [55] calibrated his model to the data of six RITs, of which two were HPR turbines. However, the loss models were evaluated only at the design point. The study by Qiu and Baines [2] employed loss model correlations that were developed and calibrated considering the data of low-pressure ratio turbines at the design point, see Refs. [52–54], and it is arguable whether these are fully representative for HPR turbine applications, especially at off-design operation.

The objective of this paper is to present a comprehensive method for the performance prediction and for the validation of RITs operating at HPR conditions based on the existing data sets of HPR turbines in the open literature. To this end, the paper presents a complete approach for turbine design and off-design modelling, calibration, validation, and analysis of the results. The work is limited to steady-state conditions. A mean-line model for the design and off-design analysis of RITs was developed and different strategies for the treatment of unchoked and choked conditions as well as subsonic and supersonic flows are presented. The model is conceived to include real-gas equations of state and a general formulation of the governing equations, in order to adapt the methodology to any working fluid and operating condition. A global sensitivity analysis based on the Monte Carlo method was applied to identify the significance level of the calibration coefficients with respect to the choking mass flow rate and the output isentropic efficiency. Afterwards, the calibration methodology is presented, where the turbine loss models are calibrated against the data of six HPR nozzled turbines from the open literature. In order to evaluate the suitability of the model, the results of the calibration were assessed by validation with two other test cases, one of which is an ORC turbine, whose features are different from the turbines used in the calibration process.

This paper contains the following novel contributions: (1) it presents in detail a mean-line modelling strategy for the treatment of choking conditions in the nozzle and the rotor at design and off-design conditions; (2) it presents an optimisation-based calibration method, which seeks to minimise the predicted deviation across every measured operating point contained within each of the test cases; (3) it provides a set of loss models tailored to HPR-RITs. The methodology and the results are intended to be used as a benchmark for the future development of radial-inflow turbines in high-pressure ratio applications.

Compared to the work by Baines [52–54] and to the most recent works in the field, i.e. Refs. [31,50,51,56], this paper extends the design and off-design methodology to high pressure ratios.

The paper is structured as follows: Section 2 presents the turbine test cases, the modelling strategies for design and off-design, and the methods for the sensitivity analysis, calibration and validation. Section 3 presents the results of the calibration. Section 4 discusses the results. The conclusions are drawn in Section 5.

2. Methods

2.1. Performance prediction methodology

This work employed a steady-state, mean-line model for the performance prediction of RITs at design and off-design conditions. The model has been conceived and implemented with the following objectives: (i) to include a complete and consistent numerical strategy for the design and performance prediction considering unchoked and choked flow conditions; (ii) to develop a tool which is general, and can be applicable to any fluid, operating condition or HPR application of interest; (iii) to ensure numerical robustness, stability and to allow for a short computational time. The model was written in the MATLAB language [57] and followed a mean-line approach, for which the thermodynamic and flow conditions were computed at the mean line in the turbine meridional plane, and were representative of mass-weighted averaged conditions over the whole section. This work focused on the modelling of the nozzle, the nozzle-rotor interspace, and of the rotor. Fig. 1 depicts a schematic of the radial-inflow turbine highlighting the main stations, the terminology and the symbols used in this paper.

The thermodynamic and flow conditions in the main modelling stations were computed by the simultaneous solution of mass continuity, energy balance, and loss equations. The fluid properties were computed by means of real-gas equations of state using the thermodynamic library CoolProp [58].

Each blade row can feature two distinguished flow patterns, corresponding to unchoked and choked flow conditions, respectively. The blade row is choked when the flow reaches sonic conditions at the point of minimum flow area, identified as the throat. For an isentropic process through a bladed element in the relative coordinate system, it can be shown that the maximum mass flow rate per unit area occurs at sonic conditions [34]. Fig. 2 illustrates that there are four possible combinations of the flow patterns, identifying the four physical situations occurring in the turbine: (a) both the nozzle and the rotor are unchoked, (b) the nozzle is unchoked and the rotor is choked, (c) the nozzle is choked and the rotor is unchoked, and (d) both the nozzle and the rotor are choked.

Different strategies can be used for design and off-design performance prediction using a mean-line model, and the reader is referred to Ref. [59] for a general overview of the topic. Fig. 3 shows the modelling modelling strategies adopted in this work.

Fig. 3 (a) depicts the workflow of the preliminary design model. The model inputs are the inlet total temperature T_{01} and pressure p_{01}, the rotational speed N, the mass flow rate $\dot{m}$, and the stage total-to-static pressure ratio PR_{ts}. In addition, a set of decision variables needs to be given as an input. This set often consists of non-dimensional variables related to the turbine geometry and turbine loading conditions, which allows expressing the design in a more general formulation. The reader is referred to Refs. [60,61] for examples of possible sets of design variables. The strategy shown in Fig. 3(a) applies to a predefined set of input variables, and a dedicated optimisation procedure needs to be applied in order to determine the optimal set of inputs. For a set of input decision variables, the design modelling strategy starts by identifying where choking occurs since the maximum turbine flow capacity is limited by the mass flow rate at choking conditions (*Step 0*). The mass continuity, energy balance, and loss equations for the nozzle are expressed, respectively, as

$$C_2 = \frac{\dot{m}}{\rho_2 \cdot \cos(\alpha_2) \cdot A_2 (1 - BF_2)} \tag{1}$$

$$h(\rho_2, T_2) = h_{01} - \frac{1}{2} C_2^2 \tag{2}$$

$$\sum_{n=1}^{n_{losses}} \Delta h_{loss,n} - h(\rho_2, T_2) + h(p_2, s_1) = 0 \tag{3}$$

where ρ_2, α_2, A_2, C_2, p_2 are the density, flow angle, flow area, absolute velocity, and static pressure at the nozzle outlet, respectively. In Eq. (1), the blockage factor BF_2 may be introduced to account for reduction in effective area due to the metal blockage and boundary layer effects. The term h denotes the specific enthalpy, and h_{01} and s_1 are the total specific enthalpy and the specific entropy computed at the nozzle inlet, respectively. The term $\Delta h_{loss,n}$ represents the specific loss contribution in the blade row, which is calculated with an empirical correlation, see Sec. 2.2. For unchoked flow conditions, the nozzle exit flow angle was computed using an empirical correlation, see Sec. 2.2. For given nozzle inlet conditions, the solution strategy adopted above allows expressing the left-hand side of Eq. (3) as a function of ρ_2 and $\dot{m}$, as illustrated in Fig. 4.

For a given value of mass flow rate, the function at the left hand side of Eq. (3) is non-monotonic with a concave shape and a single peak. In the methodology presented in this work, the condition at

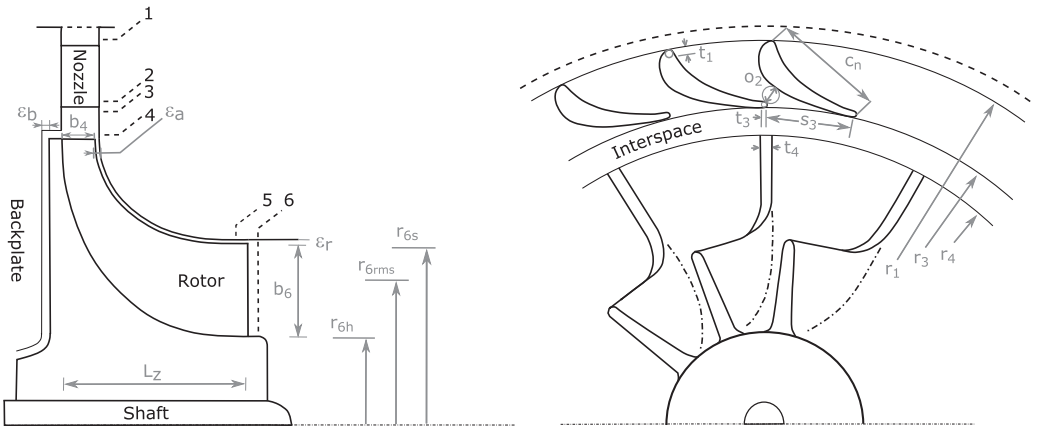

Fig. 1. Schematic of the radial-inflow turbine geometry.

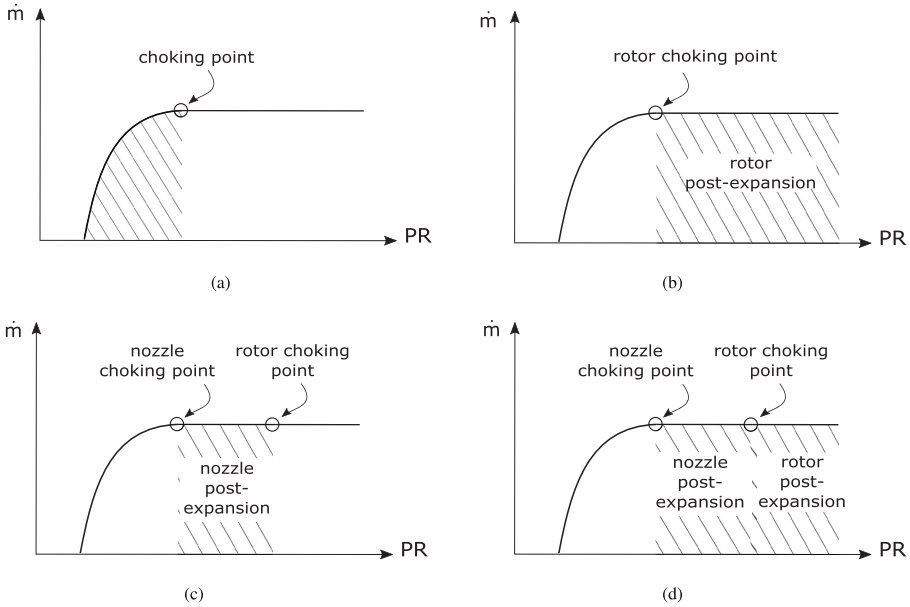

Fig. 2. Illustration of the possible turbine flow patterns occurring at off-design conditions: (a) Nozzle and rotor unchoked; (b) rotor choked and nozzle unchoked; (c) nozzle choked and rotor unchoked; (d) nozzle and rotor choked.

which the maximum of this function crosses the abscissa was identified as the *choking condition*. For small values of ṁ, when the peak is above the abscissa, there exist two values of ρ_2 which satisfy Eq. (3). The larger value corresponds to subsonic flow conditions, whereas the smaller value relates to supersonic flow conditions. By increasing the mass flow rate, the maximum of the curve shifts downwards, and eventually intersects the abscissa. Therefore, choking occurs when the subsonic and supersonic solutions coincide. When the mass flow rate exceeds the choking value, the curves in Fig. 4 show that there is no solution to the system of equations. In this case, a different set of input design variables needs to be provided as an input in order to allow for a higher design mass flow rate.

If the nozzle is unchoked, the model solves the set of nozzle Eqs. (1)–(3) (*Step 1*) and the mass continuity, the energy balance, the momentum balance and the loss equation in the nozzle-rotor interspace (*Step 2*), respectively, as follows:

$$C_4 = \frac{\dot{m}}{\rho_4 \cdot \cos(\alpha_4) \cdot A_4 (1 - BF_4)} \tag{4}$$

$$h(\rho_4, T_4) = h_{01} - \frac{1}{2} C_4^2 \tag{5}$$

$$\frac{C_3 \sin\alpha_3}{C_4 \sin\alpha_4} = \frac{r_4}{r_3} + \frac{2\pi C_f \rho_4 C_4 \sin\alpha_4 (r_3^2 - r_3 r_4)}{\dot{m}} \tag{6}$$

$$\Delta h_{vs,loss} - h(\rho_4, T_4) + h(p_4, s_3) = 0 \tag{7}$$

where $\Delta h_{vs,loss}$ is the vaneless space loss and C_f is the friction factor, which can be estimated with empirical models. The formulation of Eq. (6) was based on the analysis by Stanitz [62], as reported by Whitfield and Baines [63]. The system of Eqs. (4)–(7) was solved using a trust region solver in MATLAB [57] for a given set of guess values for α_4 and ρ_4. Afterwards, the model evaluates whether the rotor is choked (*Step 3*). To this end, the mass continuity, the energy balance and the loss equations in the rotor were solved in its relative coordinate system, as follows:

$$W_5 = \frac{\dot{m}}{\rho_5 \cdot \cos(\beta_5) \cdot A_5 (1 - BF_5)} \tag{8}$$

$$h(\rho_5, T_5) = I_4 - \frac{1}{2} W_5^2 + \frac{1}{2} U_5^2 \tag{9}$$

$$\sum_{n=1}^{n_{loss}} \Delta h_{loss,n} - h(\rho_5, T_5) + h(p_5, s_4) = 0 \tag{10}$$

where $I_4 = h_4 + 0.5W_4^2 - 0.5U_4^2$ is the rothalpy term. In the design mode, the pressure at the rotor exit, p_5, was specified by the required stage pressure ratio, and the flow angle β_5 was determined in order to match p_5. In the off-design mode, under unchoked conditions, the rotor exit pressure was unknown, and the rotor exit flow angle was computed using an empirical correlation, see Sec. 2.2. Eq. (10) was expressed as a function of the rotor throat density ρ_5, showing a trend similar to that in Fig. 4. However, in this case, the loss equation was also dependent on the turbine rotational speed. Similarly to the nozzle modelling, if the rotor was already choked, the design routine ended. Alternatively, the rotor equations were solved and the turbine design was completed by the post-processing of the data.

Fig. 3(b) shows the off-design modelling strategy. In this case an existing turbine design, or calculated as in Fig. 3(a), was the input and turbine performance maps were generated as the output. The model inputs were the same as those of the design model, except that the full turbine geometry was given as well. The mass flow rate ṁ was provided as an input for the generation of performance maps when the turbine was not choked. If the turbine is choked,

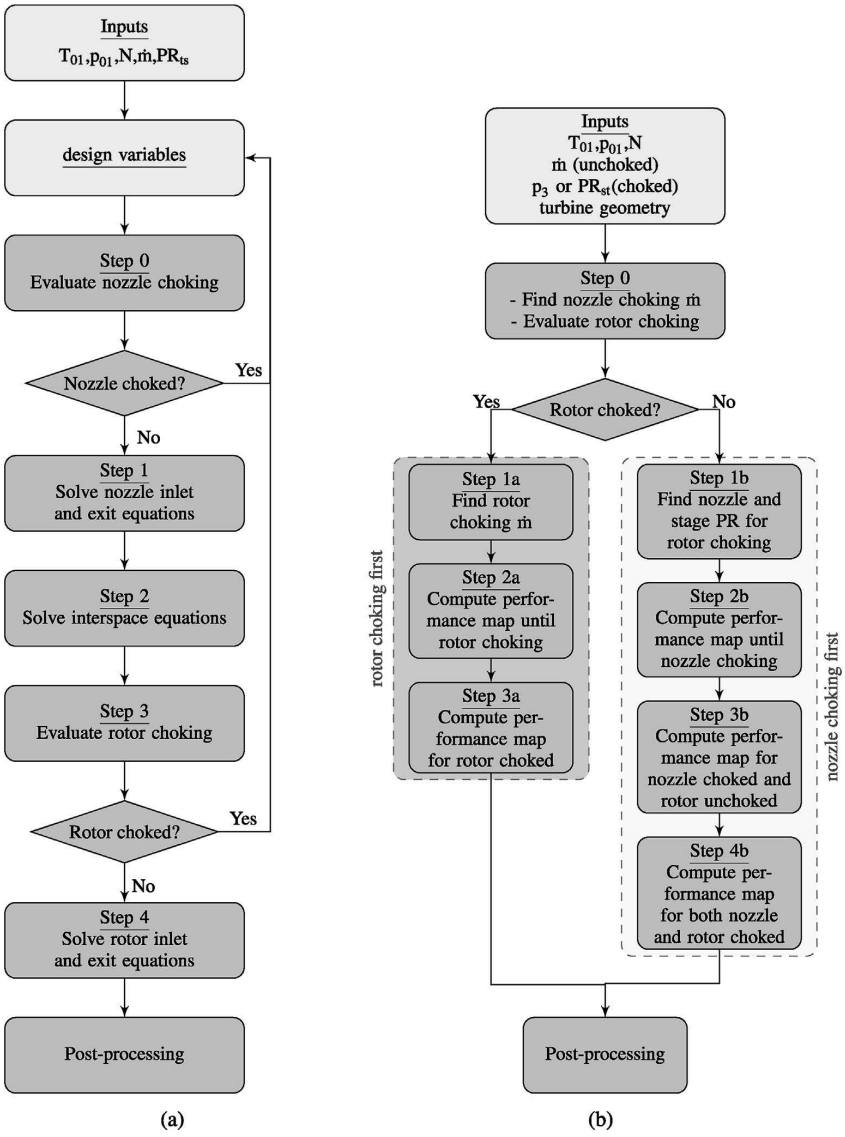

Fig. 3. Modelling strategy for high-pressure ratio RITs: (a) preliminary design model; (b) off-design model.

the mass flow rate is constant, and the outlet pressure can assume an infinitude of values. Hence, in this case, the static pressure at the turbine outlet was also specified. The workflow of Fig. 3(b) applies to a single speed line, and an iterative process was implemented to generate the full performance maps.

The off-design modelling strategy started by evaluating whether, for the given input conditions, the nozzle or the rotor is the first to choke (*Step 0*). The set of Eqs. (1)–(3) is used for the nozzle. In *Step 0*, the nozzle choking mass flow rate is found by determining the zero of the locus of maxima of Eq. (3). Afterwards, the algorithm evaluates whether the rotor was already choked at the nozzle choking mass flow rate by solving Eqs. (4)–(10). Like in the design strategy, the off-design methodology evaluates whether the rotor choking mass flow rate is smaller than the nozzle choking mass flow rate, and follows two different paths according to the result. Steps 1a-3a in Fig. 3(b) relate to the configurations 1) and 2) of Fig. 2, where the rotor chokes first. Steps 1b-4b in Fig. 3 relate to the configurations 1), 3) and 4) of Fig. 2, where the nozzle chokes first. If the rotor choked first, the choking mass flow rate and the choking density were found by determining the zero of the locus of maxima of Eq. (10) (*Step 1a*). Conversely, if the nozzle chokes first, the algorithm identifies the rotor choking point occurring at higher values of stage expansion ratio (*Step* 1b). A numerical search method was used to find the zero of Eqs. (8)–(10) by changing the rotor inlet pressure. The corresponding values of nozzle and stage pressure ratio were then recorded and used in the subsequent

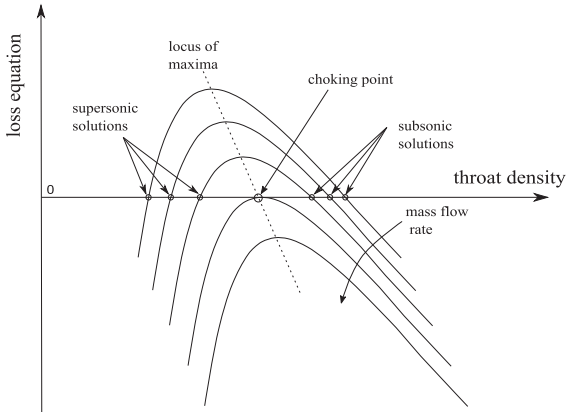

Fig. 4. Identification of the choking point for a blade row.

steps.

Nozzle and rotor unchoked (Steps 2a and 2b*).* The performance maps were generated by varying the mass flow rate up to the choking point. Equations (1)–(10) were sequentially solved for each value of mass flow rate, finding the corresponding value of pressure ratio.

Nozzle unchoked and rotor choked (Step 3a). When the rotor choking point was reached, the mass flow rate was kept constant, and the nozzle operation was fixed since any further expansion dowstream the rotor could not affect the conditions upstream the throat [34]. In this case, the rotor choking mass flow rate as well as the total-to-static pressure ratio of the stage were provided as inputs to the turbine model, and any further expansion was allowed by means of a post-expansion process after the throat. The value of choking density, previously calculated in *Step 1a*, was used to determine the values of the thermodynamic and flow conditions at the throat by applying mass continuity and the energy balance, Eqs. (8) and (9). The rotor exit density, ρ_6, after the post-expansion was found by solving the energy and mass balances and the post-expansion loss equation between the rotor throat and the exit as follows:

$$W_6 = \sqrt{2\cdot(I_4 - h(\rho_6, p_6)) + U_6^2} \tag{11}$$

$$\beta_6 = -\cos^{-1}\left[\dot{m}_{\,ch,rot}/(\rho_6 W_6 A_5(1 - BF_5))\right] \tag{12}$$

$$\Delta h_{pe,rot} - h(\rho_6, p_6) + h(p_6, s_5) = 0 \tag{13}$$

where $\Delta h_{pe,rot}$ represents the post-expansion loss, s_5 is the entropy at the throat, and $\dot{m}_{\,ch,rot}$ is the value of rotor choking mass flow rate.

Nozzle choked and rotor unchoked (Step 3b*).* The thermodynamic and flow parameters at the choked throat were found by applying mass and energy balances between the nozzle inlet and the throat. When the pressure ratio was larger than the choking value, a post-expansion was allowed at the nozzle outlet. In order to determine the conditions after the post-expansion, the energy and mass balances and the post-expansion loss equation, were solved, respectively, as follows:

$$C_3 = \sqrt{2\cdot(h_{01} - h(\rho_3, p_3))} \tag{14}$$

$$\alpha_3 = \cos^{-1}\left[\dot{m}_{\,ch,noz}/(\rho_3 C_3 A_2(1 - BF_2))\right] \tag{15}$$

$$\Delta h_{pe,noz} - h(\rho_3, p_3) + h(p_3, s_2) = 0 \tag{16}$$

In this case, $\Delta h_{pe,noz}$ represents the post-expansion losses, s_2 is the specific entropy at the throat, and $\dot{m}_{\,ch,rot}$ is the rotor choking mass flow rate.

Both nozzle and rotor choked (Step 4b*).* When both the nozzle and the rotor were choked, any further expansion downstream the rotor exit was allowed by means of a post-expansion after the rotor throat using Eqs. (14)–(16).

2.2. Empirical models for losses and flow deviation

The sets of equations described in Sec. 2.1 require the use of empirical models for the losses and the exit flow angles for each blade row. Typically, the information on possible blockage effects in the blade rows is provided empirically and depends on the specific test case. In this work, the best agreement with the experimental data was found using BF = 0 and, consequently, the blockage effects were neglected.

The loss correlations were based on the formulations by Baines [52], however some modifications were introduced. In contrast to the axial turbine field, for radial turbines there is a deep lack of techniques used to predict nozzle losses based on geometry and flow conditions [59]. In the literature, nozzle losses have been often neglected or considered of a much lower entity than the rotor losses [52]. However, experimental works [3,64] on high-pressure turbines and numerical studies [65,66] on very high-pressure ratio RITs suggest that a proper nozzle model, and associated losses, are paramount to obtain meaningful results.

In this work, three types of nozzle losses were considered: the passage loss, the trailing edge loss, and the post-expansion loss. Among the few available nozzle passage loss formulations, those by Rodgers [46] and Rohlik [67] appear to be the most reliable in the literature [68]. The formulation by Rodgers [46] was preferred since it directly relates the loss to geometry and flow parameters without resorting to the use of the boundary layer parameters, which are less straightforward to estimate. The nozzle passage loss correlation by Rodgers [46] assumes that the trailing edge and shock losses are negligible, provided that the trailing edge to chord ratio is less than 2% and that Mach numbers are lower than 1.2.

In order to fully represent HPR conditions, the losses associated to the trailing edge blockage and to high Mach numbers at the blade outlet were included in the present model. The trailing edge loss was modelled using the formulation by Glassman [55], which, according to Refs. [55,69,70], is based on the actual blade blockage and provides a more physical formulation than that based on the meridional velocity component adopted by Baines [52]. The post-expansion loss is based on the work by Aungier [39].

The vaneless space loss uses a conventional pipe-flow correlation by Khastner and Bhinder [43] often employed in the literature, see Refs. [59,63,69]. The friction factor in the interspace between nozzle and rotor was estimated using the following correlation proposed by Japikse [71]:

$$C_f = k\left(\frac{1.8\cdot 10^5}{Re_4}\right)^{0.2} \tag{17}$$

Equation (17) was developed from the experimental measurements on a number of diffusers for centrifugal compressors and

shows that the friction factor in unguided swirling flows decreases with the average Reynolds number at the exit of the vaneless space. Equation (17) was used to model the interspace loss in RITs following Whitfield and Baines [63]. Japikse [71] noted that the coefficient k in Eq. (17) varied between 0.005 and 0.02 in different applications and recommended to use the value 0.01.

The rotor model included the evaluation of losses internal and external to the blade passages. The internal losses were modelled with the passage loss, clearance loss and incidence loss correlations by Baines [52]. Moreover, rotor trailing edge and post-expansion loss models were introduced in a similar way as those of the nozzle modelling. The external losses included the effect of the rotor disc friction, and these were modelled as a sudden enthalpy drop at constant static pressure following Whitfield and Baines [63], and were predicted according to the method suggested by Daily and Nece [72].

Table 2 shows the final set of loss models. The coefficients K_{p1}, K_{p2}, K_{p3}, K_{vs} and K_{inc} were initially selected for calibration in this work, although the final set for calibration was selected after a dedicated sensitivity analysis, see Sec. 2.3.

Unlike within the axial-flow turbine field, there is a lack of well-established and reliable correlations for the deviation angle in RITs. The exit flow angle at unchoked conditions for the nozzle and the rotor was predicted using the cosine rule, where o is the throat opening and s is the vane spacing.

$$\alpha_2 = \cos^{-1}(o_2/s_2)\beta_5 = \cos^{-1}(o_5/s_5) \tag{18}$$

If the nozzle or the rotor operates at supersonic flow conditions, the off-design modelling strategy solves the post-expansion equations and determines the exit flow angle according to Eqs. (11)–(13) or Eqs. (14)–(16).

2.3. Sensitivity analysis

A sensitivity analysis was applied to the off-design turbine model in order to achieve the following: i) identify the most sensitive calibration coefficients with respect to the output mass flow rate and isentropic efficiency; ii) remove the calibration coefficients which resulted to be less sensitive to the changes in mass flow rate and efficiency, reducing the computational requirements of the simulations; iii) identify the range of values for which the calibration coefficients fulfil the choking conditions required by the test cases.

A global sensitivity analysis based on the Monte Carlo method [73] was employed. Compared to a local sensitivity analysis method, the global sensitivity analysis takes into account the mutual interactions between the different calibration coefficients. Since the Monte Carlo method is based on a probabilistic approach, the results of the sensitivity analysis were analysed in terms of their probability distribution. The Monte Carlo method was applied using a numerical model written in the MATLAB language [57], which is documented in Ref. [74]. A uniform probability distribution without correlation control was used for the input calibration coefficients. A study on the effects of increasing sampling size up to 1000 samples for each coefficient and operating point in the turbine map was performed. A number of 500 samples was selected since it provided a reasonable trade-off in terms of accuracy of the results and required computational time. Each speed line was divided into 50 points, corresponding to 25000 samples per speed line generated by the Monte Carlo method. The sensitivity analysis was applied to the turbine model using the test cases described in Sec. 2.4.

2.4. Calibration method

The methodology presented in Sec. 2.1 was applied to six test cases of HPR turbines operating with air found in the literature. These test cases were selected from the list provided in Table 1 according to the following criteria: 1) they present reliable and well-documented data; 2) they include turbine performance maps at HPR conditions; 3) they have similar geometric features, i.e. only nozzled turbines without volute and diffuser. Table 3 lists the

Table 2
Loss correlations.

Loss mechanism	Loss model	Reference
Nozzle passage	$\Delta h_{pl,noz} = K_{p1}\frac{0.05}{Re_3^{0.2}}\left[\frac{3\tan\alpha_3}{s_3/c_n}+\frac{s_3\cos\alpha_3}{b_3}\right]\frac{1}{2}C_3^2$	Rodgers [46]
Nozzle trailing edge	$\Delta h_{t,noz} = \left(\frac{Z_n t_3}{2\pi r_3\cos\alpha_3}\right)^2\frac{1}{2}C_3^2\cdot Y_3^{(*)}$	Glassman [55]
Nozzle post-expansion	$\Delta h_{pe,noz} = \left(\frac{M_3 - M_2}{M_3}\right)^2\frac{1}{2}C_3^2\cdot\frac{1}{Y_3^{(*)}}$	Aungier [39]
Interspace	$\Delta h_{vs} = K_{vs}C_f\left(\frac{L}{D}\right)\frac{1}{2}\left(\frac{C_3+C_4}{2}\right)^2$	Kastner and Bhinder [43]
Rotor incidence	$\Delta h_{inc,rot} = K_{inc}(\sin\lvert\beta_4 - \beta_{4,opt}\rvert)^2\frac{1}{2}W_4^2$	Baines [52]
Rotor passage	$\Delta h_{pl,rot} = K_p\left\{K_{p2}\left(\frac{L_H}{D_H}\right)+0.68K_{p3}\left[1-\left(\frac{r_{6rms}}{r_4}\right)^2\right]\left(\frac{\cos\beta_6}{b_6/c_r}\right)\right\}\frac{1}{2}(W_4^2+W_6^2)$	Baines [52]
Rotor clearance	$\Delta h_c = \frac{U_4^3 Z_r}{8\pi}(K_a\varepsilon_a C_a + K_r\varepsilon_r C_r + K_{ar}\sqrt{\varepsilon_a\varepsilon_r C_a C_r})$	Baines [52]
Rotor trailing edge	$\Delta h_{t,rot} = \left(\frac{Z_r t_6}{\pi(r_{6s}+r_{6h})\cos\beta_6}\right)^2\frac{1}{2}W_6^2\cdot Y_6^{(*)}$	Glassman [55]
Rotor post-expansion	$\Delta h_{pe,rot} = \left(\frac{M_{6,rel} - M_5}{M_{6,rel}}\right)^2\frac{1}{2}W_6^2\cdot\frac{1}{Y_6^{(*)}}$	Aungier [39]
Rotor disc friction	$\Delta h_{df} = 0.25K_f\frac{\overline{\rho}U_4^3 r_4^2}{\dot{m}}$ where $\overline{\rho} = \frac{\rho_4+\rho_6}{2}$ $Re_4 = \frac{\rho_4 U_4 r_4}{\mu_4}$ if $Re_4 < 3\cdot10^5$ $K_f = 3.7(\varepsilon_b/b_4)^{0.1}Re_4^{-0.5}$ if $Re_4 > 3\cdot10^5$ $K_f = 0.102(\varepsilon_b/b_4)^{0.1}Re_4^{-0.2}$	Daily and Nece [72]

* $Y_3 = \left[1+\frac{k_3-1}{2}M_3^2\right]^{\frac{k_3}{1-k_3}}$. $Y_6 = \left[1+\frac{k_6-1}{2}M_{6,rel}^2\right]^{\frac{k_6}{1-k_6}}$.

Table 3
Data of the HPR turbines selected for calibration.

	Test case	Meitner and Glassman	McLallin et al.	Simonyi rotor 1	Simonyi rotor 2	Rogo	Atkinson
	Ref.	[75]	[3]	[9]	[9]	[7]	[15]
Input conditions							
T_{01}	[K]	377.778	322.2	477.78	477.78	394	418
p_{01}	[Pa]	38610.6	137900	333706.3	333706.3	164000	354550
N	[rpm]	29550; 17730	9437–34602	17927–21911	15138–22708	12751–15939	26277–40795
Stator							
b_1	[m]	0.0147	0.0109	0.021	0.021	0.015	0.008
b_3	[m]	0.015	0.008	0.012	0.012	0.015	0.008
r_1	[m]	0.073	0.097	0.224	0.224	0.251	0.111
r_3	[m]	0.060	0.084	0.194	0.194	0.194	0.092
z_n	[−]	14	29	36	36	15	17
t_3	[m]	0.001	0.001	0.0003	0.0003	0.003	0.0012
α_{3b}	[°]	72.47	76	70	70	77	76
o_2	[m]	0.0073	0.0036	0.0091	0.0092	0.0174	0.0095
Rotor							
b_4	[m]	0.015	0.008	0.012	0.012	0.016	0.0077
r_4	[m]	0.058	0.075	0.185	0.185	0.177	0.0867
r_{6s}	[m]	0.041	0.047	0.118	0.118	0.114	0.0609
R_{6h}	[m]	0.014	0.023	0.076	0.076	0.051	0.0261
β_{4b}	[°]	0	0	0	0	0	0
β_{6b}	[°]	−56.86	−58	−55.3	−53.86	−60	−60
Z_r	[−]	22	12	14	14	13	14
t_6	[m]	0.0002	0.004	0.001	0.001	0.00076	0.0024
o_5	[m]	0.0048	0.0065	0.02	0.02	0.01706	0.0223
l_z	[m]	0.040	0.04572	0.046	0.043	0.107	0.0399
ϵ_a	[m]	0.0003	0.0003	0.0005	0.0002	0.0004	0.00075
ϵ_r	[m]	0.0004	0.0003	0.0002	0.0004	0.0004	0.0004
ϵ_b	[m]	0.0003	0.0003	0.0003	0.0003	0.0009	0.00075

employed geometry and input data for the test cases. All test cases used air as working fluid.

The calibration method consists in fitting of the loss models against the mass flow rate and efficiency maps of the selected experimental test cases. Each set of calibration coefficients can be expressed by the array

$$\overline{X} = \{K_{p1}, K_{p2}, K_{p3}, K_{inc}, K_{vs}\} \tag{19}$$

where $K_{p1}K_{p2}K_{p3}$, K_{inc} and K_{vs} are the calibration coefficients in the loss models respectively. The objective of the calibration was to minimise the overall relative root mean square error (RRMSE) in terms of mass flow rate and efficiency. The optimisation function, f, is expressed as

$$f = min\left\{\frac{1}{n_t}\sum_{i=1}^{n_t}RRMSE\left(\eta_{is,i}(\overline{X})\right), \frac{1}{n_t}\sum_{i=1}^{n_t}RRMSE\left(\dot{m}_i(\overline{X})\right)\right\} \tag{20}$$

$$RRMSE(\eta_{is}) = \sqrt{\frac{1}{n_p}\sum_{j=1}^{n_p}\left(\frac{\eta_{is,exp,j} - \eta_{is,mod,j}(\overline{X})}{\eta_{is,exp,j}}\right)^2} \tag{21}$$

$$RRMSE(\dot{m}) = \sqrt{\frac{1}{n_p}\sum_{j=1}^{n_p}\left(\frac{\dot{m}_{exp,j} - \dot{m}_{mod,j}(\overline{X})}{\dot{m}_{exp,j}}\right)^2} \tag{22}$$

where η_{is} and $\dot{m}$ indicate the isentropic efficiency and mass flow rate for $i = 1, .., n_t$ test cases and $j = 1, \ldots, n_p$ points in the performance map. The subscripts exp and mod refer to the experimental and mean-line model data, respectively. The multi-objective optimisation was performed by means of a genetic algorithm using 150 generations. When the optimisation is performed, the calibration coefficients are changed in order to provide the best possible agreement with the experimental data. Despite being mathematically consistent, this rationale does not necessarily ensure that the physics of the problem is fully respected. For this reason, two different optimisation cases were considered. In the first case, the optimisation was unconstrained, meaning that there are no specified boundaries on the calibration coefficients and that the optimiser sought the best solution from the mathematical viewpoint. In the second case, the calibration coefficients were constrained by lower and upper bounds, ensuring the correct identification of the choking point. In this case, the optimiser found a solutions which is consistent from both the mathematical and the physical viewpoints. The upper and lower bounds of the calibration coefficients for the constrained optimisation were found by applying the sensitivity analysis approach to identify the boundaries in which the choking point is correctly predicted in all the speed lines of the test case data.

2.5. Validation method

In order to assess the suitability of the loss coefficients obtained after calibration, a validation of the design and off-design models was performed.

The design model was first validated using the test cases which were used for the calibration of the off-design model. Afterwards, its results were compared with the mean-line and CFD results at the design point for an ORC turbine operating with the fluid R143a documented in Ref. [76]. This test case was selected for validation due to the presence of sufficient information regarding turbine geometry and flow conditions. The results of Ref. [76] were obtained using two commercially-available software: RITAL (Concepts NREC) for the mean-line design, and Axcent and ANSYS-CFX for the 3D geometry and CFD, respectively. The comparison of results was performed by assigning the same design specifications as in the commercial mean-line software in terms of inlet thermodynamic and flow conditions, turbine geometry and stator outlet Mach number.

The suitability of the off-design model to different geometries and operating conditions was assessed by selecting two specific experimental test cases which were not included among the test cases used for calibration. The first test case is a 2 kW ORC turbine which was documented and tested by Demierre et al. [30,31]. This test case was selected since it contains the full details of an ORC radial turbine geometry as well as off-design operating data. The turbine operates with the refrigerant R134a in the range of rotational speeds 147000–206000 rpm and pressure ratios 3.1–4.4. This test case is different to those used for calibration in the sense that it has a diffuser. In the validation, the diffuser was modelled using the equations described by Moustapha et al. [59] using a total pressure recovery coefficient of 0.55. The second test case is the Ricardo C80 turbine documented in Refs. [1,2], which was tested up to pressure ratios of 5.0. The geometry differs from those of the calibration test cases by the presence of a volute. In this case, it was assumed that the losses in the volute were small and could be incorporated in the nozzle losses. Moreover, the throat opening was not provided in the original data, and was therefore estimated using a formulation by Li et al. [42]:

$$o_2 = 2r_3 \sin\left(\frac{\theta}{2}\right)\cos\left(\frac{\theta}{2} - \alpha_{3b} - \frac{\gamma}{2}\right) \tag{23}$$

Equation (23) assumes a wedge shape for the vane trailing edge with included angle $\gamma = 11°$ for the Ricardo C80 turbine and $\theta = 2\pi/Z_s$ as the center angle in the radial plane.

3. Results

3.1. Sensitivity analysis

Fig. 5 shows the results of the global sensitivity analysis on the efficiency and the mass flow rate. In the sensitivity analysis with respect to the isentropic efficiency, the calibration coefficient K_{p2}, associated to the friction losses in the rotor passage, appears to be the most significant parameter with mean values of standardised regression coefficients between approximately 0.76 and 0.98. The calibration coefficients related to the nozzle passage loss, K_{p1}, and the rotor incidence loss, K_{inc}, appear to be the second most significant ones in some cases. The turbine efficiency results to be less sensitive to the calibration coefficient associated with the rotor secondary flows passage loss, K_{p3}. Finally, the interspace loss calibration coefficients, K_{vs}, shows very low values of mean and standard deviation, suggesting that its impact on the efficiency is insignificant. The sensitivity analysis of the calibration coefficients with respect to the mass flow rate indicates that, in most cases, K_{p2} has the largest influence on the mass flow rate. In this case, however, K_{p2} presents lower mean values and a larger scatter, which suggests that it has a smaller influence on the mass flow rate compared to the turbine efficiency. It is also noted that K_{p1} has the strongest influence on the mass flow rate in the last test case, suggesting a stronger impact of the nozzle losses in this case. The relatively high standard deviation observed in some test cases (especially for $K_{p1}K_{p2}K_{inc}$) indicates that the significance level of the calibration coefficients varies across the operating points of the turbine map and depends on the different flow conditions in the turbine. Moreover, the sensitivity analysis highlights that the significance level of the coefficients depends on the test case. At the same time, the coefficient K_{vs} appears to be the least significant from a statistical viewpoint and, henceforth, it was not included as a decision variable in the optimisation. This simplification allows a reduction of the simulation time without compromising significantly the accuracy of the results.

The sensitivity analysis was also applied to identify the range of values for which the calibration coefficients could ensure the identification of the choking point in accordance with the test cases.

3.2. Calibration

Fig. 6 shows the results of the multi-objective optimisation process with respect to the RRMSE in isentropic efficiency and mass flow rate, namely $RRMSE_\eta$ and $RRMSE_m$, for the cases of unconstrained and constrained optimisation. The optimal pareto front represented in Fig. 6 was found after approximately 120 generations. In the uncostrained optimisation, the optimal solutions range between 2.05% and 2.17% in $RRMSE_\eta$, and between 1.45% and 1.56% in $RRMSE_m$. The constrained optimisation used bounds to ensure a suitable identification of the choking point, and reduced the solution space, resulting in higher values of $RRMSE_\eta$, between 2.13% and 2.8%. Similar values of $RRMSE_m$ were found for the constrained and unconstrained optimisations. Each point in the pareto front corresponds to a set of optimal calibration coefficients, which can then be selected according to the key-decision criteria set by the designer. In order to select a final set of optimal coefficients in the pareto fronts of Fig. 6, an equal weight for the two objective functions was applied. The selected coefficients are listed in Table 4. A comparison of the calibrated coefficients with those of Baines [52]

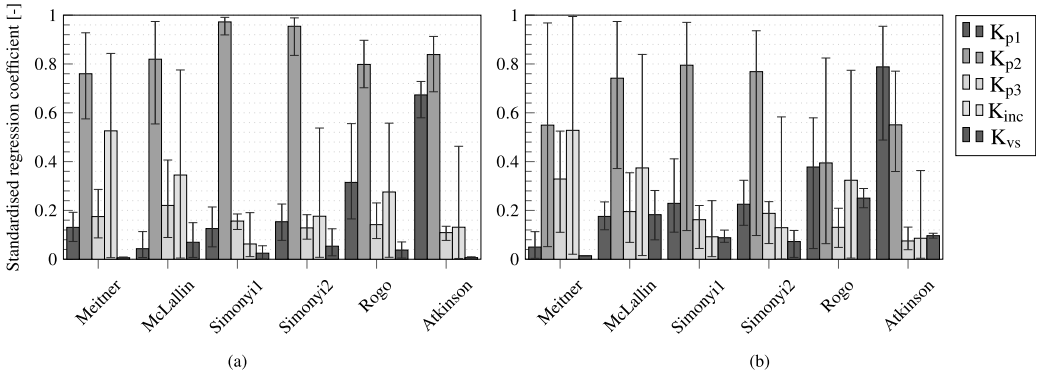

Fig. 5. Significance level of the calibration coefficients: (a) on the turbine total-to-static isentropic efficiency; (b) on the mass flow rate. The bars indicate the standard deviation from the mean value. The analysis employed the test cases listed in Table 3.

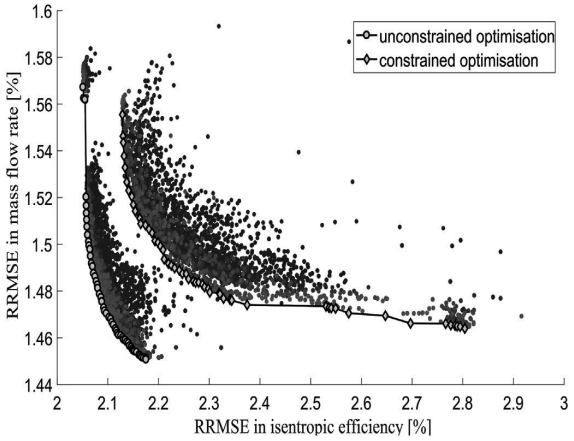

Fig. 6. Optimal pareto fronts from the unconstrained and constrained multi-objective optimisations. The colours indicate the evolution of the pareto front from the initial (◦) to the final (◦) generations. (For interpretation of the references to colour in this figure legend, the reader is referred to the Web version of this article.)

Table 4
Optimal set of calibration coefficients for an equal weight of $RRMSE_\eta$ and $RRMSE_m$ in the pareto front.

	unconstrained	constrained
K_{p1}	1.3881	1.4152
K_{p2}	0.637	0.5903
K_{p3}	0.1042	0.4036
K_{inc}	0.8952	0.8754

indicate that a 40% higher nozzle loss coefficient is required to provide a better match with the test cases, as well as lower rotor primary, secondary and incidence loss coefficients.

Fig. 7 shows a comparison of the values of $RRMSE_\eta$ and $RRMSE_m$ for the baseline, unconstrained and constrained optimisation cases. Before calibration of the loss coefficients, the maximum deviation in the single test cases higher, and the overall deviation is approximately 5.88% in the efficiency and 2.38% in the mass flow rate. After the optimisation, the overall $RRMSE_\eta$ is reduced to 2.11% and 2.04% for the constrained and unconstrained optimisations, respectively. At the same time, the overall $RRMSE_m$ is decreased to 1.54% and 1.33%, respectively. Moreover, only a small difference was found between the constrained and unconstrained test cases, as the optimal set of coefficients have also similar values, see Table 4.

Figs. 8 and 9 show a visual comparison of the performance maps before and after the calibration process for three exemplary test cases.

3.3. Validation

Fig. 10 depicts the results of the validation of the design model with the experimental test cases.

The results show that the deviation in efficiency between the model and the experimental data is between 0.1 %-points and 2.83 %-points. The largest deviation is seen for the test case by Rogo [7]. This deviation can also be seen in Fig. 8, which shows that the optimiser found the best data fit by compromising some percentage points in efficiency for the line at 100% speed. Table 5 reports the comparison between the design results of the present mean-line model and those obtained with two commercial software for the ORC turbine documented in Ref. [76]. The present mean-line model provides power and efficiency predictions closer to the CFD code, with up to 1.6% and 1.78 %-points of deviation, respectively. For the same total-to-total expansion ratio as RITAL, a maximum deviation of 8.3 %-points is reported for the rotor exit Mach number conditions. The lower flow velocity at the rotor exit suggests a higher work extraction in the rotor, possibly due to a higher rotor efficiency. This consideration is in agreement with the higher values of power output and isentropic efficiency seen in Table 5 compared to RITAL.

Fig. 11(a) and (b) show the results of the validation of the off-design model with the test case by Demierre et al. [30,31]. The mean-line model predicts the mass flow rate within less than 1% in all operating conditions. The total-to-static efficiency appears to be overpredicted in almost all operating points. The predicted values show a deviation up to 5% compared to the measured values. However, this deviation is within the uncertainty range of the experimental data.

Fig. 11(c) and (d) show the results of the validation of the off-design model with the Ricardo turbine C80. In this test case, the choking point is governed by the nozzle. A good agreement, with a value of $RRMSE_m$ of 1.75% shown in Fig. 11(d), is achieved by estimating the throat opening with Eq. (23). It is worth noting that the use of the simple cosine rule to estimate value of the nozzle throat yields a 20% lower mass flow rate. This suggests that a more detailed knowledge of the geometry in proximity of the blade

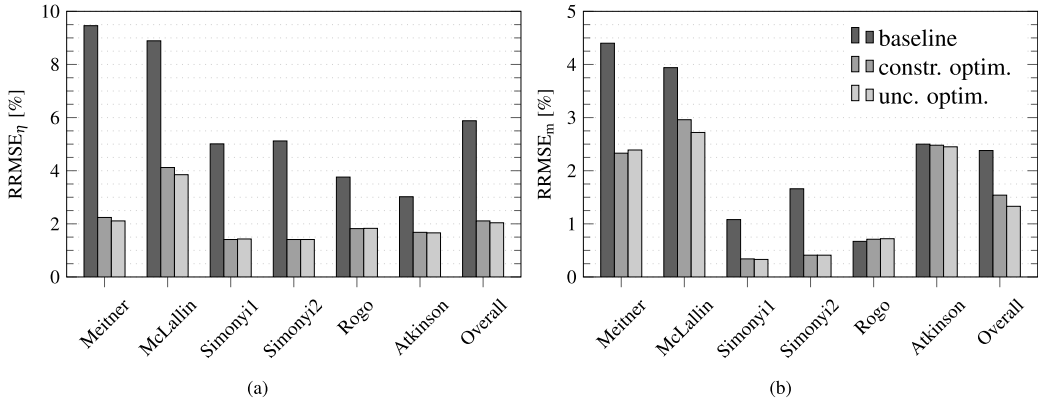

Fig. 7. Comparison of RRMSE values for the different test cases before and after the optimisation process: (a) RRMSE in isentropic efficiency; (b) RRMSE in mass flow rate.

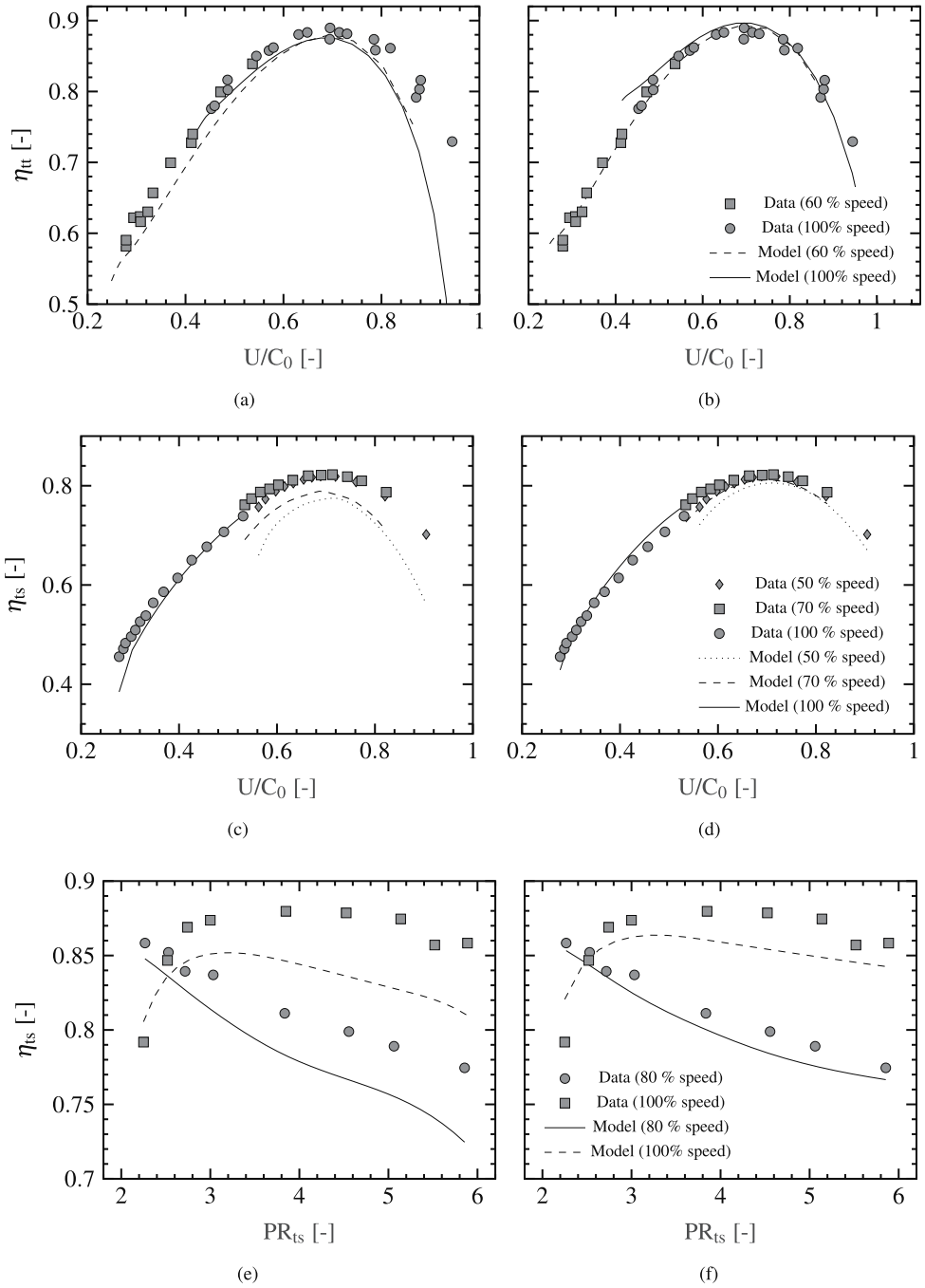

Fig. 8. Exemplary isentropic efficiency maps before (a,c,e) and after (b,d,f) the multi-objective optimisation: (a,b) Metiner and Glassmann [75] test case; (c,d) McLallin [3] test case; (e,f) Rogo [7] test case.

throat is essential to predict the correct values of mass flow rate. In terms of efficiency, the results indicate that the model predicts good agreement for low values of rotational speed and velocity ratio U/C_0, while at higher speeds the losses increase, and the maximum point is shifted towards lower values of U/C_0 of about 0.55.

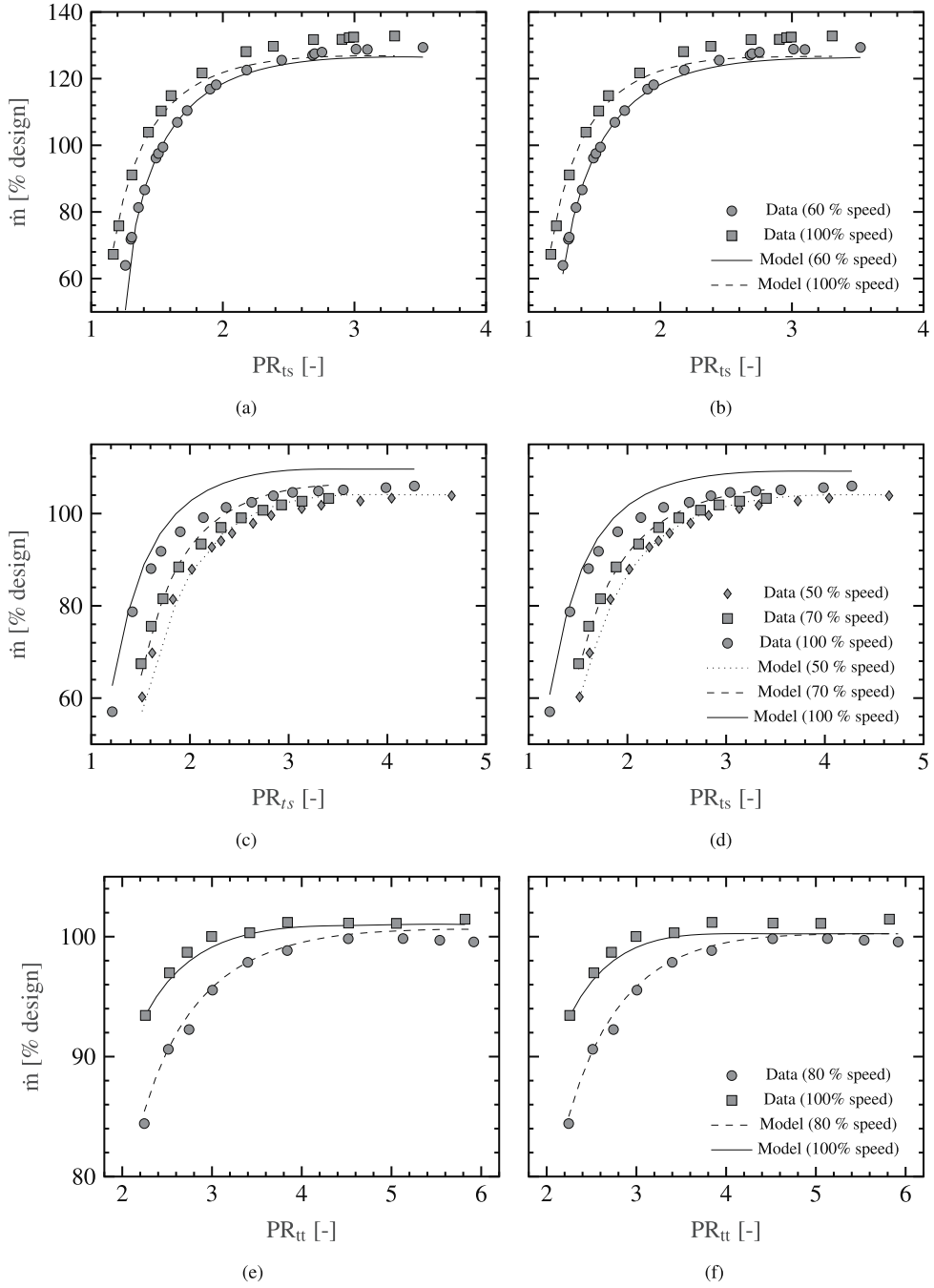

Fig. 9. Exemplary mass flow rate maps before and after the multi-objective optimisation: (a,b) Metiner and Glassmann [75] test case; (c,d) McLallin [3] test case; (e,f) Rogo [7] test case.

4. Discussion

In this work, the optimal values of the loss coefficients were identified by the best possible match in the values of mass flow rate, pressure ratio and turbine isentropic efficiency. The model may be employed for the preliminary design and performance prediction of the turbine. However, it was not the objective of this work to assess the suitability of the loss models with respect to the

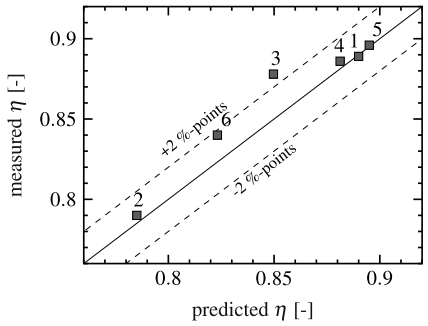

Test case	Ref.	No.	PR_{ts} [-]	ṁ [kg/s]	N [rpm]	U/C_0 [-]	η [-]	η_{exp} [-]	deviation [%]
Meitner and Glassman	[75]	1	1.54	0.260	29550	0.700	0.890 (t-t)	0.889 (t-t)	0.10%
Mc Lallin	[3]	2	3.23	0.187	31456	0.609	0.785 (t-s)	0.790 (t-s)	-0.49%
Rogo	[7]	3	4.54	1.044	164000	0.655	0.850 (t-t)	0.878 (t-t)	-2.83%
Simonyi rotor 1	[9]	4	4.99	2.361	19919	0.674	0.881 (t-t)	0.886 (t-t)	-0.48%
Simonyi rotor 2	[9]	5	4.99	2.350	18923	0.641	0.895 (t-t)	0.896 (t-t)	-0.10%
Atkinson	[15]	6	3.50	0.850	39000	0.700	0.823 (t-s)	0.840 (t-s)	-1.68%

(t-t) = total-to-total efficiency; (t-s) = total-to-static efficiency

Fig. 10. Validation of the turbine design model with experimental data.

Table 5
Comparison of the turbine design model with commercial mean-line and CFD tools presented in Ref. [76].

Parameter	Units	RITAL	CFD	present mean-line	deviation (RITAL)	deviation (CFD)
Global variables						
p_{01}/p_{06}	[−]	2.544	2.509	2.54	0.0%	1.4%
η_{ts}	[−]	76.8	83.5	81.72	4.92 pp	−1.78 pp
η_{tt}	[−]	79.8	87.6	86.68	6.88 pp	−0.92 pp
P	[kW]	393.6	421.5	414.83	5.4%	−1.6%
Stator inlet						
h_{01}	[kJ/kg]	499.2	501	499.24	0.0%	−0.4%
p_{01}	[kPa]	4989.6	4849.85	5000.00	0.2%	3.1%
Rotor inlet						
M_4	[−]	0.88	0.94	0.88	0.1%	−6.3%
p_{04}	[kPa]	4886.5	4717	4822.70	−1.3%	2.2%
T_{04}	[K]	412.2	411.9	411.71	−0.1%	0.0%
Rotor outlet						
M_6	[−]	0.363	0.364	0.33	−8.3%	−8.6%
P_{06}	[kPa]	1961.4	1933.1	1964.80	0.2%	1.6%
T_{06}	[K]	370.2	367.1	369.25	−0.3%	0.6%
h_{06}	[kJ/kg]	476.4	476.3	475.18	−0.3%	−0.2%

pp = %-points.

correct prediction of the internal flows in the turbine. In this respect, further conclusions should be drawn only after a detailed comparison with measurements or high-fidelity CFD computations [36]. Detailed CFD studies [64,66,77] on high-pressure ratio turboexpanders indicate that unsteady Reynolds-Averaged Navier Stokes (URANS) simulations can provide a reliable performance estimation.

Another important aspect concerns the accuracy in the obtained results. The optimal calibration coefficients predicted turbine efficiencies within ± 2.1%, and there are limited works in the literature that could be used for comparison. Glassman [55] calibrated the turbine losses using the data of three, low-pressure ratio turbines, showing a deviation within 1 %-point. Rodgers [46] validated a RIT model to an accuracy of ± 2% in efficiency. Baines [52,54,59] validated a set of loss correlations using the data of about 30 turbines, showing an overall RRMSE of approximately 5.80% at the best efficiency points, corresponding to 3.20%-points. This number has the same order of magnitude as that obtained in this work before the optimisation including all the off-design operating points, see Fig. 7. These examples indicate that the accuracy obtained by different performance prediction models is in the range from 1 %-point to 3.8 %-points, suggesting that the ± 2.1% accuracy in the efficiency of the present model is acceptable.

If additional datasets become available in the literature, other

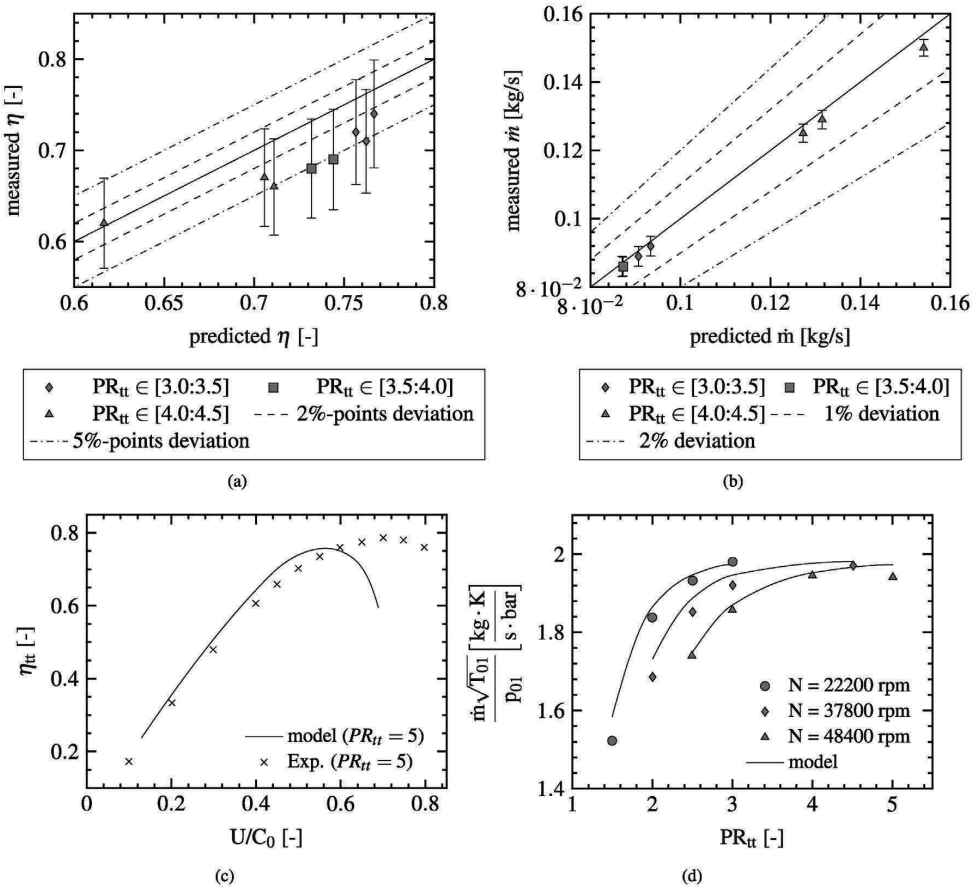

Fig. 11. Validation of the off-design turbine model: (a,b) turbine by Demierre et al. [30,31]; Ricardo C80 turbine [1,2]. The error bars represent the uncertainty in the experimental measurements.

methods such as artificial neural networks may be employed to fit the model. Previous studies [78–80] indicate that neural networks are an effective tool for empirical modelling and optimisation, especially for non-linear systems. However, neural networks require a sufficient amount of training data to ensure a good fit and avoid overfitting [81]. In case the datasets could be extended with a sufficient amount of data, response surface methods could be used to select the datasets for training the neural network [82]. If the available datasets are limited, as in this work, the optimisation method presented in this paper is the best option for refitting the calibration coefficients.

The method presented in this paper was calibrated using high-pressure ratio turbines with conventional design features, i.e. radial blade at the rotor inlet, absence of a volute and a diffuser, with rotor tip diameters between 116 and 370 mm, and using air. The same level of accuracy cannot be expected for turbines with different characteristics. The validation with the turbine by Demierre et al. [30,31], which has a tip diameter of 18 mm, uses a refrigerant as the working fluid, and has a diffuser, showed to provide a deviation up to 5 %-points in efficiency. The second case of validation was the Ricardo C80 turbine, which differed from the other turbines with a higher (80°) nozzle exit angle and by the presence of a volute. It is highlighted that the exact knowledge of the throat geometry is essential to identify the correct values of mass flow rate, and a suitable correlation, as Eq. (23), should be employed wherever possible.

This work considered only converging nozzle profiles. Reference works in the literature [36,83] indicate that the use of converging blade profiles is preferable up to an exit Mach number of 1.4, resulting in a supersonic post-expansion from the throat to the exit. For higher values of Mach number, strong shock waves and a large supersonic flow deviation occur at the blade exit, producing a dramatic drop in the turbine efficiency. In this case, converging-diverging blade profiles should be considered [36]. The loss correlations presented in this work were developed considering converging profiles blades. For this reason, it is recommended to use them up to the limit Mach number of 1.4 for the reliable application of this steady-state mean-line model.

Finally, it needs to be stressed that the model presented in this paper is subject to the limitations of all steady-state, mean-line models. The model does not attempt to reproduce the full details of the complex three-dimensional flow in the turbine and the corresponding losses. High-fidelity CFD solvers, such as unsteady Reynolds-Averaged Navier Stokes simulations [64,66,77], are required to capture the details of the complex flow field within the turbine. In this respect, the integration of mean-line methods and

CFD simulations is paramount for the complete fluid-dynamic design of the turbine [36,84].

5. Conclusions

This paper presented for the first time a comprehensive methodology for the preliminary design and performance prediction of radial-inflow turbines for high-pressure ratio applications. A single-stage, radial-inflow turbine model for preliminary design and off-design operation was developed, including consistent modelling strategies for the treatment of choking flow conditions.

A global sensitivity analysis was applied to the model to identify the significance level of the calibration coefficients in the turbine losses with respect to the isentropic efficiency and mass flow rate. The turbine loss coefficients were calibrated by minimising the deviation between predicted and measured data for the isentropic turbine efficiency and the mass flow rate across all the off-design data range of six well-documented turbines available in the open literature. The calibration method employed a multi-objective optimisation based on a genetic algorithm, which resulted in a significant reduction in the deviation between the numerical model and the experimental data compared to the baseline case (no calibration). Specifically, the RRMSE across the range of turbine operating conditions decreased from 5.9% to 2.1% in the prediction of isentropic efficiency and from 2.4% to 1.5% in the prediction of the mass flow rate.

Using the calibrated coefficients, the design model was validated against the turbine data used for calibration, and showed a maximum deviation of 2.83%. The off-design model was validated against the data of an ORC turbine and a turbine using air, both operating at high-pressure ratio conditions. Considering the experimental data uncertainty, the model provided good agreement with the ORC turbine, with less than 1% deviation in mass flow rate and about 5% deviation in efficiency. The validation with the air turbine provided good results and it was noted that a careful estimation of the blade throat, based on the detailed characteristics of the nozzle geometry, is paramount to obtain the correct values of the mass flow rate.

The developed turbine design and off-design prediction methodology is applicable to HPR turbines operating with any working fluid in the gas phase. The design and performance prediction models can be expected to provide results within the range of accuracy of the calibrated model for nozzled turbines with geometrical and loading characteristics similar to those used for calibration. A lower accuracy is expected for turbines with different characteristics. In particular, it is important to use or estimate accurate values of throat opening in order to correctly predict the maximum turbine mass flow rate.

Acknowledgements

The source of the funding is The Danish Council for Strategic Research in Sustainable Energy and Environment through Innovation Fund Denmark. The name of the project including this work is THERMCYC, and the project ID is 1305-00036B.

Nomenclature

Symbols

A	Area [m^2]
b	Blade width [m]
BF	Blockage factor [−]
C	Absolute velocity [m/s]
c_0	Spouting velocity [m/s]
c_r	Rotor chord [m]
D_H	Hydraulic diameter [m]
$\dot{m}$	Mass flow rate [kg/s]
h	Specific enthalpy [J/kg]
Δh	Enthalpy drop [J/kg]
I	Rothalpy [J/kg]
k	Specific heat ratio [−]
K_a, K_r, K_{ar}	Coefficients in Tab. 2 [-]
$K_{p1}, K_{p2}, K_{p3}, K_{vs}, K_{inc}$	Calibration coefficients [−]
l_z	Rotor axial length [m]
L_H	Hydraulic length [m]
M	Mach number [−]
N	Rotational speed [rpm]
o	Throat opening [m]
p	Static pressure [Pa]
PR	Pressure ratio [−]
r	Radius [m]
Re	Reynolds number [−]
RRMSE	Relative Root Mean Square Error [−]
s	Specific entropy [J/(kgK)]
t	Trailing edge thickness [m]
T	Temperature [K]
U	Peripheral velocity [m/s]
W	Relative velocity [m/s]
Z	Number of blades [−]

Abbreviation and acronyms

HPR	High-Pressure Ratio
ORC	Organic Rankine Cycle
RIT	Radial-Inflow Turbines

Greek letters

α	Absolute flow angle [°]
β	Relative flow angle [°]
ρ	Density [kg/m^3]
ε	Clearance gap [m]
η	Turbine isentropic efficiency [−]
γ	Nozzle wedge included angle [°]
θ	Nozzle center angle [°]

Subscripts

0	Total
1	Nozzle inlet
2	Nozzle throat
3	Nozzle exit
4	Interspace exit
5	Rotor throat
6	Rotor exit
a	Axial
b	Blade
c	Clearance
ch	Choking
h	Hub
inc	Incidence
n,noz	Nozzle
pe	Post-expansion
pl	Passage
opt	Optimal
rel	Relative
r	Radial
rot	Rotor
s	Shroud
t	Trailing edge

ts	Total-to-static
tt	Total-to-total
vs	Interspace

References

[1] Hiett G, Johnston I. Experiments concerning the aerodynamic performance of inward flow radial turbines. In: Proceedings of the institution of mechanical engineers, conference proceedings, vol. 178. London, England: SAGE Publications Sage UK; 1963. p. 28–42.
[2] Qiu X, Baines N. Performance prediction for high pressure-ratio radial inflow turbines. In: ASME turbo expo 2007: power for land, sea, and air, 14-17 may 2007, montreal, Canada, american society of mechanical engineers; 2007. p. 945–56.
[3] McLallin KL, Haas JE. Experimental performance and analysis of 15.04-centimeter-tip-diameter, radial-inflow turbine with work factor of 1.126 and thick blading. Tech. rep. USA: NASA, Washington D.C.; 1980.
[4] Kidwell J, Large G. Advanced technology components for model GTP305-2 aircraft auxiliary power system. Final report 6 May 75-15 Jul 1979, Tech. rep. Phoenix, AZ, USA: AiResearch Mfg. Co.; 1980.
[5] Rogo C, Hajek T, Chen A. Variable stator radial turbine. Tech. rep. Washington D.C., USA: NASA; 1984.
[6] Ribaud Y, Mischel C. Study and experiments of a small radial turbine for auxiliary power units. In: ASME 1986 international gas turbine conference and exhibit, 8-12 june 1986, dusseldorf, west Germany, american society of mechanical engineers; 1986. V002T04A003–V002T04A003.
[7] Rogo C. Variable area radial turbine fabrication and test program. Tech. rep. Washington D.C., USA: NASA; 1986.
[8] Rodgers C. Review of mixed flow and radial turbine options. In: 26th joint propulsion conference, 16-18 july 1990, orlando, FL, USA; 1990. p. 2414.
[9] Simonyi PS, Roelke RJ, Stabe RG, Nowlin BC, Dicicco D. Aerodynamic evaluation of two compact radial-inflow turbine rotors. Tech. rep. Washington D.C., USA: NASA; 1995.
[10] Pullen K, Baines N, Hill S. The design and evaluation of a high pressure ratio radial turbine, 14 june 1992, cologne, Germany. In: ASME 1992 international gas turbine and aeroengine congress and exposition, american society of mechanical engineers; 1992. V001T01A050–V001T01A050.
[11] Huntsman I, Hodson H, Hill S. The design and testing of a radial flow turbine for aerodynamic research. J Turbomach 1992;114(2):411–8.
[12] Huntsman I, Hodson H. An experimental assessment of the aerodynamic performance of a low-speed radial inflow turbine. In: 30th joint propulsion conference and exhibit, 27-29 june 1994, indianapolis, IN, USA; 1994. p. 1–8.
[13] Jones AC. Design and test of a small, high pressure ratio radial turbine. J Turbomach 1996;118(2):362–70.
[14] Spence S, Artt D. Experimental performance evaluation of a 99.0 mm radial inflow nozzled turbine with different stator throat areas. Proc IME J Power Energy 1997;211(6):477–88.
[15] Atkinson M. The design of efficient radial turbines for low power applications. Ph.D. thesis. University of Sussex; 1998.
[16] Doran W, Spence ST, Artt D. Experimental performance evaluation of a 99.0 mm radial inflow nozzled turbine with varying shroud profiles. Proc IME J Power Energy 2001;215(2):267–80.
[17] Feng Z, Deng Q, Li J. Aerothermodynamic design and numerical simulation of radial inflow turbine impeller for a 100 kW microturbine. In: ASME turbo expo 2005: power for land, sea, and air, 6-9 june 2005, reno, Nevada, USA, american society of mechanical engineers; 2005. p. 873–80.
[18] Spence S, Rosborough R, Artt D, McCullough G. A direct performance comparison of vaned and vaneless stators for radial turbines. J Turbomach 2006;129(1):53–61.
[19] Deng Q, Niu J, Mao J, Feng Z. Experimental and numerical investigation on overall performance of a radial inflow turbine for 100kW microturbine. In: ASME turbo expo 2007: power for land, sea, and air, 14-17 may 2007, montreal, Canada, american society of mechanical engineers; 2007. p. 919–26.
[20] Fu L, Shi Y, Deng Q, Li H, Feng Z. Integrated optimization design for a radial turbine wheel of a 100 kW-class microturbine. J Eng Gas Turbines Power 2011;134(1), 012301.
[21] Fu L, Feng Z-p, Li G-j, Deng Q-h, Shi Y, Gao T-y. Experimental validation of an integrated optimization design of a radial turbine for micro gas turbines. J Zhejiang Univ - Sci 2015;16(3):241–9.
[22] Ino N, Machida A, Ttsugawa K, Arai Y, Matsuki M, Hashimoto H, Yasuda A. Development of high expansion ratio helium turbo expander. Adv Cryog Eng 1991;37(pt B):835–44.
[23] Ghosh SK. Experimental and computational studies on cryogenic turboexpander. Ph.D. thesis. National Institute of Technology Rourkela; 2008.
[24] Larjola J. ORC power plant based on high speed technology. In: Conference on high speed technology, 21-24 august 1988, lappeenranta, Finland; 1988. p. 63–77.
[25] Van Buijtenen J, Larjola J, Turunen-Saaresti T, Honkatukia J, Esa H, Backman J, Reunanen A. Design and validation of a new high expansion ratio radial turbine for ORC application. In: Proceedings of the fifth european conference on turbomachinery - fluid dynamics and thermodynamics, 17-22 march 2003, praha, Czech republic; 2003. p. 1–14.
[26] Pei G, Li J, Li Y, Wang D, Ji J. Construction and dynamic test of a small-scale organic rankine cycle. Energy 2011;36(5):3215–23.
[27] Kang SH, Chung DH. Design and experimental study of organic rankine cycle (ORC) and radial turbine. In: ASME 2011 turbo expo: turbine technical conference and exposition, 610 june 2011. Vancouver, British Columbia, Canada: International Gas Turbine Institute; 2011. p. 1037–43.
[28] Kang SH. Design and experimental study of ORC (organic Rankine cycle) and radial turbine using R245fa working fluid. Energy 2012;41(1):514–24.
[29] Han S, Seo J, Choi B-S. Development of a 200 kW ORC radial turbine for waste heat recovery. J Mech Sci Technol 2014;28(12):5231–41.
[30] Demierre J, Favrat D, Schiffmann J, Wegele J. Experimental investigation of a thermally driven heat pump based on a double organic rankine cycle and an oil-free compressor-turbine unit. Int J Refrig 2014;44:91–100.
[31] Demierre J, Rubino A, Schiffmann J. Modeling and experimental investigation of an oil-free microcompressor-turbine unit for an organic rankine cycle driven heat pump. J Eng Gas Turbines Power 2015;137(3), 032602.
[32] Kang SH. Design and preliminary tests of ORC (organic Rankine cycle) with two-stage radial turbine. Energy 2016;96:142–54.
[33] Turunen-Saaresti T, Uusitalo A, Honkatukia J. Design and testing of high temperature micro-ORC test stand using Siloxane as working fluid. J Phys Conf 2017;821(1), 012024.
[34] Dixon SL, Hall CA. Fluid mechanics and thermodynamics of turbomachinery. Boston, USA: Butterworth-Heinemann; 2010.
[35] Wilson D, Korakianitis T. The design of high-efficiency turbomachinery and gas turbines. Cambridge, Massachusetts, USA: The MIT Press; 2014.
[36] Persico G, Pini M. Fluid dynamic design of organic rankine cycle turbines. In: Organic rankine cycle (ORC) power systems: technologies and applications; 2016. p. 253–97.
[37] Verneau A. Supersonic turbines for organic fluid rankine cycles from 3 to 1300 kW, small high pressure ratio turbines, (VKI lecture series 1987-2007). Rhode-Saint-Genése, Belgium: Von Karman Institute For Fluid Dynamics; 1987. p. 1–55.
[38] Japikse D. Characteristics of a radial inflow turbine with internal component measurements: Part I – data review. In: ASME turbo expo 2000: power for land, sea, and air, 8-11 may 2000. Munich, Germany: International Gas Turbine Institute; 2000. V001T03A042–V001T03A042.
[39] Aungier RH. Turbine aerodynamics: axial-flow and radial-flow turbine design and analysis. New York, USA: ASME Press; 2006.
[40] Serrano JR, Arnau FJ, García-Cuevas LM, Dombrovsky A, Tartoussi H. Development and validation of a radial turbine efficiency and mass flow model at design and off-design conditions. Energy Convers Manag 2016;128:281–93.
[41] Sauret E. Open design of high pressure ratio radial-inflow turbine for academic validation. In: ASME 2012 international mechanical engineering congress and exposition, 9-15 november 2012. Houston, Texas, USA: American Society of Mechanical Engineers; 2012. p. 3183–97.
[42] Li S, Krivitzky EM, Qiu X. Meanline modeling of a radial-inflow turbine nozzle with supersonic expansion. In: ASME turbo expo 2016: turbomachinery technical conference and exposition, 13-17 june. Seoul, South Korea: International Gas Turbine Institute; 2016. V02DT42A036–V02DT42A036.
[43] Kastner L, Bhinder F. A method for predicting the performance of a centripetal gas turbine fitted with a nozzle-less volute casing. In: ASME 1975 international gas turbine conference and products show, 2-6 march 1975. Houston, Texas, USA: American Society of Mechanical Engineers; 1975. p. 1–11.
[44] Glassman AJ. NASA contributions to radial turbine aerodynamic analyses. In: Automotive technol. Develop. Contractor coord. Meeting; 11-13 nov. 1980, dearborn, MI, United States; 1980. p. 1–20.
[45] Perdichizzi A, Lozza G. Design criteria and efficiency prediction for radial inflow turbines. In: Gas turbine conference and exhibition, anaheim, California, may 31-june 4; 1987. p. 1–9.
[46] Rodgers C. Mainline performance prediction for radial inflow turbines. Tech. rep. Von Karman Inst. for Fluid Dynamics, Lecture Series on Small High Pressure Ratio Turbines; 1987.
[47] Ghosh SK, Sahoo RK, Sarangi SK. Mathematical analysis for off-design performance of cryogenic turboexpander. J Fluid Eng 2011;133(3), 031001.
[48] Ventura CAM, Jacobs PA, Rowlands AS, Petrie-Repar P, Sauret E. Preliminary design and performance estimation of radial inflow turbines: an automated approach. J Fluid Eng 2012;134(3), 031102.
[49] Rahbar K, Mahmoud S, Al-Dadah RK, Moazami N. Parametric analysis and optimization of a small-scale radial turbine for Organic Rankine Cycle. Energy 2015;83:696–711.
[50] Da Lio L, Manente G, Lazzaretto A. A mean-line model to predict the design efficiency of radial inflow turbines in organic Rankine cycle (ORC) systems. Appl Energy 2017;205:187–209.
[51] Mounier V, Olmedo LE, Schiffmann J. Small scale radial inflow turbine performance and pre-design maps for Organic Rankine Cycles. Energy 2018;143:1072–84.
[52] Baines N. A meanline prediction method for radial turbine efficiency. In: Sixth international conference on turbocharging and air management systems, 3-5 november 1998. London, UK: Professional Engineering Publishing; 1998. p. 45–56.
[53] Baines N. Radial- and mixed-flow turbine options for high-boost turbochargers. In: Seventh international conference on turbochargers and turbocharging, 14-15 may 2002. London, UK: Professional Engineering Publishing Limited; 2002. p. 35–44.
[54] Baines N. Radial turbines: an integrated design approach. In: 6th conference on turbomachinery: fluid dynamics and thermodynamics, 7-11 november

Appendix D. Articles

2005, lille, France; 2005. p. 1–10.
[55] Glassman AJ. Enhanced analysis and users manual for radial-inflow turbine conceptual design code RTD. Tech. rep. Washington D.C., USA: NASA; 1995.
[56] Bahamonde S, Pini M, De Servi C, Rubino A, Colonna P. Method for the preliminary fluid dynamic design of high-temperature mini-organic rankine cycle turbines. J Eng Gas Turbines Power 2017;139(8), 082606.
[57] The mathworks inc., MATLAB - MathWorks. 2016. http://www.mathworks.com/products/matlab/.
[58] Bell IH, Wronski J, Quoilin S, Lemort V. Pure and pseudo-pure fluid thermophysical property evaluation and the open-source thermophysical property library CoolProp. Ind Eng Chem Res 2014;53(6):2498–508.
[59] Moustapha H, Zelesky MF, Baines NC, Japikse D. Axial and radial turbines. White River Junction, VT, USA: Concepts NREC; 2003.
[60] Meroni A, La Seta A, Andreasen JG, Pierobon L, Persico G, Haglind F. Combined turbine and cycle optimization for organic rankine cycle power systems – Part A: turbine model. Energies 2016;9(5):313.
[61] Robertson MC, Costall AW, Newton PJ, Martinez-Botas RF. Radial turboexpander optimization over discretized heavy-duty test cycles for mobile organic rankine cycle applications. In: Proceedings of ASME turbo expo 2016: turbomachinery technical conference and exposition, 13-17 june 2016. Seoul, South Korea: International Gas Turbine Institute; 2016. p. 1–14.
[62] Stanitz JD. One-dimensional compressible flow in vaneless diffusers of radial- and mixed-flow centrifugal compressors, including effects of friction, heat transfer and area change. Tech. rep. Washington D.C., USA: NASA; 1952.
[63] Whitfield A, Baines NC. Design of radial turbomachines. New York, NY, USA: John Wiley and Sons Inc.; 1990.
[64] Rubechini F, Marconcini M, Arnone A, Del Greco AS, Biagi R. Special challenges in the computational fluid dynamics modeling of transonic turbo-expanders. J Eng Gas Turbines Power 2013;135(10):102701.
[65] Harinck J, Pasquale D, Pecnik R, van Buijtenen J, Colonna P. Performance improvement of a radial organic Rankine cycle turbine by means of automated computational fluid dynamic design. Proc IME J Power Energy 2013;227(6):637–45.
[66] Rinaldi E, Pecnik R, Colonna P. Unsteady operation of a highly supersonic organic rankine cycle turbine. J Turbomach 2016;138(12):121010.
[67] Rohlik HE, Kofskey MG. Recent radial turbine research at the NASA lewis research center. In: ASME 1972 international gas turbine and fluids engineering conference and products show, 26-30 march 1972. San Francisco, California, USA: American Society of Mechanical Engineers; 1972. pp. V001T01A041–V001T01A041.
[68] Artt D, Spence S. A loss analysis based on experimental data for a 99.0 mm radial inflow nozzled turbine with different stator throat areas. Proc IME J Power Energy 1998;212(1):27–42.
[69] Ghosh SK, Sahoo R, Sarangi SK. Mathematical analysis for off-design performance of cryogenic turboexpander. J Fluid Eng 2011;133(3), 031001.
[70] Jung H-C, Krumdieck S. Meanline design of a 250 kW radial inflow turbine stage using R245fa working fluid and waste heat from a refinery process. Proc IME J Power Energy 2016;230(4):402–14.
[71] Japikse D. Advanced diffusion levels in turbocharger compressors and component matching. In: 1st international conference on turbocharging and turbochargers, 26-28 april 1982, london, UK; 1982. p. 143–55.
[72] Daily JW, Nece RE. Chamber dimension effects on induced flow and frictional resistance of enclosed rotating disks. Journal of Basic Engineering 1960;82(1):217–30.
[73] Metropolis N, Ulam S. The Monte Carlo method. J Am Stat Assoc 1949;44(247):335–41.
[74] Meroni A, Andreasen J, Persico G, Haglind F. Optimization of organic Rankine cycle power systems considering multistage axial turbine design. Appl Energy 2018;209:339–54.
[75] Meitner P, Glassman A. Computer program for off-design performance analysis of radial inflow turbines with rotor blade sweep. Tech. rep. Washington D.C., USA: NASA; 1983.
[76] Sauret E, Gu Y. Three-dimensional off-design numerical analysis of an organic Rankine cycle radial-inflow turbine. Appl Energy 2014;135:202–11.
[77] Marconcini M, Rubechini F, Arnone A, Del Greco AS, Biagi R. Aerodynamic investigation of a high pressure ratio turbo-expander for organic rankine cycle applications. In: Proceedings of ASME turbo expo 2012, june 11-15, copenhagen, Denmark; 2012. p. 1–10.
[78] Yusri I, Abdul Majeed A, Mamat R, Ghazali M, Awad OI, Azmi W. A review on the application of response surface method and artificial neural network in engine performance and exhaust emissions characteristics in alternative fuel. Renew Sustain Energy Rev 2018;90:665–86.
[79] Ba D, Boyaci IH. Modeling and optimization II: comparison of estimation capabilities of response surface methodology with artificial neural networks in a biochemical reaction. J Food Eng 2007;78(3):846–54.
[80] Nasouri K, Shoushtari AM, Khamforoush M. Comparison between artificial neural network and response surface methodology in the prediction of the production rate of polyacrylonitrile electrospun nanofibers. Fibers Polym 2013;14(11):1849–56.
[81] Pacheco-Vega A, Sen M, Yang KT, McClain RL. Neural network analysis of fin-tube refrigerating heat exchanger with limited experimental data. Int J Heat Mass Tran 2001;44(4):763–70.
[82] Cheng J, Li QS, Xiao R-C. A new artificial neural network-based response surface method for structural reliability analysis. Probabilist Eng Mech 2008;23:51–63.
[83] Osnaghi C. Teoria delle turbomacchine. Società Editrice Esculapio; 2013.
[84] Fiaschi D, Innocenti G, Manfrida G, Maraschiello F. Design of micro radial turboexpanders for ORC power cycles: from 0D to 3D. Appl Therm Eng 2016;99:402–10. https://doi.org/10.1016/j.applthermaleng.2015.11.087.

Applied Energy 232 (2018) 139–156

Contents lists available at ScienceDirect

Applied Energy

journal homepage: www.elsevier.com/locate/apenergy

Design of centrifugal compressors for heat pump systems

Andrea Meroni*, Benjamin Zühlsdorf, Brian Elmegaard, Fredrik Haglind

Department of Mechanical Engineering, Technical University of Denmark, Nils Koppels Allé, Building 403, 2800 Kongens Lyngby, Denmark

HIGHLIGHTS

- A mean-line model for design and analysis of centrifugal compressors is presented.
- The model is validated against five test cases including three different fluids.
- The model is coupled to that of a high-temperature heat pump and optimized.
- The optimization method accounts for trade-offs in cycle and compressor designs.
- A two-stage steam compressor yields the best cycle performance.

ARTICLE INFO

Keywords:
Turbocompressor
Validation
Preliminary design
Refrigerant
High-temperature heat pump

2010 MSC:
00-01
99-00

ABSTRACT

This work presents a mean-line model of a centrifugal compressor and a method for a coupled optimization with a heat pump system. The compressor model was validated with five test cases from the open literature including the working fluids: air, refrigerant R-134a and carbon dioxide. Afterwards, the compressor model was coupled and optimized with that of a heat pump cycle supplying steam at 150 °C. Two cycle configurations were considered: an open-loop system using steam, and a closed-loop system with five other working fluid candidates. The compressor was designed using a multi-objective optimization algorithm, which seeks to maximize simultaneously the cycle coefficient of performance and the supplied heat flow rate. The method employed in this work considers the possible trade-offs regarding cycle and compressor design criteria, and can be used to identify cost-effective solutions for the next generation of heat pumps. The obtained results suggest that a two-stage compressor using steam yields the highest values of coefficient of performance and heat supply, and at the same time requires a more challenging compressor design.

1. Introduction

Heat pump systems are regarded as a viable and attractive solution to recover excess heat from low-to-medium temperature heat sources of many industrial processes [1–3].

Chua et al. [4] and Arpagaus et al. [2] reviewed the most important advances in the field. The application of heat pump systems is currently extending to the generation of high-temperature heat (with heat sink temperatures above approximately 100 °C). The International Energy Agency (IEA) [5] produced a report on industrial heat pumps, indicating the markets, level of technological maturity, applications and barriers of heat pumps. The report highlights that the theoretical potential for application of industrial heat pumps increases significantly for heat sink temperatures up to and higher than 100 °C. Nellisen and Wolf [6] investigated the heat demand across different industries in the European market and indicated that about 626 PJ (174 TWh) of heat is reachable by industrial heat pumps, of which about 113 PJ (19%) is in the temperature range 100–150 °C. Recently, Arpagaus et al. [3] presented a comprehensive review on high-temperature heat pump (HTHP) systems, concluding that industrial HTHPs can potentially supply the industrial European demand of 113 PJ.However, the literature highlights that the development of mass-produced units is hindered by many factors, such as low awareness of the heat consumption in companies and the possible technical solutions [5,3]; lack of knowledge of comprehensive heat pump integration methods [3,5,7]; lack of available refrigerants with low global warming potential in the high-temperature range [3,8]; lack of cost-efficient solutions and long payback periods [5,8,9]; and the technical challenges related to the compressor operation at high temperatures [10].

In this respect, the centrifugal compressor (CC) technology is seen as an attractive option compared with positive displacement compressors, since it bears key advantages such as the potential for high efficiency,

* Corresponding author.
E-mail addresses: andmer@mek.dtu.dk (A. Meroni), bezuhls@mek.dtu.dk (B. Zühlsdorf), be@mek.dtu.dk (B. Elmegaard), frh@mek.dtu.dk (F. Haglind).

https://doi.org/10.1016/j.apenergy.2018.09.210
Received 12 July 2018; Received in revised form 15 September 2018; Accepted 25 September 2018
0306-2619/ © 2018 Elsevier Ltd. All rights reserved.

Appendix D. Articles

Nomenclature

Symbols

A	cross-sectional area, m^2
AR	vaned diffuser area ratio, –
AS	vaned diffuser aspect ratio, –
b	blade width, m
C	absolute velocity, m/s
C_f	diffuser friction factor, –
COP	coefficient of performance, –
CP	diffuser pressure recovery coefficient, –
d_{hb}	hydraulic diameter, m
D_f	blade diffusion factor, –
DR	degree of reaction, –
$\dot{m}$	mass flow rate, –
h	specific enthalpy, J/kg
k_s	blade surface roughness, m
K	total pressure loss coefficient, –
L_z	rotor axial length, m
L_b	blade hydraulic length, m
LWR	vaned diffuser length over width, –
M	Mach number, –
N	rotational speed, rpm
o	throat, m
p	static pressure, Pa
PR	pressure ratio, –
$\dot{Q}$	heat flow rate, W
r	radius, m
Re	Reynolds number, –
s	specific entropy, J/(kgK)
t	trailing edge thickness, m
T	temperature, K
U	peripheral velocity, m/s
$\dot{V}_{comp,in}$	compressor inlet volume flow rate, m^3/s
W	relative velocity m/s
Z	number of blades –

Abbreviation and acronyms

CC	Centrifugal Compressor
HP	Heat Pump
HTHP	High-Temperature Heat Pump
VD	Vaned Diffuser

Greek letters

α	absolute flow angle, °
β	relative flow angle, °
ρ	density, kg/m^3
ε	clearance gap, m
ε_w	wake fraction at impeller exit, –
η	compressor isentropic efficiency, –
σ	impeller slip factor, –
ϕ	flow coefficient, –
χ	secondary flow mass fraction, –
ψ	stage loading coefficient, –

Subscripts

0	total, impeller inlet
1	impeller throat static conditions
01	impeller throat total conditions
2	impeller exit static conditions
02	impeller exit total conditions
3	diffuser inlet static conditions
03	diffuser inlet total conditions
4	diffuser throat static conditions
04	diffuser throat total conditions
5	diffuser exit static conditions
05	diffuser exit total conditions
a	axial direction
b,bl	blade, back face
ch	choking
cl	clearance
h	hub
vs	interspace
vd	vaned diffuser
tt	total-to-total
ts	total-to-static
th	throat
t	trailing edge, tangential direction
sf	skin friction
s	shroud
rms	root-mean-square
rel	relative
rc	recirculation
r	radial direction, rotor
pp	pinch point
opt	optimal
mix	mixing
m	meridional direction
lim	limit value
is	isentropic
ind	inducer
Inc.	incidence
imp	impeller
id	ideal

the possibility to operate at high pressure ratios, a compact design, and oil-free operation [11,12]. The progress of the technology in the last decades, and, foremost, the introduction of high-speed generators, have made it possible to apply CCs even to smaller units in the refrigeration and heat pump fields. Hastbacka et al. [13] claimed that small centrifugal compressors are expected to replace reciprocating and screw compressors for chilled-water systems in the range 88–281 kW as their high initial cost is offset by improved energy efficiency. Süß [14] developed a centrifugal compressor for refrigeration applications with a nominal power of 7 kW, operating up to 90 krpm and achieving an overall efficiency of 70% (including the motor). Bertsch et al. [15] conducted a study on the use of micro turbo-compressors in HTHPs, concluding that such compressors are a viable alternative to traditional technology. The working fluid can range from natural to synthetic refrigerants, and the compressor can experience considerably different flow phenomena according to the selected medium. The combination of high rotational speed, the variety of possible working fluids, and the compact size often result in highly loaded compressors whose design requires the adoption of suitable numerical tools and modeling strategies.

The first step in the design of a centrifugal compressor is performed using one-dimensional preliminary design models. One-dimensional numerical methods, also called *mean-line models*, provide the design and performance estimation of the centrifugal compressor through the solution of the governing equations at the mean streamline and at the main stations of the compressor components. Compared to more

advanced methods, i.e. through-flow or computational fluid dynamics (CFD), mean-line models provide the design and performance estimation of the machine in a relatively short time and with low computational effort. Harley et al. [19] investigated different 1D methods for the performance prediction of CCs and concluded that the 1D single-zone method is the most suitable for the preliminary design process, since it provides the opportunity to analyze and reduce the internal losses even for modern designs.

At the same time, the validity of preliminary design models for CCs needs to be assessed to ensure that the accuracy and reliability criteria required in the design process are met. Table 1 lists the mean-line models that were developed for CCs and their corresponding validation methods.

All the models in Table 1 were developed and validated using test cases for a single working fluid. In particular, only three mean-line models published in the open literature employed a working fluid which is used in heat pumps, and these are the models by Schiffmann and Favrat [11], Vilim [21] and Kus and Nekså [18]. The robustness of a numerical model in its prediction capability relies not only on its accuracy for different geometries, but also on its suitability when using different working fluids. This is especially relevant for heat pump systems where, in the early design process, different working fluids can be employed, and the machine geometry and performance need to be carefully evaluated for each working fluid candidate. However, the existing literature lacks investigations on the suitability of mean-line models for the design and performance prediction of centrifugal compressors considering different working fluids. In particular, the existing loss correlations were derived from a pool of compressor data operating with air, casting doubt on the suitability when different working fluids are used.

Moreover, a widely adopted approach in the design of HP cycles is to decouple the design of the thermodynamic cycle from that of the compressor. In this case, the heat pump is typically designed by assigning a guess value in the isentropic efficiency and volume flow rate of the compressor. This approach was used in previous studies [32–37] for the design of different heat pumps and to select the most suitable working fluid. However, decoupling the design of the thermodynamic cycle from that of the compressor, may lead to inaccurate estimations of the cycle performance and complex or unfeasible compressor design solutions. Moreover, the working fluid represents an additional degree of freedom in the design process, and can greatly affect both the system and the compressor designs. In this respect, a combined design of the thermodynamic cycle and the compressor is particularly important to ensure that the working fluid selection includes considerations of the performance and the technical aspects of both the cycle and compressor.

Combined design optimization of the system and a turbomachine was recently adopted for the design of organic Rankine cycle power systems. For example, Da Lio et al. [38] proposed the design optimization of organic Rankine cycle systems using performance maps of single-stage axial turbines generated with a mean-line model and integrated into the system design model. White and Saima [39] proposed a similar approach, in which the performance maps were developed for radial-inflow turbines and were used to design the organic Rankine cycle power system. Meroni et al. [40,41] and La Seta et al. [42] presented a method for the optimization of an organic Rankine cycle system with single and multi-stage axial turbines. In the field of heat pump applications, there are few works related to the simultaneous preliminary design optimization of CCs and the thermodynamic cycle. Shiffmann and Favrat [11] developed a mean-line model for CCs and optimized the compressor for different heat pump operating points to minimize the overall seasonal energy consumption and to maximize the overall seasonal compressor isentropic efficiency. Schiffmann [12] proposed designing the centrifugal compressor by integrating the different models of the compressor components. The proposed approach showed an increase of the seasonal compressor efficiency of more than 12%-points compared to the traditional design methods. Javed et al. [43] proposed a method to design turbocompressors and heat pump systems by including different levels of design complexity, from the preliminary design with a mean-line model to the more advanced 3D impeller aerodynamic design.

None of the aforementioned works, Refs. [11,12,43], performed the design of the turbocompressor and the heat pump system including also the selection of the most suitable working fluid, which is an important key decision variable in the system design. Instead, the fluid was selected a priori in the design process. Moreover, only Ref. [43] interfaced a heat pump simulation model with that of a centrifugal compressor. In this case, the optimization method involved the use of both mean-line and CFD tools, requiring considerable time and computational efforts which might not be suitable for the screening of design solutions using different working fluids at the very early stage of the design process.

The objective of this paper is to develop a method for the combined design of high-temperature heat pumps and centrifugal compressors including the selection of the most suitable working fluid. To this end, a steady-state mean-line model of a centrifugal compressor was developed for the design and off-design performance prediction of CCs. The model formulation solves the governing equations with state-of-the-art equations of state for the estimation of the fluid thermodynamic and transport properties. Also, the method adopted in this work accounts for the onset of choking conditions in the compressor. In order to assess the suitability of the model using different working fluids, some validation test cases were performed including three working fluids: air, a synthetic refrigerant (R134a), and CO_2. The latter two test cases were the only ones in the open literature presenting well-documented data of CCs employing a fluid different from air. The compressor model was then coupled to that of a HTHP, and the combined model was

Table 1
Review of mean-line models developed for centrifugal compressors in the open literature.

Ref.	Year	Model validation
Li et al. [16]	2015	Off-Design, air compressor with vaneless and vaned diffusers
Klausner and Gampe [17]	2014	1-D, Off-Design, six air compressors
Kus and Nekså [18]	2013	Design point, CO_2 compressor
Harley et al. [19]	2012	1-D, Off-Design, three turbocharger compressors
Casey [20]	2012	0-D, Off-Design, turbocharger compressor
Vilim [21]	2010	Design point, CO_2 compressor
Schiffmann and Favrat [11]	2009	Off-design maps, R134a compressor
Veres [22]	2009	Off-design maps, three axial single and multi-stage compressors
Oh et al. [23]	1997	Off-design maps, four air compressors
Aungier [24]	1995	Off-design map, five air compressors with vaned and vaneless diffusers
Perdichizzi and Savini [25]	1985	Off-design map, air compressor with vaned diffuser, off-design
Galvas [26]	1973	Off-design map, air compressor with vaned diffuser, off-design
Rodgers [27–30]	1964	Off-design map, thirteen backswept air impellers with vaned diffuser
Coppage [31]	1956	Aeroderivative air compressor, subsonic and supersonic conditions, off-design maps

optimized.

The primary novel contributions of this paper are the following: (1) assessment of the suitability of a mean-line centrifugal compressor model and its loss correlations to different geometries and working fluids (air, R134a and CO_2); and (2) a method for the combined optimization of a heat pump equipped with centrifugal compressors enabling the selection of the most suitable working fluid in the early stage of the design process.

The results and methods may be used to support engineers and researchers in identifying cost-effective solutions in terms of design and working fluid selection for the next generation of heat pumps.

The work is structured as follows: in Section 2 the design and off-design models of the compressor, the test cases and methods used for validation, and the optimization method are presented. In Section 3 the results of the compressor model validation and the optimization method are discussed. In Section 4 the results are presented, and in Section 5 the conclusions are drawn.

2. Methods

This work employed a steady-state, mean-line model for the performance prediction of CCs at the design and off-design conditions. The model was written in the MATLAB language [44] and followed a mean-line approach, based on which the thermodynamic and flow conditions were computed at the mean streamline in the turbine meridional plane, and were representative of mass-weighted averaged conditions over the whole section. The development of the model focused on the modeling of the compressor impeller, and the vaneless and vaned diffusers. Fig. 1 depicts a schematic of the centrifugal compressor highlighting the main stations, the terminology and the symbols used in this paper. The thermodynamic and flow conditions in the main modeling stations were computed by the simultaneous solution of mass continuity, energy balance, and loss equations. The fluid properties were computed using real-gas equations of state using the thermodynamic libraries CoolProp [45] and REFPROP [46].

A key aspect in the development of the mean-line model was the identification of the choking point inside the compressor stage. Choking occurs when the local velocity of the fluid inside the compressor passages reaches the speed of sound [47]. In a compressor, choking usually occurs in the blade passages of the impeller or in the vaned diffuser at the point of minimum flow area [48]. The onset of choking is also influenced by the rotational speed of the impeller, since this will determine the value of the local relative velocity in the rotating coordinate system. When the compressor chokes, the mass flow rate cannot further increase and the performance drops abruptly, compromising the effective operational range of the machine. For any given operating condition, the method described here aims to identify the choking point by evaluating the possibility of choking conditions in the impeller inlet, the impeller outlet, or in the vaned diffuser.

2.1. Design model

Fig. 2(a) shows the workflow of the preliminary design model. The inputs to the compressor model are the inlet total temperature T_{01}, the inlet total pressure p_{01}, the rotational speed N, the mass flow rate $\dot{m}$, and the stage total-to-static pressure ratio PR_{ts}. In addition, a set of decision variables related to the compressor geometry and fluid dynamic conditions needs to be given as an input. Table 2 shows the design variables and the optimization constraints used in this work. The upper and lower boundaries are imposed to find solutions which are manufacturable, physically meaningful and technically feasible. An upper bound in the tip speed is also imposed to limit the mechanical stresses on the blades. The optimization constraints were selected from the open literature according to Refs. [11,25]. The modeling strategy of Fig. 2(a) applies to a predefined set of decision variables, and a dedicated optimization procedure needs to be applied to determine the set of decision variables producing an optimal compressor design, see Section 2.5. Not all the design variables need to be specified in the design code, and some of them may be fixed by the requirements of the specific application. The number of impeller blades, with or without splitters, can be included in the design and off-design modeling strategy either as an additional decision or input variable. In the design model the number of blades was calculated as a function of the total-to-total stage pressure ratio using an empirical correlation derived from a pool of compressor data of Ref. [49]:

$$Z_r = 12.03 + 2.544PR_{tt} \quad \text{(without splitters)} \tag{1}$$

$$Z_r = -4.527e^{1.865/PR_{tt}} + 32.22 \quad \text{(with splitters)} \tag{2}$$

where Z_r is the number of impeller blades, rounded to the closest integer value, and PR_{tt} the stage total-to-total pressure ratio. Eqs. (1) and (2) are valid for values of a design pressure ratio in the range 1.0–5.0 and 1.8–8.0, respectively.

The implementation of the design model follows the approaches by Japikse and Baines [50] and Whitfield and Baines [51].

For a given set of input and decision variables, the first step in the design modeling strategy is to identify whether the compressor stage is choked (*Step 0*). If the compressor stage is choked, the decision variables need to be changed to allow for a higher mass flow rate through the machine. Mass and energy balances, and the isentropic process formulation in the inducer throat section are expressed as

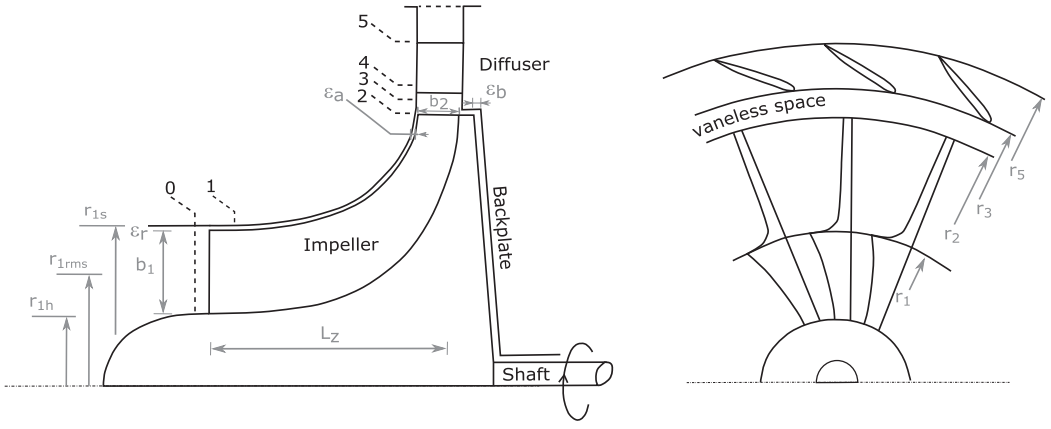

Fig. 1. Schematic of the centrifugal compressor geometry.

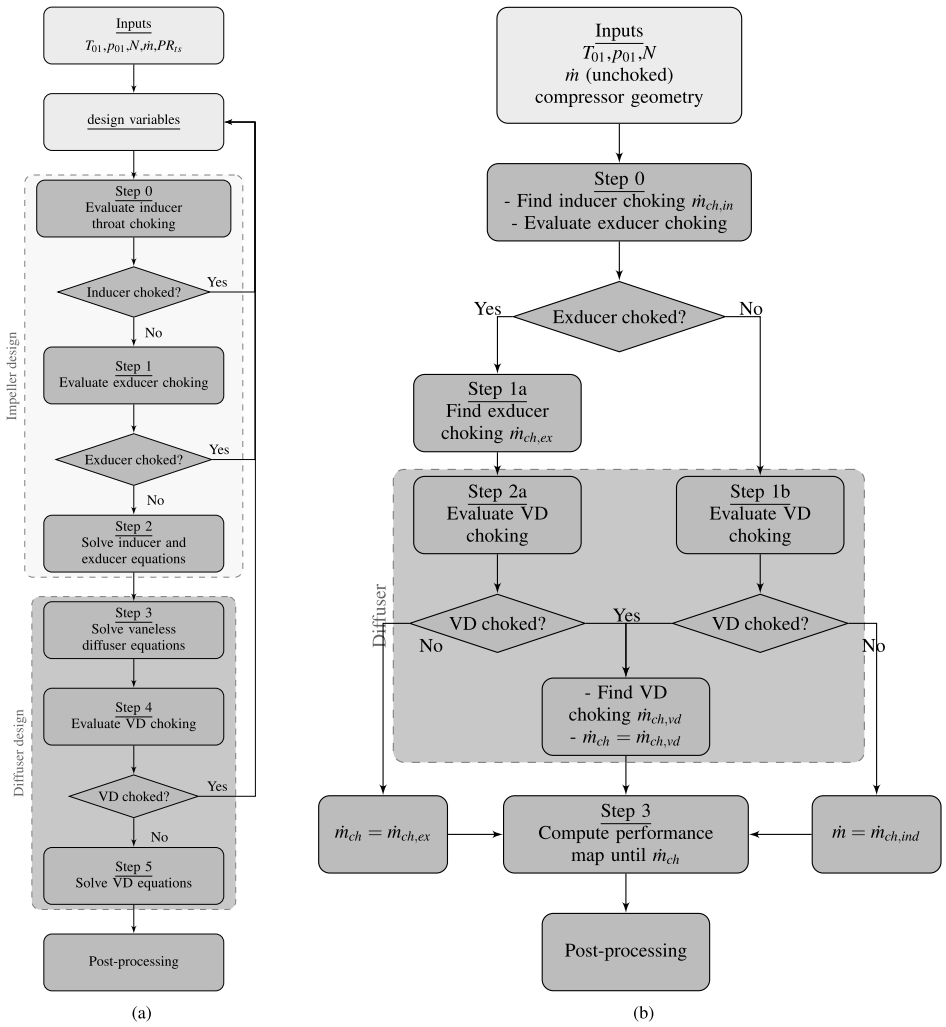

Fig. 2. Modeling strategy for centrifugal compressors: (a) preliminary design model; (b) analysis model.

$$W_1 = \dot{m}/(\rho_1 A_{\text{th},1}) \tag{3}$$

$$h_1 = h_{01} - \frac{1}{2}W_1^2 + \frac{1}{2}U_{1,\text{rms}}^2 \tag{4}$$

$$s_{01} - s_1 = 0 \tag{5}$$

where ρ_1, $A_{\text{th},1}$, W_1, $U_{1,\text{rms}}$, and h_1 are the density, cross-sectional flow area, relative velocity, root-mean-square average peripheral speed, and static specific enthalpy at the inducer throat section, respectively. The term h_{01} denotes the total specific enthalpy, and s_{01} and s_1 are the total and static specific entropies, respectively. Eq. (5) assumes an isentropic process from the inducer inlet to the throat. For given inducer inlet conditions and geometry, the solution strategy adopted above allows expressing s_{01}-s_1 as a residual function of ρ_1 and $\dot{m}$, as illustrated in Fig. 3. For a given value of mass flow rate, the residual function shows a non-monotonic behavior with a maximum. The condition at which the peak of this function crosses the abscissa was identified as the *choking condition*. For small values of $\dot{m}$, when the maximum is above the density axis, there are two values of ρ_1 which satisfy Eq. (5). The larger value represents subsonic flow conditions, whereas the smaller value corresponds to supersonic flow conditions. By increasing the mass flow rate, the peak of the curve moves downwards, and eventually crosses the abscissa. Accordingly, choking occurs when the subsonic and supersonic solutions coincide, and the Mach number at the throat is unity. Fig. 3 shows that there is no solution to the system of equations for values of mass flow rate higher than that of the choking condition. In this case, the design process ends and a different set of design variables needs to be provided to comply with the required input conditions. If choking does not occur, the modeling strategy proceeds by evaluating whether choking may be present at the exducer section (*step 1*).

To this end, the equations for mass continuity, momentum and the losses at the exducer Section 2 are expressed as

$$C_{2m} = \dot{m}/(\rho_2 A_2) \tag{6}$$

$$h_{02} = h_{01} + C_{2t}U_2 - C_{1t}U_{1,\text{rms}} \tag{7}$$

$$\sum_{n=1}^{n_{\text{loss}n}} \Delta h_{\text{loss,imp}} - h_{02} + h\left(p_{02}, s_{01}\right) = 0 \tag{8}$$

where $\Delta h_{\text{loss,imp}}$ is one of the n impeller losses, which is modeled using the empirical correlations presented in Section 2.3. To solve Eq. (7), an

Table 2
Design variables and optimization constraints of the compressor design model.

Decision variable	Description	Units	Lower boundary	Upper boundary
$\psi_{is} = \Delta h_{0,is}/U_2^2$	Isentropic stage loading coefficient	[–]	0.3	1.1
N	Rotational speed	[krpm]	1	210
r_{1s}/r_2	Inlet shroud to tip radius ratio	[–]	0.4	0.7
r_{1h}/r_{1s}	Inlet hub to shroud radius ratio	[–]	0.25	0.7
b_2/r_2	Exit blade width over radius	[–]	0.02	0.8
β_{2b}	Impeller exit blade angle	[°]	−45	0
β_{1b}	Impeller inlet average blade angle	[°]	−70	−20
Optional decision variables				
Z_r	Number of total impeller blades	[–]	6	60
Additional constraints				
$M_{1s,rel}$	Relative Mach number at impeller inlet shroud	[–]	0	1.4
$M_{1,rel}$	Relative Mach number at impeller inlet	[–]	0	0.9
W_2/W_{1s}	Ratio of exit to inlet shroud relative velocities	[–]	0.25	–
α_2	Impeller exit absolute flow angle	[°]	–	85
o_1	Impeller inlet throat	[mm]	1.49	50
DR	Stage degree of reaction	[–]	−0.1	0.9
U_2	Impeller exit peripheral speed	[m/s]	0	400
r_3/r_2	Vaneless diffuser radius ratio	[–]	1.05	2
Fixed values (if not specified)				
t_b	Blade thickness	[mm]	0.2	
ε	Impeller clearance	[mm]	0.15	
ε_b	Impeller back face clearance	[mm]	1	
k_s	Impeller surface roughness	[mm]	0.002	
b_3/b_2	Diffuser width ratio	[–]	1	
CP	Diffuser pressure coefficient	[–]	0.44	

Table 3
Modeling conditions of the high-temperature heat pump cycle.

Parameter	Value	Unit
Evaporator		
T_{eva}	100	°C
p_{eva}	$p_{sat}(T_{eva})$	Pa
Condenser		
T_{supply}	150	°C
ΔT_{pp}	3	°C
p_{cond}	$p_{sat}(T_{supply} + \Delta T_{pp})$	Pa
Subcooling (closed-loop only)		
ΔT_{sc}	5	°C

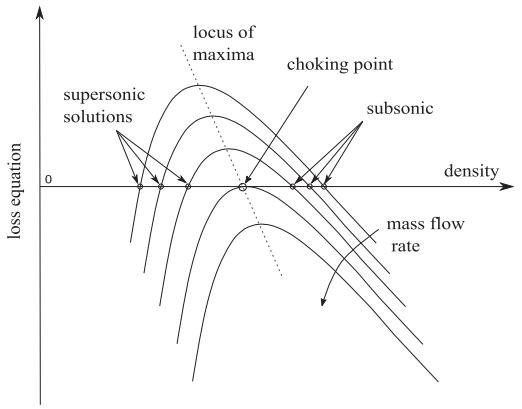

Fig. 3. Identification of the choking point for a blade row.

expression for the tangential component of the rotor exit absolute velocity, C_{2t}, was derived using the component in the meridional direction, C_{2m}, and the slip factor σ, which provides a measure of the flow deviation at the impeller exit. Based on the slip factor, a slip velocity can be computed, and the absolute and tangential velocities at the impeller exit are the following:

$$C_{2t} = \sigma U_2 - C_{2m}\tan(|\beta_{2b}|) \tag{9}$$

$$C_2 = \sqrt{C_{2m}^2 + C_{2t}^2} \tag{10}$$

$$h_2 = h_{02} - \frac{1}{2}C_2^2 \tag{11}$$

The left side of Eq. (8) can be plotted as a function of the mass flow rate and the impeller exit density, obtaining a trend similar to that of Fig. 3. Subsequently, the impeller exit is evaluated for whether or not it is choked, which results in a termination of the design process. If the impeller is not choked, Eqs. (6)–(8) are solved to determine the thermodynamic and flow conditions at the impeller exit section (*Step 2*). If the stage has only the impeller, the design process ends, and the model performs the post-processing operations necessary to compute the performance and the final design of the machine.

In the presence of a vaneless diffuser, the total pressure loss coefficient K and the ideal pressure coefficients were computed based on the specified stage exit total pressure p_{03} and pressure coefficient CP as follows:

$$K = \frac{p_{02} - p_{06}}{p_{02} - p_2} \tag{12}$$

$$p_3 = p_2 + \mathrm{CP}(p_{02} - p_2) \tag{13}$$

$$\mathrm{CP}_{id} = \mathrm{CP} + K \tag{14}$$

The vaneless diffuser exit state was then determined by solving the following set of equations for the exit density ρ_3 [50]:

$$h_3 = h(\rho_3, p_3) \tag{15}$$

$$C_3 = \sqrt{2(h_{02} - h_3)} \tag{16}$$

$$\dot{m} - C_3 \rho_3 A_2 \cos(\alpha_2)(1 - \mathrm{CP_{id}})^{-0.5} = 0 \tag{17}$$

A feature of the vaneless diffuser is that it has no throat section and, therefore, it cannot be choked [48]. If a vaned diffuser (VD) is present (*Step 4*), the model needs to evaluate whether choking may occur in its throat section according to the method followed so far. The vaned diffuser throat equations are expressed as

$$C_4 = \dot{m}/(\rho_4 A_{\mathrm{th},4}) \tag{18}$$

$$h_4 = h_{03} - \frac{1}{2} C_4^2 \tag{19}$$

$$s_{03} - s_4 = 0 \tag{20}$$

If the vaned diffuser is not choked, the governing equations are solved as follows (*Step 5*):

$$C_5 = \dot{m}/(\rho_5 \cos\alpha_5 A_5) \tag{21}$$

$$h_5 = h_{03} - \frac{1}{2} C_5^2 \tag{22}$$

$$\sum_{n=1}^{n_{\mathrm{loss}}} \Delta h_{\mathrm{loss,vd}} - h_{03} + h\left(p_5, s_3\right) = 0 \tag{23}$$

In the design mode, the pressure at the exit, p_5, was specified by the required stage pressure ratio, and the flow angle α_5 was determined to match p_5. In the off-design mode, the vaned diffuser exit pressure was unknown. In this case, the exit flow angle was approximated with the vane exit angle assuming a negligible exit flow deviation [50]. Eq. (20) was expressed as a function of the impeller exit density ρ_5, showing a trend similar to that in Fig. 3. Similarly to the impeller modeling, if the VD was already choked, the design routine ended. Alternatively, the VD equations were solved, and the compressor design was completed by the post-processing of the data.

2.2. Off-design model

Fig. 2(b) shows the off-design modeling strategy. In this case an existing compressor design, or one calculated as in Fig. 2(a), was provided as the input and compressor performance maps were generated as the output. The model inputs were the same as the design model, except that the full turbine geometry is given as well. The mass flow rate $\dot{m}$ was provided as an input for the generation of the performance maps. The workflow of Fig. 2(b) applies to a single speed line, and an iterative process was implemented to generate the performance map for different values of the compressor rotational speed.

The off-design modeling strategy started by evaluating whether, for the given input conditions, the inducer or the exducer was the first to choke (*Step 0*). The set of Eqs. (3)–(5) were used for the inducer throat. In *step 0*, the inducer choking mass flow rate is found by determining the zero of the locus of maxima of the left side function in Eq. (5).

Table 4
Loss correlations.

Loss mechanism	Loss model	Reference
Impeller incidence	$\Delta h_{\mathrm{inc}} = \frac{1}{2} W_1^2 \sin^2 \left\lvert \beta_{1,\mathrm{opt}} - \beta_1 \right\rvert$	Galvas [26]
	$\beta_{1,\mathrm{opt}} = \tan^{-1}[(A_1/A_{\mathrm{th},1})\tan\beta_{1\mathrm{b}}]$	
Impeller friction	$\Delta h_{\mathrm{sf}} = 4 C_{\mathrm{fi}} \frac{L_{\mathrm{b}}}{d_{\mathrm{hb}}} \overline{W}^2$	Galvas [26]
	$\overline{W} = max\left\{ \sqrt{(W_1^2 + W_2^2)/2)}, \sqrt{(W_{\mathrm{th},1}^2 + W_2^2)/2} \right\}$	Aungier [24]
	$L_{\mathrm{b}} \approx \frac{\pi}{8}\left(2r_2 - \left(r_{1\mathrm{s}} + r_{1\mathrm{h}}\right) - b_2 + 2L_z\right)\left(\frac{2}{(\cos\beta_{1\mathrm{s}} + \cos\beta_{1\mathrm{h}})/2 + \cos\beta_{2\mathrm{b}}}\right)$	Jansen [70]
	$d_{\mathrm{hb}} = \frac{2r_2}{\frac{Z_{\mathrm{f}}}{\pi\cos\beta_{2\mathrm{b}}} + \frac{2r_2}{b_2}} + \frac{2r_{1\mathrm{s}}}{\frac{2}{1 - r_{1\mathrm{h}}/r_{1\mathrm{s}}} + \frac{2Z_{\mathrm{f}}}{\pi(1 + r_{1\mathrm{h}}/r_{1\mathrm{s}})}\sqrt{1 + \tan^2\beta_{1\mathrm{bs}}\left(1 + \frac{(r_{1\mathrm{h}}/r_{1\mathrm{s}})^2}{2}\right)}}$	Galvas [26]
Impeller blade loading	$\Delta h_{\mathrm{bl}} = 0.05 D_f^2 U_2^2$	Coppage [31]
	$D_f = 1 - \frac{W_2}{W_1} + C_{\mathrm{df}} \frac{\Delta h_0}{U_2^2} \frac{W_2}{W_{1\mathrm{s}}}\left(\frac{Z_{\mathrm{f}}}{\pi}\left(1 - \frac{r_{1\mathrm{s}}}{r_2}\right) + 2\frac{r_{1\mathrm{s}}}{r_2}\right)^{-1}$	
Impeller clearance	$\Delta h_{\mathrm{cl}} = 0.6 \frac{\overline{\epsilon}}{b_2} \left\lvert C_{2t} \right\rvert \sqrt{\frac{4\pi}{b_2 Z_{\mathrm{f}}} \frac{r_{1\mathrm{s}}^2 - r_{1\mathrm{h}}^2}{(r_2 - r_{1\mathrm{s}})(1 + \rho_2/\rho_1)}} \left\lvert C_{2t} \right\rvert \left\lvert C_{1\mathrm{m}} \right\rvert}$	Jansen [70]
	$\overline{\epsilon} = (\epsilon_{\mathrm{a}} + \epsilon_{\mathrm{r}})/2$	
Impeller mixing	$\Delta h_{\mathrm{mix}} = \frac{1}{1 + \tan^2(\alpha_2)}\left(\frac{1 - \epsilon_{\mathrm{w}} - b^*}{1 - \epsilon_{\mathrm{w}}}\right)^2 \frac{1}{2} C_2^2$	Johnston and Dean [71]
	$\chi = 0.93\,\epsilon_{\mathrm{w}}^2 + 0.07\,\epsilon_{\mathrm{w}}$ where $b^* = 1, \chi = 0.15$	Japikse [48]
Impeller disc friction	$\Delta h_{\mathrm{df}} = 0.25 \frac{\rho_{\mathrm{i}} U_2^3 r_2^2 K_{\mathrm{f}}}{\dot{m}}$ where $\rho_{\mathrm{i}} = (\rho_1 + \rho_2)/2$	Daily and Nece [72]
	if $Re_2 = \frac{\rho_2 U_2 r_2}{\mu_2} < 3{\cdot}10^5$ $K_{\mathrm{f}} = 3.7 \frac{(\epsilon_{\mathrm{b}}/b_2)^{0.1}}{Re_2^{0.5}}$	
	if $Re_2 = \frac{\rho_2 U_2 r_2}{\mu_2} > 3{\cdot}10^5$ $K_{\mathrm{f}} = 0.102 \frac{(\epsilon_{\mathrm{b}}/b_2)^{0.1}}{Re_2^{0.2}}$	
Impeller recirculation[a]	$\Delta h_{\mathrm{rc}} = 8{\cdot}10^{-5} \sinh\left(3.5{\cdot}\alpha_2^3\right) D_f^2 U_2^2$	Oh et al. [23]
Vaned diffuser incidence	$\Delta h_{\mathrm{inc,rot}} = 0.6 \sin^2 \left\lvert \beta_4 - \beta_{4,\mathrm{opt}} \right\rvert \frac{1}{2} W_4^2$	Conrad [73]
Vaned diffuser friction	$\Delta h_{\mathrm{vd,sf}} = 2 C_{\mathrm{f,vd}} C_{\mathrm{m,vd}}^2 \frac{L_{\mathrm{b,vd}}}{d_{\mathrm{hb,vd}}}$	Conrad [73]
	$L_{\mathrm{b,vd}} = \frac{r_5 - r_3}{\cos\left(\frac{\alpha_{3\mathrm{b}} + \alpha_{5\mathrm{b}}}{2}\right)}$ $d_{\mathrm{hb,vd}} = \frac{o_4 b_4}{o_4 + b_4} + \frac{o_5 b_5}{o_5 + b_5}$	

[a] The flow angle is expressed in radians.

Afterwards, the algorithm evaluates whether the exducer is already choked for the inducer choking mass flow rate by identifying the location of the peak of the residual loss function in Eq. (8). Like in the design strategy, the off-design method evaluates whether the exducer choking mass flow rate is smaller than the inducer choking mass flow rate, and follows two different paths according to the result. If the exducer chokes first, the exducer choking mass flow rate is found by solving Eqs. (3)–(5) and finding the zero of the locus of maxima in Eq. (8). After determining the choking mass flow rate, performance maps are computed by changing the mass flow rate until obtaining the choking value (*step 3*).

A one-dimensional model has been implemented to solve the governing equations from the inlet to the outlet of the radial vaneless space (*Step 3*). Stanitz [52] presented a set of one-dimensional equations for the adiabatic flow in a vaneless radial diffuser including the effect of friction. The equations for radial and tangential momentum, mass continuity and energy balance can be derived from a fundamental control volume analysis applied to the vaneless diffuser or by rearranging and simplifying the Navier–Stokes equations [50,51]. They are formulated as

$$C_m\frac{dC_m}{dr}-\frac{C_t^2}{r}+C_f\frac{C^2\cos(\alpha)}{b}+\frac{1}{\rho}\frac{dp}{dr}=0 \tag{24}$$

$$C_m\frac{dC_t}{dr}+\frac{C_mC_t}{r}+C_f\frac{C^2\sin(\alpha)}{b}=0 \tag{25}$$

$$\frac{1}{\rho}\frac{d\rho}{dr}+\frac{1}{C_m}\frac{dC_m}{dr}+\frac{1}{b}\frac{db}{dr}+\frac{1}{r}=0 \tag{26}$$

$$h_{02}-h-\frac{1}{2}C^2=0 \tag{27}$$

where b is the vaneless space width, provided at every point by linear interpolation between the inlet and outlet values, and C_f is the friction factor which was estimated using the correlation proposed by Japikse [53] $C_f = k(1.8\cdot10^5/Re)^{0.2}$. The parameter k is an empirical constant which equals values between 0.005 and 0.02. In this work, the best match with the experimental data was found for the value 0.0050. The system of Eqs. (24)–(27) was solved using MATLAB ODE15i solver [44] using the initial values of C_m, C_t, ρ and p at the impeller exit.

In the presence of a vaned diffuser, which may choke before the impeller, *Steps 2a* and *1b* were added, evaluating whether the diffuser was choked. In that case, the choking mass flow rate was determined by solving for the zero of the locus of maxima in the set of Eqs. (21)–(23).

The volute, placed after the diffuser, was also included in the off-design modeling. The flow in the volute is treated as incompressible following the indications by Japikse and Baines [50]. Mass and energy balances, and the equations for losses accounting for the entropy generation between the volute inlet and outlet, are solved as follows:

$$\rho_4=\rho_3 \tag{28}$$

$$C_4=\dot{m}/(\rho_4A_4) \tag{29}$$

$$h_4=h_{03}-\frac{1}{2}C_4^2 \tag{30}$$

$$h_{04}-h_{04,s}=k_vC_3^2 \tag{31}$$

where k_v is an empirical coefficient set to 0.5.

2.3. Empirical models for losses and flow deviation

Several empirical correlations for losses and flow deviation in a centrifugal compressor exist, see Refs. [23,48,51,54,55]. Table 4 shows a summary of the set of loss models used in this work. These correlations were selected as they were well described in the original references and provided the best match with the data of the test cases.

To close the set of Eqs. (6)–(8), employed to solve the impeller exit state, an expression for the slip factor has to be provided. This work used the model by Wiesner [56] for the estimation of the slip factor. This model was further improved by Aungier who introduced a limit for high impeller radius ratios, accounting also for splitter blades as follows:

$$\sigma=1-\frac{\sqrt{\cos\beta_{2b}}}{Z_r^{0.7}} \tag{32}$$

Eq. (32) is valid up to the limiting radius ratio given by

$$(r_1/r_2)_{lim}=\frac{\sigma-\sigma^*}{1-\sigma^*} \tag{33}$$

$$\sigma^*=\sin(19°+0.2(90-|\beta_{2b}|)) \tag{34}$$

When the actual impeller radius ratio r_1/r_2 exceeds the limiting value $(r_1/r_2)_{lim}$, a corrected slip factor is computed as follows:

$$\sigma_{cor}=\sigma\left[1-\left(\frac{(r_1/r_2)-(r_1/r_2)_{lim}}{1-\sigma_{lim}}\sqrt{(90-\beta_{2b})/10}\right)\right] \tag{35}$$

2.4. Validation

The CC model was validated against five well-documented test cases available in the open literature. Moreover, the test cases encompass a range of different applications and employ three different working fluids: air, R134a, and CO_2. Table 5 lists the input data used to validate the mean-line model for the different test cases. In the analysis mode, the model was validated by assigning the actual geometry and comparing the performance for each test case. In the design mode, the design point specifications and the full impeller geometry were assigned, and the diffuser geometry was calculated to match the required stage pressure ratio.

2.4.1. Air compressors

The first three compressor test cases use air, and their experimental results are considered to be one of the most comprehensive experimental data sets for centrifugal compressors [57]. The three centrifugal compressors were extensively investigated in the past, and were named *Eckardt compressors* as they were tested by Dr. Dietrich Eckardt in the 1970s. The experimental investigations of Eckardt were published in a series of papers [58–60] and were performed using laser two-focus velocimetry, high-frequency pressure transducers, and conventional pneumatic probes.

The accuracy of the experimental data amounts to ±1% for the mass flow rate, ±3 rpm in rotational speed, ±0.07 °C in temperature for the baseline or ±0.2 °C with recovery factor error, ±2% on impeller exit or diffuser inlet area, ±0.25% in nominal pressure or ±0.5% for $r/r_2 < 1.1$ and angles to ±0.25° nominal or ±0.5° for $r/r_2 < 1.1$. These values were considered to be meeting or exceeding common research standards at that time [57].

2.4.2. R134a compressor

The fourth test case was a centrifugal compressor which was designed for domestic heat pump applications, and employed the refrigerant R134a. Due to the considered application, the use of a refrigerant, and the compressor size and type, this test case is particularly relevant to assess the suitability of the mean-line model using a refrigerant working fluid.

The compressor was recently designed and tested by Schiffmann and Favrat [11,61–63]. Table 5 lists the geometrical and modeling details. The compressor could be tested at high rotational speeds and employed gas lubricated bearings, allowing for oil-free operation. The measurements were performed using different probes with an accuracy of ±0.2 K in the temperature, ±0.002 MPa in the pressure, ±0.5% in the mass flow rate, and ±0.1% in the electric power [11]. The tests showed

that the compressor could achieve values of pressure ratio up to 3.3, power up to 1.8 kW, rotational speed up to 210 krpm, and internal isentropic efficiency up to 79%. No details of internal flow measurements were reported.

The experimental results proved the technical feasibility of a small-scale, oil-free and direct driven turbocompressor for domestic heat pump applications.

2.4.3. CO_2 compressor

The fifth test case is a centrifugal compressor operating with supercritical CO_2 and was tested by Wright et al. [64] at Sandia National Laboratories (SNL) under the framework of the development of advanced Brayton cycles using supercritical working fluids.

This test case is particularly relevant since the working fluid is used in the refrigeration field and there is the presence of highly challenging numerical modeling conditions close to the critical point, where the fluid properties exhibit large deviations from the ideal gas laws as well as large variations. The compressor stage consists of an impeller and a vaned diffuser. The rotor consists of six main blades and six splitter blades, whereas the diffuser consists of 17 wedge-shaped vanes. Table 5 shows the geometrical and modeling details. The compressor uses gas foil bearings, a high-speed permanent magnet motor/alternator and labyrinth gas seals to reduce the rotor cavity pressure. A small-scale loop was designed and the compressor was tested up to a rotational speed of 65 krpm, a pressure ratio of 1.65 and a mass flow rate of 1.8 kg/s. Wright et al. [64] documented values of accuracy for the experimental temperature probes of approximately 0.2 K for resistance thermometry devices, and 0.1 K for thermocouples. The test results obtained by Wright et al. [64] demonstrated the possibility of stable, controllable operation near the critical point.

In the validation, the results from the mean-line model are also compared to numerical simulations carried out to validate a CFD code documented in Pecnik et al. [65] for the impeller only and in Rinaldi et al. [66] for the impeller and vaned diffuser. The CFD code is

Table 5
Data of the experimental centrifugal compressors.

		Eckardt Impeller				
Ref.	Units	O [57–59,74]	A [57–59,74]	B [57–59,74]	Schiffmann and Favrat [11,61,63,75,76]	Sandia [21,64–66,77]
			Input conditions			
Fluid	–	Air	Air	Air	R134a	CO_2
T_{01}	K	288.15	288.15	288.15	265	305.97
p_{01}	bar	1.01	1.01	1.01	1.65	76.9
N	krpm	14–16	14–16	14–16	150–210	45–55
			Impeller			
r_{1s}	m	0.14	0.14	0.14	0.0056	0.0094
r_{1h}	m	0.045	0.06	0.0959	0.002	0.00254
r_2	m	0.2	0.2	0.2	0.01	0.01868
b_2	m	0.026	0.026	0.026	0.0012	0.00171
L_z	m	0.13	0.13	0.13	0.007693	0.1137
$Z_{r,full}$	–	20	20	20	9	6
$Z_{r,splitter}$	–	0	0	0	9	6
$LR_{splitter}$	–	0	0	0	0.5	0.7
β_{1bs}	°	−63	−63	−60	−56	−50
β_{1bh}	°	−32	−40	−45	−30.23	−40
β_{2b}	°	0	−30	−40	−45	−50
ϵ_a	mm	0.372	0.235	0.372	0.15	0.254
ϵ_r	mm	0.372	0.19	0.372	0.15	0.254
ϵ_b	mm	0.372	0.235	0.372	1	0.254
k_s	mm	0.002	0.002	0.002	0.01	0.01
t_{b1}	mm	2.11	2.11	2.11	0.1	0.762
t_{b2}	mm	1.08	1.08	1.08	0.1	0.762
			Vaneless Diffuser			
r_3/r_2	–	1.69	2.69	3.69	1.65	1.02
b_3/b_2	–	0.51	0.51	0.51	0.75	1
			Vaned Diffuser			
AR	–	–	–	–	–	2.81
AS	–	–	–	–	–	0.55
LWR	–	–	–	–	–	3.41
Z_{vd}	–	–	–	–	–	17
α_{3b}	°	–	–	–	–	71.5
α_{5b}	°	–	–	–	–	71.5
t_{b3}	m	–	–	–	–	0
t_{b5}	m	–	–	–	–	0.00335
b_5/b_2	–	–	–	–	–	1
r_5/r_2	–	–	–	–	–	1.37
			Inducer			
r_0	m	–	–	–	0.01	–
L_{ind}	m	–	—	–	0.02	–
$k_{s,ind}$	mm	–	–	–	0.1	–
			Volute			
r_4	m	–	–	–	0.0045	–

representative of the current state-of-the-art for numerical modeling of centrifugal compressors operating with CO_2, and therefore the CFD results were used as an additional benchmark for the validation of the mean-line model.

2.5. Case study and cycle modeling

The method used to design a HTHP equipped with a centrifugal compressor, was applied to the design of a high-temperature cycle of a cascade heat pump for steam generation. The heat pump was designed to supply industrial process steam at 150 °C, while utilizing heat supplied at 100 °C. The bottom cycle, not included in the present analysis, utilizes low-temperature heat sources such as excess heat or district heating while providing constant operating conditions to the top cycle.

Fig. 4 depicts two investigated cycle layouts of the heat pump system. Layout (a) is an open-loop cycle in which the working fluid is the process steam itself. The steam is returned from the process as condensate, before being directly evaporated and compressed. The compression is realized in two stages, due to the comparatively high-pressure ratio (above 5) for steam. An intercooler is included before the second-stage compressor inlet to realize a more efficient compression [67]. Layout (b) is a closed-loop, in which the working fluid is separated from the steam. The heat pump cycle is a one-stage cycle with an internal heat exchanger that preheats and evaporates the condensate before supplying the steam to the process.

Fig. 4(a) shows also the use of an electric superheater before the first compressor stage, which was adopted as a safety measure to avoid the possible presence of two-phase conditions at the compressor inlet and outlet. In the open-loop cycle, the optimal pressure ratio of the two compressor stages was calculated as the geometric mean of the overall compression ratio. As opposed to the closed-loop cycle, the open-loop cycle can employ direct contact heat exchangers rather than surface heat exchangers, since the working fluid is the same as the steam supply.

Table 3 lists the modeling conditions of the thermodynamic cycle. The evaporation temperature of the heat pump (HP) cycle was 100 °C, and the cycle supplied heat at a temperature of 150 °C. A number of different working fluids were selected according to the following criteria: (i) subcritical cycle operation, (ii) no ozone depletion potential, (iii) low global warming potential (< 150), (iv) availability of the thermodynamic and transport properties in CoolProp [45] and/or REFPROP [46]. The selected working fluids were pentane, isopentane, cyclopentane, R1233zd(E), and MM. The latter is representative for siloxanes, which are considered to be possible working fluid candidates for future HTHP applications [68].

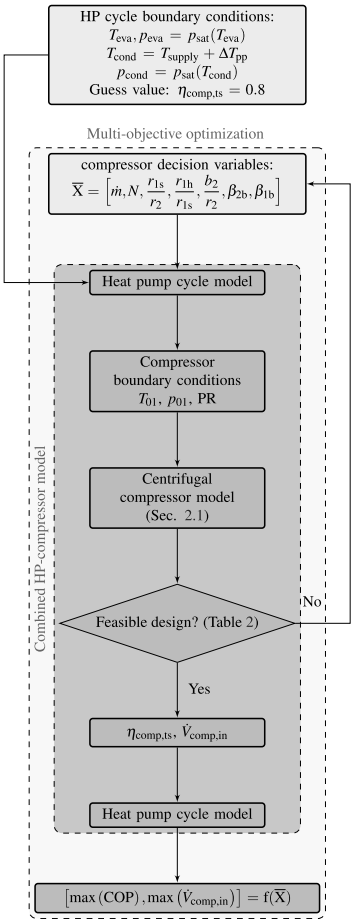

Fig. 5. Method for the combined multi-objective optimization of the heat pump cycle and the centrifugal compressor.

The compressor inlet temperature was determined by imposing a degree of superheat, which was calculated as the minimum temperature difference to avoid two-phase conditions at the compressor outlet.

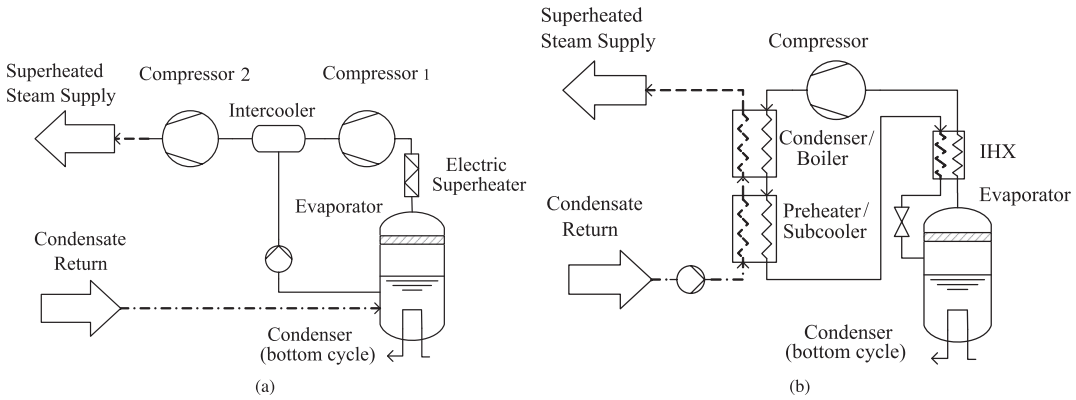

Fig. 4. Layout of the HP cycle for steam generation using: (a) an open-loop with steam and (b) a closed-loop with other working fluids.

2.6. Design optimization method

The design model of the centrifugal compressor was coupled to that of a heat pump. Fig. 5 shows the framework of the combined simulation and optimization. First, the heat pump cycle boundary conditions were set as indicated in Table 2. An initial guess value of 0.8 for the compressor isentropic efficiency was assumed. The heat pump cycle and the compressor models were then combined (inner red marked area) and subsequently optimized (outer yellow area). The array $\overline{X}$ indicates the seven decision variables of the optimization. The mass flow rate of the compressor was used as a decision variable and was optimized together with the other decision variables to maximize the cycle coefficient of performance (COP) and the compressor inlet volume flow rate as follows:

$$[\max(\mathrm{COP}),\ \max(\dot{V}_{\mathrm{comp,in}})] = \mathrm{f}(\overline{X}) \tag{36}$$

$$\overline{X} = \left[\dot{m},\ N,\ \frac{r_{1s}}{r_2},\ \frac{r_{1h}}{r_{1s}},\ \frac{b_2}{r_2},\ \beta_{2b},\ \beta_{1b}\right] \tag{37}$$

Eqs. (36) and (37) show the mathematical relation between the

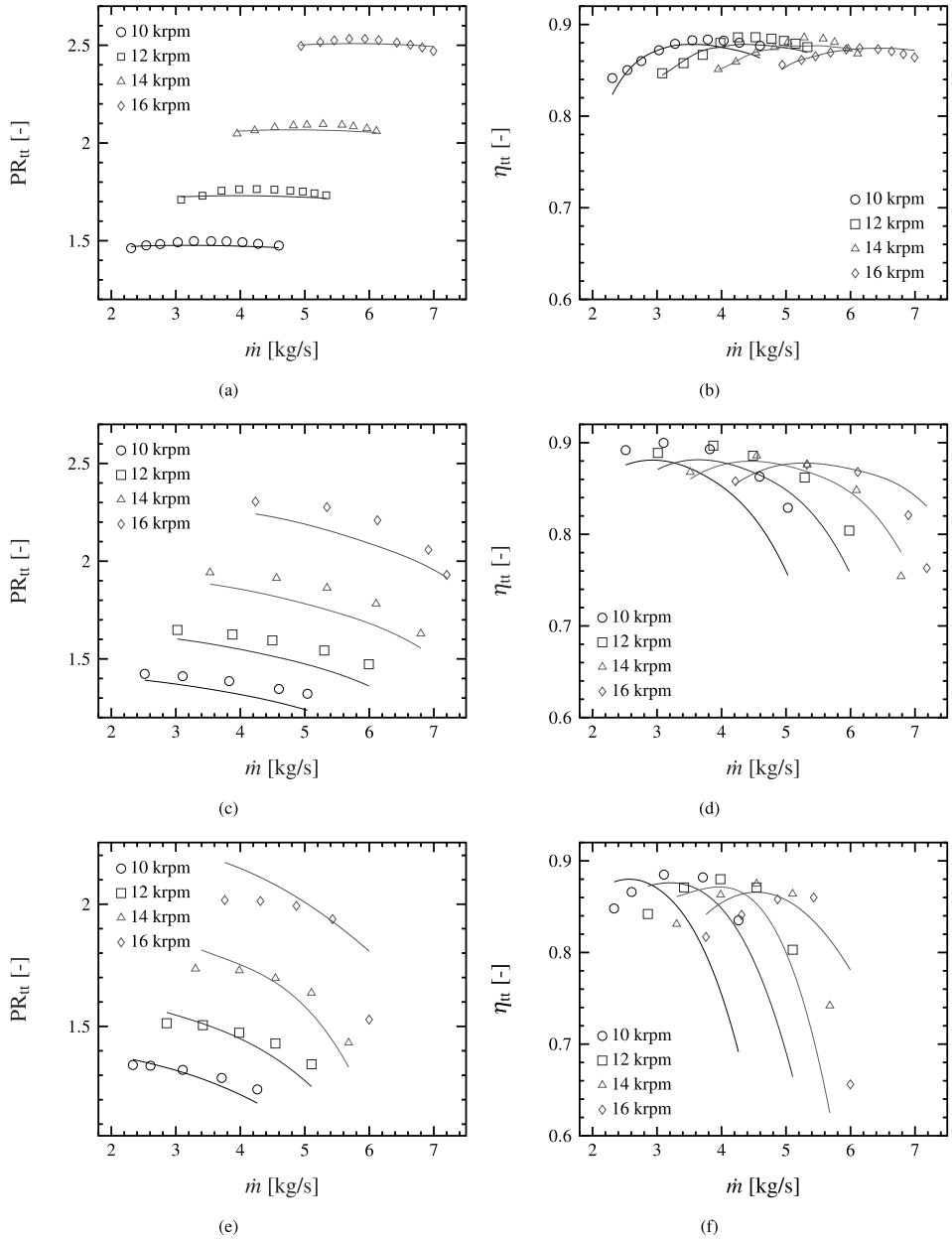

Fig. 6. Comparison between the measured (○) and predicted (–) pressure ratio and isentropic efficiency for different Eckardt impellers [58–60]: (a,b) impeller O; (c,d) impeller A; (e,f) impeller B.

cycle and the compressor models, which are interfaced through the mass flow rate and the compressor isentropic efficiency. The compressor inlet temperature and pressure, and the outlet pressure were governed by the thermodynamic cycle. Since the thermodynamic state at the compressor inlet is fixed by the cycle specifications, the maximization of the compressor inlet volume flow rate, $\dot{V}_{comp,in}$, also corresponds to maximize the supplied heat flow rate.

The decision variables of Eq. (37) were varied by the optimizer within the boundaries listed in Table 2 until achieving a technically feasible and manufacturable design. The compressor impeller outlet diameter was fixed to the value of 110 mm, which corresponds to that of the technology presented in Ref. [69] that focuses on similar heat pump applications. Fixing the compressor tip diameter allows comparing different solutions based on the same size, and makes it possible to compare with the state-of-the-art steam compressor of Ref. [69]. Since the compressor outlet diameter was fixed, the isentropic stage loading coefficient $\psi = \Delta h_{0,is}/U_2^2$ was readily calculated at the beginning of the routine and, therefore, was not optimized. The optimal number of blades was calculated using Eq. (1).

In the case of steam, where a two-stage compressor was required (see Section 2.5), the second stage was optimized assuming to be mounted on the same shaft as the first one, and the mass flow rate was calculated by mass and energy balances at the intercooler. As a result, a total of 12 decision variables was optimized in this case.

A multi-objective optimization was performed in MATLAB [44] and was based on a genetic algorithm using a population of 500 individuals and 200 generations. In the optimization of the two-stage steam compressor, a population of 1000 individuals was used instead due to the higher number of decision variables.

3. Results

3.1. Validation

Fig. 6 shows the comparison between the measured and predicted pressure ratio and isentropic efficiency for the three Eckardt impellers [58–60].

The discrepancy in pressure ratio for impeller O is within 1.4%. The model underestimates the actual pressure ratio of impeller A by up to 6%. In the case of impeller B, the highest discrepancy is seen at 16 krpm and for both low and high mass flow rates, where the model has a deviation of up to 7%. The prediction of the isentropic efficiency also follows the trends of the experimental measurements. The prediction for impeller A shows high accuracy, although the model does not reproduce the trend of the different speed lines perfectly. The maximum discrepancy is about 2%-points. The efficiency predicted by impeller A is close to that of the actual case and, like for the pressure ratio, the efficiency results are underpredicted by up to 2%-points at the best efficiency point, whereas the discrepancy is up to 6.7%-points at higher values of mass flow rate. A similar trend is observed for impeller B; however, in this case, the model predicts the peak of the efficiency curves to be at 10% to 19% lower mass flow rate than the experimental peak value. Overall, the trend of the speed lines for both the pressure ratio and the efficiency with the mass flow rate is respected in all cases, indicating that the present model can predict the compressor behavior with consistency.

Fig. 7 shows the comparison between the measured and the predicted pressure ratio for the compressor operated with R134a. In general, the agreement between the experimental data and the present model is relatively good considering the challenges related to modelling accurately mini and micro-scale turbomachinery (the maximum shaft power of the compressor is about 1.5 kW). The highest discrepancy was found at the lowest and highest values of the rotational speed, and close to the choking point where deviations in the pressure ratio up to 7% were found. Nevertheless, the model seems to capture the trend of the experimental results well. A higher deviation is found in the prediction of the compressor isentropic efficiency, see Fig. 7(b). The highest deviation is found close to the onset of surge and of choking, indicating that the presence of inlet recirculation flows close to surge is the main cause for the discrepancy between numerical and experimental data. In Fig. 7(b), the error bars related to the efficiency computed from the measurements of temperature and pressure are added as a reference. The error bars were extrapolated from Refs. [11,76], where they were calculated using the error propagation approximated by a first-order Taylor series. The experimental uncertainty in the compressor isentropic efficiency was only available for this validation test case. For some speed lines, the model prediction is within the error band of the experimental data, and in other cases, the deviation is up to 8%-points. Similar results were obtained by Schiffmann [76] and Schiffmann and Favrat [11], who showed deviations up to 8%-points using their 1D model validated with the same test case.

Fig. 8 shows the validation with the Sandia [21,64–66,77] compressor both for the 1D model and CFD calculations. The mean-line model generally shows good agreement with the experimental trends, with a maximum deviation of 15% in the enthalpy rise and 3.5%-points in the efficiency. However, a higher deviation up to 17% in the enthalpy rise is observed at 55 krpm as well as a shift of the peak efficiency from a flow coefficient of 0.03 to 0.04, corresponding to a 25% deviation. The CFD results also show a shift towards lower flow coefficients, especially at the low values of rotational speed, of about 25% compared to the experimental data. Rinaldi et al. [66] argued that such results are in a reasonable range of accuracy considering the challenges of CFD modeling close to the critical point of CO_2.

Table 6 shows the results of the validation of the design model. The

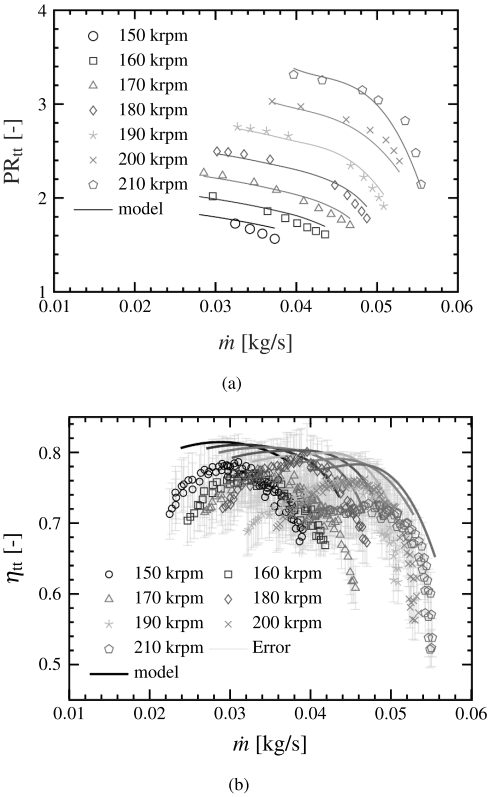

Fig. 7. Comparison between the measured and predicted results for the compressor operated with R134a and studied by Schiffmann and Favrat [11,76]: (a) pressure ratio and (b) isentropic efficiency.

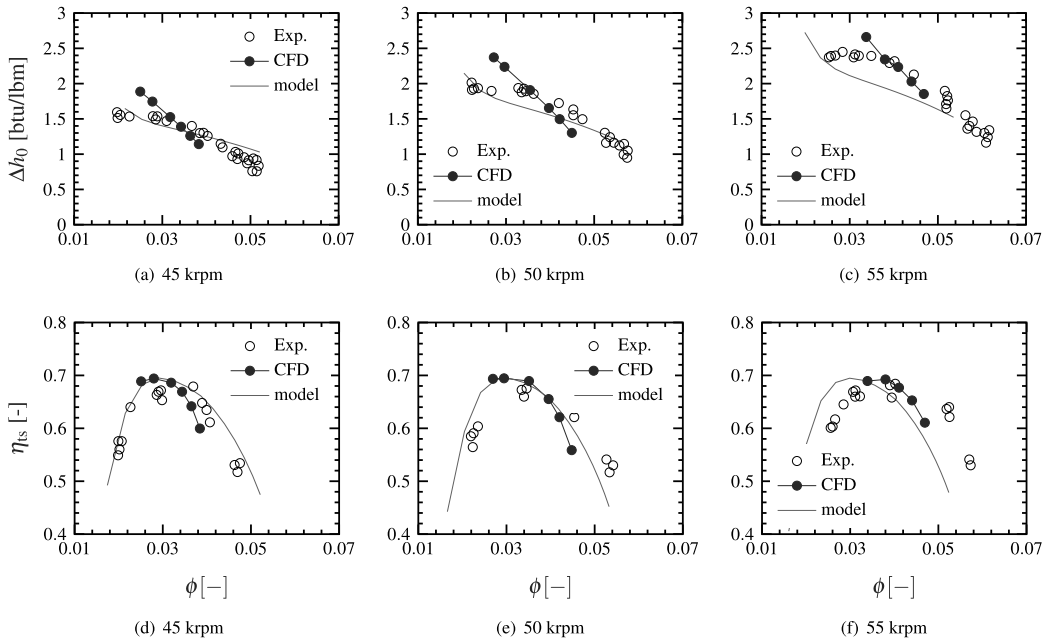

Fig. 8. Comparison between the measured and the predicted enthalpy rise and isentropic total-to-static efficiencyas a function of the flow coefficient $\phi = \dot{m}/(\rho_{01} U_2 d_2^2)$ for the Sandia compressor impeller with vaned diffuser. Experimental data from Ref. [64] and state-of-the-art CFD data from Ref. [66].

average deviation of the isentropic efficiency is within 5% for the Eckardt impellers, while it goes up to approximately 7% for the test case using R134a. Regarding the geometry, the diffuser radius ratio was found to be higher in the test cases of the Eckardt [57–59,74] impellers A and B and of the R134a compressor, the latter showing the largest increase from 1.65 to 2.23, indicating that higher losses are predicted for these cases. These results are in agreement with those found for the off-design validation and further confirm that the model is suitable for the preliminary design of centrifugal compressors using different working fluids.

3.2. Compressor design optimization

Fig. 9 shows the Pareto fronts of the optimal solutions after the multi-objective optimization for the different working fluids and in terms of COP and supply heat flow rate. The point corresponding to an equal weight of both the objective functions is selected as the best solution in the Pareto front and is indicated with the red dot. The shape of the Pareto fronts is for some fluids rather pronounced. This characteristic stems mainly from the values of the mass flow rate, which for each point in the Pareto front results as a trade-off regarding cycle performances and the minimum mass flow rate required to avoid choking in the compressor impeller.

In terms of cycle performance, the Pareto front for steam achieves the highest value of COP and supply heat flow rate, respectively, 5.46 and 1.73 MW at the best point. The fluid cyclopentane has the second highest value of COP of 4.74, but delivers 1.22 MW, corresponding to a 30% lower supply heat flow rate. The working fluid MM has a lower value of COP, around 4.54, but also supplies the lowest value of heat flow rate with approximately 0.24 MW. The fluids n-pentane and isopentane exhibit lower values of cycle COP, but values of heat flow rate higher than cyclopentane and about 19% and 6% less than steam, respectively. Finally, R1233zd(E) shows the lowest value of COP and a 57% lower supply heat flow rate of steam, respectively, 3.86 and 742.6 kW.

Fig. 9(b) shows the Pareto fronts regarding compressor total-to-

Table 6
Validation of the design model.

	Eckardt compressors				
Refs.	Impeller O [57–59,74]	Impeller A [57–59,74]	Impeller B [57–59,74]	Schiffmann [11,61,63,75,76]	Sandia [21,64–66,77]
No	1	2	3	4	5
PR_{tt} [–]	2	1.81	1.67	2.35	1.26
$\dot{m}$ [kg/s]	5.32	4.54	4.54	0.039	2.15
N [krpm]	14	14	14	180	50
ψ_{ts}	0.78	0.62	0.53	0.5	0.41
Diffuser radius ratio (model)	1.69	1.80	1.88	2.23	1.37
Diffuser radius ratio (actual)	1.69	1.69	1.69	1.65	1.3697
η_{model}	0.885	0.869	0.843	0.744	0.717
η_{exp}	0.886	0.876	0.875	0.800	0.673
Deviation	−0.03%	−0.84%	−3.70%	−7.03%	6.52%

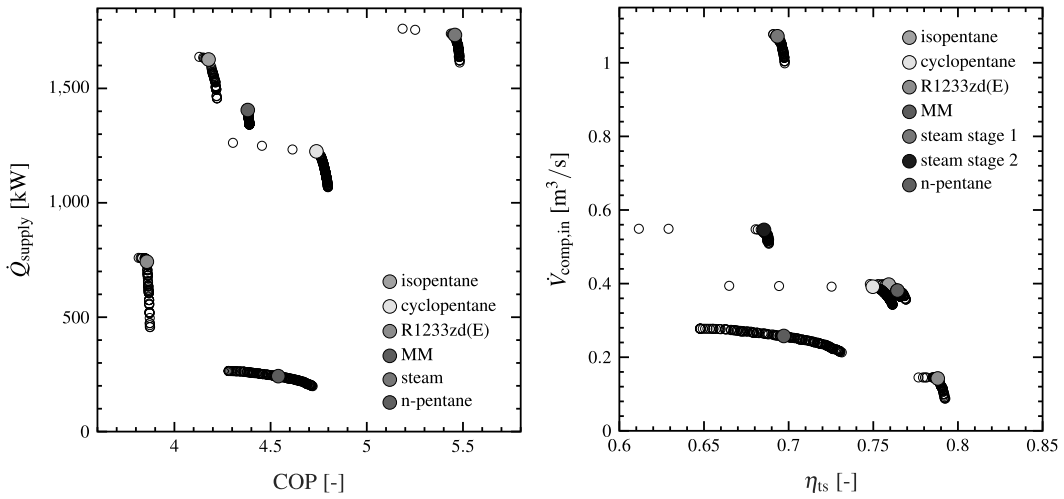

Fig. 9. Pareto fronts of the optimal solutions for the selected working fluids: (a) COP and supply heat flow rate; (b) compressor isentropic efficiency and inlet volume flow rate. The solution having an equal weight of the two objective functions is indicated with the symbol ●.

static efficiency and inlet volume flow rate. In this case, the steam compressor can accept the highest inlet volume flow rate, approximately 1.07 m^3/s, but at the expense of the lowest values of total-to-static isentropic efficiency in the two stages, about 0.69 and 0.68 in the first and the second stage, respectively. The opposite trend is seen for the other fluids which feature a higher value of compressor isentropic efficiency and a lower value of inlet volume flow rate.

Table 7 lists the results of the design optimization, and Fig. 10 shows the meridional cut layout of the obtained compressors. The optimal value of mass flow rate varies significantly among the different fluids: the highest value of 7.85 kg/s is found for R1233zd(E) and the lowest value for steam with 0.64 kg/s in the first stage. The optimal rotational speed is also very different and ranges from approximately 28.8 krpm for R1233zd(E) to 85 krpm for steam. Considering the fixed impeller diameter of 110 mm, such values of rotational speed result in acceptable values of impeller tip peripheral speed, which are well below the limit value of 500 m/s. However, values close to this limit are found for the two-stage steam compressor and stem directly from the high value of rotational speed.

The seven compressors have a significant backsweep, above 40° for all fluids except for the steam compressor, where the exit blades tend to be of the radial type. The optimal solutions were found at the upper limit of r_{1s}/r_2 for all hydrocarbons and the first stage with steam. All compressor stages, except for those with R1233zd(E) and the second stage with steam, feature a high fluid dynamic loading and high values of relative Mach number at the inlet, $M_{1s,rel}$, which exceed unity at the shroud.

The throat dimensions of all geometries are between 4.1 mm and 7.4 mm, enabling that they can be manufactured using a conventional five-axis milling machine. All of the designs feature a similar number of blades, between 18 and 22, for the same tip diameter. This suggests that they will have similar costs.

Finally, the fluid R1233zd(E) resulted in the highest values of total-to-total and total-to-static efficiency of approximately 0.91 and 0.79, respectively. These values are about 10%-points higher than those of steam. Despite the large differences in the isentropic efficiency, steam still holds the highest value of COP due to advantages in the cycle layout.

4. Discussion

The validation with the five test cases suggests that the model can predict the performance of different compressor types with reasonable accuracy under different thermodynamic conditions and applications, from the ideal gas flows of industrial air compressors to real-gas and dense flow conditions in refrigeration or CO_2 applications.

The results of the optimization with the heat pump cycle suggest that the open-loop using steam yields the highest performance in terms of COP and $\dot{V}_{comp,in}$, and it is therefore the preferred choice among all the considered working fluids for the HTHP. Finally, the results of the combination of cycle and compressor models suggest that, in the case of mechanical design issues of steam compressors or if a single-stage compressor is preferred to reduce the investment cost, a closed-loop HTHP with cyclopentane gives the second best option, although at the expense of a lower COP and supplied heat flow rate. In this case, a lower optimal rotational speed of 48 krpm is employed, thereby reducing the mechanical stresses on the impeller blades and yielding higher values of compressor isentropic efficiency.

Previous works [32–37] focused on the working fluid selection for heat pump applications by assuming a fixed value of isentropic efficiency. The thermodynamic cycle performance was analyzed in terms of COP and of the volumetric heating capacity. The latter was used as an indication of the volume flow rate at compressor inlet, and thereby the size of the compressor, for the same supply heat flow rate. This procedure assumes that the volume flow rate at the inlet of the compressor is directly related to the size of the compressor. However, the results of the present study suggest that volume flow rates in the range 0.1–1.0 m^3/s can be achieved with a compressor of comparable size and suggest that the actual volume flow rate depends on additional aspects such as the compressor stage pressure ratio, the maximum mass flow rate, the rotational speed and the working fluid itself. For the same reasons, the results of this study also suggest that the volumetric heating capacity (supplied heat flow rate over compressor inlet volume flow rate) might not be the most suitable indicator for estimating the size and, therefore, the cost of the centrifugal compressor.

This aspect further highlights the importance of applying a mean-line model together with that of the HP cycle. Moreover, the variation of the isentropic efficiency for the different fluids substantiates the

Table 7
Optimal compressor design for different working fluids.

Parameter	Units	Pentane	Isopentane	Cyclopentane	R1233zd(E)	MM	Steam (stage 1)	Steam (stage 2)
T_{01}	K	391.2	390.4	387.1	376.2	406.9	373.2	397.7
p_{01}	bar	59.27	7.22	4.16	10.42	1.00	1.01	2.29
PR_{tt}	–	2.828	2.721	2.965	2.765	3.745	2.255	2.255
$\dot{m}$	kg/s	5.73	7.45	3.88	7.85	1.30	0.64	0.69
N	rpm	46000	43985	48000	28802	34000	85001	85001
r_{1s}/r_2	–	0.70	0.70	0.70	0.53	0.70	0.70	0.68
r_{1h}/r_{1s}	–	0.33	0.27	0.34	0.32	0.29	0.26	0.64
b_2/r_2	–	0.14	0.18	0.17	0.11	0.19	0.27	0.12
β_{2b}	°	−43.6	−44.8	−44.7	−43.1	−44.91	−13.05	−5.16
β_{1b}	°	−45.1	−47.7	−49.7	−34.5	−50.6	−34.3	−44.6
T_{03}	K	428.9	429.1	430.4	429.6	429.9	476.1	504.6
U_2	m/s	264.9	253.3	276.5	165.9	195.8	489.6	489.6
C_3	m/s	105.9	88.4	118.7	67.6	81.0	199.3	212.6
β_2	°	−53.2	−55.3	−55.0	−55.1	−57.3	−33.5	−25.0
α_2	°	65.7	70.1	70.6	72.2	76.7	69.2	67.2
$M_{1s,rel}$	–	1.09	1.08	1.08	0.84	1.03	1.02	0.85
$M_{1,rel}$	–	0.89	0.88	0.88	0.71	0.81	0.88	0.76
$M_{2,rel}$	–	0.69	0.61	0.56	0.55	0.46	0.35	0.37
M_2	–		1.02	0.97	1.02	1.08	0.83	0.86
r_{1s}	m	0.0385	0.0384	0.0384	0.0291	0.0371	0.0384	0.0371
r_{1h}	m	0.0127	0.0105	0.0131	0.0094	0.0106	0.0098	0.0236
r_2	m	0.0550	0.0550	0.0550	0.055 0	0.0550	0.0550	0.0550
L_z	m	0.0360	0.0391	0.0353	0.0276	0.0371	0.0401	0.0189
b_1	m	0.0257	0.0279	0.0252	0.0197	0.0265	0.0286	0.0135
b_2	m	0.0079	0.0099	0.0093	0.0058	0.0085	0.0147	0.0065
b_3	m	0.0079	0.0099	0.0093	0.0058	0.0085	0.0147	0.0065
Z_r	–	19	19	20	19	22	18	18
$Z_{r,splitter}$	–	0	0	0	0	0	0	0
r_3	m	0.0735	0.0836	0.0738	0.0738	0.0735	0.1016	0.0996
o_1	m	0.0058	0.0052	0.0050	0.0051	0.0041	0.0068	0.0074
DR	–	0.755	0.738	0.764	0.748	0.743	0.704	0.636
η_{ts}	–	0.764	0.759	0.750	0.788	0.697	0.693	0.686
η_{tt}	–	0.892	0.851	0.886	0.907	0.838	0.796	0.797
COP	–	4.38	4.18	4.74	3.86	4.54	5.46	
$\dot{V}_{in}$	m^3/s	0.38	0.40	0.39	0.14	0.26	1.07	
$\dot{Q}_{supply}$	kW	1406	1626	1225	743	242	1734	

relevance of the presented method, since it can represent the trade-off in terms of heat capacity and COP, while providing reasonable estimates for volume flow rates and isentropic efficiencies.

The results highlight that the use of steam also requires a more challenging and expensive compressor design. The high value of rotational speed produces high-velocity flows in the impeller and diffuser passages, and requires low values of mass flow rate, leading to lower values of isentropic efficiency. For this reason, the design of a high-efficiency compressor for steam is a fluid-dynamic and technical challenge. Compared to the other fluids, the steam compressor may also experience supersonic shock losses at the inlet and mechanical resistance issues associated to the high values of peripheral speed in the impeller. In addition, the presence of two compression stages, required to deliver a pressure ratio above 5, represents a higher investment cost in the overall system. Nevertheless, this may be compensated by the absence of surface heat exchangers and the higher system COP.

The optimal design of the steam compressor obtained in this work, features a rotational speed of 85 krpm, a peripheral speed of approximately 490 m/s, blade angles in the range -15° to -5°, transonic flow conditions at the compressor inlet with relative Mach numbers in the range 0.76–1.02, and values of total-to-static isentropic efficiency of about 0.69. These results agree with those presented in the literature. Šarevski and Šarevski [78] analyzed the characteristics of a centrifugal compressor for steam applied in refrigeration and heat pump systems. They found that a pressure ratio of approximately 3.5 is the limiting value for a single stage, and for a temperature lift of 20 °C to 45 °C they found that a two-stage compressor is the optimal solution. This design philosophy is confirmed in this work, as the single-stage compressor design using the mean-line model results in excessive values of peripheral speed, supersonic Mach numbers and choking conditions inside the blade channels. In Ref. [78] the optimal blade angles at the impeller exit were found to be in the range -15° to 0° with a Mach number at the impeller inlet in the range 0.85–0.95. These values are in agreement with those of the present designs.

Madsbøll et al. [69] presented the construction and initial tests of a high-speed centrifugal compressor for a HTHP using steam as the working fluid. The authors designed the compressor at the speed of 95 krpm with blade exit angles of -10°. They showed a maximum value of compressor efficiency of 0.719 at the rotational speed 84.4 krpm, which is about 2.9%-points higher than that predicted in the present work. In the context of refrigeration applications, Süß [14] recently presented a chiller module using a centrifugal compressor which was able to achieve a COP of 14, considered to be 3 to 4 times higher than state-of-the-art equipment in the field. The compressor was designed to operate at 90 krpm and demonstrated an overall efficiency, including the motor, of 70%, which is close to the values of the optimal compressor in this paper.

Bantle [79] presented the test results for a prototype centrifugal compressor retrofitted from a turbocharger unit to be used for mechanical vapor recompression in steam driers. The centrifugal compressor was designed to deliver a thermal capacity of up to 300 kW, and tests were conducted for an inlet temperature of 105 °C. At full capacity, the turbocompressor operated at 90 krpm and achieved a pressure ratio of 2.4 with an isentropic efficiency of 72%, a mass flow rate of 0.125 kg/s and an outlet temperature of 225 °C.

The test conditions are similar to those of the first-stage steam

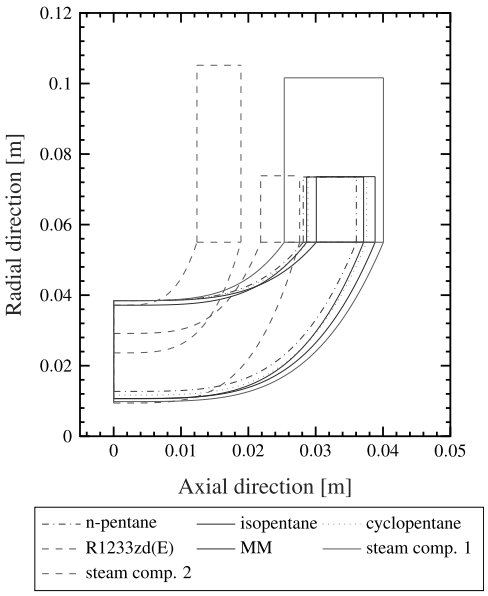

Fig. 10. Meridional cut layout of the optimal compressor designs.

compressor from the mean-line model. The efficiency of Ref. [79] is predicted to be 3%-points lower, and the mass flow rate is about 5.1 times smaller than the value 0.64 kg/s found using the optimization method. However, the different value of mass flow rate is justified by the different value of supply heat load, which in this work is maximized and found to be 5.7 times greater than the 300 kW required by Bantle [79].

More recently, the same author [80] presented the design of a two-stage compressor which is a continuation of the previous work in Ref. [79]. The two impellers feature characteristics similar to those in Table 7. The optimal pressure ratio was 2 in the first stage and 3.2 in the second stage, and it was distributed unevenly between the stages. As a result, the first-stage impeller featured an inlet relative Mach number of 1.27 at the tip, and the second impeller a Mach number of 0.96. In the optimal compressor design of the present work, the equal distribution of the pressure ratio across the stages yields a maximum value of relative Mach number of 1.02.

In terms of geometry, the two impellers presented in Ref. [80] featured exducer diameters of 115 mm and 146 mm, respectively. These values are different from the value employed in this work (110 mm) since the two turbocompressors were designed for two separate values of stage pressure ratio.

The comparison with the aforementioned works, demonstrating similar values of fluid dynamic parameters and compressor performance among the studies, indicates that the method presented in the current paper is suitable.

5. Conclusions

This paper presented a mean-line model for the design, optimization and analysis of centrifugal compressors and heat pump systems. The suitability of a mean-line centrifugal compressor model and its loss correlations, was assessed for different working fluids and geometries. Moreover, a novel method for the design and optimization of a heat pump cycle equipped with a centrifugal compressor was presented. Such a method aims to determine technically feasible solutions from the compressor and heat pump viewpoints. This approach is intended to facilitate engineers and researchers in identifying cost-effective solutions for the next-generation heat pump designs.

The compressor model was validated at design and off-design conditions with the experimental data of five test cases including three different working fluids: air, R134a, and CO_2. The off-design model showed deviations with the measured data up to 7% in the mass flow rate and 8%-points in efficiency. Overall, the model captured the trend of the experimental results. The design model was validated within 7% in the compressor isentropic efficiency. The validation suggests that the compressor model and the loss correlations can be used to simulate the performance of different machine geometries and working fluids with sufficient accuracy.

In order to show the relevance for a practical application, the proposed design method was applied to the case study of a top cycle of a high-temperature heat pump supplying steam at 150 °C. To this end, the compressor design model was coupled to the cycle design model, and a multi-objective optimization was performed. The decision variables of the compressor design model were optimized to maximize the cycle coefficient of performance and the supply heat flow rate. The method was applied to two different configurations: a closed-loop cycle using a selected refrigerant, and an open-loop using a two-stage compressor with water, which is representative of the current benchmark for such high-temperature heat pumps. In the closed-loop cycle, five working fluids were selected and analyzed.

Compared to a simple estimate of compressor efficiency and volume flow rate, the optimization of the integrated cycle and validated compressor models allowed finding more accurate results and restricting the solution space to more feasible designs also considering the compressor design criteria.

The open-loop with the two-stage water compressor achieves the highest values of coefficient of performance and heat flow rate, respectively, 5.48 and 1734 kW. At the same time, the design of a suitable water vapor compressor is found to be more challenging due to the high values of rotational speed, the low values of mass flow rate and the large pressure ratio, which in turn require the adoption of a two-stage solution. Moreover, the high values of rotational speed resulted in higher losses in the impeller and diffuser which will require special care in the fluid-dynamics design of the machine. A closed-loop with cyclopentane is indicated to be the second best option in terms of the coefficient of performance. In this case, the heat pump cycle would feature a lower coefficient of performance of 4.74 in favor of a simpler compressor design: a single-stage configuration with a backward swept impeller and lower rotational speed.

Acknowledgements

The research work was conducted within the frame of the THERMCYC project (“Advanced thermodynamic cycles utilizing low-temperature heat sources”; project ID: 1305-00036B, see http://www.thermcyc.mek.dtu.dk/) funded by Innovation Fund Denmark, The Danish Council for Strategic Research in Sustainable Energy and Environment.

References

[1] Wolf S, Blsels M. Model-based quantification of the contribution of industrial heat pumps to the European climate change mitigation strategy. In: Proceedings of the ECEEE industrial efficiency conference 2016, September 12-14, Kalkscheune, Berlin, Germany; 2016. p. 477–87.
[2] Arpagaus C, Bless F, Schiffmann J, Bertsch SS. Multi-temperature heat pumps: A literature review. Int J Refrig 2016;69:437–65.
[3] Arpagaus C, Bless F, Uhlmann M, Schiffmann J, Bertsch SS. High temperature heat pumps: Market overview, state of the art, research status, refrigerants, and application potentials; 2018.
[4] Chua KJ, Chou SK, Yang WM. Advances in heat pump systems: A review; 2010. https://doi.org/10.1016/j.apenergy.2010.06.014.
[5] IEA. Application of Industrial Heat Pumps, Final report, Part 1. Report No. HPP-AN35-1. Tech Rep; 2014.
[6] Nellissen P, Wolf S. Heat pumps in non-domestic applications in Europe: potential for an energy revolution. In: 8th EHPA European Heat Pump Forum, May 28,

Brussels, Belgium; 2015. p. 1–17.
[7] Wallerand AS, Kermani M, Kantor I, Maréchal F. Optimal heat pump integration in industrial processes. Appl Energy 2018;219:68–92.
[8] Zhang J, Zhang H-H, He Y-L, Tao W-Q. A comprehensive review on advances and applications of industrial heat pumps based on the practices in China. Appl Energy 2016;178:800–25.
[9] Jensen JK. Industrial heat pumps for high temperature process applications: A numerical study of the ammonia-water hybrid absorption-compression heat pump. Ph. D. thesis, Technical University of Denmark (DTU), Lyngby, Denmark; 2016.
[10] Bamigbetan O, Eikevik TM, Nekså P, Bantle M. Review of vapour compression heat pumps for high temperature heating using natural working fluids. Int J Refrig 2017;80:197–211.
[11] Schiffmann J, Favrat D. Design, experimental investigation and multi-objective optimization of a small-scale radial compressor for heat pump applications. Energy 2009;35(1):436–50.
[12] Schiffmann J. Integrated design and multi-objective optimization of a single stage heat-pump turbocompressor. J Turbomach 2015;137(7):071002.
[13] Hastbacka M, Dieckmann J, Bouza A. Small high speed: centrifugal compressors. ASHRAE J 2013;55(2):63–4.
[14] Süß J. A centrifugal compressor cooling system using water as working fluid. In: 12th IIR Gustav Lorentzen conference on natural refrigerants (GL2016), August 21-24, Edimburgh, UK; 2016. p. 1–7.
[15] Bertsch S, Arpagaus C, Bless F, Weickgenannt A, Schiffmann J. Theoretical investigation of a high temperature heat pump using a micro turbo compressor and water as a refrigerant. In: 13th IIR Gustav Lorentzen Conference, June 18-20, Valencia, Spain; 2018. p. 1–9.
[16] Li PY, Gu CW, Song Y. A new optimization method for centrifugal compressors based on 1D calculations and analyses. Energies 2015;8(5):4317–34.
[17] Klausner E, Gampe U. Evaluation and enhancement of a one-dimensional performance analysis method for centrifugal compressors. In: Proceedings of the Asme Turbo Expo: turbine technical conference and exposition, June 16-20, ASME, Düsseldorf, Germany; 2014. p. V02DT42A005.
[18] Kus B, Nekså P. Development of one-dimensional model for initial design and evaluation of oil-free CO2 turbo-compressor. Int J Refrig 2013;36(8):2079–90.
[19] Harley P, Spence S, Filsinger D, Dietrich M, Early J. An evaluation of 1D design methods for the off-design performance prediction of automotive turbocharger compressors. In: ASME Turbo Expo 2012: turbine technical conference and exposition, June 11-15, Copenhagen, Denmark; 2012. p. 1–11.
[20] Casey M, Robinson C. A method to estimate the performance map of a centrifugal compressor stage. J Turbomach 2012;135(2):021034.
[21] Vilim RB. A one-dimensional compressor model for super-critical carbon dioxide applications. In: 2010 International conference on advances in nuclear power plants (ICAPP'10), June 13-17, San Diego, CA, USA; 2010. p. 1–12.
[22] Veres J. Axial and centrifugal compressor mean line flow analysis method. In: 47th AIAA Aerospace sciences meeting including the new horizons forum and aerospace exposition, January 5-8. Orlando, Florida, USA: American Institute of Aeronautics and Astronautics; 2009. p. 1–38.
[23] Oh HW, Yoon ES, Chung MK. An optimum set of loss models for performance prediction of centrifugal compressors. Proc Inst Mech Eng, Part A: J Power Energy 1997;211(4):331–8.
[24] Aungier RH. Mean streamline aerodynamic performance analysis of centrifugal compressors. J Turbomach 1995;117(3):360.
[25] Perdichizzi A, Savini M. Aerodynamic and geometric optimization for the design of centrifugal compressors. Int J Heat Fluid Flow 1985;6(1):49–56.
[26] Galvas M. Fortran program for predicting off-design performance of centrifugal compressors. Tech Rep; 1973.
[27] Rodgers C. Typical performance characteristics of gas turbine radial compressors. J Eng Power 1964;86(2):161.
[28] Rodgers C. A diffusion factor correlation for centrifugal impeller stalling. J Eng Power 1978;100(4):592.
[29] Rodgers C. Efficiency of centrifugal compressor impellers. In: AGARD 282 conference proceedings, May 7-9, Brussels, Belgium; 1980. p. 1–14.
[30] Rodgers C. Static pressure recovery characteristics of some radial vaneless diffusers. Can Aeronaut Space J 1984;30:42–54.
[31] Coppage J, Dallenbach F. Study of supersonic radial compressors for refrigeration and pressurization systems. Tech Rep, Garret Corp; 1956.
[32] Chamoun M, Rulliere R, Haberschill P, Berail J. Water vapour as refrigerant for a new high temperature heat pump. In: 23rd IIR International congress of refrigeration, August 21-26, Prague, Czech Republic; 2011. p. 1–8.
[33] De Larminat P, Arnon D. Natural or synthetic refrigerants - what options for high temperature heat pumps?. In: 10th IIR Gustav Lorentzen conference on natural refrigerants, June 25-27, Delft, The Netherlands; 2012. p. 1–8.
[34] Domanski PA, Steven Brown J, Heo J, Wojtusiak J, McLinden MO. A thermodynamic analysis of refrigerants: Performance limits of the vapor compression cycle. Int J Refrig 2014;38(1):71–9.
[35] McLinden MO, Kazakov AF, Steven Brown J, Domanski PA. A thermodynamic analysis of refrigerants: Possibilities and tradeoffs for Low-GWP refrigerants. Int J Refrig 2014;38(1):80–92.
[36] Kondou C, Koyama S. Thermodynamic assessment of high-temperature heat pumps using low-GWP HFO refrigerants for heat recovery. Int J Refrig 2015;53:126–41.
[37] Bamigbetan O, Eikevik TM, Nekså P, Bantle M. Evaluation of Natural working fluids for the Development of high temperature heat pumps. In: 12th IIR Gustav Lorentzen conference on natural refrigerants GL2016, August 21-24, Edimburgh, UK; 2016. p. 1–8.
[38] Da Lio L, Manente G, Lazzaretto A. Predicting the optimum design of single stage axial expanders in ORC systems: Is there a single efficiency map for different working fluids? Appl Energy 2016;167:44–58.
[39] White M, Sayma AI. Improving the economy-of-scale of small organic rankine cycle systems through appropriate working fluid selection. Appl Energy 2016;183:1227–39.
[40] Meroni A, Andreasen JG, Persico G, Haglind F. Optimization of organic Rankine cycle power systems considering multistage axial turbine design. Appl Energy 2018;209:339–54.
[41] Meroni A, La Seta A, Andreasen JG, Pierobon L, Persico G, Haglind F. Combined turbine and cycle optimization for organic rankine cycle power systems – Part A: turbine model. Energies 2016;9(5). 313, 1–15.
[42] La Seta A, Meroni A, Andreasen JG, Pierobon L, Persico G, Haglind F. Combined turbine and cycle optimization for organic rankine cycle power systems – Part B: application on a case study. Energies 2016;9(6). 393, 1–17.
[43] Javed A, Arpagaus C, Bertsch S, Schiffmann J. Small-scale turbocompressors for wide-range operation with large tip-clearances for a two-stage heat pump concept. Int J Refrig 2016;69:285–302.
[44] The Mathworks Inc. MATLAB - MathWorks; 2016. URL http://www.mathworks.com/products/matlab/.
[45] Bell IH, Wronski J, Quoilin S, Lemort V. Pure and pseudo-pure fluid thermophysical property evaluation and the open-source thermophysical property library coolprop. Ind Eng Chem Res 2014;53(6):2498–508.
[46] Lemmon EW, Huber ML, McLinden MO. NIST reference fluid thermodynamic and transport properties–REFPROP; 2002.
[47] Dixon SL, Hall CA. Fluid mechanics and thermodynamics of turbomachinery. 7th ed. Oxford, UK: Butterworth-Heinemann; 2014.
[48] Japikse D. Centrifugal compressor design and performance. Wilder, VT, USA: Concepts ETI Inc.; 1996.
[49] Xu C, Amano RS. Empirical design considerations for industrial centrifugal compressors. Int J Rotat Mach 2012;2012:1–15.
[50] Japikse D, Baines N. Introduction to turbomachinery. Norwich, VT, USA: Concepts ETI; 1994.
[51] Whitfield A, Baines NC. Design of radial turbomachines. New York, NY, USA: John Wiley and Sons Inc.; 1990.
[52] Stanitz JD. One-dimensional compressible flow in vaneless diffusers of radial-and mixed-flow centrifugal compressors, including effects of friction, heat transfer and area change. Tech Rep, NASA; 1952.
[53] Japikse D. Advanced diffusion levels in turbocharger compressors and component matching. In: 1st International conference on turbocharging and turbochargers, April 26-28, London, UK; 1982. p. 143–55.
[54] Aungier RH. Centrifugal compressors: a strategy for aerodynamic design and analysis. New York, NY, USA: ASME Press; 2000.
[55] Botha BW, Moolman A. Determining the impact of the different losses on centrifugal compressor design. R&D J 2005;21(3):1–9.
[56] Wiesner FJ. A review of slip factors for centrifugal impellers. J Eng Gas Turbines Power 1967;89(4):558–66.
[57] Japikse D. A critical evaluation of three centrifugal compressors with pedigree data Sets: Part 5 studies in component performance. J Turbomach 1987;109(1):1.
[58] Eckardt D. Instantaneous measurements in the jet-wake discharge flow of a centrifugal compressor impeller. J Eng Power 1975;97(3):337.
[59] Eckardt D, Trültzsch K, Weimann W. Vergleichende Strömungsuntersuchungen an drei Radialverdichter-Laufrädern mit konventionellen Meßverfahren, Ph.D. thesis; 1977.
[60] Eckardt D. Flow field analysis of radial and backswept centrifugal compressor impellers. I-Flow measurements using a laser velocimeter. In: Proceedings of the twenty-fifth annual international gas turbine conference and exhibit and twenty-second annual fluids engineering conference, March 9-13, New Orleans, Louisiana, USA; 1980. p. 77–86.
[61] Schiffmann J, Favrat D. Theoretical design of a high-speed low power radial turbocompressor. In: 6th European turbomachinery conference, 7-11 March, Lille, Francel 2005. p. 1–11.
[62] Schiffmann J, Favrat D. High-speed low power radial turbocompressor for oil-free heatpumps. In: International Compressor engineering conference at Purdue, July 17-20; 2006. p. 1–8.
[63] Demierre J, Rubino A, Schiffmann J. Modeling and experimental investigation of an oil-free microcompressor-turbine unit for an organic rankine cycle driven heat pump. J Eng Gas Turbines Power 2015;137(3):1–10.
[64] Wright SA, Radel RF, Vernon ME, Rochau GE, Pickard PS. Operation and analysis of a supercritical CO_2 brayton cycle. Tech Rep; 2010.
[65] Pecnik R, Rinaldi E, Colonna P. Computational fluid dynamics of a radial compressor operating with supercritical CO_2. J Eng Gas Turbines Power 2012;134(12):122301.
[66] Rinaldi E, Pecnik R, Colonna P. Computational fluid dynamic simulation of a supercritical CO_2 compressor performance map. J Eng Gas Turbines Power 2015;137(7):072602.
[67] Šarevski VN, Šarevski MN. Energy efficiency of the thermocompression refrigerating and heat pump systems. Int J Refrig 2012;35:1067–79.
[68] Colonna P, Nannan NR, Guardone A, Lemmon EW. Multiparameter equations of state for selected siloxanes. Fluid Phase Equilib 2006;244(2):193–211.
[69] Madsbøll H, Weel M, Kolstrup A. Development of a water vapor compressor for high temperature heat pump applications. In: 24th IIR international congress of refrigeration, August 16-22, Yokohama, Japan; 2015. p. 1–8.
[70] Jansen W. A method for calculating the flow in a centrifugal impeller when entropy gradients are present. In: Royal Society conference on internal aerodynamics (turbomachinery), 19-21 July, Cambridge, UK; 1967. p. 133–46.
[71] Johnston JP, Dean RC. Losses in vaneless diffusers of centrifugal compressors and pumps: analysis, experiment, and design. J Eng Power 1966;88(1):49.

Appendix D. Articles

[72] Daily JW, Nece RE. Chamber dimension effects on induced flow and frictional resistance of enclosed rotating disks. J Basic Eng 1960;82(1):217–30.
[73] Conrad O, Raif K, Of MW. The calculation of performance maps for centrifugal compressors with vane-island diffusers. Proceedings of the twenty-fifth annual international gas turbine conference and exhibit and twenty-second annual fluids engineering conference, March 9-13. New Orleans, Louisiana, USA: American Society of Mechanical Engineers; 1980. p. 135–47.
[74] Eckardt D. Detailed flow investigations within a high-speed centrifugal compressor impeller. J Fluids Eng 1976;98(3):390.
[75] Schiffmann J, Favrat D. Experimental investigation of a direct driven radial compressor for domestic heat pumps. Int J Refrig 2009;32(8):1918–28.
[76] Schiffmann J. Small-scale and oil-free turbocompressor for refrigeration applications. In: 22nd International compressor engineering conference at Purdue, 14-17 July, West Lafayette, Indiana, USA; 2014. p. 1–11.
[77] Monge B. Design of supercritical carbon dioxide centrifugal compressors, Ph.D. thesis, University of Seville, Seville, Spain; 2014.
[78] Šarevski MN, Šarevski VN. Characteristics of water vapor turbocompressors applied in refrigeration and heat pump systems. Int J Refrig 2012;35(5):1484–96.
[79] Bantle M. Turbo-compressors: Prototype tests of mechanical vapour re-compression for steam driers. In: 12th IEA heat pump conference, June, Rotterdam, The Netherlands; 2017.
[80] Bantle M. Steam compression and the development of a cost effective turbo compressor. In: Elmegaard B, Zühlsdorf B, Reinholdt L, Bantle M, editors. Book of presentations of the international workshop on high temperature heat Pumps. Kgs. Lyngby: Technical University of Denmark (DTU); 2017. p. 137–41.

st of Figures

1.1 Current working domain of ORC and HP systems: (a) ORC domain based on system power capacity and heat source temperature (adapted from [6, 7]); (b) HP domain in terms of source and supply temperatures (adapted from [8, 9]). 2

1.2 Heat demand by industrial sector in 33 European countries. Adapted from Ref. [21]. 3

1.3 Exemplary turbine stage with nozzle, rotor and velocity triangles. See the Nomenclature for symbols. 5

1.4 Installed ORC units by manufacturer, power output, and expander type. Data collected from the literature, see Refs. [6, 12, 13, 18] and from the company websites, see Refs. [30–49]. Companies which abandoned the development of their product line are not included. The term *unknown* indicates that the information on the expander type is not available. The term *combination* indicates that the manufacturer employs a combination of different expander technologies. 6

1.5 Number of installed units in the period 1995-2016. Data collected from the literature, see Refs. [6, 12, 13, 18] and from the company websites, see Refs [30–49]. The term "n.a." indicates that the data are not available. 7

1.6 Charts for preliminary selection of compressor technology. Adapted from [150]. 13

1.7 Manufacturers of high-temperature heat pumps based on maximum supply temperature and compressor type. SC = screw compressor; PC = piston compressor; CC = centrifugal compressor. Adapted from Refs. [8, 152–161]. 14

2.1 Methodology for combined optimization of the cycle and multistage turbine for (a) the conservative design approach and (b) the advanced design approach. From Ref. [72]. 21

2.2 Schematic of the axial-flow turbine geometry and meridional cut layout. 22

2.3 Flowchart of the single-stage axial turbine model. From Ref. [211]. 23

2.4 Decision variables and nomenclature in the blade-to-blade plane for the single-stage axial turbine model. From Ref. [211]. 24

2.5 Schematic of the multistage axial-flow turbine geometry and meridional cut layout. 25

2.6 Exemplary blade profiles and representation of the conservative (left) and advanced (right) design approaches. 27

2.7 Methodology for combined optimization of the cycle and single-stage axial turbine using mixtures. 31

2.8 ORC unit and modeling conditions for the case of waste heat recovery from the jacket water of a 60 MW marine diesel engine. From Ref. [215]. 34

2.9 ORC unit and modeling conditions for the case of waste heat recovery from from the exhaust gases, the scavenge air and the jacket water cooling system of a 37 MW marine diesel engine. From Ref. [215]. 35

2.10 Computational results for the Hannover turbine test cases using the CFD tool ANSYS CFX®: (a) rotor mesh discretisation at the midspan; (b) contours of the specific entropy at i) the rotor inlet, ii) the rotor outlet, and iii) the measurement station; (c) static pressure field in the meridional plane; (d) contours of tangential velocity in the meridional plane. From [211]. 36

2.11 Experimental and numerical results for the fourth stage of the Hannover turbine in terms of (a) static temperature, (b) static pressure, (c) axial velocity, (d) absolute and relative velocity and (e) flow angles at the nozzle inlet, the nozzle outlet and the rotor outlet . From Ref. [211]. 38

2.12 Comparison of results between TURAX and Verneau data [66]. pp = percentage-points. The breakdown of losses is shown in the chart. 40

2.13 Sensitivity analysis and significance of decision variables of the axial turbine model. Morris screening method [261] applied to the Hannover turbine test case. From Ref. [211]. 41

2.14 Profiles of total temperature, total pressure, absolute flow angle, absolute velocity at the stage outlet. Data from experimental results [248], Gerolymos et al. [252], Croce at al. [253] and TURAX for the Hannover turbine test case [72]. 44

2.15 (a) Four-stage subsonic Hannover turbine test case (adapted from [248]); (b) meridional cut layout of the four-stage Hannover turbine; (c) two-stage supersonic ORC turbine test case [258]; (d) meridional cut layout of the two-stage supersonic ORC turbine. From Ref. [72]. 45

2.16 Results of the uncertainty analysis on the assumed parameters of the two-stage supersonic turbine: (a) scatterplot of uncertainty in turbine efficiency; (b) corresponding cumulative distribution function; (c) ranking of the uncertain parameters based on significance level. From Ref. [72]. 47

2.17 Specific entropy-temperature diagram for the following binary mixtures in the molar composition range 0.0 to 1.0: (a) R45fa/pentane and (b) propane/isobutane. 48

2.18 Optimal power output for the optimal cycle and constant η_{tt} (▲), for the optimal cycle and optimal η_{tt} (■), and the optimal total-to-total turbine efficiency (●) vs. molar composition of the selected mixtures. Heat source with (a,b) and without (c,d) limitation on the heat source outlet temperature. Adapted From Ref. [215]. 49

2.19 Temperature-thermal power diagram for the optimal R245fa/pentane mixture with and without outlet temperature limit. From Ref. [215]. 50

2.20 Hot fluid, working fluid temperature glide and superheating in the evaporator. No temperature constraint. From Ref. [215]. 50

2.21 Breakdown of losses in terms of (a) turbine efficiency debit; (b) aspect ratio; (c) volume flow rate (VFR) and size parameter (SP). In the figure, the two mixtures are (a) R245fa/pentane and (b) propane/isobutane at their optimal molar compositions and for the cases with and without outlet temperature limit, respectively. Adapted from Ref. [215]. 51

2.22 Performance Index (PI) and optimal net power output of the working fluid candidates according to (a,c) the conservative and (b,d) the advanced design approaches. From Ref. [72]. 56

2.23 Meridional profile geometry of the two best working fluid candidates, and Mach numbers and stage reactions of the five best working fluid candidates: (a) conservative and (b) advanced design approaches. From Ref. [72]. 58

2.24 Turbine design efficiency and minimum number of stages of the working fluid candidates according to (a,c) the conservative and (b,d) the advanced design approaches. From Ref. [72]. 59

3.1 Representation of the geometry of the radial-inflow turbine. From Ref. [95]. . . 64

3.2 Illustration of the possible turbine flow patterns occurring at off-design conditions: (a) Nozzle and rotor unchoked; (b) rotor choked and nozzle unchoked; (c) nozzle choked and rotor unchoked; (d) nozzle and rotor choked. From Ref. [95]. 65

3.3 modeling strategy for high-pressure ratio RITs: (a) preliminary design model; (b) off-design model. From Ref. [95]. 66

3.4 Identification of the choking point for a blade row. From Ref. [95]. 67

3.5 Significance level of the calibration coefficients: (a) on the turbine total-to-static isentropic efficiency; (b) on the mass flow rate. The bars indicate the standard deviation from the mean value. The analysis employed the test cases listed in Table B.1. From Ref. [95]. 74

3.6 Optimal pareto fronts from the unconstrained and constrained multi-objective optimizations. The colours indicate the evolution of the pareto front from the initial (●) to the final (●) generations. From Ref. [95]. 76

3.7 Comparison of RRMSE values for the different test cases before and after the optimization process: (a) RRMSE in isentropic efficiency; (b) RRMSE in mass flow rate. From Ref. [95]. 77

3.8 Exemplary isentropic efficiency maps before (a,c,e) and after (b,d,f) the multi-objective optimization: (a,b) Metiner and Glassmann [314] test case; (c,d) McLallin [98] test case; (e,f) Rogo [102] test case. From Ref. [95]. 78

3.9 Exemplary mass flow rate maps before and after the multi-objective optimization: (a,b) Meitner and Glassmann [314] test case; (c,d) McLallin [98] test case; (e,f) Rogo [102] test case. From Ref. [95]. 79

3.10 Validation of the turbine design model. From Ref. [95]. 80

3.11 Validation of the off-design turbine model: (a,b) turbine by Demierre et al. [125, 126]; Ricardo C80 turbine [96, 97]. The error bars represent the uncertainty in the experimental measurements. From Ref. [95]. 81

4.1 Schematic of the centrifugal compressor geometry. From Ref. [315]. 85

4.2 modeling strategy for centrifugal compressors: (a) preliminary design model; (b) analysis model. From Ref. [315]. 86

4.3 Identification of the choking point for a blade row: (a) residual of the loss equation, and (b) Mach number. From Ref. [315]. 88

4.4 Layout of the HP cycle for steam generation using: (a) an open-loop with steam and (b) a closed-loop with other working fluids. From Ref. [315]. 93

4.5 Entropy-temperature diagram for the test cases used for validation: (a) air compressors; (b) R134a compressor; (c) CO_2 compressor. 94

4.6 Methodology for the combined multi-objectived optimization of the heat pump cycle and the centrifugal compressor. 96

4.7 Comparison between the measured (○) and predicted (–) pressure ratio and isentropic efficiency for different Eckardt impellers: (a,b) impeller O; (c,d) impeller A; (e,f) impeller B. From Ref. [315]. 98

4.8 Comparison between the measured and predicted results for the compressor operated with R134a and studied by Schiffmann and Favrat [182, 329]: (a) pressure ratio and (b) the isentropic efficiency. From Ref. [315]. 99

4.9 Comparison between the measured and predicted enthalpy rise and isentropic total-to-static efficiency as a function of the flow coefficient $\phi = \dot{m}/(\rho_{01} U_2 d_2^2)$ for the Sandia compressor impeller with vaned diffuser. Experimental data from Ref. [183] and state-of-the-art CFD data from Ref. [326]. From Ref. [315]. . . . 100

4.10 Pareto fronts of the optimal solutions in terms of COP and supply heat flow rate for the selected working fluids. The solution having an equal weight of the two objective functions is indicated with the symbol ●. From Ref. [315]. 102

4.11 Pareto fronts of the optimal solutions in terms of compressor isentropic efficiency and inlet volume flow rate for the selected working fluids. The solution having an equal weight of the two objective functions is indicated with the symbol ●. From Ref. [315]. 103

4.12 Meridional cut layout of the optimal compressor designs. From Ref. [315]. . . . 105

A.1 Estimation of (a) basic profile loss x_p and (b) lift parameter F_L. Adapted from Craig and Cox [222]. 138

A.2 (a) Contraction ratio for average profiles and (b) profile loss ratio against Reynolds number effect. Adapted from Craig and Cox [222]. 139

A.3 Trailing edge thickness losses. Adapted from Craig and Cox [222]. 139

A.4 Profile loss increment for (a) blade back radius losses and (b) Mach number loss for convergent blading. Adapted from Craig and Cox [222]. 140

A.5 (a) Secondary loss-basic loss factor and (b) Secondary loss- aspect ratio factor. Adapted from Craig and Cox [222]. 141

A.6 Annulus wall loss. Adapted from Craig and Cox [222]. 142

A.7 Shrouded efficiency loss. Adapted from Craig and Cox [222]. 142

C.1 Number of total impeller blades for centrifugal compressors: (a) without splitter blades; (b) with splitter blades. Adapted from [317]. 157

C.2 Meridional layout of Eckardt's centrifugal compressor stages (dimensions in mm). Adapted from Ref. [167]. 158

List of Tables

1.1 Documented multistage ORC axial turbines. From [72]. 9

1.2 RITs designed and tested at pressure ratios above 3 from the open literature. From Ref. [95]. 11

1.3 Well-documented experimental activities on centrifugal compressors from the open literature. 15

1.4 Mean-line models developed for centrifugal compressors in the open literature. . 15

2.1 Decision variables of the multistage turbine model. From Ref. [72]. 26

2.2 Optimizing parameters and constraints of TURAX. Adapted from Ref. [215]. . . 33

2.3 Comparison between the predicted and measured quantities for the fourth stage of the Hannover turbine. From [211]. pp = percentage-points. 39

2.4 Comparison of results between TURAX and Verneau data [66]. pp = percentage-points. From Ref. [211]. 40

2.5 Comparison between numerical and experimental results [247, 248] for the four-stage Hannover turbine. From Ref. [72]. 43

2.6 Comparison of results between TURAX and Verneau [66, 257] data on a two-stage ORC turbine. From Ref. [72]. 46

2.7 Optimal turbine and cycle design parameters. From Ref. [215]. 53

2.8 Selected working fluid candidates for the case study of waste heat recovery from a 37 MW marine diesel engine with heat source temperature of 235 °C. From Ref. [72]. 54

2.9 Ranking of the optimal working fluid candidates. From Ref. [72]. 57

3.1 Decision variables of the design model for RITs. 67

3.2 Loss correlations. 72

3.3 Optimal set of calibration coefficients for an equal weight of $RRMSE_\eta$ and $RRMSE_m$ in the pareto front. From Ref. [95]. 76

4.1 Design variables and optimization constraints of the compressor design model. From Ref. [315]. 87

4.2 Loss correlations. From Ref. [315]. 92

4.3 Modeling conditions of the heat pump cycle. From Ref. [315]. 95

4.4 Validation of the design model. From Ref. [315]. 101

4.5 Optimal compressor design for different working fluids. From Ref. [315]. 104

A.1 Decision variables **(1-12)** and input variables of TURAX for the Hannover [246, 247] and Verneau [66] single-stage turbine test cases. From Ref. [211]. 146

A.2 Decision and input variables of TURAX for the Hannover [247, 248] and Verneau [66, 257] multistage turbine test cases. From Ref.[72]. 147

B.1 Data of the HPR turbines selected for calibration. From Ref. [95]. 152

C.1 Data of the experimental centrifugal compressors. 159

Breathe.
Let go.
And remind yourself
that this very moment
is the only one you know
you have for sure.

— Oprah Winfrey

DTU Mechanical Engineering
Section of Thermal Energy
Technical University of Denmark

Nils Koppels Allé, Bld. 403
DK-2800 Kgs. Lyngby
Denmark
Phone (+45) 4525 4131
Fax (+45) 4588 4325
www.mek.dtu.dk
ISBN: 978-87-7475-541-8

DCAMM
Danish Center for Applied Mathematics and Mechanics

Nils Koppels Allé, Bld. 404
DK-2800 Kgs. Lyngby
Denmark
Phone (+45) 4525 4250
Fax (+45) 4593 1475
www.dcamm.dk
ISSN: 0903-1685